

Kinji Asaka
Hidenori Okuzaki *Editors*

Soft Actuators

Materials, Modeling, Applications,
and Future Perspectives

 Springer

Soft Actuators

Kinji Asaka • Hidenori Okuzaki
Editors

Soft Actuators

Materials, Modeling, Applications,
and Future Perspectives

 Springer

Editors

Kinji Asaka
National Institute of Advanced
Industrial Science and Technology
(AIST)
Osaka, Japan

Hidenori Okuzaki
University of Yamanashi
Kofu, Japan

ISBN 978-4-431-54766-2 ISBN 978-4-431-54767-9 (eBook)
DOI 10.1007/978-4-431-54767-9
Springer Tokyo Heidelberg New York Dordrecht London

Library of Congress Control Number: 2014949897

© Springer Japan 2014

This work is subject to copyright. All rights are reserved by the Publisher, whether the whole or part of the material is concerned, specifically the rights of translation, reprinting, reuse of illustrations, recitation, broadcasting, reproduction on microfilms or in any other physical way, and transmission or information storage and retrieval, electronic adaptation, computer software, or by similar or dissimilar methodology now known or hereafter developed. Exempted from this legal reservation are brief excerpts in connection with reviews or scholarly analysis or material supplied specifically for the purpose of being entered and executed on a computer system, for exclusive use by the purchaser of the work. Duplication of this publication or parts thereof is permitted only under the provisions of the Copyright Law of the Publisher's location, in its current version, and permission for use must always be obtained from Springer. Permissions for use may be obtained through RightsLink at the Copyright Clearance Center. Violations are liable to prosecution under the respective Copyright Law.

The use of general descriptive names, registered names, trademarks, service marks, etc. in this publication does not imply, even in the absence of a specific statement, that such names are exempt from the relevant protective laws and regulations and therefore free for general use.

While the advice and information in this book are believed to be true and accurate at the date of publication, neither the authors nor the editors nor the publisher can accept any legal responsibility for any errors or omissions that may be made. The publisher makes no warranty, express or implied, with respect to the material contained herein.

Printed on acid-free paper

Springer is part of Springer Science+Business Media (www.springer.com)

Preface

A variety of soft actuators has so far been developed not only from the fundamental viewpoint of basic material science, chemistry, physics, and biology but also from the engineering viewpoint for the practical applications to light-weight, low-cost, no-noise, less-pollution, and high-efficiency micro- and macro-artificial muscles and soft robotic systems. This book “Soft Actuators: Materials, Modeling, Applications, and Future Perspectives” reviews current and comprehensive research and development of soft actuators, and encompasses interdisciplinary studies of materials science and chemistry, mechanics, electronics, robotics, and bioscience. The topics of this book update the preceding book (in Japanese) entitled “Soft Actuators which Drive Future Technologies -Recent R&D Activities Focused on Polymers and Biomaterials-” edited by Prof. Yoshihito Osada (Riken) and Prof. Takahisa Taguchi (AIST) published by CMC Publishing Co., Ltd. in 2010.

Chapters 1 and 2 of this book provide an overview of the current status of materials, properties, applications, and market of soft actuators, including background and history of soft actuators with typical references as milestones of the progress. Chapters 3–5 describe thermo-driven soft actuators using temperature-responsive gels and nanofibers. Electro-driven soft actuators, which are also known as electro-active polymer (EAP) actuators, utilizing ionic and electric conductive polymers, carbon nanotubes, ionic liquid gels, dielectric elastomers and gels, and piezoelectric polymers were intensively discussed in Chaps. 6–15. On the other hand, light-driven soft actuators based on photochromism, photoisomerization, and photoredox reaction were described in Chaps. 16–18, while Chaps. 19 and 20 cover the topics on magneto-driven actuators, both of which enable operation of soft actuators by remote control. Furthermore, various motion models and control methods of soft actuators were examined in Chaps. 21–26, which are crucially important for the practical applications to Braille displays, soft micro-robots for medical applications, micro-pumps, and transducers evaluated in Chaps. 27–32. Finally, Chaps. 33–35 focus on next-generation bio-actuators based on biomaterials to provide future perspectives for artificial muscle technology of bio-nanomachines.

These topics covered in this book not only promote further research and development of soft actuators, but also lead the way to their utilization and industrialization. Readers can obtain detailed, useful information about materials, methods of synthesis, fabrication, and measurements. The new ideas offered in this book will provide inspiration and encouragement to researchers and developers as they explore new fields of applications for soft actuators.

Osaka, Japan
Kofu, Japan
June 2014

Kinji Asaka
Hidenori Okuzaki

Contents

Part I Introduction

- 1 Progress and Current Status of Materials and Properties of Soft Actuators** 3
Hidenori Okuzaki
- 2 Current Status of Applications and Markets of Soft Actuators** 19
Kinji Asaka and Kayo Nakamura

Part II Materials of Soft Actuators: Thermo-Driven Soft Actuators

- 3 Electromagnetic Heating** 33
Takeshi Yamauchi
- 4 Thermo-Responsive Nanofiber Mats Fabricated by Electrospinning** 43
Hidenori Okuzaki
- 5 Self-Oscillating Gels** 55
Ryo Yoshida

Part III Materials of Soft Actuators: Electro-Driven Soft Actuators

- 6 Ionic Conductive Polymers** 81
Kunitomo Kikuchi and Shigeki Tsuchitani
- 7 Conducting Polymers** 95
Keiichi Kaneto

8 Humidity-Sensitive Conducting Polymer Actuators	111
Hidenori Okuzaki	
9 Carbon Nanotube/Ionic Liquid Composites	127
Takushi Sugino, Kenji Kiyohara, and Kinji Asaka	
10 Ion Gels for Ionic Polymer Actuators	141
Masayoshi Watanabe, Satoru Imaizumi, Tomohiro Yasuda, and Hisashi Kokubo	
11 Ionic Liquid/Polyurethane/PEDOT:PSS Composite Actuators	157
Hidenori Okuzaki	
12 Dielectric Gels	169
Toshihiro Hirai	
13 Dielectric Elastomers	183
Seiki Chiba	
14 Development of Actuators Using Slide Ring Materials and Their Various Applications	197
Hiromitsu Takeuchi	
15 Piezoelectric Polymers	203
Yoshiro Tajitsu	
 Part IV Materials of Soft Actuators: Light-Driven Soft Actuators	
16 Spiropyran-Functionalized Hydrogels	219
Kimio Sumaru, Toshiyuki Takagi, Shinji Sugiura, and Toshiyuki Kanamori	
17 Photomechanical Energy Conversion with Cross-Linked Liquid-Crystalline Polymers	231
Jun-ichi Mamiya	
18 Photoredox Reaction	245
Tetsu Tatsuma	
 Part V Materials of Soft Actuators: Magneto-Driven Soft Actuators	
19 Magnetic Fluid Composite Gels	255
Toshihiro Hirai	
20 Magnetic Particle Composite Gels	271
Tetsu Mitsumata	

Part VI Modeling

21 Molecular Mechanism of Electrically Induced Volume Change of Porous Electrodes 287
 Kenji Kiyohara, Takushi Sugino, and Kinji Asaka

22 Material Modeling 299
 Yutaka Toi

23 Distributed Parameter System Modeling 313
 Kentaro Takagi, Gou Nishida, Bernhard Maschke, and Kinji Asaka

24 Modeling and Feedback Control of Electro-Active Polymer Actuators 327
 Norihiro Kamamichi, Kentaro Takagi, and Shigenori Sano

25 Motion Design-A Gel Robot Approach 343
 Mihoko Otake

26 Motion Control 355
 Minoru Hashimoto

Part VII Applications

27 Application of Nano-Carbon Actuator to Braille Display 371
 Isao Takahashi, Tomomasa Takatsuka, and Munemitsu Abe

28 Underwater Soft Robots 385
 Kentaro Takagi, Zhi-Wei Luo, and Kinji Asaka

29 IPMC Actuator-Based Multifunctional Underwater Microrobots 401
 Shuxiang Guo and Liwei Shi

30 Medical Applications 423
 Tadashi Ihara

31 Micro Pump Driven by a Pair of Conducting Polymer Soft Actuators 435
 Masaki Fuchiwaki

32 Elastomer Transducers 447
 Mikio Waki and Seiki Chiba

Part VIII Next-Generation Bio-Actuators

33 Tissue Engineering Approach to Making Soft Actuators 463
 Toshia Fujisato, Shunya Takagi, Tomohiro Nakamura, and Hiroshi Tsutsui

34 ATP-Driven Bio-machine 475
Daisuke Inoue, Arif Md. Rashedul Kabir, Kazuki Sada,
Jian Ping Gong, and Akira Kakugo

35 Employing Cytoskeletal Treadmilling in Bio-Actuator 489
Ken-Ichi Sano, Ryuzo Kawamura, and Yoshihito Osada

Index 499

Part I
Introduction

Chapter 1

Progress and Current Status of Materials and Properties of Soft Actuators

Hidenori Okuzaki

Abstract In this chapter, brief history and current status of soft actuators made of various materials driven by different stimuli are described with typical references as milestones of the progress. The soft actuators originated from unique characteristics of cross-linked polymer gels for understanding their physical and chemical properties of dimensional changes and phase transitions induced by various environmental stimuli such as pH, salt, solvent, heat, light, and electric field. The ‘explosion’ of research and development of soft actuators in the 1990s extended over a variety of materials such as conductive polymers, elastomers, carbon nanotubes, and biomaterials, which had driven further progress in soft actuators not only from the fundamental viewpoint of basic science and materials chemistry and physics but also from the engineering viewpoint for the practical applications to light-weight, low-cost, no-noise, less-pollution, and high-efficiency micro- and macro-artificial muscles and soft robotic systems.

Keywords Bio-actuator • Carbon nanotube • Conductive polymer • Elastomer • Gel • Soft actuator

1.1 Introduction

Soft actuators made of synthetic or natural materials, capable of converting chemical or physical energy into mechanical work in response to various environmental stimuli such as pH, salt, solvent, heat, humidity, electric or magnetic field, and light, have attracted considerable attention for biomimetic or bioinspired systems which underlie the motility of all living organisms. Differing from conventional mechanical transducers such as electric motors, combustion engines, and hydraulic pumps in which the motion is generated via changes of relative positions between their components, the soft actuators exhibit flexible motion through shape or volume changes due to accumulation and integration of

H. Okuzaki (✉)

Interdisciplinary Graduate School of Medicine and Engineering, University of Yamanashi,
4-4-37 Takeda, Kofu 400-8511, Japan

e-mail: okuzaki@yamanashi.ac.jp

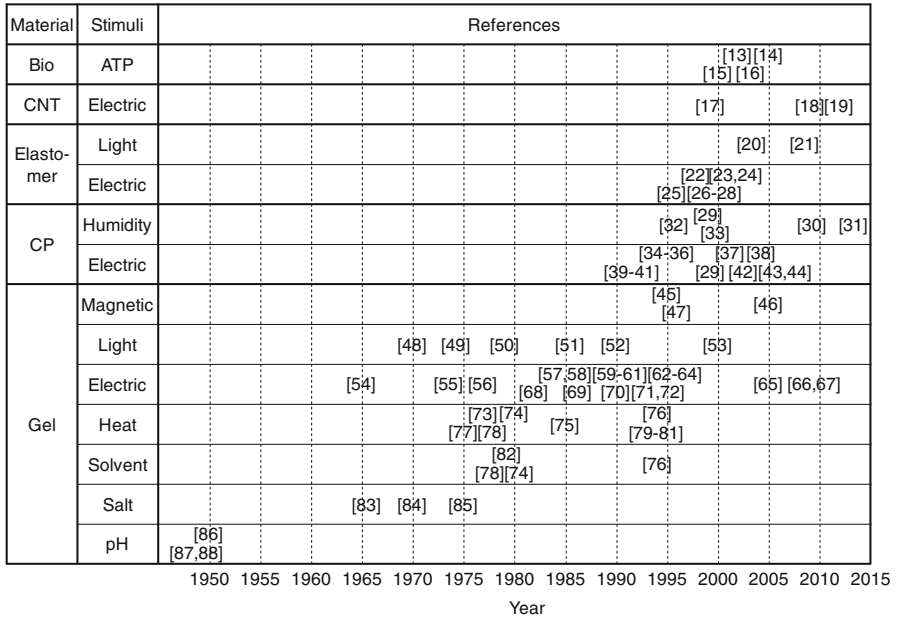


Fig. 1.1 List of typical soft actuators using various materials driven by different stimuli

microscopic conformational changes at the molecular level into a macroscopic large deformation of the actuator materials.

A variety of soft actuators has so far been developed not only from the fundamental viewpoint of basic science and materials chemistry and physics, but also from the engineering viewpoint for the practical applications to light-weight, low-cost, no-noise, less-pollution, and high-efficiency micro- and macro-artificial muscles and soft robotic systems [1–12]. The soft actuators may be classified according to the material and stimuli as listed in Fig. 1.1, in which typical references are cited chronologically as milestones of the progress in research and development of soft actuators:

- (a) gel (pH, salt, solvent, heat, light, electric and magnetic fields)
- (b) conductive polymer (CP) (electric field and humidity)
- (c) elastomer (electric field and light)
- (d) carbon nanotube (CNT) (electric field etc.)
- (e) biomaterial (ATP etc.)

1.2 Gel Actuators

1.2.1 *pH-Responsive Gels*

In 1949 Katchalsky and Kuhn [86–88] reported that water-swollen gels such as poly(acrylic acid) (PAA) crosslinked with glycerin or poly(vinyl alcohol) (PVA) via esterification can convert chemical energy directly into mechanical work under isometric conditions. The PAA gel exhibited reversible contraction and expansion in length by ca. 20 % repeatedly in response to alternate addition of acid and base. The principle was based on the reversible ionization of polyelectrolyte bearing carboxylic acid groups caused by pH changes, in which the dimensional changes of the gel was dependent on the degree of crosslinking.

1.2.2 *Salt-Responsive Gels*

Katchalsky et al. developed chemomechanical engines working on chemical melting and crystallization of crosslinked collagen fibers by treating with solutions of salts such as LiBr, KSCN, or Urea [83]. The mechanochemical engine generated high power-to-weight ratio of 30 mW/g (collagen) which was close to that of skeletal muscles (50 mW/g). Furthermore, Sussman and Katchalsky built chemomechanical turbines [84] and thermodynamic study of mechanochemical availability was theoretically investigated [85]. The power density and efficiency of energy conversion of the mechanochemical turbine attained as high as 0.79 J/g and 40 %, respectively.

1.2.3 *Solvent-Responsive Gels*

Tanaka discovered that hydrolyzed poly(acrylamide) (PAAm) gels immersed in acetone-water mixtures underwent a discontinuous volume collapse as large as 350-fold when the acetone concentration increased and reached a critical value [74]. According to the Flory–Huggins theory, the drastic volume change is accounted for by the osmotic pressure of protons dissociated from the carboxylic acid groups formed by hydrolysis of the PAAm network. Suzuki devised a solvent-responsive ‘gel-arm’ made of poly(vinylalcohol)-poly(acrylic acid)-poly(allylamine) (PVA-PAA-PAIAm) rubberlike elastic gel films by means of a repeated freezing (at $-50\text{ }^{\circ}\text{C}$) and thawing (at room temperature) processes [76]. The cryoSEM image clearly shows that the resulting gel has a porous structure, which favors fast diffusion of solvent between inside and outside the gel. The PVA-PAA-PAIAm gel film showed rapid contraction and expansion (30 % under free loading and 10 % under 0.2 MPa) by altering the solvent between acetone and water, where the power density attained as high as 0.1 W/g that was close to the value of skeletal muscles.

1.2.4 *Thermo-Responsive Gels*

Osada developed chemomechanical systems based on a polymer association between poly(methacrylic acid) (PMMA) and poly(ethylene glycol) (PEG) through hydrogen bonding [77]. The PMMA membrane in the PEG solution contracted by more than 40 % under isotonic conditions with increasing the temperature from 20 to 30 °C, where contractile stress generated in the membrane was 4–6 kg/cm² under isometric conditions.

Poly(*N*-isopropylacrylamide) (PNIPAM), a typical thermo-responsive polymer with a lower critical solution temperature (LCST) in water at 32 °C, has been paid considerable attention not only from thermodynamic and kinetic of phase transition [75] but also for the promising applications in actuators, sensors, drug delivery systems, and cell cultures. Okano et al. found that a crosslinked PNIPAM gel bearing comb-like grafted side chains made of the PNIPAM exhibited fast deswelling compared to the conventional PNIPAM homopolymer gel [79], mechanism of which was based on a much greater aggregation force operating within the grafted side chains where the trapped water was rapidly squeezed out from the gel. Hirasa synthesized thermo-responsive poly(vinyl methyl ether) (PVME) gel crosslinked by γ -ray irradiation, which also showed a LCST in water at 37 °C [76]. The PVME gel fibers with a spongy-like porous structure prepared above the LCST exhibited quick and reversible swelling and shrinking where the fiber diameter changed from 400 nm at 20 °C to 200 nm at 40 °C.

Yoshida introduced the Belousov-Zhabotinsky (BZ) reactions in a thermo-responsive PNIPAM copolymer gel [81]. The ‘BZ gel’ shows mechanical oscillation induced by the chemical oscillation due to the periodic redox changes of Ru complex in the BZ reaction, where the phase transition temperature of the gel shifts from 33 °C at Ru²⁺ in the reduced state (orange) to 36 °C at Ru³⁺ in the oxidized state (green) owing to the change in the hydrophilic/hydrophobic nature of polymer chains.

1.2.5 *Electro-Responsive Gels*

Electrically induced dimensional changes of gels was observed by Hamlen et al. in 1965 using a PVA-PAA fiber containing finely dispersed platinum powders [54]. When a negative voltage is applied, the fiber expands since the solution becomes alkaline due to evolution of hydrogen, while the fiber shrinks under positive voltages because the solution becomes acidic. Later, Grodzinski showed that collagen membrane immersed in an electrolyte solution deformed in the presence of an external electric field [55, 56]. The mechanism resulted from field-induced changes in inter-membrane salt concentration which in turn modify the internal double layer repulsive forces between the charged fibrils. DeRossi reported that a PVA-PAA membrane underwent shape changes by applying DC voltage, which

was attributed to the change in ionization state of the membrane induced by electrochemical reactions near the electrodes [58, 69].

Since the first discovery of phase transitions in polymer gels by Tanaka in 1977 [73, 74, 78, 82], a variety of stimuli-responsive gels was widely and deeply studied from both fundamental and practical aspects (Fig. 1.1). He also demonstrated that the phase transition was also induced by the application of an electric field across the gel [68]. The electric forces on the charged sites of the network produce a stress gradient along the electric field lines in the gel, where there exists a critical stress below which the gel is swollen and above which the gel collapses. On the other hand, Osada and Hasebe found a crosslinked hydrogel inserted between a pair of electrodes underwent contraction by releasing water droplets in air [57]. When an external electric field is applied across the gel, the macro- and micro-ions receive electrical forces in the opposite direction. However, the macro-ions are stationary since they are chemically fixed to the polymer network, while the counter ions are mobile, capable of migrating along the electric field to the electrode.

From 1986 to 1991 the project “Development of Biomimetic Energy-Transducing Devices” was performed through Special Coordination Funds of Science and Technology Agency of the Japanese Government (Fig. 1.2) aimed at clarifying the mechanism of biomolecular machinery systems and designing the biomimetic energy-transducing devices. The project yielded many advanced gel actuators such as electro-responsive ‘gel-fish’ and ‘robot-hand’ made of PVA-PAA gels [61, 70, 71] (Toyota Central R&D Labs., Inc.). Okuzaki and Osada succeeded in fabricating a novel polymer gel actuator, namely ‘gel-looper’, with electrically driven worm-like motility [59]. The mechanism is based on an electrokinetic molecular assembly reaction of cationic surfactant molecules on the negatively charged hydrogel, which brings about a contraction of the gel surface due to hydrophobic aggregation of alkyl chains of the surfactant molecules. It was found that the gel-looper walked at a constant velocity of 25 cm/min in water by repeating bending and stretching under an alternating voltage.

Oguro and Asaka independently developed ionic polymer-metal composite (IPMC) actuators utilizing a nafion membrane whose surfaces were chemically plated with gold or platinum [60, 64] (Fig. 1.3). The IPMC bent toward the anode by applying an electric field, the mechanism of which was associated with the difference of swelling degree at both sides caused by an electrophoretic transport of protons carrying with water molecules. The IPMC actuators are flexible and suitable for downsizing capable of driving at low voltages (0.5–3 V), which provides medical applications such as micro-active catheters and guide wires. However, most of them operate in an electrolyte solution or in a swollen state. Recently, Asaka et al. developed tri-layer actuators utilizing a fluorinated polymer membrane containing ionic liquid as an active layer sandwiched between two bucky-gel layers consisting of single-walled carbon nanotubes dispersed in the ionic liquid as electrodes [65, 67]. The bucky-gel actuator shows reversible bending more than 8,000 cycles at 30 Hz in air, which is associated with the electrophoretic polarization of ionic liquid in the active layer.

DEVELOPMENT OF BIOMIMETIC ENERGY-TRANSDUCING DEVICES

= RESULTS OF THE SECOND HALF TERM =

1 2

3 4

Gel actuators developed in the first half term.
1 ; Thermo-responsive gel actuator, 2 ; Electrically driven gel actuator
3 ; Solvent-sensitive gel actuator, 4 ; Artificial fish driven electrically

This study was performed through Special Coordination Funds of Science and Technology Agency of the Japanese Government.

Fig. 1.2 Brochure of research project “Development of Biomimetic Energy-Transducing Devices” by Science and Technology Agency of the Japanese Government

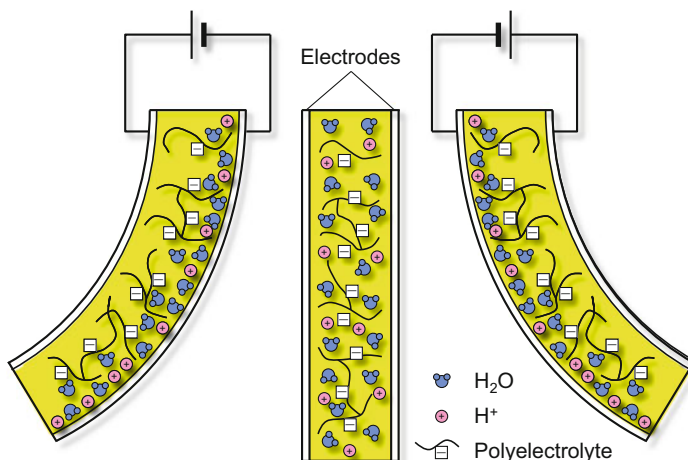


Fig. 1.3 Electro-responsive bending of ionic polymer-metal composite (IPMC)

Hirai first reported that dielectric gels made of PVA swollen in dimethyl sulfoxide exhibited rapid contraction of 8 % within 0.1 s under an electric field of 250 V/mm [62, 72]. Furthermore, plasticized poly(vinyl chloride) (PVC) gels showed amoeba-like pseudopodial deformations and applied to an electro-active artificial pupil. It was found that a displacement of 470 μm in the radial direction, corresponding to 100 % of the thickness of the pupil, was achieved within 6 s under 400 V [66].

1.2.6 Photo-Responsive Gels

Photo-responsive gels were investigated by designing polymers tethering photo-sensitive chromophores, such as azobenzene (*cis-trans* isomerization) [48], spirobenzopyrane (ring opening and closing) [49], *N,N*-dimethylamino groups (photo-ionization) [50], triphenylmethane leucocyanide groups (photo-ionization) [51] in the side or main chains. The mechanism of photo-responsive soft actuators was based on changes in polarity, free volume, hydrophilicity/hydrophobicity, having advantages such as fast response, remote operation, easy to downsize, and high efficiency. Suzuki and Tanaka reported the phase transition of gels induced by visible light, where the transition mechanism was due to the direct heating of the network polymers by light [52]. On the other hand, Misawa et al. showed a laser-induced volume phase transition of gels, in which the radiation force generated by a focused laser beam induced reversible shrinkage in polymer gels [53]. This can be explained in terms of the direct influence on the balance between repulsive intermolecular forces to expand the polymer network (electrostatic or hydrophobic repulsion) and attractive forces to shrink it (hydrogen bonding or van der Waals interactions).

1.2.7 *Magneto-Responsive Gels*

The magnetic field is also available for remote operation of soft actuators. Hirai fabricated PVA gels incorporating with magnetic fluids where strain of the magnetic gel was proportional to the square of the magnetic field [45]. On the other hand, Zrinyi developed ‘ferrogels’ made of crosslinked PVA hydrogels filled with magnetic particles (Fe_3O_4) with an average size of 10–12 μm and unidirectional magnetoelastic behavior was studied [47]. The elongation of ferrogel can be described by the Hook law where the modulus of the gel is not influenced by the presence of inhomogeneous external magnetic field. Recently, Mitsumata and coworkers demonstrated that the magnetic gels made of κ -carrageenan containing barium ferrite as ferromagnetic particles showed giant storage modulus reduction ($\sim 10^7$ Pa) before and after magnetization [46], which might be associated with that the magnetic particles would rotate or move under the magnetic fields due to the demagnetizing effect.

1.3 Conductive Polymer Actuators

1.3.1 *Electro-Responsive Conductive Polymers*

Conductive polymers (CP), such as polypyrrole, polythiophene, polyaniline, and their derivatives, show dimensional changes resulting from electrochemical doping, characterized by transportation of solvated ions between the interior of the polymer matrix and the surrounding electrolyte solution, electrostatic repulsion, and/or structural distortion through oxidation of π -conjugated polymers (Fig. 1.4) [3, 4, 6, 9, 10]. When the dopant ions are too large to dedope from the polymer matrix, the reduction of conductive polymers results in an expansion due to the intercalation of small cations from the electrolyte solution into the polymer matrix to compensate their charges.

In 1990 Baughman first evaluated CPs as electromechanical actuators for the direct conversion of electrical energy to mechanical energy, in which large dimensional changes upon electrochemical doping and dedoping provided the mechanical response for proposed extensional and fibrous actuators, fluid flow controlling devices using unimorph or bimorph actuators, micromechanical tweezers with paired bimorph actuators, and Bourdon tube actuators [3]. Otero [41], Pei, and Inganäs [39, 40] demonstrated that bilayers consisting of an electro-active conjugated polymer such as polypyrrole and non-conductive flexible film exhibited bending in an electrolyte solution due to the reversible volume changes caused by doping and dedoping of the polypyrrole layer. Kaneto and MacDiarmid fabricated polyaniline actuators driven by proton-mediated redox reaction between two states of leuco-emeraldine salt and emeraldine salt. They demonstrated that ‘backbone-

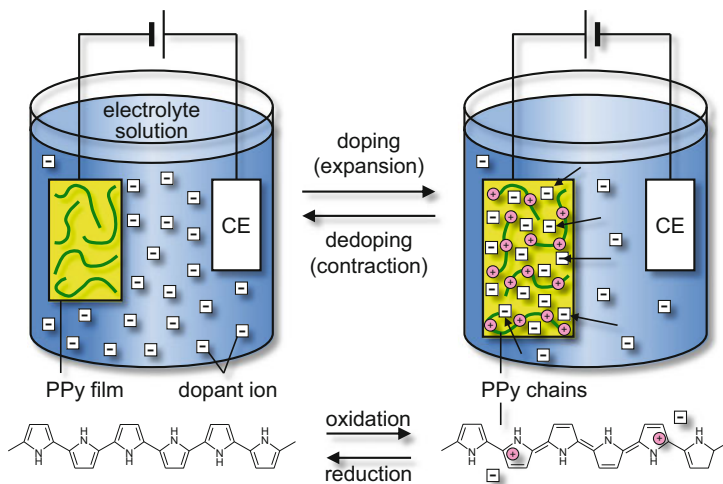


Fig. 1.4 Electrochemical volume changes of polypyrrole film based on reversible doping and dedoping

type' actuator responded to the frequency of higher than 44 Hz, while 'shell-type' actuator operated in air [35, 36].

Smela and coworkers fabricated polypyrrole micro-actuators utilizing a micro-electro-mechanical system (MEMS) technique. The micro-cubes 300 μm on a side with hinges made of micro-actuators based on polypyrrole-gold bilayers showed rapid opening-closing within 1 s [34]. Furthermore, micro-robotic arms with the polypyrrole-gold bilayers succeeded in manipulating a glass bead with 100 μm in diameter.

Kaneto et al. reported that electrochemically synthesized polypyrrole films showed high strain and stress of 12.4 % and 22 MPa, respectively, which was applied to diaphragm pumps and tactile displays [38, 42]. The speed of contraction (13.8 %/s) [44] is slower compared to a real muscle (300 %/s) because diffusion of dopant ions in the conductive polymer matrix is the rate-determining step. Most of the CPs exhibit dimensional changes in an electrolyte solution or in a swollen state, while a few reports have been investigated on solid-state polymers in a redox gas atmosphere or that employ polyelectrolyte gel and ionic liquid [37].

1.3.2 Humidity-Responsive Conductive Polymers

In 1996 Okuzaki first observed that electrochemically synthesized polypyrrole films underwent rapid bending due to water vapor sorption [32], and developed polymer motors, capable of transducing chemical free energy change of sorption directly into continuous rotation [12]. Furthermore, films made of polypyrrole [29, 33] and poly(3,4-ethylenedioxythiophene)/poly(4-styrenesulfonate) (PEDOT/PSS) [30]

underwent contraction in air under application of an electric field, which was explained by desorption of water vapor caused by Joule heating. The contractile strain and stress generated in the PEDOT/PSS films attained 2.5 % and 17 MPa at 50 %RH, respectively, where work capacity was 174 kJ/m³. Recently, Ma and Langer (MIT) developed humidity-responsive polymer films made of polypyrrole as a rigid matrix and polyol-borate as a dynamic network, which exhibited rapid and continuous locomotion due to the sorption of water vapor [31]. A film generator assembled with a piezoelectric element outputs alternating electricity at ~0.3 Hz, with a peak voltage of ~1.0 V.

1.4 Elastomer Actuators

1.4.1 *Electro-Responsive Elastomers*

Dielectric elastomers (DEs) are voltage-responsive polymers, in which high efficiency and durability are expected because of a low electric current suppressing from electrochemical degradation and thermal decomposition. Hirai et al. investigated electrostrictive properties of polyurethane elastomers with various components in hard and soft segments [25]. When an electric field was applied through both electrodes, the polyurethane elastomer contracted, where the strain was proportional to the square of the electric field in a range of ± 200 V/m. The DE actuators utilizing silicone or acrylic rubbers with carbon or silver grease as compliant electrodes were reported by Pelrine et al. (SRI International) [22–24], where a large deformation of the DE (>100 %) under an electric field could be explained by the Maxwell stress (Fig. 1.5). Although the DE actuators have advantages such as simple structure and a variety of elastomeric materials, they have drawbacks such as high driving voltages (>1,000 V), few flexible and stretchable electrodes compliant to the large deformation of the DE actuators, and prestrains applied prior to operate the DE actuators. Aimed at decreasing the driving voltage and/or increase the electrostriction of the DE actuators, composites with inorganic fillers having higher dielectric constants and blends with plasticizers to lower Young's modulus are commonly investigated [11].

Zhang et al. reported high and fast strains of up to 4 % within an electric field of 150 MV/m achieved by electrostriction in an electron-irradiated poly(vinylidene fluoride-trifluoroethylene) copolymer exhibiting typical relaxor ferroelectric behavior [26]. The expanding and contracting of polar regions under an electric fields, coupled with a large difference in the lattice strain between the polar and nonpolar phases, generate an ultra high strain response. On the other hand, Lehmann and coworkers developed ferroelectric liquid crystalline elastomers (FLCEs) [27, 28]. Ultrathin (<100 nm) FLCE films exhibit 4 % strain at only 1.5 MV/m, which is obtained by combing the properties of ferroelectric liquid crystals with those of a polymer network.

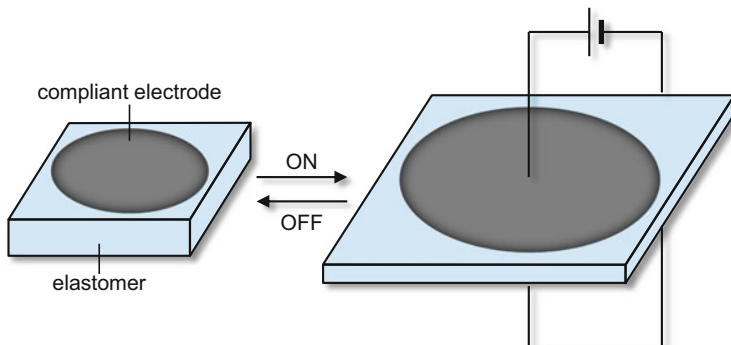


Fig. 1.5 Electro-responsive dimensional changes of dielectric elastomer caused by Maxwell stress

1.4.2 Photo-Responsive Elastomers

Ikeda et al. demonstrated that liquid crystalline films, prepared by thermal polymerization of liquid crystal monomer and diacrylate crosslinker both of which had azobenzene moieties, were precisely bent along the any chosen direction by using linearly polarized light [20]. The mechanism is based on the microscopic changes in size and ordering in the liquid crystalline domains caused by *trans-cis* isomerization of the azobenzene moieties aligned along the direction of light polarization. Furthermore, Yamada and Mamiya et al. fabricated a light-driven plastic motor using liquid crystalline elastomers where the light energy is converted directly into mechanical rotation [21].

1.5 Carbon Nanotube Actuators

In 1999 Baughman and coworkers reported novel electromechanical actuators based on sheets of single-walled carbon nanotubes (CNTs), the mechanism of which was based on the quantum chemical-based expansion due to electrochemical double-layer charging [17]. The CNT actuator shows the strain and stress of $>0.2\%$ and 0.75 MPa , respectively, for more than 140,000 cycles between $\pm 0.5\text{ V}$ at 1 Hz and still works at $>1\text{ kHz}$. Aimed at improving electrically powered artificial muscles, CNT aerogel actuators, having giant elongations (220%) and elongation rate ($3.7 \times 10^4\% \text{ s}^{-1}$) at 5 kV , are developed operating at temperatures from 80 to $1,900\text{ K}$ [18]. The mechanism of the CNT aerogel actuator is associated with the giant Poisson's ratios (~ 15), where ballooning in the width direction is due to periodic corrugation in the same direction during nanotube sheet cycling. Recently, guest-filled, twist-spun CNT yarns are developed as electrolyte-free muscles that provide fast, high-force, large-stroke torsional and tensile actuation [19]. More than

10^6 torsional and tensile actuation cycles are demonstrated, wherein a muscle spins a rotator at an average speed of 11,500 rpm or delivers 3 % tensile contraction at 1,200 cycles/min that can be powered by not only heat, electric field, and light but also absorption of hydrogen.

1.6 Bio-Actuators

One of the promising candidates of future materials for soft actuator is bio-actuators. Montemagno et al. fabricated bio-actuators consisting of an engineered substrate, an F_1 -adenosine triphosphate synthase (F_1 -ATPase) biomolecular motor, and fabricated nanopropellers [15]. It was found that rotation of the nanopropellers was initiated with 2 mM adenosine triphosphate (ATP). Kakugo et al. developed an ATP fueled bio-actuator, namely 'gel machines', constructed from chemically crosslinked actins and myosins [13]. The chemically crosslinked actin filaments (F-actin) move along a chemically crosslinked myosin fibrous gel with a velocity as high as that of native F-actin, by coupling to ATP hydrolysis.

Morishima and Kitamori et al. proposed a concept to use intrinsic cellular mechanical functions where cultured cardiomyocytes can be used in microchip prototype devices as intrinsically pulsatile microactuators converting biochemical energy into mechanical energy to drive both solid microstructures and fluid in a microchip [16]. Xi and Montemagno fabricated novel bio-actuators through self-assembly of muscle cells into bundles on MEMS devices [14]. A microdevice had two 'legs' extending from the body and walked at the maximum speed of 38 $\mu\text{m/s}$ by repeated bending and stretching synchronized with pulsating motion of the bundles of muscle cells self-assembled on the beam of the microdevice.

References

1. Katchalsky A, Zwick M (1955) Mechanochemistry and ion exchange. *J Polym Sci* 16:221–234
2. Osada Y (1987) Conversion of chemical into mechanical energy by synthetic polymers (chemomechanical systems). In: Olive S, Henrici-Olive G (eds) *Advance in Polymer Science*, 82. Springer, Berlin/Heiderberg, pp 1–46
3. Baughman RH, Shacklette LW, Elsenbaumer RL, Plichta E, Becht C (1990) Conducting polymer electromechanical actuators. In: Bredas JL, Chance RR (eds) *Conjugated polymeric materials: opportunities in electronics, optoelectronics, and molecular electronics*. Kluwer Academic, The Netherlands, pp 559–582
4. Baughman RH, Shacklette LW, Elsenbaumer RL, Plichta EJ, Becht C (1991) Micro electro-mechanical actuators based on conducting polymers. In: Lazarev PI (ed) *Molecular electronics*. Kluwer Academic, The Netherlands, pp 267–289
5. DeRossi D, Kajiwara K, Osada Y, Yamauchi A (eds) (1991) *Polymer gels: fundamentals and biomedical applications*. Plenum, New York/London

6. Otero TF, Rodríguez J (1993) Electrochemomechanical and electrochemopositioning devices: artificial muscles. In: Aldissi M (ed) *Intrinsically conducting polymers: an emerging technology*. Kluwer Academic, The Netherlands, pp 179–190
7. Osada Y, Gong JP (1998) Soft and wet materials: polymer gels. *Adv Mater* 10:827–836
8. Bar-Cohen Y (ed) (2001) *Electroactive polymer (EAP) actuators as artificial muscles, reality, potential and challenges*. SPIE, Bellingham
9. Smela E (2003) Conjugated polymer actuators for biomedical applications. *Adv Mater* 15:481–494
10. Madden JDW, Vandesteeg NA, Anquetil PA, Madden PGA, Takshi A, Pytel RZ, Lafontaine SR, Wieringa PA, Hunter IW (2004) Artificial muscle technology: physical principles and naval prospects. *IEEE J Ocean Eng* 29:706–728
11. Brochu P, Pei Q (2010) Advances in dielectric elastomers for actuators and artificial muscles. *Macromol Rapid Commun* 31:10–36
12. Okuzaki H, Kuwabara T, Funasaka K, Saido T (2013) Humidity-sensitive polypyrrole films for electro-active polymer actuators. *Adv Funct Mater* 23:4400–4407
13. Kakugo A, Sugimoto S, Gong JP, Osada Y (2002) Gel machines constructed from chemically cross-linked actins and myosins. *Adv Mater* 14:1124–1126
14. Xi J, Schmidt JJ, Montemagno CD (2005) Self-assembled microdevices driven by muscle. *Nat Mater* 4:180–184
15. Soong RK, Bachand GD, Neves HP, Olkhovets AG, Craighead HG, Montemagno CD (2000) Powering an inorganic nanodevice with a biomolecular motor. *Science* 290:1555–1558
16. Morishima K, Tanaka Y, Sato K, Ebara M, Shimizu T, Yamato M, Kikuchi A, Okano T, Kitamori T (2003) Bio actuated microsystem using cultured cardiomyocytes. In: *Proceedings of the micro total analysis systems*. Squaw Valley, CA, USA, pp 1125–1128
17. Baughman RH, Cui C, Zakhidov AA, Iqbal Z, Barisci JN, Spinks GM, Wallace GG, Mazzoldi A, DeRossi D, Rinzler AG, Jaschinski O, Roth S, Kertesz M (1999) Carbon nanotube actuators. *Science* 284:1340–1344
18. Aliev AA, Oh J, Kozlov E, Kunznetsov AA, Fang S, Fonseca AF, Ovalle R, Lima MD, Haque H, Gartstein YN, Zhang M, Zakhidov AA, Baughman RH (2009) Giant-stroke, superelastic carbon nanotube aerogel muscles. *Science* 323:1575–1578
19. Lima MD, Li N, Andrade MJ, Fang S, Oh J, Spinks GM, Kozlov ME, Haines CS, Suh D, Froughi J, Kim J, Chen Y, Ware T, Shin MK, Machado LD, Fonseca AF, Madden JDW, Voit WE, Galvao DS, Baughman RH (2012) Electrically, chemically, and potonically powered torsional and tensile actuation of hybrid carbon nanotube yarn muscles. *Science* 338:928–932
20. Yu Y, Nakano M, Ikeda T (2003) Directed bending of a polymer film by light. *Nature* 425:145
21. Yamada M, Kondo M, Mamiya J, Yu Y, Kinoshita M, Barrett CJ, Ikeda T (2008) Photomobile polymer materials: towards light-driven plastic motors. *Angew Chem Int Ed* 47:4986–4988
22. Pelrine RE, Kornbluh RD, Joseph JP (1998) Electrostriction of polymer dielectrics with compliant electrodes as a means of actuation. *Sens Actuators A* 64:7–85
23. Pelrine R, Kornbluh R, Pei Q, Joseph J (2000) High-speed electrically actuated elastomers with strain greater than 100 %. *Science* 287:836–839
24. Pelrine R, Kornbluh R, Kofod G (2000) High-strain actuator materials based on dielectric elastomers. *Adv Mater* 12:1223–1225
25. Hirai T, Sadato H, Ueda T, Kasazaki T, Kurita Y, Hirai M, Hayashi S (1996) Polyurethane-elastomer-actuator. *Die Angew Makromol Chem* 240:221–229
26. Zhang QM, Bharti V, Zhao X (1998) Giant electrostriction and relaxor ferroelectric behavior in electron-irradiated poly(vinylidene fluoride-trifluoroethylene) copolymer. *Science* 280:2101–2104
27. Lehmann W, Hartmann L, Kremer F, Stein P, Finkelmann H (1999) Direct and inverse electro-mechanical effect in ferroelectric liquid crystalline elastomers. *J Appl Phys* 86:1647–1652
28. Lehmann W, Skupin H, Tolksdorf C, Gebhard E, Zentel R, Kruger P, Losche M, Kremer F (2001) Giant lateral electrostriction in ferroelectric liquid-crystalline elastomers. *Nature* 410:447–450

29. Okuzaki H, Kunugi T (1998) Electrically induced contraction of polypyrrole film in ambient air. *J Polym Sci Polym Phys* 36:1591–1594
30. Okuzaki H, Suzuki H, Ito T (2009) Electromechanical properties of poly(3,4-ethylenedioxythiophene)/poly(4-styrene sulfonate) films. *J Phys Chem B* 113:11378–11383
31. Ma M, Guo L, Anderson DG, Langer R (2013) Bio-inspired polymer composite actuator and generator driven by water gradients. *Science* 339:186–189
32. Okuzaki H, Kunugi T (1996) Adsorption-induced bending of polypyrrole films and its application to a chemomechanical rotor. *J Polym Sci Polym Phys* 34:1747–1749
33. Okuzaki H, Funasaka K (2000) Electromechanical properties of a humido-sensitive conducting polymer film. *Macromolecules* 33:8307–8311
34. Smela E, Inganäs O, Lundström I (1995) Controlled folding of micrometer-sized structures. *Science* 268:735–738
35. Kaneto K, Kaneko M, Min Y, MacDiarmid AG (1995) “Artificial muscles”: electrochemical actuators using polyaniline films. *Synth Met* 71:2211–2212
36. Takashima W, Kaneko M, Kaneto K, MacDiarmid AG (1995) The electrochemical actuator using electrochemically-deposited poly-aniline film. *Synth Met* 71:2265–2266
37. Lu W, Fadeev AG, Qi B, Smela E, Mattes BR, Geoffrey JD, Spinks M, Mazurkiewicz J, Zhou D, Wallace GG, MacFarlane DR, Forsyth SA, Forsyth M (2002) Use of ionic liquids for π -conjugated polymer electrochemical devices. *Science* 297:983–987
38. Hara S, Zama T, Takashima W, Kaneto K (2004) TFSI-doped polypyrrole actuator with 26 % strain. *J Mater Chem* 14:1516–1517
39. Pei Q, Inganäs O (1992) Electrochemical application of the bending beam method. 1. Mass transport and volume changes in polypyrrole during redox. *J Phys Chem* 96:10507–10514
40. Pei Q, Inganäs O (1992) Conjugated polymers and the bending cantilever method: electrical muscles and smart devices. *Adv Mater* 4:277–278
41. Otero TF, Angulo E, Rodriguez J, Santamaria C (1992) Electrochemomechanical properties from a bilayer: polypyrrole/non-conducting and flexible material - artificial muscle. *J Electroanal Chem* 341:369–375
42. Hara S, Zama T, Sewa S, Takashima W, Kaneto K (2003) Highly stretchable and powerful polypyrrole linear actuators. *Chem Lett* 32:576–577
43. Spinks GM, Mottaghitaleb V, Bahrami-Samani M, Whitten PG, Wallace GG (2006) Carbon-nanotube-reinforced polyaniline fibers for high-strength artificial muscles. *Adv Mater* 18:637–640
44. Zama T, Tanaka N, Takashima W, Kaneto K (2006) Fast and large stretching bis(trifluoromethanesulfonyl)imide-doped polypyrrole actuators and their applications to small devices. *Polym J* 38:669–677
45. Hirai T (1995) Actuator materials from polymer gels. Polymer gels responding to electric and magnetic field. *J Mater Sci Soc Jpn* 32:59–63
46. Mitsumata T, Nagata A, Sakai K, Takimoto J (2005) Giant complex modulus reduction of κ -carrageenan magnetic gels. *Macromol Rapid Commun* 26:1538–1541
47. Zrinyi M, Barsi L, Buki A (1996) Deformation of ferrogels induced by nonuniform magnetic fields. *J Chem Phys* 104:8750–8756
48. Agolini F, Gay FP (1970) Synthesis and properties of azoaromatic polymers. *Macromolecules* 3:349–351
49. Smets G, De Blauwe F (1974) Chemical reactions in solid polymeric systems. Photomechanical phenomena. *Pure Appl Chem* 39:225–238
50. Aviram A (1978) Mechanophotochemistry. *Macromolecules* 11:1275–1280
51. Irie M, Kunwathakun D (1986) Photoresponsive polymers. 8 reversible photostimulated dilation of polyacrylamide gels having triphenylmethane leuco derivatives. *Macromolecules* 19:2476–2480
52. Suzuki A, Tanaka T (1990) Phase transition in polymer gels induced by visible light. *Nature* 346:345–347

53. Juodkazis S, Mukai N, Wakaki R, Yamaguchi A, Matsuo S, Misawa H (2000) Reversible phase transitions in polymer gels induced by radiation forces. *Nature* 408:178–181
54. Hamlen RP, Kent CE, Shafer SN (1965) Electrolytically activated contractile polymer. *Nature* 206:1149–1150
55. Yannas IV, Grodzinski AJ (1973) Electromechanical energy conversion with collagen fibers in an aqueous medium. *J Mechanochem Cell Mobilily* 2:113–125
56. Grodzinski AJ, Shoenfeld NA (1977) Tensile forces induced in collagen by means of electromechanochemical transductive coupling. *Polymer* 18:435–443
57. Osada Y, Hasebe M (1985) Electrically activated mechanochemical devices using polyelectrolyte gels. *Chem Lett* 14:1285–1288
58. DeRossi D, Parrini P, Chiarelli P, Buzzigoli G (1985) Electrically induced contractile phenomena in charged polymer networks: preliminary study on the feasibility of musclelike structures. *Trans Am Soc Artif Intern Organs* 31:60–65
59. Osada Y, Okuzaki H, Hori H (1992) A polymer gel with electrically driven motility. *Nature* 355:242–244
60. Oguro K, Kawami Y, Takenaka H (1992) Bending of an ion-conducting polymer film-electrode composite by an electric stimulus at low voltage. *J Micromachine Soc* 5:27–30
61. Shiga T, Hirose Y, Okada A, Kurauchi T (1992) Bending of poly(vinyl alcohol)-poly(sodium acrylate) composite hydrogel in electric fields. *J Appl Polym Sci* 44:249–253
62. Hirai T, Nemoto H, Hirai M, Hayashi S (1994) Electrostriction of highly swollen polymer gel: possible application for gel actuator. *J Appl Polym Sci* 53:79–84
63. Kishi R, Suzuki Y, Ichijo H, Hirasu O (1994) Electrical deformation of thermotropic liquid-crystalline polymer gels. *Chem Lett* 23:2257–2260
64. Asaka K, Oguro K, Nishimura Y, Mizuhara M, Takenaka H (1995) Bending of polyelectrolyte membrane-platinum composites by electric stimuli I. Response characteristics to various waveforms. *Polym J* 27:436–440
65. Fukushima T, Asaka K, Kosaka A, Aida T (2005) Fully plastic actuator through layer-by-layer casting with ionic-liquid-based bucky gel. *Angew Chem Int Ed* 44:2410–2413
66. Hirai T, Ogiwara T, Fujii K, Ueki T, Kinoshita K, Takasaki M (2009) Electrically active artificial pupli showing amoeba-like pseudopodial deformation. *Adv Mater* 21:2886–2888
67. Mukai K, Asaka K, Sugino T, Kiyohara K, Takeuchi I, Terasawa N, Futaba DN, Hata K, Fukushima T, Aida T (2009) Highly conductive sheets from millimeter-long single-walled carbon nanotubes and ionic liquids: application to fast-moving, low-voltage electromechanical actuators operable in air. *Adv Mater* 21:1582–1585
68. Tanaka T, Nishio I, Sun ST, Nishio SU (1982) Collapse of gels in an electric field. *Science* 218:467–469
69. DeRossi D, Chiarelli P, Buzzigoli G, Domenichi C, Lazzeri L (1986) Contractile behavior of electrically activated mechanochemical polymer actuators. *Trans Am Soc Artif Intern Organs* 32:157–162
70. Shiga T, Kurauchi T (1990) Deformation of polyelectrolyte gels under the influence of electric field. *J Appl Polym Sci* 39:2305–2320
71. Shiga T, Hirose Y, Okada A, Kurauchi T (1993) Bending of ionic polymer gel caused by swelling under sinusoidally varying electric fields. *J Appl Polym Sci* 47:113–119
72. Hirai T, Nemoto H, Suzuki T, Hayashi S, Hirai M (1993) Actuation of poly(vinyl alcohol) gel by electric field. *J Intell Mater Syst Struct* 4:277–279
73. Tanaka T, Ishiwata S, Ishimoto C (1977) Critical behavior of density fluctuations in gels. *Phys Rev Lett* 38:771–774
74. Tanaka T, Fillmore DJ, Sun ST, Nishio I, Swislow G, Shah A (1980) Phase transitions in ionic gels. *Phys Rev Lett* 45:1636–1639
75. Tanaka T, Sato E, Hirokawa Y, Hirotsu S, Peetermans J (1985) Critical kinetics of volume phase transition of gels. *Phys Rev Lett* 55:2455–2458
76. Suzuki M, Hirasu O (1993) An approach to artificial muscle using polymer gels formed by micro-phase separation. *Adv Polym Sci* 110:242–261

77. Osada Y, Saito Y (1975) Mechanochemical energy conversion in a polymer membrane by thermo-reversible polymer-polymer interactions. *Makromolekulare Chem* 176:2761–2764
78. Tanaka T (1978) Collapse of gels and the critical endpoint. *Phys Rev Lett* 40:820–823
79. Yoshida R, Uchida K, Kaneko Y, Sakai K, Kikuchi A, Sakurai Y, Okano T (1995) Comb-type grafted hydrogels with rapid deswelling response to temperature changes. *Nature* 374:240–242
80. Osada Y, Matsuda A (1995) Shape memory in hydrogels. *Nature* 376:219
81. Yoshida R, Takahashi T, Yamaguchi T, Ichijo H (1996) Self-oscillating gel. *J Am Chem Soc* 118:5134–5135
82. Tanaka T, Fillmore DJ (1979) Kinetics of swelling of gels. *J Chem Phys* 70:1214–1218
83. Steinberg IZ, Oplatka A, Katchalsky A (1966) Mechanochemical engines. *Nature* 210:568–571
84. Sussman MV, Katchalsky A (1970) Mechanochemical turbine: a new power cycle. *Science* 167:45–47
85. Sussman MV (1975) Mechanochemical availability. *Nature* 256:195–198
86. Kuhn W, Hargitay B, Katchalsky A, Eisenberg H (1950) Reversible dilation and contraction by changing the stage of ionization of high-polymer acid networks. *Nature* 165:514–516
87. Katchalsky A (1949) Rapid swelling and deswelling of reversible gels of polymeric acids by ionization. *Experimentia* 5:319–320
88. Kuhn W (1949) Reversible dehnung und kontraktion bei änderung der ionisation eines netzwerkes polyvalenter fadenmolekulionen. *Experimentia* 5:318–319

Chapter 2

Current Status of Applications and Markets of Soft Actuators

Kinji Asaka and Kayo Nakamura

Abstract In this chapter, the current status of applications and markets of soft actuators will be described with reference to some published patents in the expected application fields.

Keywords Automobile • Biomedical device • Consumer electronics • Electroactive polymer • Energy harvesting • Haptics • Robotics • Sensor

2.1 Introduction

Soft actuators are one of the most promising technologies of various emerging applications such as haptics, biomedical fields, MEMS, robotics, etc. Among the various materials of soft actuators reported in this book, electrically driven polymer actuators, so called electroactive polymer (EAP) actuators, are especially of practical interest for various industries [1–3]. The EAP actuators are broadly classified as electronic and ionic EAPs. Electronic EAPs respond to an electronic field, whereas ionic EAPs change shape by the transfer of ions by applying voltages [1]. Each type has various advantages and disadvantages. Table 2.1 lists main EAP materials and the properties thereof.

Due to various properties, such as lightness, softness, ease of processing, high compliance and low cost of soft actuators, they have become very attractive for applications in various fields, such as consumer electronics, biomedical applications, robotics, etc. In this chapter, applications of soft actuators will be described with reference to some published patents in the expected application fields.

K. Asaka (✉)
Health Research Institute, National Institute of Advanced Industrial Science and Technology (AIST), 1-8-31, Ikeda, Osaka 563-8577, Japan
e-mail: asaka-kinji@aist.go.jp

K. Nakamura
Property Co, Ltd., 6-12-7, Nishi-shinjuku, Shinjuku, Tokyo 160-0023, Japan

Table 2.1 List of main EAP materials and the properties thereof

EAP type	EAP materials	Advantages	Disadvantages
Ionic EAP	Ionic polymer (IP) – Nafion/Pt, Au, C – Flemion/Pt, Au – Ionic gel/Nano-carbon Conducting polymer (CP) – Polypyrrole – Polythiophene, PEDOT – Polyaniline Carbon nanotube (CNT)	– Low drive voltage – Relatively high response – Large displacement – Soft material – Can be activated in both wet and dry conditions.	– Low electromechanical efficiency – Relatively low actuation force (Bending EAPs)
Electronic EAP	Piezo-electric (PE) – PVdF, P (VdF-TrFE) Electrostrictive (ES) – P(VdF-TrFE), P (VdF-TrFE-CFE) Dielectric Elastomer (DE) – Acrylic, Silicone	– High response – Large actuation force – High mechanical energy density – High efficiency	– High drive voltage – No effect of voltage polarity

2.2 Current Status of Applications of Soft Actuators

2.2.1 Groundbreaking Studies

Soft actuator researches started from the research of direct transfer from chemical energy to mechanical work by using polymer gels [4]. As a Japanese pioneer patent relating to this research, Japanese Unexamined Patent Application Publication No. 1977–28482 (JP-A-1977-28482), “ENERGY CONVERSION AND SHAPE CONVERSION METHODS THROUGH THE MEDIUM OF POLYMERIC COMPOSITIONS”, (Applicant: HIDETOSHI TUSCHITANI, YOSHIIHITO OSADA) discloses a method that transfers chemical energy to mechanical work and changes shape by deforming polymer gels by pH changes reversibly. In this patent, with the application of this method, liquid and gas flow control valves and destruction of the bedrock were presented as examples. Among various driving methods of soft actuators, for example by pH control, temperature control, solvent control, etc., electrical control is the best method for the various applications, since the system itself becomes compact by using this method. As the Japanese pioneer patent of the electrically driven polymer gel, Japanese Patent No. 01592684 (JP 01592684), “BENDING METHOD OF POLYMER MATERIALS” (TOYOTA

CENTRAL LABS., Inc.) discloses a bending actuator based on electrically driven polymer gels. With the application of JP 01592684, an artificial fish with a fin of electrically driven bending polymer gel, was developed.

Based on these groundbreaking studies, JP 1966645; US 5268082 (OSAKA NATIONAL RESEARCH INSTITUTE) discloses an ionic polymer metal composite actuator, which opened the door to the research and development of the practical device of soft actuators. This patent is known to be a representative patent of ionic polymer actuators. As representative patents of electronic-type polymer actuators, US 6343129, 6940211, 7049732, (SRI INTERNATIONAL) discloses dielectric elastomer actuators.

Based on these studies, research and development of practical devices of EAP actuators has become vigorous worldwide including in Japan, Europe and North America.

2.2.2 Current Status of Technology of EAP Actuators for Applications

As previously described in Sect. 2.1, EAP actuators are broadly classified as ionic and electronic types; and nowadays, there are various kinds of EAP actuators that have different responses and mechanical properties. Therefore, it is possible to select the EAP actuators for each application. JP-A-2010-175360, “MICROCHEMICAL CHIP” (PANASONIC Co.) is the application patent focusing on the properties of various polymer actuators. In this patent, a conducting polymer actuator was selected since other polymer actuators have issues with the selected applications. For instance, according to the patent, heat-driven polymer gels needs a large system; electrically driven polymer gels have high electrical energy consumption; and dielectric elastomers need a high driving voltage.

However, in general, there are many patents which insist on the novelty of the use itself and do not consider the properties and applicability of the EAP actuators.

2.2.3 Consumer Electronics

The field that is applied most for is “IMAGE DEVICE AND IMAGE APPARATUS”. Table 2.2 lists the representative patents. For instance, JP 4972779, “OPTICAL UNIT AND IMAGING APPARATUS” discloses an optical unit and an imaging apparatus that have the features of “AUTOFOCUS” and “HAND SHAKE CORRECTION” driven by EAP actuators. Since a small “IMAGE APPARATUS”, which can be mounted on mobile phones, needs both low costs, scalability and high functions, EAP actuators are very attractive devices in this field, since they have a high power density, lightweight, noiseless, require a low driving

Table 2.2 Representative patents relating to consumer electronics

Bulletin number	Title	Applicant	EAP actuator used
JP 4758211	Camera shake correction unit and photographing apparatus	Fujifilm	DE
JP 4972779	Optical unit and imaging apparatus	Konica Minolta Opto Products	DE, ES, IP
JP 4324743	Stage structure of the imaging element and imaging device	Casio Computer	IPMC
JP 4501085	Optical element module and imaging device	Sony	IP
JP 4435290	Lens holder driving apparatus and imaging device using the surface drive polymer actuator	Panasonic	IP
JP 5029140	Variable shape optical elements, optical device and imaging apparatus	Konica Minolta Opto Products	EAP
JP 5188924	Imaging lens unit	Kantatsu	EAP
WO200585930	Adaptive optical element comprising a polymer actuator	SIEMENS	DE
US7679839	Optical lens displacement systems	BAYER MATERIALSCIENCE	DE
EP2270555	Optical liquid lens with a buffer elastic film	SAMSUNG ELECTRONICS	DE, ES, IP

voltage and have an ease of molding into any shape. JP 5029140, “VARIABLE SHAPE OPTICAL ELEMENTS, OPTICAL APPARATUS AND IMAGING APPARATUS” and WO200585930, “ADAPTIVE OPTICAL ELEMENT COMPRISING A POLYMER ACTUATOR” disclose shape-variable lenses using EAP actuators, which is quite a different method from mechanical transfer of optical lenses that is disclosed in other patents.

Another important field in consumer electronics is haptics. Many patents which provide haptic (touch-sense) feedback to the user interface (such as touch panel, etc.) have already been filed. Table 2.3 lists the representative patents. This technology can be applied to all types of user interfaces, such as touch pads, touch screens and keypads of PCs, mobile phones, PDAs, video game consoles, GPS systems, etc. Therefore, this technology can contribute remarkably to a wide range of user interfaces, and is expected to be a significant development in the near future.

Other important patents in relation to consumer electronics are as follows.

JP-A-2010-140717, “SWITCHING ELEMENT WITH MECHANICAL MOVEMENT” (HITACHI ELECTRIC Co.) and JP-A-2010-159780, “BRAKE DEVICE USING CONDUCTING POLYMER ACTUATORS” (PANASONIC Co.) disclose devices that make use of the advantages of EAP actuators such as the capability for low power consumption operation, and being small and light. The EAP actuators are the best devices for the application of these small apparatuses.

Table 2.3 Representative patents relating to haptics

Bulletin number	Title	Applicant	EAP actuator used
JP 4633074	Polyelectrolyte film actuator and touch panel using the same	Japan Aviation Electronics Industry	IP
JP-A-2010-86500	Operation device	KDDI, Hitachi,	CP
JP-A-2011-22495	Protrusion pattern forming device with a display function	Sony	IP
WO2010054014	Electroactive polymer transducers for tactile feedback devices	Bayer Materials Science	DE
WO2011123599	System and method for providing haptic stimuli based on position	Immersion	EAP
WO2009154158	Actuator and input device using the same	ALPS ELECTRIC	IP
US7342573	Electrostrictive polymer as a combined haptic-seal actuator	NOKIA	IP

JP 5151896, “VIBRATION DAMPING DEVICE” (KONICA MINOLTA Co.) discloses vibration damping devices using the EAP actuators. Although vibration damping devices using piezo-electric actuators are well-known, to use EAP actuators gives the possibility of application to a vibration body which piezo-electric actuators cannot control. Nowadays, various information apparatuses are used in the home and office, and noises generated by them are a serious problem. The vibration damping devices using EAP actuators may be adopted as one of the solutions in the near future.

JP-A-2011-123685, “ANTENNA DEVICE AND COMMUNICATION APPRATUS” (SONY MOBILE COMMUNICATIONS INC.) discloses antenna devices that can be applied to small communication devices such as mobile phone terminals, etc. JP-A-2008-206144, “SELF-DEFORMABLE ANTENNA APPRATUS” (JAMSTEC, RIKEN, AIST) provides a technology for controlling the direction of an antenna freely by using an ionic EAP actuator. The technology for controlling the direction of the antenna and a solar cell panel in aerospace by using EAP actuators was also reported.

2.2.4 Biomedical Devices

Biomedical fields are also among those to which many application patents of EAP actuators have already been filed. Table 2.4 lists the representative patents. From Table 2.4, it can be interpreted that the most important applications are micro-pumps for medical uses and microchips for analysis, and various EAP actuators have been adopted as electromechanical parts for these devices, such as

Table 2.4 Representative patents relating to biomedical devices

Bulletin number	Title	Applicant	EAP actuator used
JP 3071524	Micropump	Nidec	EAP
JP 4646530	Actuator element and method of driving the same	Eamex	IP
JP 4481826	Catheter for thrombolysis	Boston Scientific	CP
JP 4374436	Grip forceps system	Tohoku University	IP
JP 4679241	Endoscope	Olympus Medical Systems	DE
JP 4657082	Ultrasound therapeutic apparatus	Olympus Medical Systems	ES
JP 4961898	Capsule type medical apparatus	Konica Minolta Opto Products	CP
JP 5021366	Treatment implementation and endoscope operation system with the same	Olympus Medical Systems	EAP
JP-A-2010-175360	Microchemical chip	Panasonic	CP
JP-A-2011-208597	Micropump	Eamex	CP
US20050085693	Activated polymer articulated instruments and methods of insertion	INTUITIVE SURGICAL	IP
US7407074	Electroactive polymer-based actuation mechanism for multi-fire surgical fastening instrument	ETHICON ENDO SURGERY	EAP
US7566297	Electroactive polymer based artificial sphincters and artificial muscle patches	BOSTON SCIENTIFIC SCIMED	CP

diaphragms of micro-pumps and micro-valves of microchips. Another important application is the “artificial organ”, which is disclosed in JP 4646530, “ACTUATOR ELEMENT AND ITS DRIVING METHOD”. This application was expected since the early stages of the research into EAP actuators. Moreover, many application patents for active catheters, active endoscopes, ultrasonic therapy apparatuses and medical treatment tools have been filed.

2.2.5 Robotics

Applications of soft actuators to robotics are not only the purpose of the research at the early stage; the ultimate goal of the research is to realize artificial muscles by applying soft actuators. In the current stage, the practical application of soft

actuators to robotics to realize artificial muscles is difficult. Here, the following two patents are shown as examples of the application of EAP actuators to robotics:

1. JP 3976129, “PARALLEL LINK MECHANISM AND ARTIFICIAL JOINT DEVICE USING THE SAME” (HONDA MOTOR Co. Ltd.)
2. JP 3817259, “CONDUCTING POLYMER ACTUATOR”, (PANASONIC Co.)

US7966074, “APPARATUS AND METHOD FOR ENHANCING MUSCULAR MOVEMENT” (SAMSUNG ELECTRONICS Co.) and JP-A-2010-051416, “MOTION ASSISTING APPARATUS OF ANKLE JOINT AND ITS CONTROL METHOD” (NABTESCO Co.) disclose the applications of the motion assisting apparatus for the nursing of elderly people and rehabilitation work.

2.2.6 Other Applications of Soft Actuators

Many applied patents have already been filed in other fields including the field of automobiles. Table 2.5 lists the representative patents. It can be seen from Table 2.5 that there are patents of EAP actuators that apply to various parts of automobiles, such as dampers, steering, power transmission devices, tires, sheets, air bags, etc. However, there are few patents that are truly effective in this field.

In recent patents, as summarized in Table 2.6, new applications for information apparatuses based on EAP actuators were provided in the field of automobiles. For instance, JP 5182353, “INFORMATION PRESENTING DEVICE” discloses a steering device with EAP actuators for providing a driver with support information by means of haptics. JP-A-2013-023107, “VEHICLE SYSTEM” discloses a control method of the deformation of EAP actuators which are embedded in the tires of a vehicle in order to improve the running performance thereof.

2.2.7 Energy Harvesting and Sensor

Table 2.7 summarizes the representative patents in this field. JP-A-2012-16917, “ELECTROSTATIC CAPACITY VARIATION TYPE POWER GENERATION ELEMENT” discloses energy harvesting devices using dielectric elastomer EAP devices. In recent years, the research of the energy harvesting, based on various EAPs, is being developed from a basic and practical point of view.

Table 2.5 Representative patents on automobile

Bulletin number	Title	Applicant	EAP actuator used
JP-A-2005-083530	Variable damping force damper	Honda Motor	CP
JP-A-2005-104416	Steering device	Honda Motor	CP
JP-A-2005-112200	Pneumatic tire	Honda Motor	CP
JP-A-2006-348085	Cushion actuator obtained using ionic liquid, and part for vehicle composed of the same	Nissan Motor	IP
JP-A-2011-106564	Power transmission device	Honda Motor	EAP
JP-A-2009-216130	Shock absorber	KYB	EAP
JP-A-2012-203798	Information presentation system	Denso IT Laboratory	EAP
US20030168936	Electro-active polymer as a fuel vapor control valve actuator	SIEMENS VDO AUTOMOTIVE	DE
US7516982	Gas bag module	TRW AUTOMOTIVE SAFETY SYSTEMS	EAP
WO2006062608	Tunable vehicle structural members and methods for selectively changing the mechanical properties thereto	GENERAL MOTORS	PE

Table 2.6 Representative patents relating to information apparatuses in the field of automobiles

Bulletin number	Title	Applicant	EAP actuator used
JP-A-2011-242386	Transparent composite piezoelectric combined touch sensor and haptic actuator	Immersion	PE
JP-A-2012-062040	Information presentation device	Nippon Soken, Denso	ES
JP-A-2012-203798	Information presentation system	Denso IT Laboratory	EAP
JP-A-2013-023107	Vehicle system	Sumitomo Rubber Industries	EAP

Table 2.7 Representative patents relating to energy harvesting and sensors

Bulletin number	Title	Applicant	EAP actuator used
JP-A-2011-087387	Polymer actuator and polymer sensor using the same	Eamex	IP
WO10/095581	Multi-laminating transformation sensor	Kuraray	IP
JP-A-2012-164917	Electrostatic capacity variation type power generation element	Fuji film	DE
US7034432	Electroactive Polymer Generators	SRI International	IP

2.3 Current and Expected Markets for Soft Actuators

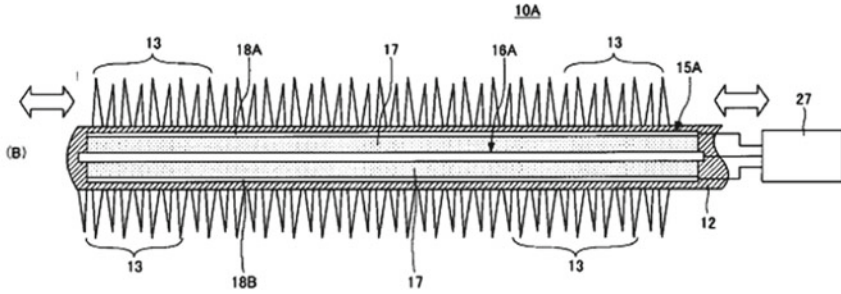
JP 4245964, “DECORATIVE AQUARIUM AND DECORATIVE DISPLAY UNIT” (EAMEX Co.) discloses a robotic ornamental fish with an ionic EAP actuator as a fin thereof, which is the world’s first commercial product using an EAP actuator. Hereafter, more commercial products using EAP actuators will be expected in various fields. Here, current and future expected markets for soft actuators will be discussed.

In recent years, parts which are mounted on portable terminals need not only to be smaller and lighter but also have more sophisticated functions. Therefore, soft actuators, which can meet both needs, are a very attractive technology for these kinds of new fields. They are being applied to apparatuses for everyday uses as driving units that are noiseless and can be driven with low-drive voltages and low-power consumption.

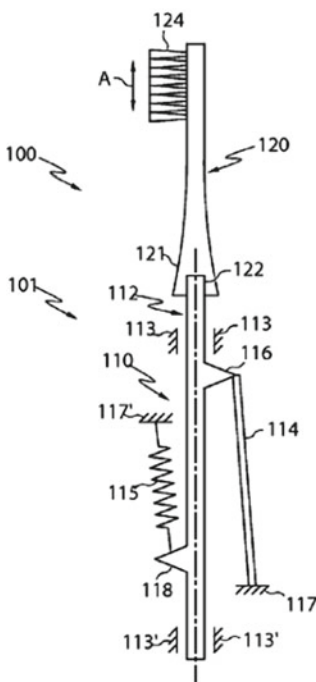
An example of an applied patent of EAP actuators to a new field that utilizes the advantage of their noiselessness as compared to other actuators is JP-A-2013-063262, “COSMETIC TOOL” (SHISEIDO Co., Ltd.) (Fig. 2.1). Previously, an electric mascara applicator was proposed which was rotated and vibrated by electro-magnetic motor easier application of mascara. However, it had problems; heavy to use and too noisy. In order to solve these problems, the above patent discloses a technology that employs a conducting polymer actuator. JP-A-2013-83049, “SLAT ANGLE CHANGE DEVICE” (AISIN SEIKI Co., Ltd.) (Fig. 2.1) discloses a slat angle adjusting device for horizontal blinds using the EAP actuator in order to solve the same issues. Moreover, various patents which disclose daily necessities using EAP actuators have been filed, e.g., “the electric toothbrush” in US 2013025079, “LINEAR ELECTRO-POLYMER MOTORS AND DEVICES HAVING THE SAME” (Braun) (Fig. 2.1), JP-A-2008-142108, “MASSAGING APPARATUS” (YAMAHA Co.), JP-A-2012-64441, “LIGHTING DEVICE” (KONICA MINOLTA OPTO PRODUCTS Co., Ltd.).

In recent years, growing interest has been focused on environmental issues. One of the most effective methods to solve a part of this issue is to use solar cells as a clean energy source. However, the important issue for the effective use of the solar light and the maintenance of the device is the removal of snow from the solar cell panel. JP-A-2011-060836, “SOLAR CELL MODULE APPARATUS” (OBAYASHI Co.) (Fig. 2.2) discloses a technique that cleans the snow from the solar cell panel by the vibration which is provided by the deformation of the dielectric elastomer actuators. This method is able to accomplish the purpose using low power consumption compared to using a piezoelectric device.

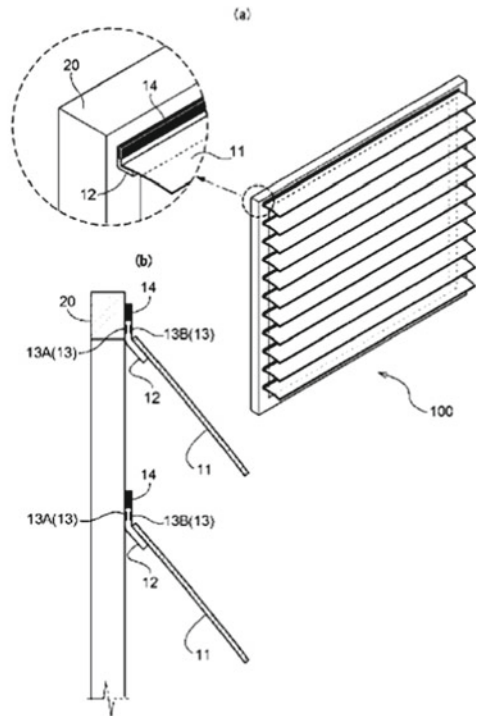
As the patents of electric-acoustic transducers that can reproduce a music signal with a high sound quality by using a small device producing large vibrational amplitude, two patent applications were filed. One is JP-A-2011-223478, “POLYMER ACTUATOR AND ELECTROACOUSTIC TRANSDUCER USING THE SAME; AND ELECTRONIC EQUIPMENT” (NEC Co.), which adopts conducting



JP-A-2013-063262



US2013025079

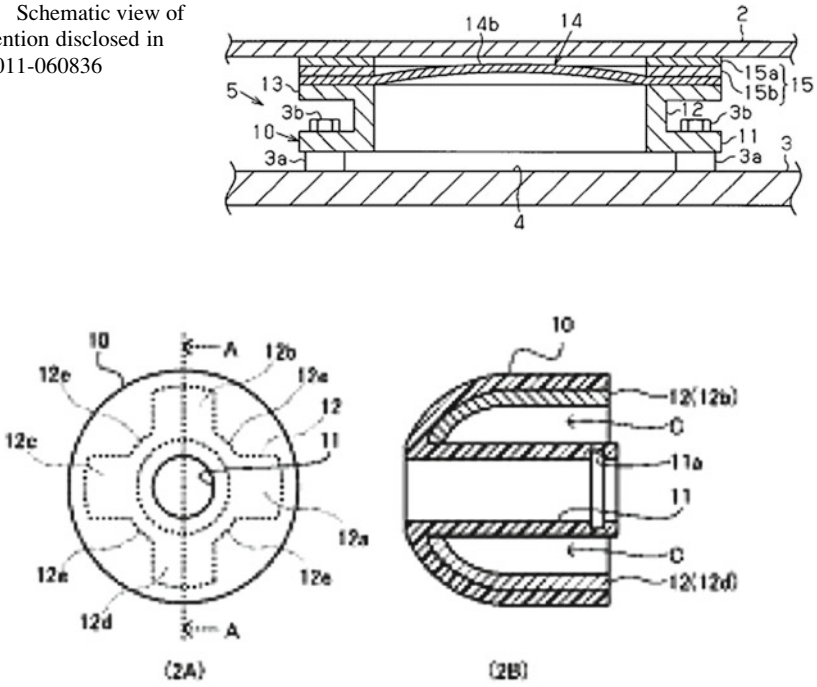


JP-A-2013-83049

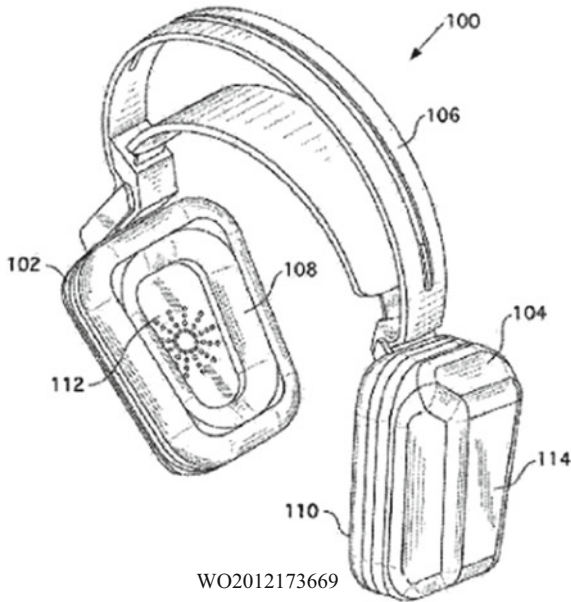
Fig. 2.1 Schematic views of disclosed inventions. JP-A-2013-063262 US2013025079 JP-A-2013-83049

polymer polyaniline actuators as the EAP actuator. The other is WO2012173669 (Fig. 2.3), “AUDIO DEVICES HAVING ELECTROACTIVE POLYMER ACTUATORS” (BAYER MATERIAL SCIENCE Co.), which adopts dielectric elastomer actuators. Meanwhile, JP 5024065, “EARPHONE” (YAMAHA Co.) (Fig. 2.3) discloses a technique by which an EAP actuator deforms an ear canal insertion

Fig. 2.2 Schematic view of the invention disclosed in JP-A-2011-060836



JP 5024065



WO2012173669

Fig. 2.3 Schematic view of disclosed inventions. JP 5024065 WO2012173669

part of an earphone in the radial direction of a sound conduction tube so that the earphone can be used more comfortably and held more securely.

A typical example of an application patent in the welfare field is JP-A-2006-034574, "BEDSORE CONTACT ARRESTER AND BEDSORE CONTACT PREVENTION SYSTEM" (MITSUBISHI ELECTRIC Co.). Moreover, a Braille display which is disclosed in JP 4705992, "DOT DISPLAY DEVICE" (ALPS ELECTRIC Co., Ltd.) and JP 5066754, "POLYMER ACTUATOR ELEMENT AND BRAILLE DISPLAY USING THE SAME" (UNIVERSITY OF YAMANASHI, TAKANO Co., Ltd.) is one of the most promising applications for EAP actuators.

2.4 Conclusion

As previously described, the technical fields for the application patents of EAP actuators have spread through various fields such as daily necessities, consumer electronics, musical instruments, portable terminals including speakers etc., environmental applications including solar cells etc. and welfare applications including Braille devices etc. As compared to conventional electro-magnetic motors with their heavy and hard structures and noise problems, soft, lightweight and noiseless EAP actuators have an affinity with humans and the advantages of low power consumption and low drive voltages that are strong points for applications both economically and environmentally. Therefore, they will be expected to produce various applied patents in human friendly applied fields.

References

1. Bar-Cohen Y (ed) (2004) *Electroactive polymer actuators as artificial muscles, reality, potential, and challenges*, 2nd edn. SPIE, Washington
2. Kim KJ, Tadokoro S (eds) (2007) *Electroactive polymers for robotic applications*. Springer, London
3. Carpi F, Smela E (eds) (2009) *Biomedical applications of electroactive polymer actuators*. Wiley, West Sussex
4. DeRossi D, Kajiwaru K, Osada Y, Yamauchi A (eds) (1991) *Polymer gels: fundamentals and biomedical applications*. Plenum, New York

Part II
Materials of Soft Actuators:
Thermo-Driven Soft Actuators

Chapter 3

Electromagnetic Heating

Takeshi Yamauchi

Abstract In this study, we demonstrated the surface modification of carbon microcoil (CMC) with grafting polymers onto the CMC and prepared composite material of poly(*N*-isopropyl acrylamide) (PNIPAM) gel as thermo-sensitive polymer gels by electromagnetic heating. The properties of the material such as content of carbon micro-coils, swelling ratio, breaking strength, and thermo-sensitivity, and its function as drug carrier were evaluated. The composite gels were shrunken with increase of temperature as well as normal PNIPAM gel and responded to electromagnetic waves with the presence of contained CMCs which absorb electromagnetic waves and generate heat. The surface temperature of composite gel was reached 43 °C within 150 s and changed its shape with squeezed water.

Keywords Carbon micro coil • Electromagnetic heating • Graft polymerization • Thermo-sensitive polymer

3.1 Introduction

Recently, there has been much research work with respect to soft actuator response to thermal stimulus, particularly as thermal energy is easy to generate into various of transitions such as structure phase transition, metal-insulator transition, magnetic phase transition. Flexible actuators have been developed using structure memory metals which have the capability to change its structure by Martensite transition. The actuators fabricated with micro size have been applied to various kinds of medical devices.

Poly (*N*-isopropyl acrylamide) (PNIPAM) gel is well known as a thermo-sensitive polymer gel, and has been actively studied for application to smart materials. Since PNIPAM has a lower critical solution temperature (LCST) at approximately 35 °C, the PNIPAM gel can be swollen at a lower temperature and shrunken at higher temperature than LCST [1–4]. There has been various research

T. Yamauchi (✉)

Faculty of Engineering, Niigata University, 8050, Ikarashi 2-nocho, Nishi-ku,
Niigata 950-2181, Japan

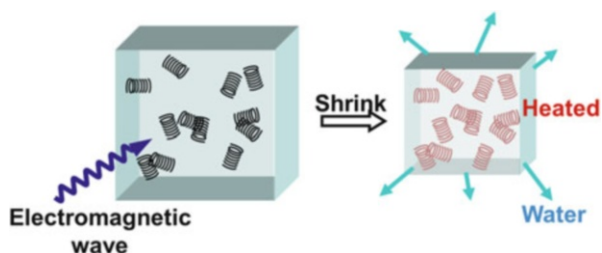
e-mail: yamauchi@gs.niigata-u.ac.jp

works using PINPM for biomedical application such as drug delivery carriers, bio culture sheet, and blood tube bulbs [5–7]. Materials changed physical properties by external thermal condition. Human body temperature is localized and changed easily.

As the gel works by external thermo stimulus, it is difficult to maintain its shape without an increase in temperature from the external environment. Development of NIPAM gel which can control its physical properties by internal thermo stimulus is useful for high grade bio-medical application. Carbon microcoils (CMCs) were focused on to solve this problem because it has been reported that CMCs generate heat with electromagnetic irradiation [8–10]. The surface temperature of CMCs reached more than 500 °C within several minutes with 2.45 GHz microwave irradiation. This material also showed novel electrical properties and anti-bacterial effect. The composite material of CMCs and PNIPAM would change its shape with internal thermo energy which generate by electromagnetic irradiation. For high-grade nano-materials, it is necessary for nano-materials to form a self-organized structure by external stimuli. However, due to the low dispersibility and low stabilization of CMCs it is very difficult to achieve a uniform dispersion of CMCs in various solvents and polymer matrices. Tsubokawa et al. have successfully reported the surface grafting of polymers onto carbon materials, such as carbon black, graphite, carbon nanotubes, and carbon fibers [11–13]. Additionally it was reported that polymer radicals formed by the decomposition of macro azo-initiator and bis-peroxides were effectively trapped by carbon black surface [12].

In this study, thermo-sensitive polymers were grafted onto CMCs by thermal decomposition of Perhexa C. The radical graft polymerization was initiated by the peroxyester groups introduced onto a CMC surface. Composite material of PNIPAM gels containing CMCs was prepared by photo-polymerization.

It is expected that the contained CMCs generate heat with electromagnetic irradiation and the composite gel is shrunken without alteration in the external environment (Scheme 3.1). The properties of the composite materials such as content of CMCs, swelling ratio, breaking strength, thermo-sensitivity, and sensitivity to electromagnetic wave were evaluated.



Scheme 3.1 Thermo-sensitive soft actuator by electromagnetic heating

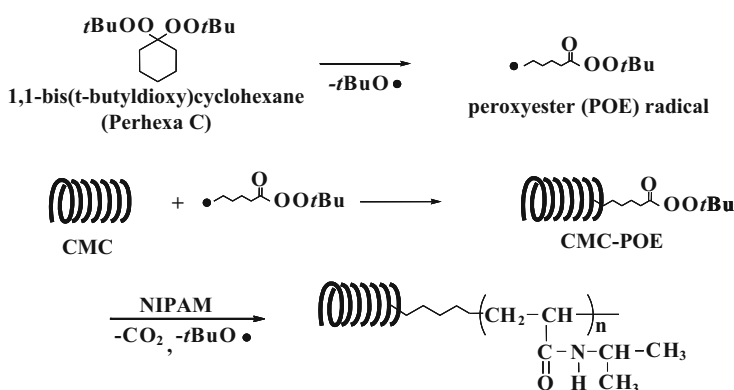
3.2 Surface Modification of CMCs

Carbon micro coil (CMC) is a carbon fiber with helical structure and has high grade mechanical and electrical properties. It has also reported that CMC was generated heat with electromagnetic irradiation. For the high-grade composite material of CMC and polymer matrix, it has required that modification of CMC surface with polymer. The introduction of thermo-sensitive polymer onto CMCs was carried out through the trapped peroxyester radicals formed by the thermal decomposition of Perhexa C. A typical example was as follows: 0.50 g of CMCs and 10.0 mL of Perhexa C were placed in a polymerization tube. After degasification by four freeze-thaw cycles, the solution was sealed off under vacuum. The sealed tube was heated at 70 °C in a constant temperature oil bath with stirring. After the reaction, resulting CMCs were dispersed in methanol, and the dispersion was centrifuged at 1.5×10^4 rpm until polymer-grafted CMCs were precipitated completely. The procedure was repeated three times, dried in vacuo at room temperature, and stored in a refrigerator.

It is well known that bis-peroxides, such as Perhexa C, are used in the preparation of block copolymers in the radical polymerization, because these peroxides form peroxyester radicals [12]. For example, Perhexa C has two decomposition temperatures, giving a 10 h half-life and is decomposed by two-step mechanism, initially decomposition of alternative peroxide groups at 60 °C and finally decomposition of residual peroxide groups at 100 °C (Scheme 3.2).

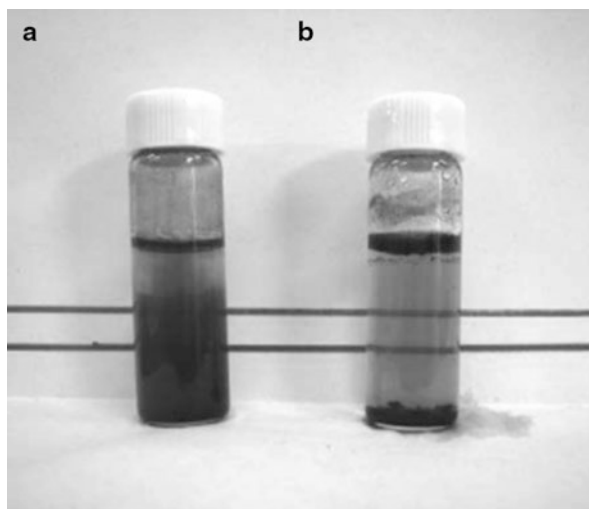
PNIPAM was introduced onto CMCs using Perhexa C and the amount of polymer grafted onto CMCs was calculated 6 % by infrared spectroscopy and thermal calorimetry.

The dispersibility of PNIPAM-grafted CMCs in water was investigated. Figure 3.1 shows the dispersibility of untreated and PNIPAM-grafted CMCs in



Scheme 3.2 Radical polymerization of Poly(*N*-isopropylacrylamide) (PNIPAM) by peroxyester group introduced on carbon microcoil(CMC)

Fig. 3.1 Improvement of dispensability of carbon microcoils against water solution. (a) poly(*N*-isopropylacrylamide) grafted carbon microcoils at room temperature, (b) poly(*N*-isopropylacrylamide) grafted carbon microcoils at 80 °C



water. Untreated CMCs precipitated after 30 s. conversely PNIPAM grafted CMC gave a stable dispersion in good solvent for grafted polymer. These results indicate that by grafting PNIPAM onto a CMCs surface, the solubility of CMCs was drastically improved by grafted polymer chains on the surface which interfere with the aggregation of the CMC in solvent (Fig. 3.1a). PNIPAM-grafted CMCs showed very unique properties against thermal condition. PNIPAM-grafted CMCs were significantly aggregated at 80 °C (Fig. 3.1b). The precipitated speed was the same as the untreated CMCs. It was found that untreated CMCs were difficult to disperse in water solution even with ultrasonic irradiation, although PNIPAM-grafted CMCs could be dispersed again by shaking the bottle at room temperature. PNIPAM-grafted CMCs showed this dissociation and aggregation with temperature repeatedly. It appeared that the solubility of PNIPAM grafted CMCs was controlled by external thermo energy.

3.3 Preparation of Composite Gels

The composite gels were prepared by photo-polymerization with irradiation of ultraviolet light. *N*-isopropyl acrylamide, monomer, *N,N'*-methylenebisacrylamide, cross linker, and 2,2'-Azobis(2-amidinopropane)dihydrochloride, initiator were dissolved in water. Untreated CMCs and PNIPAM-grafted CMCs were added respectively to this solution with stirring. The gelation was carried out by irradiating with ultraviolet light for several hours. Obtained gels were immersed in water until it reached an equilibrium condition.

The properties of the composite materials such as content of CMCs, swelling ratio, breaking strength, thermo-sensitivity, and sensitivity to electromagnetic wave were evaluated.

Content of CMCs was calculated from weight of dry gel and that of CMCs contained in the gel. The swollen gels were dried for several days and powdered. Weight of the powdered dry gels and that of CMCs contained in the gel were calculated from thermogravimetric analysis using with a micro-thermobalance (DSC-50, Shimadzu Corporation, Japan). Swelling ratio was calculated from the weight of swollen gel in equilibrium condition and that of the dry gel. The swollen gels were dried for several days after measuring of their weights, and subsequently the weights of the dry gels were measured. Breaking strength was evaluated by compression test using a digital push-pull pressure gauge (Model RX-1, Aikoh Engineering Co., Ltd., Japan). The swollen gels were compressed with conical-shaped tip at room temperature, and the strength was measured when the gels were broken.

The black colored composite gel membranes were prepared by photopolymerization (Fig. 3.2). Normal PNIPAM gel without CMCs was transparent (Fig. 3.2a) and large black aggregates of CMCs were observed in the gel containing untreated CMCs (Fig. 3.2b). On the other hand, PNIPAM-grafted CMCs were evenly dispersed in PNIPAM gels, and the gel containing PNIPAM-grafted CMCs was wholly black (Fig. 3.2c). It was estimated that grafted PNIPAM, hydrophilic polymer at polymerization temperature, augmented hydrophilic of CMCs, and the coils were kept dispersed in water while polymerization and contained in PNIPAM gel uniformly. Content of PNIPAM-grafted CMC was as same as that of untreated CMC, since as same quantity of PNIPAM-grafted CMCs as untreated CMCs were added for polymerization of the gels (Table 3.1). PNIPAM gels containing CMCs had slightly smaller swelling ratio than normal PNIPAM gel. The breaking strength of PNIPAM gel containing PNIPAM-grafted CMCs was the same as that of the normal gel. Compared with the strength of the gel containing untreated CMCs, mechanical properties of PNIPAM gel containing PNIPAM-grafted CMCs were substantially improved. It was estimated that contained CMCs inconsiderably inhibited swelling of the gels and untreated CMCs deteriorated the breaking strength of the PNIPAM gel, however, the grafted PNIPAM headed off the deterioration. The CMCs were uniformly dispersed and the grafted polymer on CMC would form a physical interaction with thermo-sensitive polymer network in the gel and improved its mechanical strength.

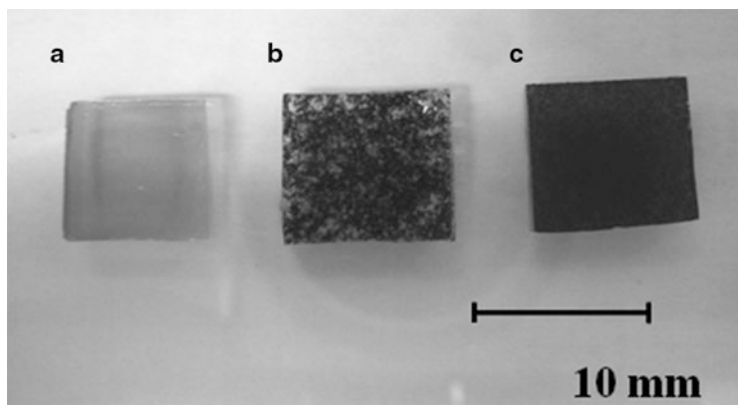


Fig. 3.2 Photograph of poly(*N*-isopropylacrylamide) gels. (a) without carbon microcoils, (b) contained untreated carbon microcoils, (c) contained polymer grafted carbon microcoils

Table 3.1 Properties of carbon microcoils contained poly(*N*-isopropylacrylamide) gels

Contained CMC	Swelling ratio (%)	Content of CMCs (%)	Breaking strength (N)
None	2.3×10^3	–	0.37
Untreated CMCs	2.0×10^3	6.6	0.13
PNIPA M-grafted CMCs	1.8×10^3	6.6	0.49

3.4 Sensitivity of Composite Gels Against Electromagnetic Wave

Thermo-sensitivity was evaluated by relationship between temperature and volume alteration modulus, and differential scanning calorimetry using with a micro-thermobalance (DSC-50, Shimadzu Corporation, Japan). The gels were heated in a constant-temperature bath by an elevated temperature process, their sizes were measured from 20 to 40 °C at 5 °C intervals after the gels were allowed to stand for several hours and shrunken almost-totally at each temperature. LSCT of the composite gels were evaluated from peaks of differential scanning calorimetric curves in elevated temperature process.

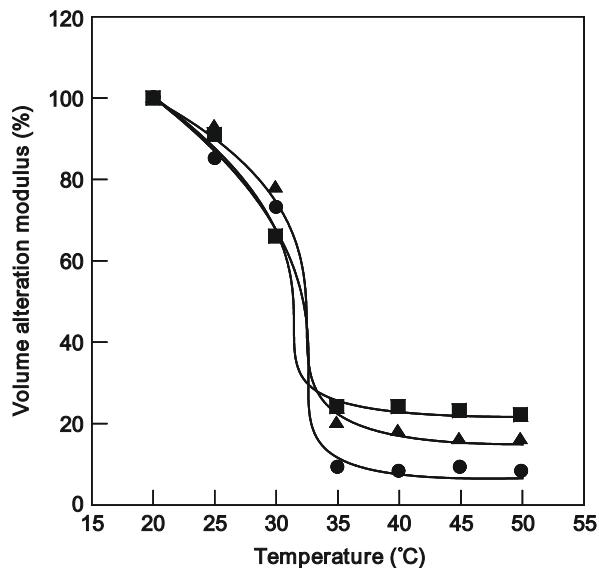
The volume alteration modulus was defined as follows:

$$\text{Volume alternation modulus (\%)} = \frac{\text{Volume at each temperature}}{\text{Volume at 20 } ^\circ\text{C}} \times 100$$

Sensitivity of the composite gels to electromagnetic wave was evaluated by irradiating electromagnetic wave (2.45 GHz, in range of wavelength CMC absorbs) with a microwave oven (NE-A750, Matsushita Electric Industrial Co., Ltd.).

The composite gels changed their volume with temperature and shrank remarkably from 100 to 20 % at around 35 °C as well as normal PNIPAM gel (Fig. 3.3).

Fig. 3.3 Thermo-sensitive characteristics of various PNIPAM gels. *Filled circle*: without carbon microcoils, *filled triangle*: contained untreated carbon microcoils, *filled square*: contained polymer grafted carbon microcoils



During the shrinking process of composite gels, no CMC eluted off from the composite gels. As a result of differential scanning calorimetry, the endothermic peaks attributed to remarkable shrinkage of PNIPAM gel at LSCT were observed at about 35 °C in DSC curves of the composite gels and normal gel. These results suggested that the composite gels maintained their thermo-sensitivity to shrink with increases in temperature, and the gels had almost the same LCST as normal PNIPAM gel at around 35 °C. It is expected that the contained CMCs generate heat and the composite gel shrink with electromagnetic irradiation without temperature change.

The surface temperature of composite gels with 2.45 GHz microwave irradiation was investigated (Fig. 3.4). The surface temperature of CMCs containing polymer gel was increased with irradiation time and reached 43 °C within 150 s. The composite gels generate thermo-energy by absorbed electromagnetic waves. It is reported that cancer cell is exterminated above 42.5 °C. These composite materials would work as not only as a drug delivery carrier which release drug with internal thermal energy by electromagnetic waves and also as a hyperthermia therapy effect for cancer. The composite gel changed its shape and squeezed solvent from the bulk of the gels with 20 wt% water being released from the gel. PNIPAM has lower critical solution temperature (LSCT) at about 35 °C, and hydrophilic property of polymer was extremely changed into hydrophobic property at LSCT (Fig. 3.5). These results suggest that the PNIPAM responded to internal thermal condition and transformed physical property of CNT from hydrophilicity into hydrophobicity.

Fig. 3.4 Relationship between surface temperature of various PNIPAM gels and irradiation time of electronic micro wave (2.45 GHz). *Filled circle*: Without carbon microcoils, *filled triangle*: Contained untreated carbon microcoils, *filled square*: Contained polymer grafted carbon microcoils

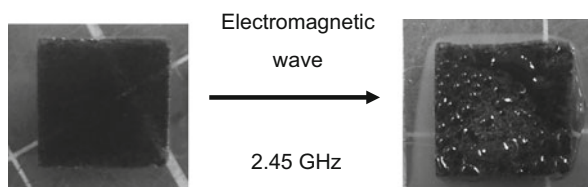
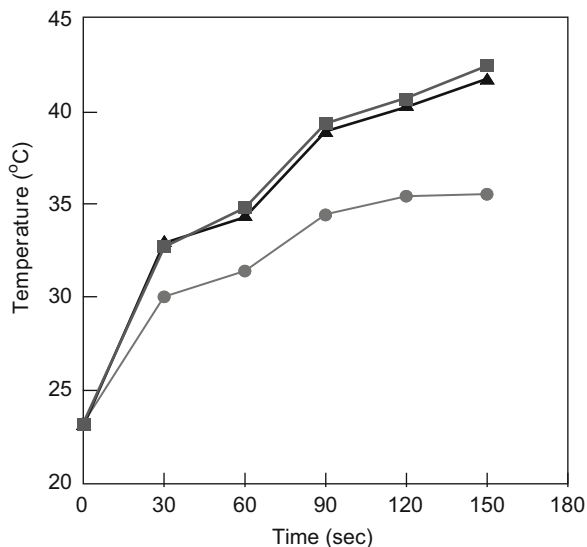


Fig. 3.5 Photograph of poly(*N*-isopropylacrylamide) gels contained polymer grafted carbon microcoils with irradiation of electronic micro wave (2.45 GHz)

3.5 Conclusions

Thermo-driven soft actuators by electromagnetic heating were developed using carbon micro fiber with helical structure. The composite gels with CMC and thermo-sensitive polymer gel changed shape by electromagnetic irradiation. It was found that the composite gel responded to electromagnetic wave with the presence of contained CMCs which absorbed electromagnetic wave and generated heat without alteration in the external environment. Carbon micro fiber was effectively generated by thermal energy with irradiating magnetic wave and composite material shrank by itself to release solution. The composite material can use as drug delivery system with hyperthermia effect. It would be possible to develop novel thermo-driven soft actuators by electromagnetic heating possessing hieratical multi-phase transition. It was also found that thermo-sensitive polymer grafted with carbon nanomaterial such as nanotube, fullerene, and carbon coil can control micro scale self-organization by external stimulus.

Acknowledgement The author appreciates the help received from Dr. Norio Tsubokawa (Niigata university), Dr. Kenji Kawabe, Dr. Yukio Hishikawa, and Dr. Seiji Motojima (CMC Technology Development Co. Ltd.).

References

1. Fujishige S et al (1989) Phase transition of aqueous solutions of poly(*N*-isopropylacrylamide) and poly(*N*-isopropylmethacrylamide). *J Phys Chem* 93:3311–3313
2. Hirotsu S et al (1987) Volume-phase transitions of ionized *N*-isopropylacrylamide gels. *J Chem Phys* 87(2):1392–1394
3. Aoyagi T et al (2000) Novel bifunctional polymer with reactivity and temperature sensitivity. *J Biomater Sci Polym Ed* 11(1):101–110
4. Díez-Peña E et al (2002) Thermal properties of cross-linked poly(*N*-isopropylacrylamide) [P(*N*-iPAAm)], poly(methacrylic acid) [P(MAA)], their random copolymers [P(*N*-iPAAm-co-MAA)], and sequential interpenetrating polymer networks (IPNs). *Macromolecules* 35:2667–2675
5. Yoshida T et al (2003) Newly designed hydrogel with both sensitive thermoresponse and biodegradability. *J Polym Sci A Polym Chem* 41(6):779–787
6. Maeda T et al (2006) Hydroxylated poly(*N*-isopropylacrylamide) as functional thermoresponsive materials. *Biomacromolecules* 7(2):545–549
7. Yang J et al (2007) Reconstruction of functional tissues with cel sheet engineering. *Biomaterials* 28(34):5033–5043
8. Chen X et al (1999) The growth patterns and morphologies of carbon micro-coils produced by chemical vapor deposition. *Carbon* 37(11):1817–1823
9. Motojima S et al (2003) Electromagnetic wave absorption property of carbon microcoils in 12–110 GHz region. *J Appl Phys* 94:2325–2330
10. Motojima S et al (2003) Electromagnetic wave absorption properties of carbon microcoils/PMMA composite beads in W bands. *Carbon* 41(13):2658–2660
11. Tsubokawa N et al (1992) Grafting of poly(organophosphazenes) onto carbon black surface. *J Macromol Sci Pure Appl Chem A29*:311–321
12. Tsubokawa N (2005) Preparation and properties of polymer-grafted carbon nanotubes and nanofibers. *Polym J* 37:637–655
13. Tsubokawa N et al (2002) Grafting of polymers onto carbon-fiber surface by ligand-exchange reaction of poly(vinyl ferrocene-co-vinyl monomer) with polycondensed aromatic rings of the surface. *J Polym Sci A Polym Chem* 40:1868–1875

Chapter 4

Thermo-Responsive Nanofiber Mats Fabricated by Electrospinning

Hidenori Okuzaki

Abstract Copolymers of *N*-isopropylacrylamide and stearyl acrylate (PNIPA-SAX) with various SA feed ratios ($X = 1\text{--}10$ mol%) were synthesized and electrospun into nanofiber mats. It was found that average diameter of nanofibers electrospun at concentration of 25 % and voltage of 30 kV linearly increased from 165 nm (PNIPA) to 497 nm (PNIPA-SA10) with increasing the SA content. The PNIPA-SAX ($X = 3\text{--}10$ mol%) nanofiber mats were insoluble in water at 25 °C, in which inter-polymer and inter-fiber physical cross-links were formed through hydrophobic interaction of stearyl side-chains. With increasing the temperature from 25 to 40 °C the PNIPA-SA3 nanofiber mat exhibited significant volume contraction of 66 %, while that of a single nanofiber estimated by AFM measurements was found to be 37 %. The results allowed us to conclude that not only swelling-deswelling but also dissociation-association of the nanofibers via hydrophobic interactions were crucially important for the macroscopic volume changes of the nanofiber mats.

Keywords Electrospinning • LCST • Nanofiber • PNIPA • Stearyl acrylate

4.1 Introduction

Poly(*N*-isopropylacrylamide) (PNIPA), a typical thermo-responsive polymer with a lower critical solution temperature (LCST) in water at 32 °C [1], has been paid considerable attention not only from the fundamental viewpoint of thermodynamics and kinetics of phase transition but also for the promising applications in sensors, actuators, drug delivery systems, and cell cultures [2–5], where rapid volume changes of gels are crucially important for the practical use. Since swelling-deswelling of cross-linked gels is caused by collective diffusion of polymer

H. Okuzaki (✉)

Interdisciplinary Graduate School of Medicine and Engineering,
University of Yamanashi, 4-4-37 Takeda, Kofu 400-8511, Japan
e-mail: okuzaki@yamanashi.ac.jp

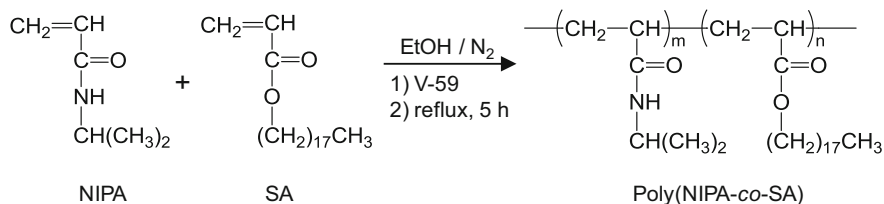
networks in a fluid, the relaxation time (τ) of volume change can be expressed as $\tau = R^2/\pi^2 D$, where R and D are characteristic length of a gel and collective diffusion coefficient of a polymer network, respectively [6, 7]. The equation describes the relaxation time is proportional to the square of the characteristic length of a gel, which clearly demonstrates that downsizing of gels would significantly enhance the rate of volume changes. Lyon et al. [8] synthesized PNIPA nanometer-scaled gel particles and studied on dynamics of swelling-deswelling by using time-resolved transmittance measurements. They found that upon inducing a temperature-jump, deswelling of gel particles occurred on the microsecond time scale. However, individual gel particles are unable to produce macroscopic volume change or detectable stress.

Electrospinning, a facile, inexpensive, and template-free method, which enables fabrication of nanometer-scaled fibers, has been applied to various polymer solutions and melts [9–12], where electrospun nanofibers are directly deposited on a grounded target as a randomly oriented mat. Although PNIPA can be electrospun from various solvents [13, 14], the resulting mats dissolve in water below the LCST, while above the LCST nanofibers unravel and disperse in water, which is ascribed to lacks of inter-polymer and inter-fiber cross-links to keep its shape in the swollen state. Kim et al. fabricated poly(vinyl alcohol) nanofibers by electrospinning of polymer solution containing glyoxal by which subsequent heat treatment formed cross-links between polymer chains [15]. On the other hand, poly(2-hydroxyethyl methacrylate) nanofibers were synthesized via reactive electrospinning process where photoinduced polymerization and cross-linking of polymers took place simultaneously [16]. However, PNIPA has no reactive sites such as hydroxyl groups capable of forming chemical cross-links.

Previously, we have succeeded in fabricating a fast thermo-responsive nanofiber mat of PNIPA copolymerized with stearyl acrylate (SA) [17], which was physically cross-linked via hydrophobic interactions of stearyl side-chains. However, role and effect of hydrophobic interactions of stearyl side-chains on thermal phase transition, electrospinning, and dimensional change of nanofiber mats were not so far investigated systematically. In this chapter, poly(NIPA-*co*-SA)s with various SA contents are newly synthesized and characterized by H^1 NMR, GPC, and thermal phase-transition analyses. Furthermore, morphology and dimensional changes of the electrospun nanofiber mats are also investigated by means of SEM, optical microscope, and AFM techniques.

4.2 Experimental

Poly(NIPA-*co*-SA) was synthesized by free radical copolymerization of *N*-isopropylacrylamide (NIPA, Tokyo Kasei) with stearyl acrylate (SA, Aldrich) used as a hydrophobic monomer bearing a long alkyl chain. The copolymerization was carried out in pure ethanol under reflux for 5 h under a nitrogen bubbling in the presence of 2,2'-azobis(2-methylbutyronitrile) (V-59, Wako) used as an



Scheme 4.1 Synthesis of poly(NIPA-*co*-SA). V-59 denotes 2,2'-azobis(2-methylbutyronitrile) used as an initiator

initiator (Scheme 4.1). After polymerization, the solution was dialyzed in a large amount of ethanol at room temperature for 3 days to remove unreacted monomers and initiator. The copolymer in the solution was precipitated in lukewarm water above the LCST and separated by filtration, washed with the lukewarm water for several times, and then freeze-dried with a freeze dryer (DC400, Yamato). Copolymer composition was evaluated with a ^1H NMR spectrometer (Unity plus-400, Varian) from the ratio of the area at 4.0 ppm (singlet) due to the C-2 proton of isopropyl groups to that at 0.9 ppm (triplet) attributed to the terminal methyl protons of stearyl groups [18]. Molecular weights and polydispersity index were measured with a GPC (UFLC, Shimadzu) using THF as an eluent and calibrated with polystyrene standards. Temperature dependence of transmittance for aqueous solutions of PNIPA and poly(NIPA-*co*-SA) was measured at a wavelength of 500 nm in a temperature range from 7 to 40 °C at 0.2 °C intervals after reaching the equilibrium with a UV-vis-NIR spectrometer (V-670, JASCO) equipped with a Peltier thermostatted cell holder. Prior to the measurement, the 1 wt%-solutions of PNIPA and poly(NIPA-*co*-SA) were centrifuged at 3,000 rpm for 5 min to remove insoluble part and impurities.

Electrospinning was performed on methanol solutions of PNIPA and poly(NIPA-*co*-SA). About 1 mL of the methanol solution was poured into a glass syringe (12 mm in diameter) and DC voltages up to 30 kV were applied to a single-hole spinneret (260 μm in diameter) by a variable high-voltage power supply (HJPQ-30P1, Matsusada). The electrospun fibers were collected on a slide glass (4 \times 2.5 cm) placed on an aluminum-covered grounded flat plate (10 \times 10 cm) where a gap between the spinneret and the target electrode was 20 cm. Diameter of the electrospun nanofibers was measured with a SEM (JSM-6510, JEOL). Thermo-responsive dimensional change of the nanofiber mats (2 cm \times 2 cm \times 20 μm) was measured from 25 to 40 °C at a heating rate of 0.1 °C/min with a digital video camera. AFM images of a single nanofiber electrospun on a Si wafer were measured in pure water with a SPM (SPM-9600, Shimadzu) equipped with a thermostatic solution-cell by a tapping mode at a frequency of 0.2 Hz.

4.3 Results and Discussion

4.3.1 Synthesis and Characterization of PNIPA and PNIPA-SAX

The copolymer composition, molecular weights and polydispersity index of the poly(NIPA-*co*-SA) are listed in Table 4.1, where PNIPA-SAX denotes the poly(NIPA-*co*-SA) copolymer with different SA feed ratios ($X = 1\text{--}10\text{ mol}\%$). It is found that the molar ratios of NIPA to SA evaluated by the ^1H NMR (Y) exceed the monomer feed ratios (X) by 30 % except for PNIPA-SA1 (by 80 %). This indicates that SA units are incorporated into the copolymer preferentially to NIPA units, suggesting a larger reactivity ratio of the SA in comparison with the NIPA indicative of a block-like copolymer [19]. The number-average molecular weight (M_n) is less dependent on the copolymer composition varying between 18,000 and 22,000 g/mol while the weight-average molecular weight (M_w) increases with the SA content, leading to increasing the polydispersity index (M_w/M_n) from 1.48 to 2.33.

Figure 4.1 shows temperature dependence of transmittance for aqueous solutions of PNIPA and PNIPA-SAX. The transmittance of the PNIPA solution drops in a narrow temperature range around 32 °C, corresponding to a LCST, which represents a coil-globule transition of polymer chains (inset) and subsequent aggregation of hydrophobic globules being responsible for the scattering of visible light [20]. An increase of the SA incorporated in the copolymer not only shifts the LCST to lower temperatures but also decreases the sharpness of the temperature-dependent transmittance change. Moreover, the PNIPA-SAX solutions remain turbid even at 7 °C, transmittance of which decreases with the SA content, suggesting a formation of micelle-like aggregates of hydrophobic stearyl side-chains in water that cannot dissociate entirely below the LCST (inset) [18]. Indeed, the aggregate size of the PNIPA-SA3 measured at 15 °C by a light scattering technique was 2–3 μm . A gradual increase of the transmittance above 30 °C for the PNIPA-SAX at $X = 5\text{--}10\text{ mol}\%$ is due to a formation of aggregates being removed from the solution as precipitates.

Table 4.1 Copolymer composition, molecular weights, and polydispersity index of various polymers

Polymer	X ^a (mol%)	Y ^b (mol%)	M _n (g/mol)	M _w (g/mol)	M _w /M _n
PNIPA	0	–	22,100	32,800	1.48
PNIPA-SA1	1	1.8	18,700	35,400	1.89
PNIPA-SA3	3	3.9	18,200	35,200	1.93
PNIPA-SA5	5	6.6	21,500	42,600	1.98
PNIPA-SA8	8	10.1	21,300	45,200	2.12
PNIPA-SA10	10	12.6	21,200	49,400	2.33

^a[SA]/([NIPA] + [SA]) × 100 = n/(m + n) × 100

^bBy ^1H NMR

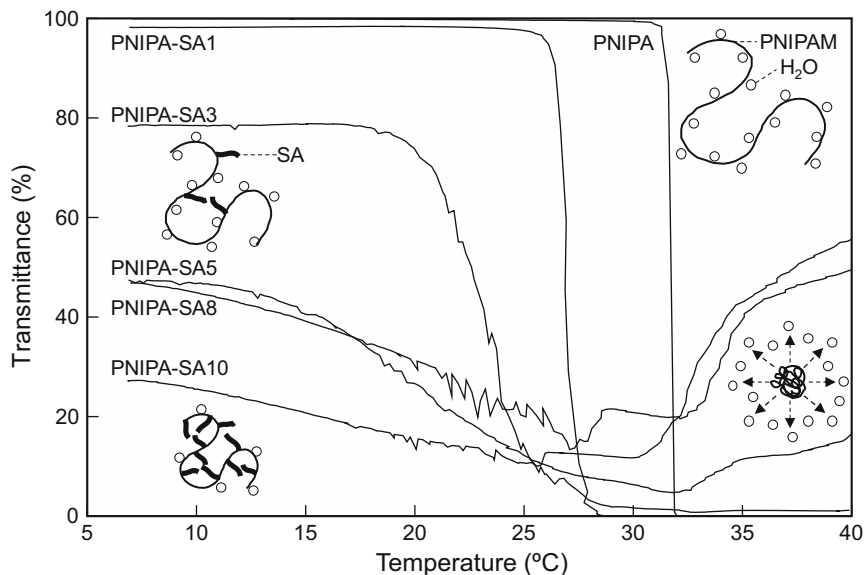


Fig. 4.1 Temperature dependence of transmittance for PNIPA and PNIPA-SAX aqueous solutions (ca. 1 wt%) and schematic illustrations of possible conformational changes of polymers (insets)

4.3.2 Electrospinning and Morphology of PNIPA and PNIPA-SAX

Figure 4.2 shows SEM micrographs of the PNIPA-SA3 electrospun at various concentrations (C) and voltages (E). When the applied voltage reaches a critical value, the electrostatic force overcomes the surface tension of the polymer solution, thereby ejecting a jet from the spinneret. Since the polymer chains and solvent molecules bear the same (positive) charge, they repel each other and the droplets become smaller due to the separation while traveling in air during a few milliseconds from the spinneret to the grounded target. Meanwhile, evaporation of solvent molecules takes place rapidly because the separation of droplets produces high surface area to volume. Consequently, electrospun fibers are directly deposited on the grounded target as a randomly oriented mat. It is seen from Fig. 4.2 at $C = 15\%$ numerous micrometer-sized beads are deposited on the target at E up to 30 kV, which is ascribed to the lack of sufficient entanglements to form a coherent fiber due to the low solution viscosity [13]. The beads and fibers coexist in a C range of 20–25% where the fibers become a major part with increasing the C and/or E , while a further increase of C yields thicker fibers with diameters larger than 1 μm . At $C = 25\%$ and $E = 30\text{ kV}$, we have succeeded in fabricating bead-free fibers with an average diameter of 207 nm. To clarify the role and effect of SA on changes in morphology and fiber diameter, PNIPA and PNIPA-SAX are electrospun at the same conditions ($C = 25\%$ and $E = 30\text{ kV}$) and results are shown in Fig. 4.3.

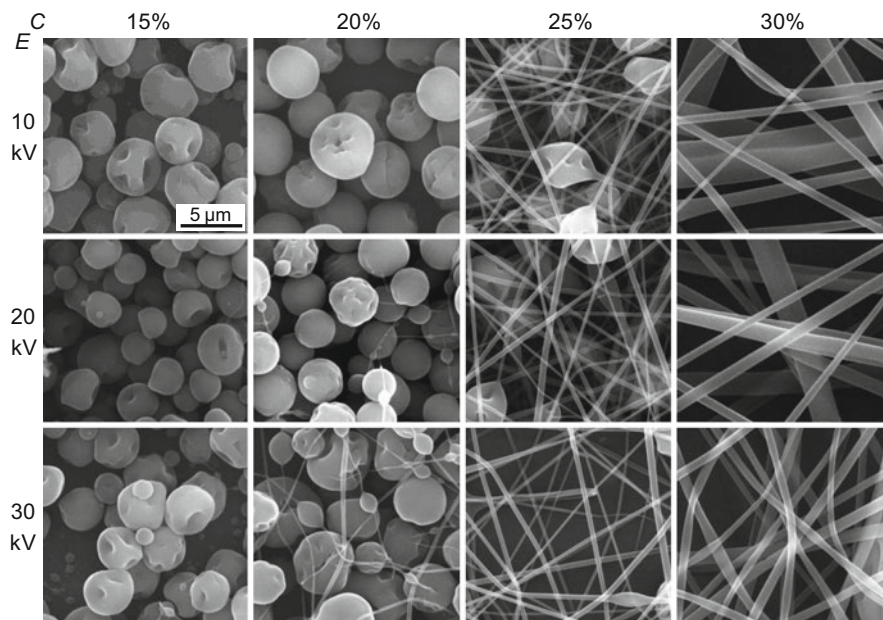


Fig. 4.2 SEM micrographs of PNIPA-SA3 electrospun at various concentrations (C) and voltages (E)

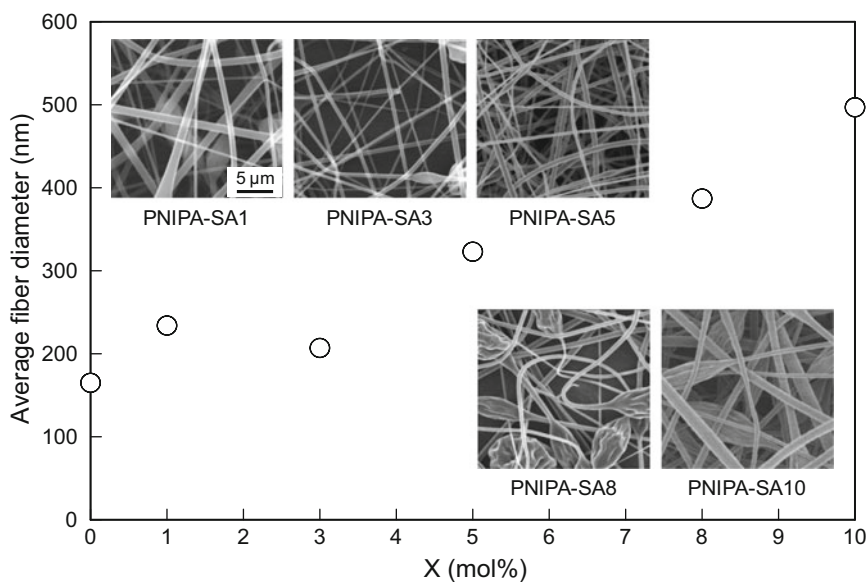


Fig. 4.3 Changes in average fiber diameter and SEM micrograph of nanofiber mats on SA feed ratio (X). The electrospinning was performed at $C = 25$ wt% and $E = 30$ kV

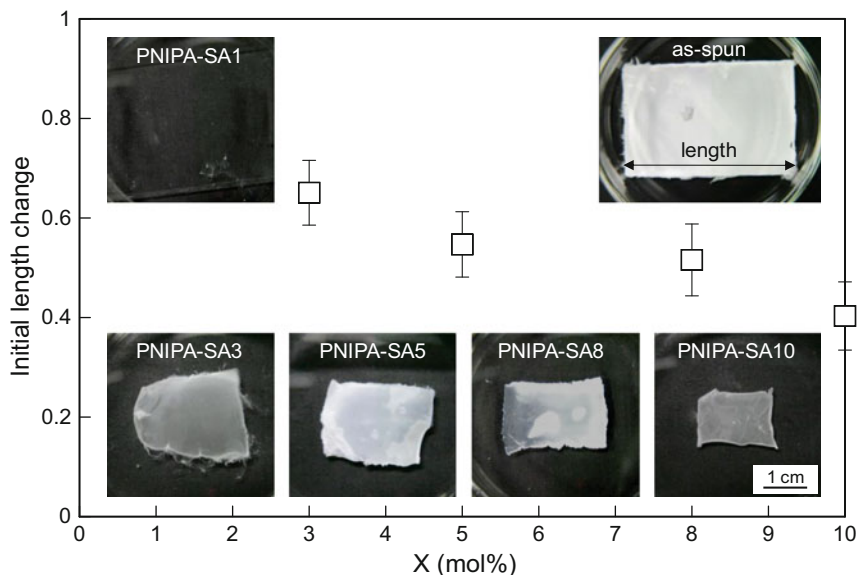


Fig. 4.4 Changes in initial length and optical image of various nanofiber mats ($25 \text{ mm} \times 40 \text{ mm} \times 20 \text{ }\mu\text{m}$) measured in pure water at $25 \text{ }^\circ\text{C}$ on SA feed ratio (X). The electrospinning was performed at $C = 25 \text{ wt}\%$ and $E = 30 \text{ kV}$ for 5 h

It is found that average fiber diameter linearly increases from 165 nm (PNIPA) to 497 nm (PNIPA-SA10), probably due to the increase of the M_w as well as the stearyl side-chains that may enhance inter-chain interactions. Rabolt et al. [14] reported on electrospinning of PNIPA with a higher M_w of 300,000 g/mol from various solvents and found that fiber diameter increased from 400 nm to 17 μm with increasing the concentration from 6 to 18 %. By comparison, the average fiber diameters are much smaller, which may be attributed to the lower molecular weight having less entanglement of polymer chains [21].

4.3.3 Thermo-Response of Nanofiber Mats

The nanofiber mats ($2.5 \text{ cm} \times 4 \text{ cm} \times 20 \text{ }\mu\text{m}$) deposited on glass substrates fabricated by electrospinning at $C = 25 \%$ and $E = 30 \text{ kV}$ for 5 h are immersed in pure water at $25 \text{ }^\circ\text{C}$. As shown in Fig. 4.4, the as-spun PNIPAM and PNIPA-SA1 nanofiber mats dissolve in water at $25 \text{ }^\circ\text{C}$ ($< \text{LCST}$) whereas unravel and disperse in water at $40 \text{ }^\circ\text{C}$ ($> \text{LCST}$), which is ascribed to lacks of inter-polymer and inter-fiber cross-links to keep their shapes in a swollen state [17]. In contrast, the PNIPA-SAX nanofiber mats ($X = 3\text{--}10 \text{ mol}\%$) are insoluble in water at $25 \text{ }^\circ\text{C}$ but spontaneously peel from the substrate, demonstrating that the stearyl side-chains form physical cross-links between polymer chains and nanofibers through

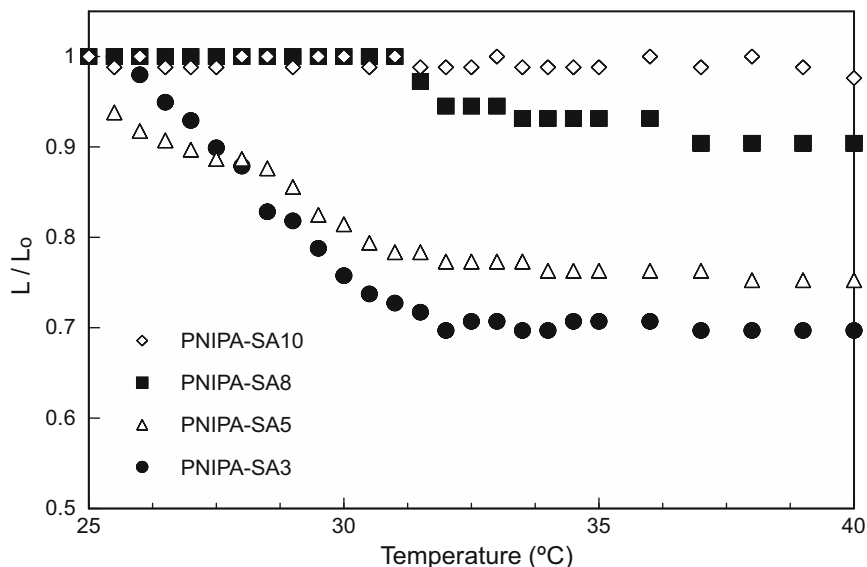


Fig. 4.5 Temperature dependence of relative length change (L/L_0) for various nanofiber mats ($20 \text{ mm} \times 20 \text{ mm} \times 20 \text{ }\mu\text{m}$) measured in pure water from 25 to 40 °C at a heating rate of $0.1 \text{ }^\circ\text{C min}^{-1}$

hydrophobic interactions [22]. It is noted that the nanofiber mats shrink in water, which becomes remarkable with increasing the SA content from 35 % (PNIPA-SA3) to 60 % (PNIPA-SA10) due to surface tension to minimize the surface area, relaxation of inner stress, and/or inter-fiber hydrophobic interaction. Although the SA content varies the diameter of nanofibers and morphology, the nanofiber mats shrink in water rapidly regardless of the SA content. This indicates that the mesh is so loose that water can readily diffuse and penetrate into the mat.

A clear indication of thermo-response of the nanofiber mats is demonstrated in Fig. 4.5. One can see the nanofiber mat of PNIPA-SA3 significantly deswells with increasing the temperature from 25 °C and reaches ca. 70 % of its initial length at temperatures higher than 32 °C, corresponding to volume contraction of 66 % by assuming the isotropic volume change. An increase of the SA content results in a decrease of the relative length change (L/L_0) and thermo-response is no longer observed for the PNIPA-SA10 similarly to the temperature-dependent transmittance (Fig. 4.1), which is ascribed to that the nanofiber mat of the PNIPA-SA10 already shrinks in water at 25 °C through hydrophobic interaction of SA side-chains (Fig. 4.4). In order to evaluate dynamics of thermo-responsive behavior, time-dependent deswelling-swelling of PNIPA-SA3 nanofiber mat is demonstrated in Fig. 4.6. It is well known that deswelling of PNIPA bulk gel becomes very slow after a certain period and it requires a few days to reach the equilibrium state, which is ascribed to the formation of a dense skin layer on the gel surface which strongly hinders diffusion of water [3]. Interestingly, PNIPA-SA3 nanofiber mat exhibits

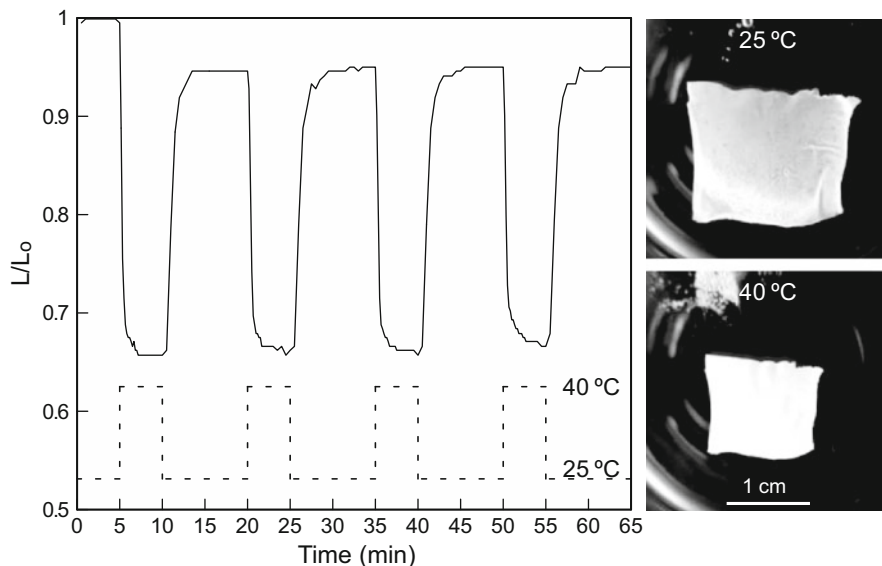


Fig. 4.6 Reversibility and reproducibility of time-dependent deswelling and swelling of PNIPA-SA3 nanofiber mat (20 mm × 20 mm × 20 μm) in pure water between 25 and 40 °C

rapid and significant shrinkage by 34 % of its initial length within 2 min after a jump in temperature from 25 to 40 °C, which suggests no skin layer forms on the surface of the nanofiber and will be discussed later. On the other hand, decreasing the temperature from 40 to 25 °C brings about rapid swelling up to 95 % of the initial length within 4 min and reversible swelling-deswelling was repeated at least 4 times. It is important to note that swelling rate of the nanofiber mat is more than one order of magnitude faster than bulk gels [23] because swelling rate of gels is controlled by diffusion of polymer networks and characteristic size of the gel. In other words, the rapid swelling of the nanofiber mat might be associated with a larger specific surface area of the mat and small diameters of nanometer-scaled fibers fabricated by electrospinning.

To clarify the mechanism of swelling-deswelling of the nanofiber mat in more detail, AFM measurements were performed on a single PNIPA-SA3 nanofiber and results were shown in Fig. 4.7. Since the average diameter of nanofibers in a dry state is 207 nm (Fig. 4.3), the nanofiber with height and width of 187 and 2,520 nm, respectively, in water at 25 °C (a) appears to be in a swollen state, the flat shape of which may result from depression by a cantilever probably due to the low elastic modulus of the nanofiber. It is noted that a rise in the temperature to 40 °C (b) causes significant decrease of width (760 nm) but increase of height (384 nm), indicating the nanofiber shrunk into more stiff cylindrical shape due to deswelling. The volume change of the nanofiber estimated from cross-sectional areas at 25 and 40 °C is ca. 37 % which is nearly half that of the nanofiber mat (66 %) as shown in Fig. 4.5. The fact demonstrates that not only swelling-deswelling but also

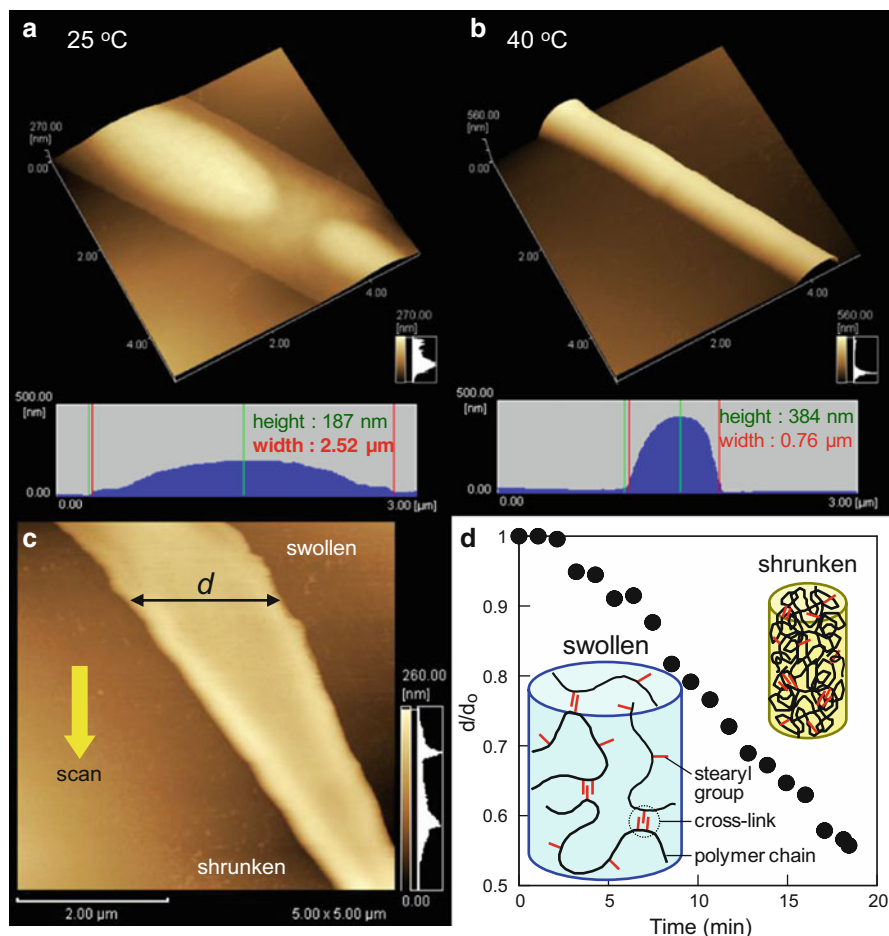


Fig. 4.7 AFM images of a single PNIPA-SA3 nanofiber measured at 25 °C (a) and 40 °C (b) with a thermostatic solution-cell by a tapping mode at a frequency of 0.2 Hz. Note that AFM images of (a) and (b) represent the same area. (c) Temperature-modulated AFM image and (d) time-dependent deswelling of a single PNIPA-SA3 nanofiber measured by a tapping mode at a frequency of 0.2 Hz where solution-cell is heated from 25 to 40 °C when scanning starts

dissociation-association of the nanofibers via hydrophobic interactions are crucially important for the macroscopic volume changes of the nanofiber mat. Furthermore, we have successfully measured for the first time shrinking process of a single nanofiber by means of a temperature-modulated AFM technique where solution-cell is heated from 25 to 40 °C when scanning starts. It is seen from Fig. 4.7c that a nanofiber becomes finer as the scan proceeds (from top to bottom), which reveals deswelling of the nanofiber where formation of bumps around the edges during the deswelling is probably due to the slow heat conduction from the surface to the core of the nanofiber. Figure 4.7d shows time dependence of deswelling evaluated from

a scanning frequency (0.2 Hz). Relatively slow deswelling of the nanofiber is ascribed to sluggish heat conduction through water in the thermostatic solution-cell because stirring of water is not allowed during the AFM measurement. It should be emphasized that deswelling of the nanofiber takes place linearly with elapse of time, which strongly suggests no skin layer forms on the surface of the nanofiber. Shibayama and coworkers [24] investigated shrinking kinetics of PNIPA gels by means of small-angle neutron scattering coupled with static/dynamic light scattering. They found that skin formation plays a major role in slow shrinking kinetics and evaluated thickness of skin layer to be ca. 3 μm . By comparison with the thickness of the skin layer, the diameters of PNIPA-SA3 nanofibers in the swollen state are smaller, which evidently indicates that nanofiber transforms directly from a swollen state to a shrunk state without formation of a skin layer that significantly slows down the rate of deswelling.

4.4 Conclusions

In conclusion, the thermo-responsive dimensional changes of poly(NIPA-co-SA) nanofiber mats originate from the swelling-deswelling of the nanofibers and their dissociation-association through hydrophobic interactions, where the SA content strongly affects the thermo-responsive volume change of the nanofiber mats. Furthermore, it is worthy to note that (1) the LCST of polymers can be tuned by choosing alkyl chain-length of hydrophobic monomer and its composition and (2) not only morphology of mat but also fiber diameter can be controlled by electrospinning conditions, which will open up a new field of applications to fast thermo-responsive actuators or drug delivery systems.

References

1. Heskins M, Guillet JE (1968) Solution properties of poly(*N*-isopropylacrylamide). *J Macromol Sci Chem* 2:1441–1455
2. Kumoda M, Takeoka Y, Watanabe M (2003) Template synthesis of poly(*N*-isopropylacrylamide) minigels using interconnecting macroporous polystyrene. *Langmuir* 19:525–528
3. Yoshida R, Uchida K, Kaneko Y, Sakai K, Kikuchi A, Sakurai Y, Okano T (1995) Comb-type grafted hydrogels with rapid deswelling response to temperature changes. *Nature* 374:240–242
4. Yoshida R, Sakai K, Okano T, Sakurai Y (1993) Pulsatile drug delivery systems using hydrogels. *Adv Drug Delivery Rev* 11:85–108
5. Yamato N, Akiyama Y, Kobayashi J, Yang J, Kikuchi A, Okano T (2007) Temperature-responsive cell culture surfaces for regenerative medicine with cell sheet engineering. *Prog Polym Sci* 32:1123–1133
6. Tanaka T, Fillmore DJ (1979) Kinetics of swelling of gels. *J Chem Phys* 70:1214–1218
7. Tanaka T, Sato E, Hirokawa Y, Hirotsu S, Peetermans J (1985) Critical kinetics of volume phase transition of gels. *Phys Rev Lett* 55:2455–2458

8. Wang J, Gan D, Lyon LA, El-Sayed MA (2001) Temperature-jump investigations of the kinetics of hydrogel nanoparticle volume phase transitions. *J Am Chem Soc* 123:11284–11289
9. Reneker DH, Chun I (1996) Nanometre diameter fibres of polymer, produced by electrospinning. *Nanotechnology* 7:216–223
10. MacDiarmid AG, Jones WE Jr, Norris ID, Gao J, Johnson AT Jr, Pinto NJ, Hone J, Han B, Ko FK, Okuzaki H, Llaguno M (2001) Electrically-generated nanofibers of electronic polymers. *Synth Met* 119:27–30
11. Okuzaki H, Takahashi T, Miyajima N, Suzuki Y, Kuwabara T (2006) Spontaneous formation of poly(*p*-phenylenevinylene) nanofiber yarns through electrospinning of a precursor. *Macromolecules* 39:4276–4278
12. Okuzaki H, Takahashi T, Hara Y, Yan H (2008) Uniaxially aligned carbon nanofibers derived from electrospun precursor yarns. *J Polym Sci Polym Phys* 46:305–310
13. Okuzaki H, Kobayashi K, Yan H (2009) Non-woven fabric of poly(*N*-isopropylacrylamide) nanofibers fabricated by electrospinning. *Synth Met* 159:2273–2276
14. Rockwood DN, Chase DB, Akins RE Jr, Rabolt JF (2008) Characterization of electrospun poly(*N*-isopropyl acrylamide) fibers. *Polymer* 49:4025–4032
15. Ding B, Kim H-Y, Lee S-C, Shao C-L, Lee D-R, Park S-J, Kwang G-B, Choi K-J (2002) Preparation and characterization of a nanoscale poly(vinyl alcohol) fiber aggregate produced by an electrospinning method. *J Polym Sci Polym Phys* 40:1261–1268
16. Kim SH, Kim S-H, Nair S, Moore E (2005) Reactive electrospinning of cross-linked poly(2-hydroxyethylmethacrylate) nanofibers and elastic properties of individual hydrogel nanofibers in aqueous solutions. *Macromolecules* 38:3719–3723
17. Okuzaki H, Kobayashi K, Yan H (2009) Thermo-responsive nanofiber mats. *Macromolecules* 42:5916–5918
18. Ringsdorf H, Venzmer J, Winnik FM (1991) Fluorescence studies of hydrophobically modified poly(*N*-isopropylacrylamide). *Macromolecules* 24:1678–1686
19. Matsuda A, Sato J, Yasunaga H, Osada Y (1994) Order–disorder transition of a hydrogel containing an *n*-alkyl acrylate. *Macromolecules* 27:7695–7698
20. Fujishige S, Kubota K, Ando I (1989) Phase transition of aqueous solution of poly(*N*-isopropylacrylamide) and poly(*N*-isopropylmethacrylamide). *J Phys Chem* 93:3311–3313
21. Lyons J, Li C, Ko F (2004) Melt-electrospinning part I: processing parameters and geometric properties. *Polymer* 45:7597–7603
22. Osada Y, Matsuda A (1995) Shape memory in hydrogels. *Nature* 376:219
23. Okeyoshi K, Abe T, Noguchi Y, Furukawa H, Yoshida R (2008) Shrinking behavior of surfactant-grafted thermosensitive gels and the mechanism of rapid shrinking. *Macromol Rapid Commun* 29:897–903
24. Norisuye T, Kida Y, Masui N, Tran-Cong-Miyata Q, Maekawa Y, Yoshida M, Shibayama M (2003) Studies on two types of built-in inhomogeneities for polymer gels: frozen segmental concentration fluctuations and spatial distribution of cross-links. *Macromolecules* 36:6202–6212

Chapter 5

Self-Oscillating Gels

Ryo Yoshida

Abstract Stimuli-responsive polymer gels and their application to smart materials have been widely studied. On the other hand, as a novel biomimetic gel, we developed gels with an autonomous self-oscillating function like a heart muscle, which was firstly reported in 1996. We designed the self-oscillating gels by utilizing the oscillating reaction, called the Belousov-Zhabotinsky (BZ) reaction which is recognized as a chemical model of the TCA cycle in organisms. The self-oscillating gel is composed of a poly(*N*-isopropylacrylamide) network in which the metal catalyst for the BZ reaction is covalently bonded. In a closed solution containing the reactants other than the catalyst, the gel undergoes spontaneous cyclic swelling–deswelling changes without any on–off switching of external stimuli. Their potential applications include several kinds of functional material systems, such as biomimetic soft-actuators and autonomous mass transport systems. Here recent progress on the novel polymer gels is introduced.

Keywords Biomimetic actuators • BZ reaction • Polymer gels • Self-oscillation

5.1 Introduction

As mentioned in the other chapters, many kinds of stimuli-responsive polymers and gels and their applications to soft actuators (artificial muscles) inspired by living systems have been studied. Other than stimuli-responsive function, one of characteristic and important behaviors in living systems is autonomous oscillation, that is, spontaneous changes with temporal periodicity (called “temporal structure”) such as heartbeat, brain waves, pulsatile secretion of hormone, cell cycle, and biorhythm. However, there are few studies on polymer and gel systems undergoing self-oscillation under constant condition without any on-off switching of external stimuli. If such autonomous systems can be realized by using completely synthetic polymers, unprecedented biomimetic materials may be created.

R. Yoshida (✉)

Department of Materials Engineering, School of Engineering,
The University of Tokyo, 7-3-1 Hongo, Bunkyo-ku, Tokyo 113-8656, Japan
e-mail: ryo@cross.t.u-tokyo.ac.jp

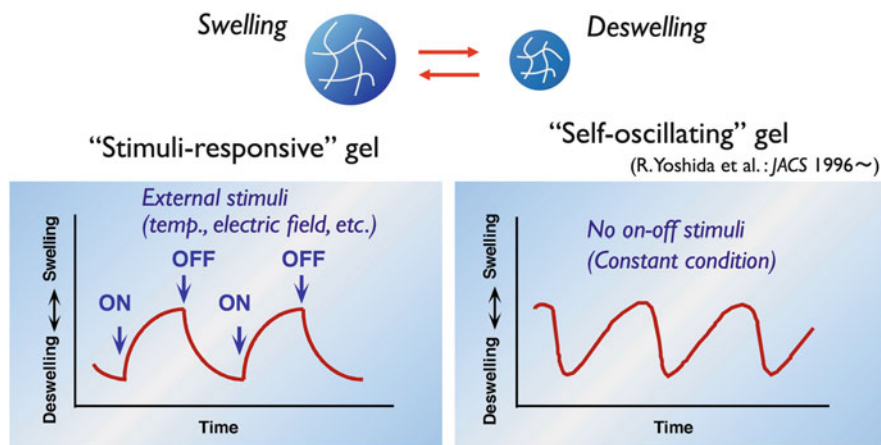


Fig. 5.1 Stimuli-responsive and self-oscillating gels

From this viewpoint, we have studied polymer gels with autonomous function. As one method, we designed a coupling system of pH responsive gel and pH-oscillating reaction. By soaking pH-responsive gels in a solution of pH-oscillating reaction in a continuous stirred tank reactor (CSTR), autonomous and periodic swelling-deswelling changes of the gel were realized [1, 2]. In this system, however, oscillating outer solution is created by CSTR and swelling-deswelling changes of the gel occur in response to the oscillating outer condition. Therefore, we attempted to develop a novel gel that provides mechanical oscillation by itself without external control in a complete closed and non-oscillating outer solution. We succeeded in developing such a self-oscillating polymer and gels by incorporating oscillating chemical reaction in polymer network, i.e., by constructing built-in circuit of energy conversion cycle producing mechanical oscillation within polymer network itself. In contrast to conventional stimuli-responsive gels, we have developed “self-oscillating” polymer gels that autonomously undergo periodic swelling/deswelling oscillation without on-off switching of external stimuli in a closed solution (Fig. 5.1).

5.2 Design of Self-Oscillating Polymer Gel

5.2.1 Oscillating Chemical Reaction: The Belousov-Zhabotinsky Reaction

For the design of such a gel, the Belousov-Zhabotinsky (BZ) reaction [3–6], which is well-known as an oscillating reaction which spontaneously exhibits temporal rhythm and spatial pattern, was focused. The overall process is the oxidation of an organic substrate, such as malonic acid (MA) or citric acid, by an oxidizing agent

(typically bromate ion) in the presence of a catalyst under acidic condition. Metal ions or metal complexes with high redox potentials (1.0–1.4 V/SHE), such as cerium ion, ferroin, or ruthenium tris(2,2'-bipyridine) ($\text{Ru}(\text{bpy})_3^{2+}$) are widely used as catalysts. While the reaction proceeds, the catalyst undergoes spontaneous redox oscillation, showing periodical changes in color of the solution under stirring condition and concentric or spiral wave patterns under stationary condition. The wave of oxidized state propagating in the medium is called a “chemical wave”. The understanding of the BZ reaction in terms of the Field-Körös-Noyes (FKN) mechanism [5] allows us to divide the overall reaction into three main processes: consumption of Br^- ions (process A), autocatalytic formation of HBrO_2 accompanying oxidation of catalyst (process B), and formation of Br^- ions accompanying reduction of catalyst (process C). These processes proceed cyclically with the arrow of time; $\text{A} \rightarrow \text{B} \rightarrow \text{C} \rightarrow \text{A} \rightarrow \dots$. The elementary reactions which constitute each process have been elucidated by many researchers. The BZ reaction is often analogically compared with the TCA cycle which is a key metabolic process taking place in the living body, and it is recognized as a chemical model for understanding several autonomous phenomena in biological systems.

5.2.2 Mechanism of Self-Oscillation

We attempted to convert the chemical oscillation of the BZ reaction into a mechanical change in gels and generate an autonomous swelling-deswelling oscillation under non-oscillatory outer conditions. For this purpose, we prepared the gel composed of poly(*N*-isopropylacrylamide) (PNIPAAm) and $\text{Ru}(\text{bpy})_3$ which is covalently bonded to the PNIPAAm network (Fig. 5.2). When the poly(NIPAAm-*co*- $\text{Ru}(\text{bpy})_3$) gel is immersed in the catalyst-free BZ solution containing the substrates (MA, NaBrO_3 and nitric acid), the reaction occurs in the gel by the catalytic function of the polymerized $\text{Ru}(\text{bpy})_3$. The redox changes of the polymerized catalyst moiety ($\text{Ru}(\text{bpy})_3^{2+} \rightleftharpoons \text{Ru}(\text{bpy})_3^{3+}$) change the volume phase transition temperature of the gel as well as the swelling ratio because the hydrophilicity of the polymer chains increases at the oxidized Ru(III) state and decreases at the reduced Ru(II) state. As a result, the gel exhibits an autonomous swelling-deswelling oscillation with the redox oscillation in the closed solution under constant condition. We reported the “self-oscillating” gel in 1996 for the first time [7], and since then we have developed many kinds of biomimetic or smart material systems (Fig. 5.3) [8–44].

5.2.3 Self-Oscillating Behavior on Several Scales

The self-oscillation can be induced on several scales from the order of polymer chain to bulk gel (Fig. 5.4). In the case of the uncrosslinked linear polymer, the polymer solution exhibits self-oscillations of optical transmittance and viscosity

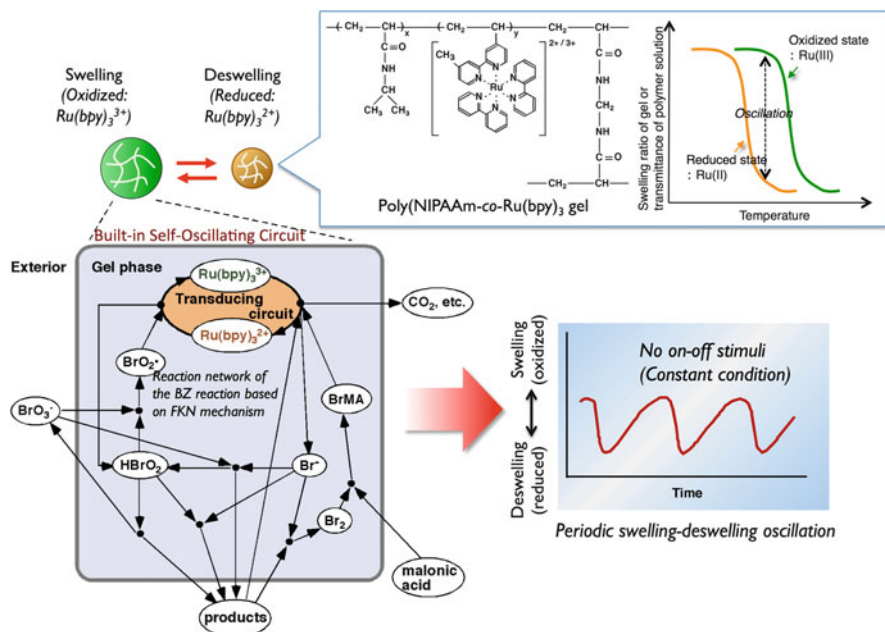


Fig. 5.2 Design concept of self-oscillating gel by using the BZ reaction

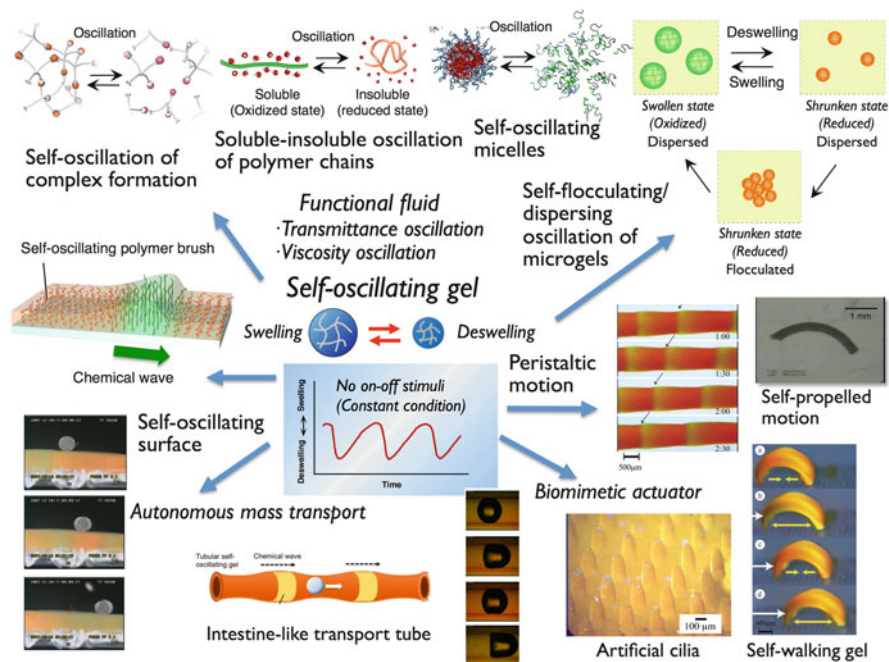


Fig. 5.3 Evolution of the self-oscillating polymer gels

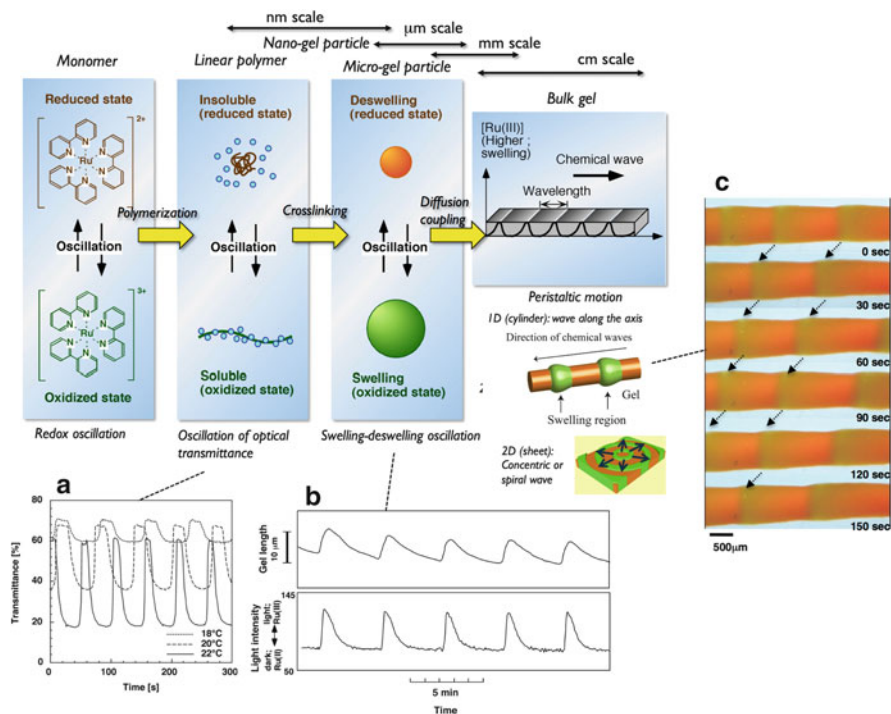


Fig. 5.4 Self-oscillation on several scales. **(a)** Self-oscillating profiles of optical transmittance for poly(NIPAAm-co-Ru(bpy)₃) solution. **(b)** Periodic redox changes of the miniature cubic poly(NIPAAm-co-Ru(bpy)₃) gel (*lower*) and the swelling-deswelling oscillation (*upper*) at 20 °C. Color changes of the gel accompanied by redox oscillations (*orange*: reduced state, *light green*: the oxidized state) were converted to 8-bit grayscale changes (*dark*: reduced, *light*: oxidized) by image processing. Transmitted light intensity is expressed as an 8-bit grayscale value. **(c)** Time course of peristaltic motion of poly(NIPAAm-co-Ru(bpy)₃-co-AMPS) gel in a solution of the BZ substrates at 18 °C. The *green* and *orange* colors correspond to the oxidized and reduced states of the Ru moiety in the gel, respectively

due to spontaneous cyclic soluble-insoluble changes of the polymer (Fig. 5.4a). When the gel is much smaller than chemical wavelength, redox changes occur homogeneously in the gel without pattern formation [9]. Then the swelling-deswelling change of the gel becomes isotropic (Fig. 5.4b). On the other hand, when the gel size is larger, chemical waves spontaneously evolve and propagate in the gel by coupling with diffusion of intermediates [10–12]. Then peristaltic motion of the gel is created. Figure 5.4c shows time course of peristaltic motion of the cylindrical gel in a solution of the BZ substrates [10]. The green and orange colors correspond to the oxidized and reduced states of the Ru moiety in the gel, respectively. The chemical waves propagate in the gel at a constant speed in the direction of the gel length. Considering the orange (Ru(II)) and green (Ru(III)) zones represent simply the shrunken and swollen parts respectively, the locally swollen and shrunken parts move with the chemical wave, like the peristaltic motion of living worm or intestine.

5.3 Control of Self-Oscillating Chemomechanical Behaviors

5.3.1 Concentration and Temperature Dependence of Oscillation

Oscillating behavior of the BZ reaction changes depending on concentration and temperature as characteristics of chemical reaction. Typically, the oscillation period increases with a decrease in the initial concentration of substrates. Further, in general, the oscillation frequency (the reciprocal of the period) of the BZ reaction tends to increase as the temperature increases, in accordance with the Arrhenius equation. The swelling-deswelling amplitude of the gel increases with an increase in the oscillation period and amplitude of the redox potential changes [9]. Therefore the swelling-deswelling amplitude of the gel is controllable by changing the initial concentration of substrates as well as temperature.

5.3.2 On-Off Regulation of Self-Oscillation by External Stimuli

Further, on-off regulation of the self-oscillation by external stimuli such as temperature change [13], addition and removal of organic acid [14], photo-irradiation is possible [15–17]. In particular, Ru(bpy)₃ has photo-sensitivity at the reduced state. By photo-irradiation, it creates the other reaction pathway to stop or cause the oscillation by producing an intermediate to act as an inhibitor (Br⁻) or an activator (HBrO₂), depending on the composition of the BZ solution [6]. By utilizing such photochemical characteristics of the BZ reaction, photo-regulation of self-oscillating motion of the gel was experimentally demonstrated [15, 16]. Balazs et al. [45, 46] theoretically demonstrated light-guided motility of the gel by model simulation.

In this photo-regulation system utilizing the photo-sensitivity of Ru(bpy)₃, there is no difference in hydrated state of the polymer chains (consequently swelling state of the gel) between photo-irradiated and non-irradiated conditions. On the other hand, we design photo-regulated self-oscillating systems based on hydration and dehydration change of the polymer by photo-irradiation. For this purpose, spirobenzopyran (Sp) was introduced into the poly(NIPAAm-co-Ru(bpy)₃) as a photochromic site [17]. Even under acidic condition necessary for the BZ reaction, photochromism of the spirobenzopyran occurs and the lower critical solution temperature (LCST) of the polymer solution shifts to lower temperature with isomerization from McH to Sp by photo-irradiation. As a result, on-off switching of the soluble-insoluble self-oscillation for the polymer solution is possible by photo-irradiation. Theoretical simulation of chemomechanical behaviors corresponding to this photoregulation system is also demonstrated [47].

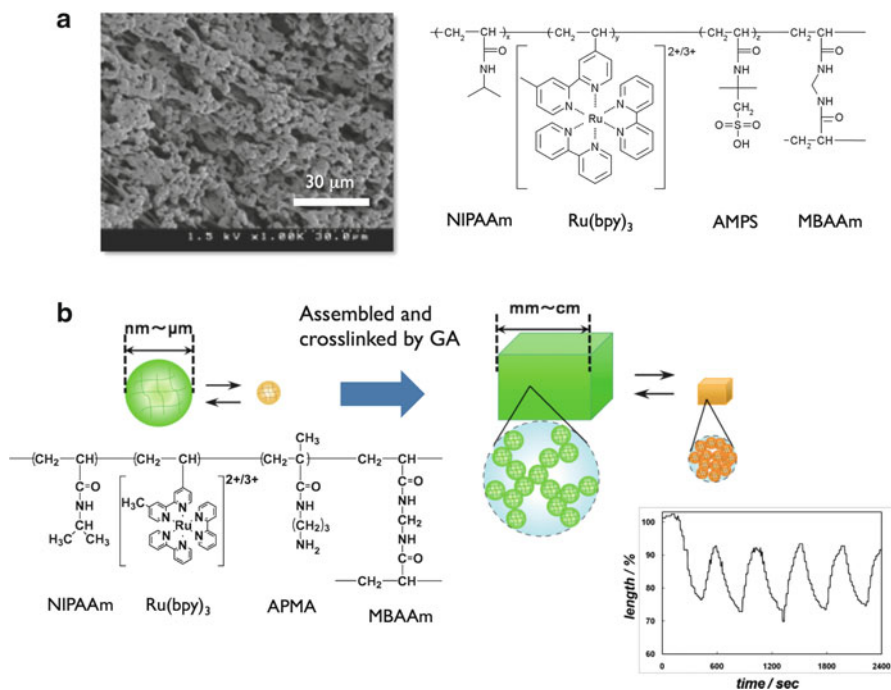


Fig. 5.5 Control of interior morphology of gels for fast response and increasing swelling-deswelling amplitude. (a) Microgel-aggregated gel structure formed by solvent effect. Chemical structure of poly(NIPAAm-co-Ru(bpy)₃-co-AMPS) gel (right) and the SEM photograph of the gel (left). (b) Crosslinking after assembling gel particles prepared by precipitation polymerization

5.3.3 Control of Self-Oscillating Behaviors by Designing Chemical Structure of Gel

The self-oscillating behaviors can also be controlled by designing chemical and physical structures of the gels. There are several variations of the gels with different chemical components. For example, it was found to be effective to copolymerize 2-acrylamido-2'-methylpropanesulfonic acid (AMPS) to a poly(NIPAAm-co-Ru(bpy)₃) gel network to generate a large amplitude of volume change of the gel because the gel had a microphase-separated structure due to the effect of the poor solvent in the polymerization process (Fig. 5.5a) [18].

The operating conditions for the self-oscillation are limited to conditions under which the BZ reaction occurs. For potential applications as functional bio- or biomimetic materials, it is necessary to design a self-oscillating polymer which acts under biological environments. To induce self-oscillation of polymer systems under physiological conditions, BZ substrates other than organic ones (MA, citric acid, etc.) must be built into the polymer system itself. For this purpose, we have synthesized a quarternary copolymer which includes both pH-control and oxidant-

supplying sites in the poly(NIPAAm-*co*-Ru(bpy)₃) chain at the same time [19]. By using this polymer, self-oscillation by adding only the organic acid (i.e., MA) was actually observed.

In order to induce self-oscillation while maintaining a larger amplitude at higher temperatures and around body temperature for potential applications to biomaterials, etc., we prepared a self-oscillating gel composed of a thermosensitive *N,N'*-ethylmethacrylamide (EMAAM) polymer exhibiting a higher LCST than that of PNIPAAm [20]. The self-oscillating behavior of the poly(EMAAM-*co*-Ru(bpy)₃) gel was investigated by comparing against gels composed of a thermosensitive NIPAAm polymer with a lower LCST or non-thermosensitive *N,N'*-dimethylacrylamide (DMAAM) polymer. The design concept of self-oscillation at higher temperatures without a decrease in swelling-deswelling amplitude was demonstrated by utilizing a thermosensitive polymer exhibiting a higher LCST.

5.3.4 Remarkable Swelling-Deswelling Changes by Assembled Self-Oscillating Microgels

Typically, there are several strategies to improve the response of gels, such as introducing porous microstructures, decreasing the size of the gels. And also, in a living muscle, there exists hierarchical structure to amplify the microscopic movements of actin-myosin to macroscopic displacements. Such a hierarchical structure was introduced into the self-oscillating gel to get large amplitude of swelling/deswelling oscillation [21]. The soft actuators assembled from self-oscillating sub-micron-sized particles (microgels) were fabricated (Fig. 5.5b). Firstly, the microgels composed of NIPAAm, Ru(bpy)₃ and *N*-(3-aminopropyl) methacrylamide hydrochloride (APMA) were prepared by aqueous free radical precipitation polymerization. Then the microgels were assembled and crosslinked by using the glutaric dialdehyde to induce a chemical reaction between the amino groups located on microgel exterior. The resulting macrogels exhibited large displacements due to cooperative dispersing/flocculating motion of constituent microelements.

5.3.5 Comb-Type Self-Oscillating Gel

Further, as another method to improve the response of gels, it is effective to introduce grafted side chains with freely mobile ends on the backbone networks of gels. For example, it was demonstrated that the comb-type grafted PNIPAAm gels exhibited a fast deswelling response to temperature change by the guiding effect of hydrophobic interaction between side chains that have freely mobile ends [48, 49]. These network-arranged designs are expected to be applicable for improving the swelling/deswelling kinetics to the redox change in the self-oscillating gel.

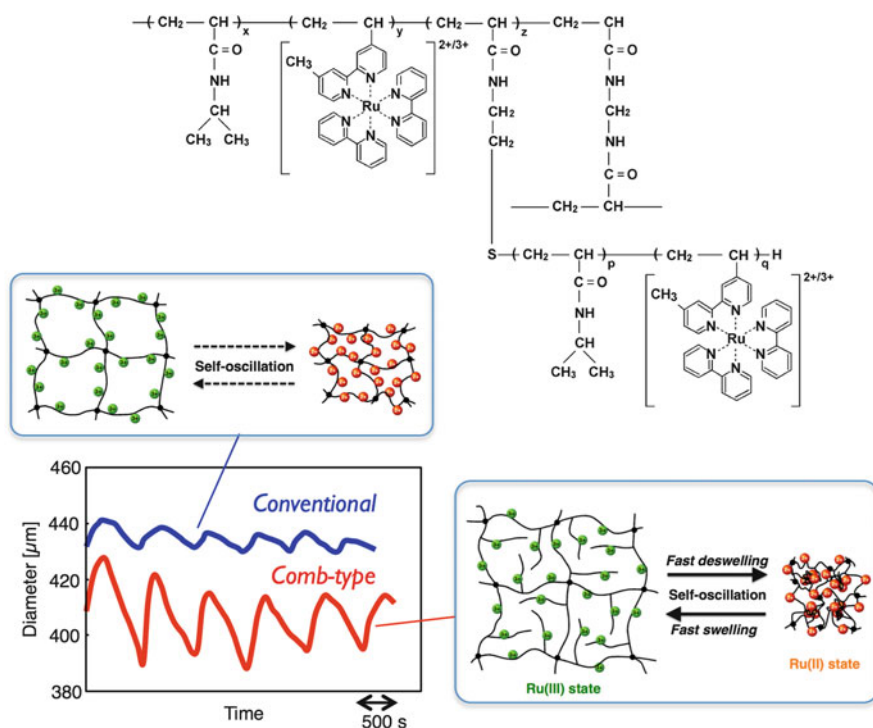


Fig. 5.6 Chemical structure of comb-type poly(NIPAAm-co-Ru(bpy)₃)-grafted poly(NIPAAm-co-Ru(bpy)₃) gel and self-oscillating behaviors for conventional poly(NIPAAm-co-Ru(bpy)₃) gel and the comb-type gel at 20 °C in the BZ substrate solution containing NaBrO₃, MA, and HNO₃

We designed a novel comb-type self-oscillating gel that has Ru(bpy)₃ on both the main and side chains (Fig. 5.6) [22]. Different from the conventional type of self-oscillating gel in which Ru(bpy)₃ is immobilized only on main chains, faster swelling/deswelling changes are obtained because the grafted side chains with freely mobile ends can respond to the redox change of Ru(bpy)₃ more quickly than the main chains. As a result, self-oscillation with a larger swelling-deswelling amplitude was achieved.

5.4 Design of Biomimetic Soft-Actuators

5.4.1 Ciliary Motion Actuator Using Self-Oscillating Gel (Artificial Cilia)

By utilizing such swelling-deswelling oscillation of the gel, novel biomimetic actuators may be created. As applications to autonomous biomimetic actuators, ciliary motion actuators (artificial cilia) [23, 24] and self-walking gels [25], etc.

were realized. Recently, microfabrication technologies such as photolithography are also attempted for preparation of microgels. Since any shape of gel can be created by these methods, application as a new manufacturing method for soft microactuator, microgel valve, gel display, etc. is expected. One of the promising fields of the MEMS is micro actuator array or distributed actuator systems. The actuators, which have a very simple actuation motion such as up and down motion, are arranged in an array form. If their motions are random, no work is extracted from this array. However, by controlling them to operate in a certain order, they can generate work as a system. A typical example of this kind of actuation array is a ciliary motion micro actuator array. There have been many reports on this system. Although various actuation principles have been proposed, all the previous work is based on the concept that the motion of actuators is controlled by external signals. If a self-oscillating gel plate with a micro projection structure array on top were realized, it would be expected that the chemical wave propagation would create dynamic rhythmic motion of the structure array. This proposed structure could exhibit spontaneous dynamic propagating oscillation producing a ciliary motion array [23, 24].

A gel plate with micro projection array was fabricated by molding. First, moving mask deep-X-ray lithography was utilized to fabricate a PMMA plate with a truncated conical shape microstructure array. This step was followed by evaporation of a Au seed layer and subsequent electroplating of nickel to form the metal mold structure. Then, a PDMS mold structure was duplicated from the Ni structure and utilized for gel molding. The formation of gel was carried out by vacuum injection molding. A structure with a height of 300 μm and bottom diameter of 100 μm was successfully fabricated by the described process (Fig. 5.7). The propagation of chemical reaction wave and dynamic rhythmic motion of the micro projection array were confirmed by chemical wave observation and displacement measurements. Motion of the top with 5 μm range in both lateral and vertical directions, and elliptical motion of the projection top were observed. The feasibility of the new concept of the ciliary motion actuator made of self-oscillating polymer gel was successfully confirmed. The actuator may serve as a micro-conveyer to transport objects on the surface.

5.4.2 Self-Walking Gel

Further, we successfully developed a novel biomimetic walking-gel actuator made of self-oscillating gel [25]. To produce directional movement of gel, asymmetrical swelling-deswelling is desired. For these purposes, as a third component, hydrophilic 2-acrylamido-2'-methylpropanesulfonic acid (AMPS) was copolymerized into the polymer to lubricate the gel and to cause anisotropic contraction. During polymerization, the monomer solution faces two different surfaces of plates; a hydrophilic glass surface and a hydrophobic Teflon surface. As the thickness of the spacer is thin (0.5 mm), the surface property of the plate may affect the

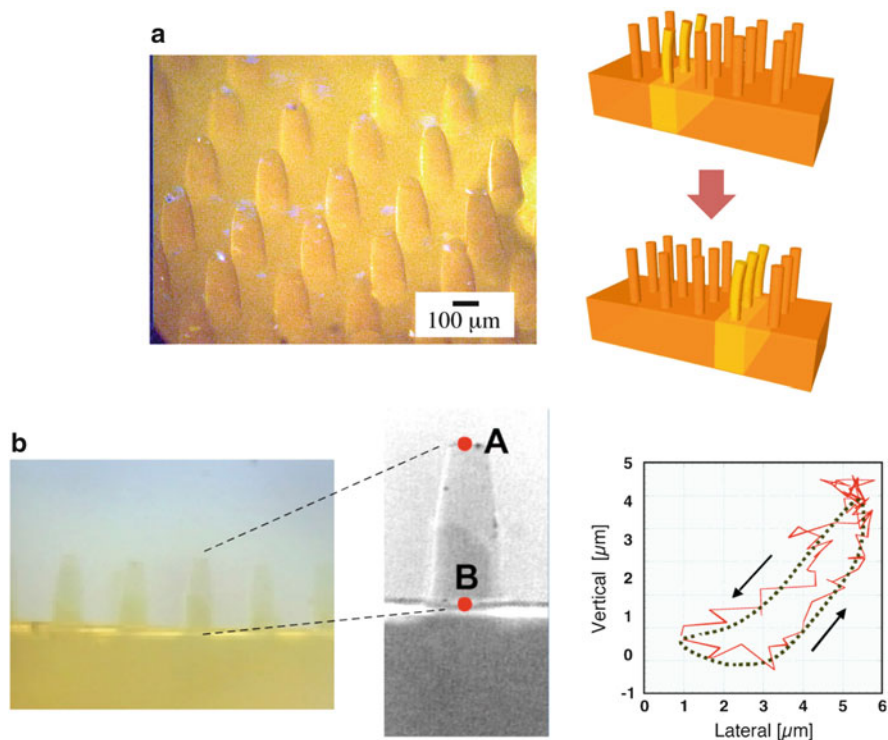


Fig. 5.7 Ciliary motion actuator (artificial cilia) using self-oscillating gel. (a) Poly(NIPAAm-co-Ru(bpy)₃) gel with micro projection structure array on the surface. (b) Cross-sectional view of the micro projection and measured motion of the projection top

distribution of the monomer in the solution. Since Ru(bpy)₃²⁺ monomer is hydrophobic, it easily migrates to the Teflon surface side. As a result, a non-uniform distribution along the height is formed by the components, and the resulting gel has gradient distribution for the content of each component in the polymer network.

In order to convert the bending and stretching changes to one-directional motion, we employed a ratchet mechanism. A ratchet base with an asymmetrical surface structure was fabricated. On the ratchet base, the gel repeatedly bends and stretches autonomously. Figure 5.8 shows successive profiles of the “self-walking” motion of the gel like a looper in the BZ substrate solution under constant temperature. During stretching, the front edge can slide forward on the base, but the rear edge is prevented from sliding backwards. Oppositely, during bending, the front edge is prevented from sliding backwards while the rear edge can slide forward. This action is repeated, and as a result, the gel walks forward. The walking velocity of the gel actuator was approximately 170 μm/min. Since the oscillating period and the propagating velocity of chemical wave change with concentration of substrates in the outer solution, the walking velocity of the gel can be controlled. By using the gel with gradient structure, other type of actuator which generates a pendulum motion is also realized [26].

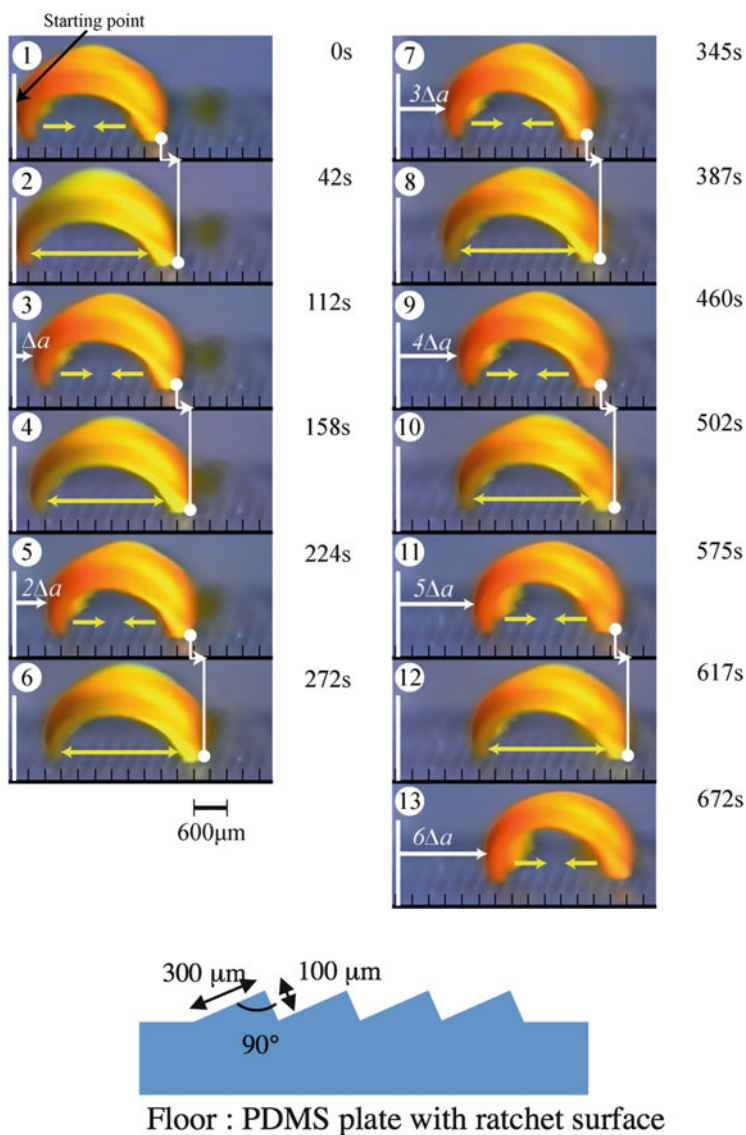


Fig. 5.8 Time course of self-walking motion of the gel actuator in a solution of the BZ substrates at 18 °C. During stretching, the front edge can slide forward on the base, but the rear edge is prevented from sliding backwards. Oppositely, during bending, the front edge is prevented from sliding backwards while the rear edge can slide forward. This action is repeated, and as a result, the gel walks forward

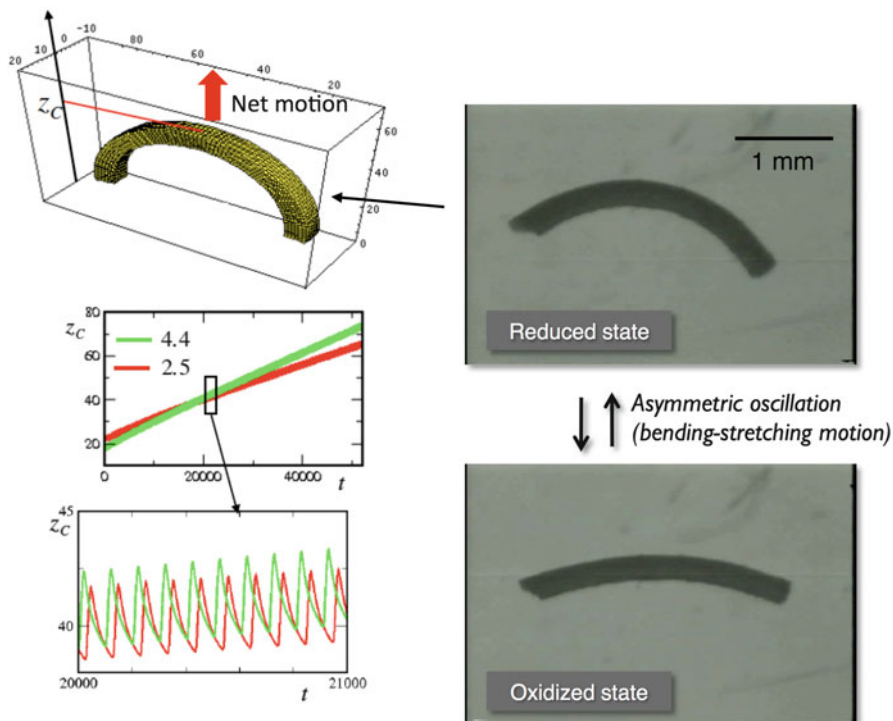


Fig. 5.9 Self-propelled motion of the self-oscillating gel. *Right*: The self-oscillating bending-stretching behaviors of the gel with a gradient in the cross-link density prepared by photo-polymerization. *Left*: The theoretical simulation. Time evolution of the z -coordinates of the centers of the samples, z_c

5.4.3 Self-Propelled Motion

Further, self-propelled motion of gels was theoretically demonstrated and experimentally realized by utilizing the gels [27]. The cylindrical self-oscillating gel with a gradient in crosslinking density was prepared by photo-polymerization. To introduce gradient structure, during the gelation, light was irradiated from one side to the pre-gel solution in a glass capillary. The resulting gel has denser crosslinking at the photo-irradiated side, and bends to the direction at the reduced state. In the catalyst-free BZ solution, the gel repeated bending and stretching motion, and the position of the center of the gel apparently shifts slowly upwards (towards the region with lower cross-link density) (Fig. 5.9).

Control of the motion by preparing a composite gel made of self-oscillating and non-active gels was also attempted [28]. For this purpose, heterogeneous BZ gel was prepared. The disk-shaped self-oscillating gels were arranged around the corners of a polygonal sheet of poly(acrylamide) (PAAm) gel. Wave propagation was controlled by changing the patch size, catalyst content of the BZ gel, and spacing between the patches.

5.4.4 Theoretical Simulation of the Self-Oscillating Gel

The self-oscillating gels construct provides unique material systems which contain reaction–diffusion and chemomechanical motion. Since the chemical reaction and the mechanical motion are affected each other with a feedback control, the oscillating behaviors of gels become more complicated compared with conventional stimuli-responsive gels. Then theoretical simulation becomes effective tool for understanding the chemomechanical behaviors. Balazs et al. [45–47, 50–53] developed a mathematical model for simulating chemomechanical behaviors of the self-oscillating gels. Since reported in 2006 [50], they have demonstrated several aspects of the self-oscillating behavior for the gel by theoretical simulation. Many interesting phenomena and possible actuating behaviors, some of which were experimentally realized, were demonstrated theoretically. The investigations from theoretical studies will provide helpful guidelines for creating autonomously moving objects, which can be used for robotic applications.

5.5 Design of Autonomous Mass Transport Systems

5.5.1 Self-Driven gel Conveyor: Autonomous Transportation on the Self-Oscillating Gel Surface by Peristaltic Motion

In order to realize self-driven gel conveyor as novel autonomous mass transport system, we attempted to transport an object by utilizing the peristaltic motion of the self-oscillating gel. A model object, a cylindrical or spherical PAAm gel was put on the surface of self-oscillating gel sheet [18, 29–31]. It was observed that the object was transported on the gel surface with the propagation of the chemical wave as it rolled (Fig. 5.10a). The velocity and the inclination angle of the chemical wave were changed by changing the concentrations of the outer solution. For the controlled chemical waves with several inclination angles and velocities, whether the cylindrical gel could be transported or not was estimated. It was found that the cylindrical PAAm gel was not transported when the inclination angle was less than approximately 3° . The mass transportability did not depend on the velocity of the chemical wave, but on the diameter of the cylindrical PAAm gel and the inclination angle of the wave front. For analysing this result, we have proposed a model to describe the mass transport phenomena based on the Hertz contact theory, and the relation between the transportability and the peristaltic motion was investigated. As a result of calculation from the theoretical equation, the minimum inclination angle was 3° and it was the same as the angle resulted from the experiment. It was supported by the model that the sheer wave front of the peristaltic motion was necessary to transport cylindrical gels.

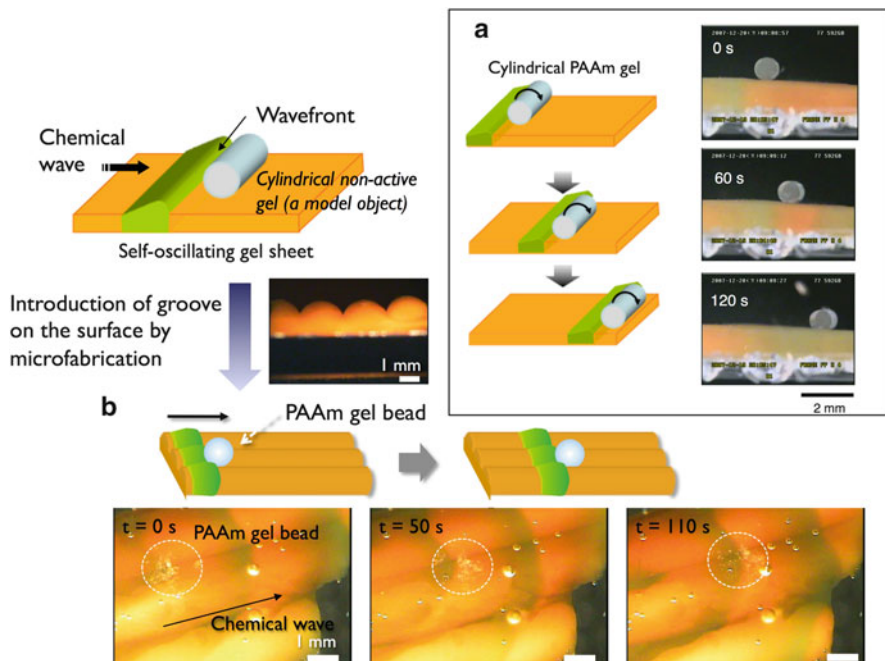


Fig. 5.10 Autonomous mass transport with wave propagation on the surface of self-oscillating gel (gel conveyor). (a) Schematic illustration of mass transport on the peristaltic surface and observed transport of cylindrical PAAm gel on the self-oscillating gel sheet in a solution of the BZ substrates. (b) The grooved self-oscillating gel sheet prepared by the PDMS template. Schematic illustration of mass transport on the peristaltic surface and transport of poly(AAm-co-AMPS) gel beads on the grooved surface

Then, the surface figure capable of transporting microparticles in one direction was designed to fabricate more versatile self-driven gel conveyor. The self-oscillating gel having a grooved surface was fabricated by using PDMS template and the effectiveness of the surface design was investigated. Poly(AAm-co-AMPS) gel beads with the diameter of several hundred μm to several mm were transported on the grooved surface of the self-oscillating gel by its autonomous peristaltic motions (Fig. 5.10b) [29]. It was found that the traveling direction of the peristaltic motion could be confined to the direction along the grooves by designing the groove-distance shorter than the wavelength of the chemical wave. Consequently, several gel beads were transported in parallel.

The influences of these surface properties on the transport behaviors were also investigated [30]. Instead of the homopolymer gel of PAAm, several kinds of copolymer gels consisting of AAm with AMPS, *N*-(3-aminopropyl)methacrylamide hydrochloride (APMA), *N*-(hydroxymethyl)acrylamide (HMAAm), and methyl methacrylate (MMA) were prepared as model cargos with different surface properties; positive or negative charge, more hydrophilicity or hydrophobicity, respectively. It was found that the adhesion force between the cylindrical poly(AAm-co-MMA)

gel and the self-oscillating gel sheet was too strong to apply the transport model because of their hydrophobic interaction. The adhesive force to prevent transportation is not significant for the other gels, which agrees with the prediction from swelling, zeta potential, and contact angle measurements. Then the effect of surface roughness on the transportation was investigated. It was found that higher surface roughness is more effective in transporting the loaded gel because frictional force increases and the moment of force of the rotational motion increases.

5.5.2 Autonomous Intestine-Like Motion of Tubular Self-Oscillating Gel

Further, to construct autonomous mechanical pumping systems like an intestine, we fabricated the self-oscillating gel in a tubular shape [32] (Fig. 5.11). Tubular self-oscillating gels were fabricated by photopolymerization. Several kinds of tubular

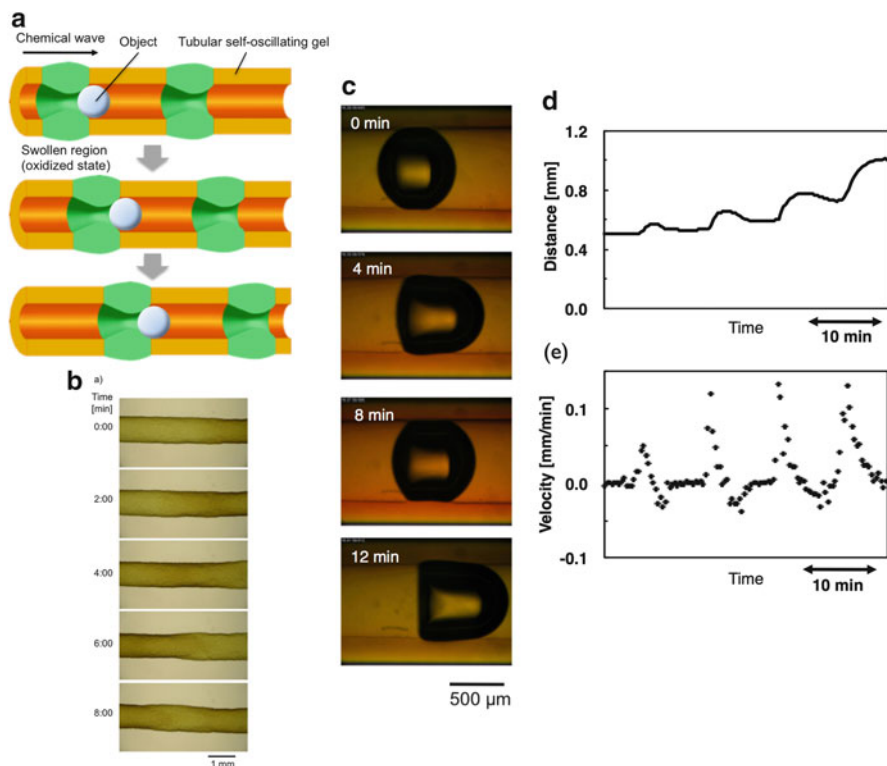


Fig. 5.11 (a) Schematic illustration of autonomous mass transport by peristaltic pumping of a tubular self-oscillating gel. (b) Time course images of the peristaltic motion of the tubular poly(NIPAAm-co-Ru(bpy)₃-co-AMPS) gel. (c) The behavior of the autonomous transport of a CO₂ bubble in the gel tube by peristaltic pumping. (d) Change in the position of the bubble. (e) The velocity of the bubble

self-oscillating gels that exhibit autonomous peristaltic motion were prepared. First, a tubular poly(NIPAAm-*co*-Ru(bpy)₃) gel adhered to the inner wall of a glass capillary was prepared and the periodic inner diameter changes during the BZ reaction were analyzed. Second, by removing the gel from the glass capillary, a tubular gel that can swell and deswell freely without a mechanical restraint was prepared. Then, a tubular gel with interpenetrating network structure composed of self-oscillating and non-oscillating polymers was prepared. It was shown that these tubular self-oscillating gels exhibited various behaviors of peristaltic motions.

In addition, it was demonstrated that an object was autonomously transported in the gel tube by the peristaltic pumping motion similar to an intestine. Figure 5.11c shows the behavior of a CO₂ bubble in the tubular poly(NIPAAm-*co*-Ru(bpy)₃) gel. When the chemical wave reaches the contact point, the bubble is squashed and deformed by swelling of the gel layer at the point. Then the bubble is mechanically pushed forward by the peristaltic pumping mechanism. After the wave passes through, the gel layer deswells and the squashed bubble returns back to the initial round shape. Due to a decrease in pushing force and a negative pressure, the bubble moves backward slightly. After that, the movement of the bubble stops for a while. As a result, the movement was intermittent. By repeating this process, the bubble is transported in the gel tube. Figure 5.11d, e shows the changes in the position and the velocity of the bubble, respectively. The velocity was calculated by differentiating the position with time. It is obvious that a net movement of the bubble occurs by repeating backward and forward movements. Potential applications to artificial intestines, artificial digestive tracts, etc. can be expected. Furthermore, there is a possibility of autonomous flow of an inner fluid. We are investigating an application to a novel micropump for microfluidic systems.

5.5.3 Self-Oscillating Polymer Brushes

Recently, surface modification techniques for polymer chains have made a lot of progress with the development of new polymer synthesis methods. In particular, surface-initiated atom transfer radical polymerization (SI-ATRP) is one of the most effective modification methods for preparing a well-defined dense polymer brush structure, or polymer brush, on substrates. Thus, a self-oscillating polymer brush prepared by SI-ATRP can be expected to create a new self-oscillating surface with autonomic function like a cilia, which will lead to potential applications to transporting systems for nano-materials or flow control in micro fluidics.

We prepared the self-oscillating polymer brush on glass substrates through SI-ATRP (Fig. 5.12) [33]. The self-oscillating polymer was grafted onto the inner surface of a glass capillary. Figure 5.12b shows the image observed by fluorescence microscope, which shows that the self-oscillating polymer brush was successfully modified onto the inner surface of the capillary. Then the catalyst-free BZ solution was fed into the capillaries and the BZ reaction on the inner surface was observed by fluorescence microscope. Spatiotemporal image analyses were performed in different locations (1–4) of the glass capillary and the oscillating profiles of the

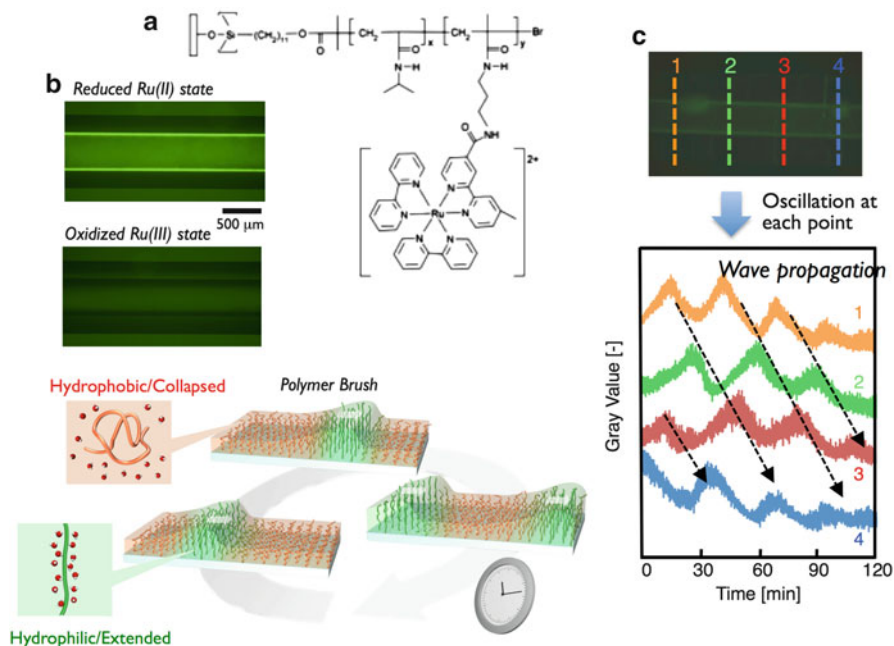


Fig. 5.12 Preparation of self-oscillating polymer brush by surface-initiated atom transfer radical polymerization (SI-ATRP). (a) Chemical structure of the self-oscillating polymer brush. (b) Images of glass capillary modified with the self-oscillating polymer brush observed by fluorescence microscope. (c) Oscillating profile of fluorescence intensity at each position for the self-oscillating polymer brush modified on inner surface of glass capillary. The solution containing MA, NaBrO₃ and HNO₃ is enclosed in the capillary at 25 °C

fluorescence intensity were compared (Fig. 5.12c). It was found that oscillations occurred at each position with a phase difference. This suggests that the chemical wave propagates in the self-oscillating polymer brush layer on the inner surface of the glass capillary. A self-oscillating surface to generate spontaneous periodic changes was able to be demonstrated by using synthetic polymers, as a novel autonomous functional surface which has potential applications in systems such as nano-transport systems.

5.6 Self-Oscillating Fluids

5.6.1 Transmittance and Viscosity Oscillation of Polymer Solution and Microgel Dispersion

In the case of the uncrosslinked linear polymer (poly(NIPAAm-co-Ru(bpy)₃), as shown in Fig. 5.4, the polymer undergoes spontaneous cyclic soluble-insoluble changes and the transmittance of the polymer solution oscillates autonomously with

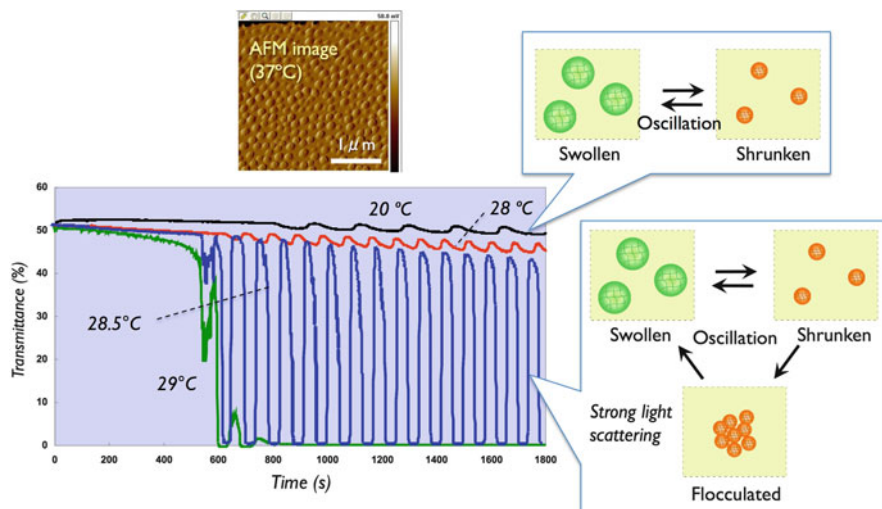


Fig. 5.13 Self-oscillating profiles of optical transmittance for microgel dispersions at several temperatures

redox changes of the copolymerized $\text{Ru}(\text{bpy})_3$ [34]. Further, we prepared submicron-sized poly(NIPAAm-*co*- $\text{Ru}(\text{bpy})_3$) gel beads by surfactant-free aqueous precipitation polymerization and analyzed the oscillating behavior of the microgel dispersions [35–38]. The microgel dispersion also exhibited transmittance oscillation due to swelling and deswelling changes of the microgels. With increasing temperature, the oscillation period decreased and the amplitude increased a little. When the temperature increased near to the volume phase transition temperature of the reduced microgel, the microgels showed dispersing/flocculating oscillation as well as swelling-deswelling oscillation (Fig. 5.13) because the reduced and shrunken microgels lost colloidal stability, which resulted in a remarkable increase of amplitude in optical transmittance oscillation. Due to such behaviors, as mentioned before, the macroscopic self-oscillating gel prepared by crosslinking the assembled microgels exhibits a faster response and leads to larger amplitude of swelling-deswelling oscillation [21].

In both cases of the polymer solution and the microgel dispersion, viscosity oscillation was observed with optical transmittance oscillation [39–41]. In the microgel dispersion, it was found that the viscosity oscillation occurs with exhibiting two different waveforms; a simple pulsatile waveform or a complex waveform with two peaks per period. The difference in waveform is due to the difference in the oscillating behavior of the microgels: swelling/deswelling or dispersing/flocculating oscillation. The oscillating behavior can be controlled by changing the concentration of microgels, $\text{Ru}(\text{bpy})_3$ contents, crosslinking density, etc. It is expected that these polymer solutions and microgel dispersions are applied as novel functional fluid.

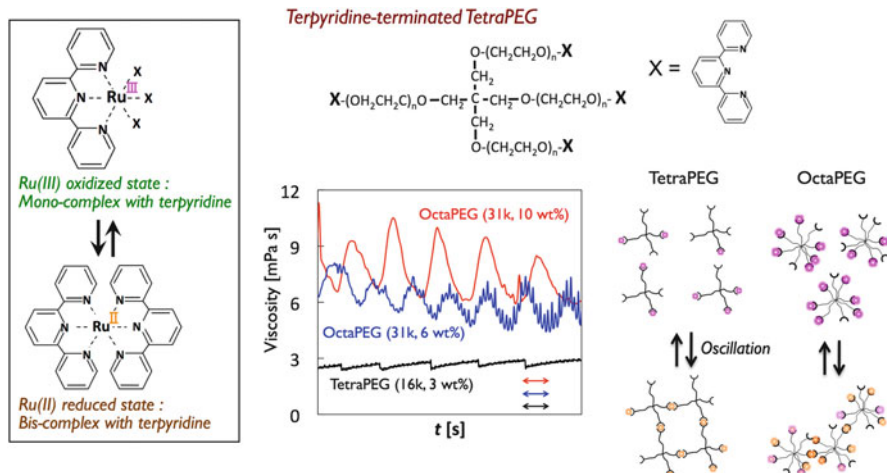


Fig. 5.14 Autonomous viscosity oscillation by reversible complex formation of terpyridine-terminated branched-PEG in the BZ reaction. Oscillating profiles of viscosity of the aqueous solution containing Ru(terpy)₂-tetra or Ru(terpy)₂-octa PEG, HNO₃, NaBrO₃ and MA at 25 °C

5.6.2 Autonomous Viscosity Oscillation by Reversible Complex Formation of Terpyridine-Terminated PEG in the BZ Reaction

We realized autonomous viscosity oscillations of a polymer solution based on different mechanisms, that is, an autonomous viscosity oscillation of polymer solutions coupled with metal–ligand association/dissociation between Ru and terpyridine (tpy), driven by the BZ reaction [42, 43] (Fig. 5.14). The tpy ligand for the Ru catalyst was attached to the terminals of poly(ethylene glycol) (PEG) with different numbers of branches (linear-, tetra-, and octa-PEG). It is well known that mono-tpy coordination is stable when Ru is oxidized (Ru(tpy)³⁺), whereas bis-tpy coordination is stable when the Ru centre is reduced (Ru(tpy)₂²⁺) [54]. In the oxidized state, these polymers existed as solutions. In contrast, when the Ru centre was reduced, gels were obtained for the tetra- and octa-PEG owing to the formation of a three-dimensional polymer network through Ru–tpy coordination. By increasing the number of PEG branches, we succeeded in decreasing the number of crosslinking points necessary for gelation. This was qualitatively explained by the tree-like structure theory stating a rate of reaction of crosslinking point for a branched polymer at gelation point. Further, the gelation kinetics of the octa-PEG system were approximately four times faster than those of the tetra-PEG system.

The polymer solutions exhibited self-oscillation of absorbance and viscosity when BZ substrates were added to the solutions of Ru²⁺-tpy-modified tetra-/octa-PEG. This indicated that the Ru(tpy)₂²⁺ attached to the polymer ends could work as a metal catalyst for the BZ reaction. The viscosity oscillation profiles of the tetra- and octa-PEG were compared under the optimised conditions for each

system (Fig. 5.14). As expected, the octa-PEG was much more effective than the tetra-PEG system in providing a large oscillation amplitude as well as a higher viscosity baseline. For the octa-PEG, the viscosity baseline and amplitude were approximately two times higher and ten times larger, respectively, than for the tetra-PEG system. This is likely because the number of crosslinking points necessary for gelation was decreased by increasing the branch number of PEG, as predicted from the tree-like structure theory. As a result, the maximum value of crosslinking points in oscillation is closer to that necessary for gelation. Thus, viscosity oscillation occurred in the region of higher viscosity with a larger amplitude.

5.6.3 Self-Oscillating Micelles

Further, we prepared a novel block copolymer (“self-oscillating micelle”) that could undergo spontaneous unimer–micelle oscillation under constant conditions [44]. Diblock copolymer (PEO-*b*-P(NIPAAm-*r*-Ru(bpy)₃)) was successfully prepared by RAFT random copolymerization of NIPAAm and vinyl monomer having Ru(bpy)₃ side chain from poly(ethylene oxide) (PEO)-based macro-CTA (Fig. 5.15). Rhythmical oscillation of the scattering intensity and hydrodynamic radii of the block copolymer solution driven by the BZ reaction was demonstrated without any on-off switching of external stimuli. This is the first report on a synthetic block copolymer that realizes the novel concept of self-assembly assisted by a dissipative structure.

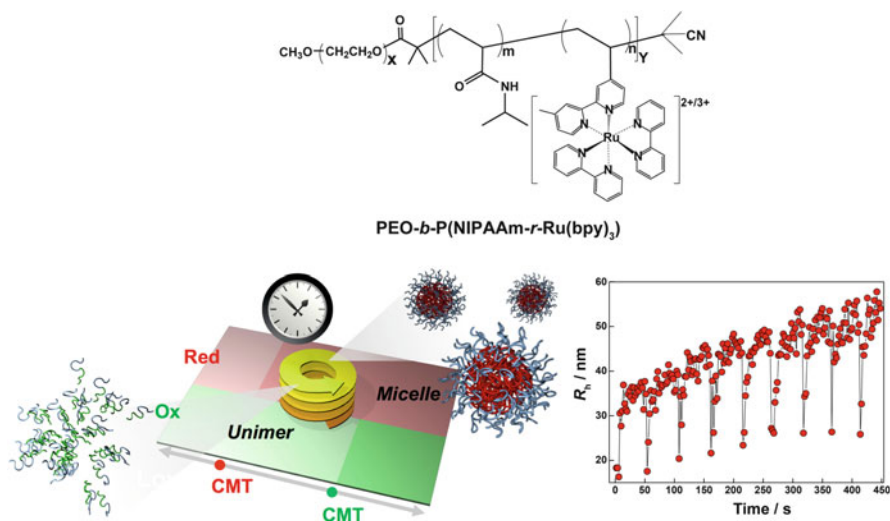


Fig. 5.15 Upper: Chemical structure of PEO-*b*-P(NIPAAm-*r*-Ru(bpy)₃). Lower: Schematic illustration of unimer/micelle oscillation and the oscillating profiles of R_h of the diblock copolymer determined by time-resolved DLS measurements

5.6.4 BZ Reaction in Protic Ionic Liquids

We realized the BZ reaction using hydrated protic ionic liquid (PIL) as a reaction medium [55]. It was found for the first time that the BZ oscillation reaction occurred in certain hydrated PILs without adding strong acid such as HNO_3 . Furthermore, unprecedented stable and long-lasting self-oscillation can be realized when concentrations of the BZ substrates are optimized. Investigation of more optimized ion structures for a stable and long-lasting BZ reaction under mild conditions is now in progress for evolution of the self-oscillating gels.

5.7 Future Prospects

As mentioned above, we developed novel “self-oscillating” polymer gels which exhibit autonomous swelling-deswelling oscillation under constant external condition like a heart muscle. Since the first report in 1996 [7], we have systematically studied the polymer gels, and we will continue to advance our research by studying new polymer systems. In this chapter, our recent progress on the self-oscillating polymer gels as functional materials were summarized. As an innovative study to propose novel potential of polymer gels and achieve an autonomous behavior by coupling chemical and mechanical oscillations in polymer systems, the study has attracted much attention in the many research fields of polymer science, material science, physical chemistry, theoretical simulation, biophysics, etc. Robotics is one of those fields, and applications to autonomous soft actuators will be extensively expected. Many similar studies following the same mechanism will be possible in future. But more innovative researches, which are not simple applied researches just only improving or utilizing the gels, will be necessary.

References

1. Yoshida R, Ichijo H, Hakuta T, Yamaguchi T (1995) Self-oscillating swelling and deswelling of polymer gels. *Macromol Rapid Commun* 16:305–310
2. Yoshida R, Yamaguchi T, Ichijo H (1996) Novel oscillating swelling-deswelling dynamic behaviour for pH-sensitive polymer gels. *Mater Sci Eng C* 4:107–113
3. Field RJ, Burger M (eds) (1985) *Oscillations and traveling waves in chemical systems*. Wiley, New York
4. Epstein IR, Pojman JA (1998) *An introduction to nonlinear chemical dynamics: oscillations, waves, patterns, and chaos*. Oxford University Press, New York
5. Field RJ, Körös E, Noyes RM (1972) Oscillations in chemical systems. II. Through analysis of temporal oscillation in the bromate-cerium-malonic acid system. *J Am Chem Soc* 94:8649–8664
6. Amemiya T, Ohmori T, Yamaguchi T (2000) An Oregonator-class model for photoinduced behavior in the $\text{Ru}(\text{bpy})_3^{2+}$ -catalyzed Belousov-Zhabotinsky reaction. *J Phys Chem A* 104:336–344

7. Yoshida R, Takahashi T, Yamaguchi IH (1996) Self-oscillating gel. *J Am Chem Soc* 118:5134–5135
8. Yoshida R (2010) Self-oscillating gels driven by the Belousov-Zhabotinsky reaction as novel smart materials. *Adv Mater* 22:3463–3483
9. Yoshida R, Tanaka T, Onodera S, Yamaguchi T, Kokufuta E (2000) In-phase synchronization of chemical and mechanical oscillations in self-oscillating gels. *J Phys Chem A* 104:7549–7555
10. Maeda S, Hara Y, Yoshida R, Hashimoto S (2008) Peristaltic motion of polymer gels. *Angew Chem Int Ed* 47:6690–6693
11. Takeoka Y, Watanabe M, Yoshida R (2003) Self-sustaining peristaltic motion on the surface of a porous gel. *J Am Chem Soc* 125:13320–13321
12. Sasaki S, Koga S, Yoshida R, Yamaguchi T (2003) Mechanical oscillation coupled with the Belousov-Zhabotinsky reaction in gel. *Langmuir* 19:5595–5600
13. Ito Y, Nogawa N, Yoshida R (2003) Temperature control of the Belousov-Zhabotinsky reaction using a thermo-responsive polymer. *Langmuir* 19:9577–9579
14. Yoshida R, Takei K, Yamaguchi T (2003) Self-beating motion of gels and modulation of oscillation rhythm synchronized with organic acid. *Macromolecules* 36:1759–1761
15. Shinohara S, Seki T, Sakai T, Yoshida R, Takeoka Y (2008) Chemical and optical control of peristaltic actuator based on self-oscillating porous gel. *Chem Commun* 4735–4737
16. Shinohara S, Seki T, Sakai T, Yoshida R, Takeoka Y (2008) Photoregulated wormlike motion of a gel. *Angew Chem Int Ed* 47:9039–9043
17. Yamamoto T, Yoshida R (2013) Self-oscillation of polymer and photo-regulation by introducing photochromic site to induce LCST changes. *React Func Polym* 73:945–950
18. Murase Y, Maeda S, Hashimoto S, Yoshida R (2009) Design of a mass transport surface utilizing peristaltic motion of a self-oscillating gel. *Langmuir* 25:483–489
19. Hara Y, Yoshida R (2008) Self-oscillating polymer fueled by organic acid. *J Phys Chem B* 112:8427–8429
20. Hidaka M, Yoshida R (2011) Self-oscillating gel composed of thermosensitive polymer exhibiting higher LCST. *J Control Release* 150:171–176
21. Suzuki D, Kobayashi T, Yoshida R, Hirai T (2012) Soft actuators of organized self-oscillating microgels. *Soft Matter* 8:11447–11449
22. Mitsunaga R, Okeyoshi K, Yoshida R (2013) Design of comb-type self-oscillating gel. *Chem Commun* 49:4935–4937
23. Tabata O, Kojima H, Kasatani T, Isono Y, Yoshida R (2003) Chemo-mechanical actuator using self-oscillating gel for artificial cilia. In: *Proceedings of the international conference on MEMS 2003*, pp 12–15
24. Tabata O, Hirasawa H, Aoki S, Yoshida R, Kokufuta E (2002) Ciliary motion actuator using self-oscillating gel. *Sens Actuators A* 95:234–238
25. Maeda S, Hara Y, Sakai T, Yoshida R, Hashimoto S (2007) Self-walking gel. *Adv Mater* 19:3480–3484
26. Maeda S, Hara Y, Yoshida R, Hashimoto S (2008) Control of dynamic motion of a gel actuator driven by the Belousov-Zhabotinsky reaction. *Macromol Rapid Commun* 29:401–405
27. Kuksenok O, Yashin VV, Kinoshita M, Sakai T, Yoshida R, Balazs AC (2011) Exploiting gradients in cross-link density to control the bending and self-propelled motion of active gels. *J Mater Chem* 21:8360–8371
28. Yashin VV, Suzuki S, Yoshida R, Balazs AC (2012) Controlling the dynamic behavior of heterogeneous self-oscillating gels. *J Mater Chem* 22:13625–13636
29. Murase Y, Hidaka M, Yoshida R (2010) Self-driven gel conveyor: autonomous transportation by peristaltic motion of self-oscillating gel. *Sens Actuators B* 149:272–283
30. Murase Y, Takeshima R, Yoshida R (2011) Self-driven gel conveyor: effect of interactions between loaded cargo and self-oscillating gel surface. *Macromol Biosci* 11:1713–1721
31. Yoshida R, Murase Y (2012) Self-oscillating surface of gel for autonomous mass transport. *Colloids Surf B: Biointerfaces* 99:60–66

32. Shiraki Y, Yoshida R (2012) Autonomous intestine-like motion of tubular self-oscillating gel. *Angew Chem Int Ed* 51:6112–6116
33. Masuda T, Hidaka M, Murase Y, Akimoto AM, Nagase K, Okano T, Yoshida R (2013) Self-oscillating polymer brushes. *Angew Chem Int Ed* 52:7468–7471
34. Yoshida R, Sakai T, Ito S, Yamaguchi T (2002) Self-oscillation of polymer chains with rhythmical soluble-insoluble changes. *J Am Chem Soc* 124:8095–8098
35. Suzuki D, Sakai T, Yoshida R (2008) Self-flocculating/self-dispersing oscillation of microgels. *Angew Chem Int Ed* 47:917–920
36. Suzuki D, Yoshida R (2008) Temporal control of self-oscillation for microgels by cross-linking network structure. *Macromolecules* 41:5830–5838
37. Suzuki D, Yoshida R (2008) Effect of initial substrate concentration of the Belousov-Zhabotinsky reaction on self-oscillation for microgel system. *J Phys Chem B* 112:12618–12624
38. Suzuki D, Yoshida R (2010) Self-oscillating core/shell microgels. *Polymer J* 42:501–508
39. Hara Y, Yoshida R (2008) A viscosity self-oscillation of polymer solution induced by the BZ reaction under acid-free condition. *J Chem Phys* 128:224904
40. Suzuki D, Taniguchi H, Yoshida R (2009) Autonomously oscillating viscosity in microgel dispersions. *J Am Chem Soc* 131:12058–12059
41. Taniguchi H, Suzuki D, Yoshida R (2010) Characterization of autonomously oscillating viscosity induced by swelling/deswelling oscillation of the microgels. *J Phys Chem B* 114:2405–2410
42. Ueno T, Bundo K, Akagi Y, Sakai T, Yoshida R (2010) Autonomous viscosity oscillation by reversible complex formation of terpyridine-terminated poly(ethylene glycol) in the BZ reaction. *Soft Matter* 6:6072–6074
43. Ueki T, Takasaki Y, Bundo K, Ueno T, Sakai T, Akagi Y, Yoshida R (2014) Autonomous viscosity oscillation via metallo-supramolecular terpyridine chemistry of branched poly(ethylene glycol) driven by the Belousov-Zhabotinsky reaction. *Soft Matter* 10:1349–1355
44. Ueki T, Yoshida R (2013) Self-oscillating micelles. *Chem Commun* 49:6947–6949
45. Dayal P, Kuksenok O, Balazs AC (2010) Designing autonomously motile gels that follow complex paths. *Soft Matter* 6:768–773
46. Dayal P, Kuksenok O, Balazs AC (2009) Using light guide the self-sustained motion of active gels. *Langmuir* 25:4298–4301
47. Kuksenok O, Balazs AC (2013) Modeling the photoinduced reconfiguration and directed motion of polymer gels. *Adv Funct Mater* 23:4601–4610
48. Kaneko Y, Sakai K, Kikuchi A, Yoshida R, Sakurai Y, Okano T (1995) Influence of freely mobile grafted chain length on dynamic properties of comb-type grafted poly(N-isopropylacrylamide) hydrogels. *Macromolecules* 28:7717–7723
49. Yoshida R, Uchida K, Kaneko Y, Sakai K, Kikuchi A, Sakurai Y, Okano T (1995) Comb-type grafted hydrogels with rapid de-swelling response to temperature changes. *Nature* 374:240–242
50. Yashin VV, Balazs AC (2006) *Science* 314:798–801
51. Yashin VV, Kuksenok O, Balazs AC (2010) Modeling autonomously oscillating chemo-responsive gels. *Prog Polym Sci* 35:155–173
52. Yashin VV, Kuksenok O, Dayal P, Balazs AC (2012) Mechano-chemical oscillations and waves in reactive gels. *Rep Prog Phys* 75:066601
53. Yashin VV, Kuksenok O, Balazs AC (2010) Computational design of active, self-reinforcing gels. *J Phys Chem B* 114:6316–6322
54. Lohmeijer BGG, Schubert US (2002) Supramolecular engineering with macromolecules: an alternative concept for block copolymers. *Angew Chem Int Ed* 41:3825–3829
55. Ueki T, Watanabe M, Yoshida R (2012) Belousov-Zhabotinsky reaction in protic ionic liquids. *Angew Chem Int Ed* 51:11991–11994

Part III
Materials of Soft Actuators:
Electro-Driven Soft Actuators

Chapter 6

Ionic Conductive Polymers

Kunitomo Kikuchi and Shigeki Tsuchitani

Abstract Electro active polymers (EAPs) are attracting considerable interest due to their special characteristics, including high flexibility and low weight. Ionic conductive polymers have the potential to play a main role in the realization of smart systems for applications such as bio inspired and autonomous robotics, medical devices, and aerospace. Ionic polymer-metal composites (IPMCs) are one of the most promising EAP materials for the artificial muscle-like actuators and sensors. Typical applications of IPMC are soft robotic actuators, since they are suitable for micro actuators in devices used in the human body due to their flexibility and good biological compatibility. In this chapter, the fundamental aspects of the IPMC, i.e., typical fabrication methods, evaluation techniques for testing, recent results of fabrication of miniaturized IPMC, and recent developments of materials of ion conductive polymer actuators are described.

Keywords Electro active polymer • Ionic conductive polymer • Ionic liquid • Miniaturization

6.1 Introduction

Polymer actuators are attracting considerable interest due to their special characteristics, including high flexibility and low weight. Ionic polymer-metal composites (IPMCs) are one of the most promising electro active polymer (EAP) materials for the artificial muscle-like actuators. The schematic structure and basic driving mechanisms of IPMC are shown in Fig. 6.1. They consist of an ionic conductive polymer gel membrane with thin noble-metal electrodes on both membrane surfaces. When applying a voltage between the electrodes, the counter cation moves to the cathode side with dragging water. Therefore, IPMC bends toward anode side due to the pressure gradient in the ionic polymer. A large ionic current gives the IPMC actuator a soft and relatively powerful motion. IPMC actuators have a

K. Kikuchi (✉) • S. Tsuchitani

Department of Opto-Mechatronics, Faculty of Systems Engineering, Wakayama University,
930 Sakaedani, Wakayama 640-8510, JAPAN

e-mail: kikuchi@sys.wakayama-u.ac.jp

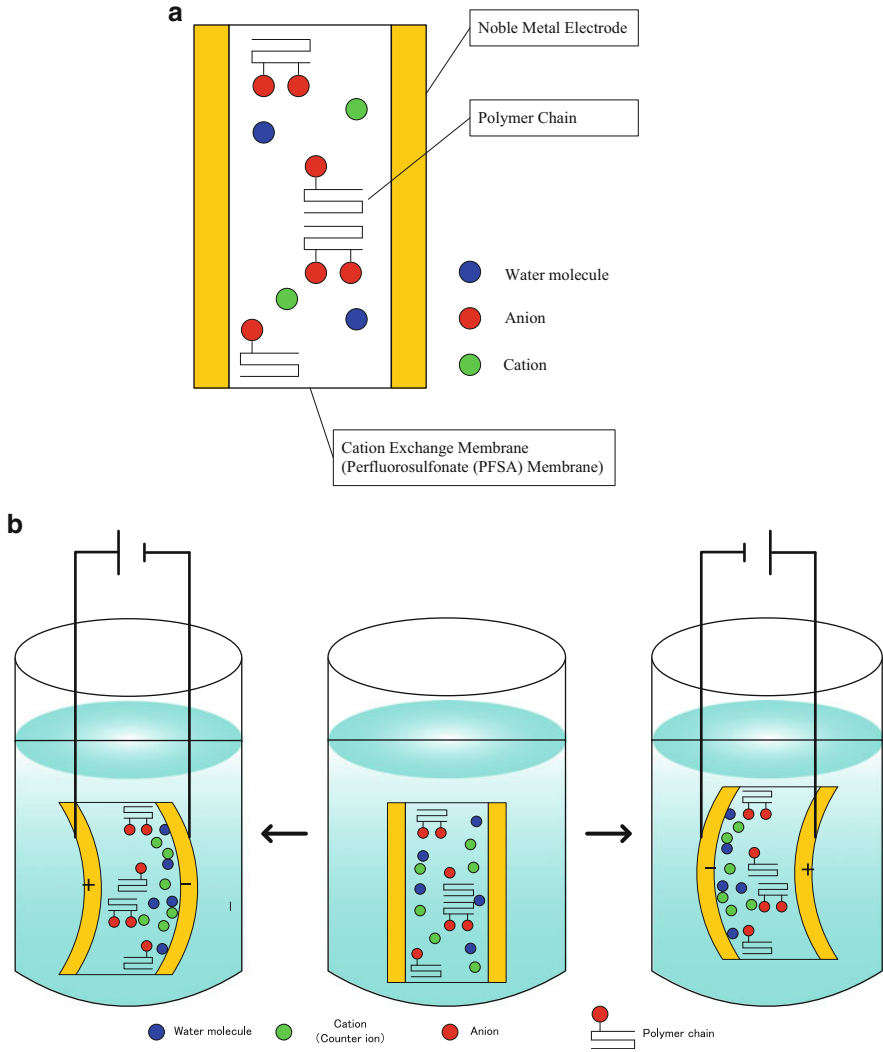


Fig. 6.1 Structure of cation-exchange-polymer-based IPMC. (a) Structure of IPMC; (b) Schematic representation of bending of IPMC

number of advantages that make them attractive to use for soft robotics and biomedical applications [1, 2]:

- Low driving voltage (1–3 V)
- Relatively high response (up to several hundreds of Hz)
- Large deformation
- Flexibility
- Excellent formability
- Driving in water or in wet condition

Oguro et al. [3] firstly reported the bending response of the perfluorosulfonic acid membrane (Nafion[®] 117) plated with platinum electrodes, being activated by low voltages, about 1 V, in 1992, which was named IPMC [4]. Shahinpoor et al. also reported a similar idea [5]. IPMC is also known as the ionic conductive polymer gel films (ICPF) [6].

In this chapter, the fundamental aspects of the IPMC fabrication methods, evaluation techniques for testing, recent results of miniaturized IPMC, and recent developments of materials of ion conductive polymer actuators are described.

6.2 Fabrication Methods

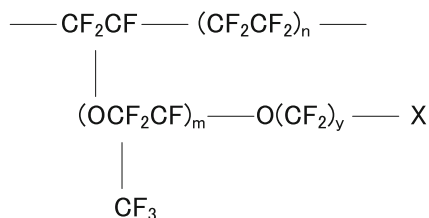
6.2.1 Ionic Polymers

There are a number of different types of ionic polymers available. Ionic polymers usually used for the IPMC are perfluorosulfonic acid or perfluorocarboxylic acid polymers as shown in Fig. 6.2 [7]. Commercially available products of membranes of perfluorosulfonic acid type can be obtained from DuPont (Nafion[®]). Also, Asahi Glass Co. produces perfluorocarboxylic acid type (Flemion[®]).

Many researches on IPMCs have been carried out on Nafion[®] 117 which is a membrane whose typical thickness is 183 μm [8]. Also, Nafion[®] is available in the form of membranes of different thickness, thermoplastic beads and dispersing solutions. Thin films of Nafion[®] can be obtained by casting their dispersing solution and evaporating the solvent or by hot moulding thermoplastic beads of their polymers and changing $-\text{SO}_2\text{F}$ to $-\text{SO}_3^-$ by hydrolysis.

Nafion[®] is a Teflon-based polymer with short side-chains terminated by ionic groups. Therefore, Nafion[®] has excellent chemical and thermal stability. However, the dissolution of these ionic groups causes the membrane to swell significantly when the material is hydrated (absorbing as much as 38 % of its dry weight in water) [8]. The cations can be free from ionic groups and move within the polymer matrix. On the other hand, the anions are covalently fixed to the fluorocarbon backbone. For this reason, IPMC usually operate in water or wet conditions.

Fig. 6.2 Chemical Structure of perfluorinated ion exchange polymer. $X = \text{SO}_3^-$: perfluorosulfonic acid polymer; COO^- : perfluorocarboxylic polymer; or SO_2F : thermoplastic polymer



6.2.2 *Plating Methods*

The electrodes of IPMC are one of the most significant components for durable and high-performance one because both faces of the ionic conductive polymer membrane must be plated with conductive electrodes in order to apply a voltage effectively to it. Therefore, the electrodes for optimum performance of IPMC actuator should have the following criteria:

- Good adhesion to the ionic polymer
- High electric conductivity
- Large electrochemical interfacial area
- Large electrochemical window (high over potential to redox reactions)
- Inertness
- Flexibility (high ductility)
- Nontoxicity

The most used methods to form electrodes onto the membranes for fulfilling the above criteria are based on an ion exchange (adsorption) process and subsequent chemical reduction process [9–18]. Noble metals such as platinum or gold are generally used as the electrode materials, although other materials such as silver [19], copper [20], palladium [21], and carbon [22] have been proposed.

These fabrication methods based on the chemical plating are generally composed of four steps as follows:

1. Surface treatment (or roughening) process of the membrane
2. The adsorption (or ion exchange) process of metallic ions into the membrane
3. The reduction (or primary plating) process of the metallic ions
4. Developing (or secondary plating) process of the electrodes

Oguro et al. firstly found the bending response of Nafion[®] 117 chemically plated with platinum electrodes [4]. However, a platinum electrode has a narrower electrochemical window and is mechanically harder than a gold electrode. Hence, a chemical plating method with a gold electrode has been developed for the IPMC actuator [12]. This plating method has been developed for optimizing the electrode structure, which has large electrochemical area and soft mechanical property.

6.3 Evaluation Techniques of IPMC

The typical measuring setup for the displacement of IPMC is shown in Fig. 6.3 [23]. IPMC strip is clamped by the electrodes and the displacement at the measurement point is measured by a LASER displacement sensor. The applied voltage and driving current are simultaneously measured the electrochemical measurement

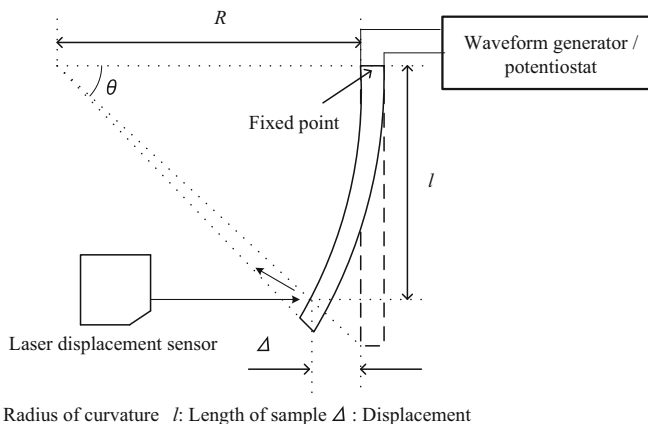


Fig. 6.3 Measuring setup for the displacement of IPMC

setup such as a potention/galvano stat. Because the measurement displacement is varied by the length of IPMC at the measurement point from the fix point (free length), the curvature calculated from the displacement δ by the following equation:

$$\frac{1}{R} = \frac{2\delta^2}{l^2 + \delta^2} \quad (6.1)$$

where R is the radius of curvature and l is the free length.

The blocking force is also measured by a load cell. The relationship between the blocking force F and the curvature $\frac{1}{R}$ is:

$$\frac{1}{R} = \frac{M - Fl}{EI} \quad (6.2)$$

where M is the bending moment, EI is the rigidity of the IPMC.

The electrochemical characteristics of IPMC and electrodes are important in understanding the fundamental actuation mechanism of IPMCs. Therefore, electrochemical analyses including voltammetry, AC impedance, and capacitance measurements on IPMC samples has been carried out in wet solutions or in dry condition [24, 25].

In order to understand the physics of transduction in IPMC, the morphology of Nafion[®] is characterized using small-angle X-ray scattering (SAXS) [26].

Moreover, Fourier-transform infrared (FTIR) spectroscopy is used to investigate and characterize the molecular structure of cations-containing Nafion[®] membranes [27, 28].

6.4 Recent Developments

6.4.1 IPMC Containing Ionic Liquids

During the past decade, much work has been done on the development of IPMC actuator in water or wet conditions. Water has favorable interactions with Nafion[®] polymer and the low viscosity. Generally, Nafion[®] membranes will absorb up to 38 % of their dry weight in water and achieve an ionic conductivity of 0.10 S/cm when fully hydrated [8].

When a voltage is applied between the two electrodes in water, the IPMC bends toward the higher potential side due to movement of hydrated counter ions and the accompanying electro-osmotic water flow [9, 23, 29]. First, IPMC bends to the anode side quickly (within 0.1 s), then slowly back to the cathode side (back-relaxation), and finally stops in a stable position [30–32]. It's not uncommon to observe cantilever-type IPMCs which exhibit large deformation of bending curvature angle of more than 90° when a voltage of few volts is applied.

The ionic forms of IPMC affect the response speed, the bending amplitude and the back-relaxation of the electromechanical response [32]. In order to these results, bending models for conventional IPMCs with metallic counter cations have been developed by many researchers. Asaka et al. suggested that bending is caused by a change in the local volume of the polyelectrolyte membrane due to electroosmotic water flow [9, 13, 29]. De Gennes et al. developed a more comprehensive theory using phenomenological equations for the electric current and water permeation generated by the electric field and the pressure gradient [33]. In this theory, the pressure field is coupled with the deformation of the IPMC. Yamaue et al. extended de Gennes's theory and developed an electro-stress diffusion coupled model, which is a more formal model for the deformation dynamics of an IPMC in an electric field in water [34]. In conventional IPMCs that operate in water, the local swelling in the polyelectrolyte membrane due to water permeation caused by electro-osmosis and the pressure gradient in the membrane plays an important role in transduction.

Unfortunately water-swollen membranes gradually lose the solvent because of water volatility when IPMCs containing water are used in air. Also, IPMC actuators can lose water because of the small electrochemical stability window of water (1.23 V). Both water evaporation and electrolysis lead to a deterioration of the actuation performance of IPMC [16].

Recently, IPMCs that can operate in air have been developed by incorporating ionic liquids in them [24, 27, 35–38]. Ionic liquids have a number of advantages as follows:

- Low vapor pressure
- Thermal stability
- Electrochemical stability (High potential window)
- High ionic conductivity

Bennett et al. showed that a Nafion[®]-based ionic-liquid-swollen IPMC could operate for over 250,000 cycles in air with less than a 30 % reduction in the free strain [26, 35]. Wang et al. demonstrated that Flemion[®]-based IPMCs containing ionic liquids could operate in air with good stability for 10,000 s [36, 37]. Bennett et al. proposed a model in which ionic liquids (instead of water, which is used in conventional IPMCs) were used as diluents to swell the IPMC; this resulted in counter ions being displaced from the ion exchange sites of the ionic polymer and increased the mobility of the counter ions [38].

We have also developed IPMCs containing ionic liquids. Ionic liquids were incorporated at room temperature by soaking IPMCs in mixtures of water and ionic liquids. We confirmed their long-term stability when they were operated in air; their bending curvature fluctuated by less than 21 % during 180 min of operation as shown in Figs. 6.4 and 6.5 [24]. Also, humidity of operating environment of IPMC affects the electrochemical response of it [27].

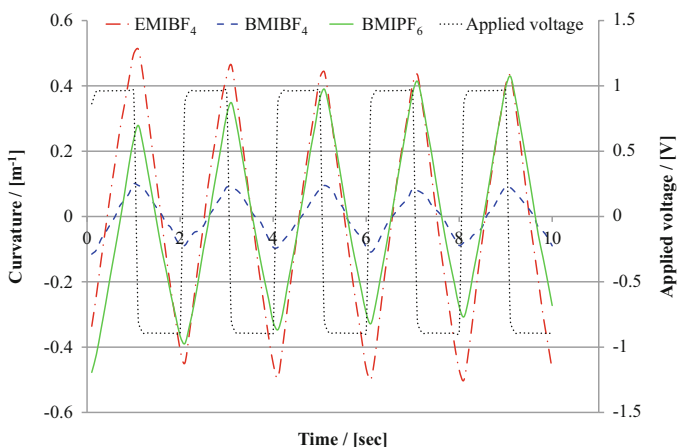
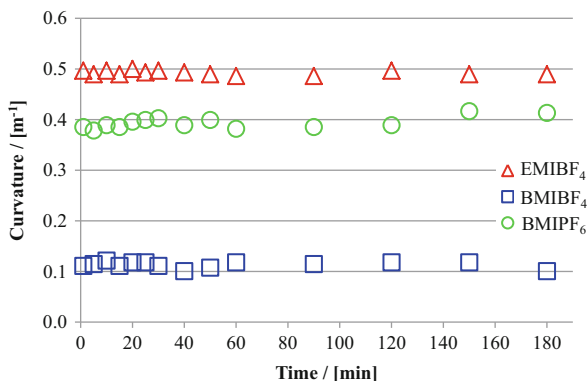


Fig. 6.4 Curvature response curves of IPMCs with three kinds of ionic liquids when square wave voltages with a frequency of 0.5 Hz and an amplitude of 1.0 V were applied for 10 s. “Reprinted with permission from Kikuchi and Tsuchitani [24]. Copyright (2009), AIP Publishing LLC”

Fig. 6.5 Time histories of the amplitude of the curvature response curves of IPMCs with three kinds of ionic liquids during 180 min operation in air when square wave voltages with a frequency of 0.5 Hz and an amplitude of 1.0 V were applied. “Reprinted with permission from Kikuchi and Tsuchitani [24]. Copyright (2009), AIP Publishing LLC”



6.4.2 Fabrication Techniques for Miniaturized IPMCs

By forming patterned electrodes, IPMC will be capable of complex motions such as peristaltic movement. Also, typical applications of IPMC are soft robotic actuators, since they are suitable for micro actuators in devices used in the human body due to their flexibility and good biological compatibility. Therefore, several methods have been developed for fabricating miniaturized IPMCs and patterned electrode of IPMC, including photolithography [39, 40], laser machining [41], mechanical milling [1], plasma etching [42].

We have also developed a fabrication technique for miniaturized IPMCs with an electroless gold plating using a selective plasma treatment [43, 44]. Our proposed method can provide a simple and direct fabrication process without covering process of the side wall compared to the previous study, because this treatment prevents the formation of the electrode on the side wall which creates a short-circuit between the driving electrodes.

The proposed method (selective gold plating method) consists of the following four processes as follows:

- (I) Covering a Nafion[®] membrane by a stencil mask
- (II) Plasma etching and surface modification of the membrane
 - (II-1) O₂ plasma etching
 - (II-2) CF₄ or SF₆ plasma treatment
- (III) Removal of the stencil mask from the Nafion[®] membrane
- (IV) Electroless gold plating
 - (IV-1) Adsorption process
 - (IV-2) Reduction process

The membrane which is not covered by the stencil mask is etched away from the surface to the backside by O₂ plasma etching (process II-1). This process is adequate for large-area processing, and can alleviate thermally and mechanically damages of the membrane, because the membrane is etched chemically. The CF₄ or SF₆ plasma treatment (process II-2) prevents the adsorption and the reduction of the gold complex from the etched surface (side wall) of the membrane during the electroless plating.

Figure 6.6 shows a photograph of miniaturized IPMCs after the electroless gold plating of one-cycle which has line-and-space patterns with an average width of 98 μm. In this case, Nafion[®] NR-212 membrane with a thickness of 51 μm and lateral dimensions of 15 × 15 mm² was used. The selective plasma irradiation onto the Nafion[®] was performed through a stencil mask which has a 100-μm-wide line-and-space pattern by using a RIE equipment.

From the results, the average dimensional error against the size of the mask was ~7%. This error came from the insufficient contact of the stencil mask with the membrane. In photolithography which is a typical microfabrication method, the ionic polymer is exposed to the organic solvents used in development and removal

Fig. 6.6 Fabrication result of IPMCs after electroless gold plating

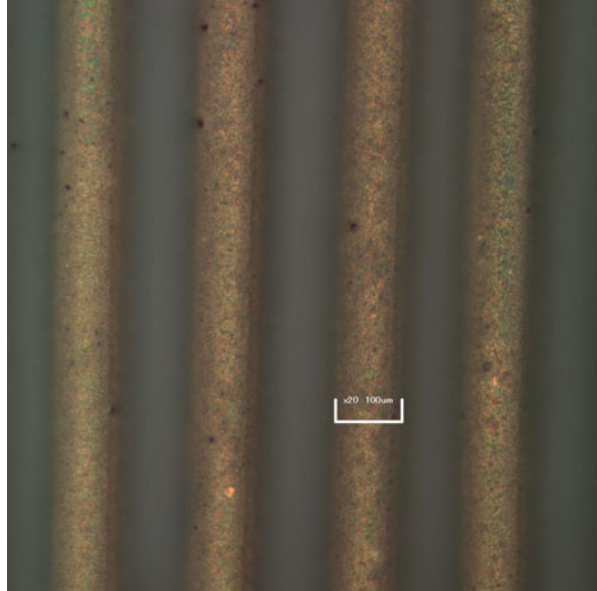
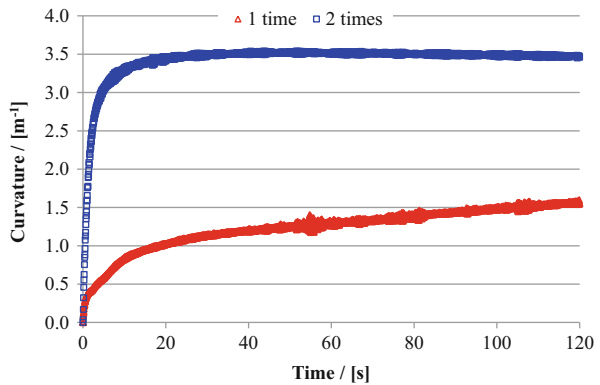


Fig. 6.7 Time history of curvature of a piece of miniaturized IPMC driven by an DC applied voltage (1.0 V)



of the photoresist and those included in the photoresist, and also to water for rinsing. This swells the ionic polymer by about 10 % (linear expansion) of its original size due to adsorption of solvents, which remarkably reduces the patterning accuracy [8]. Therefore, processing accuracy is quite improved in the present method compared to that of the previous method using photolithography techniques (average dimensional error: 10 %) [40].

Figure 6.7 shows the time history of the bending curvature of a piece of fabricated IPMC specimen with 1 time and 2 times plating (0.1 mm × 10 mm) operated in water when a DC voltage (1.0 V) was applied during 120 s. From the results, they can be activated by low voltage without cutting process of side wall of IPMC.

6.4.3 Materials

Dry actuators that can be fabricated simply through layer-by-layer casting with bucky gel which consists of ionic liquids and a single-wall carbon nanotube have been developed [45, 46]. Also, ionic polymer conductor network composite (IPCNC) including Nafion[®] membrane actuators, Nafion[®] coated with layer-by-layer (LbL) Au nanoparticle/poly(allylamine hydrochloride) (PAH) composite actuators, and Nafion[®] with vertically aligned carbon nanotube (VA-CNT)/Nafion[®] composite actuators have been developed [47, 48].

These actuators can be driven by low voltage and have long-time operation stability in air. Therefore, they are one of the most promising ion conductive polymer actuators as well as IPMC.

6.5 Conclusion

In this chapter, the fundamental aspects of the IPMC fabrication methods, evaluation techniques for testing, recent results of miniaturized IPMC, and recent developments of materials of ion conductive polymer actuators are described.

Ionic conductive polymers are suitable for applications such as bio inspired and autonomous robotics, medical devices, and aerospace because they have many unique characteristics such as low voltage driving, large deformation and flexibility.

References

1. Pugal D, Kim SJ, Kim KJ, Leang KK (2010) IPMC: recent progress in modeling, manufacturing, and new applications. In: Proceedings of the SPIE electroactive polymer actuators and devices (EAPAD), vol 7642, p 76420U. doi:10.1117/12.84828
2. Carpi F, Smela E (eds) (2009) Biomedical applications of electroactive polymer actuators. Wiley, Chichester. doi:10.1002/9780470744697
3. Oguro K, Kawami Y, Takenake H (1992) Bending of an ion-conducting polymer film-electrode composite by an electric stimulus at low voltage. *J Micromach Soc* 5:27–30
4. Bar-Cohen Y (ed) (2004) Electroactive polymer (EAP) actuators as artificial muscles: reality, potential, and challenges, 2nd edn. SPIE, Washington
5. Shahinpoor M (1992) Conceptual design, kinematics and dynamics of swimming robotic structures using ionic polymeric gel muscles. *Smart Mater Struct* 1:91–94. doi:10.1088/0964-1726/1/1/014
6. Tadokoro S, Konyo M, Oguro K (2004) Modeling IPMC for design of actuation mechanisms. In: Bar-Cohen Y (ed) Electroactive polymer (EAP) actuators as artificial muscles: reality, potential, and challenges, 2nd edn. SPIE, Washington, pp 385–427. doi:10.1117/3.547465.ch13

7. Yeo RS, Yeager HL (1985) Structural and transport properties of perfluorinated ion-exchange membrane. In: Conway BE, White RE, Bockris JOM (eds) *Modern aspects of electrochemistry*. Plenum, New York, pp 437–504
8. DuPont™ Nafion® membranes and dispersion. http://www2.dupont.com/FuelCells/en_US/products/naflon.html
9. Asaka K, Oguro K, Nishimura Y, Mizuhara M, Takenaka H (1995) Bending of polyelectrolyte membrane-platinum composites by electric stimuli I. Response characteristics to various waveforms. *Polym J* 27:436–440
10. Tadokoro S, Murakami T, Fuji S, Kanno R, Hattori M, Takamori T, Oguro K (1996) An elliptic friction drive element using an ICPF (ion conducting polymer gel film) actuator. In: *Proceedings of the IEEE international conference on robotics and automation*, pp 205–212
11. Shahinpoor M, Bar-Cohen Y, Simpson JO, Smith J (1998) Ionic polymer-metal composites (IPMCs) as biomimetic sensors, actuators and artificial muscles – a review. *Smart Mater Struct* 7:R15. doi:10.1088/0964-1726/7/6/001
12. Oguro K, Fujiwara N, Asaka K, Onishi K, Sewa S (1999) Polymer electrolyte actuator with gold electrodes. In: *Proceedings on the SPIE smart structures and materials 1999: electroactive polymer actuators and devices*, vol 3669, pp 64–71. doi:10.1117/12.349698
13. Fujiwara N, Asaka K, Nishimura Y, Oguro K, Torikai E (2000) Preparation of gold-solid polymer electrolyte composites as electric stimuli-responsive materials. *Chem Mat* 12 (6):1750–1754
14. Onishi K, Sewa S, Asaka K, Fujiwara N, Oguro K (2000) Bending response of polymer electrolyte actuator. In: *Proceedings of the SPIE smart structures and materials 2000: electroactive polymer actuators and devices (EAPAD)*, vol 3987, pp 121–128. doi:10.1117/12.387770
15. Shahinpoor M, Kim KJ (2000) The effect of surface-electrode resistance on the performance of ionic polymer-metal composite (IPMC) artificial muscles. *Smart Mater Struct* 9:543–551. doi:10.1088/0964-1726/9/4/318
16. Shahinpoor M, Kim KJ (2001) Ionic polymer-metal composites: I. Fundamentals. *Smart Mater Struct* 10:819–833
17. Kim KJ, Shahinpoor M (2003) Ionic polymer–metal composites: II. Manufacturing techniques. *Smart Mater Struct* 12:65–79
18. Shahinpoor M (2003) Ionic polymer–conductor composites as biomimetic sensors, robotic actuators and artificial muscles – a review. *Electrochim Acta* 48:2343–2353. doi:10.1016/S0013-4686(03)00224-X
19. Chung CK, Fung PK, Hong YZ, Ju MS, Lin CCK, Wu TC (2006) A novel fabrication of ionic polymer-metal composites (IPMC) actuator with silver nano-powders. *Sens Actuators B Chem* 117(2):367–375. doi:10.1016/j.snb.2005.11.021
20. Pugal D, Jung K, Aabloo A, Kim KJ (2010) Ionic polymer–metal composite mechano-electrical transduction: review and perspectives. *Polym Int* 59(3):279–289. doi:10.1002/pi.2759
21. Aoyagi W, Omiya M (2013) Mechanical and electrochemical properties of an IPMC actuator with palladium electrodes in acid and alkaline solutions. *Smart Mater Struct* 22:055028. doi:10.1088/0964-1726/22/5/055028
22. Heo S, Kim KJ, Lee DY, Vemuri S, Lee MH (2005) Multiwalled carbon nanotube/IPMC nanocomposite. In: *Proceedings of the SPIE smart structures and materials 2005: electroactive polymer actuators and devices (EAPAD)*, vol 5759, p 194. doi:10.1117/12.592267
23. Asaka K, Oguro K (2009) IPMC actuators: fundamentals. In: Carpi F, Smela E (eds) *Biomedical applications of electroactive polymer actuators*. Wiley, Chichester, pp 103–119. doi:10.1002/9780470744697
24. Kikuchi K, Tsuchitani S (2009) Nafion®-based polymer actuators with ionic liquids as solvent incorporated at room temperature. *J Appl Phys* 106:053519. doi:10.1063/1.3204961
25. Nakamura T, Ihara T, Horiguchi T, Mukai T, Asaka K (2009) Measurement and modeling of electro-chemical properties of ion polymer, metal composite by complex impedance analysis. *SICE J Control Measure Syst Integr* 2(6):373–378

26. Bennett M, Leo D (2005) Morphological and electromechanical characterization of ionic liquid/Nafion polymer composites. In: Proceedings on the SPIE smart structures and materials 2005: electroactive polymer actuators and devices (EAPAD), vol 5759, pp 506–517. doi:[10.1117/12.599849](https://doi.org/10.1117/12.599849)
27. Kikuchi K, Sakamoto T, Tsuchitani S, Asaka K (2011) Comparative study of bending characteristics of ionic polymer actuators containing ionic liquids for modeling actuation. *J Appl Phys* 109:073505. doi:[10.1063/1.3556434](https://doi.org/10.1063/1.3556434)
28. Panwar V, Lee C, Ko SY, Park JO, Park S (2012) Dynamic mechanical, electrical, and actuation properties of ionic polymer metal composites using PVDF/PVP/PSSA blend membranes. *Mat Chem Phys* 35:928–937. doi:[10.1016/j.matchemphys.2012.05.081](https://doi.org/10.1016/j.matchemphys.2012.05.081)
29. Asaka K, Oguro K (2000) Bending of polyelectrolyte membrane platinum composites by electric stimuli, part II. Response kinetics. *J Electroanal Chem* 480:186–198. doi:[10.1016/S0022-0728\(99\)00458-1](https://doi.org/10.1016/S0022-0728(99)00458-1)
30. Onishi S, Sewa S, Asaka K, Fujiwara N, Oguro K (2001) Morphology of electrodes and bending response of the polymer electrolyte electrodes and bending response of the polymer electrolyte actuator. *Electrochim Acta* 46:737–743. doi:[10.1016/S0013-4686\(00\)00656-3](https://doi.org/10.1016/S0013-4686(00)00656-3)
31. Asaka K, Fujiwara N, Oguro K, Onishi K, Sewa S (2001) State of water and ionic conductivity of solid polymer electrolyte membranes in relation to polymer actuators. *J Electroanal Chem* 505:24–32. doi:[10.1016/S0022-0728\(01\)00445-4](https://doi.org/10.1016/S0022-0728(01)00445-4)
32. Asaka K, Mori N, Hayashi K, Nakabo Y, Mukai T, Luo ZW (2004) Modeling of the electromechanical response of ionic polymer metal composites (IPMC). In: Proceedings on the SPIE, smart structures and materials 2004: electroactive polymer actuators and devices (EAPAD), vol 5385, pp 172–181. doi:[10.1117/12.539090](https://doi.org/10.1117/12.539090)
33. Gennes PG, Okumura K, Shahinpoor M, Kim KJ (2000) Mechanoelectric effects in ionic gels. *Europhys Lett* 50(4):513–518. doi:[10.1209/epl/i2000-00299-3](https://doi.org/10.1209/epl/i2000-00299-3)
34. Yamaue T, Mukai H, Asaka K, Doi M (2005) Electrostress diffusion coupling model for polyelectrolyte gels. *Macromolecules* 38(4):1349–1356. doi:[10.1021/ma047944j](https://doi.org/10.1021/ma047944j)
35. Bennett MD, Leo DJ (2004) Ionic liquids as stable solvents for ionic polymer transducers. *Sens Actuators A Phys* 115(1):79–90. doi:[10.1016/j.sna.2004.03.043](https://doi.org/10.1016/j.sna.2004.03.043)
36. Wang J, Xu C, Taya M, Kuga Y (2006) Flemion-based actuator with ionic liquid as solvent. In: Proceedings of the SPIE smart structures and materials 2006: electroactive polymer actuators and devices (EAPAD), vol 6168, p 61680R. doi:[10.1117/12.658548](https://doi.org/10.1117/12.658548)
37. Wang J, Xu C, Taya M, Kuga Y (2007) A Flemion-based actuator with ionic liquid as solvent. *Smart Mater Struct* 16:S214–S219. doi:[10.1088/0964-1726/16/2/S03](https://doi.org/10.1088/0964-1726/16/2/S03)
38. Bennett MD, Leo DJ, Wilkes GL, Beyer FL, Pechar TW (2006) A model of charge transport and electromechanical transduction in ionic liquid-swollen Nafion membranes. *Polymer* 47:6782–6796. doi:[10.1016/j.polymer.2006.07.061](https://doi.org/10.1016/j.polymer.2006.07.061)
39. Oh IK, Jeon JH, Lee YG (2006) Multiple electrode patterning of ionic polymer metal composite actuators. In: Proceedings of the SPIE smart structure and materials 2006: electro active polymer actuators and devices (EAPAD), vol 6168, p 616828. doi:[10.1117/12.658436](https://doi.org/10.1117/12.658436)
40. Kikuchi K, Tsuchitani S, Miwa M, Asaka K (2008) Formation of patterned electrode in ionic polymer-metal composite using dry film photoresist. *IEEE Trans Electric Electron Eng* 3 (4):452–454. doi:[10.1002/tee.20299](https://doi.org/10.1002/tee.20299)
41. Nakabo Y, Mukai T, Asaka K (2005) Kinematic modeling and visual sensing of multi-DOF robot manipulator with patterned artificial muscle. In: Proceedings of the IEEE international conference on robotics and automation, pp 4326–4331. doi:[10.1109/ROBOT.2005.1570784](https://doi.org/10.1109/ROBOT.2005.1570784)
42. Kikuchi K, Taniguchi T, Han H, Tsuchitani S (2012) Improvement of a formation method of patterned electrodes for IPMC by selective plasma treatment. *Proc EuroEAP* 2012:26–27
43. Kikuchi K, Taniguchi T, Miki H, Tsuchitani S (2013) Evaluation of driving characteristics of miniaturized ionic polymer actuator fabricated by a selective plasma treatment method. *Proc EuroEAP* 2013:38–39

44. Chen Z, Tan X (2010) Monolithic fabrication of ionic polymer-metal composite actuators capable of complex deformation. *Sens Actuators A Phys* 157(2):246–257. doi:[10.1016/j.sna.2009.11.024](https://doi.org/10.1016/j.sna.2009.11.024)
45. Fukushima T, Asaka K, Kosaka A, Aida T (2005) Layer-by-layer casting fabrication of soft actuator based on single-walled carbon nanotubes and ionic liquids. *Angew Chemie Int Ed* 44 (16):2410–2413. doi:[10.1002/anie.200462318](https://doi.org/10.1002/anie.200462318)
46. Mukai K, Asaka K, Kiyohaya K, Sugino T, Takeuchi I, Fukushima T, Aida T (2008) High performance fully plastic actuator based on ionic-liquid-based bucky gel. *Electrochim Acta* 53 (17):5555–5562. doi:[10.1016/j.electacta.2008.02.113](https://doi.org/10.1016/j.electacta.2008.02.113)
47. Liu S, Montazami R, Liu Y, Jain V, Lin M, Heflin JR, Zhang QM (2009) Layer-by-layer self-assembled conductor network composites in ionic polymer metal composite actuators with high strain response. *Appl Phys Lett* 95:023505. doi:[10.1063/1.3179554](https://doi.org/10.1063/1.3179554)
48. Liu Y, Zhao R, Ghaffari M, Lin J, Liu S, Cebeci H, Villoria RG, Montazami R, Dong Wang D, Wardle BL, James R, Heflin JR, Zhang QM (2012) Equivalent circuit modeling of ionomer and ionic polymer conductive network composite actuators containing ionic liquids. *Sens Actuators A Phys* 181:70–76. doi:[10.1016/j.sna.2012.05.002](https://doi.org/10.1016/j.sna.2012.05.002)

Chapter 7

Conducting Polymers

Keiichi Kaneto

Abstract Soft actuators based on conducting polymers are discussed in terms of strain, stress and stability taking the mechanism into consideration. The actuation is generated by the insertion of anions from the electrolyte solution, which is triggered by electrochemical redox reactions. Characteristics of the actuation in polypyrrole, polyaniline, polythiophene, and poly(3,4-ethylenedioxythiophene) (PEDOT) are described. The maximum strain and stress are reported to be 39.9 % and 22 MPa, respectively, in polypyrrole actuator. However, the strain is usually less than 10 %. The stress (contraction force) originates from the elasticity of conducting polymers or Young's modulus. Creeping under tensile loads, which is intimate issue in soft actuators, is discussed in terms of conformation change of polymer chains and shape memory effect. The actuation generated by sorption and desorption of moisture controlled with electrical heating is also introduced with the mechanism and characteristics.

Keywords Artificial muscle • Conducting polymer • Creeping • Electrochemomechanical deformation • Shape memory • Soft actuator • Stress–strain

7.1 Introduction

Artificial muscle is a future device to realize human friendly welfare robots mimicking living body. The artificial muscle, which is defined as a transducer of chemical energy into the contraction force of elastic materials, is too complicated to fabricate. Therefore, presently soft actuators with simple structure have been developed using synthetic polymers. The soft actuators are characterized by self-deformation with stimuli, softness, light-weight and silent movement, contrasting to piezoelectric actuators and shape-memory alloys.

Table 7.1 shows performance in various soft actuators [1–7] driven by electrical stimulus as well as the skeletal muscle for comparison. Conducting polymers have been interested in, because the relatively large strain and stress are generated by the application of low voltages [8–11]. The form of deformation in conducting polymer

K. Kaneto (✉)

Kyushu Institute of Technology, 3-3-72-804, Arato, Chuoku, Fukuoka 810-0062, Japan

e-mail: smartk@s7.dion.ne.jp

Table 7.1 Performance of various soft actuators

Materials	Form of deformation	Voltage (V)	Strain (%)	Stress (MPa)	Response time (s)	Cycle stability	Environment and remarks
Skeletal muscle	Expansion and contraction	–	20	0.1–0.4	0.1	⊙	Wet [1]
Ionic polymer and metal composites	Bending	2–3	>3	30	0.1	○	Wet [2]
Conducting polymers	Expansion and contraction	1–2	39	22	1	△	Wet [3]
Dielectric elastomers	Expansion and contraction	5,000	100	8	0.2–1	⊙	Dry [4]
Polymer gels	Bending	800	1.3	0.015	0.1	⊙	Dry (Organic Solvent) [5]
Hydro gels	Bending	2–3	–	–	–	○	Wet [6]
Carbon nanotubes	Bending	3–4	0.9	0.1	5	○	Wet (Ionic Liquid) [7]

is expansion and contraction, being similar to that of skeletal muscle. The other polymers except for dielectric elastomers exhibit bending motion. The bending motion is magnified by the bimorph structure and fun for the demonstration, however, is hard to utilize for the practical application.

In this chapter, mechanism, measurement, characteristics, performance and some other interesting features in conducting polymer soft actuators are mentioned.

7.2 Mechanism of Actuation

Conducting polymers, polypyrrole (PPy), polythiophene (PT), polyaniline (PANi) and poly(3,4-ethylenedioxythiophene) (PEDOT) are shown in Fig. 7.1, which have been well studied for soft actuators. These are π -conjugated linear polymers and semiconductor (or insulator) at the neutral state. Upon either electrochemical or chemical oxidation the conducting polymers turn highly conductive with the conductivity larger than several S/cm (metal like). The electrochemical oxidation takes place by removing π -electron via an external circuit and generating of positive charges (polaron or bipolaron) [12]. The schematic picture of polaron in PPy is shown in Fig. 7.1e. The polaron (or bipolaron) is delocalized along the polymer chain by about three unit rings, and is drifted by electric field as the charge carrier.

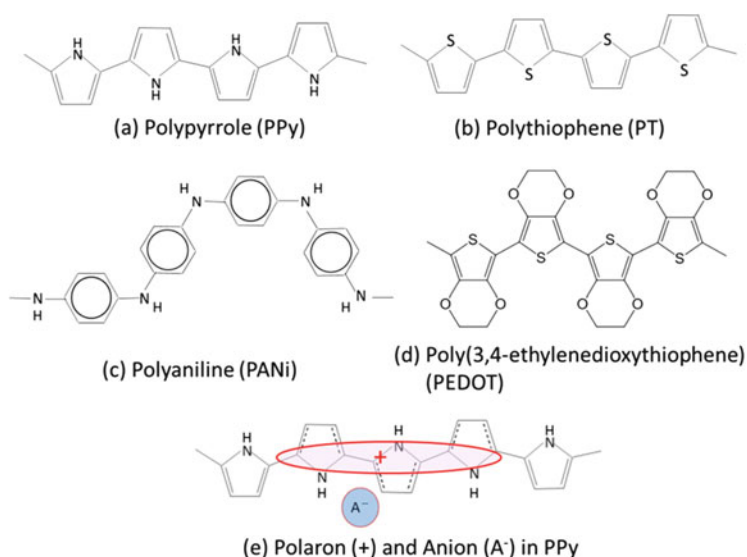


Fig. 7.1 Conducting polymers studied for soft actuator

7.2.1 Electrochemomechanical Actuation

The electrochemical oxidation is accompanied with insertion of anions from electrolyte solution, resulting in the expansion of conducting polymers by the volume of total inserted anions [1]. The degree of oxidation, namely, density of polaron (number of anion) can be controlled by the applied voltage to the conducting polymer (working electrode) against counter electrode. The considerably large swelling is demonstrated, when bulky anions are employed in electrolyte solution at high level of oxidization [3]. The deformation is named as electrochemomechanical deformation (ECMD). On the other hand, the chemical oxidation, which occurs spontaneously depending on the activity of oxidizing agent, is uncontrollable.

The mechanism of actuation in conducting polymers is shown in Fig. 7.2 for two modes of (a) anion drive and (b) cation drive actuations [13, 14]. Usually, conducting polymers are synthesized by either chemical or electrochemical oxidative polymerization of monomers; hence, the as-grown form is oxidized. Oxidized state is stiff compared with the reduced state, because of ionic crosslink at the polaron site with the presence of anion as shown in the right hand side of Fig. 7.2 and also delocalization of π -electron [14]. By the electrochemical reduction, the conducting polymers undergo two routes depending on the size of anions involved in polymerization process as shown in Fig. 7.2a, b. When small anion like ClO_4^- and bis-trifluoromethansulfonylimide (TSFI^-) is employed, the anion moves out from the bulk of conducting polymers into electrolyte solution during electrochemical reduction. In this route the reduced state is shrunk and the actuation is named as the anion drive shown by Fig. 7.2a. On the other hand, large anion like dodecylbenzenesulfonic (DBS^-) acid is used; the anion with long alkyl chain is entangled and immobilized in polymer network [13]. In this case, the conducting polymers are reduced by insertion of cation from electrolyte solution, hence swollen by the volume of additional cations as shown by cation drive in Fig. 7.2b.

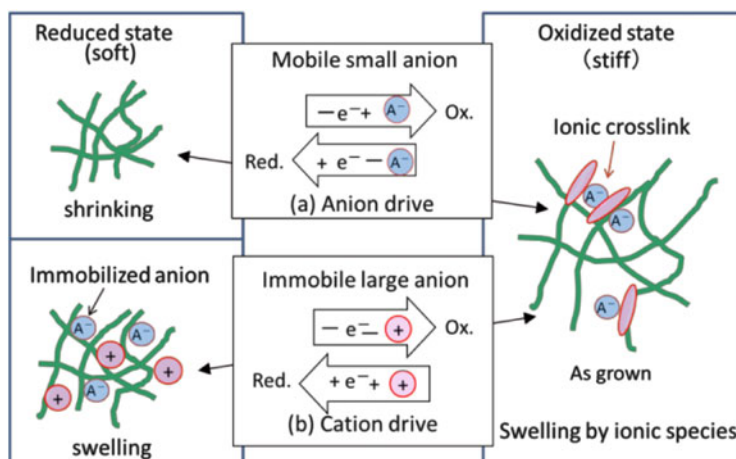


Fig. 7.2 Mechanism of ECMD in conducting polymers

7.2.2 Water Vapor Sorption Based Actuation

Besides the ECMD mechanism, conducting polymer actuators have been fabricated using water vapor induced swelling phenomenon [15–17]. Oxidized conducting polymer is salt form with the ionic bond between positive charges (polaron and bipolaron) and anions. The salt form is favorable to absorb water vapor, resulting in swelling. A film of oxidized conducting polymer is electrically conductive, and can be heated by passing a current with Joule heating. The heating evaporates the absorbed water, then the film shrinks. By turning off the current, the film cools down and absorbs moisture, resulting in swell again. Based on this mechanism, characteristics of conducting polymer actuators are studied for PPy and PEDOT in detail [16, 17].

7.3 Measurement of Actuation

By electrochemical reaction the conducting polymers change the dimension, which can be measured using a handmade apparatus shown in Fig. 7.3 [9, 13, 14]. The conducting polymer films with the approximate dimension of length of 10 mm, width of 2 mm and thickness of 10 μm was hung with a wire connected to working electrode in a glass cell with a pinhole at the bottom. The other end of film was connected through the pinhole to a plate of reflector, on which a weight of load was put to give an isotonic tension to the film. The change of film length was measured by a laser displacement meter under the reflector. Rectangular or triangle voltages are

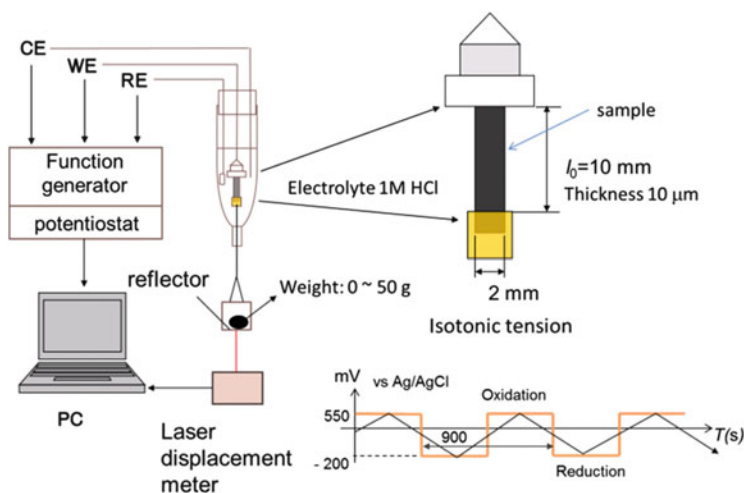
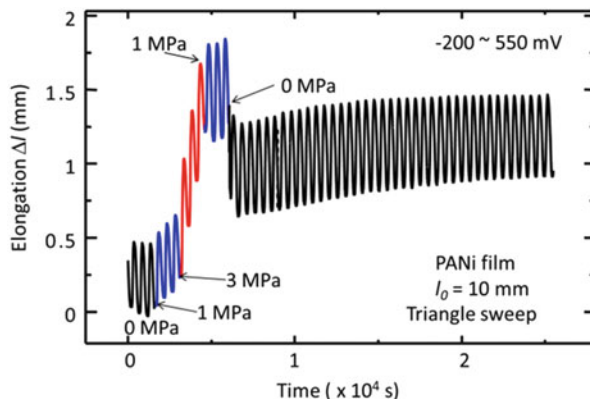


Fig. 7.3 Experimental setup for the measurement of ECMD in conducting polymer films, the typical waveforms of applied voltage are shown at the bottom

Fig. 7.4 Typical time dependence of electrochemomechanical elongation in PANi film under various load stresses



were applied to the film by a computer control system. Using this apparatus, the change of film length can be directly measured at various tensile loads.

Typical response of ECMD in PANi film is shown in Fig. 7.4 under tensile load stresses [18]. Short cycle response is due to elongation and contraction of the film by ECMD. The shift of elongation originates from creeping of the film under load stresses, and is enhanced by electrochemical cycles. It should be noted that the elongation of short cycle Δl after the application of tensile load of 3 MPa is increased, compared with that of the initial cycle at 0 MPa. This phenomenon is a training effect of actuators [18], and is discussed later.

7.4 Characteristics and Performance

7.4.1 Basic Characteristics in Conducting Polymer Actuators

Figure 7.5 depicts stress (σ)-strain (ϵ) curves in DBS doped PPy (PPy/DBS) film for the oxidized and reduced states [13]. Most conducting polymers behave similar in the magnitudes. The σ and ϵ are related with $\sigma = \epsilon E$, where E is Young's modulus. The result indicates that the oxidized state is stiffer than that of the reduced state by 2–3 times. The linear portion of the curves is the region of Hooke's law or elasticity. This elasticity indicates, for example, that 10 MPa stress approximately induces 5% strain balancing to contraction force of the elastic body.

Load stress (f) and actuation strain ($\Delta l/l_0$) curves in PPy and PANi films are shown in Fig. 7.6. Δl is the incremental length at f and l_0 is the original length of the film. The linear dependence between $\Delta l/l_0$ and f gives an empirical relation [19] of $\Delta l/l_0 = \Delta l_0/l_0 - f/E'$, where Δl_0 is the elongation at $f = 0$ MPa and E' is a constant related to Young's modulus. The f_0 in Fig. 7.4 is so called blocking force or the maximum contraction force of actuators. The result of Fig. 7.6 indicates that actuations in PPy and PANi are similar in the magnitudes of strain and stress

Fig. 7.5 Stress–strain curves in PPy/DBS film

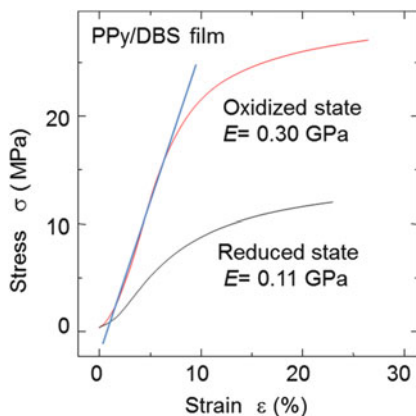
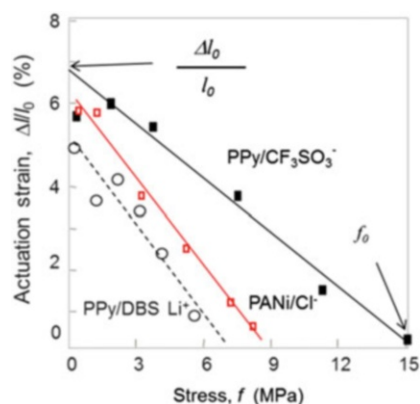


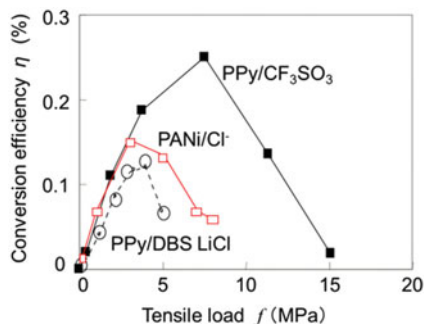
Fig. 7.6 Stress–strain curves in actuation of conducting polymers, PPy and PANi



curves, also being consistent with the static stress and strain curves shown in Fig. 7.5. For example, E' of PPy/DBS from Fig. 7.6 is obtained to be 0.14 GPa using the relation of $\Delta l_0/l_0 - f_0/E' = 0$, and corresponds to the middle of E .

Figure 7.7 shows energy conversion efficiencies in PPy and PANi actuators [20], that is, the ratio of mechanical output energy of $W_{\text{Mout}} = fS\Delta l_0$ to electrical input energy of $W_{\text{Ein}} = \int V i dt$, where S is cross section of the film, V is applied voltage and i is current for the actuator. The efficiency is small, because the most of W_{Ein} is stored in film as the secondary battery, which can be recovered during reduction or elongation. If the electrical energy is harvested during reduction, the efficiency should be increased. An interesting result is that the maximum efficiency was obtained at the half of blocking stress, indicating the W_{Ein} is nearly constant.

Fig. 7.7 Typical energy conversion efficiencies in PPy and PANi actuators derived from Fig. 7.6



7.4.2 Polypyrrole Actuator

Characteristics and performances of typical conducting polymer actuators are tabulated in Table 7.2. The maximum strain is the value at the load stress free. PPy has been widely studied among conducting polymers, because of the easy preparation by electrochemical deposition, stable actuation and large strain. The largest ECMD was reported for gel like porous PPy film, demonstrating the strain of 39.9 % [39]. Generally, in the anion drive actuators, the larger the anion the larger the strain. In addition, the large strain has been observed by the effect of solvation, in which ion is surrounded by solvent and forms cluster. It is also noted that even in cation drive mode the PPy film obtained by electrodeposition in DBS acid is strongly anisotropic, and the expansion of the film thickness direction is reported to be 35 % [25]. PPy prepared by chemical method has not been studied for the actuation, since it has been hard to obtain the high quality material, so far.

The PPy actuator based on water vapor absorption mechanism [15, 16] is also shown in Table 7.2. The strain depends on the ambient humidity and power of heating. For instance, PPy film with the conductivity of 94 S/cm, length 35 mm, width 4 mm and thickness 38 μm was heated by applied voltage of 3 V and current of 70 mA, resulted in 1.5 % strain at relative humidity (RH) of 50 %. In PEDOT/PSS film [17] with the conductivity of 3 S/cm, the applied voltage of 35 V gave the strain of 3.3 %. The response times for contraction and expansion are several tens second depending on the applied voltage.

7.4.3 Polyaniline Actuator

The merits of PANi are the stable operation in aqueous electrolytes, and the film can be chemically prepared by mass production using the cheap raw material [40]. The demerits of PANi actuator are that the actuator has to be operated in a strong acid (HCl) of pH < 1 with rather small strain of 3.2 %. By using high salt (3 M NaCl) concentration as the supporting electrolyte, the pH was increased to 3 and a larger strain of 6.7 % was obtained [29].

Table 7.2 Characteristics and performances of typical ECMD in various conducting polymers

Conducting polymers	Electrolyte solution	Strain (%)	Stress (MPa)	Preparation	Remarks and reference	
PPy	TBATFSI/H ₂ O	26.5	Blocking 7.6	ECD TBATFSI/ MB	Anion drive. [21]	
	NaPF ₆ /H ₂ O	12.4	Blocking 22	ECD BACF ₃ SO ₃ / MB	Anion drive. [22]	
	LiCl/H ₂ O	4.9	Blocking 5	ECD DBS/H ₂ O	Cation Drive. [23]	
	TBAPF ₆ /PC	2	At 5.0	ECD TBAPF ₆ /PC	Anion Drive. [24]	
	NaDBS/H ₂ O	thickness change 35	–	ECD NaDBS/H ₂ O	Cation Drive [25]	
	NaDEHS/CH ₃ CN/ H ₂ O	30	–	ECD NaDEHS/ H ₂ O	Anion Drive [26]	
	Ionic liquid: BMPTFSI	5	–	ECD LiTFSI/ MB/DP	Cation drive [27]	
	Ionic liquid: EMITFSA	2.5–3.0	0–6.5	ECD TBAPF ₆ /PC	Cation Drive [28]	
	Joule heating	1.5	–	ECD TBAClO ₄ / PC	Water Vapor, RH46–52 % [16]	
PANi	HCl/H ₂ O	6.7	Blocking 9	Chemical HCl	Anion drive. [29]	
	HCl/H ₂ O	0.92	Blocking 34	Chemical AMPS	Anion drive [30]	
	Ionic Liquid: BMIMBF ₄	0.28	–	Chemical	Cation drive [31]	
PAT	PHT	TBABF ₄ /CH ₃ CN	3.5	–	Chemical	Anion drive [32] 347 (2007)523
	PMT	TBAPF ₆ /PC	2.1	–	ECD. TBAPF ₆ /PC	Anion drive [33]
PEDOT	TBAPF ₆ /PC	2	–	ECD. TBAPF ₆ /PC	Anion and Cation drive [34]	
	TBACF ₃ SO ₃ /PC	2–3	At 1.35	ECD. TBACF ₃ SO ₃ / PC	Cation drive. [35]	
	KCl/H ₂ O	1.4	At 2	ECD. TBACF ₃ SO ₃ / MB	Cation drive [36]	
	Ionic liquid EMITFSI/PEO: PTHF IPN	0.75	–	Chemical FeCl ₃	Bilayer [37]	

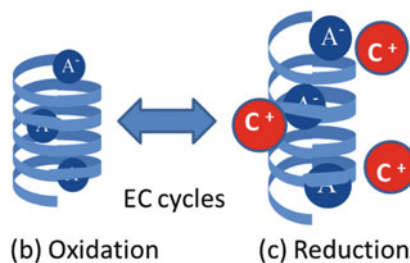
(continued)

Table 7.2 (continued)

Conducting polymers	Electrolyte solution	Strain (%)	Stress (MPa)	Preparation	Remarks and reference
	Ionic liquid BMITFSI etc./	Bending beam		Chemical	Bilayer Anion [38]
	Joule heating	3.3		Chemical	Water Vapor, RH20–90 % [17]

TBA tetrabutylammonium, *AMPS* 2-acrylamido-2-methyl-propane-1-sulfonic acid, *PC* propylene carbonate, *DEHS* di-(2-ethylhexyl) sulfosuccinate, *EMI* 1-ethyl-3-methylimidazolium, *MB* methyl benzoate, *DP* dimethyl phthalate, *BMP* 1-butyl-1-methylpyrrolidinium, *BMIM* 1-butyl-3-methyl imidazolium, *PTHF* poly(tetrahydrofurane), *IPN* Inter-Penetrating Network

Fig. 7.8 Schematic drawing of helical structure of PEDOT and EC cycles



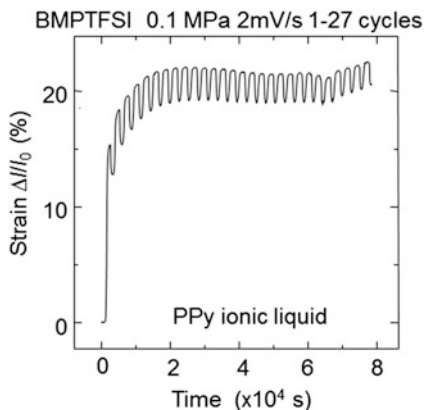
7.4.4 Polyalkylthiophene and PEDOT Actuators

Poly(alkylthiophene), PAT, is rather hard to prepare either chemically or electrochemically for tough film suitable to actuator. This is reason why few study in electrochemical devices and also because of small strain and unstable actuation [32, 41]. On the other hand for the instability of PAT actuators, PEDOT being polythiophene derivative is remarkably stable in air and electrochemical cycles. However, the ECMD strains reported are small as shown in Table 7.2, the ECMD is mostly cation drive mode due to the PEDOT structures. It is proposed that PEDOT prepared by electrochemical polymerization takes the helical structure, and the anions are thought to be immobilized inside helix [36] as shown in Fig. 7.8.

7.4.5 Ionic Liquids

Ionic liquids (ILs) have attracted much attention because of the large ion mobility, stability, inflammability and large electrochemical window. ECMDs using ILs have been studied for many soft actuators including conducting polymers, carbon nano-tube and IPMC as discussed in other chapters. ILs are consisting of large cations

Fig. 7.9 Initial creeping of PPy actuator in ionic liquid by EC reduction



and anions, therefore, the response of ECMD is usually slow. ECMD in conducting polymers and ILs mostly exhibit cation drive mode, even anions are smaller than cations [27, 28].

As shown in Fig. 7.9 the electrochemical cycle of PPy in IL starts by reduction and swelling with cation doping, and never begins by oxidation [42]. This is explained as follows. Conducting polymer films as-synthesized and oxidized form repel ILs and do not wet with ILs. The fact indicates that inside film is filled with dopant anions, then, cations and ILs initiate to move into the film to attain the concentration equilibrium of IL inside and outside of film. The initial large creeping is due to insertion of IL into the film. The mechanism is reasonable and favorable, contrary to that anions move out by reduction, due to high concentration of the ionic liquid in electrolyte. The strain of ECMD is small and approximately 1–2 %, since the cation of ionic liquid moves solely in the conducting polymer without making solvation. In another word, large strain may not be expected in conducting polymer and ionic liquid actuators.

7.5 Creep and Related Phenomena

Creeping is observed under tensile stress, when a load stress goes over the elastic or Hook's law region. In soft actuators the creeping is literally serious issues for the precise positioning [14, 18, 24]. Creeping results from (1) slipping of polymer chains, (2) breaking and yielding of chains and (3) conformation change of polymer alignment. Creeping is significantly enhanced during EC cycles [18] as shown in Fig. 7.10a, which is compared with the mechanical creeping of Fig. 7.10b without EC cycles. The reason is that ions move dynamically in the polymer network during electrochemical cycles generating and degenerating ionic crosslinks. This is named as electrochemical (EC)-creeping and a few studies [18, 24] are reported. The creeping due to (1) and (2) is the permanent deformation and that by (3) is recovered by removing the tensile load and EC cycles [14]. As shown in

Fig. 7.10 (a) EC creep and (b) mechanical creep in PANi film

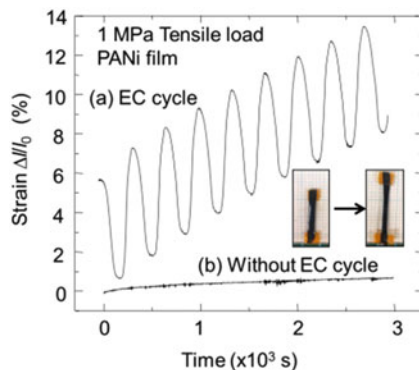


Fig. 7.11 Recovery of creep

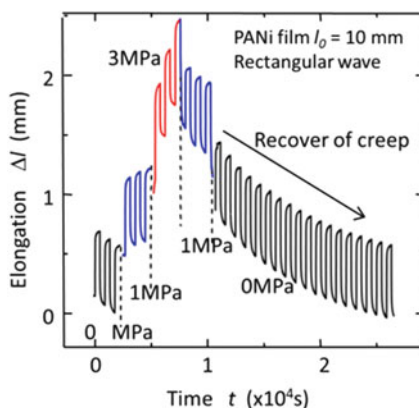


Fig. 7.11 the recovery of EC creep is clearly observed in PANi film, when operated by a rectangular wave forms, somehow different from the case of triangular sweep (Fig. 7.4).

The training, memory effects and recovery of creep are resulted from the conformation change of polymer chains [14, 18]. The mechanism of training effect is that the tensile stress stretches polymer chains to be anisotropic and enhances the electrochemical activity of the film. The stretched conformation is frozen or fixed with ionic crosslink, resulting in the shape memory. By removing the tensile stresses and EC cycles, stretched polymer chains come back to original shape by the elasticity of polymer chains (thermal relaxation), resulting in recovery of creeping.

7.6 Conclusion

Various approaches have been attempted to enhance the strain and stress to the level of demands for practical applications. The largest strain of 39 % and stress of 22 MPa are better than those of a typical skeletal muscle of 20 % and 0.1 MPa,

respectively. Conducting polymer actuators have some superiority compared with the other soft actuators, however, the total performance is still below the commercial level, so far. The conducting polymer actuators are suffering from issues of cycle life, response time. The cycle life has been improved by the operation of moderate potential spans and employing ionic liquids with wide potential window. In use of ionic liquid, the cycle life has been elongated to some extent; however, the strain is not satisfactory. The response time in typical conducting polymers are around 1 s, which is not quick enough for the application. We believe that using conformation change of polymer structure could be a possible mechanism for the innovative soft actuators.

References

1. Mirfakhrai T, Madden JDW, Baughman RH (2007) Polymer artificial muscles. *Mater Today* 10:30–38. doi:[10.1016/S1369-7021\(07\)70048-2](https://doi.org/10.1016/S1369-7021(07)70048-2)
2. Asaka K, Oguro K, Nishimura Y, Mizutani M, Takenaka H (1995) Bending of polyelectrolyte membrane-platinum composites by electric stimuli. I. Response characteristics to various wave-forms. *Polym J* 27:436–440. doi:[10.1295/polymj.27.436](https://doi.org/10.1295/polymj.27.436)
3. Hara S, Zama T, Takashima W, Kaneto K (2005) Free-standing gel-like polypyrrole actuators doped with bis(perfluoroalkylsulfonyl)imide exhibiting extremely large strain. *Smart Mater Struct* 14:1501–1510. doi:[10.1088/0964-1726/14/6/042](https://doi.org/10.1088/0964-1726/14/6/042)
4. Pelrine R, Kornbluh R, Pei Q, Joseph J (2000) High-speed electrically actuated elastomers with strain greater than 100 %. *Science* 287:836–839. doi:[10.1126/science.287.5454.836](https://doi.org/10.1126/science.287.5454.836)
5. Hirai T, Sadatoh H, Ueda T, Kasazaki T, Kurita Y, Hirai M, Hayashi S (1996) Polyurethane elastomer actuator. *Angew Makromol Chemie* 240:211–229. doi:[10.1002/apmc.1996.052400121](https://doi.org/10.1002/apmc.1996.052400121)
6. Osada Y, Okuzaki H, Hori H (1992) A polymer gel with electrically driven motility. *Nature* 355:242–244. doi:[10.1038/355242a0](https://doi.org/10.1038/355242a0)
7. Fukushima T, Asaka K, Kosaka A, Aida T (2005) Fully plastic actuator through layer-by-layer casting with ionic-liquid bucky gel. *Angew Chem Int Ed* 44:2410–2413. doi:[10.1002/anie.200462318](https://doi.org/10.1002/anie.200462318)
8. Baughman RH (1996) Conducting polymer artificial muscles. *Synth Met* 78:339–353. doi:[10.1016/0379-6779\(96\)80158-5](https://doi.org/10.1016/0379-6779(96)80158-5)
9. Kaneto K, Min Y-G, MacDiarmid AG (1994) Conductive polyaniline laminates. U.S-Patent 5,556,700
10. Otero TF, Sansinena JM (1995) Artificial muscles based on conducting polymers. *Bioelectrochem Bioenerg* 38:411–414. doi:[10.1016/0302-4598\(95\)01802-L](https://doi.org/10.1016/0302-4598(95)01802-L)
11. Hara S, Zama T, Takashima W, Kaneto K (2005) Free-standing polypyrrole actuators with response rate of 10.8 % s⁻¹. *Synth Met* 149(2–3):199–201. doi:[10.1016/j.synthmet.2005.01.003](https://doi.org/10.1016/j.synthmet.2005.01.003)
12. Bredas JL, Wudl F, Heeger AJ (1987) Polarons and bipolarons in doped polythiophene: a theoretical investigation. *Solid State Commun* 63:577–580. doi:[10.1016/0038-1098\(87\)90856-8](https://doi.org/10.1016/0038-1098(87)90856-8)
13. Sendai T, Suematsu H, Kaneto K (2009) Anisotropic strain and memory effect in electrochemomechanical strain of polypyrrole films under high tensile stresses. *Jpn J Appl Phys* 48:051506. doi:[10.1143/JJAP.48.051506](https://doi.org/10.1143/JJAP.48.051506) (4 pages)
14. Kaneto K, Hashimoto H, Tominaga K, Takashima W (2011) Shape retention in polyaniline artificial muscles. *Jpn J Appl Phys* 50:021603. doi:[10.1143/JJAP.50.021603](https://doi.org/10.1143/JJAP.50.021603) (5 pages)

15. Okuzaki H, Kunugi T (1996) Adsorption-induced bending of polypyrrole films and its application to a chemomechanical rotor. *J Polym Sci B Polym Phys* 34:1735–1749. doi:10.1002/(SICI)1099-0488(19960730)34:10<1747::AID-POLB5>3.0.CO;2-N
16. Okuzaki H, Kunugi T (1998) Electrically induced contraction of polypyrrole film in ambient air. *J Polym Sci B Polym Phys* 36:1591–1594. doi:10.1002/(SICI)1099-0488(19980715)36:9<1591::AID-POLB16>3.3.CO;2-W
17. Okuzaki H, Suzuki H, Ito T (2009) Electrically driven PEDOT/PSS actuators. *Synth Metal* 159:2233–2236. doi:10.1016/j.synthmet.2009.07.054
18. Tominaga K, Hashimoto H, Takashima W, Kaneto K (2011) Training and shape retention in conducting polymer artificial muscles. *Smart Mater Struct* 20:124005. doi:10.1088/0964-1726/20/12/124005 (6 pages)
19. Spinks GM, Truong VT (2005) Work-per-cycle analysis for electromechanical actuators. *Sens Actuators A* 119:455–461. doi:10.1016/j.sna.2004.10.010
20. Kaneto K, Fujisue H, Kunifusa M, Takashima W (2007) Conducting polymer soft actuators based on polypyrrole films-energy conversion efficiency. *Smart Mater Struct* 16:S250–S255. doi:10.1088/0964-1726/16/2/S08
21. Hara S, Zama T, Takashima W, Kaneto K (2004) TFSI-doped polypyrrole actuator with 26 % strain. *J Mater Chem* 14:1516–1517. doi:10.1039/b404232h
22. Hara S, Zama T, Takashima W, Kaneto K (2004) Artificial muscles based on polypyrrole actuators with large strain and stress induced electrically. *Polym J* 36:151–161. doi:10.1295/polymj.36.151
23. Fujisue H, Sendai T, Yamato K, Takashima W, Kaneto K (2007) Work behaviors of soft actuators based on cation driven polypyrrole. *Bioinsp Biomim* 2:S1–S5. doi:10.1088/1748-3182/2/2/S01
24. Madden JD, Ringerknecht D, Anquetil PA, Hunter IW (2007) Creep and cycle life in polypyrrole actuators. *Sens Actuators A* 133:210–217. doi:10.1016/j.sna.2006.03.016
25. Smela E, Gadegaard N (2001) Volume change in polypyrrole studied by atomic force microscopy. *J Phys Chem B* 105:9395–9406. doi:10.1021/jp004126u
26. Foroughi J, Spinks GM, Wallace GG (2011) High strain electromechanical actuators based on electrodeposited polypyrrole doped with di-(2ethylhexyl)sulfosuccinate. *Sens Actuators B* 155:278–284. doi:10.1016/j.snb.2010.12.035
27. Yamato K, Tominaga K, Takashima W, Kaneto K (2009) Stability of electrochemomechanical strains in polypyrrole films using ionic liquids. *Synth Met* 159:839–842. doi:10.1016/j.synthmet.2009.01.016
28. Ding J, Zhou D, Spinks G, Wallace GG, Forsyth S, Forsyth M, MacFarlane D (2003) Use of ionic liquid as electrolytes in electromechanical actuator systems based on inherently conducting polymers. *Chem Mater* 15:2392–2398. doi:10.1021/cm020918k
29. Takashima W, Nakashima M, Pandey SS, Kaneto K (2004) Enhanced electrochemomechanical activity of polyaniline films towards high pH region: contribution of Donnan effect. *Electrochim Acta* 49:4239–4244. doi:10.1016/j.jelectacta.2004.04.020
30. Smela E, Lu W, Mattes BR (2005) Polyaniline actuators: Part I PANi(AMPS) in HCl. *Synth Metal* 151:26–42. doi:10.1016/j.synthmet.2005.03.009
31. Lu W, Mattes BR (2005) Factors influencing electrochemical actuation of polyaniline fibers in ionic liquids. *Synth Met* 152:53–56. doi:10.1016/j.synthmet.2005.07.122
32. Fuchiwaki M, Takashima W, Kaneto K (2002) Soft actuators based on poly(3-alkylthiophene) films upon electrochemical oxidation and reduction. *Mol Cryst Liq Cryst* 374:513–520. doi:10.1080/10587250210420
33. Xi BB, Truong VT, Whitten P, Ding J, Spinks GM, Wallace GG (2006) Poly(3-methylthiophene) electrochemical actuators showing increased strain and work per cycle at higher operating stresses. *Polymer* 47:7720–7725. doi:10.1016/j.polymer.2006.08.063
34. Vandesteeg N, Madden PG, Madden JD, Anquetil PA, Hunter IW (2003) Synthesis and characterization of EDOT-based conducting polymer actuators. *Smart Struct Mater EAPAD* 5051:349–356. doi:10.1117/12.484418

35. Kiefer R, Bowmaker GA, Cooney RP, Kilmartin PA, Sejdic JT (2008) Cation driven actuation for free standing PEDOT film prepared from propylene carbonate electrolytes containing TBACF₃SO₃. *Electrochim Acta* 53:2593–2599. doi:[10.1016/j.electacta.2007.10.033](https://doi.org/10.1016/j.electacta.2007.10.033)
36. Kaneto K, Takayanagi K, Tominaga K, Takashima W (2012) How to improve electrochemo-mechanical strain in conducting polymers. In: Proceedings of SPIE electroactive polymer actuators and devices (EAPAD), vol 8340, pp 83400K-1~7. doi:[10.1117/12.917879](https://doi.org/10.1117/12.917879)
37. Plesse C, Khaldhi A, Wang Q, Cattan E, Eyssie D, Chevrot C, Vidal F (2011) Polyethylene oxide-polytetrahydrofurane-PEDOT conducting interpenetrating polymer networks for high speed actuators. *Smart Mater Struct* 20:124002. doi:[10.1088/0964-1726/20/12/124002](https://doi.org/10.1088/0964-1726/20/12/124002) (8 pages)
38. Cho MS, Seo HJ, Nam JD, Choi HR, Koo JC, Song KG, Lee Y (2006) A solid state actuator based on the PEDOT/NBR system. *Sens Actuators B* 119:621–624. doi:[10.1016/j.snb.2006.01.021](https://doi.org/10.1016/j.snb.2006.01.021)
39. Hara S, Zama T, Takashima W, Kaneto K (2005) Gel-like polypyrrole based artificial muscles with extremely large strain. *Polym J* 36:933–936. doi:[10.1295/polymj.36.933](https://doi.org/10.1295/polymj.36.933)
40. Kaneto K, Kaneko M, Min Y, MacDiarmid AG (1995) Artificial muscle: electromechanical actuators using polyaniline films. *Synth Metal* 71:2211–2212. doi:[10.1016/0379-6779\(94\)03226-V](https://doi.org/10.1016/0379-6779(94)03226-V)
41. Fuchiwaki M, Takashima W, Kaneto K (2001) Comparative study of electrochemomechanical deformation of poly(3-alkylthiophene)s, polyaniline and polypyrrole films. *Jpn J Appl Phys* 40:7110–7116. doi:[10.1143/JJAP.40.7110](https://doi.org/10.1143/JJAP.40.7110)
42. Kaneto K, Shinonome T, Tominaga K, Takashima W (2011) Electrochemical creeping and actuation of polypyrrole in ionic liquid. *Jpn J Appl Phys* 50:091601. doi:[10.1143/JJAP.50.091601](https://doi.org/10.1143/JJAP.50.091601) (5 pages)

Chapter 8

Humidity-Sensitive Conducting Polymer Actuators

Hidenori Okuzaki

Abstract Free-standing films made of poly(3,4-ethylenedioxythiophene) doped with poly(4-styrenesulfonate) (PEDOT/PSS) were prepared by casting water dispersion of its colloidal particles. Specific surface area, water vapor sorption, and electro-active polymer actuating behavior of the resulting films were investigated by means of sorption isotherm, and electromechanical analysis. It was found that the non-porous PEDOT/PSS film, having a specific surface area of $0.13 \text{ m}^2/\text{g}$, sorbed water vapor of $1,080 \text{ cm}^3(\text{STP})/\text{g}$, corresponding to 87 wt%, at relative water vapor pressure of 0.95. Upon application of 10 V, the film underwent contraction of 2.4 % in air at 50 % relative humidity (RH) which significantly increased to 4.5 % at 90 % RH. The principle lay in desorption of water vapor sorbed in the film due to Joule heating, where electric field was capable of controlling the equilibrium of water vapor sorption. The film generated contractile stress as high as 17 MPa under isometric conditions and work capacity attained $174 \text{ kJ}/\text{m}^3$, where Young's modulus of the film increased from 1.8 to 2.6 GPa by application of 6 V at 50 % RH. On the basis of this phenomenon, linear actuators utilizing PEDOT/PSS films were successfully developed and applied to leverage actuator and Braille cell.

Keywords Desorption • Humidity • Joule heating • Linear actuator • PEDOT/PSS

8.1 Introduction

Polymers which undergo dimensional changes in response to various environmental stimuli are capable of transducing chemical or physical energy directly into mechanical work. Conducting polymers, such as polypyrrole, polythiophene, and polyaniline, have attracted considerable attention because dimensional changes resulting from electrochemical doping, characterized by transportation of solvated ions between inside of the polymer matrix and the surrounding electrolyte solution, electrostatic repulsion, and/or structural distortion through oxidation of π -conjugated

H. Okuzaki (✉)

Interdisciplinary Graduate School of Medicine and Engineering, University of Yamanashi,
4-4-37 Takeda, Kofu 400-8511, Japan

e-mail: okuzaki@yamanashi.ac.jp

polymers, can be applied to produce electro-active polymer (EAP) actuators or artificial muscles [1–3]. Most of them operate in an electrolyte solution or in a swollen state, while few reports have been investigated on solid-state polymers in a redox gas atmosphere or that employ a polyelectrolyte or ionic liquid [4–6].

Since the first observation of a curious phenomenon whereby electrochemically synthesized polypyrrole (PPy) films underwent rapid bending due to water vapor sorption, we devised polymer motors capable of transducing chemical free energy change of sorption directly into continuous rotation [7–9]. Furthermore, we found that the PPy film contracted in air under application of an electric field [7, 10, 11], which was explained by desorption of water vapor caused by Joule heating. Unlike conducting polymer actuators driven by the electrochemical doping and dedoping, this system operated in air without using an electrolyte solution and counter/reference electrodes. However, the PPy film exhibits contractile strain of ca. 1 % [11] which is smaller than other EAP actuators [1–6]; besides the electrochemical synthesis is inefficient taking time compared with facile casting or printing process, which limits mass production and reduction in costs for practical applications.

This chapter deals with a novel EAP actuator utilizing poly(3,4-ethylenedioxythiophene) (PEDOT) films prepared by casting water dispersion of PEDOT doped with poly(4-styrenesulfonate) (PEDOT/PSS) as colloidal particles [12–15]. The PEDOT/PSS is a conductive polymer having a hierarchical structure: the sequence of monomer units of PEDOT and PSS (primary structure) forms a poly-ion complex through electrostatic interactions (secondary structure). The poly-ion complex disperses in water as a colloidal gel particle (tertiary structure) where hydrophobic PEDOT molecules aggregate to form physical cross-links between the PSS chains [16]. Therefore, the PEDOT/PSS colloidal gel particles can be shaped into various shapes such as thin coatings on various substrates [17], fibers [18, 19], and free-standing thick films (quaternary structure) [12–15]. Here, the PSS has two functions: one is the dopant ions of the doped PEDOT cations to compensate the charges; and the other is the dispersant of hydrophobic PEDOT molecules in the form of colloidal particles to disperse in water. Herein we investigate specific surface area, water vapor sorption, and EAP actuating behavior of the PEDOT/PSS films by means of sorption isotherm, and electromechanical analysis. Furthermore, we have developed linear actuators utilizing PEDOT/PSS films and applied to leverage actuator and Braille cell.

8.2 Experimental

PEDOT/PSS was commercially available in the form of water dispersion as Clevios P AG (Heraeus). Free-standing films were prepared by casting the PEDOT/PSS dispersion containing 3 wt% of ethylene glycol in a Teflon dish and allowing it to solidify by evaporation of solvent at 60 °C for 6 h and subsequent annealing at 160 °C for 1 h in a vacuum. Specific surface area of the PEDOT/PSS film was evaluated with a Belsorp-mini II (Bel Japan) by means of a free space measurement

technique at 77 K using Kr as a sorbent. Water vapor sorption of the film was measured by a volumetric method using a Belsorp-aqua3 (Bel Japan) at each water vapor pressure after reaching the equilibrium state. Prior to the measurement, the film was cut into small pieces and dried at 160 °C for 6 h under a nitrogen stream until the weight reached a constant in order to remove sorbed water completely. Electrical conductivity of the PEDOT/PSS film was measured by a normal four-point method with a Lorester (MCP-T610, Dia Instruments). The EAP actuating behavior of the films (10–50 mm long, 2 mm wide, and 17 μm thick) was measured in air at 25 °C and various RHs with an electromechanical cell equipped with an inductive displacement sensor (EX-416 V, Keyence). Temperature at the film surface was measured with an infrared thermometer (THI-500S, Tasco) and a thermographic image was obtained with a thermovision (CPA-2200, Chino). RH in the vicinity of the film surface was measured with a hygrometer (THP-728, Shinyei). Contractile stress generated by application of an electric field was measured under isometric condition using the electromechanical cell equipped with a strain gauge (LTS-500GA, Kyowa), where evaluation of Young's modulus was carried out from stress–strain curves measured at a constant strain rate of 10 %/min.

8.3 Results and Discussion

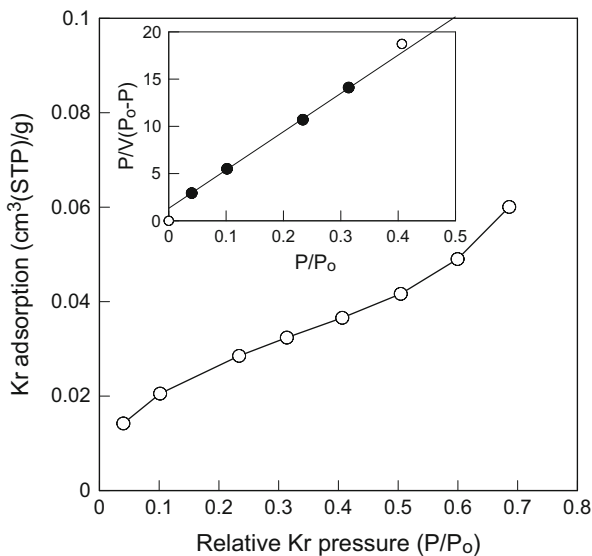
8.3.1 Specific Surface Area

Since dimensional changes of PEDOT/PSS films are caused by reversible sorption and desorption of water vapor [12–15], specific surface area of the film was evaluated by means of sorption isotherm at 77 K using Kr as a sorbent. It is seen from Fig. 8.1 that the isothermal adsorption curve belongs to the type II of IUPAC classification described by Brunauer-Emmett-Teller (BET) equation as follows [20]:

$$\frac{P}{V(P_0 - P)} = \frac{1}{V_m C} + \frac{(C - 1)P}{V_m C P_0} \quad (8.1)$$

where V_m and V are the volumes of Kr adsorbed in a monolayer and in the film, respectively. P and P_0 are Kr pressure and saturated Kr pressure, respectively, and C is a constant involving the heat of adsorption. As shown in the inset of Fig. 8.1, the BET plot shows a linear relation in a relative Kr pressure (P/P_0) range between 0.04 and 0.31. Using the data of V_m (0.025 cm³(STP)/g), where STP denotes standard temperature and pressure at 0 °C and 1 atm, BET specific surface area (A_{BET}) can be calculated according to the following equation:

Fig. 8.1 Isothermal sorption curve of Kr for PEDOT/PSS film and BET plot (*inset*) measured at 77 K



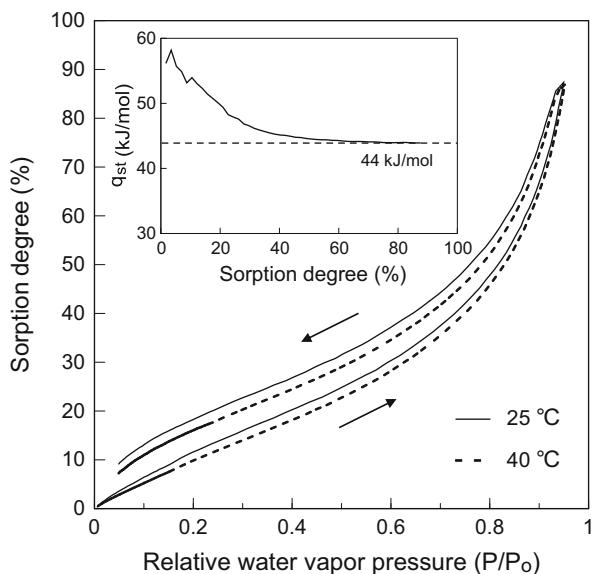
$$A_{BET} = \frac{V_m}{22414} \times 6.02 \times 10^{23} \times a_{Kr} \quad (8.2)$$

where a_{Kr} is the cross sectional area of a Kr molecule (0.202 nm^2). The value of A_{BET} for the PEDOT/PSS film is calculated to be $0.13 \text{ m}^2/\text{g}$ [13] that is three orders of magnitude smaller than that of porous materials such as silica gels ($300\text{--}500 \text{ m}^2/\text{g}$) [21] and alumina ($200\text{--}400 \text{ m}^2/\text{g}$) [22]. This implies that the PEDOT/PSS cast film is non-porous despite the fact that the film is formed by aggregation of PEDOT/PSS colloidal particles with diameters of several-tens nm dispersing in water, which might be associated with that void space of the film is filled with water soluble glassy PSS [23].

8.3.2 Water Vapor Sorption

Since the PEDOT/PSS contains ca. 70 wt% of PSS, a typical hydrophilic polyelectrolyte bearing sulfonic acid groups stabilizing the dispersion in water, the films made of PEDOT/PSS may absorb moisture in ambient atmosphere. Figure 8.2 shows isothermal sorption curves of the PEDOT/PSS films measured at $25 \text{ }^\circ\text{C}$ (solid lines) and $40 \text{ }^\circ\text{C}$ (broken lines). The sorption degree increases with increasing the relative water vapor pressure and the value attains 87 wt%, corresponding to $1,080 \text{ cm}^3(\text{STP})/\text{g}$, at relative water vapor pressure of 0.95, which is one order of magnitude larger than the PPy films [24] because of the hydrophilic PSS. At the same relative water vapor pressure, the sorption degree for desorption is higher than that for sorption, indicative of a hysteresis involving thermodynamically

Fig. 8.2 Isothermal sorption and desorption curves of water vapor for PEDOT/PSS film measured at 25 °C (solid lines) and 40 °C (broken lines). Inset: isosteric heat of sorption as a function of water vapor sorption



irreversible processes that can be interpreted by conformational changes of hydrated PSS chains and/or condensation of water vapor sorbed in the film. It is also seen from Fig. 8.2 that a rise in the temperature from 25 to 40 °C lowers the sorption degree, demonstrating the sorption of water vapor to the PEDOT/PSS film is an exothermic process. Although direct calorimetric measurement of isosteric heat of sorption (q_{st}) is more accurate, the q_{st} can be estimated from two isothermal sorption curves measured at different temperatures by a change in the water vapor pressure at the same degree of sorption using Clausius-Clapeyron equation as follows [25]:

$$q_{st} = \frac{RT_1T_2}{T_2 - T_1} (\ln P_2 - \ln P_1) \quad (8.3)$$

where R is the gas constant and P_1 and P_2 are water vapor pressures at temperatures T_1 and T_2 , respectively. The inset of Fig. 8.2 shows changes in the isosteric heat of sorption as a function of sorption degree evaluated using the two sorption isotherms at 25 and 40 °C. At sorption degree of 3.5 wt%, the q_{st} attains 58.2 kJ/mol, while an increase of the sorption degree brings about a decrease of the value to 43.9 kJ/mol, being consistent with the heat of water condensation (44 kJ/mol) [13, 26]. The fact demonstrates that at low sorption degree water molecules are initially adsorbed directly onto the most active sites such as hydrophilic sulfonic acid groups of the PSS forming the first monomolecular layer, giving rise to higher energy of interaction between water and the sorption sites. As these active sites were occupied, further sorption of water molecules subsequently occurs on the less active sites or on the already adsorbed water molecules covering the active sites, creating

additional water layers. At higher sorption degree, the interaction between water molecules is dominant rather than between polymer and water, which gives lower values of q_{st} close to the heat of water condensation.

8.3.3 Contraction Under Electric Field

Figure 8.3 shows time profiles of length change, electric current, surface temperature of the PEDOT/PSS film, and RH in the vicinity of the film surface. When DC 10 V is applied to the film (50 mm long, 2 mm wide, and 17 μm thick) under the thermostatic conditions (25 $^{\circ}\text{C}$, 50 % RH), the film undergoes significant contraction in response to the electric field. The degree of contraction reaches 1.2 mm, corresponding to a strain of 2.4 % [12], which is more than twice that of the PPy films (ca. 1 %) [11]. Here, the PEDOT/PSS film contracts in air without the use of an electrolyte solution or redox gas, indicating the mechanism differs from the electrochemical doping [1–3]. The electric current passing through the film is about 95 mA, and the temperature at the film surface rises from 25 to 64 $^{\circ}\text{C}$. It is noted that RH in the vicinity of the film surface abruptly rises by application of the electric

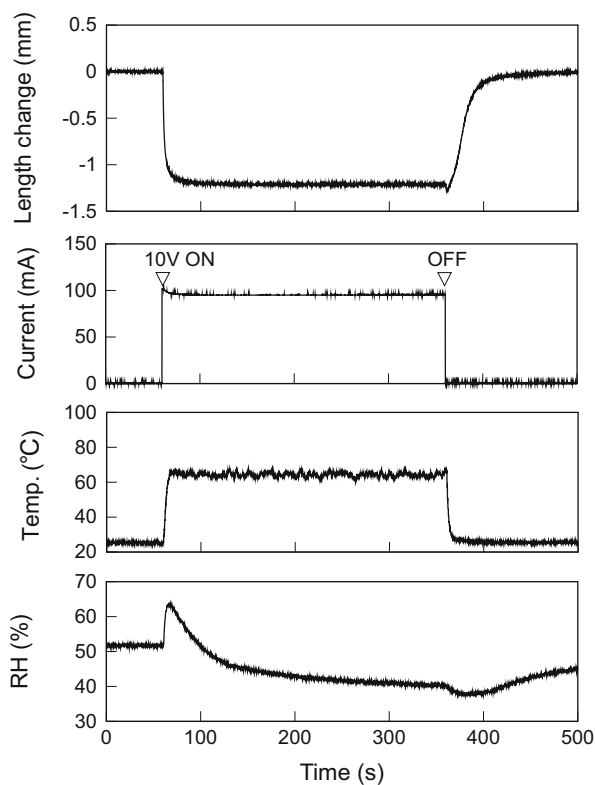
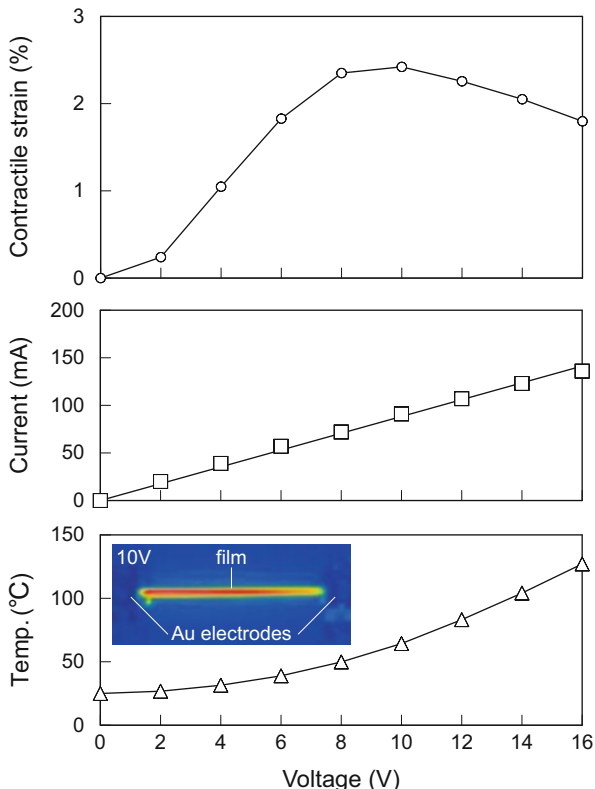


Fig. 8.3 Time profiles of length change, electric current, surface temperature of PEDOT/PSS film (50 mm long, 2 mm wide, and 17 μm thick), and RH in the vicinity of the film surface under 10 V measured at 25 $^{\circ}\text{C}$ and 50 % RH

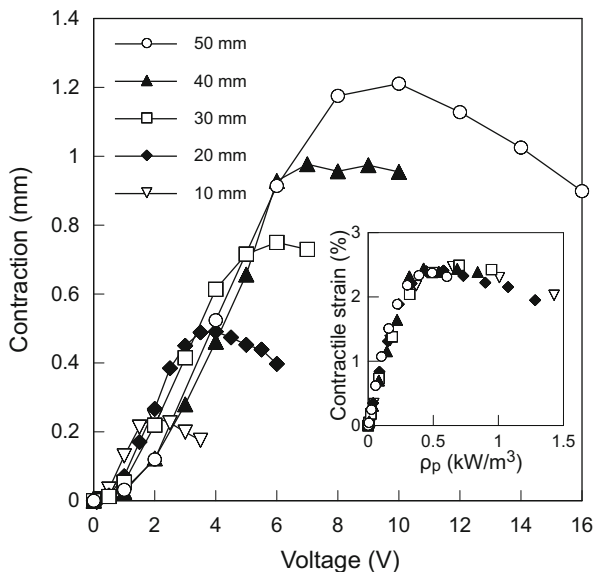
Fig. 8.4 Voltage dependence of contractile strain, electric current, and surface temperature of PEDOT/PSS film (50 mm long, 2 mm wide, and $17\ \mu\text{m}$ thick) measured at $25\ ^\circ\text{C}$ and 50 % RH. *Inset:* thermographic image of the film under 10 V



field, demonstrating that the water vapor sorbed in the film desorbs and scatters into ambient air. A gradual decrease of the RH will be due to the temperature rise near the film because saturated water vapor pressure increases with temperature. On the other hand, a drop of the RH, when the electric field is switched off, can be explained in terms of resorption of water vapor from the air surrounding the film.

To clarify the role and effect of the electric field on the film contraction, various voltages are applied to the film at 50 % RH and the results are shown in Fig. 8.4. The electric current is proportional to the voltage, and resistance of the film (R) calculated from the slope of the current-voltage relationship is $113\ \Omega$, which is in good agreement with the value expected from the conductivity ($150\ \text{S/cm}$) measured by a normal four-point method, demonstrating the film is ohmic in the experimental range of the electric field. The temperature of the film rises with the square of voltage, indicative of Joule heating. As shown in the inset of Fig. 8.4, the color of the thermographic image indicates the temperature around the ends and edges of the film (yellow) is lower than that in the center (red) by ca. $5\ ^\circ\text{C}$, which is due to the thermal diffusion to the electrodes or atmosphere. On the other hand, the contractile strain, defined as the percentage of contraction to initial length of the film, increases with the voltage and reaches the maximum (2.4 %) at 10 V where the

Fig. 8.5 Voltage dependence of contraction for PEDOT/PSS films (2 mm wide and 17 μm thick) with different lengths (10–50 mm) measured at 25 $^{\circ}\text{C}$ and 50 % RH. Inset: relation between contractile strain and electric power density (ρ_p) for various films



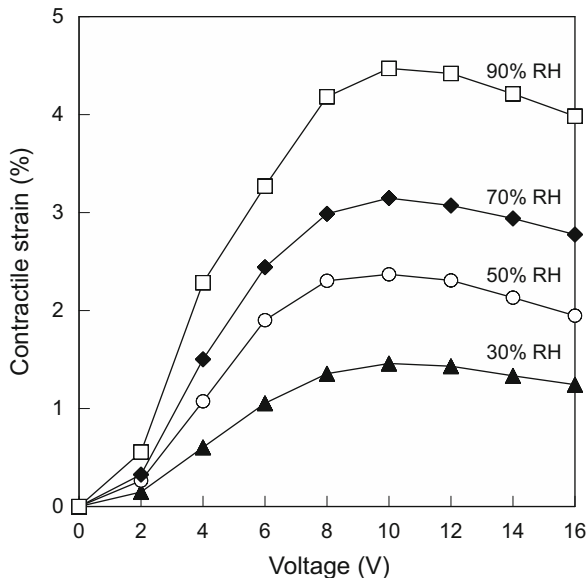
film may almost be dried above this temperature (64 $^{\circ}\text{C}$) at 50 % RH. A further increase of the voltage, however, results in a decrease of the value, which might be explained by thermal expansion of the film [27]. The coefficient of linear thermal expansion at voltages higher than 10 V is calculated as ca. $1 \times 10^{-4} \text{ K}^{-1}$, which is smaller than that of the PPy film ($2.4 \times 10^{-4} \text{ K}^{-1}$). A similar tendency is observed for the films with different lengths (10–50 mm) as shown in Fig. 8.5. One can see that an increase of the film length not only increases the contraction but also shifts the “optimum” voltage at which the contraction becomes a maximum toward a higher voltage due to the higher resistance of the film (R).

Using the parameters of the electric current (I), voltage (E), and the film volume (V_{film}), electric power density (ρ_p), defined as the volumetric rate at which electrical energy is transferred to work, is calculated by Joule’s law as follows:

$$\rho_p = \frac{EI}{V_{\text{film}}} = \frac{I^2 R}{V_{\text{film}}} \quad (8.4)$$

As shown in the inset of Fig. 8.5, we should emphasize that the relationship between contractile strain and ρ_p fits a single master curve regardless of the film length. Since the ρ_p represents the rate of heat production through Joule heating, the dimensional change of the PEDOT/PSS films can be described as follows: In ambient air, water vapor sorbs in the film through hydration of PSS chains, leading to the film expansion. Upon application of the electric field, the dimensional change of the film is caused by two processes both due to Joule heating: one is the contraction by desorption of water vapor, and the other is the thermal expansion of polymer chains. On the other hand, when the electric field is turned off, the film

Fig. 8.6 Voltage dependence of contractile strain of PEDOT/PSS films (50 mm long, 2 mm wide, and 17 μm thick) measured at 25 $^{\circ}\text{C}$ and various RHs



reverts to the initial length through the resorption of water vapor from the air and/or cooling of the film by thermal diffusion and convection. Indeed, thermal contraction of the PPy film in the absence of electric field measured by a thermal mechanical analysis was consistent with contraction caused by Joule heating [11]. Therefore, contraction of the PEDOT/PSS film might be based on the same principle. Moreover, the contractile strain can be improved by increasing water vapor sorption at higher RHs as shown in Fig. 8.6. One can see that a rise in the RH from 30 to 90 % RH increases the contractile strain in the whole experimental range of the applied voltage, where the value attains 4.5 % at 90 % RH that is three times larger than that at 30 % RH [12].

8.3.4 Stress Generation and Modulus Change

Under isometric condition, the film generates a contractile stress by application of an electric field. It is seen from Fig. 8.7, the contractile stress measured at 25 $^{\circ}\text{C}$ and 50 % RH rises with increasing the applied voltage and the value reaches as high as 17 MPa, corresponding to an equivalent contractile force of 59 gf, which is four orders of magnitude larger than its own weight (2.5 mg). A further increase of the voltage decreases the stress due to the thermal expansion, similarly to the film contraction (Fig. 8.4). Although the contractile stress is smaller than the highest stress of 120 MPa reported on carbon nanotube-reinforced polyaniline fibers [28], the value is larger than skeletal muscle in animals (0.3 MPa) [29] and conducting polymers driven by the electrochemical doping (3–5 MPa) [30], which can be

Fig. 8.7 Voltage dependence of contractile stress generated in PEDOT/PSS film (50 mm long, 2 mm wide, and 17 μm thick) measured at 25 $^{\circ}\text{C}$ and 50 % RH

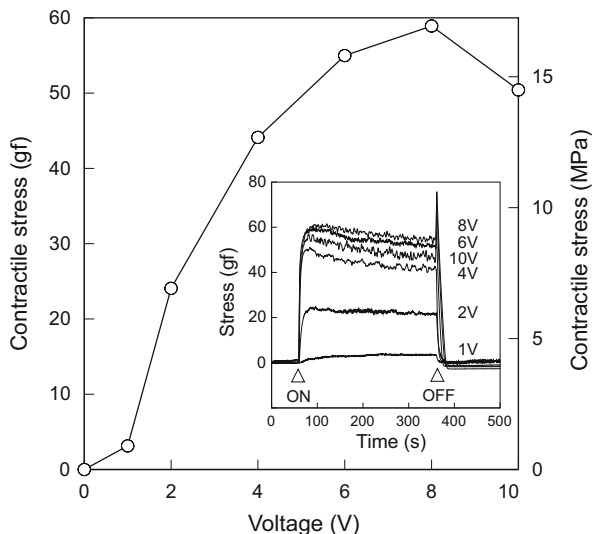
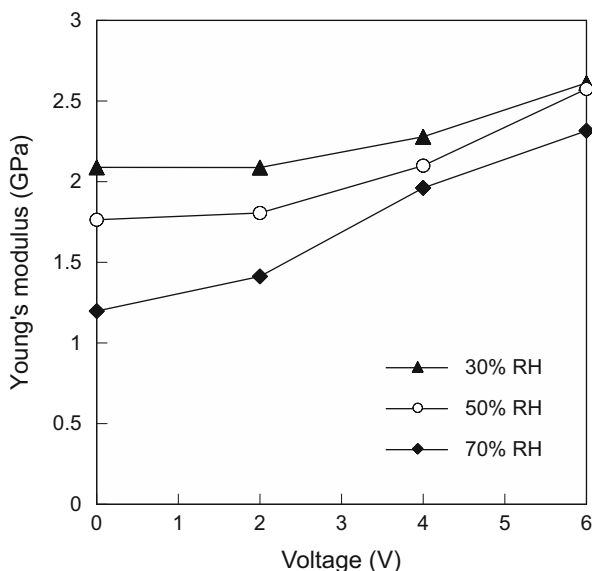


Fig. 8.8 Changes in Young's modulus of PEDOT/PSS film (50 mm long, 2 mm wide, and 17 μm thick) measured at 25 $^{\circ}\text{C}$ and a constant strain rate of 10 %/min under various voltages and RHs



associated with larger elastic modulus of the film. It is seen from Fig. 8.8 that Young's modulus of the PEDOT/PSS film measured at 25 $^{\circ}\text{C}$ and 50 % RH is found to be 1.8 GPa which is higher than the skeletal muscles (10–60 MPa) [31] and the conducting polymers in the electrolyte solution (0.6–1.2 GPa) [30]. It should be noted that the Young's modulus increases to 2.6 GPa by application of 6 V, indicating a 44 % gain, which can be interpreted in terms of plasticizing effect of water molecules that may increase the motion of polymer chains to lower the

elasticity of the film [32]. In fact, the elastic nature of the film is strongly affected by the humidity: Young's modulus at 30 % RH (2.1 GPa, 10.4 % of water content) decreases to nearly half at 70 % RH (1.2 GPa, 24.9 % of water content) despite the sorption-induced film expansion in the same RH change is only 1.9 % [12]. On the other hand, the Young's modulus are less dependent on the RH as the voltage becomes higher since the water vapor sorbed in the film is more forced to desorb by application of the higher voltages. The results were reproducible since the measurements were carried out after reaching the equilibrium at each RH and applied voltage.

8.3.5 Work Capacity and Energy Efficiency

Suppose that the contractile strain (γ) when the film is loosened so as to make the film contract until the stress (σ) becomes almost zero corresponds to the value of free loading contraction (Fig. 8.4), the volumetric work capacity (W), representing elastic energy stored in the film, can be estimated as follows [11, 30]:

$$W = \frac{1}{2} \times \sigma \times \gamma \quad (8.5)$$

Although the performance of the PEDOT/PSS actuator depends on environmental conditions such as relative humidity, at 10 V and 50 % RH, the W value is calculated to be 174 kJ/m³ which is much higher than the skeletal muscles (8–40 kJ/m³) [31], ionic polymer-metal composites (5.5 kJ/m³) [33], and the conducting polymers (73 kJ/m³) [30]. Here, the W represents maximum energy calculated using maximum values of stress and strain, therefore actual work capacity might be smaller than the value of W . If we define the energy efficiency (η) as the ratio of work capacity to electric energy, we obtain the η using the parameters of E , I , and V_{film} (1.7×10^{-9} m³) as follows:

$$\eta(\%) = \frac{W \times V_{\text{film}}}{E \times I \times t} \times 100 \quad (8.6)$$

where t is a typical response time, about 5 s. It is found that the value of η is 6×10^{-3} % which is smaller compared with other soft actuators because most of the electric energy is dissipated as the heat through Joule heating and/or relatively slow response, similarly to the SMA actuators [34] and liquid crystal elastomers [35].

8.3.6 Applications to Linear Actuators

Figure 8.9 shows a linear actuator in which both ends of the PEDOT/PSS film (50 mm long, 2 mm wide, and 16 μ m thick) were clamped by two Au-plated chucks

Fig. 8.9 Photographs of linear actuator utilizing PEDOT/PSS film

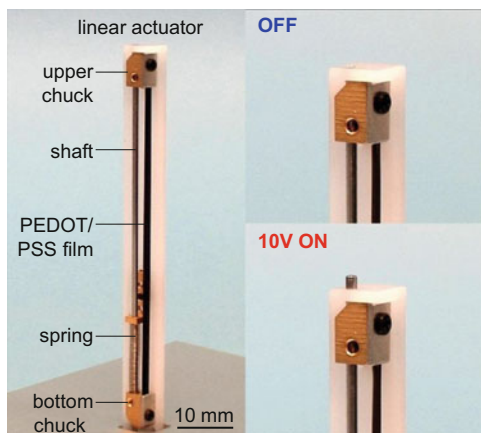
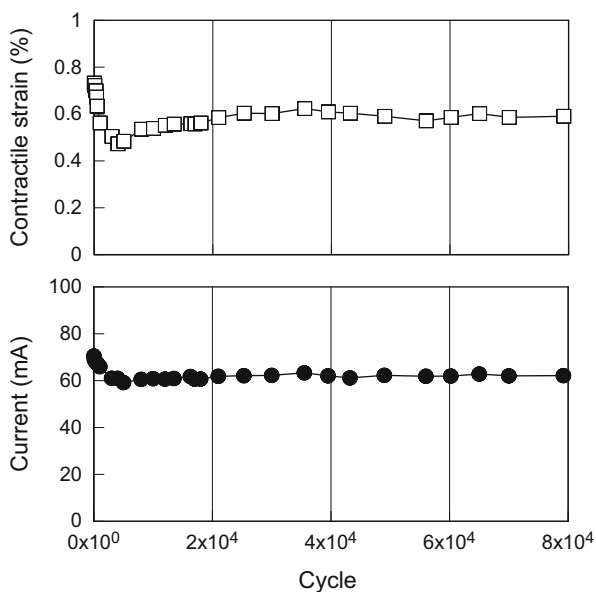


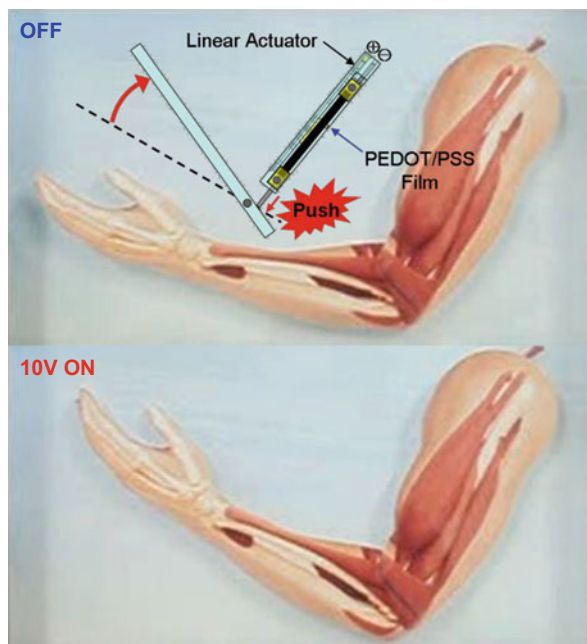
Fig. 8.10 Changes in contractile strain and current for PEDOT/PSS linear actuator when a cycle of 10 V on for 5 s and off for 15 s was repeated at 50 % RH



as electrodes [14]. Upon application of an electric field, a shaft slides up against a compressive force of a spring due to the film contraction where the bottom chuck is movable lifting up the shaft. When the electric field is turned off, the shaft rapidly slides down to the initial position in the course of the film expansion with the help of an expansive force of the spring. Since the linear actuator operates in ambient air without electrochemical reactions in an electrolyte solution or redox gas atmosphere, high reproducibility of motion may be achieved.

To examine durability of the film, a cycle of turning 10 V on for 5 s and off for 15 s was repeated at 50 % RH. It is seen from Fig. 8.10 that the contractile strain

Fig. 8.11 Photographs of leverage actuator ‘PolyMuscle’ using PEDOT/PSS linear actuator



slightly decreases to about 80 % of the initial strain until 10^3 cycles due to a creep of the film which increases the resistance and decreases the electric current. After 10^3 cycles, the film gradually contracts probably due to the rearrangement of polymer chains, which may partly recover the film contraction. After 8×10^4 cycles, the film finally breaks where both contractile strain and electric current are kept constant from 10^3 cycles until breaking, suggesting the PEDOT has superior stability of electrical conductivity [14]. The stress concentrates and deformation or breaking may take place at structural defects, such as microvoids or microfractures formed during the casting. On the other hand, reproducibility and reliability may deteriorate at higher RH, where creep of the film becomes more remarkable because of the plasticization of PSS chains.

Figure 8.11 shows a leverage actuator, namely ‘PolyMuscle’, in which the linear actuator drives leverage, leading to a large displacement of a beam [14]. On the other hand, the PEDOT/PSS films can also be applied to a Braille cell consisting of six linear actuators, keyboard, and controller. As shown in Fig. 8.12, the Braille cell can display Japanese characters of “Ya”, “Ma”, “Na”, and “Shi” by driving the individual linear actuators. Similarly, shape memory alloy (SMA) actuators are driven by electrical Joule heating where deformation is caused by thermal phase transition between austenitic and martensitic phases [34]. However, it is difficult to control not only phase transition temperature decided by the composition of alloys but also intermediate states between the two phases. In contrast, the PEDOT/PSS actuator can provide various contraction states according to the applied voltage.

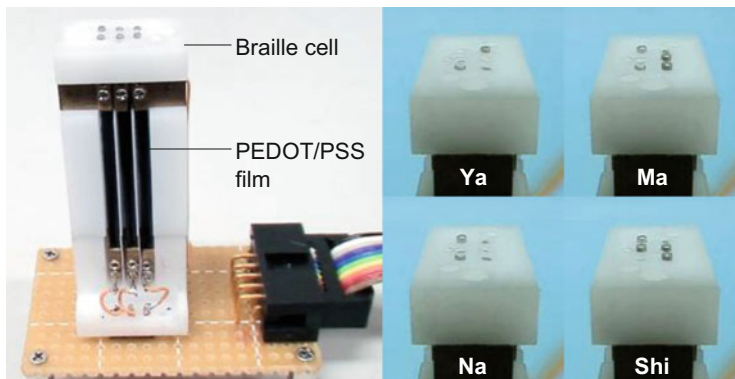


Fig. 8.12 Photographs of Braille cell using PEDOT/PSS linear actuators

8.4 Conclusions

We should emphasize here the PEDOT/PSS films exhibit electromechanical performance with large contractile strain, stress, and work capacity in ambient atmosphere without using an electrolyte solution and counter/reference electrodes where the electric field is capable of controlling the equilibrium of water vapor sorption. Furthermore, the PEDOT/PSS actuator operates at voltages one or two orders of magnitude lower than dielectric elastomers [36] and piezoelectric actuators [37] because the dimensional change of the film is caused by the electric current but the electric field. Furthermore, novel EAP actuators such as leverage actuator (PolyMuscle) and Braille cell utilizing the PEDOT/PSS linear actuators were fabricated. Thus, the cooperation between the electrical conductivity and hygroscopic nature of conducting polymers can provide an insight into the development of new class of EAP actuators or artificial muscles working in air. Moreover, various conducting polymers or composites that undergo dimensional changes in response to water vapor sorption can be employed on the same principle.

References

1. Smela E, Inganäs O, Lundström I (1995) Controlled folding of micrometer-sized structures. *Science* 268:1735–1738
2. Baughman RH, Shacklette LW, Elsenbaumer RL, Plichta EJ, Becht C (1991) Micro electro-mechanical actuators based on conducting polymers. In: Lazarev PI (ed) *Molecular electronics*. Kluwer Academic, The Netherlands, pp 267–289
3. Otero TF, Rodríguez J (1993) Electrochemomechanical and electrochemopositioning devices: artificial muscles. In: Aldissi M (ed) *Intrinsically conducting polymers: an emerging technology*. Kluwer Academic, The Netherlands, pp 179–190
4. Pei Q, Inganäs O (1993) Conjugated polymers as smart materials, gas sensors and actuators using bending beams. *Synth Met* 55–57:3730–3735

5. Sansinena JM, Olazábal V, Otero TF, Polo da Fonseca CN, De Paoli M-A (1997) A solid state artificial muscle based on polypyrrole and a solid polymeric electrolyte working in air. *Chem Commun* 2217–2218
6. Lu W, Fadeev AG, Qi B, Smela E, Mattes BR, Ding J, Spinks GM, Mazurkiewicz J, Zhou D, Wallace GG, MacFarlane DR, Forsyth SA, Forsyth M (2002) Use of ionic liquid for π -conjugated polymer electrochemical devices. *Science* 297:983–987
7. Okuzaki H, Kuwabara T, Funasaka K, Saido T (2013) Humidity-sensitive polypyrrole films for electro-active polymer actuators. *Adv Funct Mater* 23:4400–4407
8. Okuzaki H, Kunugi T (1996) Adsorption-induced bending of polypyrrole films and its applications to a chemomechanical rotor. *J Polym Sci Polym Phys* 34:1747–1749
9. Okuzaki H, Kuwabara T, Kunugi T (1997) A polypyrrole rotor driven by sorption of water vapour. *Polymer* 38:5491–5492
10. Okuzaki H, Kunugi T (1998) Electrically induced contraction of polypyrrole films in ambient air. *J Polym Sci Polym Phys* 36:1591–1594
11. Okuzaki H, Funasaka K (2000) Electromechanical properties of a humido-sensitive conducting polymer film. *Macromolecules* 33:8307–8311
12. Okuzaki H, Suzuki H, Ito T (2009) Electrochemical properties of poly(3,4-ethylenedioxythiophene)/poly(4-styrene sulfonate) films. *J Phys Chem B* 113:11378–11383
13. Okuzaki H, Hosaka K, Suzuki H, Ito T (2010) Effect of temperature on humido-sensitive conducting polymer actuators. *Sens Actuators A* 157:96–99
14. Okuzaki H, Hosaka K, Suzuki H, Ito T (2013) Humido-sensitive conducting polymer films and applications to linear actuators. *React Funct Polym* 73:986–992
15. Okuzaki H, Suzuki H, Ito T (2009) Electrically driven PEDOT/PSS actuators. *Synth Met* 159:2233–2236
16. Takano T, Masunaga H, Fujiwara A, Okuzaki H, Sasaki T (2012) PEDOT nanocrystal in highly conductive PEDOT:PSS polymer films. *Macromolecules* 45:3859–3865
17. Hohnholz D, Okuzaki H, MacDiarmid AG (2005) Plastic electronic devices through line patterning of conducting polymers. *Adv Funct Mater* 15:51–56
18. Okuzaki H, Ishihara M (2003) Spinning and characterization of conducting microfibers. *Macromol Rapid Commun* 24:261–264
19. Okuzaki H, Harashina Y, Yan H (2009) Highly conductive PEDOT/PSS microfibers fabricated by wet-spinning and dip-treatment in ethylene glycol. *Eur Polym J* 45:256–261
20. Brunauer S, Emmett PH, Teller E (1938) Adsorption of gases in multimolecular layers. *J Am Chem Soc* 60:309–319
21. Dutta D, Chatterjee S, Pillai KT, Pujari PK, Ganguly BN (2005) Pore structure of silica gel: a comparative study through BET and PALS. *Chem Phys* 312:319–324
22. Ertl G, Knözinger H, Weitkamp J (eds) (1999) Preparation of solid catalysis. Wiley-VCH, Weinheim
23. Yan H, Arima S, Mori Y, Kagata T, Sato H, Okuzaki H (2009) Poly(3,4-ethylenedioxythiophene)/poly(4-styrenesulfonate): correlation between colloidal particles and thin films. *Thin Solid Films* 517:3299–3303
24. Okuzaki H, Kondo T, Kunugi T (1999) Characteristics of water in polypyrrole films. *Polymer* 40:995–1000
25. Ross S, Oliver JP (eds) (1964) On physical adsorption. Interscience, New York
26. Barrow GM (ed) (1961) Physical chemistry. McGraw-Hill, New York
27. Okuzaki H, Funasaka K (2000) Electro-responsive polypyrrole film based on reversible sorption of water vapor. *Synth Met* 108:127–131
28. Spinks GM, Mottaghitaleb V, Bahrami-Samani M, Whitten PG, Wallace GG (2006) Carbon-nanotube-reinforced polyaniline fibers for high-strength artificial muscles. *Adv Mater* 18:637–640
29. Alexander RM (1992) Exploring biomechanics. Freeman WH Company, New York
30. Santa AD, De Rossi D, Mazzoldi A (1997) Performance and work capacity of a polypyrrole conducting polymer linear actuator. *Synth Met* 90:93–100

31. Madden JDW, Vandesteeg NA, Anquetil PA, Madden PGA, Takshi A, Pytel RZ, Lafontaine SR, Wieringa PA, Hunter IW (2004) Artificial muscle technology: physical principles and naval prospects. *IEEE J Ocean Eng* 29:706–728
32. Okuzaki H, Kuwabara T, Kondo T (1998) Role and effect of dopant on sorption-induced motion of polypyrrole films. *J Polym Sci Polym Phys* 36:2635–2642
33. Nemat-Nasser S, Wu Y (2003) Comparative experimental study of ionic polymer-metal composites with different backbone ionomers and in various cation forms. *J Appl Phys* 93:5255–5267
34. Bergamasco M, Salsedo F, Dario P (1989) Shape memory alloy micromotors for direct-drive actuation of dexterous artificial hands. *Sens Actuators* 17:115–119
35. Thomsen DL III, Keller P, Naciri J, Pink R, Jeon H, Shenoy D, Ratna BR (2001) Liquid crystal elastomers with mechanical properties of a muscle. *Macromolecules* 34:5868–5875
36. Pelrine R, Kornbluh R, Pei Q, Joseph J (2000) High-speed electrically actuated elastomers with strain greater than 100 %. *Science* 287:836–839
37. Lee JK, Marcus MA (1981) The deflection-bandwidth product of poly(vinylidene fluoride) benders and related structures. *Ferroelectrics* 32:93–101

Chapter 9

Carbon Nanotube/Ionic Liquid Composites

Takushi Sugino, Kenji Kiyohara, and Kinji Asaka

Abstract Both carbon nanotubes and ionic liquids are very attractive materials in the present scientific fields. Recently, we combine these two materials into the polymer matrix to make a conductive electrode film which expands and contracts when alternative square voltages are applied. We utilize these interesting phenomena for electroactive polymer actuators (electric-driven soft actuators). In this chapter, we introduce recent studies for electroactive polymer actuators composed of carbon nanotube/ionic liquid composites and their application potential for a thin and light Braille display as well.

Keywords Additives • Braille display • Carbon nanotube • Electroactive polymer • Ionic liquid

9.1 Introduction

Polymer actuators, especially, electroactive polymer (EAP) actuators are of great interest as new class of motion drives and controls because they are soft, flexible, light weight and show large deformation compared to conventional actuators such as metal motors and piezoelectric actuators [1, 2]. EAP actuators are classified into two groups; one is ionic EAP actuator and the other is electronic EAP actuator. In particular, ionic EAP (i-EAP) actuators have advantages in their low voltage operation and their large deformation. Representative i-EAP actuators consist of ionic polymer-metal composites (IPMC) [3], conductive polymers such as polyaniline [4] and polypyrrole [5], and carbon nanotubes (“bucky paper”) [6].

Up to the end of twentieth century, most i-EAP actuators needed water or organic solvent to drive because the electrolytes soluble into water or organic solvent were used. That is the reason why these conventional i-EAP actuators

T. Sugino (✉) • K. Kiyohara
Artificial Cell Research Group, Health Research Institute, Advanced Industrial Science and Technology (AIST), Ikeda, Osaka 563-8577, Japan
e-mail: takushi-sugino@aist.go.jp

K. Asaka
Health Research Institute, National Institute of Advanced Industrial Science and Technology (AIST), Ikeda, Osaka 563-8577, Japan

could not show their best performance in air because of evaporation of water or organic solvent in the polymer electrolytes. On these backgrounds, we produced a new class of i-EAP actuators composed of carbon nanotube (CNT), ionic liquid (IL), and base polymer (BP) [7]. We call this new class of i-EAP actuators as “bucky gel” actuators. These new actuators can show stable and long-cycle actuation in air under low voltage (below 3 V) due to the nonvolatility and wide electrochemical stability of ILs. Furthermore, both the electrode and the electrolyte layers are simply prepared by a casting method without any chemical or electrochemical reaction used to make the electrodes of IPMC (chemical plating) and conductive polymer (electrochemical reaction) actuators, respectively. The bucky gel actuators have a three-layered structure where an electrolyte layer is laminated by two electrode layers and they show a bending deformation against the anode side when voltages are applied. The actuation properties of bucky gel actuators depend on species of ILs, kinds of nano-carbon, additives, and so on. We introduce recent progress of bucky gel actuators and application example for an ultra-light and thin refreshable Braille display.

9.2 Fabrication of Bucky Gel Actuator and the Actuation Mechanism

Our bucky gel actuators have a three-layered structure as shown in Fig. 9.1a. One electrolyte film is laminated with two electrode films by heat-pressing at 70 °C. A typical preparation procedure is described below. The electrode film was prepared from single-walled carbon nanotube (SWCNT; purified HiPco® grade) as a carbon source, polyvinylidene fluoride-co-hexafluoropropylene (PVDF-HFP; Kynar Flex® 2801) as a base polymer, and 1-ethyl-3-methylimidazolium tetrafluoroborate (EMIBF₄) as an ionic liquid. 20 wt% of SWCNT, 32 wt% of PVDF-HFP, and 48 wt% of EMIBF₄ were dissolved in 9 mL of N,N-dimethylacetamide (DMAc) and stirred for more than 1 day at room temperature, then sonicated in an ultrasonic bath for 24 h. The obtained gelatinous black solution was cast into a Teflon mold and the solvent was dried. As a result, a black self-standing electrode film was obtained. The thickness of electrode film is controllable by casting amount. The

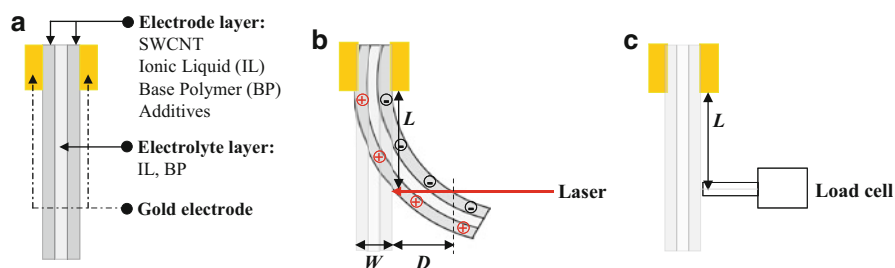


Fig. 9.1 Schematic representation of three-layered actuator (a), experimental setup for displacement measurement (b), and bending force (c) (Reproduced with permission from Sugino et al. [8])

electrolyte film is prepared by the similar casting method. 50 wt% of PVDF-HFP and 50 wt% of EMIBF₄ were dissolved in the solvent mixture of 4-methyl-2-pentanone and propylene carbonate anhydrous and cast into an aluminum mold. After drying solvent, an opaque self-standing gel electrolyte was obtained. The thickness of electrolyte film was between 10 and 20 μm .

The three-layered bucky gel actuators show a bending motion against the anode side when voltages are applied. The electric charge to induce the bending motion is stored in the electrode layer capacitively. We investigated the actuation mechanisms by a combination of symmetry analysis, elasticity theory, and experimental results in the scale of micrometer [9]. We found that the cathode expands and the anode contracts resulting in the bending motion toward the anode side. We consider that this dimensional change is induced concertedly by changing of C–C bond distance in CNTs [6, 10], volume exclusion effect by charging/discharging of ions into the electrode layers [11], and electrostatic effect in the electrical double layer [12]. Kiyohara et al. have investigated the actuation mechanism of the bucky gel actuator theoretically in the scale of nanometer by a method of Monte Carlo simulation [13, 14]. The actuation mechanism is still under discussion. Detailed discussion about the actuation mechanism of bucky gel actuator is described in Chap. 22.

9.3 Measurements

The actuation (bending motion) was directly monitored by a laser displacement meter (KEYENCE LC2100). The three-layered actuator strip with 1 mm (width) \times 10 mm (length) size was clipped by two gold current collectors. Alternative square voltages were applied to the actuator strip to activate. A Potentio/Galvanostat (HOKUTO DENKO, HA-501G) with a wave generator (YOKOGAWA ELECTRIC model FC200) was used to apply voltage. The voltage, current, and displacement were simultaneously recorded by an oscilloscope (YOKOGAWA DL708). The displacement at 5 mm away (free length, L) from the fixed end of gold current collector was monitored. The monitored displacement (D) was converted to the strain difference (ε) between two electrodes in order to normalize actuator size and compare each actuation from different actuator samples by using the following Eq. (9.1):

$$\varepsilon = 2WD/(L^2 + D^2), \quad (9.1)$$

where W is the thickness of actuator strip.

In Eq. (9.1), we assume that there is no distortion of the cross sections in the actuator during bending. The bending force at 4 mm away from the fixed end of the gold current collector was monitored with a load cell (KYOWA LTS-50GA). The actuator strip with the size of 2 \times 10 mm was used for the bending force measurements. The experimental setup to measure displacement and bending force are shown in Fig. 9.1b, c. The ionic conductivity of IL was evaluated by an impedance spectroscopy (SOLARTRON 1250 Impedance/Gain-phase analyzer). The cyclic voltammetry was performed to characterize the electrical capacitance of actuator

electrode in a sealed two-electrode cell using a HOKUTO DENKO HSV-100 model. The conductivity of the electrode film was studied by the four probe DC current method by using a HOKUTO DENKO Potentio/Galvanostat HA-151 model as a galvanostat mode with a YOKOGAWA ELECTRIC FC220 model wave generator. The conductivity of the electrode film was calculated from the slope of current–voltage curve. The Young’s modulus of electrode film was evaluated by a stress–strain measurement using TMA/SS6000 (SEIKO INSTRUMENTS Inc.).

9.4 Influence of ILs

Ionic liquids (ILs) used as the internal electrolyte of bucky gel actuators are one of crucial material to determine the actuation performance. So, we investigated the influence of ILs. We studied the electrochemical and electromechanical properties of bucky gel actuator by using seven kinds of ILs [15]. The chemical structure of ILs and some physical properties [16] of ILs are summarized in Table 9.1. We measured the frequency dependence of bending displacements with alternative triangle voltages. The frequency dependence of strain (ϵ) for bucky gel actuators including various kinds of ILs is depicted in Fig. 9.2. The actuator with EMIBF₄ as an internal electrolyte shows the best actuation response among actuators with seven kinds of ILs. The actuation response becomes worse with increasing the length of alkyl chain in the imidazolium-cation. This result is due to dramatic decreasing of the ionic conductivity with increasing the length of alkyl chain.

We succeeded to fit the results of bending displacements by an electrochemical kinetic model (a double-layer charging kinetic model). In the kinetic model, we considered that the electrode layers of actuator were fully charged at low frequencies of applied voltage, on the other hand, there is not enough time for the electrodes to be fully charged at higher frequencies. Therefore, the stored charge (Q) decreases with increasing the frequency of applied voltage. According to this consideration, the strain difference (ϵ) is proportional to the stored charge. We used a simple equivalent circuit model in order to make the electrochemical kinetic model quantitatively as shown in Fig. 9.3. C_1 is the double-layer capacitance of each electrode of actuator and is replaced by the capacitance $C = C_1/2$. R is the resistance of ionic gel electrolyte. R is calculated from the ionic conductivity κ ($=$ thickness/ $R \times$ area). The stored charge $Q(f)$ at a frequency (f Hz) is represented by the following Eq. (9.2):

$$Q(f)/Q_0 = 1 - 4CRf(1 - \exp(-1/4CRf)), \quad (9.2)$$

where Q_0 is the stored charge at a limit of low frequency. And the strain difference (ϵ) is given by the following Eq. (9.3):

$$\epsilon = \epsilon_0 Q(f)/Q_0, \quad (9.3)$$

where ϵ_0 is the strain at a limit of low frequency.

Table 9.1 Chemical structure and physicochemical property of IL

Ionic liquid	Cation	Anion	T_{mp} (°C)	η (cP) at 25 °C	κ (mS cm ⁻¹)	d (g cm ⁻³)
EMIBF ₄		BF ₄ ⁻	14.6	31.8	13.6	1.28
BMIBF ₄			-71	118.3	3.43	1.21
HMIBF ₄			-82	223.8	1.04	1.15
OMIBF ₄			-80	422.0	0.576	1.11
EMITFSI		(CF ₃ SO ₂) ₂ N ⁻	-16	28.0	8.40	1.52
A-3		BF ₄ ⁻	-	-	-	-
A-4			(CF ₃ SO ₂) ₂ N ⁻	-	-	-

T_{mp} melting point, η viscosity, κ electric conductivity, d density

Fig. 9.2 Frequency dependence of strain of bucky gel actuators including various ILs (Reproduced with permission from Takeuchi et al. [15])

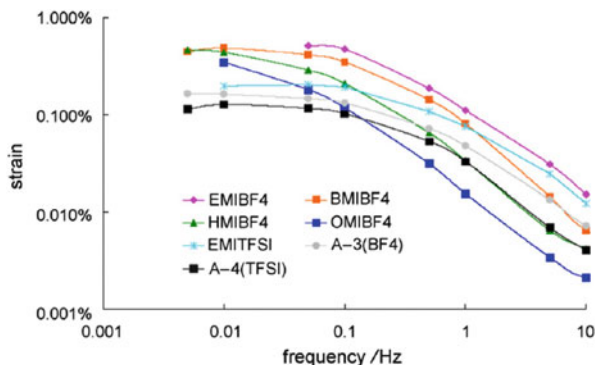
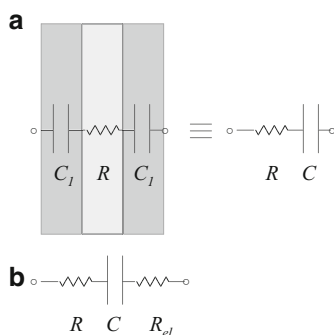


Fig. 9.3 Equivalent circuit model of the three-layered bucky gel actuator. The circuit model without the electrode resistance (R_{el}) (a) and the circuit model with R_{el} (b)



In this study, we also took into account the electrode resistance (R_{el}) in the equivalent circuit model. In the case of considering R_{el} , we just replaced R to $R + R_{el}$ in Eq. (9.2). We obtained around 10 S cm^{-1} for the conductivity of electrode from the four probe DC current method. From this result, we roughly estimated R_{el} as $16.6 \text{ } \Omega\text{cm}^2$ for the electrode with $60 \text{ } \mu\text{m}$ -thickness and 1 cm^2 -area. We observed a better fitting against experimental results of strain when we considered the conductivity of the electrode film, especially when IL has higher ionic conductivity. This implies that the response of bucky gel actuator must be improved by using the electrolyte with higher ionic conductivity and the electrode with higher electric conductivity as well. The capacitance of the electrode layer, the ionic conductivity of gel electrolyte layer, the strain at a limit of low frequency, and the time constant (CR) are summarized in Table 9.2. From these results, we conclude that not only the ionic transfer speed but also the size difference between cation and anion of IL affect the actuation response of bucky gel actuators. Further detailed study on an impedance model analysis for the pore structure of the electrode layer of bucky gel actuators was reported elsewhere [17].

Table 9.2 Obtained parameters for the electrode, the time constant (CR), and the strain at a limit of low frequency used for simulation

Ionic liquid	C ($F g^{-1}$)	C ($F cm^{-2}$)	κ ($mS cm^{-1}$)	R (Ωcm^2)	CR (s)	$R+R_{el}$ (Ωcm^2)	$C(R+R_{el})$ (s)	ϵ_0 (%)
EMIBF ₄	45.5	0.0312	1.71	1.17	0.0365	17.77	0.554	0.53
BMIBF ₄	45.3	0.0338	0.312	6.41	0.217	23.01	0.778	0.45
HMIBF ₄	44.8	0.0286	0.134	14.9	0.426	31.50	0.901	0.48
OMIBF ₄	44.6	0.0286	0.014	143	4.09	159.6	4.565	0.60
EMITFSI	49.2	0.0338	1.33	1.50	0.0507	18.10	0.612	0.21
A-3	35.4	0.0286	0.393	5.09	0.146	21.69	0.620	0.17
A-4	41.6	0.0286	0.729	2.74	0.0784	19.31	0.553	0.13

$$R_{el} = 16.6 \Omega cm^2$$

9.5 Nano-Carbon Materials

Carbon electrode is a key issue for Li-battery, supercapacitors, and actuators. Among carbon materials, SWCNT has been focused as a practically promising carbon species because of its high conductivity, large surface area, large capacitance, and high mechanical stiffness. So, we use SWCNT as a carbon source for the conductive material in the electrode layer of bucky gel actuator. In this section, we introduce some examples of EAP actuators that consist of other carbon species and ionic liquids.

We tested other carbon species such as activated carbon nanofiber (ACNF) and vapor grown carbon fiber (VGCF) to fabricate bucky gel actuators [18]. We believe that SWCNT is one of the best carbon species for the electrodes of bucky gel actuator, however, SWCNT has a drawback, that is, poor dispersibility into solvents or polymers. On the contrary, ACNF and VGCF have a characteristic feature of their good dispersibility. Furthermore, ACNF (ACNF-25 from Gunei Chemical Industry Co. Ltd) has larger specific surface area ($2,500 m^2 g^{-1}$) than that of SWCNT (purified grade HiPco[®], $500 m^2 g^{-1}$), on the other hand, VGCF (from Showa Denko K. K.) has smaller specific surface area ($13 m^2 g^{-1}$). These two carbon fibers may be good for comparison. The actuator only with ACNF or VGCF as carbon material of the electrode showed smaller bending performance (strain (ϵ)) compared to the actuator with SWCNT. We found the best mixing condition between SWCNT (76 wt%) and ACNF (24 wt%). With this best mixing condition, the actuator (SWCNT+ACNF) showed larger strain compared to the actuator only with SWCNT as a carbon source. Total weight ratio of nano-carbon (SWCNT+ACNF) is 23 wt% in the electrode layer, other components are composed of 31 wt% of PVDF-HFP and 46 wt% of IL. We also used a unique SWCNT that is called as 'super-growth' SWCNT (SG-SWCNT). SG-SWCNT is produced by a water-assisted modified CVD method reported by Hata et al. [19]. SG-SWCNT is impurity (catalyst) free SWCNT with large specific surface area ($\sim 1,000 m^2 g^{-1}$). From these characteristic points of view, SG-SWCNT could be most suitable

carbon material for bucky gel actuators. We produced polymer-free electrodes for EAP actuators. The electrode layer consists of 50 wt% of SG-SWCNT and 50 wt% of EMITFSI and the electrolyte layer is composed of 50 wt% of PVDF-HFP and 50 wt% of EMITFSI. The SG-SWCNT actuator showed very fast and large bending deformation compared to conventional SWCNT bucky gel actuators. The actuator exhibits 2.28 \% s^{-1} as a strain speed and showed very quick actuation even at the frequency of 100 Hz. Mukai and Giménez et al. found that such high speed actuation is originated from an oxidation/reduction (redox) reaction (Faradaic mechanism) in addition to capacitive charge (non-Faradaic mechanism) [20, 21].

Biso et al. utilized multi-walled carbon nanotube (MWCNT) to prepare EAP actuator including ionic liquid (BMIBF₄) and PVDF [22]. The composition of the MWCNT actuator is MWCNT (30 wt%), PVDF (35 wt%), and BMIBF₄ (35 wt%). They observed the maximum strain of ca. 1 % that is comparable to the actuation performance of SWCNT-based bucky gel actuators. Torop et al. used carbide-derived carbon (CDC) which is a type of amorphous carbon as a carbon source instead of using SWCNT [23, 24]. CDC has a well-defined nanoporous structure. The pore size can be controlled by template metal size and synthesis temperature. They investigate the actuation properties of CDC actuators and observed the largest strain of 0.62 % ($\pm 2.0 \text{ V}$ at 0.005 Hz) and the generated stress of 0.3 MPa when they used a CDC which has the largest pore size (ca. 1.0 nm). They succeeded to improve the actuation of CDC actuator dramatically by using gold foil on the surface of carbon electrode. As a result, they observed the strain of 2.2 % ($\pm 2.0 \text{ V}$ at 0.5 Hz). Saito et al. used activated carbon (AC) (20 wt%) and acetylene black (12 wt%) as carbon source, ionic liquid (EMITFSI (60 wt%)) and PVDF-HFP (8 wt%) to prepare the electrode film (ca. 50 μm) [25]. A photocurable polymer TSR-1920 and EMITFSI were used to make an electrolyte gel film (ca. 150 μm). The actuator has ca. 250 μm -thickness and 5 mm-free length. Their actuator showed 0.35 mm bending displacement during 150 s with the applied voltage of 1.5 V.

9.6 Improving the Actuation Properties by Using Additives

EAP actuators are expected to show their large displacement, quick response, and strong bending force. It is, however, difficult to satisfy these three parameters at the same time. For example, when we can improve the displacement, one or two of other parameters go to decrease the performance. In the previous last two sections, we introduced the influence of ionic liquids and nanocarbons on the actuation properties of bucky gel actuators. Our bucky gel actuators show their deformation by the accumulation of charge into the electrode layers. So, actuators can show their fast and large bending deformation due to the fast and large electrical charge. Therefore, it is considered that improving the ionic conductivity of electrolyte layer and/or improving of electrical conductivity of the electrode layer with large capacitance are effective ways.

Table 9.3 The maximum strain (ϵ_{\max}) and the maximum generated stress (σ_{\max}) for each actuator at 0.005 Hz at ± 2.0 V. Obtained capacitance (C), conductivity (κ), and Young's modulus (Y) of the electrode

Actuator ^a	ϵ_{\max} (%)	σ_{\max} (MPa)	C (F cm ⁻²)	κ (mS cm ⁻¹)	Y (MPa)
SWCNT(50)-1IL	0.69	1.9	0.0339	17	280
SWCNT/PANI(50/50)-1IL	2.0	8.8	0.0885	32	440
SWCNT/MCM41(50/50)-1IL	1.1	1.9	0.0356	8.1	170

^aThe wt% of each component to make the electrode film is following: SWCNT(50)-1IL: SWCNT (19.9 wt%)/PVDF-HFP (31.9 wt%)/EMIBF₄ (48.2 wt%), SWCNT/PANI(50/50)-1IL: SWCNT (16.7 wt%)/PANI (16.7 wt%)/PVDF-HFP (26.7 wt%)/EMIBF₄ (39.9 wt%), SWCNT/MCM41(50/50)-1IL: SWCNT (16.6 wt%)/MCM-41 (16.6 wt%)/PVDF-HFP (26.6 wt%)/EMIBF₄ (40.1 wt%)

In this section, we introduce other strategy to improve the actuation properties. The electrical energy stored by the accumulate charges need to be converted to the mechanical energy effectively for the actuators to show their large bending and strong bending force. From this point of view, we investigated the influence of additives in the electrode layers of bucky gel actuators [8, 26, 27]. We can tune the electrochemical properties and electromechanical properties of the electrodes by changing the kinds of additives and/or by changing the packing density of additives. We tested both non-conductive and conductive nanoparticles as additives. We chose MCM-41 (mesoporous silica) as a non-conductive additive and polyaniline (PANI), polypyrrole (PPy), and carbon black (CB) as a conductive additive. We found that the conductive additive was more effective than non-conductive additive. The same weight % (16.7 wt%) of additive against SWCNT was used to make the electrode film. The maximum strain (ϵ_{\max}) and the maximum generated stress (σ_{\max}) are summarized together with other characteristic properties of the electrode such as capacitance (C), conductivity (κ) and Young's modulus (Y) in Table 9.3. As seen in Table 9.3, the bucky gel actuator with PANI exhibited the highest conductivity and largest capacitance resulting in showing maximum strain of 2.0 % and the largest generated stress of 8.8 MPa [26]. These values are almost comparable to the actuation performance of conductive polymer actuators including ILs [3, 4]. The strain (2.0 %) observed for the actuator with PANI (SWCNT/PANI(50/50)-1IL) is ca. three times larger than that of actuator without any additives (SWCNT(50)-1IL). The generated stress of SWCNT/PANI(50/50)-1IL is more than four times larger than that of SWCNT(50)-1IL.

The actuator with PANI additive showed the best actuation performance as mentioned above [26, 27]. So, the actuator with PANI was chosen as a model actuator to investigate the influence of ILs and thickness of actuator [8]. Some selected electromechanical data are summarized in Table 9.4. Firstly, we studied the influence of IL species. As described in Sect. 9.4, EMIBF₄ was the best IL as an internal electrolyte rather than EMITFSI and EMITfO (1-ethyl-3-methylimidazolium trifluoromethanesulfonate). Secondly, we changed the amount of IL.

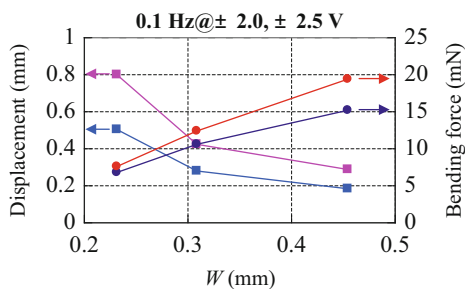
Table 9.4 Influence of species of IL and amount of IL. The thickness (W), displacement (D), strain (ϵ), and bending force (F) for each actuator at 0.1 Hz with applied voltage of ± 2.0 and ± 2.5 V

Actuator ^a	W (μm)	V (V)	D (mm)	ϵ (%)	F (mN)
SWCNT/PANI(50/50)-1IL (IL = EMIBF ₄)	236	2.0	0.37	1.1	6.6
		2.5	0.42	1.2	8.0
SWCNT/PANI(50/50)-2IL (IL = EMIBF ₄)	232	2.0	0.51	1.4	6.9
		2.5	0.80	2.2	7.7
SWCNT/PANI(50/50)-3IL (IL = EMIBF ₄)	356	2.0	0.17	0.74	5.2
		2.5	0.26	1.1	6.9
SWCNT/PANI(50/50)-1IL (IL = EMITfO)	219	2.0	0.58	1.6	6.6
		2.5	0.75	2.0	7.5
SWCNT/PANI(50/50)-2IL (IL = EMITfO)	215	2.0	0.49	1.3	2.2
		2.5	0.81	2.1	2.8
SWCNT/PANI(50/50)-1IL (IL = EMITFSI)	450	2.0	0.030	0.17	2.6
		2.5	0.049	0.27	7.1
SWCNT/PPy(50/50)-2IL (IL = EMIBF ₄)	203	2.0	0.56	1.4	5.3
		2.5	0.78	1.9	7.2

^aThe size of actuator is 2 mm-width \times 10 mm-length for measurements

The equimolar amount of IL is used to prepare each electrode film when same numerical value is seen in the last part of abbreviation ($-*IL$)

Fig. 9.4 Thickness dependence of displacement and bending force. *Closed-square* denotes the displacement (*blue* at 2.0 V, *pink* at 2.5 V) and *closed-circle* denotes the bending force (*dark-blue* at 2.0 V, *red* at 2.5 V) (Reproduced with permission from Sugino et al. [8])



When double portion of EMIBF₄ compared to SWCNT/PANI(50/50)-1IL was used to make the actuator with PANI (SWCNT/PANI(50/50)-2IL), the actuator (SWCNT/PANI(50/50)-2IL) showed ca. 2 time larger strain (2.2 %) without losing bending force (7.7 mN) at voltage of 2.5 V at 0.1 Hz compared to the actuator of SWCNT/PANI(50/50)-1IL. Similar good actuation (strain and bending force) was observed when PPy was used as a conductive additive instead of using PANI. Finally, we optimized the actuator thickness for the actuator of SWCNT/PANI (50/50)-2IL. The thickness dependence of displacement and bending force was depicted in Fig. 9.4. As seen in Fig. 9.4, it was found that the optimum thickness for SWCNT/PANI(50/50)-2IL (IL = EMIBF₄) is in between 270 and 310 μm .

When the thickness of actuator is 454 μm , the actuator, SWCNT/PANI(50/50)-2IL, exhibits 20 mN (bending force) and about 0.3 mm (bending displacement) at voltage of 2.5 V at 0.1 Hz.

9.7 Application

i-EAP actuators have been expected to be used in practical applications such as drug delivery, active microcatheter, micropump, and tactile display [1, 2]. First commercial production by using i-EAP was produced by a Japanese company (Eamex Co.) in 2002. They produced the fish robots. They used i-EAP to control the caudal of fish robot by electromagnetic induction. Here, we show one of application potential for our bucky gel actuators.

In present information society, we can get huge number of visual information through internet quite easily. This is due to the development of liquid crystal display (LCD) on mobile phones, laptop computers, and other mobile tools such as iPad. On the contrary, visually impaired people cannot receive benefit from such convenient information tools because all the information is shown on LCD. Refreshable Braille display is one of the most important communication tools for visually impaired people. Most Braille displays adopt the piezoelectric ceramic actuator to lift up and down the Braille dot. Nowadays the Braille display is commercially available but is not suitable for mobile use because of the size and weight ($\sim\text{kg}$). In such situation, we had a motivation to produce an ultra-light and thin Braille display by using our bucky gel actuators [28]. This new Braille display has a size of 65 mm-length \times 30 mm-width \times 3 mm-thickness and the weight is only 5 g (Fig. 9.5). Our Braille display is composed by six cells, that is, it has 36 Braille dots which are driven by 36 bucky gel actuators. Visually impaired people could recognize Braille characters on our prototype of Braille display by their finger touch. However, we need to improve the durability. Improving the durability is now in progress.

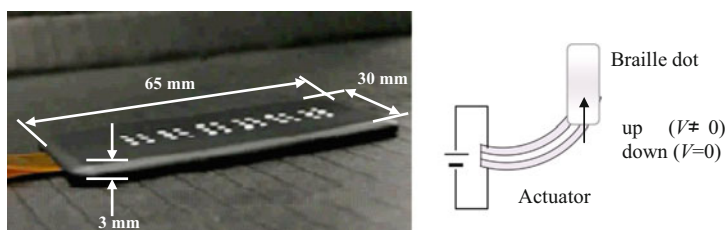


Fig. 9.5 A photo of very thin (ca. 3 mm) Braille display by using bucky gel actuators (*left*) and a schematic drawing of lifting up and down the Braille dot by bucky gel actuator (*right*) (Reproduced with permission from Sugino et al. [8])

9.8 Conclusions

In this chapter, we introduced recent progress to improve the actuation properties of carbon nanotube/ionic liquid composites (bucky gel actuators). We also demonstrated the application potential of bucky gel actuators for an ultra-light and thin Braille display. We are convinced that our bucky gel actuator will be appreciable in some medical welfare devices in the near future.

Acknowledgements The authors thank to Mr. Abe M, Mr. Takahashi I, and their colleagues (Sendai R&D center of Alps Electric Co. Ltd.), Prof. Nakano Y, Dr. Arai T (Keio Univ.), and Prof. Someya T, Dr. Sekitani T (Univ. of Tokyo) for their collaborations in the Braille project (the grant from Ministry of Health, Labor and Welfare of Japan in 2009 FY and 2010 FY). A part of this work was supported by Grant-in-Aid for Scientific Research (C) from Japan Society for Promotion of Science (JSPS) KAKENHI (23560822).

References

1. Bar-Cohen Y (ed) (2001) Electroactive polymer (EAP) actuators as artificial muscles, reality, potential, and challenges. SPIE, Washington
2. Carpi F, Smela E (eds) (2009) Biomedical applications of electroactive polymer actuators. Wiley, West Sussex
3. Akle BJ, Bennett MD, Leo DJ (2006) High-strain ionomeric-ionic liquid electroactive actuators. *Sens Actuators A* 126:173–181
4. Kaneko M, Fukui M, Takashima W, Kaneto K (1997) Electrolyte and strain dependences of chemomechanical deformation of polyaniline film. *Synth Met* 84:795–796
5. Zhou D, Spinks GM, Wallace GG, Tiyapiboonchaiya C, MacFarlane DR, Forsyth M, Sun J (2003) Solid state actuators based on polypyrrole and polymer-in-ionic liquid electrolytes. *Electrochim Acta* 48:2355–2359
6. Baughman RH, Cui C, Zakhidov AA, Iqbal Z, Barisci JN, Spinks GM, Wallace GG, Mazzorzi A, Rossi DD, Rinzler AG, Jaschinski O, Roth S, Kertesz M (1999) Carbon nanotube actuators. *Science* 284:1340–1344
7. Fukushima T, Asaka K, Kosaka A, Aida T (2005) Fully plastic actuator through layer-by-layer casting with ionic-liquid-based bucky gel. *Angew Chem Int Ed* 44:2410–2413
8. Sugino T, Shibata Y, Kiyohara K, Asaka K (2012) CNT/conductive polymer composites for low-voltage driven EAP actuators. *Proc SPIE* 8340:63400T-1-8
9. Kiyohara K, Sugino T, Takeuchi I, Mukai K, Asaka K (2009) Expansion and contraction of polymer electrodes under applied voltage. *J Appl Phys* 105:063506-1-8 (Erratum: (2009) *J Appl Phys* 105:119902-1)
10. Chan CT, Kamitakahara WA, Ho KM (1987) Charge-transfer effects in graphite intercalates: *ab initio* calculations and neutron-diffraction experiment. *Phys Rev Lett* 58:1528–1531
11. Hahn M, Barbieri O, Campana FP, Kötz R, Gallay R (2006) Carbon based double layer capacitors with aprotic electrolyte solutions: the possible role of intercalation/insertion processes. *Appl Phys A* 82:633–638
12. Oren Y, Glatt I, Livnat A, Kafri O, Soffer A (1985) The electrical double layer charge and associated dimensional changes of high surface area electrodes as detected by moiré deflectometry. *J Electroanal Chem* 187:59–71
13. Kiyohara K, Asaka K (2007) Monte Carlo simulation of electrolytes in the constant voltage ensemble. *J Chem Phys* 126:214704–214714

14. Kiyohara K, Asaka K (2007) Monte Carlo simulation of porous electrodes in the constant voltage ensemble. *J Phys Chem C* 111:15903–15909
15. Takeuchi I, Asaka K, Kiyohara K, Sugino T, Terasawa N, Mukai K, Fukushima T, Aida T (2009) Electromechanical behavior of fully plastic actuators based on bucky gel containing various internal ionic liquids. *Electrochim Acta* 54:1762–1768
16. Ohno H (ed) (2006) Ionic liquid II- marvelous developments and colorful near future. CMC, Tokyo
17. Takeuchi I, Asaka K, Kiyohara K, Sugino T, Mukai K, Randriamahazaka H (2010) Electrochemical impedance spectroscopy and electromechanical behavior of bucky-gel actuators containing ionic liquids. *J Phys Chem C* 114:14627–14634
18. Takeuchi I, Asaka K, Kiyohara K, Sugino T, Terasawa N, Mukai K, Shiraishi S (2009) Electromechanical behavior of a fully plastic actuator based on dispersed nano-carbon/ionic-liquid-gel electrodes. *Carbon* 47:1373–1380
19. Hata K, Futaba DN, Mizuno K, Namai T, Yumoto M, Iijima S (2004) Water-assisted highly efficient synthesis of impurity-free single-walled carbon nanotubes. *Science* 306:1362–1364
20. Mukai K, Asaka K, Hata K, Otero TF, Oike H (2011) High-speed carbon nanotube actuators based on an oxidation/reduction reaction. *Chem Eur J* 17:10965–10971
21. Giménez P, Mukai K, Asaka K, Hata K, Oike H, Otero TF (2012) Capacitive and faradic charge components in high-speed carbon nanotube actuator. *Electrochim Acta* 60:177–183
22. Biso M, Ricci D (2009) Multi-walled carbon nanotubes plastic actuator. *Phys Stat Solid B* 246:2820–2823
23. Torop J, Palmre V, Arulepp M, Sugino T, Asaka K, Aabloo A (2011) Flexible supercapacitor-like actuator with carbide-derived carbon electrodes. *Carbon* 49:3113–3119
24. Torop J, Sugino T, Asaka K, Jänes A, Lust E, Aabloo A (2012) Nanoporous carbide-derived carbon based actuators modified with gold foil: prospect for fast response and low voltage applications. *Sens Actuators B* 161:629–634
25. Saito S, Katoh Y, Kokubo H, Watanabe M, Maruo S (2009) Development of a soft actuator using a photocurable ionic gel. *J Micromech Microeng* 19:035005 (5 pages)
26. Sugino T, Kiyohara K, Takeuchi I, Mukai K, Asaka K (2009) Actuator properties of the complexes composed by carbon nanotube and ionic liquid: the effect of additives. *Sens Actuators B* 141:179–186
27. Sugino T, Kiyohara K, Takeuchi I, Mukai K, Asaka K (2011) Improving the actuating response of carbon anotube/ionic liquid composites by the addition of conductive nanoparticles. *Carbon* 49:3560–3570
28. Fukuda K, Sekitani T, Zschieschang U, Klauk H, Kuribara K, Yokota T, Sugino T, Asaka K, Ikeda M, Kuwabata H, Yamamoto T, Takimiya K, Fukushima T, Aida T, Takamiya M, Sakurai T, Someya T (2011) A 4 V operation, flexible Braille display using organic transistors, carbon nanotube actuators, and organic static random-access memory. *Adv Funct Mater* 21:4019–4027

Chapter 10

Ion Gels for Ionic Polymer Actuators

Masayoshi Watanabe, Satoru Imaizumi, Tomohiro Yasuda,
and Hisashi Kokubo

Abstract Ionic polymer actuators are driven by the migration or diffusion of ions and generally exhibit significant deformation (i.e., bending) under low-voltage (<5 V) applications. However, the durability of conventional ionic polymer actuators decreases under open atmosphere owing to the evaporation of solvents, which are essential for the movement of ions, from the actuators. In order to overcome this drawback, ionic polymer actuators that can be operated under open atmosphere and even under vacuum are being developed using ionic liquids (ILs). Combining macromolecules with ILs as additives can result in highly ion-conducting polymer electrolytes (ion gels) suitable for applications in ionic polymer actuators. However, the contribution of polymeric materials to the high performance of IL-based polymer actuators is yet to be elucidated. In this chapter, IL-based polymer electrolytes comprising block copolymers and polyimides are demonstrated to enable easily processable ionic polymer actuators with high performance and durability. The displacement response is also analyzed using our proposed displacement model.

Keywords Block copolymer • Electric double-layer capacitor • Ionic liquid • Polyimide • Polymer actuator • Polymer electrolyte

10.1 Introduction

Polymer actuators are defined as polymeric moving parts that are driven by external stimuli such as voltage application and photo-irradiation. In particular, electroactive polymer (EAP) actuators driven by voltage applications are expected to be part of the next-generation driving parts because they are easily controllable and have unique features such as soft motion, low mass, and easy and flexible processing. EAP actuators are classified into two groups: Electronic polymer

M. Watanabe (✉) • S. Imaizumi • H. Kokubo
Department of Chemistry and Biotechnology, Yokohama National University, Tokiwadai,
Hodogaya-ku, Yokohama 240-8501, Japan
e-mail: mwatanab@ynu.ac.jp

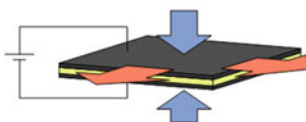
T. Yasuda
Cooperative Research and Development Center, Yokohama National University, Tokiwadai,
Hodogaya-ku, Yokohama 240-8501, Japan

EAP (Electroactive Polymer) Actuators

Polymeric materials that expand/shrink or bend with voltage application

Electronic EAP

Motive force: Coulombic attraction
Working E : High (> 1 kV)
Working conditions: Dry



Ionic EAP

Motive force: Transport of ions (migration, diffusion)
Working E : Low (< 5 V)
Working conditions: Wet

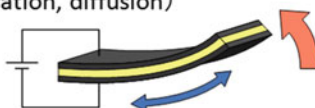


Fig. 10.1 Classification of electroactive polymer (EAP) actuators and their motive force and working voltage and conditions

actuators and ionic polymer actuators (Fig. 10.1) [1–4]. Electronic EAP actuators are driven by coulombic attraction (i.e., Maxwell force) between two flexible electrodes deposited on both sides of an insulating elastomer membrane [2]. The application of high voltage (> 1 kV) generates an attractive force between the two electrodes, which collapses the elastomer. Electronic polymer actuators can operate under dry conditions but require a high-voltage application. In contrast, ionic EAP actuators are driven by the migration or diffusion of ions and generally exhibit large deformation (usually a bending motion) under low voltage (< 5 V), as seen in conducting polymer actuators [3, 5], ionic-polymer metal composite actuators [4, 6], and carbon nanotube actuators [7]. However, conventional ionic polymer actuators are less durable under open atmosphere owing to the evaporation of solvents, which are essential for the movement of ions, from the actuators. Moreover, the narrow potential windows of the solvents limit the applied voltage and frequently induce side reactions that deteriorate the actuators.

Ionic polymer actuators that can be operated under open atmosphere and even under vacuum are possible through the use of ionic liquids (ILs) [8–10]. ILs are molten salts at ambient temperature, and they have attracted considerable attention because of their unique properties such as thermal stability, negligible volatility, non-flammability, and high ionic conductivity [11–15]. Here, we show that the combination of macromolecules with ILs as additives can result in highly ion-conducting polymer electrolytes [16–21] that are suitable for application in ionic polymer actuators. Compatible binary systems, where ILs are solidified (i.e., gelled) by polymers, can be used as the polymer electrolytes (ion gels) [18, 22, 23]. Even in the absence of solvents, ion gels feature fast ion transport that is decoupled from the segmental motion of the polymers, leading to relatively high ionic conductivities even at their glass transition temperatures [24]. The high ionic conductivity of the ion gels over a wide temperature range and under open and dry conditions is quite promising for electrolyte applications in ionic polymer actuators.

10.2 Materials for Ionic Polymer Actuators Using Ionic Liquids

Ionic polymer actuators based on polymer electrolytes that contain ILs have an electric double-layer capacitor (EDLC) structure and are driven by electric double-layer charging and discharging and are not accompanied by redox reactions. Generally, ionic polymer actuators consist of three materials: the IL, electrode material, and polymer (Fig. 10.1). There are many studies on the effect of the IL and electrode-material structures on the performance of ionic polymer actuators [25–31]. Ionic polymer actuators require electrode materials with high electron conductivity and high surface area in order to achieve high EDL capacitance and rapid charging and discharging in order to achieve large and rapid deformation. Accordingly, carbon nanotubes [10, 25], nonelectrolytically plated noble metals [9, 29], and conducting polymers [8, 26] are typical electrode materials. Indeed, actuators with these electrodes exhibit large and rapid deformation and are stable even after thousands of cycles. However, few studies on IL-based ionic polymer actuators have focused on polymeric materials. In fact, commercially available poly(vinylidene fluoride-*co*-hexafluoropropylene) (P(VDF-*co*-HFP)) and Nafion™ are widely used for IL-based ionic polymer actuators because they have good electrochemical and mechanical properties [6, 9, 10, 25–31]. However, the transduction from electrical energy into mechanical energy (to generate force and displacement) should correlate closely with the properties of the polymeric materials. The optimization of polymeric materials for actuators is crucial and should result in improved performance. Additionally, such investigations may contribute to the fundamental understanding of transduction mechanisms. For these reasons, polymeric materials for polymer actuators using ILs have begun to be studied [32–35]. For instance, Long and coworkers prepared block copolymers for IL-containing polymer actuators [32–34], and Hatipoglu et al. demonstrated the applicability of sulfonated poly(arylene ether sulfone) for actuators [35].

Generating polymeric materials that improve the performance of IL-based polymer actuators remains a great challenge [36–39]. Furthermore, it is important to explore the applicability of ubiquitous and inexpensive carbon materials such as activated carbon to IL-based polymer actuators [31, 36–39]. In this chapter, IL-based polymer electrolytes comprising block copolymers and polyimides are demonstrated in order to generate easily processable IL-based ionic polymer actuators with high performance and durability. Ionic polymer actuators were fabricated using these polymer electrolytes, activated carbon (AC), and highly conducting carbon materials in order to reduce the electrode resistance. The conducting carbons include acetylene black (AB), vapor-grown carbon fiber (VGCF), and Ketjen black (KB). The displacement response is also analyzed using our proposed displacement model [38].

10.3 Polymer Actuator Prepared by Self-Assembly of an ABA-Triblock Copolymer

Block copolymers are of great interest as they could enable easily processable and mechanically reliable polymer electrolytes via self-assembly. ABA-triblock copolymers, polystyrene-*block*-poly(methyl methacrylate)-*block*-polystyrene (SMS), synthesized by successive atom-transfer radical polymerizations [40, 41] (Fig. 10.2) were hybridized with an ionic liquid, [C₂mim][NTf₂] (1-ethyl-3-methylimidazolium bis(trifluoromethanesulfonyl)amide) [37]. Polystyrene (PSt) and poly(methyl methacrylate) (PMMA) are incompatible and compatible, respectively, with [C₂mim][NTf₂] [42]; thus, preferential dissolution of [C₂mim][NTf₂] in the PMMA phase was expected. Polymer electrolytes consisting of SMS and [C₂mim][NTf₂] were prepared by the cosolvent evaporation method with tetrahydrofuran. Atomic force microscopy (AFM) images of the ion gels indicated that PSt phase-separates to form spherical domains that serve as physical crosslinking points because PSt is not compatible with [C₂mim][NTf₂]; in contrast, a continuous PMMA phase with dissolved [C₂mim][NTf₂] formed and provided ion conduction paths (Fig. 10.2) [37]. The change in the ionic conductivity of the SMS-[C₂mim][NTf₂] polymer electrolytes (ion gels) as a function of their composition was well rationalized by this two-phase model. Accordingly, the ion gels were formed by the self-assembly of SMS and preferential dissolution of [C₂mim][NTf₂] into the PMMA phase. The viscoelastic properties of the gels could be easily controlled

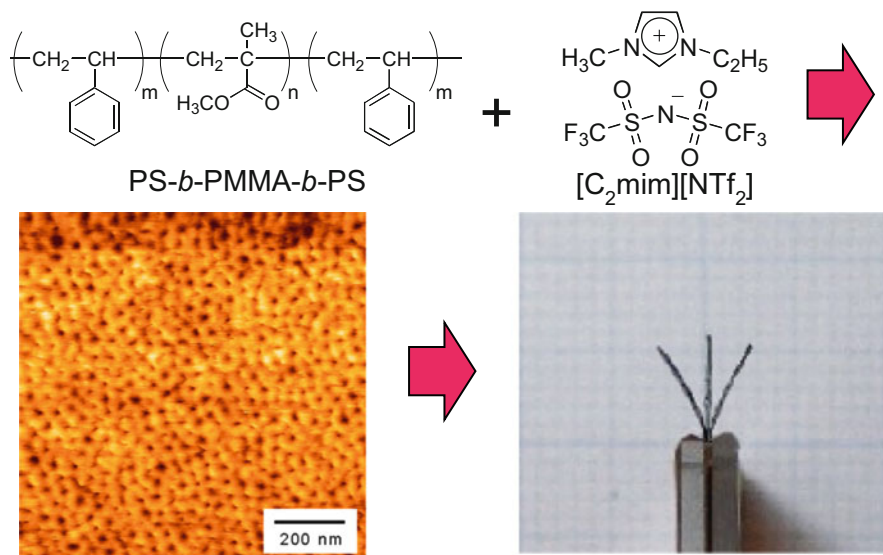
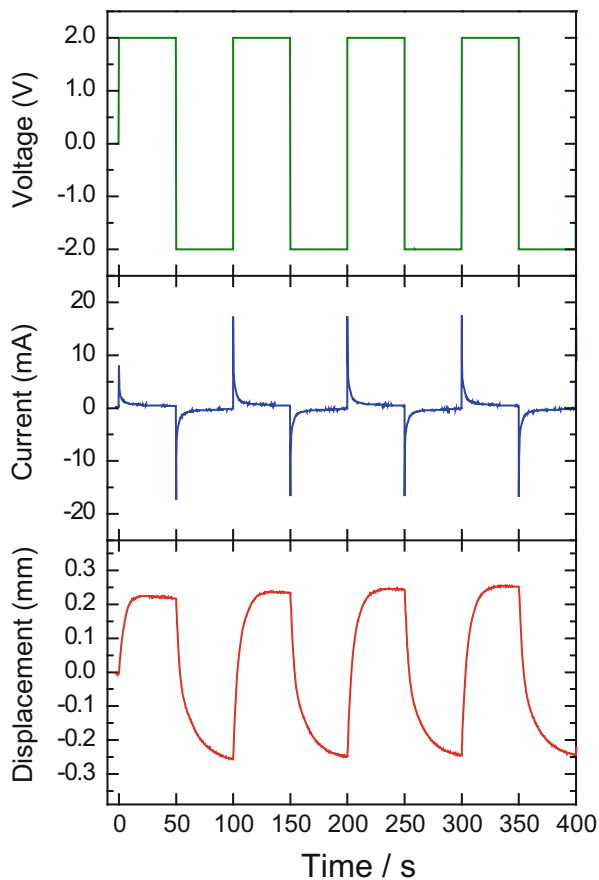


Fig. 10.2 Preparation of polymer electrolytes by self-assembly of ABA-type block copolymers and ionic liquids and their application in ionic polymer actuators. Cited from Imaizumi et al. [37]

Fig. 10.3 Current and displacement responses of an ion-gel actuator based on SMS (20 wt%) and [C₂mim][NTf₂] versus the application of ± 2.0 V rectangular voltage with a cycle of 100 s. Cited from Imaizumi et al. [37]



by changing the weight fraction of polystyrene in the SMS and [C₂mim][NTf₂] concentration in the ion gels.

The ion gels that exhibit high ionic conductivities ($>10^{-3}$ S cm⁻¹) at room temperature were used as the electrolyte for an ionic polymer actuator with a trilaminar structure consisting of the ion-gel electrolyte sandwiched between two composite carbon electrodes containing high-surface-area AC powders. The carbon electrodes were prepared by hot pressing a mixture of AC, KB, P(VDF-co-HFP), and [C₂mim][NTf₂] to form the electrode membranes, which were attached to both sides of the ion-gel electrolyte by hot pressing to fabricate a monolithic trilaminar membrane.

Figure 10.3 shows the current and bending displacement responses of an ion gel actuator versus the application of rectangular voltage [37]. When voltage is applied to the actuator, charging current that exponentially decays with time is observed. No faradaic current was observed in the cyclic voltammetry (data not shown) analyses within the voltage range ± 2.0 V. These results indicate that charging

and discharging of the EDL formed at the interface between the carbon materials and $[C_2mim][NTf_2]$ in the electrode layer is responsible for displacement of the actuator. The bending displacement was always directed toward the anodic side; this behavior is widely observed in ionic polymer actuators containing ILs [9, 10, 27–30]. Interestingly, the diffusivity of the cations is larger than that of the anions in most cases, even when the van der Waals radius of the cations is larger than that of the anions [43, 44]; this phenomenon appears to be related to the side-specific bending. The mechanism of bending will be discussed in the following section. The displacement of the actuator increased with increasing charge stored at the electric double-layer between the AC and IL.

10.4 Ionic Polymer Actuator Based on a Multi-Block Copolymer and Its Driving Mechanism

To elucidate the side-specific bending of the SMS- $[C_2mim][NTf_2]$ actuators, two solid polymer electrolytes that were composed of polyether-segmented polyurethaneurea (PEUU) and either a nonvolatile ionic liquid ($[C_2mim][NTf_2]$) or a lithium salt (lithium bis(trifluoromethanesulfonyl)amide; $Li[NTf_2]$), were prepared for use as ionic polymer actuators (Fig. 10.4) [38]. These salts were preferentially dissolved in the polyether phases to generate ion-conduction paths. PEUU was selected as the polymer matrix because of the expectation that the cations move faster than the anions in $[C_2mim][NTf_2]$ -doped PEUU and vice versa for $Li[NTf_2]$ -doped PEUU [43, 45]. The ionic transport mechanism in the polyethers was discussed in terms of the diffusion coefficients and ionic transference numbers of the incorporated ions, which were estimated using pulsed-field

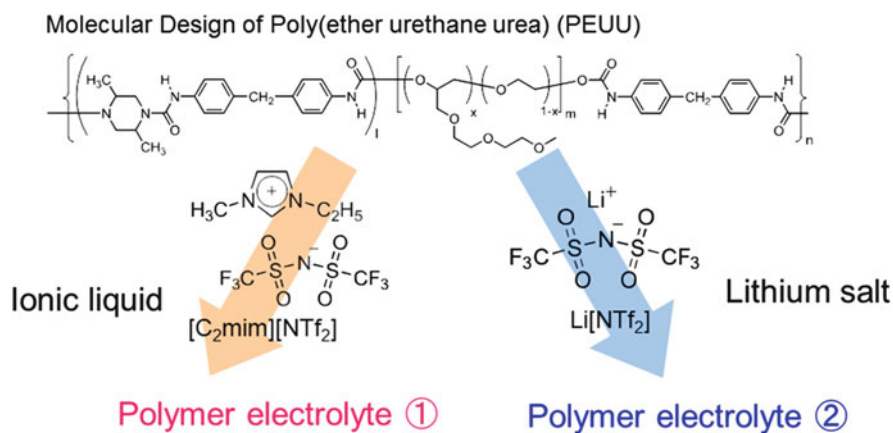


Fig. 10.4 Structure of poly(ether urethane urea) (PEUU) and its polymer electrolytes with $[C_2mim][NTf_2]$ and $Li[NTf_2]$

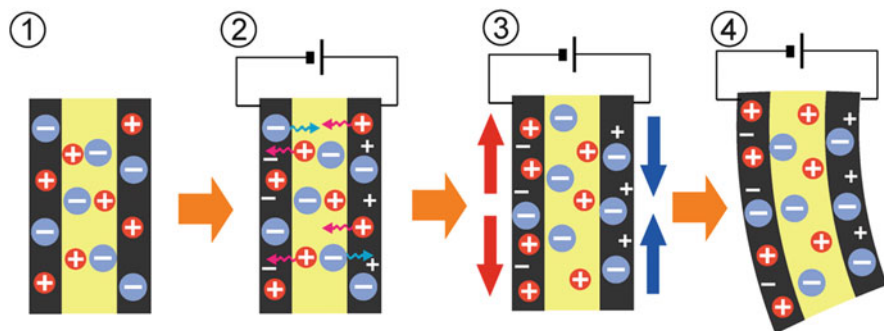


Fig. 10.5 A plausible mechanism for the deformation of an ionic polymer actuator with an electric double-layer capacitor structure

gradient spin-echo (PGSE) NMR. There was a distinct difference in the ion-transport properties of each polymer electrolyte that was caused by the difference in the magnitude of the interactions between the cations and polyether. In this electrolyte, anion diffusion was much faster than in the polyether/Li[NTf₂] electrolyte, whereas the cation diffused faster than the anion in the polyether/[C₂mim][NTf₂] electrolyte [38].

Ionic polymer actuators, which have a solid-state EDLC structure, were prepared using these polymer electrolyte membranes and ubiquitous carbon materials (AC and AB). A simple model of the actuation mechanisms was proposed by taking the differences in the ionic transport properties into consideration. Figure 10.5 shows a plausible mechanism for deformation that involves the following phenomena:

- (1) The ionic polymer actuators have an EDLC structure, in which the electrode layers consist of a matrix polymer, salt, AC, and AB.
- (2) Upon the application of voltage, EDL charging and ion migration occurs.
- (3) Because of the differences in the cationic and anionic mobilities and their ionic sizes, the volume of the electrode layers changes and concentration polarization occurs in addition to EDL charging.
- (4) This volume change causes displacement.

According to this model, a simple equation that presents the magnitude of displacement (d) as a function of the charge stored at EDL of an actuator (Q), cationic and anionic transference numbers (t_+ and t_- , respectively), and cationic and anionic volumes (v_+ and v_- , respectively) was derived (Fig. 10.6), where V_0 is the volume of each electrode, q is the ionic charge, and L and h represent the shape of an actuator, as shown in Fig. 10.6 [38]. This model discriminates the behavior of the actuators in terms of the products of the transference numbers and ionic volumes. Figure 10.7 and Table 10.1 show the ionic van der Waals volume of each ion in the actuators and the important parameters that determine the displacement of the two actuators. It is interesting to note that t_+ ($t_+ = D_+/(D_+ + D_-)$),

$$d = \frac{L^2}{3h} \cdot \frac{Q}{V_0} \cdot \frac{1}{q} (t_+ v_+ - t_- v_-)$$

Shape factor (determined by actuator shape)

Accumulated charge per unit volume of electrode

Volume change by unit charge (Intrinsic parameter determined by transference number t_+ and ionic volume v_+ .)

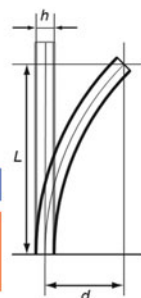


Fig. 10.6 A simple equation that presents the magnitude of displacement (d) as functions of the charge stored at the EDL of an actuator (Q), the cationic and anionic transference numbers (t_+ and t_- , respectively), and the cationic and anionic volume (v_+ and v_- , respectively), where V_0 is the volume of each electrode, q is the ionic charge, and L and h represent the shape of an actuator

Fig. 10.7 Ionic van der Waals volumes of the ions contained in PEUU-based ionic polymer actuators

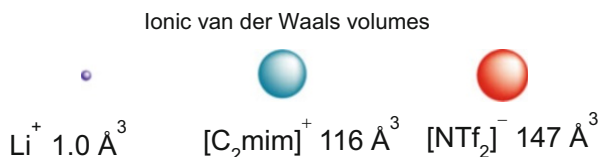


Table 10.1 Salt concentration, ionic conductivity, cationic transference number, and $t_+ v_+ - t_- v_-$ values for the PEUU electrolytes

Electrolyte	C_{salt} (mol kg ⁻¹)	σ (S cm ⁻¹) at 25 °C	t_+	$t_+ v_+ - t_- v_-$ (Å ³)
PEUU/[C ₂ mim][NTf ₂]	2.0	1.4×10^{-3}	0.62	16
PEUU/Li[NTf ₂]	0.86	3.4×10^{-3}	0.20	-117

where D represents the diffusivity) was determined to be larger than 0.5 via the PGSE-NMR measurements of [C₂mim][NTf₂]-doped PEUU and lower than 0.5 for Li[NTf₂]-doped PEUU. Importantly, the direction of deformation depends on the sign of $t_+ v_+ - t_- v_-$: The term $t_+ v_+ - t_- v_-$ is positive for [C₂mim][NTf₂]-doped PEUU and negative for Li[NTf₂]-doped PEUU, which predicts displacement to opposite sides (i.e., the anodic side for the former and the cathodic side for the latter). The absolute value of $t_+ v_+ - t_- v_-$ is much larger for Li[NTf₂]-doped PEUU than [C₂mim][NTf₂]-doped PEUU. Actuators with electrolytes with large $|t_+ v_+ - t_- v_-|$ values may undergo the same displacement with a smaller Q . This property contributes to faster motion and/or lower power consumption.

Figure 10.8 shows the applied voltage, current, and displacement of the actuators using PEUU [38]. It is very interesting to note that the displacement direction differs depending on the salt incorporated in PEUU, which is in agreement with the prediction of the displacement model in Fig. 10.5 and equation in Fig. 10.6. It is also notable that, despite the large difference in the charging current depending on the doped salts, the magnitude of the displacement is similar. The large difference in the current arises from the difference in the ionic conductivity (Table 10.1), and the

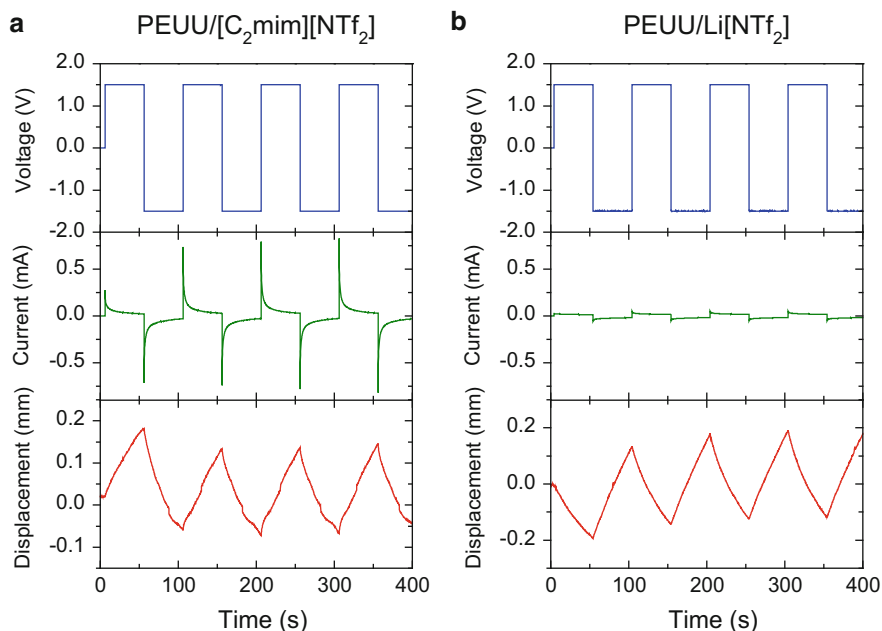
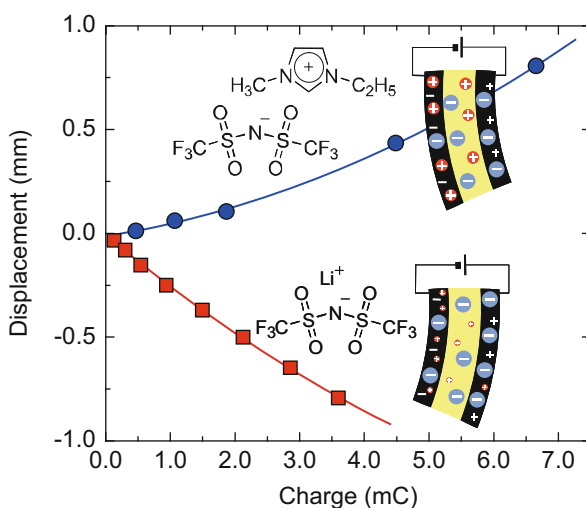


Fig. 10.8 Current and displacement response of actuators using (a) PEUU-[C₂mim][NTf₂] and (b) PEUU-Li[NTf₂] electrolytes driven by a square waveform voltage of ± 1.5 V at a frequency of 0.01 Hz. Cited from Imaizumi et al. [38]

Fig. 10.9 Displacement of PEUU-based ionic polymer actuators as a function of accumulated charge (Q). The displacement direction switches depending on the salt incorporated in PEUU. Cited from Imaizumi et al. [38]



Li[NTf₂]-doped PEUU has a much lower ionic conductivity; however, the $|t_{+}v_{+} - t_{-}v_{-}|$ value is much larger. This is the reason for the large displacement of the Li[NTf₂]-doped actuator despite the small charging current. Figure 10.9 shows the displacement of the two actuators as a function of stored charge at the

EDL of each actuator [38]. The magnitude of displacement was in good agreement with the magnitude calculated from the equation in Fig. 10.6 when the stored charge was small.

10.5 Sulfonated Polyimide for a High-Performance Ionic Polymer Actuator

Although the block copolymers discussed in the preceding sections are of great interest as building blocks for ion gels without chemical crosslinking, the mechanical strength of the gels with doped ILs was insufficient. Generally speaking, there is an inverse relationship between high ionic conductivity and mechanical strength of ion gels (i.e., IL-doped polymer electrolytes) in these actuators; the former is essential for a large and rapid response while the latter is important for durability and generation of a large force. Therefore, polymer electrolytes with both high ionic conductivity and reliable mechanical strength are required for high-performance polymer actuators. Through a broad exploration of polymeric materials, we developed polymer polymer electrolytes comprising soluble sulfonated polyimide (SPI) and $[C_2mim][NTf_2]$ IL (Fig. 10.10) [39]. Polyimides are representative engineering plastics that have high thermal stability, good film formability, and high mechanical strength. Studies on the application of polyimides in electrochemically functional materials have begun. In particular, SPIs are expected to be alternatives to Nafion™ in the polymer electrolyte membranes of polymer electrolyte fuel cells (PEFCs) [46]. Previously, we reported the first example of polymer electrolytes consisting of ILs and SPIs for non-humidified PEFCs [47, 48].

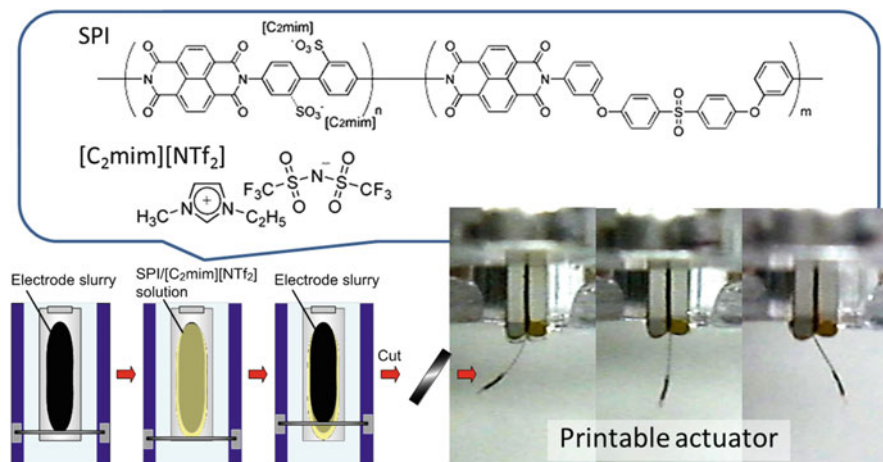


Fig. 10.10 Printable polymer actuators derived from ionic liquid, soluble polyimide, and ubiquitous carbon materials. Cited from Imaizumi et al. [39]

Table 10.2 Ionic conductivities and storage moduli of different polymer-[C₂mim][NTf₂] electrolytes

Polymer	$f_{\text{polymer}}/\text{wt}\%$ ^a	$\sigma/\text{mS cm}^{-1}$ ^b	E'/MPa ^c
SPI	25	0.83	37
SPI	33	0.29	220
SPI	50	0.0017	1,100
SPI	100	—	6,300
P(VDF- <i>co</i> -HFP) ^d	17	3.5	1.4
PMMA ^e	21	0.98	0.16

^aPolymer weight percent in [C₂mim][NTf₂]-based electrolytes^bIonic conductivity measured at 20 °C^cStorage tensile modulus measured at 30 °C^dPrepared by dissolving P(VDF-*co*-HFP) in [C₂mim][NTf₂] at 130 °C, followed by cooling to room temperature^eNetwork polymer cross-linked by ethylene glycol dimethacrylate (1 mol% vs. MMA monomer)

In SPI/IL electrolytes, the rigid aromatic backbones of SPI impart strength to the films and the sulfonate groups and their counter-cations provide compatibility with ILs. As a result, the polymer electrolytes of SPIs exhibit both favorable mechanical properties and high ionic conductivity.

Table 10.2 summarizes the ionic conductivities (at 20 °C) and storage tensile moduli (E') of different SPI-[C₂mim][NTf₂] electrolytes and related polymer electrolytes, as determined by dynamic viscoelastic measurements at 30 °C [39]. The SPI-[C₂mim][NTf₂] electrolytes have high ionic conductivity (0.83 mS cm⁻¹) that is comparable to that of the ion gel prepared from chemically cross-linked PMMA (0.98 mS cm⁻¹) [18]; however, the elastic modulus of the electrolytes is more than two orders of magnitude higher ($>10^7$ Pa) than that of the ion gel. The P(VDF-*co*-HFP)-based electrolyte has a high conductivity and high modulus, which result from a microporous structure that is generated by the phase separation of spherulites during film formation [49]. [C₂mim][NTf₂] appears to be incorporated mainly into the porous structure, which results in leakage of the ionic liquid during long-term use of the actuator.

The concurrent high ionic conductivity and high mechanical strength in the SPI-[C₂mim][NTf₂] electrolytes appear to arise from the rigid polymer backbone and microscopic structure. Dynamic mechanical measurements of the SPI-IL electrolytes indicated that the hydrophobic and ionic groups are phase-separated and that the ionic liquid is preferentially incorporated in the ionic domains [39]. The clustered ionic groups form ion-conducting channels, while the hydrophobic groups provide a rigid framework. A tapping-mode AFM phase image of the SPI-IL electrolytes also supports the microphase-separated structures (Fig. 10.11a) [39]. This assumption coincides well with percolation-type changes in the ionic conductivity and elastic modulus of the SPI-IL electrolytes, as shown in this study and our previous work [39, 47]. It has also been reported that SPIs that were prepared to replace perfluorinated sulfonic acid membranes in fuel cells have similar microphase-separated structures [50, 51].

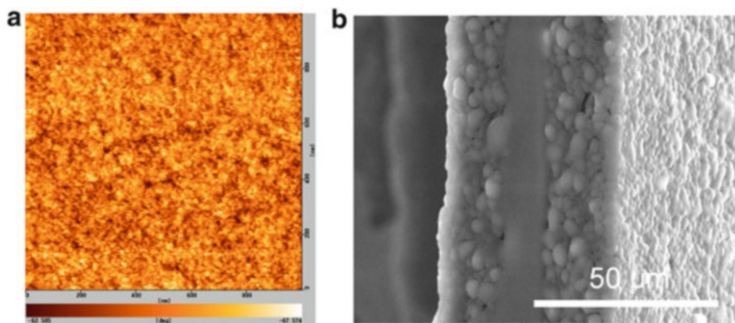
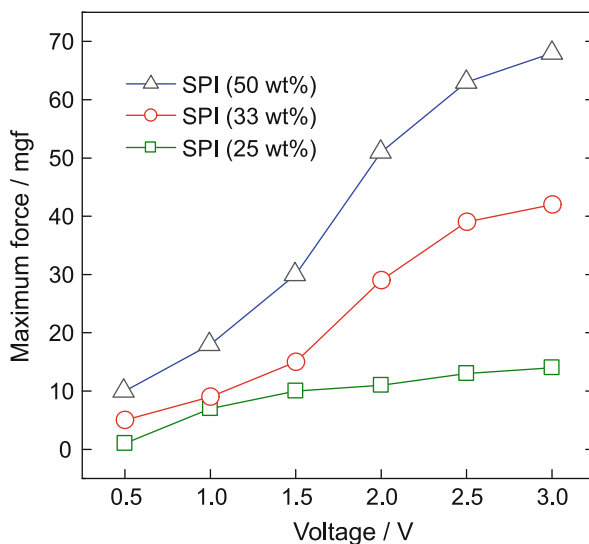


Fig. 10.11 (a) Tapping mode AFM phase image of SPI-[C₂mim][NTf₂] (SPI: 25 wt%) and (b) SEM image of a cross-sectional view of an SPI actuator

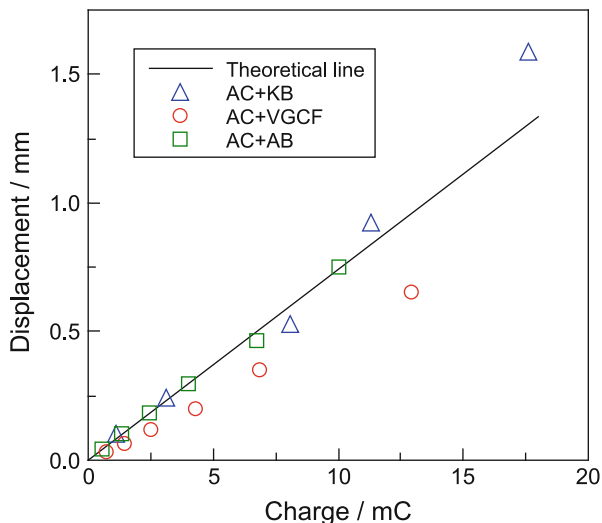
Fig. 10.12 Maximum generative force of actuators using electrolytes with different SPI weight fractions as a function of voltage. Cited from Imaizumi et al. [39]



Polymer actuators based on the SPI-[C₂mim][NTf₂] electrolytes were prepared using AC together with a highly electron-conducting carbon such as AB, VGCF, and KB. Trilaminar-structured actuators were successfully prepared by a layer-by-layer printing method (Figs. 10.10 and 10.11b) [39]. Thanks to the relatively high modulus of the SPI-[C₂mim][NTf₂] electrolytes, the electrolyte and electrode layers could be significantly thinner (Fig. 10.11b). Adhesion between the electrolyte and electrodes was also greatly improved by the use of the layer-by-layer printing method.

Figure 10.12 shows the maximum generative force of the SPI-[C₂mim][NTf₂] actuators at each applied voltage. The maximum force depends on the applied voltage and SPI composition in the electrolyte layer and increases with applied voltage and SPI fraction. Specifically, the actuator with an electrolyte containing 50 wt% SPI generates a force of 68 mgf (stress of 67 MPa) at 3.0 V, and this

Fig. 10.13 Displacements of SPI actuators with different electron-conducting carbon additives in response to rectangular waveform voltages at a frequency of 0.05 Hz as a function of accumulated charge (Q). Cited from Imaizumi et al. [39]



composition reaches a force 70 times higher than its weight (~ 1 mg), which is comparable to the results for other IL-based actuators [9, 10, 25]. The dependence of the generative force on the SPI weight fraction corresponds well with the differences in the elastic moduli of the electrolytes, as listed in Table 10.2. Furthermore, the displacement, response speed, and durability of the actuators depend on the combination of carbons. In particular, the actuators with mixed AC/KB carbon electrodes exhibited relatively large displacement and high-speed response and retained 80 % of the initial displacement even after more than 5,000 cycles. As shown in Fig. 10.13 [39], the displacement of the actuators was proportional to the electric charge accumulated in the electrodes, regardless of the types of carbon materials, and agreed well with the displacement model, where the solid line is drawn based on the equation in Fig. 10.6.

Acknowledgements This work was supported in part by Grants-in-aid for Scientific Research on Priority Areas (No. 438-19016014 and No.452-17073009) and Basic Research A (No. 23245046) from the MEXT of Japan.

References

1. Bar-Cohen Y (2004) Electroactive polymer (EAP) actuators as artificial muscles: reality, potential, and challenges. SPIE Press, Washington
2. Pelrine R, Kornbluh R, Pei QB, Joseph J (2000) High-speed electrically actuated elastomers with strain greater than 100 %. *Science* 287:836–839
3. Smela E (2003) Conjugated polymer actuators for biomedical applications. *Adv Mater* 15:481–494

4. Shahinpoor M (2003) Ionic polymer–conductor composites as biomimetic sensors, robotic actuators and artificial muscles—a review. *Electrochim Acta* 48:2343–2353
5. Kaneto K, Kaneko M, Min Y, MacDiarmid AG (1995) “Artificial muscle”: electromechanical actuators using polyaniline films. *Synth Met* 71:2211–2212
6. Asaka K, Oguro K, Nishimura Y, Mizuhata M, Takenaka H (1995) Bending of polyelectrolyte membrane–platinum composites by electric stimuli I. Response characteristics to various waveforms. *Polym J* 27:436–440
7. Baughman RH, Cui C, Zakhidov AA, Iqbal Z, Barisci JN, Spinks GM, Wallace GG, Mazzoldi A, Rossi DD, Rinzler AG, Jaschinski O, Roth S, Kertesz M (1999) Carbon nanotube actuators. *Science* 284:1340–1344
8. Lu W, Fadeev AG, Qi B, Smela E, Mattes BR, Ding J, Spinks GM, Mazurkiewicz J, Zhou D, Wallace GG, MacFarlane DR, Forsyth SA, Forsyth M (2002) Use of ionic liquids for π -conjugated polymer electrochemical devices. *Science* 297:983–987
9. Bennett MD, Leo DJ (2004) Ionic liquids as stable solvents for ionic polymer transducers. *Sens Actuators A* 115:79–90
10. Fukushima T, Asaka K, Kosaka A, Aida T (2005) Fully plastic actuator through layer-by-layer casting with ionic-liquid-based bucky gel. *Angew Chem Int Ed* 44:2410–2413
11. Welton T (1999) Room-temperature ionic liquids. Solvents for synthesis and catalysis. *Chem Rev* 99:2071–2083
12. Wasserscheid P, Keim W (2000) Ionic liquids—new “solutions” for transition metal catalysis. *Angew Chem Int Ed* 39:3772–3789
13. Wilkes JS (2002) A short history of ionic liquids—from Molten salts to neoteric solvents. *Green Chem* 4:73–80
14. Seddon KR (2003) Ionic liquids: a taste of the future. *Nat Mater* 2:363–365
15. Plechkova NV, Seddon KR (2008) Applications of ionic liquids in the chemical industry. *Chem Soc Rev* 37:123–150
16. Watanabe M, Yamada SI, Sanui K, Ogata N (1993) High ionic conductivity of new polymer electrolytes consisting of polypyridinium, pyridinium and aluminium chloride. *J Chem Soc Chem Commun* 929–931
17. Noda A, Watanabe M (2000) Highly conductive polymer electrolytes prepared by in situ polymerization of vinyl monomers in room temperature molten salts. *Electrochim Acta* 45:1265–1270
18. Susan MABH, Kaneko T, Noda A, Watanabe M (2005) Ion gels prepared by in situ radical polymerization of vinyl monomers in an ionic liquid and their characterization as polymer electrolytes. *J Am Chem Soc* 127:4976–4983
19. Carlin RT, Fuller J (1997) Ionic liquid–polymer gel catalytic membrane. *Chem Commun* 1345–1346
20. Fuller J, Breda AC, Carlin RT (1997) Ionic liquid–polymer gel electrolytes. *J Electrochem Soc* 144:L67–L70
21. He Y, Lodge TP (2008) Thermoreversible ion gels with tunable melting temperatures from triblock and pentablock copolymers. *Macromolecules* 41:167–174
22. Ueki T, Watanabe M (2008) Macromolecules in ionic liquids: progress, challenges, and opportunities. *Macromolecules* 41:3739–3749
23. Ueki T, Watanabe M (2012) Polymers in ionic liquids: dawn of neoteric solvents and innovative materials. *Bull Chem Soc Jpn* 85:33–50
24. Seki S, Susan MABH, Kaneko T, Tokuda H, Noda A, Watanabe M (2005) Distinct difference in ionic transport behavior in polymer electrolytes depending on the matrix polymers and incorporated salts. *J Phys Chem B* 109:3886–3892
25. Mukai K, Asaka K, Kiyohara K, Sugino T, Takeuchi I, Fukushima T, Aida T (2008) High performance fully plastic actuator based on ionic-liquid-based bucky gel. *Electrochim Acta* 53:5555–5562
26. Vidal F, Plesse C, Teyssié D, Chevrot C (2004) Long-life air working conducting semi-IPN/ionic liquid based actuator. *Synth Met* 142:287–291

27. Takeuchi I, Asaka K, Kiyohara K, Sugino T, Terasawa N, Mukai K, Shiraishi S (2009) Electromechanical behavior of a fully plastic actuator based on dispersed nano-carbon/ionic-liquid-gel electrodes. *Carbon* 47:1373–1380
28. Terasawa N, Takeuchi I, Matsumoto H, Mukai K, Asaka K (2011) High performance polymer actuator based on carbon nanotube-ionic liquid gel: effect of ionic liquid. *Sens Actuators B* 156:539–545
29. Akle BJ, Bennett MD, Leo DJ (2006) High-strain ionomeric–ionic liquid electroactive actuators. *Sens Actuators A* 126:173–181
30. Torop J, Palmre V, Arulepp M, Sugino T, Asaka K, Aabloo A (2011) Flexible supercapacitor-like actuator with carbide-derived carbon electrodes. *Carbon* 49:3113–3119
31. Kokubo H, Honda T, Imaizumi S, Dokko K, Watanabe M (2013) Effects of carbon electrode materials on performance of ionic polymer actuators having electric double-layer capacitor structure. *Electrochem* 81:849–852
32. Gao R, Wang D, Heflin JR, Long TE (2012) Imidazolium sulfonate-containing pentablock copolymer–ionic liquid membranes for electroactive actuators. *J Mater Chem* 22:13473–13476
33. Green MD, Wang D, Hemp ST, Choi JH, Winey KI, Heflin JR, Long TE (2012) Synthesis of imidazolium ABA triblock copolymers for electromechanical transducers. *Polymer* 53:3677–3686
34. Wu T, Wang D, Zhang M, Heflin JR, Moore RB, Long TE (2012) RAFT synthesis of ABA triblock copolymers as ionic liquid-containing electroactive membranes. *ACS Appl Mater Interfaces* 4:6552–6559
35. Hatipoglu G, Liu Y, Zhao R, Yoonessi M, Tigelaar DM, Tadigadapa S, Zhang QM (2012) A highly aromatic and sulfonated ionomer for high elastic modulus ionic polymer membrane micro-actuators. *Smart Mater Struct* 21:055015
36. Saito S, Katoh Y, Kokubo H, Watanabe M, Maruo S (2009) Development of a soft actuator using a photocurable ionic gel. *J Micromech Microeng* 19:035005
37. Imaizumi S, Kokubo H, Watanabe M (2012) Polymer actuators using ion-gel electrolytes prepared by self-assembly of ABA-triblock copolymers. *Macromolecules* 45:401–409
38. Imaizumi S, Kato Y, Kokubo H, Watanabe M (2012) Driving mechanisms of ionic polymer actuators having electric double layer capacitor structures. *J Phys Chem B* 116:5080–5089
39. Imaizumi S, Ohtsuki Y, Yasuda T, Kokubo H, Watanabe M (2013) Printable polymer actuators from ionic liquid, soluble polyimide, and ubiquitous carbon materials. *ACS Appl Mater Interfaces* 5:6307–6315
40. Patten TE, Xia J, Abernathy T, Matyjaszewski K (1996) Polymers with very low polydispersities from atom transfer radical polymerization. *Science* 272:866–868
41. Tsarevsky NV, Matyjaszewski K (2007) “Green” atom transfer radical polymerization: from process design to preparation of well-defined environmentally friendly polymeric materials. *Chem Rev* 107:2270–2299
42. Ueki T, Karino T, Kobayashi Y, Shibayama M, Watanabe M (2007) Difference in lower critical solution temperature behavior between random copolymers and a homopolymer having solvatophilic and solvophobic structures in an ionic liquid. *J Phys Chem B* 111:4750–4754
43. Tokuda H, Hayamizu K, Ishii K, Susan MABH, Watanabe M (2004) Physicochemical properties and structures of room temperature ionic liquids. 1. Variation of anionic species. *J Phys Chem B* 108:16593–16600
44. Tokuda H, Hayamizu K, Ishii K, Susan MABH, Watanabe M (2005) Physicochemical properties and structures of room temperature ionic liquids. 2. Variation of alkyl chain length in imidazolium cation. *J Phys Chem B* 109:6103–6110
45. Tokuda H, Tabata S, Susan MABH, Hayamizu K, Watanabe M (2004) Design of polymer electrolytes based on a lithium salt of a weakly coordinating anion to realize high ionic conductivity with fast charge-transfer reaction. *J Phys Chem B* 108:11995–12002

46. Hickner M, Ghassemi H, Kim YS, Einsla BR, McGrath JE (2004) Alternative polymer systems for proton exchange membranes (PEMs). *Chem Rev* 104:4587–4611
47. Lee SY, Ogawa A, Kanno M, Nakamoto H, Yasuda T, Watanabe M (2010) Nonhumidified intermediate temperature fuel cells using protic ionic liquids. *J Am Chem Soc* 132:9764–9773
48. Yasuda T, Nakamura S, Honda Y, Kinugawa K, Lee SY, Watanabe M (2012) Effects of polymer structure on properties of sulfonated polyimide/protic ionic liquid composite membranes for nonhumidified fuel cell applications. *ACS Appl Mater Interfaces* 4:1783–1790
49. Michot T, Nishimoto A, Watanabe M (2000) Electrochemical properties of polymer gel electrolytes based on poly(vinylidene fluoride) copolymer and homopolymer. *Electrochim Acta* 45:1347–1360
50. Essafi W, Gebel G, Mercier R (2004) Sulfonated polyimide ionomers: a structural study. *Macromolecules* 37:1431–1440
51. Bae B, Yoda T, Miyatake K, Uchida H, Watanabe M (2010) Proton-conductive aromatic ionomers containing highly sulfonated blocks for high-temperature-operable fuel cells. *Angew Chem Int Ed* 49:317–320

Chapter 11

Ionic Liquid/Polyurethane/PEDOT:PSS Composite Actuators

Hidenori Okuzaki

Abstract The transparent ionic liquid/polyurethane (IL/PU) gels were synthesized by addition reaction of polyol and diisocyanate in the presence of 1-ethyl-3-methylimidazolium bis(trifluoromethylsulfonyl)imide. With increasing the IL content from 0 to 40 wt%, both ionic conductivity and electric-double-layer capacitance increased from 3.1×10^{-5} S/cm and 9.6 pF/cm^2 to 8.8×10^{-5} S/cm and 277 pF/cm^2 , respectively, while the compression modulus slightly decreased from 0.49 to 0.44 MPa. The IL/PU/PEDOT:PSS composites were fabricated by sandwiching the IL/PU gel between two conductive polymer films made of poly(3,4-ethylenedioxythiophene) doped with poly(4-styrenesulfonate) (PEDOT:PSS) as soft and flexible electrodes. Upon application of an electric field, the IL/PU/PEDOT:PSS composite showed quick and intensive bending toward anode, where the bending displacement attained 3.8 mm at IL = 40 wt% and 2 V, corresponding to the strain of 0.32 %.

Keywords Actuator • Conductive polymer • Ionic liquid • PEDOT:PSS • Polyurethane

11.1 Introduction

Polymers that undergo dimensional changes in response to various environmental stimuli are capable of transducing chemical or physical energy directly into mechanical work [1–7]. Oguro and Asaka first developed ionic polymer-metal composite (IPMC) actuators utilizing a nafion membrane whose surfaces were chemically plated with gold or platinum [8]. They found that the IPMC actuator bent toward the anode by applying an electric field, the mechanism of which was associated with the difference of swelling degree at both sides caused by an electrophoretic transport of protons carrying with water molecules. The IPMC actuators are flexible and suitable for downsizing capable of driving at low voltages, which provides medical applications such as micro-active catheters and guide

H. Okuzaki (✉)

Interdisciplinary Graduate School of Medicine and Engineering, University of Yamanashi,
4-4-37 Takeda, Kofu 400-8511, Japan
e-mail: okuzaki@yamanashi.ac.jp

wires. However, most of them operate in an electrolyte solution or in a swollen state, while few reports have been investigated on solid-state polymers with ionic liquid [9, 10] working in ambient atmosphere. Asaka reported tri-layer actuators utilizing a fluorinated polymer membrane containing ionic liquid as an active layer sandwiched between two bucky-gel layers consisting of single-walled carbon nanotubes dispersed in the ionic liquid as electrodes [11]. The motion of these actuators is based on a deformation of polymer matrices caused by an electrophoretic polarization of ionic liquid in the active layer. These actuators are generally categorized as “ionic electro-active polymers (EAPs)” [12].

On the other hand, dielectric elastomer (DE) actuators utilizing silicone or acrylic rubbers were reported by Perline et al. (SRI International) [13], where large deformation of the DE (>100 %) under an electric field could be explained by Maxwell stress. However, the DE actuators have drawbacks such as high driving voltages (>1,000 V) and few flexible and stretchable electrodes compliant to the large deformation of the DE actuators. Aimed at decreasing the driving voltage and/or increase the electrostriction of the DE actuators, composites with inorganic fillers such as TiO_2 , BaTiO_3 , and SrTiO_3 to increase the dielectric constant and blends with plasticizers to lower Young's modulus are commonly investigated. In contrast to the ionic EAPs, these actuators are categorized as “electric EAPs” [12].

So far as the authors know, only a few research on composites of elastomer and ionic liquid for the applications to EAP actuators have been investigated [14–16]. If the composites of elastomer with ionic liquid got complementary advantages of the ionic and electric EAPs and redeemed each defects, they may provide an insight into the development of novel low-voltage and high-strain EAP actuators working in ambient atmosphere. In this study, we fabricated ionic liquid/polyurethane elastomer (IL/PU) composite gels and mechanical and electrical properties were investigated by means of compression test and AC impedance analysis. Moreover, IL/PU/PEDOT:PSS composites were fabricated by sandwiching the IL/PU gel between two conductive polymer films made of poly(3,4-ethylenedioxythiophene) doped with poly(4-styrenesulfonate) (PEDOT:PSS) as soft and flexible electrodes. The EAP actuating behavior of the IL/PU/PEDOT:PSS composite was demonstrated.

11.2 Experimental

Polyurethane (PU) elastomers were synthesized via addition reaction of 80 wt% of polyester-type polyol (Nippollan 4748, Nippon Polyurethane Industry) with 20 wt% of aliphatic-type diisocyanate (HC-210, Nippon Polyurethane Industry) by heating at 80 °C for 1 h. It is obvious that the PU elastomer is chemically cross-linked by urethane bonds formed between the hydroxyl and isocyanate groups, where the cross-linking density of the PU elastomer is strongly dependent on the composition ratio between the polyol and diisocyanate. 1-Ethyl-3-methylimidazolium bis(trifluoromethylsulfonyl)imide ([EMI][TFSI], Tokyo Chemical Industry) as an ionic liquid (IL) was used as received. The IL/PU gels were synthesized by the

addition reaction similarly to the PU elastomer in the presence of 10–40 wt% of [EMI][TFSI]. The mechanical properties of the resulting disk-like PU elastomer and IL/PU gels (1 mm thick and 30 mm in diameter) were evaluated by a compression test with a mechanical tester (EZ-TEST, Shimadzu) measured at a constant strain rate of 100 %/min, where compressive moduli were calculated from the initial slope of the stress–strain curves. The electrical properties of the disk-like IL/PU gels (1 mm thick and 30 mm in diameter) were measured at $1\text{--}10^6$ Hz by an AC impedance technique with a frequency response analyzer (1255WB, Solartron) equipped with a sample holder (SH1-Z, Toyo). The analyses of Cole–Cole plots and equivalent circuits were carried out using a ZPlot (Solartron).

The soft and flexible electrodes were fabricated by casting the PEDOT:PSS aqueous dispersion containing 0.75 wt% of xylitol at 60 °C for 6 h and subsequent heat treatment at 120 °C for 2 h [17]. The thickness of the resulting PEDOT:PSS film was ca. 14 μm with an electrical conductivity of 286 S/cm measured by a four-point technique using a Loresta-GP (MCP-T610, Mitsubishi Chemical Analytech). The rectangular strip of the IL/PU gel (25 mm long, 5 mm wide, and 100 μm thick) was sandwiched between two PEDOT:PSS films and suspended from a Kelvin clip by holding the upper part of 5 mm. The bending of the IL/PU/PEDOT:PSS composite actuator under an electric field applied using a function generator (HB-305, Hokuto Denko) equipped with a potentiostat (HAL-3001, Hokuto Denko) was demonstrated by measuring the displacement at the position of 5 mm from the bottom end of the composite actuator with a laser displacementometer (LK-H050, Keyence).

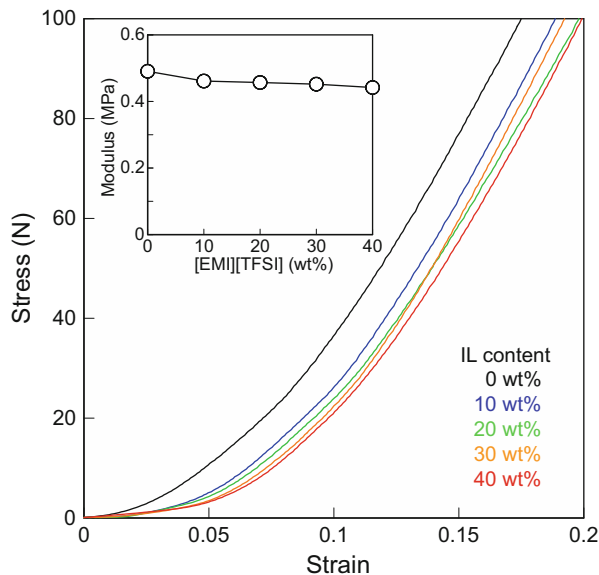
11.3 Results and Discussion

11.3.1 Mechanical Properties of IL/PU Gels

The polyurethane (PU) is a typical elastomer with high strength, wear resistance, and dielectric constant. On the other hand, the ionic liquid (IL) is a room-temperature molten salt with non-volatility, non-flammability, chemical and thermal stability, and high ionic conductivity. As a result of the screening experiment of various ionic liquids, 1-ethyl-3-methylimidazolium bis(trifluoromethylsulfonyl) imide ([EMI][TFSI]) showed high miscibility with PU and the resulting IL/PU gels were uniform and transparent at $\text{IL} \leq 40$ wt%, indicative of a homogeneous structure at least in size of wavelength of visible light. On the other hand, at $\text{IL} > 40$ wt% the IL partly leaked out on the surface of the IL/PU gel, which demonstrates that the maximum uptake of the IL in PU is ca. 40 wt%.

In order to clarify the effect of IL on mechanical properties of the IL/PU gels, compression test was performed and results are shown in Fig. 11.1. When the disk-like PU and IL/PU gels (1 mm thick and 30 mm in diameter) are compressed, stress gradually increases at strains lower than 0.05 and abruptly rises and attains 100 N at

Fig. 11.1 Stress–strain curves of IL/PU gels (1 mm thick and 30 mm in diameter) with various IL contents measured at a constant strain rate of 100 %/min. The inset represents dependence of compression modulus of IL/PU gels on IL content



strains of 0.17–0.2. It should be noted that the IL never exuded from the gel even under 100 N, corresponding to the load of ca. 10 kg, which demonstrates the good miscibility between the PU and IL at IL < 40 wt%. At the same strain the stress becomes smaller with increasing the IL content, indicating the decrease of compression modulus. Indeed, the compression modulus calculated from the initial slope of the stress–strain curves slightly decreases from 0.49 MPa (IL = 0 wt%) to 0.44 MPa (IL = 40 wt%) as shown in the inset of Fig. 11.1, which is probably due to the plasticizing effect of the IL and/or decrease of network density of the PU elastomer. At room temperature, the PU elastomer is already in a rubbery state because of its low glass transition temperature, suggesting few effects of the IL as the plasticizer. Therefore, the slight decrease of the compression modulus may be associated with the drop of the network density caused by decreasing the volume fraction of the PU elastomer due to the dilution effect during the synthesis.

11.3.2 Electrical Properties of IL/PU Gels

A clear indication of the importance of IL on electrical properties is seen in the AC impedance analysis. As shown in Fig. 11.2, Cole–Cole plots of the IL/PU gels show a semicircle at higher frequencies with a straight line at lower frequencies, which can be expressed by a Randles equivalent circuit consisting of a gel resistant (R_g) in series with the parallel combination of an electric-double-layer capacitance (C_{dl}) and an impedance of a faradic reaction composed of charge

Fig. 11.2 Cole–Cole plots of IL/PU gels (1 mm thick and 10 mm in diameter) with various IL contents measured in a frequency range of 1–10⁶ Hz and Randles equivalent circuit (*inset*)

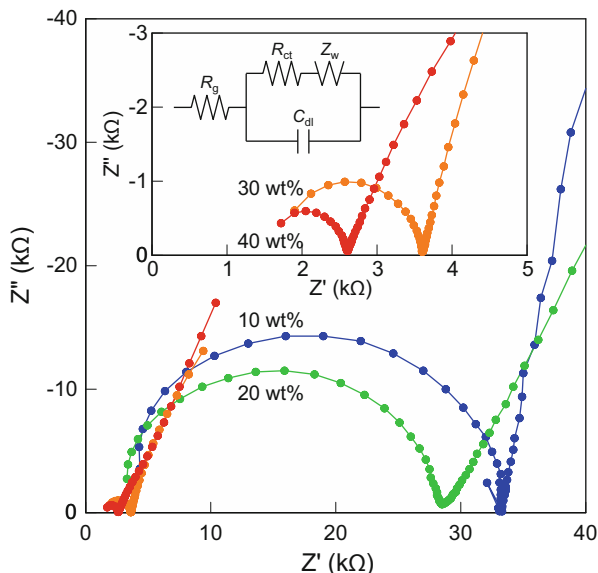
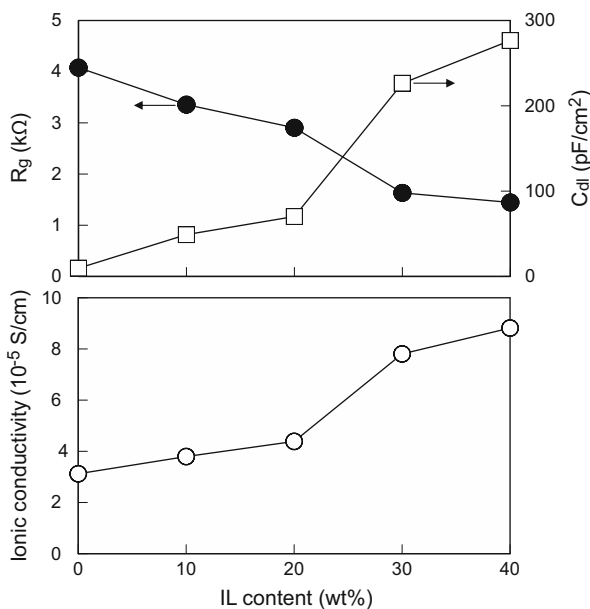


Fig. 11.3 Changes in gel resistance (R_g), electric-double-layer capacitance (C_{dl}), and ionic conductivity (σ) of IL/PU gels on IL content



transfer resistance (R_{ct}) and a Warburg impedance (Z_w) representing the diffusion of ions as shown in the inset of Fig. 11.2 [18]. One can see that the semicircle in the Cole–Cole plot becomes smaller and slightly shifts toward lower resistance with increasing the IL content from 10 to 40 wt%, indicative of changes in the parameters of the equivalent circuit. As shown in Fig. 11.3, a rise in the IL content

brings about a decrease of the R_g owing to the increase of ionic conductivity (σ) calculated as follows:

$$\sigma = d/R_g S \quad (11.1)$$

where d and S are the gel thickness (0.1 cm) and electrode surface area (0.785 cm²), respectively. It is found that the ionic conductivity is in proportion to the IL content and the value attains as high as 8.8×10^{-5} S/cm at IL = 40 wt%, which is comparable to that of polyether-segmented polyurethaneurea (PEUU) and [EMI][TFSI] composites at the similar IL content [19]. On the other hand, the C_{dl} significantly increases by two orders of magnitude from 9.6 pF/cm² (IL = 0 wt%) to 277 pF/cm² (IL = 40 wt%) owing to the polarization of IL.

11.3.3 EAP Actuating Behavior of IL/PU/PEDOT:PSS Composites

The IL/PU/PEDOT:PSS composite was fabricated by sandwiching a rectangular strip of the IL/PU gel (25 mm long, 5 mm wide, and 100 μ m thick) between two PEDOT:PSS films (25 mm long, 5 mm wide, and 14 μ m thick) as flexible electrodes (Fig. 11.4). Since the PEDOT:PSS film becomes soft and sticky by addition of xylitol and subsequent heating [17], a strongly adhered lamination is formed with the IL/PU gel. The resulting IL/PU/PEDOT:PSS composite actuator (25 mm long, 5 mm wide, and ca. 130 μ m thick) is suspended from a Kelvin clip by holding the upper part of 5 mm. It is seen from Fig. 11.4 that when a DC voltage is applied through the PEDOT:PSS electrodes with a function generator, the IL/PU/PEDOT:PSS composite actuator quickly bends toward anode. Figure 11.5 shows time profiles of bending displacement and current of the IL/PU/PEDOT:PSS composite (IL = 40 wt%) under various voltages. The application of an electric field brings about a rapid increase of the bending displacement within a few seconds and reaches an equilibrium. On the other hand, after removal of the electric field, the actuator immediately recovers to its original straight shape, demonstrating the reversible response to the electric field.

In general, there are two main mechanisms of the ionic EAP actuators: one is based on an electric-double-layer capacitor such as IPMC and bucky gel actuators [8, 10, 11], the other is based on a Faradic reaction such as conductive polymer actuators [5–7, 9]. Since the charging and discharging currents flow though the IL/PU/PEDOT:PSS composite in response to ON and OFF the electric field without the Faradic current, the mechanism of bending is mainly associated with the polarization caused by electrophoretic diffusion of IL in the PU matrices based on the electric-double-layer capacitor similarly to the IPMC actuators. Indeed, the PU elastomer without IL did not show any bending at the same voltages, which implies that the IL plays a predominant role in the ionic EAP actuating behavior of

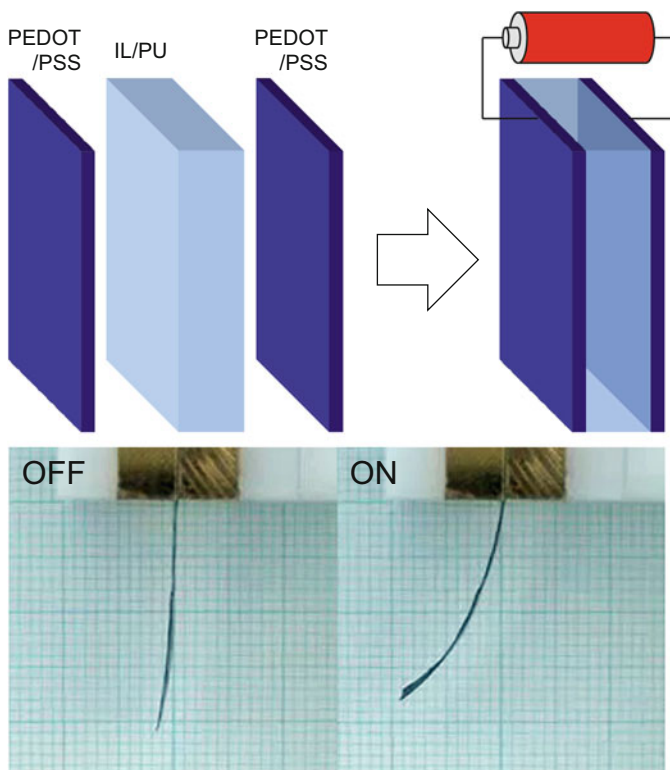


Fig. 11.4 Schematic illustration of IL/PU/PEDOT:PSS composite actuator (20 mm long, 5 mm wide, and 130 μm thick) fabricated by sandwiching IL/PU gel between two PEDOT:PSS films as electrodes and optical images of IL/PU/PEDOT:PSS composite actuator with and without electric field

the IL/PU/PEDOT:PSS composites. To clarify the mechanism in more detail, cyclic voltammograms (CV) of the IL/PU/PEDOT:PSS composite (IL = 40 wt%) were measured at different voltages and the results are shown in Fig. 11.6. It is found that the CV curves show the box-type characteristics, indicative of the electric double-layer capacitor. It is noted that the CV curve slightly shows a redox behavior at voltages higher than 1.5 V, indicating the electrochemical reaction of the PEDOT. Since the PSS anions are too big to move, reduction of the PEDOT may bring about an intercalation of $[\text{EMI}]^+$ to compensate their charges [20]. The results allow us to conclude that the mechanism of bending is mainly associated with the electric double-layer capacitor where the redox reaction of the PEDOT:PSS electrodes may simultaneously take place at higher voltages.

Figure 11.7 shows the voltage dependence of strain and maximum current of the IL/PU/PEDOT:PSS composite actuators with various IL contents. The strain (γ), representing the percentage of the length change at both sides to the initial length of the IL/PU gel, was calculated from the bending displacement (δ) using the thickness ($d = 100 \mu\text{m}$) and length ($L = 20 \text{ mm}$) of the gel as follows [21]:

Fig. 11.5 Time profiles of bending displacement and current of IL/PU/PEDOT:PSS composite actuator (20 mm long, 5 mm wide, and 130 μm thick) measured under various voltages (IL = 40 wt%)

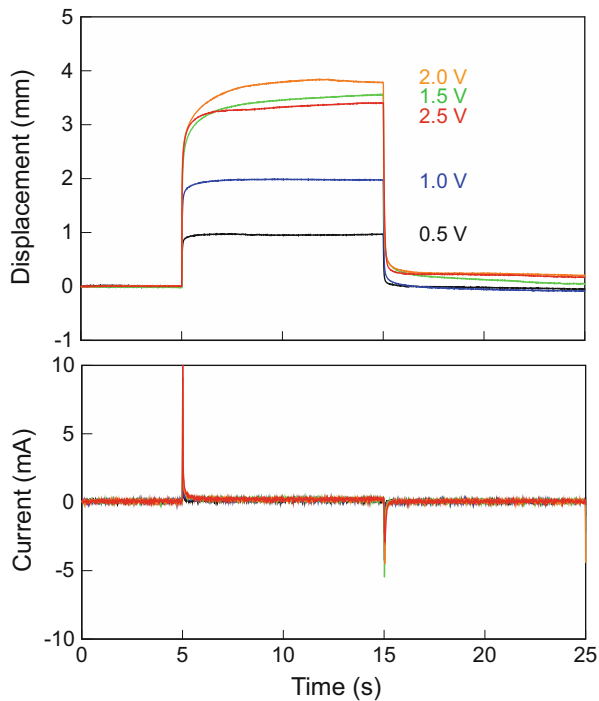


Fig. 11.6 Cyclic voltammograms of IL/PU/PEDOT:PSS composite actuator (20 mm long, 5 mm wide, and 130 μm thick) measured at various voltages (IL = 40 wt%)

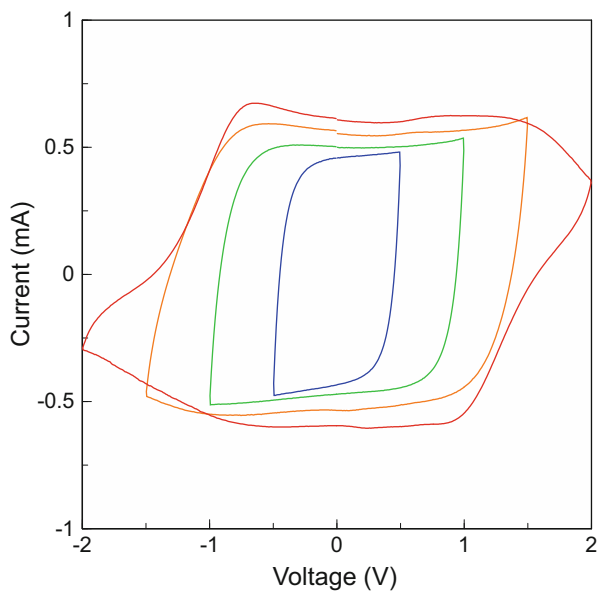
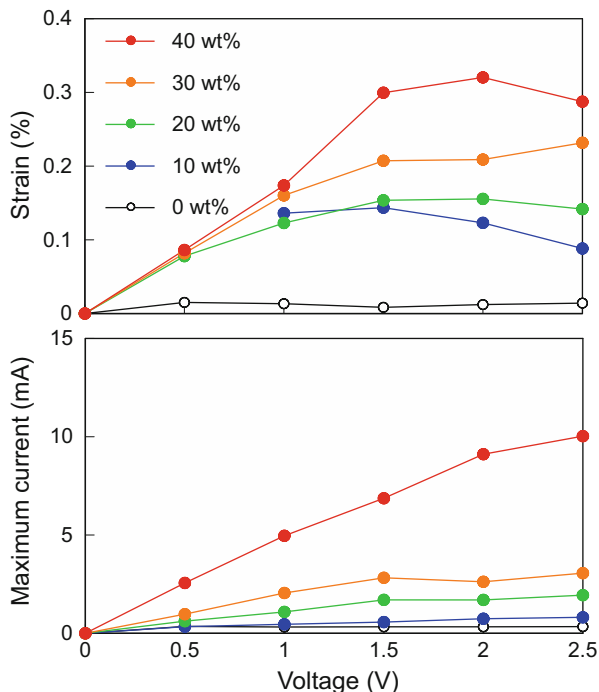


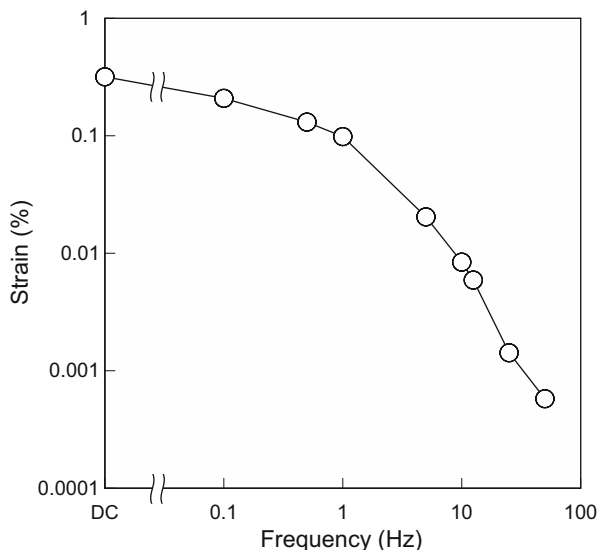
Fig. 11.7 Voltage dependence of strain and maximum current of IL/PU/PEDOT:PSS composite actuators (20 mm long, 5 mm wide, and 130 μm thick) with various IL contents



$$\gamma = 2d\delta \times 100 / (L^2 + \delta^2) \tag{11.2}$$

With increasing both applied voltage and IL content, the strain becomes larger and attains 0.32 % at 2 V and IL = 40 wt%, which is comparable to those of IL/carbon nanotube gel actuators [21]. A further increase of the voltage, however, results in a slight decrease of the strain though the maximum current is proportional to the applied voltage, which is probably due to the relaxation of the PU chains and/or electrochemical reactions of PEDOT:PSS electrodes. Since the EAP actuating behavior of the IL/PU/PEDOT:PSS composites is consistent with the ionic conductivity (σ) and electric-double-layer capacitance (C_{dl}) of the IL/PU gels (Fig. 11.3), the mechanism of bending can be explained in terms of the volume difference at both sides of the gel caused by polarization of IL with different ionic sizes and mobilities [19]. Figure 11.8 shows frequency dependence of strain for the IL/PU/PEDOT:PSS composite actuator (IL = 40 wt%) measured at 2 V. Although the strain becomes smaller as the frequency becomes higher, the composite actuator is still bending at frequencies higher than 10 Hz. This can be associated with the soft and flexible IL/PU gel as well as the PEDOT:PSS electrodes with high ionic and electric conductivities, respectively. The preliminary study on the lifetime of the IL/PU/PEDOT:PSS composite actuator showed that the actuator still worked after 70,000 cycles at 1 Hz, corresponding to about 20 h operation, indicating high stability and reproducibility of motion. Compared with other compliant electrodes

Fig. 11.8 Frequency dependence of strain for IL/PU/PEDOT:PSS composite actuator (20 mm long, 5 mm wide, and 130 μm thick, IL = 40 wt%) measured at 2 V



such as IL/carbon nanotube composite and chemically plated gold or platinum, the PEDOT:PSS is really cheaper and compliant electrodes can be fabricated by a facile wet-process such as spin-coating, bar-coating, dip-coating, and spray-coating. Therefore, the EAP actuators utilizing the soft and flexible PEDOT:PSS electrodes will open up a new field of low-cost printed actuators or paper actuators for the practical applications [22].

11.4 Conclusions

The uniform and transparent IL/PU gels composed of PU elastomer and [EMI] [TFSI] were synthesized and mechanical and electrical properties were investigated. It was found that with increasing the IL content from 0 to 40 wt%, the compression modulus of the IL/PU gels slightly decreased from 0.49 MPa to 0.44 MPa, while both ionic conductivity and electric-double-layer capacitance increased and the values respectively attained 8.8×10^{-5} S/cm and 277 pF/cm² at IL = 40 wt%. The IL/PU/PEDOT:PSS composites, fabricated by sandwiching the IL/PU gel between two PEDOT:PSS films as flexible electrodes, exhibited quick and intensive bending toward anode under the electric field, where the bending displacement attained 3.8 mm at IL = 40 wt% and 2 V, corresponding to the strain of 0.32 %. Moreover, the IL/PU/PEDOT:PSS composite actuator worked at frequencies higher than 10 Hz.

References

1. Osada Y, Okuzaki H, Hori H (1992) A polymer gel with electrically driven motility. *Nature* 355:242–244
2. Yoshida R, Uchida K, Kaneko Y, Sakai K, Kikuchi A, Sakurai Y, Okano T (1995) Comb-type grafted hydrogels with rapid deswelling response to temperature changes. *Nature* 374:240–242
3. Hirai T, Ogiwara T, Fujii K, Ueki T, Kinoshita K, Takasaki M (2009) Electrically active artificial pupil showing amoeba-like pseudopodial deformation. *Adv Mater* 21:2886–2888
4. Yoshida R, Takahashi T, Yamaguchi T, Ichijo H (1996) Self-oscillating gel. *J Am Chem Soc* 118:5134–5135
5. Smela E, Inganäs O, Lundström I (1995) Controlled folding of micrometer-sized structures. *Science* 268:1735–1738
6. Otero TF, Cortés MT (2003) Artificial muscles with tactile sensitivity. *Adv Mater* 15:279–282
7. Hara S, Zama T, Takashima W, Kaneto K (2005) Free-standing gel-like polypyrrole actuators doped with bis(perfluoroalkylsulfonyl)imide exhibiting extremely large strain. *Smart Mater Struct* 14:1501–1510
8. Asaka K, Oguro K, Nishimura Y, Mizuhara M, Takenaka H (1995) Bending of polyelectrolyte membrane-platinum composites by electric stimuli I. Response characteristics to various waveforms. *Polym J* 27:436–440
9. Lu W, Fadeev AG, Qi B, Smela E, Mattes BR, Ding J, Spinks GM, Mazurkiewicz J, Zhou D, Wallace GG, MacFarlane DR, Forsyth SA, Forsyth M (2002) Use of ionic liquid for π -conjugated polymer electrochemical devices. *Science* 297:983–987
10. Lee JW, Yoo YT (2009) Anion effects in imidazolium ionic liquids on the performance of IPMCs. *Sens Actuators B* 137:539–546
11. Fukushima T, Asaka K, Kosaka A, Aida T (2005) Fully plastic actuator through layer-by-layer casting with ionic-liquid-based bucky gel. *Angew Chem Int Ed* 44:2410–2413
12. Bar-Cohen Y (ed) (2001) Electroactive polymer (EAP) actuators as artificial muscles, reality, potential and challenges. SPIE, Bellingham
13. Pelrine R, Kornbluh R, Pei Q, Joseph J (2000) High-speed electrically actuated elastomers with strain greater than 100 %. *Science* 287:836–839
14. Inoue Y, Yan H, Okuzaki H (2011) Electromechanical properties and actuating behavior of ionic liquid/polydimethylsiloxane gels. *Kobunshi Ronbunshu* 68:122–126
15. Goujon LJ, Khaldi A, Maziz A, Plesse C, Nguyen GTM, Aubert PH, Vidal F, Chevrot C, Teyssié D (2011) Flexible solid polymer electrolytes based on nitrile butadiene rubber/poly(ethylene oxide) interpenetrating polymer networks containing either LiTFSI or EMITFSI. *Macromol* 44:9683–9691
16. Festin N, Maziz A, Plesse C, Teyssié D, Chevrot C, Vidal F (2013) Robust solid polymer electrolyte for conducting IPN actuators. *Smart Mater Struct* 22:104005
17. Li Y, Masuda Y, Iriyama Y, Okuzaki H (2012) Stretchable and highly conductive polymer films. *Trans Mater Res Soc Jpn* 37:303–306
18. Randles JEB (1947) Kinetics of rapid electrode reactions. *Discuss Faraday Soc* 1:11–19
19. Imaizumi S, Kato Y, Kokubo H, Watanabe M (2012) Driving mechanism of ionic polymer actuators having electric double layer capacitor structures. *J Phys Chem B* 116:5080–5089
20. Otero TF, Martinez JG, Hosaka K, Okuzaki H (2011) Electrochemical characterization of PEDOT:PSS-Sorbitol electrodes. Sorbitol changes cation to anion interchange during reactions. *J Electroanal Chem* 657:23–27
21. Terasawa N, Mukai K, Asaka K (2012) Improved performance of an activated multi-walled carbon nanotube polymer actuator, compared with a single-walled carbon nanotube polymer actuator. *Sens Actuators B* 173:66–71
22. Okuzaki H, Takagi S, Hishiki F, Tanigawa R (2014) Ionic liquid/polyurethane/PEDOT:PSS composites for electro-active polymer actuators. *Sens Actuators B* 194:59–63

Chapter 12

Dielectric Gels

Toshihiro Hirai

Abstract Dielectric gels of various types are recently found electrically active, and can be used for actuators. Polymer gels swollen with large amount of dielectric solvent deforms by applying dc voltage. The deformation is based on the solvent flow (or ion drag) through the polymer network. They shows contractile, bending, and crawling deformation. Advantages are very swift deformation in air, small electric current, and large strain up to over 10 % depending on the degree of crosslinks among the polymer chain. Disadvantages are low durability because of the solvent bleed-out, and relatively high voltage.

Dielectric elastomers (sometime gel-like) can be good candidate when the polymer chains are flexible enough and sensitive enough to the electric field, although flexible polymer chains can not take the role of solvents. Similarity to the gel is that the electrically induced asymmetric charge distribution causes the bending deformation. Advantages of this system are low electric current, relatively swift deformation at high voltage, and good durability. Disadvantages of this system are requirement of high voltage, small strain, and basically very limited stress. For attaining large strain, very high voltages are necessary for the actuation such as over 10 kV/mm. We show the cases of polyurethane and poly(methyl methacrylate-*b*-*n*-butyl acrylate-*b*-methyl methacrylate) triblock copolymer.

Plasticized polymer system provides another possibility, and we think at this moment the best candidate from the viewpoint of easy processing and variable possibilities. Polymers with large content of plasticizer (we call this category as “polymer gel” in stead of plasticized polymer) shows peculiar deformation such as amoeba-like creep deformation. In some cases, we investigated the gels show high power, high toughness, very low current, and variable application possibilities. The characteristics comes out from the very large dielectric constant from the cooperative interaction between the polymer and plasticizer both of which have very low dielectric constant. By applying the characteristic properties, not only the electro-mechanical function but also the electro-optical functions and mechano-electric functions are found.

T. Hirai (✉)

Fiber Innovation Incubator, Faculty of Textile Science and Technology, Shinshu University,
3-15-1 Tokida, Ueda-shi 386-8567, Japan
e-mail: tohirai@shinshu-u.ac.jp

Through these investigations, we could conclude the dielectric gels have great possibilities as novel type of electro-active materials.

Keywords Actuator • Artificial muscle • Dielectric gel • Electro-mechanical deformation • Electro-optical function • Impact sensor • Light deflection

12.1 General Background

Polymer gel actuator was proposed long time ago using hydrogel [1]. After the discovery of discrete volume change as a phase transition, the researches on the gel heated-up since the variable phenomena have been found and their potential has been recognized [2, 3]. On the electrical actuation of polymer gels have also been investigated from the viewpoint of highly efficient controllable actuator [4, 5]. Most of the researches on these gel actuators were carried out on hydrogels. In the hydrogel actuator, bleed-out of water is usually inevitable, and the practical actuation in air is difficult as it is. In the case of polyelectrolyte gel actuators, they can be actuated at low voltage such as below 10 V in order to avoid the electrochemical reaction on the electrodes.

On the other hand, dielectric gel had been considered difficult to be actuated by controlling electric field. However poly(vinyl alcohol) (PVA) gel swollen with dielectric solvent was actuated very efficiently in air without the presence of water [6]. The mechanism was revealed as solvent drag (or “ion drag”) induced deformation [7–14]. The motion of the gel was far much faster than that of conventional methods for the gels. Disadvantage of this method is durability in terms of physical strength and bleeding of the solvent.

Elastomer with flexible polymer structure seems to be the best choice for electrically active actuator. We found amorphous polyurethane elastomer (PU) deforms easily by applying dc electric field [15, 16]. The PU as electrically active materials was investigated by controlling soft segment chain length and chemical structure [17]. It turned out that the asymmetrically accumulated charge caused bending strain of the polyurethane films, and the direction can be controlled by modifying the chemical structure of the soft segment [18]. However, the strain of the dielectric elastomers can not be increased without applying very high voltage like 50 kV/mm. There are intensive works on the dielectric elastomer actuators and various successful applications have been proposed [19, 20].

Slightly different from solvent swollen polymer gels, we mentioned plasticized polymers, typically that of poly(vinyl chloride) (PVC). In the case of plasticized PVC (PVC gel), bleed-out of plasticizer is very small and almost negligible compared to the highly swollen polymer gels. Durability and stability is far much better from the viewpoint of practical application. The PVC gel showed huge electrically induced elastic-deformation, amoeba-like pseudopodial creep deformation [21–23]. The application has also been investigated as an optical device [24].

The mechanism of the amoeba-like deformation has been explained as an asymmetric charge distribution but not accompanied the solvent drag [23, 25, 26]. Even if the case, the effect is negligibly small. It has been suggested recently that the dielectric properties of the PVC gels are peculiar and depend on the chemical structure of plasticizer [27–30]. They implied the so-called “colossal” dielectric constant.

Plasticizers does not bleed out of the gel body, but the deformation accompanies polymer chain rearrangement together with that of plasticizer, and realized huge strain in the vicinity of near the anode surface [31–33].

New function expected for future possibility of dielectric gels will also be mentioned in this chapter. The colossal dielectric constant of the plasticized gels expands the application [27]. For instance, electro-optical function or the electrical control of refractive index can be possible. We also revealed the proportionality can be varied by changing the gels [34]. The effect observed on PVC gel was much larger than that of nitrobenzene as a control. PVA gel could also show very efficient electro-optical function.

Electrically induced colossal dielectric nature of these materials suggests that the gels can be used as mechano-electric sensor with high sensitivity. The experiment revealed the validity of the idea, and the gels turned out to be an efficient touch sensor or mechano-electrical energy conversion device [35].

Electro-mechanical oscillation was demonstrated on polyethylene terephthalate (PET) film. In the case of PVC gel, PVC and plasticizer, lead to a interesting oscillatory deformation [36]. They are similar phenomena but the mechanism is different each other.

Through these researches, it turned out that not only the dielectric gels but also almost every dielectric polymers have great possibilities as excellent electro-active materials.

12.2 Electroactive Dielectric Actuators

12.2.1 *Gels Swollen with Dielectric Solvent*

12.2.1.1 Behavior of Dielectric Solvent Under dc Electric Field

When we look back the history of electrical activation of dielectric materials, even an argon gas could be activated by applying an dc electric field [37]. Dielectric solvent has been considered inactive to the electric field in common sense. However, they are revealed to be active in 1960s. First recognized as electrohydrodynamic instability and pressure generation by ion drag [14, 38]. The idea was, then, applied to ion drag pump [39, 40]. Some challenges had been carried out for practical applications [41–44]. (Fig. 12.1 Ion drag)

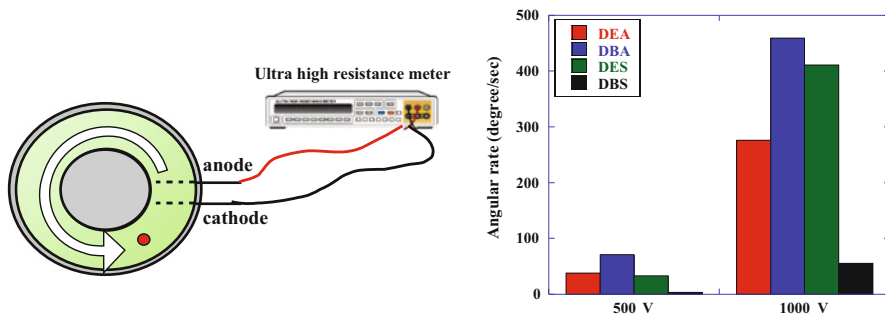


Fig. 12.1 Electrically induced flow of a dielectric organic solvent. Solvent (DMSO) flow was induced from cathode to anode. Electrode (comb) distance is 2 mm. Applied voltage over 100 V is enough for inducing an “ion drag” flow. Flow rate increased with the voltage

12.2.1.2 Highly Swollen Chemically Crosslinked Dielectric Gel

So it is not difficult to expect electrical actuation of the dielectric gels from the fore mentioned researches. However we have no idea of those phenomena when we came across the electrical actuation of an dielectric gel at the first time.

In the research of highly swollen PVA hydrogel, however, we had vast amount experience and knew already the solvent flow or water diffusion in the gels. But if the diffusion causes the bleed-out of solvent, it is not desirable as an actuator. Fortunately, the solvent leak is depressed and some asymmetric pressure distribution was induced in the dielectric PVA-dimethyl sulfoxide (DMSO) gel, resulting in the very efficient electrical actuation in air [6, 45]. Contractile deformation depended on the degree of chemical-crosslinks induced in the gel network. We demonstrated over 10 % of contractile strain could be induced. The voltage required for the contractile deformation was 1 kV for the gel of thickness of 4 mm [9]. Careful observation, however, revealed the gel deformed asymmetrically on the electrodes. The gel tend to swell on cathode and shrink on anode. When the gold sheet was employed as flexible electrodes, although they are fragile, we could have observed the gel bent very swiftly in air [13]. It took 40 ms to attain 90° of bending on the gel of 2 mm thickness and 2 × 1 cm (length × width) [46]. By applying the ion drag theory, the bending deformation could be estimated in the low bending deformation range. At higher bending deformation or at high voltage region the fitting became poor. The phenomena suggested the role of electro-rheological process became important. The other characteristic deformation is “crawling” on the electrode array. The gel could be expanded on the anode by accumulating the charge-tapped solvent ejected from cathode side, on which the gel became thinner, thus, resulting in the worm-like crawling deformation. This type deformation can only be realized at very low degree of chemical-crosslink. For instance in the case of PVA-DMSO gel, the solvent content is over 98 % by weight. Therefore, this type of the gel is difficult for practical application as it is in spite of some advantages (Fig. 12.2 Gel bending, crawling, contractile).

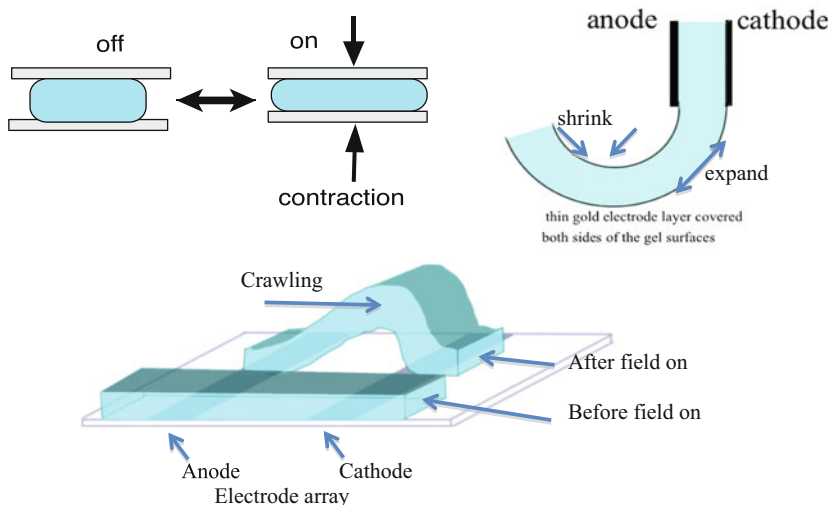


Fig. 12.2 Electrically induced PVA-DMSO gel deformation. (1) Contractile deformation was applied for the fluttering motion of the plastic wing. Strain was over 10 % at the voltage of 250 V/mm, and the rate is ca. 10 Hz. (2) Bending deformation of PVA-DMSO gel. Thickness of the gel was 2 mm. Bending angle increased with voltage. Curves were estimated theoretically. (3) Crawling deformation on a electrode array. Gel rose up on cathode and the gel on anode slide to the cathode

12.2.2 Possibility of Elastomers as Electroactive Dielectric Actuator

From the studies on highly swollen polymer gels, it is clear that solvent leak or bleed out have to be overcome for the practical use in air. To avoid the presence of solvent, the best way is to employ the soft materials without solvent. From this viewpoint, polyurethane (PU) was investigated, since many controlling factors contribute to the physical properties of the elastomer [15]. Detailed analysis on the relationship between the chemical structure and electro-mechanical function revealed several interesting features of PU [16, 17, 47–49]. However under the voltage range of 10 kV/mm, PU coated with gold nano-layer showed swift bending motion, but could not attain large strain and high durability, neither. Further detailed and systematic development is necessary for the practical application. We could anyway have shown the bending deformation can be controlled by varying chemical structures, such as crosslinking density, functional groups (hard segment and soft segment), etc. The bending direction was turned to be controllable by the space charge distribution. It is well known that the sheets or films of the elastomers have not necessarily homogeneous structures but often have inhomogeneous structure [50], and this makes the controlling factor complicated.

We investigated another type of elastomer from tri-block copolymer. Tri-block copolymer of poly(methyl methacrylate (MMA)-*b*-*n*-butylacrylate (nBA)-*b*-MMA)

was investigated [51]. The concept of the actuator of this material is nano-scale phase separation of each component in the polymer film. If the stiff segment of MMA forms continuous phase the sheet will be electrically inactive because of the stiffness of the sheet. But it will be soft and can be electrically active, when the nBA forms percolated continuous phase and PMMA forms and takes the role of isolated physical-crosslinking point. For attaining the phase separation, we investigated the effect of casting solvent and successfully the continuous phase control was accomplished [52]. However to attain the large strain, the control of segment chain length or mixing small amount of diblock copolymer will be effective. This method will provide high possibility for the efficient control of motility in future.

12.2.3 *Plasticized Polymer (PVC Gel)*

As pointed out above, highly swollen gel and elastomers from conventional dielectric polymers have some limitations. We changed viewpoint to plasticized polymers. Poly(vinyl chloride) is most popular among the plasticized polymers, and has long experience with wide range of plasticizers, although it has some unpopularity from the viewpoint of chloride containing material.

As a candidate of dielectric material with high dielectric constant, plasticized PVC is the lowest ranking. When we started the electrostriction measurement, actually no striction was detected in d3 direction as expected. But I observed a very slight deformation on the vicinity of anode surface through optical micrograph. That was the amoeba-like pseudopodial creep deformation or electrotactic creep deformation on the anode (Fig. 12.3 Creep).

The creep deformation was first applied for folding type bending motion by Zulhash [21]. It was very efficient, but unusual way of bending, that is, the creep onto the other surface of anode tip leads the gel bend to the direction. The layer crept out on to the anode was very thin but pull the whole gel body bend in the direction finally. When the electric field is off, it swiftly restores original shape. The gel contains anomalously large amount of plasticizer. Content of plasticizer reaches up to 80 % by weight, so we call the plasticized PVC as “PVC gel” (Fig. 12.4 Bending).

The creep deformation of the PVC gel showed fairly large power such as tacking or attractive force to the anode. We have been investigated how to utilize the unique deformation for practical devices. One way is micro-soft gripper that can hold fragile tiny parts for electronic device as an example. The other way is to utilize the creep deformation of the transparent PVC gel directly for instance as a focus controllable lens [24, 53] (Fig. 12.5 Lens, gripper, contractile).

The mechanism of the PVC gel deformation has been clarified to be originated asymmetric charge distribution on anode, that is, negative charge accumulation on the anode plays important role for the deformation [27]. The charge accumulation was suggested to be attributable to the colossal dielectric constant that is induced by applying dc electric field at higher concentration of the plasticizer in the gel. The

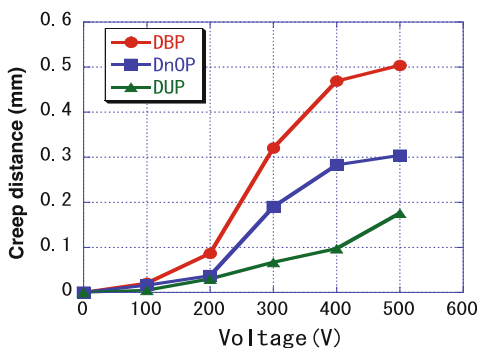
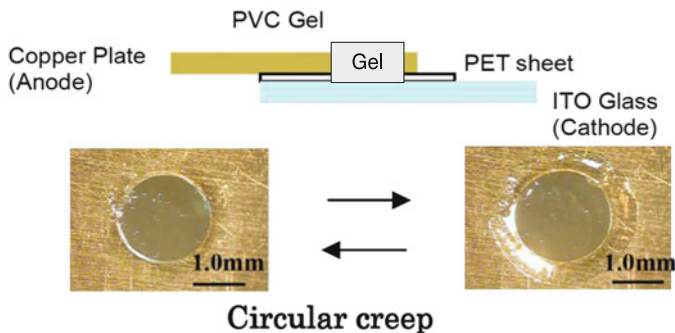
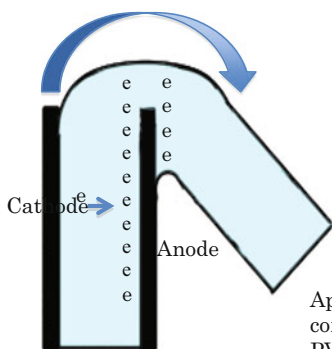


Fig. 12.3 Amoeba-like pseudopodial creep deformation of PVC gel. Creep deformation is non-linear to the applied electric field. Deformation depends very much to the plasticizer



Sample name	Angular velocity / degree s ⁻¹
PVC-DEA gel	522
PVC-DBA gel	1162
PVC-DES gel	899
PVC-DBS gel	153

Applied voltage is 2.5 kV/mm, 100 degree bending completed in 100 ms on PVC-DBA gel in air. PVC:DBA=1:8 by weight, thickness=0.25 mm

Fig. 12.4 Bending deformation observed on PVC gel. The gel bends on the tip of anode and totally different from ordinal bending deformation, that is, it is a creep-induced bending. Contractile deformation of Maxwell type is very small and almost negligible. Bending speed is very high

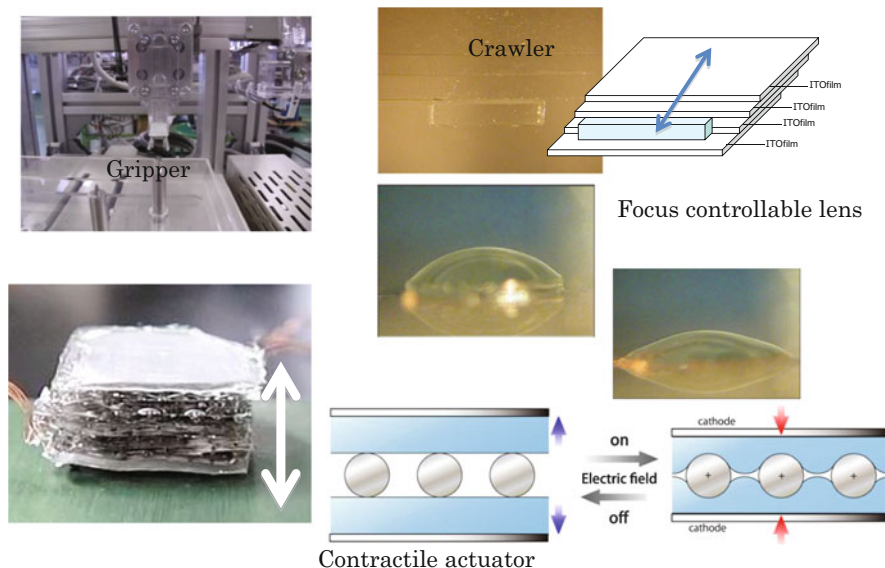


Fig. 12.5 Application of PVC gel for (1) lens, (2) gripper, and (3) contractile actuators. Gripper is for the factory machine. Crawler is for transporter. Lens is for optical device

dielectric constant of the PVC gels reaches from 10^3 to 10^4 at 1 Hz around, although those of PVC and plasticizers are usually around 5–10 at most. The phenomena are often occurs for adipate plasticizers but not remarkable for phthalate plasticizers [54], suggesting that the colossal dielectric constant was induced by cooperative phenomena between the polymer and the plasticizer (Fig. 12.6 Ali).

12.2.4 Solid Crystalline Polymer Film

Poly(ethylene terephthalate) (PET) or nylons are most commonly used conventional polymers, and have been known to be inactive to the electric field, and this is true from the viewpoint of high modulus for the deformation and small dielectric properties. But electrostatic behavior of these polymers can be utilized for the actuators, for instance, as oscillators [36]. PVC gel can also be applied for oscillator, and the mechanism is almost the same as that of PET film, although the tacking to anode or creep deformation on to the anode is different from that of PET [36]. The oscillation is an enforced vibration by tacking force or attractive force to the anode only, and repulsive force from cathode does not take any role (Fig. 12.7 PET, PVC gel oscillation).

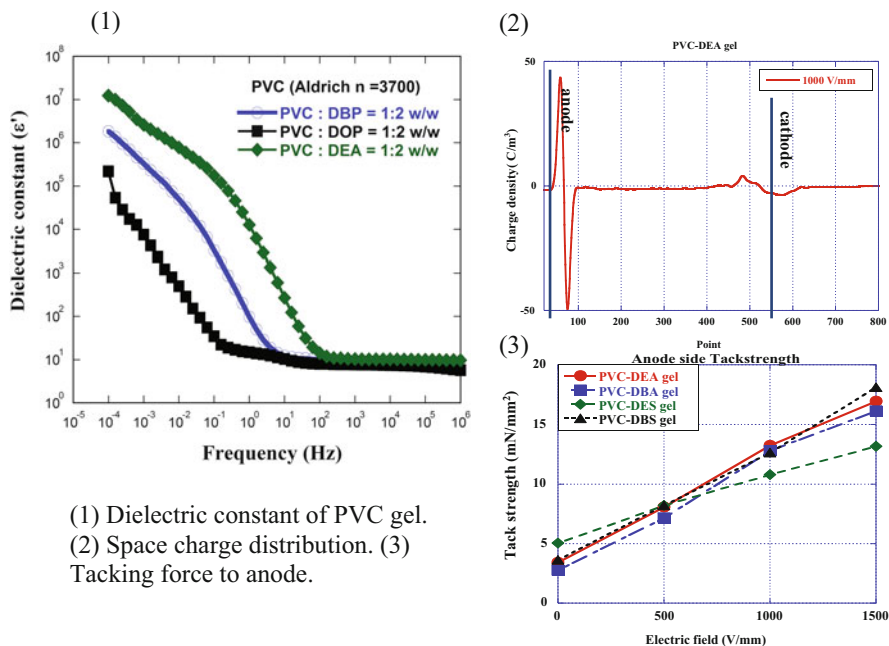


Fig. 12.6 Dielectric characteristics of PVC gel plasticized with dibutyl adipate (DBA). (1) Permittivity dependence on the frequency, (2) Space charge distribution, (3) Tacking force to anode

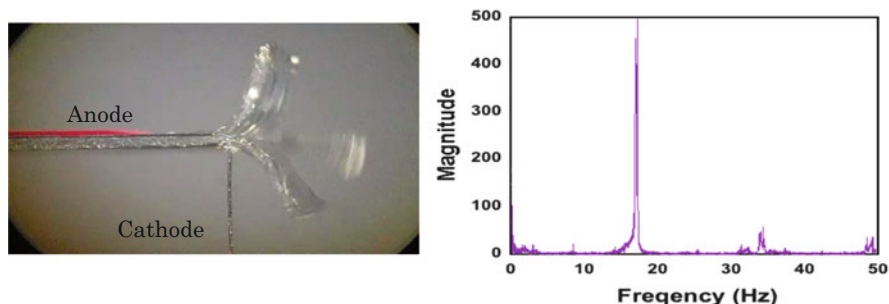


Fig. 12.7 Oscillation of PVC gel. PET can also be a good oscillator, and can be used as micro-fan. Electrode array is different for PVC gel from the case of PET film

12.3 Electro-Optical Functions

On the electro-optical function, the gel, in appearance, implied huge Kerr effect. PVA-NMP gel, on the other hand, showed very large Pockels effect. Once we accept the colossal dielectric constant emerged through the interaction between polymer and plasticizer, the application of the gel expands to various fields. We are investigating on the electro-optical function and mechano-electric function on the

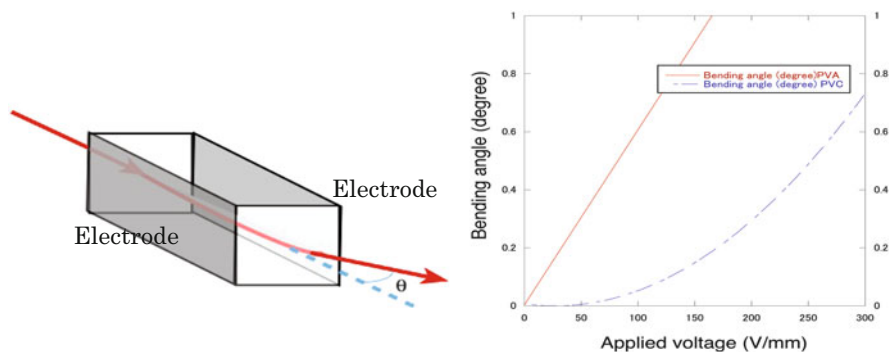


Fig. 12.8 Electro-optical function of dielectric gels (PVC gel and PVA gel)

various polymer systems. On PVC gel, light could be bent by applying a dc field with proportionality to the square of the field. The effect observed was much larger than that of nitrobenzene as a control. PVA gel with *N*-methylpyrrolidone showed proportional dependency to the applied dc electric field [34]. The electrical phenomena did not accompany any serious hysteresis, and on-and-off control was possible. The electro-optical effect is also found to depend on the plasticizer and its concentration in remarkable manner [55] (Fig. 12.8 EO effect on PVC gel and PVA).

As the control, PVC, PVA, plasticizers, solvents (DMSO, NMP) themselves did not show any electro-optical phenomena such as observed in the gels.

The mechanism of these functions are originated from the colossal dielectric properties of the gels and cooperative interaction between PVC and coexisting low molecular weight compounds (plasticizers and/or solvent), although the further details are under investigation. The cooperative phenomena on the dielectric materials have been attracting strong interests for years [56, 57].

12.4 Mechano-Electric Functions

The other function observed on the PVC gels was as an impact sensor [35]. The gels with thickness of submillimeter could generate voltage of ca. 1.5 V/cm² with the impact of 10 g of steel ball falling from 10 cm height. These functions depend on the combination of plasticizers or solvent coexisting in the materials.

PVC gel can be considered to be homogeneous, although the homogeneity depends seriously on the preparation conditions. The gels did not show any electrostrictive deformation in d3 direction, suggesting the mechanism for the crystalline materials, which has large poling effect, can not be applied, and actually very small voltage could be attained by pressing the gel. The mechanism of the piezo-function of the “homogeneous” non-poled soft polymer material has been considered as the following, that is, PVC rich gel can negatively charge on the

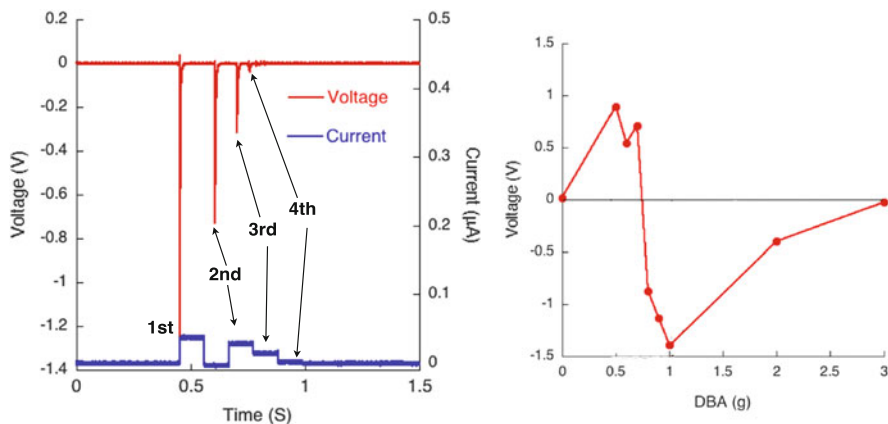


Fig. 12.9 Dielectric gel as an impact sensor. PVC gel implied voltage generation that could be controlled by the content of plasticizer

impact surface because of the friction between polymer phase and plasticizer phase, and in the plasticizer rich gel can bear positive charge on the vicinity of electrode surface. The experimental results can be explained by the triboelectric series [35]. Further detail will be clarified and the method can be applied practically for the sensor and/or energy harvesting systems (Fig. 12.9 Tanaka).

12.5 Concluding Remarks

The dielectric polymers or polymer composites of conventional use can be possible actuators and sensors as have been recognized just recently. Scientific understanding is still underway as this field is interdisciplinary area. I hope the application of conventional polymer in this way might cause very reasonable and big innovation in near future. For example, the nano- and micro-fiber weaving, which has been considered difficult to manipulate such a thin fiber because of the low tenacity, by using electrical motility of the fibers [58, 59]. These technology might be applied for totally new devices of various functions.

We can provide a guideline as described above for the electroactive dielectric gel, although the mechanism is still remains some ambiguity. The parameters that controls the phenomena became clearer during this decade [60]. I am very convincing the future of the soft actuator from conventional polymers, as the control of nano-level control or manipulation of the structure is developing very rapidly. This field will make burst into “nano-tech controlled molecularly assembled devices” for the society of “ambient technology” [61].

References

1. Katchalsky A (1949) *Experientia* 5:319
2. Osada Y (1987) Conversion of chemical into mechanical energy by synthetic polymers (Chemomechanical System). In: *Advances in polymer science*, vol 82, Springer, Berlin
3. Tanaka T, Ishiwata S, Ishimoto C (1977) Critical behavior of density fluctuations in gels. *Phys Rev Lett* 38(14):771–774
4. Osada Y, Okuzaki H, Hori H (1992) A polymer gel with electrically driven motility. *Nature* 355:242–244
5. Tanaka T et al (1982) Collapse of gels in an electric field. *Science* 218:467–469
6. Hirai T et al (1991) Fluttering wings – first step for flying up-above into the sky? Preprints of second symposium on polymer gels, December 10–11, Tsukuba, Japan, p 129
7. Hirai T et al (1991) Actuation of poly(vinyl alcohol) gel by applying electric field. Preprints of second symposium on polymer gels, pp 67–68
8. Hirai T et al (1991) Actuation of PVA gel by electric field. *Polymer Prep* 40(7):2116–2118
9. Hirai T et al (1993) Actuation of poly(vinyl alcohol) gel by electric field. *J Intell Mater Syst Struc* 4:277–279
10. Hirai M, Hirai T, Ueki T (1994) Growing process of scattering density fluctuation of a medium distance in the hydrogel of poly(vinyl alcohol) under stretching. *Macromolecules* 27(4):1003–1006
11. Hirai T et al (1994) Electrostriction of highly swollen polymer gel: possible application for gel actuator. *J Appl Polym Sci* 53(1):79–84
12. Hirai M et al (1995) Electrically induced reversible structural change of a highly swollen polymer gel network. *J Chem Soc Faraday Trans* 91:473–477
13. Hirai T et al (2000) Electroactive non-ionic gel and its application. In: Bar-Cohen Y (ed) *Proceedings of the SPIE, smart structures and materials 2000: electroactive polymer actuators and devices (EAPAD)*, vol 3987, pp 281–290
14. Stuetzer OM (1959) Ion drag pressure generation. *J Appl Phys* 30(7):984–994
15. Hirai T et al (1996) Polyurethane elastomer actuator. *Angew Makromol Chem* 240:221–229
16. Watanabe M et al (1997) Bending deformation of monolayer polyurethane film induced by an electric field. *Chem Lett* 1997:773–774
17. Watanabe M et al (1999) Effects of polymer networks on the bending electrostriction of polyurethanes. In: Elgsaeter A, Stokke BT (eds) *The Wiley polymer networks group review*, vol 2. Wiley
18. Watanabe M, Hirai T (2004) Close relationship between bending-electrostrictive response and space charge distribution in a polyurethane film. *J Appl Phys* 43:1446–1448
19. Kornbluh R et al (2000) Ultra-high strain response of elastomeric polymer dielectrics. In: *Materials research society symposium proceedings. Electroactive Polymers (EAP)*, vol 600, pp 119–130
20. Pelrine R et al (2001) Applications of dielectric elastomer actuators. In: *Proceedings of the SPIE international society for optical engineering. Electroactive polymer actuators and devices*, vol 4329, pp 335–349
21. Uddin MZ et al (2001) Electrically induced creeping and bending deformation of plasticized poly(vinyl chloride). *Chem Lett* 2001:360–361
22. Hirai T et al (2003) Electroactive artificial muscle: nonionic polymer gels and elastomers. In: Mohan S, Dattaguru B, Gopalakrishnan S (eds) *Proceedings of the SPIE, smart materials, structures, and systems*, vol 5062, pp 378–388
23. Hirai T et al (2003) Quick and large electrostrictive deformation of non-ionic soft polymer materials. In: Bar-Cohen Y (eds) *Proceedings of the SPIE, smart structures and materials 2003: electroactive polymer actuators and devices (EAPAD)*, vol 5051, pp 198–206
24. Hirai T, Ogiwara T, Fujii K, Ueki T, Kinoshita K, Takasaki M (2009) Electrically active artificial pupil showing amoeba-like pseudopodial deformation. *Adv Mater* 21(28):2886–2888

25. Hirai T, Uddin MZ, Zheng J, Watanabe M, Shirai H (2002) Electroactive artificial muscle: non-ionic polymer gels and elastomers. In: Proceedings of international conference on smart materials, structures & systems. Microart, Bangalore
26. Uddin MZ et al (2002) Creeping and novel huge bending of plasticized PVC. *J Robot Mechatr* 14(2):118–123
27. Ali M et al (2011) Influence of plasticizer content on the transition of electromechanical behavior of PVC gel actuator. *Langmuir* 27(12):7902–7908
28. Ali M, Hirai T (2011) Characteristics of the creep-induced bending deformation of a PVC gel actuator by an electric field. *J Mater Sci* 46(24):7681–7688
29. Ali M, Hirai T (2012) Effect of plasticizer on the electric-field-induced adhesion of dielectric PVC gels. *J Mater Sci* 47(8):3777–3783
30. Ali M, Hirai T (2012) Relationship between electrode polarization and electrical actuation of dielectric PVC gel actuators. *Soft Mater* 8:3694–3699
31. Xia H, Ueki T, Hirai T (2011) Direct observation by laser scanning confocal microscopy of microstructure and phase migration of PVC gels in an applied electric field. *Langmuir* 27(3):1207–1211
32. Xia H, Takasaki M, Hirai T (2010) Actuation mechanism of plasticized PVC by electric field. *Sens Actuators A Phys* 157:307–312
33. Xia H, Hirai T (2010) Electric-field-induced local layer structure in plasticized PVC actuator. *J Phys Chem B* 114(33):10756–10762
34. Satou H, Hirai T (2013) Electromechanical and electro-optical functions of plasticized PVC with colossal dielectric constant. In: Proceedings of SPIE, electroactive polymer actuators and devices (EAPAD), vol 8687, p 868728-1-7
35. Tanaka Y, Hirai T (2013) Mechanoelectric function of plasticized poly(vinyl chloride) for impact sensor and energy harvesting. In: 62nd SPSJ symposium on macromolecules, polymer preprints, Japan, vol 3635. The Society of Polymer Science, Kanazawa University, Kanazawa, Japan. p 2ESB1
36. Tsurumi D, Hirai T (2013) Electrically induced oscillatory motion of dielectric soft polymer materials. In: 62nd SPSJ symposium on macromolecules, polymer preprints, Japan, vol 3637. The Society of Polymer Science, Japan. p 2ESB12
37. Chattok AP (1899) On the velocity and mass of the ions in the electric wind in air (fifth series). *Phil Mag* 48(294):401–420
38. Stuetzer OM (1959) Instability of certain electrohydrodynamic systems. *Phys Fluids* 2(6):642–648
39. Pickard WF (1963) Ion drag pumping. II. Experiment. *J Appl Phys* 34(2):251–258
40. Pickard WF (1963) Ion drag pumping. I. Theory. *J Appl Phys* 34(2):246–250
41. Jorgenson GV, Will E (1962) Improved ion drag pump. *Rev Sci Instrum* 33(1):55–56
42. Fujita H (1988) Micro-actuator and micromechanical parts. *IEEJ Trans* 108(3):214–217
43. Tsuchida N, Satou H, Ueda M (1983) The mobilities of various impurity ions in silicone oil. *IEEE Trans Jpn* 103(1):47–52
44. Tsuchida N, J O, Murata R, Yamada Y, Imai K (1993) Studies on DC micro motor employing EHD stream by ion drag. *IEEE Trans Jpn* 113(12):1442–1448
45. Hirai T (1991) High speed responding polymer gel actuator. Japan patent has been requested
46. Hirai T, Hirai M, Hayashi S, Ueki T (1992) Study of the conformational change of amylose induced by complexation with iodine using synchrotron X-ray small-angle scattering. *Macromolecules* 25(24):6699–6702
47. Watanabe M et al (2003) A pumping technique using electrohydrodynamic flow inside a gel. *IEEE Trans Dielectr Electr Insul* 10(1):181–185
48. Watanabe M et al (1999) Effects of polymer networks on the bending electrostriction of polyurethanes. In: Wiley polymer networks group review series, vol 2 (Synthetic versus Biological Networks), pp 213–221
49. Watanabe M et al (2000) Hysteresis in bending electrostriction of polyurethane films. *J Appl Polym Sci* 79(6):1121–1126

50. Xiu Y et al (1993) Morphology-property relationship of segmented polyurethaneurea: influences of soft-segment structure and molecular weight. *J Appl Polym Sci* 48:867–869
51. Jang Y, Hirai T (2011) A control method for triblock copolymer actuators by nano-lamellar pattern. *Soft Mater* 7(22):10818–10823
52. Jang Y et al (2011) Performance of PMMA-PnBA-PMMA dielectric film actuator with controllable phase morphology. *Sens Actuators A Phys* 168:300–306
53. Yasuda A, Kinoshita T, Hirai T (2011) Focusing device and imaging device. Seiko Precision Inc., Chiba, p 10
54. Hirai T et al (2012) Plasticized poly(vinyl chloride) gel as super paraelectric actuator. In: IUMRS-international conference on electronic materials (IUMRS-ICEM 2012), 23–28 September, 2012. The Materials Research Society of Japan (MRS-J), Pacifico Yokohama, Yokohama, Japan
55. Sato H, Gotoh Y, Hirai T (2013) The electro-optic effect of PVA gel and PVC gel. In: 62nd SPSJ symposium on macromolecules, polymer preprints, Japan, vol 3639. The Society of Polymer Science, Kanazawa University, Kanazawa, Japan, p 2ESB13
56. Haken H, Wagner M (1973) Cooperative phenomena. Springer, Berlin
57. Zwicky F (1933) On cooperative phenomena. *Phys Rev* 43(4):270–278
58. Xia H, Hashimoto Y, Hirai T (2012) Electric-field-induced actuation of poly(vinyl alcohol) microfibers. *J Phys Chem C* 116:23236–23242
59. Xia H, Hirai T (2013) New shedding motion, based on electroactuation force, for micro- and nanoweaving. *Adv Eng Mater Commun* 2013:1–4
60. Hirai T, Zheng J, Watanabe M, Shirai H (2001) Electrically active polymer materials: application of non-ionic polymer gel and elastomers for artificial muscles. In: Tao XM (ed) *Smart fibres, fabrics and clothing: fundamentals and applications*. CRC, Boca Raton
61. Sakurai T (2012) Smart community and ambient electronics. *Panasonic Tech J* 58(1):4–7

Chapter 13

Dielectric Elastomers

Seiki Chiba

Abstract Electroactive polymer transducers have many features that are desirable for various devices. An especially attractive type of electroactive polymer is dielectric elastomer.

Dielectric elastomer, based on the field-induced deformation of elastomeric polymers with compliant electrodes, can produce a large strain response, a fast response time and high electromechanical efficiency. This unique performance, combined with other factors such as low cost, suggests many potential applications, a wide range of which are under investigation. Applications that effectively exploit the properties of dielectric elastomers include artificial muscle actuators for robots; low-cost, light-weight linear actuators; solid-state optical devices; diaphragm actuators for pumps and smart skins; acoustic actuators; and rotary motors. Dielectric elastomers may also be used to generate electrical power from mechanical deformation.

Keywords Actuators • Artificial muscles • Dielectric elastomers • Direct drive • EAP • Electroactive polymers • Generators • Renewable energy • Sensors

13.1 Introduction

Electro active polymers (EAPs) are used for actuators that can electrically control their motions to resemble those of actual muscles. Thus, they are called artificial muscles. In addition, since EAPs are often made of flexible materials, they have also come to be called “soft actuators” in recent years. There are many types of EAPs such as dielectric elastomers [1, 2], ionic polymer-metal composites [3], electroconductive Polymers [4], and ion polymer gels [5]. Figure 13.1 shows typical EAPs.

EAP can be generally classified into two categories: electrochemical polymers and field-activated polymers [6]. Electrochemical polymers use electrically driven mass transport of ions or electrically charged species to effect a change in the shape (or vice versa). Field-activated polymers use an electric field to effect a shape change by acting directly on charges within the polymer (or vice versa). Each type of EAP has advantages and disadvantages for the applications. Electrochemical

S. Chiba (✉)

Chiba Science Institute, 3-8-18 Yagumo, Meguro-ku, Tokyo, Japan

e-mail: schiba947@gmail.com

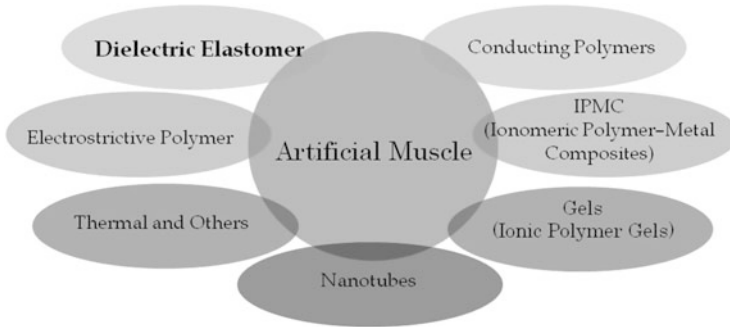


Fig. 13.1 Typical Electro Active Polymers (EAPs)

polymers typically can exert relatively high pressures and can be driven by low voltages. However, they are relatively slow and limited in size (since they are dependent on molecular transport), require high current and relatively energy inefficient. They can operate best over a narrow range of temperatures and must often be kept moist [6]. In contrast, field-activated polymers can be fast, efficient, and relatively insensitive to temperature and humidity fluctuations. These polymers can operate at relatively high voltages and low currents, that usually requires additional voltage conversion components but makes the size and capacity of wires and interconnects lighter and less critical [6].

A type of field-activated EAP transducer that embodies the desirable properties of polymer is dielectric elastomers [2].

Dielectric elastomer (DE) is a new transducer technology uses rubber like polymer (elastomer) as actuator materials. They have been gaining attention as technologies that have reached the practical use level as actuators and even as devices that can generate electricity efficiently [7].

13.2 Background on DE Artificial Muscles

DE is a new smart material with characteristics and properties not seen in other materials. The basic element of DE is a very simple structure comprised of thin polymer films (elastomers) sandwiched by two electrodes made of a flexible and elastic material, and can operate as an electric control actuator.

Using a DE actuator makes it possible to achieve a highly efficient transduction from electric energy into mechanical energy (the theoretical transduction efficiency is 80–90 % [8], which translates into a considerable energy saving compared to other actuator technologies such as electric motors with gearboxes. At the material level, this material has fast speed of response (over 50,000 Hz has been demonstrated for small strains), with a high strain rate (up to 380 % as shown in Fig. 13.2) [9], high actuation pressure (up to 8 MPa), and power density of 1 W/g (for comparison, human muscle is 0.2 W/g and an electric motor with gearbox is 0.05 W/g) [8].

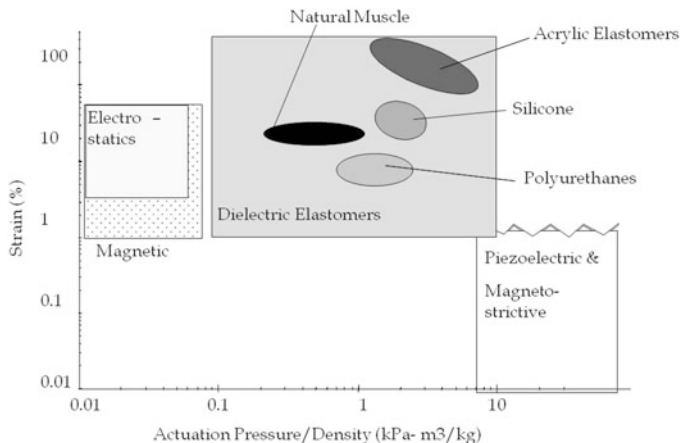
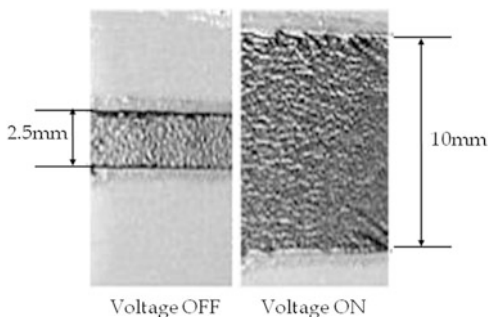


Fig. 13.2 Acrylic elastomers showing 380 % linear strain

Fig. 13.3 Performance of DE is similar to that of natural muscle



The energy density of DE has reached 3.4 J/g, about 21 times that of single-crystal piezoelectrics and more than two orders of magnitude greater than that of most commercial actuators [2, 8]. As can be seen in Fig. 13.3, DEs not only outperform existing actuator technologies in various areas but also are similar to natural muscle in that they fill the “actuator gap” between other actuation technologies [10]. That is, DEs have an actuation pressure/density that is bigger than that of electrostatic actuators and magnetic actuators, and cause strains that are bigger than that of piezo electric actuators and magneto strictive actuators.

13.3 Principle of Operation of DEs

DE transducers are based on the electromechanical response of an elastomeric dielectric film with compliant electrodes on each surface. Actuators based on DE technology operate on the simple principle shown in Fig. 13.4. When a voltage is

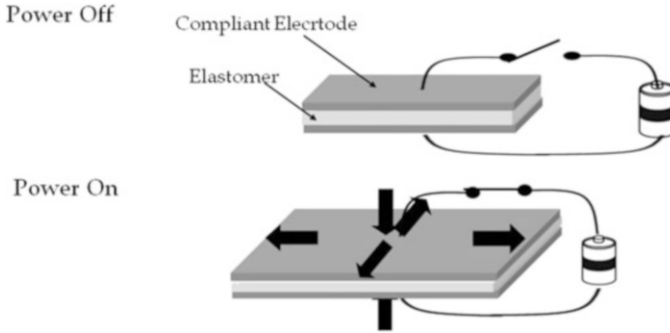


Fig. 13.4 Principle of operation of DEs

applied across the compliant electrodes, the polymer shrinks in thickness and expands in area.

The net volume change of the polymer materials that we investigate is small because of their high bulk moduli. Therefore, the electrodes must be compliant, to allow the film to strain. The observed response of the film is caused primarily by the interaction between the electrostatic charge on the electrodes. Simply put, the opposite charges on the two electrodes attract each other, while the like charges on the electrodes repel each other. Using this simple electrostatic model, we can derive the effective pressure produced by the electrodes on the film as function of the applied voltage. The pressure, ρ , is

$$\rho = \epsilon \epsilon_0 E^2 = \epsilon \epsilon_0 (V/t)^2 \quad (13.1)$$

where ϵ_0 and ϵ are the permittivity of free space (8.85×10^{-12} F/m) and the relative permittivity (dielectric constant) of polymer, respectively; E is the applied electric field in V/m; V is the applied voltage; and t is the film thickness. The response of the polymer is functionally similar to that of electrostrictive polymers, in that the response is directly related to the square of the applied electric field.

Two observations made from Eq. (13.1) clarify the difference between Maxwell stress actuation and the use of conventional air-gap electrostatic actuators. First, ϵ for polymers is typically in the range 2–12, whereas for air ϵ is 1. Thus the actuation pressure is increased substantially via polymers rather than air the same electric field. Another difference is that typical air-gap actuators have an additional factor of 0.5 in their equivalent pressure expression, i.e., the polymers double the actuation pressure independent of the dielectric constant. The reason for this difference is that the polymers can stretch in area rather than just contract in thickness. Polymers have two modes of converting electrical to mechanical energy. In contrast to polymers, air-gap actuators are typically made of rigid materials that can convert electrical to mechanical energy via only one mode of motion, such as the convergence of opposite electrodes.

DEs also have other advantages over air-gap electrostatic actuators, even though both are based on electrostatic force. Several polymers have been identified with breakdown strength of 300 MV/m or more in thin films, but breakdown strength this high are difficult to achieve consistently in air-gap electrostatic devices [9].

As mentioned above, the three effects, i.e., “two-mode coupling,” “high dielectric susceptibility,” and “high electric strength,” greatly contribute to the actuation pressure of the DEs.

13.4 Materials, Fabrication, Performance and Operating Considerations of DE Actuators

As a result of testing many materials so far, the best-performing materials (those with greatest strains) are based on commercially available formulations of silicone rubber and acrylic elastomer, as shown in Fig. 13.3 and Table 13.1 [11].

DEs can be fabricated in a variety of ways. The polymer films themselves can be cast, coated, or spun. Dip coating can be used to make complex shapes [9, 10]. All of these polymer fabrication methods have been used to make DE actuator materials. The optimal choice of fabrication method depends on the application as well as on cost and performance tradeoffs.

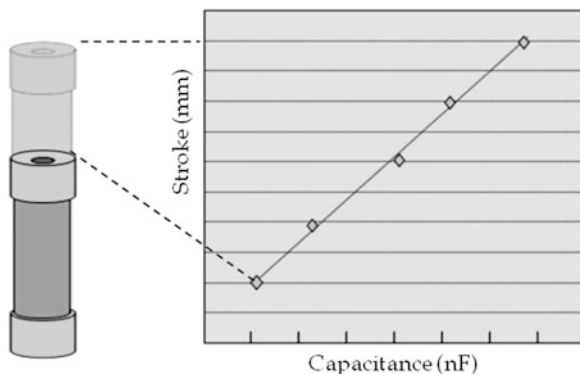
Spin coating generally makes the most uniform, highest-quality polymer films. It can also be used to make the thinnest films [10].

The environmental tolerance of DE appears good for a variety of applications. Silicon DE in Particular may have exceptional temperature performance. Silicon materials can operate at the temperatures ranging from $-50\text{ }^{\circ}\text{C}$ to over $250\text{ }^{\circ}\text{C}$, and we have successfully demonstrated Silicon DE actuators at over $260\text{ }^{\circ}\text{C}$ in preliminary testes.

Table 13.1 Properties and performance of best silicones and acrylics

Parameter	Acrylics	Silicones
Maximum actuation Strain (%)	380	120
Maximum actuation pressure (MPa)	7.2	3.0
Maximum specific energy density in actuation (MJ/m^3)	3.4	0.75
Maximum frequency response (Hz)	>50,000	>50,000
Maximum electric field (MV/m)	440	350
Relative dielectric constant	4.8	2.5–3.0
Dielectric loss factor	0.005	<0.005
Average elastic modulus (MPa)	2.0–3.0	0.1–2.0
Mechanical loss factor	0.18	0.05
Maximum electromechanical coupling, k^2	0.9	0.8
Maximum overall efficiency (%)	>80	>80
Durability (cycles)	>10,000,000	>10,000,000
Operating range ($^{\circ}\text{C}$)	-10 to 90	-100 to 260

Fig. 13.5 Linear relation between capacitance and stroke of actuator



Acrylic DE is likely to have a more modest range of operating temperatures, but we have demonstrated good actuation between $-10\text{ }^{\circ}\text{C}$ and $+70\text{ }^{\circ}\text{C}$ using acrylic. Table 13.1 summarizes the relevant properties and performance of the best acrylic and silicon materials.

The elastomer has excellent workability which enables the shape design of devices with sizes from micrometers to several meters. Also, as elastomers are light and deform like rubbers, they can show flexible movements like bionic actions. They can express “flexible and natural feeling” which systems with motors cannot imitate. A wide array of proof-of-principle devices for use in leg robots (see Chap. 33), swimming robots, snakelike robots, compact inspection robots, geckolike robots for climbing up perpendicular walls or across ceilings, and flying robots, as well as in achieving compatibility with living organisms are currently developed [8, 12]. The main feature of DEs is that they do not use any gears and cams, thus enabling high efficiency and safe and smooth driving even if the speed or direction of movement are suddenly changed.

In addition, as there is a direct proportionality between the change in the capacitance and elongation of DE actuators, they can be used for pressure- and position-sensors (see Fig. 13.5) [11].

13.5 Application of DE Actuators

Part of the great promise of DE technology is its versatility which resides in its considerable range of configurations. It can convert electrical energy into mechanical motion in a planar format (motion perpendicular to the plane or motion in the plane); in a cylindrical shape (motion along or perpendicular to the axis of the cylinder); and in other three-dimensional shapes (motion perpendicular to or tangential to the surface of the shape). The configurations can be single or multiple layers, in externally biased single-phase configurations or internally biased multiphase configurations. Details of the application will be discussed in Chap. 33.

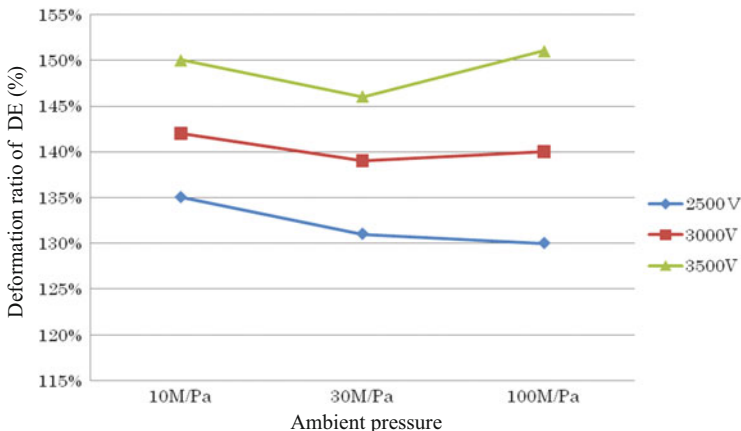


Fig. 13.6 Deformation ratio of DE actuators at different ambient pressures and applied voltages

We will discuss more unique feature of DE actuators in this section: In a recent experiment, we have verified that the DE type of electroactive polymer can maintain good operational characteristics even in an ultrahigh-pressure environment by showing that the electroactive strain response to an applied voltage was unaffected by externally applied pressures of up to 100 MPa [13]. Figure 13.6 shows the deformation ratio of DE actuators at different ambient pressures and applied voltages.

13.6 Principle of DE Generators

The operation principle in the generator mode is the transformation of mechanical energy into electric energy by deformation of the DE. Functionally, this mode resembles piezoelectricity, but its power generation mechanism is fundamentally different [7]. With DE, electric power can be generated even by a slow change in the shape of DE, while for piezoelectric devices impulsive mechanical forces are needed to generate the electric power [14]. Also, the amount of electric energy generated and conversion efficiency from mechanical to electrical energy can be greater than that from piezoelectricity [7, 15]. Figure 13.7 shows the operating principal of DE power generation.

Application of mechanical energy to DE to stretch it causes compression in thickness and expansion of the surface area. At this moment, electrostatic energy is produced and stored on the polymer as electric charge. When the mechanical energy decreases, the recovery force of the DE acts to restore the original thickness and to decrease the in-plane area. At this time, the electric charge is pushed out to

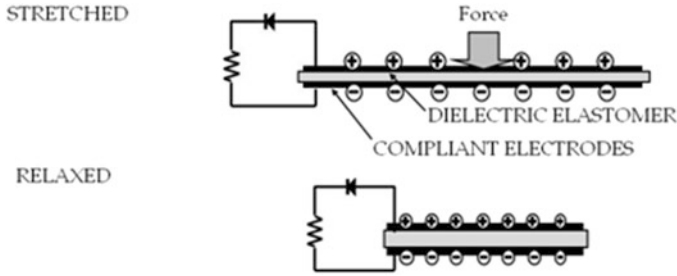


Fig. 13.7 Operating principle of DE power generation

the electrode direction. This change in electric charge increases the voltage difference, resulting in an increase of electrostatic energy.

$$C = \epsilon_0 \epsilon A / t = \epsilon_0 \epsilon b / t^2 \quad (13.2)$$

where ϵ_0 is the dielectric permittivity of free space, ϵ is the dielectric constant of the polymer film, A is the active polymer area, and t and b are the thickness and the volume of the polymer. The second equality in Eq. (13.2) can be written because the volume of elastomer is essentially constant, i.e., $At = b = \text{constant}$.

The energy output of a DE generator per cycle of stretching and contraction is

$$E = 0.5C_1 V_b^2 (C_1 / C_2 - 1) \quad (13.3)$$

where C_1 and C_2 are the total capacitances of the DE films in the stretched and contracted states, respectively, and V_b is the bias voltage.

Considering then changes with respect to voltages, the electric charge Q on a DE film can be considered to be constant over a short period of time and in the basic circuit. Since $V = Q/C$, the voltages in the stretched state and the contracted state can be expressed as V_1 and V_2 , respectively, and the following equation is obtained:

$$V_2 = Q / C_2 = (C_1 / C_2) (Q / C_1) = (C_1 / C_2) V_1 \quad (13.4)$$

Since $C_2 < C_1$, the contracted voltage is higher than the stretched voltage, corresponding to the energy argument noted above. The higher voltage can be measured and compared with predictions based on the DE theory. In general, experimental data based on high impedance measurements are in excellent agreement with predictions [16]. When the conductivity is assumed to be preserved in the range of electric charging, Q remains constant.

Figure 13.8a shows a typical scope trace from contraction of DE. Figure 13.8b shows a simplified circuit for oscilloscope measurement of voltage. The voltage peak generated for one cycle is typically on the order of a few ms to several tens of ms for a piezoelectric element. However, in the case of DE, the peak width is on the order of 150–200 ms or longer [7]. The long power-generation pulse duration of DE

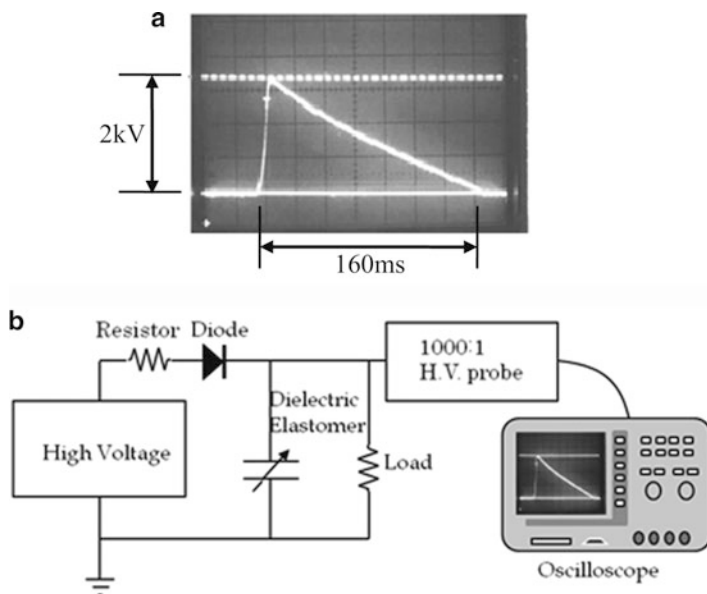


Fig. 13.8 Voltage for compression of DE and measurement circuit (a) Typical scope trace from contraction of DE. Voltage spike occurs at contraction and gradually back to (stretched) voltage due to load resistance. (b) Measurement circuit of generated energy

can allow for the direct use of generated energy for activities such as lighting LEDs or as a power source for high-speed wireless devices [17]. Due to both the long pulse duration and the high energy density of DE in power generation mode, mechanical energy can be effectively converted to electric energy even at low frequencies.

13.7 Innovative DC Generation System by DE Generators

DE generator applications can be categorized into point generator applications, such as an alternator in an automobile, or distributed generator applications, such as harvesting wind power over a broad area [18].

In point generation applications, DE can be used for traditional point generator applications as a direct replacement for electromagnetic generators. One can, for example, connect a DE generator to an internal combustion engine to make a fuel-powered generator. For these traditional point generator applications, DE may offer lower cost, lighter weight, smaller size, or other advantages. However, it must be acknowledged that for these traditional high frequency point applications, DE is a new technology competing against a mature technology that is well suited for the task. Hence, while DE may eventually become competitive in traditional

high-speed generator applications, other uses for both point and distributed generators may better exploit the advantages of DE in the nearer term.

For point generator applications, DE is much more competitive if the mechanical input is intrinsically low frequency or variable speed. For these applications, conventional generators must use transmissions with their added cost, complexity, and size, thus making DE more competitive in the low frequency domain.

DE can be made in large area, low cost sheets with high performance [19]. This capability suggests novel ways to capture energy that is distributed over large areas. Wind and wave energy are two clear examples of distributed power sources that might benefit from large area generators.

Incidentally, wave or wind power generators using conventional rotors generate AC electric power, and thus for their usage, it must be converted into DC power. On the other hand, the DE systems generate DC power. It can be used without the conversion. This indicates that the DE system is very advantageous for constructing a high-efficiency, local self-sufficiency electric power system which enables the activation of local industries

Details of such applications will be discussed in the Chap. 33.

We will discuss more fundamental issue in this section: An energy transduction technology that operates efficiently over a range of frequencies is important for practical energy harvesting devices such as ocean wave power generators. DE is based on the change in capacitive energy of a deformable dielectric and is a candidate for such applications. A simple scale model of DE-based wave energy harvesting system was tested in a wave tank over a range of wave periods from 0.7 to 3 s and wave heights of 3 and 6 cm. The energy output was found to be largely independent of wave period (See Fig. 13.9.) [17].

Conventional wave power generators have a tendency for a slight modification from the optimum natural period to cause a considerable decrease in generation efficiency, but the DE based generator produces stable generated electricity over a range from a short to a long period, which, on average, represents approximately 70 % of the maximum value. This is the first case in the world where this kind of electric output has been shown to be possible.

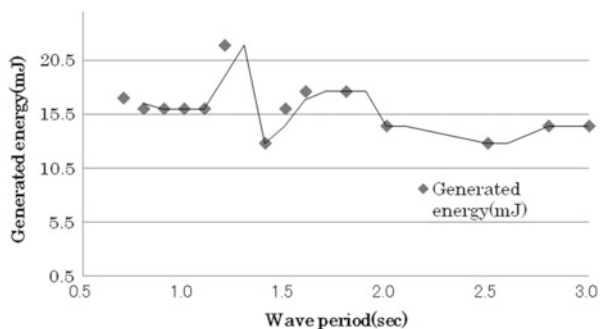


Fig. 13.9 Generated energy as a function of wave period

13.8 Future of DE System

DE is potentially the dream material for a wide range of applications in actuators and power generation devices. However, although research on DE as a generator material has advanced rapidly in recent years, material and application technologies remain not fully developed. Commercialization efforts and development of structures suitable for mass production must be strengthened in order to keep pace with diverse and constantly changing social needs. Future research will be oriented to develop the technologies for diverse applications and to establish a production system that answers market needs.

13.8.1 *Toward the Future*

13.8.1.1 Super Artificial Muscle

According to current research and development projects, in 5 years it will be possible to produce a “super artificial muscle” having a strain of 15 % with an output pressure of 8 MPa. In the near future, this material could be used in prosthetic or orthotic devices that will allow people that are disabled to carry out activities at the same level or better than fully able-bodied people. Moreover, large numbers of DE actuators could be embedded into buildings or other structures to cancel out or reduce the vibration from earthquakes and thereby prevent the collapse of or damage to buildings.

The super artificial muscles could also improve the efficiency of electric transport systems. DE can be used to make a lightweight and efficient motor drive. Light and highly efficient automobiles will be possible, creating a dream vehicle with low energy consumption.

13.8.1.2 Carbon Management

In the near future, it will be possible to offer a small but powerful generator that answers diverse needs, which will not only stimulate the industrial development of these regions (such as new farming fishery businesses, plant factories, carbon dioxide fixation factories, and derived purification businesses), but also contribute to the decrease of carbon dioxide emissions.

In the future, it may be possible to set a large-scale generator system in areas such as a desert using a Stirling engine or a large-scale array with DE sheets, by coupling it to a solar system as a thermal source. As production costs, installation costs, and maintenance costs are remarkably low, an almost revolutionary approach would be utilized for reducing CO₂ emissions.

Hydrogen is currently being touted as a next-generation transportable fuel, and research work is being conducted on its applications. However, there are several basic problems to solve before being able to consider hydrogen as a cheap and stable means of storing energy. Sequestration of carbon dioxide also requires the use of huge amounts of energy and so almost any approach that relies on non-renewable fuels is not carbon friendly. Compared with these other approaches, we are expecting that DE generators may become one of the promising technologies to the solution of these problems in the future.

References

1. Pelrine R, Chiba S (1992) Review of artificial muscle approaches. In: Proceedings of the third international symposium on micromachine and human science, Nagoya, Japan
2. Pelrine R, Kornbluh R, Pei Q, Joseph J (2000) High speed electrically actuated elastomers with over 100 % strain. *Science* 287(5454):836–839
3. Oguro K, Fujiwara N, Asaka K, Onishi K, Sewa S (1999) Polymer electrolyte actuator with gold electrodes. In: Proceedings of the SPIE's 6th annual international symposium on smart structures and materials, SPIE Proc, vol 3669, pp 64–71
4. Otero TF, Sansiñena JM (1998) Soft and wet conducting polymers for artificial muscles. *Adv Mater* 10(6):491–494
5. Osada Y, Okuzaki H, Hori H (1992) A polymer gel with electrically driven motility. *Nature* 355:242–244
6. Kornbluh R, Pelrine R, Chiba S (2004) Silicon to silicon: stretching the capabilities of micromachines with electroactive polymers. *IEEJ Trans Sens Micromech* 124(8):266–271
7. Chiba S, Waki M, Kornbluh R, Pelrine R (2008) Innovative power generators for energy harvesting using electroactive polymer artificial muscles. In: Bar-Cohen Y (ed) *Electroactive polymer actuators and devices (EAPAD)*, Proceedings of the SPIE, vol 6927, pp 692–715, 1–9
8. Chiba S, Stanford S, Pelrine R, Kornbluh R, Prahald H (2006) Electroactive polymer artificial muscle. *JRSJ* 24(4):38–42
9. Pelrine R, Kornbluh R, Chiba S (2002) Artificial muscle for small robots and other micromechanical devices. *IEEE Trans Jpn* 122-E(2):97–101
10. Chiba S (2002) MEMS and NEMS applications of dielectric elastomer and future trends. *Electr Pack Technol* 18(1):32–38
11. Kornbluh R, Bashkin J, Pelrine R, Prahald H, Chiba S (2004) Medical applications of new electroactive polymer artificial muscles. *Seikei Kakou* 16(10):631–637
12. Pei Q, Rosenthal M, Pelrine R, Stanford R, Kornbluh R (2003) Multifunctional electroelastomer roll actuators and their application to biomimetic walking robots. In: Bar-Cohen Y (ed) *Proceedings of the SPIE, smart structures and materials, electroactive polymer actuators and devices (EAPAD)*, San Diego, March 2003
13. Chiba S, Waki M, Sawa T, Yoshida T, Kornbluh R, Pelrine R (2011) Electroactive polymer artificial muscle operable in ultra-high hydrostatics pressure environment. *IEEE Sens J* 11(1):3–4
14. Ashida K, Ichiki M, Tanaka M, Kitahara T (2000) Power generation using Piezo element: energy conversion efficiency of Piezo element. In: Proceedings of the JAME annual meeting, pp 139–140
15. Jean-Mistral C, Basrour S, Chaillout J (2010) Comparison of electroactive polymer for energy scavenging applications. *Smart Mater Struct* 19:085012

16. Chiba S, Waki M, Wada T, Hirakawa Y, Masuda K, Ikoma T (2013) Consistent ocean wave energy harvesting using electroactive polymer (dielectric elastomer) artificial muscle generators. *Appl Energy* 104:497–502
17. Chiba S et al (2007) Extending applications of dielectric elastomer artificial muscle. In: *Proceedings of the SPIE, San Diego, 18–22 March 2007*
18. Chiba S, Pelrine R, Kornbluh R, Prahlah H, Stanford S, Eckerle J (2007) New opportunities in electric power generation using electroactive polymers (EPAM). *Jpn Inst Energy* 86(9):743–747
19. Chiba S, Kornbluh R, Pelrine R, Waki M (2008) Low-cost hydrogen production from electroactive polymer artificial muscle wave power generators. In: *Proceedings of the world hydrogen energy conference, Brisbane, Australia, 16–20 June 2008*

Chapter 14

Development of Actuators Using Slide Ring Materials and Their Various Applications

Hiromitsu Takeuchi

Abstract Recently, the driving source with excellent lightweight properties and silence is requested. Therefore, a variety of polymer actuator is actively researched and developed. Polymer dielectric actuator shows an excellent characteristic in the response and the energy efficiency in these actuator. However, dielectric actuator has the fault with high drive voltage. To overcome this fault, a novel polymeric material (sliding material) was adopted. Moreover, we made the artificial arm that moved with dielectric actuator.

Keywords Artificial arm • Polymer dielectric actuators

14.1 Introduction

Being in the automobile industry, I have been able to offer convenience and comfort to automobile users by means of high-polymer technologies.

For the purpose of further social contribution through the high-polymer technologies nurtured by the automobile industry, I began developing high-polymer actuators, i.e., artificial muscle. Although some research and development of high-polymer actuators has already been undertaken [1–6], from among the existing types I chose to focus on dielectric elastomer actuators, which are superior in output and energy efficiency, as candidates for artificial muscle. A high drive voltage of several kV has been impeding practical use of the high-polymer dielectric actuator. To solve this problem, I focused on slide ring materials (SRM) [7, 8].

This study was done in collaboration with Tokyo University, Advanced Softmaterials Inc., and Yokohama Rehabilitation Center, with the support of New Energy and Industrial Technology Development Organization (NEDO).

H. Takeuchi (✉)

Research Center, Toyoda Gosei Co., Ltd, 1-1 Higashi-Takasuka, Futatsudera, Amashi, Aichi 490-1207, Japan

e-mail: tg22918@toyoda-gosei.co.jp

14.2 Development of Dielectric Elastomer Actuator

As shown in Fig. 14.1, the dielectric elastomer actuator is a sheet composed of a dielectric layer made from insulating rubber and elastic electrode layers made from electrode rubber. When voltage is applied between the elastic electrodes, the dielectric layer is squeezed by the coulomb force acting between the electrodes, and an output (displacement and force) is generated in a planar direction. The output becomes zero when the voltage is turned off, as the dielectric layer returns to its original thickness. Soft materials, which are easily deformed by coulomb force, are required to drive it with a lower voltage; however, materials that do not suffer from hysteresis loss are required to drive it continuously with good responsiveness. Hysteresis loss not only deteriorates the responsiveness of the actuator drastically, but also causes a fatal flaw for an actuator by not accurately returning to its original length. SRM, a new material invented by Ito of Tokyo University [8], is an elastomer material with superior flexibility and almost no settling. This can be said to be an ideal material for dielectric elastomer actuators, due to its mechanical properties.

Because the driving source for dielectric elastomer actuators is the coulomb force acting between the electrodes, the higher the dielectric constant of the dielectric layer material, the higher the coulomb force, resulting in a higher actuator output being generated. As compared with the relative dielectric constant of about two of silicone rubber and about four of acrylic rubber, the relative dielectric constant of SRM is about ten, resulting in a coulomb force five times greater than silicone rubber and 2.5 times greater than acrylic rubber, eventually resulting in higher actuator output.

As just described, SRM is superior in mechanical and dielectric properties as a material for the dielectric layers of dielectric actuators; however, it has been posing a problem in durability due to its lower dielectric breakdown strength. For that reason, the focus of the development has been on creating a thin film with higher dielectric breakdown strength.

As for the improvement of dielectric breakdown strength, two main approaches were implemented, as described below. In the first step, the dielectric breakdown strength of the material itself was improved.

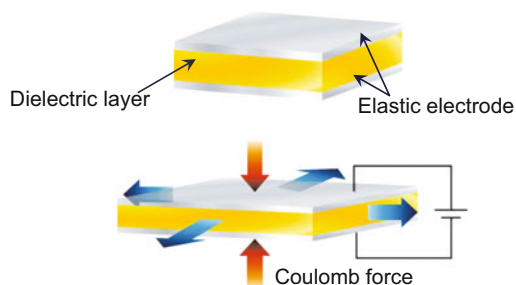


Fig. 14.1 Principles of dielectric elastomer actuator

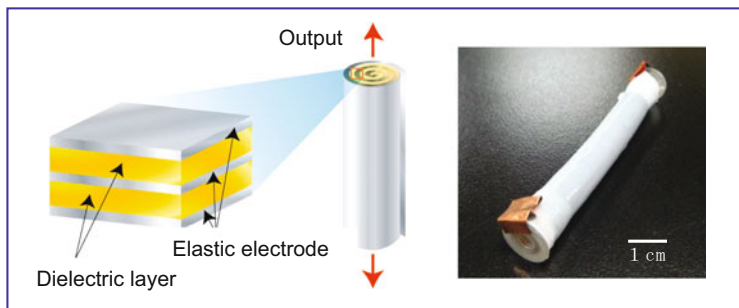


Fig. 14.2 Structure of actuator

A composite material was developed by combining SRM with resins with higher dielectric breakdown strength, such as polycarbonate and silicone, etc. Compatibility of resins of higher dielectric breakdown strength with SRM was improved so as to exploit the low hysteresis loss property of SRM, and then a crosslinking method was developed to add flexibility.

The second step was the development of SRM thin-film formation technology.

The roll-type structure shown in Fig. 14.2 was employed so as to efficiently draw out the actuator output. This actuator is made by rolling up a laminated sheet of SRM thin-film and electrode thin-film. The SRM thin-film is required to have no pinholes, etc., which become the starting point of dielectric breakdown.

Also required is a technology to roll up the sheet without generating air bubbles between layers. The targeted dielectric breakdown strength and low-voltage driving were achieved by developing a thin-film formation technology suited for SRM solution, and considering a technology for rolling up soft SRM thin-film with uniform tension.

Significant results were obtained by carrying out material development and technology development in an integrated manner. The drive starting voltage, which used to require several kV, was reduced down to several hundred volts, and a force of 2 N, displacement of 2 mm was achieved.

14.3 Application Development

14.3.1 Application as Artificial Muscle

Dielectric elastomer actuators are characterized by high energy efficiency, in addition to light weight, silent running, and flexibility, which are qualities they have in common with muscles. As a welfare device exploiting these characteristics, the development of an electric artificial arm was implemented. Commonly,

Current lineup trend of artificial arm products and next-generation development direction

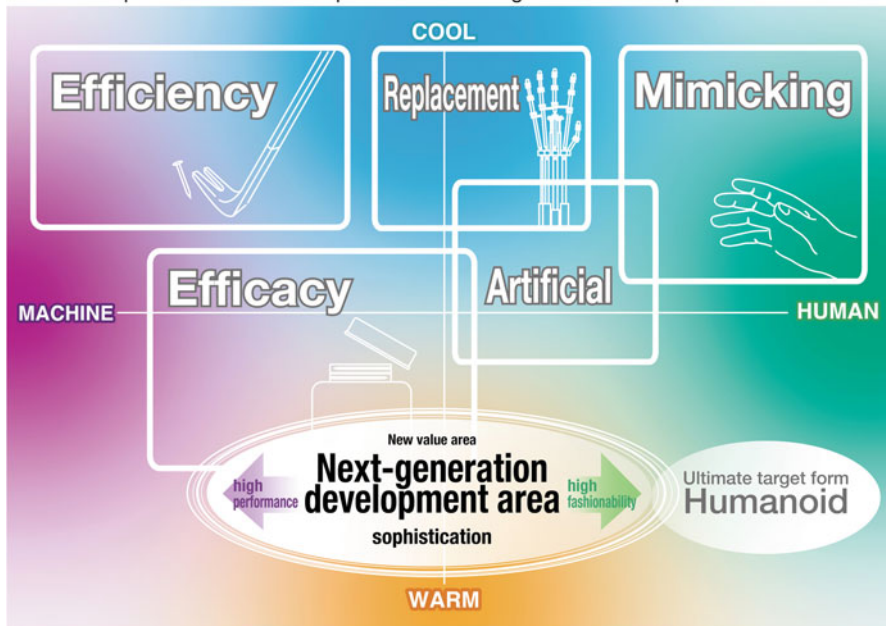


Fig. 14.3 Mapping of design concept

conventional artificial arms are driven by electromagnetic motors. Such artificial arms pose problems such as “heavy, hard to use,” “loud operating noise,” and “requires a larger battery,” etc.; however, these problems can be solved by dielectric elastomer actuators.

Artificial arms have a negative image as opposed to artificial legs, which have a positive image as a device to show, owing to the pursuance of designability and functionality as displayed in the scenes from recent Paralympics games. This may be caused by the fact that more attractive-looking, decorative artificial arms are produced in Japan, rather than electrical artificial arms advancing in popularity. For that reason, we pursued a design to generate a positive image of electric artificial arms. First, we conducted a survey on artificial arms to find out what kind of designs and functions they have, and then mapped the result in terms of “human \leftrightarrow machine,” and “cool \leftrightarrow warm” (Fig. 14.3). Based on this mapping, we fabricated a test model after setting the direction of the design. Points of interest are the flowing lines of the finger portion, which give an image of slender and supple lady’s fingers, and the decoration on the finger portion, which provides the enjoyment of adding replacements like nail art (Fig. 14.4). We succeeded making the arm hold a circular vessel by sensing the voltage generated when muscles contract (myoelectricity) to drive the dielectric elastomer actuators.

14.3.2 Application to General Machinery

We found out that vibration can be generated by using the laminated sheet that was developed as artificial muscle. Figure 14.5 shows the vibration device under consideration. Vibration is generated by the up-and-down motion of the vibration portion in the center, which then vibrates an enclosure, etc. via the frame. Figure 14.5 shows the vibration mechanism. The laminated sheet elongates when the driving voltage is turned ON, and the center portion is moved downward by gravity. The laminated sheet returns to its original length when the driving voltage is turned OFF, and the center portion also returns to its original position. Vibration can be generated by repeating ON and OFF. The magnitude of vibration varies depending on the deformation extent of the laminated sheet and the weight of the center portion. It has been confirmed that the amount of vibration amplitude can be maintained up to 100Hz.

When vibrating at 1 Hz, a vibration that reproduces a human pulse can be obtained, leading to initiating the development of these as devices for stress reduction.



Fig. 14.4 Myoelectric artificial arm

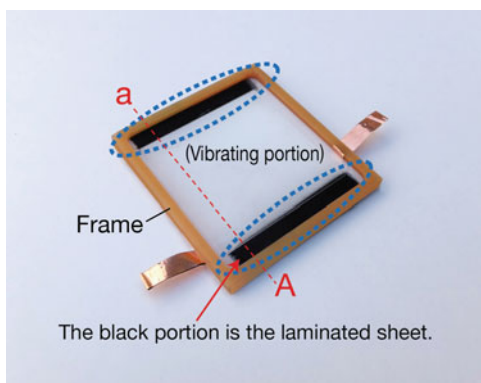


Fig. 14.5 Vibration device

In the case of optical devices, they are currently under consideration as a driving source that can halve the space, weight, and power consumption when compared to driving sources of electromagnetic vibration generation.

14.4 For the Future

Development will continue, with the aim of driving at 100 V or lower. As for the development of artificial arms, we will implement the prototyping of models for specific usage scenarios, before shifting to demonstration experiments.

We will also aim for applications to other medical welfare products, and even to general machinery.

References

1. Kaneto K et al (2007) *Smart Mater Struct* 16:S250
2. Smela E et al (1995) *Science* 268:1735
3. Pei Q, Inganas O (1993) *Synth Met* 55–57:3730
4. Asaka K et al (2000) *J Electroanal Chem* 480:186
5. Fukushima T et al (2005) *Angew Chem Int Ed* 44:2410
6. Pelrine R et al (2000) *Science* 287:5454
7. Ito K, Kato K (2012) *High Polymers, Japan* 61:398
8. Ito K et al (2007) *Soft Mater* 3:1456

Chapter 15

Piezoelectric Polymers

Yoshiro Tajitsu

Abstract The study of the piezoelectric polymers has advanced in the last few decades, and their practical application to sensor and actuator devices has progressed. The piezoelectric polymers in practical use are divided into the following classes with different piezoelectric characteristics: chiral polymers (optically active polymers), ferroelectric polymers, and cellular electrets. The piezoelectricity of a chiral polymer is in response to shear strain, that of a ferroelectric polymer is in response to tensile strain, and that of cellular electrets is in response to strain perpendicular to film surface. In this chapter, the fundamental properties and applications of these different types of polymers are systematically discussed.

Keywords Chirality • Electrets • Ferroelectricity • Optically active polymers • Piezoelectricity • Poly-L-lactic acid • Polypeptide • Polyvinylidene fluoride

15.1 Introduction

The development of new human-machine interface (HMI) for mobile devices such as smartphones etc., has been actively progressed. As a key material of such HMIs, the piezoelectric element has attracted attention. Organic piezoelectric materials such as piezoelectric polymers, are transparent, light and flexible, and the fabrication of thin films is easy, resulting in high expectations of their application as actuators and sensors for many years [1–9]. However, the large resonance essential to drive an actuator cannot be induced. This is because the mechanical loss of piezoelectric polymers is almost the same as that of general polymeric materials. Moreover, the piezoelectric constant of piezoelectric polymers is no more than one-tenth that of practical piezoelectric ceramics [4–6]. On the other hand, elucidation of the crystal growth and higher-order structure of the crystalline polymers has progressed significantly [3, 7–9]. Following the progress in the research, various novel control technologies for higher-order structures have been established. To achieve this, the properties of piezoelectric polymers have also

Y. Tajitsu (✉)

Department of Electrical and Electronic Engineering, Faculty of Engineering Science, Kansai University, Suita, Osaka, Japan

e-mail: tajitsu@ipku.kansai-u.ac.jp

been significantly improved. Concrete examples of organic piezoelectric materials in current use are poly-L-lactic acid (PLLA) as a chiral piezoelectric polymer, porous polypropylene (cellular PP) as a cellular electret, and polyvinylidene fluoride (PVDF) as a ferroelectric polymer [3, 6, 8, 10]. First, the history of piezoelectric polymers is reviewed. The first research report on piezoelectric polymers was published in 1955. Its theme was the piezoelectricity of wood [3] and the author was Dr. Eiichi Fukada, who is known as “father of piezoelectric polymers” worldwide. The existence of piezoelectricity in silk, hemp, and wool was subsequently proved. Collagen, which is a protein, is a type of polypeptide having a molecular structure in which amino acids are linked by a peptide bond (CONH) [3, 4, 7, 8]. Research on piezoelectricity in many types of polypeptides and their compounds has been carried out. The shear piezoelectricity of biological materials such as silk, wool, skin, horns, blood vessel walls, muscles, teeth, and shells has been demonstrated. Typical synthetic polymers in which many amino acids are bonded through a covalent bond whose piezoelectricity has been investigated are poly-L-alanine (PA), poly- γ -methyl-L-glutamate (PMLG), and poly- γ -benzyl-L-glutamate (PBLG) [3, 4, 7, 8].

Lead zirconate titanate (PZT) ceramic, in which lead zirconate is occluded in lead titanate crystals, is the most popular one of actual piezoelectric material in actual use [5]. PZT crystal has a unique ordered structure in which the ionized atoms are arranged. Therefore, when an electric field is applied to PZT, large internal displacement of the ions is induced. As a result, PZT was a high dielectric constant and also exhibits ferroelectricity. In contrast, the main chain molecules of polymers are formed by covalent bonds. Thus, until the end of the 1970s, it was considered that polymer materials do not exhibit ferroelectricity or have a large dielectric constant [2, 3]. This established theory was overturned by the discovery of ferroelectricity in PVDF. It is now widely accepted that ferroelectric polymers exist [2, 3].

Furthermore, electrets are among the most important piezoelectric organic materials [10]. Traditional electrets were insulating materials such as carnauba wax. The fabrication process of traditional electrets was apply a high voltage to an insulating material at a high temperature. In traditional electrets, the positive charges and negative charges are separately trapped on opposite sides of a film surface. In general, the piezoelectric constant of an electret is lower than that of piezoelectric organic materials such as PVDF. However, it was recently reported that cellular electrets have large piezoelectric constants that are almost as high as that of PZT ceramic.

15.2 Macroscopic Piezoelectricity of Polymers

Piezoelectricity is the ability of dielectrics to generate an electric charge in response to mechanical stress. The opposite effect also is occurs: the application of an electric voltage produces mechanical strain in piezoelectric materials. Both these

effects can be measured, making piezoelectric materials effective in sensors and transducers. In considering the piezoelectricity of a polymer film, the strain s_m (extension: $m = 1-3$, shear strain: $m = 4-6$) induced by an electric field E_i ($i = 1-3$) is represented by the equations below. The electric displacement D_i ($i = 1-3$) induced by stress T_m (tensile stress: $m = 1-3$, shear stress: $m = 4-6$) is also give [1-11].

$$D_i = d_{im}T_m \quad (15.1)$$

$$s_m = d_{im}E_i \quad (\text{opposite effect}) \quad (15.2)$$

Here, d_{im} ($i = 1-3$, $m = 1-6$) is a piezoelectric tensor.

In general, amorphous components are always present in complex high-order structures in polymer films with piezoelectricity, including electret type piezoelectric films. Therefore, the macroscopic symmetry of a piezoelectric polymer film must be considered on the basis of point group theory. For a right-handed system ($x_1-x_2-x_3$), asymmetry is imparted to a film by conventional methods such as drawing and poling [4, 7]. The directions of the coordinate axes are different in each type of piezoelectric polymer material [3, 4, 7, 8, 11]. In particular, it is necessary to ensure that the directions of the coordinate axes do not become mixed, as shown in Fig. 15.1. The purpose of drawing is to macroscopically arrange the chain molecules in a polymer film along the same direction in the entire film [3, 4, 7, 8, 11]. In contrast, the purpose of poling is to macroscopically arrange the dipole moments of the molecules along the same direction in the entire film,. Actually, the macroscopic piezoelectricity of an isotropic film does not occur even when piezoelectricity exists in the crystal state. The point group of drawn and poled films of ferroelectric polymers such as PVDF is C_{2v} , as shown in Fig. 15.1. The symmetry is the same as that of the PVDF crystal. In the poling process a high voltage is applied perpendicular to the film surface. However, drawn and poled PVDF films exhibit high macroscopic tensile piezoelectricity. In this case, the direction of the x_1 -axis is taken along the fiber orientation axis, and the direction of the x_3 -axis is parallel to the poling direction. Five independent piezoelectric tensors, d_{31} , d_{32} , d_{33} , d_{15} , and d_{24} , exist as shown in Fig. 15.1.

Next, we consider the case of a chiral polymer film. The point group of a drawn polymer film without chirality is $D_{\infty v}$ [3, 4, 7, 8, 11], as shown in Fig. 15.1. In this case, it is important that a mirror plane perpendicular to the film surface exists. Furthermore, in this case, no piezoelectricity arises. However, the molecule of a chiral polymer such as PLLA has chirality, as shown in Fig. 15.1. Its point group is $D_{\infty v}$. As a result, two independent piezoelectric tensors, d_{14} and d_{25} ($= -d_{14}$), exist.

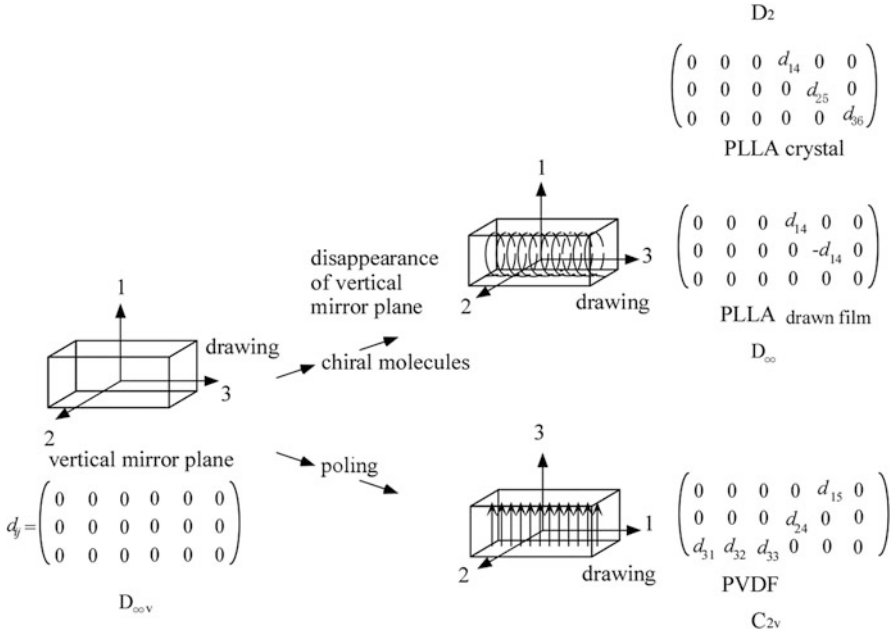


Fig. 15.1 Macro symmetry of polymer film

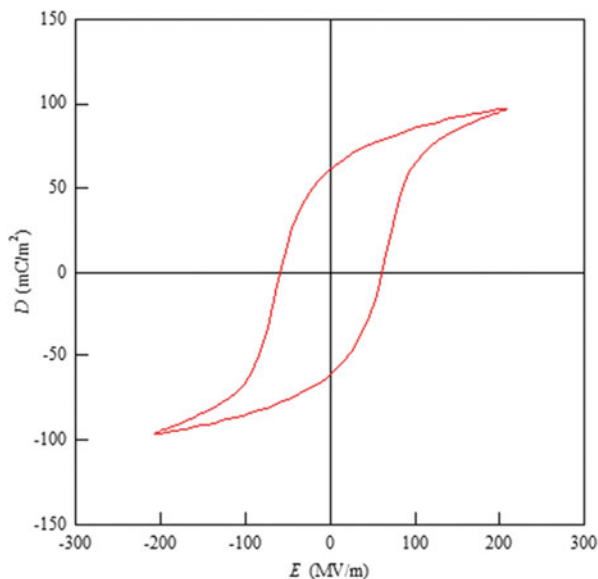
15.3 Typical Piezoelectric Polymers in Practical Use

In this section, typical piezoelectric polymers are surveyed and their characteristic features enabling their use as sensors and actuators are introduced.

15.3.1 Polyvinylidene Fluoride (PVDF)

The most well-known piezoelectric macromolecule is the ferroelectric polymer PVDF. Its large residual polarization was discovered found when a strong electric field was applied to a stretched PVDF film. It was reported by Kawai [2, 3] in 1969 that PVDF has a high piezoelectric constant of 5 pC/N. Both the poling process and the drawing process are essential for piezoelectricity to occur in a PVDF film. This discovery was the starting point of the study of ferroelectricity in polymers. As shown in Fig. 15.2, PVDF exhibits a *D-E* hysteresis loop [2, 3]. In other words, the macroscopic piezoelectricity of PVDF is not observed if spontaneous polarization does not arise in this *D-E* hysteresis loop. That is, the same poling process as that for piezoelectric PZT ceramic, is required to induce the piezoelectricity in a PVDF film. In the poling process, a DC voltage is applied to the sample to generate residual polarization. In the case of PVDF, an electric field of 50 MV/m or more

Fig. 15.2 Hysteresis loop of PVDF film drawn along one axis



must be applied at room temperature. This is difficult for a PVDF film with a thickness of $100\ \mu\text{m}$ or more because we must apply a large voltage of over $5\ \text{kV}$ without inducing breakdown or discharge phenomena. Therefore, in practice, thermal poling by the application of a dc voltage of several kV to a PVDF film at a temperature higher than room temperature is carried out. To induce piezoelectricity more effectively in a PVDF film, a uniaxial stretching process to orient the chain molecules is necessary in advance. When these treatments are applied to a PVDF film, its point group becomes C_{2v} , as shown in Fig. 15.1. The point group of a PVDF crystal is also C_{2v} . Thus, the point group of an entire PVDF film is the same as that of a PVDF crystal. The piezoelectric tensor in this case is summarized in Fig. 15.1. Here, we consider this result in detail. The point groups were should not be the same since a PVDF film is a single crystal. It is coincidental that the point group of a poled PVDF film with single-axis orientation is the same as that of a single crystal. That is, a PVDF film has a complicated higher-order structure; therefore, it does not show translational symmetry. This is a very important point in clarifying the macroscale piezoelectricity of PVDF films.

Many applications of piezoelectric PVDF films have been commercially realized in the U.S. and Europe [2–6]. In the acoustic field, these include the pickup of a loudspeaker, a guitar, and a violin. Also, microphones, and sonar (underwater microphones) used by a submarine or ship are included. In the field of security, piezoelectric PVDF films with a large area placed under a carpet have been used to detect intruders. In the field of traffic control, piezoelectric cables is embedded in roads have been used to detect the speed of vehicles, and vehicles ignoring traffic lights, and to obtain information on the occupancy of parking lots. They have also been used in switches, sensors in water meters, for nondestructive detection, and in

keyboards. They have also been employed as oscillating sensors for the vibratory control of washing machines and in eyeball sensors, sphygmomanometers, stethoscopes, and over 250,000 pacemakers as medical sensors. Moreover, ultrasonic image sensors and sensors that measure the pressure of the soles to feet have been developed that use PVDF films. Thus, PVDF films have a proven track record in many fields. PVDF sensors are also used as ultrasonic elements. Since the acoustic impedance of a PVDF film is closer to that of a living body or water than that of conventional electrostrictive ceramics, the propagation loss in the case of ultrasonic transmission and reception is small. As a result, PVDF devices are highly sensitive. Also, the separation of transmission and reception in a short pulse is possible. Therefore, high-resolution and broadband characteristics are acquired. Since PVDF films are soft, they are easy to process into the shapes of concave and convex lenses. Another use of PVDF devices is to converge an ultrasonic beam without an acoustic lens. Also the focus and depth of focus in the design of PVDF devices can be adjusted as required. Moreover, since elements with a large area are obtained easily, large transducers are realized easily. Also, since thin film elements are obtained easily, high-frequency transducers can be obtained. Thus, PVDF films have many attractive features. Taking advantage of these features, they are practically used in probes for hydrophones, ultrasonic diagnostic equipment, ultrasonic nondestructive-testing equipment, and acoustic microscopes.

15.3.2 *Poly-L-Lactic Acid (PLLA)*

First, the PLLA crystal structure is introduced to clarify the origin of the macroscopic piezoelectricity of PLLA films. The crystal structure is based on a base-centered orthorhombic unit cell [12, 13], as shown in Fig. 15.3. Here, a , b , and c are the lengths of the unit cell, which contains two $10/3$ helical chains arranged along the c -axis. Thus, PLLA is a chiral polymer, and in the crystal the chain molecules form a helical structure. The crystal structure of PLLA is characterized by this helical structure. That is, the piezoelectric characteristics of the PLLA crystal are governed by this helical structure. The point group of the PLLA crystal is D_2 . When the c -axis corresponds to the x_3 -axis, the a -axis corresponds to the x_1 -axis, and the b -axis corresponds to the x_2 -axis, three independent piezoelectric tensors, d_{14} , d_{25} , and d_{36} , are present, as shown in Fig. 15.1. After close investigation, the origin of the observed macroscopic piezoelectricity, where charges are induced on the film surface as shear stress is applied to a PLLA film, is understood as follows [7, 9]. At the microscopic scale, some carboxyl bonds (C=O) rotate, as shown in Fig. 15.3. Shear stress is applied to the chain molecules in PLLA with a $10/3$ helical structure through its side chain. All the atoms in the chain molecules are displaced. In particular, the plane on which the CO bond and carboxyl bond (C=O) exist is rotated. As a result, the C=O bond, which has a larger dipole moment than the other bond, is displaced. The rotation of the C=O bond changes the polarization of the entire long-chain molecule, resulting in the shear piezoelectricity of PLLA.

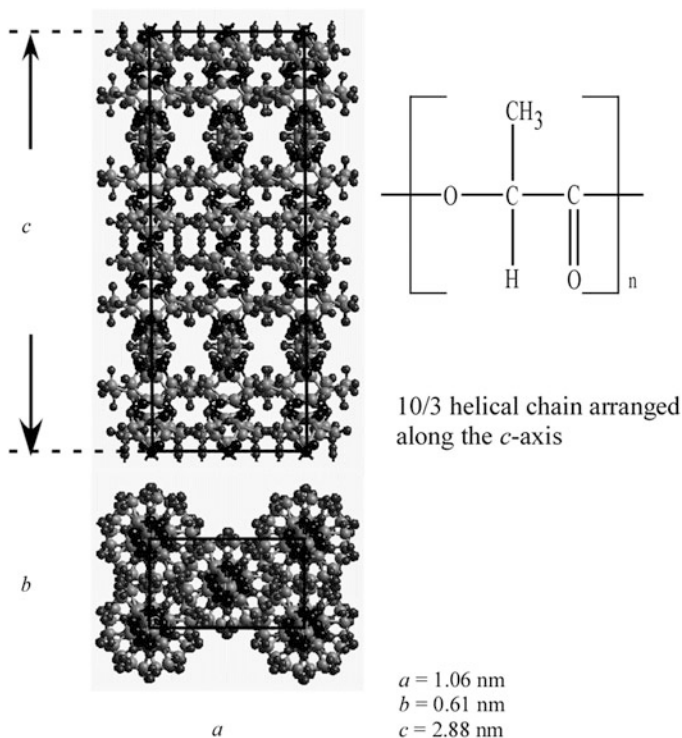


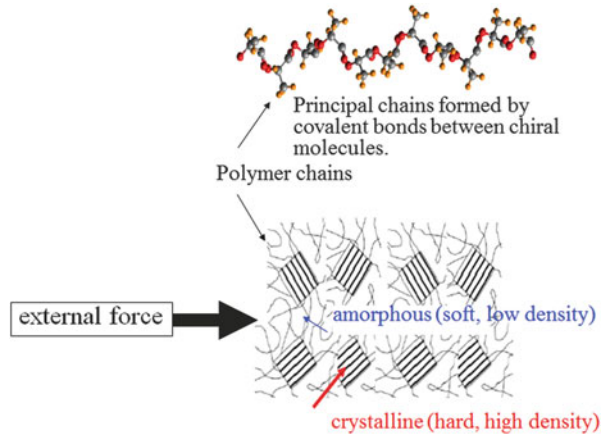
Fig. 15.3 Crystal structure of PLLA

We must change the notation to distinguish the new d_{14}^m , d_{25}^m , and d_{36}^m from the macroscopic piezoelectric tensors d_{14} and d_{36} in the entire PLLA film, as shown in Fig. 15.1. On the other hand, we must point out the difference between the point group in the crystal state, D_2 , and that in the entire film, D_∞ . The point group of an oriented PLLA film corresponds to the orientation distribution of the c -axis of each PLLA crystal around the x_3 -axis (drawing axis) in the entire PLLA film.

15.3.2.1 Improving the Piezoelectricity of PLLA Films

The piezoelectricity of PLLA is expressed when the atoms of the chain molecules move under the application of an external force. The atoms of a chain molecule are not easily displaced by an external force because the binding force of a covalent bond in PLLA is larger than that of an ionic bond in ceramics. On the other hand, an external force does not propagate through the amorphous region of PLLA. The power (force) is not sufficient to displace atoms in the chain molecules in the crystalline polymer film, as shown in Fig. 15.4. As a result, the piezoelectric constant is small. Improvement of the material properties, such as piezoelectricity and mechanical strength, and the development of processing technology for PLLA

Fig. 15.4 Higher-order structure of PLLA



films are key factors that will enable the increased use of PLLA films as flexible piezoelectric sensors. To improve the properties of PLLA films, it is necessary for the mechanical properties of the amorphous region to approach those of the crystallites. We have reported that changing the higher-order structure of PLLA by applying a high-pressure forging process [14] and supercritical CO_2 ($s\text{-CO}_2$) treatment [15] is an effective means of improving its piezoelectricity. However, these processes are difficult to apply to industrial production because their productivity is low. In the previous section, it was explained that PLLA films with 100 % crystallinity cannot be obtained through conventional methods. Thus, a one-to-one correspondence has not been found between the macroscale piezoelectric properties and the crystal characteristics. It has been observed that a PLLA film contains complex higher-order structures with various scales [16] in increasing order of size from single-chain molecules to a macroscopic film, including crystalline and amorphous regions and PLLA crystals. The existence of these complex higher-order structures in the PLLA film is the reason why the piezoelectric constant of PLLA is lower than those of conventional piezoelectric ceramics. Advanced technical skills are required to manufacture PLLA films with high piezoelectricity. To improve the piezoelectricity of PLLA films, we have employed a triblock copolymer with hard and soft parts to establish a new force propagation path between the crystallites while maintaining the application of stress to the crystallites [16]. The triblock copolymer is a pure acrylic symmetric block copolymer consisting of a center block of poly(butyl acrylate) (PBA), corresponding to its soft part, and two side blocks of poly(methyl methacrylate) (PMMA), corresponding to its hard part (hereafter denoted as PMMA-b-PBA-b-PMMA). The piezoelectric constant of most samples was more than 10 pC/N, more than twice that of conventional uniaxially drawn PLLA films. Also, the Young's modulus of most samples was from 1 to 2 GN/m². Also, we found that the glass transition temperature increases with increasing PMMA-b-PBA-b-PMMA content. It was found from atomic force microscope (AFM) images that, upon the addition of PMMA-b-PBA-b-PMMA, the

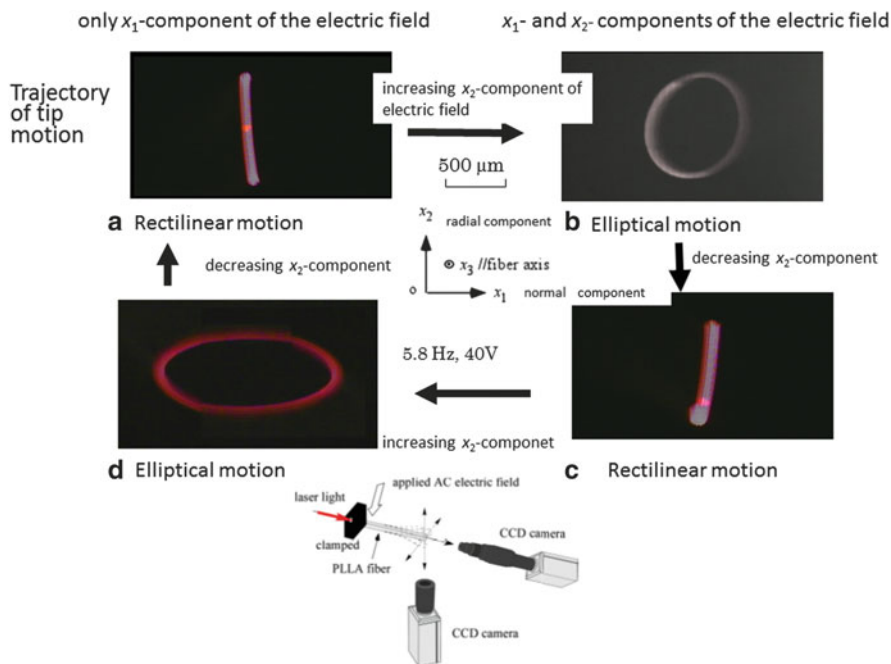


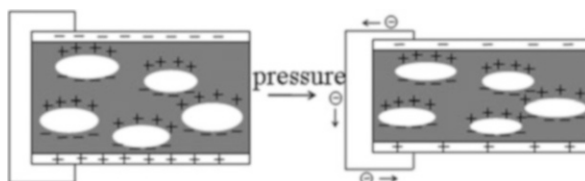
Fig. 15.5 Demonstration of PLLA fiber actuator

grain structure in the PLLA/[PMMA/PBA/PMMA] film became more homogenous than that in the reference PLLA film. Thus, to realize PLLA films with high piezoelectricity, it is important that a homogeneous higher-order structure is formed [16].

15.3.2.2 PLLA Fiber Actuator

We have investigated the application of chiral polymers to actuators with flexibility (soft actuators). However, before we can apply the shear piezoelectricity of a chiral polymer to a soft actuator, some difficult problems must be solved. For example, using shear strain, it is more difficult to include stretching and contraction than with tensile strain. Also, the chiral polymer membrane has a very small piezoelectric constant of at least two orders of magnitude less than that of inorganic ferroelectrics. However, we found that the PLLA fibers have the largest shear piezoelectricity (over 10 pC/N) among chiral polymers. Thus, we attempted to realize the electrically controlled complex motion of a PLLA fiber induced by its shear piezoelectricity such as that observed in an actuator. The results obtained were as follows [17–19]. The control of the bending motion of a PLLA fiber induced by its shear piezoelectricity upon applying an electric field was successfully demonstrated using the experimental apparatus shown in Fig. 15.5. We propagated laser light into

Fig. 15.6 Cellular PP electret



a PLLA fiber because of its similar transparency to polymeric optical fibers such as PMMA fibers. The high-speed charge-coupled device (CCD) camera used to record the motion faced the incident laser light. The CCD camera was focused on the tip of the PLLA fiber. Here, to measure the piezoelectric motion under the application of a controlled electric field, one end of the PLLA fiber was clamped, as shown in Fig. 15.5 [17]. In the experiments, a controlled sinusoidal voltage was applied to the PLLA fiber, and the direction of the transmitted laser light varied with the bending of PLLA fiber owing to its shear piezoelectric motion. The complex motion of the tip of the PLLA fiber could be controlled by applying an electric field with various directions and strengths. On the basis of these experimental results, we believe that there is a strong possibility of realizing a chiral polymeric fiber actuator using piezoelectric PLLA [17–19].

15.3.3 Cellular and Porous Electrets

Electrets, which retain residual polarization semi-permanently, are dielectrics. Usually, a polymer film with high insulation performance is used as an electret. A European research group [10, 20] has realized a large piezoelectric constant of 100 pC/N in an electret with a two-layer structure consisting of a hard film placed on a soft porous film. The piezoelectric mechanism in this electret is as follows. In this electret, the electric charge accumulates at the interface between the soft and hard layers. If pressure is applied to this film, electric charges are induced on both electrodes since the strains of the two layers are markedly different. As a result, high piezoelectricity in the electret is observed. The same research group also reported a soft electret using cellular PP with a large piezoelectric constant of up to 500 pC/N. A schematic diagram (sectional view) of the cellular PP electret is shown in Fig. 15.6 [10, 20]. Many long and slender holes exist in the film. Positive and negative electric charges were trapped on the upper and lower sides of each hole, respectively, when corona discharge was applied. Since the thickness of each hole markedly changes when pressure is applied in the thickness direction of the film, a large amount of electric charge is induced on both electrodes. Because of this unique structure, cellular PP has a large piezoelectric constant. Also, Fig. 15.6 shows the mechanism of the ferroelectric behavior of cellular PP [10, 20]. With increasing applied electric field, the sign of the trapped electric charges is reversed because of the plasma discharge induced within each hole. Therefore, the induced

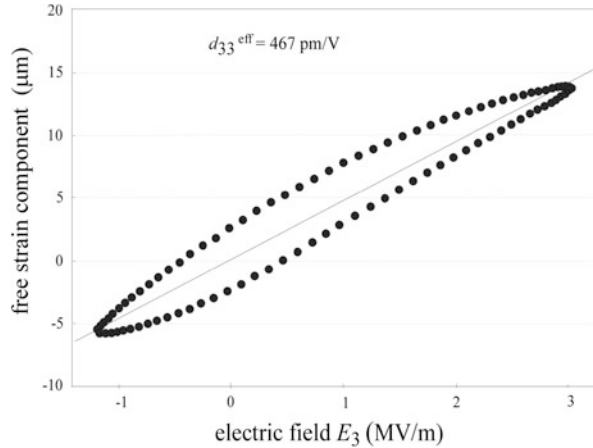
electric charge on the electrode exhibits hysteresis. In general, electrets have not exhibited ferroelectric hysteresis, and the ferroelectric hysteresis observed in cellular PP was the first case of its observation in an electret. Thus, cellular PP is as a ferroelectret. In ferroelectrets such as cellular PP, positive charges exist on one side of each hole and negative charges exist on the opposite side. The pairs of positive and negative charges result in a huge dipole moment. When a strong electric field is applied to cellular PP, ferroelectric hysteresis is observed because the positive and negative charges replace each other in each hole. Moreover, since the thickness of each hole markedly changes with the external force, the piezoelectric constant is very large [10, 20].

Many applications using the softness and high piezoelectricity of cellular PP have already been developed, for example, noncontact ultrasonic imaging, ultrasonic receivers, legless chair sensors, floor sensors for a wide area, musical instrument pickups, and broadband microphones. A new sensing device with flexibility and a large area has been developed that comprises cellular PP and an amorphous silicon field-effect transistor (FET) [20]. In this device, a 70- μm -thick cellular PP layer was bonded on a substrate fabricated from 50- μm -thick polyimide film using epoxy resin. The thickness of the bonding layer was 1–5 μm . This device is directly applicable as a piezoelectric film switch, a pressure sensor, and a microphone.

15.4 Polymeric Composite Systems

There has been considerable research on piezoelectric composite systems consisting of ceramics and polymer materials with high power and flexibility to realize novel actuators. In this section, the interesting topic of polymeric composite systems is introduced. A piezoelectric actuator called a macro-fiber composite (MFC), which was developed by Langley Laboratory of National Aeronautics and Space Administration (NASA), is a new device with unique performance [21–23]. The piezoelectric constant of the MFC, which is a plate with a thickness about 0.3 mm, is about ten times that of PVDF, and the MFC exhibits reasonable flexibility. The fabrication process of the MFC is as follows. First, after spinning PZT ceramic, bundles of PZT fibers are bonded by epoxy resin. Then, a large dc voltage is applied parallel to the fiber axis of the bundled PZT fibers to obtain the MFC [21–23]. Therefore, upon applying strain to the MFC, a voltage can be induced owing to the nonzero piezoelectric constant d_{33} . The piezoelectric strain of the MFC is dependent on the electric field, as shown in Fig. 15.7 [21–23]. The MFC can be used as an actuator and as a sensor [21–23], and it has been applied to systems in airplanes and space rockets. Typical examples of such applications are as follows. The MFC has been attached to the wings of a helicopter, and the vibration of the wings was controlled by the MFC acting as an actuator. As an advanced example, some MFCs has been installed in the tail unit of an airplane, and the vibration of the airplane was controlled by active control using the MFCs. Moreover, the MFC was successfully used to attenuate the vibration of the prop

Fig. 15.7 Induced strain of MCC under application of voltage



stick of a space shuttle. MFC sensors are used in space shuttles to inspect the bolt joints in sealed chambers and the pedestal of the rocket booster. Also, the MFC can be inserted in the washer of a bolt to control the torque at the time of bolting.

15.5 Summary

Piezoelectric polymers have now been studied for over half a century. The study of piezoelectric polymers has reached a stage where the piezoelectricity of a polymer film can be arbitrarily tailored. We believe that there is a strong possibility of realizing novel piezoelectric polymer actuators and sensors with flexibility, softness, transparency, and lightness.

References

1. Galetti P, DeRossi D, DeReggi A (1988) Medical applications of piezoelectric polymers. Gordon and Breach, New York
2. Wang T, Herbert J, Glass A (1988) The applications of ferroelectric polymers. Blackie, Glasgow
3. Nalwa H (ed) (1995) Ferroelectric polymers. Marcel Dekker, Inc., New York
4. Fukada E (2000) History and recent progress in piezoelectric polymers. IEEE Trans Ultrason Ferroelectr Freq Control 47:1110–1119
5. Uchino K (2000) Ferroelectric devices. Marcel Dekker, Inc., New York
6. Lang SB (2005) Guide to the literature of piezoelectricity and pyroelectricity. Ferroelectrics 321:91–204
7. Fukada E (2006) Recent developments of polar piezoelectric polymers. IEEE Trans Dielectr Electr Insul 13:1110–1119

8. Carpi F, Smela E (eds) (2009) Biomedical applications of electroactive polymer actuators. Wiley, Chichester
9. Tajitsu Y (2013) Fundamental study on improvement of piezoelectricity of poly(L-Lactic Acid) and its application to film actuators. *IEEE Trans Ultrason Ferroelectr Freq Control* 60:1625–1629
10. Bauer S, Gerhard R, Sessler G (2008) Ferroelectrets: soft electroactive foams for transducers. *Phys Today* 57:7–43
11. Nye J (1985) Physical properties of crystals. Clarendon, Oxford
12. Kobayashi J, Asahi T, Fukada E, Shikinami Y (1995) Structural and optical properties of polylactic acid. *J Appl Phys* 77:2957–2972
13. Aleman C, Lotz B, Puiggali J (2001) Crystal structure of the alpha-form of poly(L-lactide). *Macromolecules* 34:4795–4801
14. Tajitsu Y (2002) Giant optical rotatory power and light modulation by polylactic acid film. In: Bar-Cohen Y, Zhang QM, Fukada E, Bauer S, Chrisey DB, Danforth SC (eds) Materials research society symposium proceedings: topics in electroactive polymers and rapid prototyping, Boston, November 2001, vol 698. Warrendale, Pennsylvania, pp 125–136
15. Imoto K, Tahara K, Yamakita T, Tajitsu Y (2009) Piezoelectric motion of poly-L-lactic acid film improved by supercritical CO₂ treatment. *Jpn J Appl Phys* 48:09KE06
16. Shiomi Y, Onishi K, Nakiri T, Imoto K, Ariura F, Miyabo A, Date M, Fukada E, Tajitsu Y (2013) Improvement of piezoelectricity of poly(L-lactide) film by using acrylic symmetric block copolymer as additive. *Jpn J Appl Phys* 52:09KE02
17. Honda M, Hayashi K, Morii K, Kawai S, Morimoto Y, Tajitsu Y (2007) Piezoelectricity of chiral polymeric fibers. *Jpn J Appl Phys* 46:7122–7124
18. Sawano M, Tahara K, Orita Y, Nakayama M, Tajitsu Y (2008) New design of actuator using shear piezoelectricity of a chiral polymer, and prototype device. *Polym Int* 59:365–370
19. Ito S, Imoto K, Takai K, Kuroda S, Kamimura Y, Kataoka T, Kawai N, Date M, Fukada E, Tajitsu Y (2012) Sensing using piezoelectric chiral polymer fiber. *Jpn J Appl Phys* 51:09LD16
20. Graz I, Kaltenbrunner M, Keplinger C, Schwodiauer R, Bauer S, Lacour S, Wagner S (2006) Flexible ferroelectret field-effect transistor for large-area sensor skins and microphones. *Appl Phys Lett* 89:073501–073503
21. Mossi K, Selby G, Bryant M (1998) Tin-layer composite unimorph ferroelectric driver and sensor properties. *Mater Lett* 35:39–49
22. Williams R, Inman D, Schultz M, Hyer M, Wilkie W (2004) Nonlinear tensile and shear behaviour of macro fiber composite actuators. *J Comp Mater* 38:855–869
23. Blinzler B, Goldberg R, Binienda W (2012) Macroscale independently homogenized subcells for modeling braided composites. *AIAA J* 50:1873–1884

Part IV
Materials of Soft Actuators: Light-Driven
Soft Actuators

Chapter 16

Spiropyran-Functionalized Hydrogels

Kimio Sumaru, Toshiyuki Takagi, Shinji Sugiura, and Toshiyuki Kanamori

Abstract Photoresponsive actuators composed of a hydrogel functionalized with spiropyran are described. The hydrogel exhibits drastic shrinking in rapid response to blue light irradiation in acidic aqueous systems, and is examined for the application of several photoresponsive actuator systems. Rod-like hydrogel bends drastically after 1 s light irradiation, and microrelief is formed instantly on the hydrogel sheet by the micropatterned light irradiation. Based on these characteristics of the hydrogel, a photo-controllable microfluidic system is constructed with a hydrogel sheet, and the microchannels with arbitrary width, height and pathway are formed instantly by the micropatterned light irradiation. Also independent and parallel control of microvalve array by local light irradiation is demonstrated for a similar microfluidic system combined with fixed microchannel.

Keywords Hydrogel • Microchannel • Microrelief • Microvalve • Photoresponse • Rod bending • Spiropyran

16.1 Introduction

Light, as an electromagnetic wave with the wavelength less than 1 μm , can be irradiated locally to the arbitrary area with a resolution and precision of micrometer scale at any desired timing. Therefore, it is potentially a powerful control means to operate many microscopic objects in an independent or parallel manner. Due to the rapid progress in the optoelectronics in recent years, control technology by light with such advantages has been increasingly important and feasible. In these circumstances, we found that a hydrogel composed of a thermoresponsive polymer and a photochromic chromophore exhibited rapid and drastic shrinking in quick response to blue light irradiation and returned gradually to the former swollen state after stopping the irradiation, and this photo-responsive shrinking was repeatable [1]. Due to such a unique photoresponse based on the reversible photoisomerization, the hydrogel was expected to be a key material in the examination of

K. Sumaru (✉) • T. Takagi • S. Sugiura • T. Kanamori
National Institute of Advanced Industrial Science and Technology (AIST), Tsukuba Central
5, 1-1-1 Higashi, Tsukuba, Ibaraki 305-8565, Japan
e-mail: k.sumaru@aist.go.jp

wet and soft system, which can be controlled flexibly by light. In this chapter, we briefly review the past studies on photoresponsive hydrogels in the beginning, and describe the characteristics and the mechanism of the characteristic light-volume transduction of the hydrogel we developed. Then we discuss on its application as light-driven soft actuators with respect to several examples of our examinations.

16.2 Past Researches on Photoresponsive Hydrogels

Before describing the hydrogel we have studied, we review past important studies in this research field. In the pioneering research on photoresponsive hydrogels, Irie et al. reported that the volume of the hydrogel functionalized with leuco chromophore increased largely by UV irradiation [2, 3]. Although the photoresponsive swelling was very slow and degradation of leuco chromophore requiring high energy UV light was critical due to the side reaction, it was shown experimentally for the first time that the signal of light irradiation could be transduced to the change in the volume of material.

Without using photochromic reaction, Suzuki and Tanaka demonstrated the photoinduced shrinking by using the hydrogel composed of poly (N-isopropylacrylamide) (pNIPAAm), which was well known thermoresponsive polymer [4]. The pNIPAAm hydrogel colored with chlorophyll exhibited drastic shrinking in response to the intensive irradiation with visible light. This photoresponsive shrinking was induced by the temperature rise through the conversion of light absorbed by chlorophyll to heat (“thermal-mode”). Although there is a limitation in the spatial resolution due to inevitable influence of the thermal diffusion, such a thermal-mode scheme is important and useful in the implementation of photoresponsive actuators for its simplicity and robustness.

16.3 Spiropyran-Functionalized Hydrogel Actuators

16.3.1 Mechanism and Characteristics

As a trigger to start our study on the photoresponsive hydrogel introduced in this section, we found that pNIPAAm functionalized with spiropyran chromophore (pSpNIPAAm) dehydrated drastically upon blue light irradiation in acidic aqueous solution at around pH 3 [5]. First of all, we describe the mechanism of this photoresponsive dehydration, which is an elementary step of the characteristic photoresponsive shrinking of the pSpNIPAAm hydrogel. We observed that the pSpNIPAAm (functionalized with 1 mol% chromophore) acidic aqueous solution in the temperature range from 25 to 30 °C, which had been transparent and yellowish in the dark, turned colorless and turbid in quick response to the irradiation

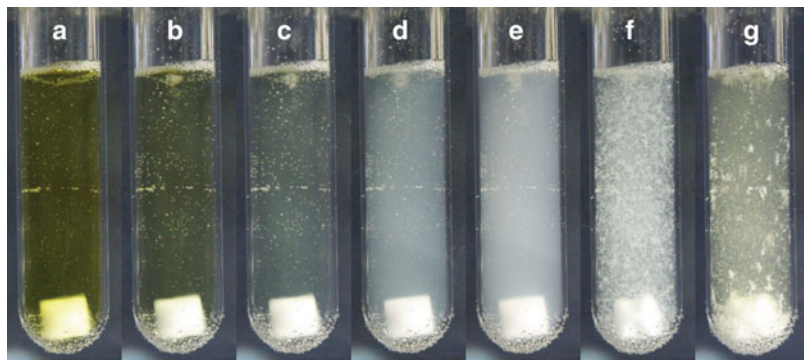


Fig. 16.1 Photoinduced change in the appearance of 0.10 wt% pSpNIPAAm aqueous solution accompanied by blue light irradiation at 31.5 °C. (a) Before the irradiation, after irradiation for (b) 20 s, (c) 25 s, (d) 30 s, (e) 35 s, (f) 50 s, and (g) 5 min after stopping irradiation and stirring (Reproduced with permission from Sumaru et al. [5]. Copyright 2004 American Chemical Society)

of with the wavelength of 436 nm, and the pSpNIPAAm precipitated in a subsequent few minutes (Fig. 16.1). After stopping the irradiation, the solution returned to its original yellowish transparent state in one or a few hours, and this reversible change was repeatable for at least ten times without any detectable degradation.

Then, in order to clarify the photoisomerization of the chromophore and accompanied change in its property triggering such a drastic dehydration of polymer at no more than 1 mol % functionalization, we carried out the detailed analysis on the absorbance spectra of the aqueous solution of spiropyran-functionalized polymers measured at various conditions of coexisting proton concentration in the dark or under light irradiation [6]. As a result, we found that most of the chromophores were in a protonated open-ring form, which was positively-charged and exhibited yellow color due to strong absorbance at around 420 nm in the acidic and dark condition. Irradiated with blue light absorbed by the chromophores in the state, whereas most of them isomerized effectively to a nonionic and hydrophobic form through the photo-induced ring closure and proton dissociation. Then most of the chromophores returned to the original protonated open-ring form gradually in an hour after stopping the irradiation. As the evidence of photoinduced proton dissociation, we observed the conductivity increase and the pH decrease in the aqueous solution of spiropyran-functionalized polymers in the sharp response to the light irradiation [6, 7]. From these observations, we concluded the following mechanism for the drastic photoinduced dehydration of pSpNIPAAm; the chromophores isomerized by light into a nonionic and hydrophobic form collapsed the hydration of pNIPAAm main chain while they stabilized it in a protonated open-ring form in the dark before irradiation. In addition to such a drastic change in the property of the chromophore accompanied by the loss of net charge, it was also very important that the hydration of pNIPAAm had been delicately balanced at slightly below its lower critical solution temperature (LCST) in aqueous solution.

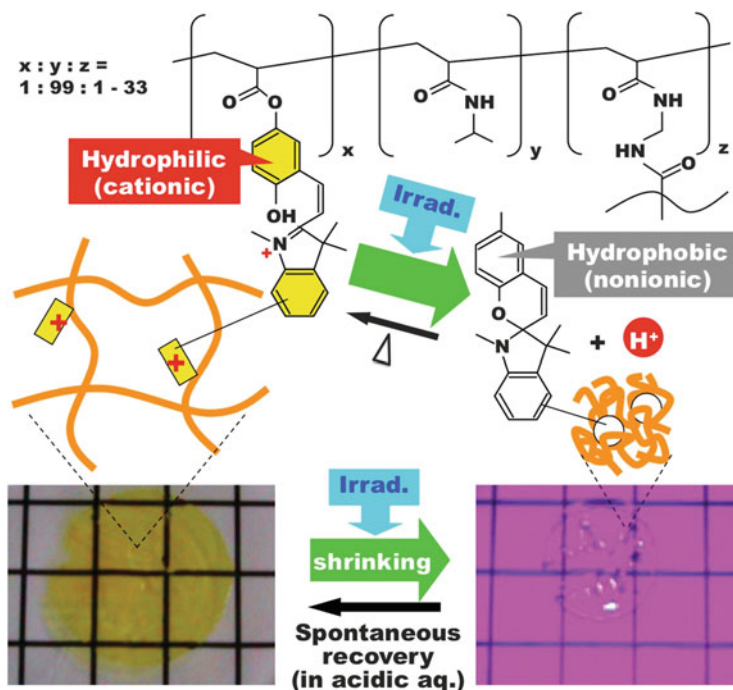


Fig. 16.2 Photo-induced shrinking of pSpNIPAAm hydrogel (Reproduced with permission from Sumaru et al. [8]. Copyright 2013 Taylor & Francis Group, LLC)

Based on these findings, we prepared the cross-linked hydrogel composed of the pSpNIPAAm expecting drastic and repeatable photoresponsive shrinking [1]. We observed that the hydrogel, which had been swollen in the acidic aqueous system, shrank by 70 % in quick response to blue light irradiation, and returned gradually in an hour to the former swollen state after stopping the irradiation. This drastic and quick photoresponsive shrinking was induced in the temperature range between 20 and 30 °C, and was repeatable for many times (Fig. 16.2). Since there had been no report examples of hydrogels showing such a rapid, drastic and repeatable volume change induced by visible light irradiation, the prepared hydrogel was expected to be a key material in constructing photo-controllable wet and soft systems.

16.3.2 Bending of Rod Actuator

To examine the control the macroscopic movement by light, we examined the photoinduced shape change of a rod-like hydrogel composed of pSpNIPAAm [9]. We prepared the rod-like hydrogel by synthesizing the pSpNIPAAm hydrogel

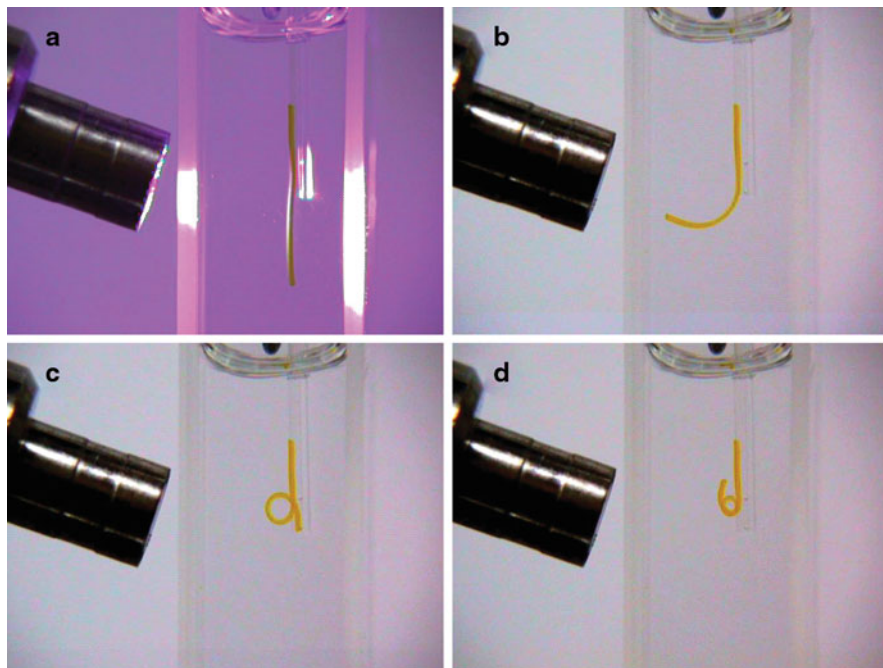


Fig. 16.3 Photo-induced bending of rod-like pSpNIPAAm hydrogels. (a) Under irradiation for 1 s, (b) 5 s, (c) 20 s and (d) 60 s after stopping irradiation

in a glass capillary tube with 0.3 mm inner diameter through radical copolymerization. The rod-like hydrogel was immersed in acidic aqueous solution containing 5 mM HCl with one of its end fixed. Then we irradiated blue light with 436 nm wavelength to one side of the rod-like hydrogel for a second. Figure 16.3 shows the change in its shape after the irradiation. Due to the asymmetric distribution of the light intensity provided by the irradiation to one side, the hydrogel shrank drastically in the directly irradiated side while it maintained the swelling state almost constant. As a result, the rod-like hydrogel started to bend toward the irradiated direction in response to the temporary irradiation, and continued bending even after stopping the irradiation until its end rotated by one and a half turns in a minute forming a loop with 1 mm inner diameter.

This feature of the huge deformation induced by the light irradiation for only one second was originated from the “memory effect” in which the distribution in the isomerization ratio brought by the temporary irradiation was maintained stably for a while due to the slow, but spontaneous back isomerization of the chromophore from the photo-induced closed-ring form described above. As a result, we had to wait long before next actuation, and the actual operation would be semi-one-directional although the process was basically reversible. With respect to this point, we examined the structure of spiropyran showing faster back isomerization, and found that methoxy substitution at 8' position accelerate the spontaneous back

isomerization by 20 times [10]. We confirmed that the rod-like hydrogel functionalized with the spiropyran with that structure bent only while the irradiation, stopped to bend when the irradiation was stopped, and then returned to the former state in a few minutes [9].

16.3.3 Surface Profile Modulation of Sheet Actuator

Further we examined on-demand control of the surface profile of the pSpNIPAAm hydrogel sheet in microscopic scale by light [11]. First, we prepared a pSpNIPAAm hydrogel sheet of initial thickness of about 250 μm on an acrylated glass surface so that the hydrogel sheet was attached covalently to the surface of the flat glass plate. In response to the local light irradiation, the thickness of the hydrogel sheet decreased rapidly in the irradiated area to the half of the original thickness in a few minutes. Even after stopping the irradiation, the hydrogel sheet retained the shrunk state stably for about 10 min, and then swelled gradually to the former swollen state.

Then, we applied the micropatterned irradiation onto the pSpNIPAAm hydrogel sheet by using a computer-controlled micropattern irradiation system. As a result, a very sharp microrelief was formed on the surface of hydrogel sheet right after micropatterned irradiation for 1 s. Figure 16.4 shows the demonstration of 3-dimensional control of the microrelief profile. A microrelief with 4-step height was formed readily just by irradiation 3 micropatterns sequentially. The resultant fine microrelief was retained stably after stopping irradiation for at least 10 min and then diminished gradually in 2 h. Since the temperature distribution in such a microscopic scale could not be maintained for as long as 10 min, this result indicated clearly that this microrelief formation was not based on the thermal-mode process.

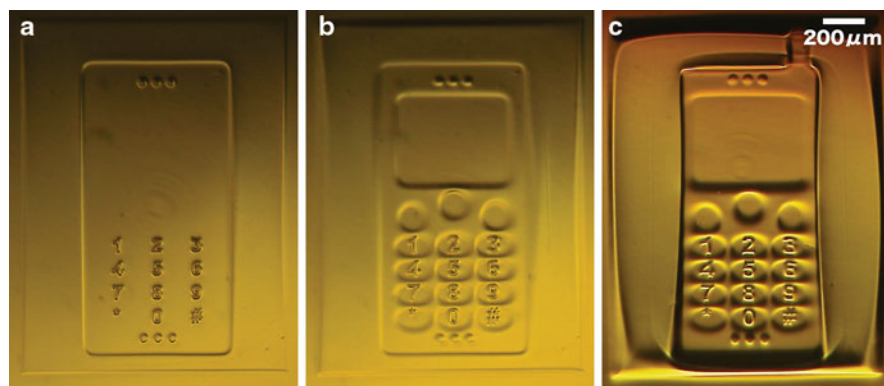


Fig. 16.4 Process of a microrelief formation by stepwise micropatterned irradiation on pSpNIPAAm hydrogel sheet. The photos show the microscopic images after (a) first, (b) second and (c) third irradiation

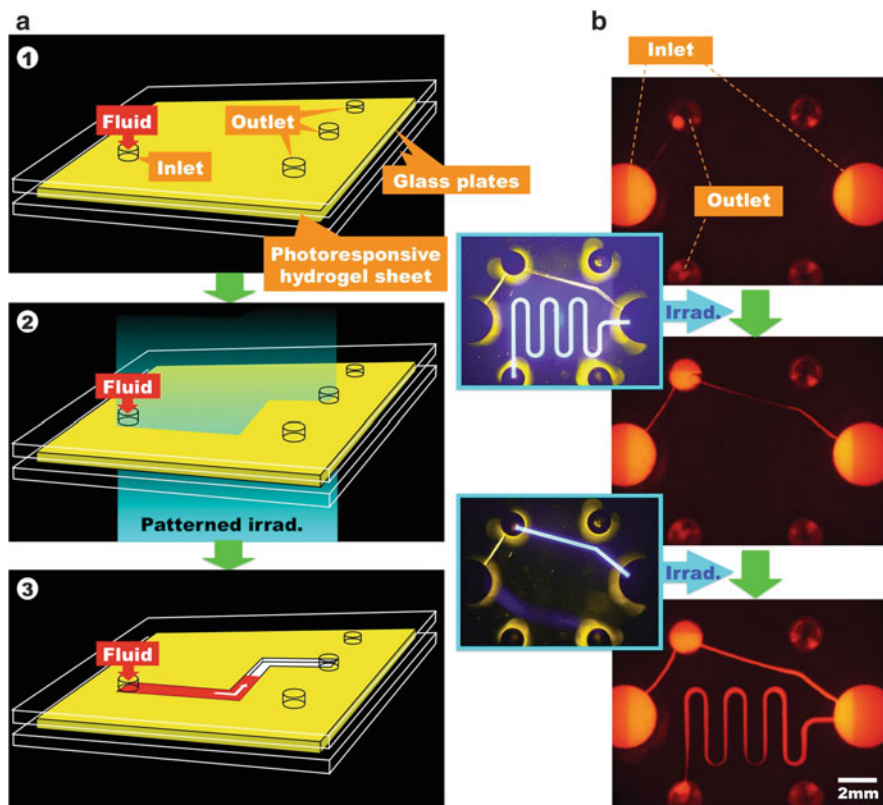


Fig. 16.5 Universal control of a microfluidic system by patterned light irradiation based on local thickness modulation of pSpNIPAAm hydrogel sheet. (a) Schematic illustration showing the structure and working principle (Reproduced with permission from Sumaru et al. [8]. Copyright 2013 Taylor & Francis Group, LLC). (b) Experimental demonstration (Reproduced with permission from Sugiura et al. [12]. Copyright 2013 Royal Society of Chemistry)

The microrelief was retained for longer time by interval irradiation of the micropattern or continuous irradiation at low intensity. In addition, we confirmed that microrelief was renewed by the irradiation of different micropattern in the area after the former microrelief had diminished.

16.3.4 On-demand Formation of Arbitrary Microchannel

Next we examined to apply this instant formation of microrelief induced by micropattern irradiation to a new microfluidic system with unconventional flexibility of design [12]. The working principle is shown in Fig. 16.5a. The system is constructed by mounting another glass plate with multiple inlet and outlet ports,

on the photoresponsive hydrogel sheet attached to a glass plate. When the light is irradiated in a pattern along an arbitrary path linking an arbitrary inlet port and an arbitrary outlet port, the hydrogel in the irradiated area shrinks and decreases its thickness. Resultantly, a microchannel is formed in an “on-demand” manner, and a fluid supplied from the inlet is led to the outlet along the microchannel. The depth of the formed microchannel is also controllable by choosing the irradiation intensity to induce the hydrogel shrinking. Accordingly, microchannels with an arbitrary width and depth along arbitrary path can be formed at an arbitrary timing.

We prepared actually a universal microfluidic system according to the above scheme, and carried out practical demonstrations. The experimental result was shown in Fig. 16.5b. Before irradiation, the fluorescent latex suspension supplied from an inlet port remained still exhibiting no detectable leakage. After micropatterned irradiation, a microchannel was formed instantly in the hydrogel sheet along the irradiated pattern, and the latex suspension started to flow through the newly-formed microchannels within a few minutes. Based on the conversion of light to the volume change of the photoresponsive hydrogel, a straight microchannel, a bent microchannel, a serpentine microchannel and branched microchannels were appended just by irradiating micropatterns stepwisely. This methodology in the scheme we proposed was expected to provide microfluidic systems with the highly flexible means to control mass transfer.

16.3.5 Individual Control of Microvalve Array

Further, we constructed an integrated photoresponsive microvalve array combining the basic design of microfluidic control utilizing a photoresponsive hydrogel sheet described above and conventional fixed microchannel [12]. The system was constructed by stacking a polydimethylsiloxane microchannel chip and a glass plate with the pairs of through-holes, on a photoresponsive hydrogel sheet attached to a glass plate, and ten photoresponsive microvalves were integrated within 1 cm² (Fig. 16.6). In response to the light irradiation in the area including a pair of through-holes, the hydrogel shrank locally inducing the opening of the microvalve, and the conduction was obtained from the inlet to the outlet resultantly. We confirmed that the individual microvalves were successfully controlled by local light irradiation while they had stopped stably the flow of fluid applied at the pressure of 5 kPa before the irradiation.

In the photoresponsive microvalves fabricated by incorporating pieces of the hydrogels at prescribed positions in microfluidic channel [14], quite high precision and reproducibility were required for the size and position of the hydrogel pieces to achieve both the stable stopping before irradiation and the prompt opening upon irradiation. On the other hand, such a requirement was easily cleared in the construction stacking a flat glass plate on a photoreponsive hydrogel sheet with uniform thickness attached to another flat glass plate.

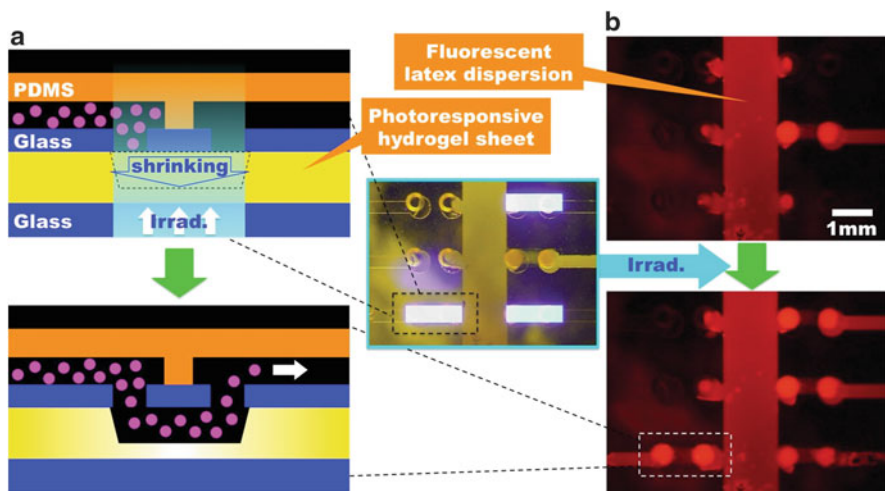


Fig. 16.6 Individual control of a microvalve array by patterned light irradiation based on local thickness modulation of pSpNIPAAm hydrogel sheet. (a) Schematic illustration showing the structure and working principle. (b) Experimental demonstration (Reproduced with permission from Sumaru et al. [8]. Copyright 2013 Taylor & Francis Group, LLC)

In clear contrast to the methods based on the conversion of light to heat [15, 16], the photoresponsive valve openings working in pure “photon mode” would be unsusceptible to thermal interference between adjacent microvalves even in such a case that many of highly integrated microvalves were manipulated at the same time. Further, unlike the methods based on the thermal melting [13, 17–19] and wettability change [20] of materials caused by light irradiation, fluid flow could be controlled reversibly.

16.4 Conclusions and Future Outlook

As mentioned in the beginning of this chapter, light can be applied locally and instantly from distant light source. Further, the rapid progress in the optoelectronics in recent years has been provided light-based control methods with a high compatibility with information technology, which is very important in their automations. Actually, a computer-controlled system composed of a digital micromirror device enabled micropattern irradiation with a significant flexibility and precision, which was essential especially in our examinations using the photoresponsive hydrogel sheets introduced above.

However, the hydrogel introduced in this chapter can be driven by light only in weakly acidic environment [6], and this has been a severe limitation to the biological utility. Recently, it was reported that volume change of a hydrogel was implemented by the photoresponsive change in the inclusion of azobenzene in

cyclodextrin, which was substantially unaffected by pH [21]. Due to these findings and future examination, on-demand control of the hydrogel via photoresponsive volume change as we demonstrated will be applied directly to the biological utility.

In addition to the photoresponsive hydrogels, we have developed various photoresponsive cell culture surfaces. Although only weak light having no direct influence to the cells is generally available in the areal micropatterned irradiation, these surfaces transduced such a weak light to the change in the surface properties which can affect the cultured cells [8, 22–25]. Combining these surfaces with the micropattern irradiation, we examined the manipulation of cultured cells as microscopic objects, and demonstrated the preparation of micropatterned co-culture and selective elimination of unwanted cells from the cells cultured on the substrate. We anticipate that photoresponsive polymer materials, which are wet and soft including those hydrogels introduced above, will contribute to the innovation of the technologies related to the chemistry and biology by the integration of the researches in this field.

Acknowledgements The authors gratefully acknowledge Dr. András Szilágyi and Dr. Taku Satoh for their cooperation in our research on the development and the application of photoresponsive hydrogels. The authors also acknowledge financial supports by Grant-in-Aids for Scientific Research (B) (No. 20350110) from Japan Society of Promotion of Science (JSPS), Industrial Technology Research Grant Program in 2002 and 2005 from the New Energy Development Organization (NEDO), and the Creation and Support Program for Start-ups from Universities in 2005 from Japan Science and Technology Agency (JST).

References

1. Sumaru K, Ohi K, Takagi T, Kanamori T, Shinbo T (2006) Photo-responsive properties of poly (N-isopropylacrylamide) hydrogel partly modified with spirobenzopyran. *Langmuir* 22:4353
2. Irie M, Kungwachakun D (1986) Photoresponsive polymers. 8. Reversible photostimulated dilation of polyacrylamide gels having triphenylmethane leuco derivatives. *Macromolecules* 19:2476
3. Mamada A, Tanaka T, Kungwachakun D, Irie M (1990) Photoinduced phase transition of gels. *Macromolecules* 23:1517
4. Suzuki A, Tanaka T (1990) Phase transition in polymer gels induced by visible light. *Nature* 346:345
5. Sumaru K, Kameda M, Kanamori T, Shinbo T (2004) Characteristic phase transition of aqueous solution of poly(N-isopropylacrylamide) functionalized with spirobenzopyran. *Macromolecules* 37:4949
6. Sumaru K, Takagi T, Satoh T, Kanamori T (2013) Photo-induced reversible proton dissociation of spirobenzopyran in aqueous systems. *J Photochem Photobiol A Chem* 261:46
7. Sumaru K, Kameda M, Kanamori T, Shinbo T (2004) Reversible and efficient proton dissociation of spirobenzopyran-functionalized poly(N-isopropylacrylamide) in aqueous solution triggered by light irradiation and temporary temperature rise. *Macromolecules* 37:7854
8. Sumaru K, Sugiura S, Takagi T, Kanamori T (2013) Photoresponsive polymers for control of cell bioassay systems. In: Dumitriu S, Popa V (eds) *Polymeric biomaterials*, 3rd edn. CRC Press, Boca Raton, pp 683–708

9. Satoh T, Sumaru K, Takagi T, Kanamori T (2011) Fast-reversible light-driven hydrogels consisting of spirobenzopyranfunctionalized poly(Nisopropylacrylamide). *Soft Mater* 7:8030
10. Satoh T, Sumaru K, Takagi T, Takai K, Kanamori T (2011) Isomerization of spirobenzopyrans bearing electron-donating and electron-withdrawing groups in acidic aqueous solutions. *Phys Chem Chem Phys* 13:7322
11. Szilagyí A, Sumaru K, Sugiura S, Takagi T, Shinbo T, Zrinyi M, Kanamori T (2007) Rewritable microrelief formation on photoresponsive hydrogel layers. *Chem Mater* 19:2730
12. Sugiura S, Szilagyí A, Sumaru K, Hattori K, Takagi T, Filipcsei G, Zrinyi M, Kanamori T (2009) On-demand microfluidic control by micropatterned light irradiation of a photoresponsive hydrogel sheet. *Lab Chip* 9:196
13. Moriguchi H, Wakamoto Y, Sugio Y, Takahashi K, Inoue I, Yasuda K (2002) An agar-microchamber cell-cultivation system: flexible change of microchamber shapes during cultivation by photo-thermal etching. *Lab Chip* 2:125
14. Sugiura S, Sumaru K, Ohi K, Hiroki K, Takagi T, Kanamori T (2007) Photoresponsive polymer gel microvalves controlled by local light irradiation. *Sens Actuators A Phys* 140:176
15. Sershen SR, Mensing GA, Ng M, Halas NJ, Beebe DJ, West JL (2005) Independent optical control of microfluidic valves formed from optomechanically responsive nanocomposite hydrogels. *Adv Mater* 17:1366
16. Chen G, Svec F, Knapp DR (2008) Light-actuated high pressure-resisting microvalve for on-chip flow control based on thermo-responsive nanostructured polymer. *Lab Chip* 8:1198
17. Hattori A, Moriguchi H, Ishiwata S, Yasuda K (2004) A 1480-nm/1064-nm dual wavelength photo-thermal etching system for non-contact three-dimensional microstructure generation into agar microculture chip. *Sens Actuators B Chem* 100:455
18. Park J-M, Cho Y-K, Lee B-S, Lee J-G, Ko C (2007) Multifunctional microvalves control by optical illumination on nanoheaters and its application in centrifugal microfluidic devices. *Lab Chip* 7:557
19. Hua Z, Pal R, Srivannavit O, Burns MA, Gulari E (2008) A light writable microfluidic flash memory: optically addressed actuator array with latched operation for microfluidic applications. *Lab Chip* 8:488
20. Caprioli L, Mele E, Angilè FE, Girardo S, Athanassiou A, Camposeo A, Cingolani R, Pisignano D (2007) Photocontrolled wettability changes in polymer microchannels doped with photochromic molecules. *Appl Phys Lett* 91:113113
21. Yamaguchi H, Kobayashi Y, Kobayashi R, Takashima Y, Hashidzume A, Harada A (2012) Photoswitchable gel assembly based on molecular recognition. *Nat Commun* 3:603
22. Tada Y, Sumaru K, Kameda M, Ohi K, Takagi T, Kanamori T, Yoshimi Y (2006) Development of a photoresponsive cell culture surfaces: regional enhancement of living cell adhesion induced by local light irradiation. *J Appl Polym Sci* 100:495
23. Edahiro J, Sumaru K, Tada Y, Ohi K, Takagi T, Kameda M, Shinbo T, Kanamori T, Yoshimi Y (2005) In-situ control of cell adhesion using photoresponsive culture surface. *Biomacromolecules* 6:970
24. Kikuchi K, Sumaru K, Edahiro J, Ooshima Y, Sugiura S, Takagi T, Kanamori T (2009) Stepwise assembly of micropatterned co-cultures using photoresponsive culture surfaces and its application to hepatic tissue arrays. *Biotechnol Bioeng* 100:552
25. Sumaru K, Kikuchi K, Takagi T, Yamaguchi M, Satoh T, Morishita K, Kanamori T (2013) On-demand killing of adherent cells on photo-acid-generating culture substrates. *Biotechnol Bioeng* 110:348

Chapter 17

Photomechanical Energy Conversion with Cross-Linked Liquid-Crystalline Polymers

Jun-ichi Mamiya

Abstract Cross-linked liquid-crystalline (LC) polymers with a photochromic moiety show photoinduced deformation with change in molecular shape and alignment of photochromic compounds. Molecular-level photoisomerization of the photochromic moieties can give rise to macroscopic deformation of the materials, allowing one to convert light energy directly into mechanical work. The photomechanical effects extend the applicability of azobenzene-containing polymers towards light-driven actuators and artificial muscles. Recently, the effect of structure–property relationships and crosslinking density on the photomechanical property of photochromic polymers was investigated. Various motions based on the photoinduced deformation of the LC polymers were achieved by forming the polymer materials. This chapter summarizes the recent progress in photoinduced movements and light-driven actuation property of the LC polymers, in particular cross-linked LC polymers with a photochromic property.

Keywords Cross-linked polymer • Energy conversion • Liquid crystal • Photochromism • Photomobile material

17.1 Introduction

To achieve a sustainable society, creation of new energy conversion system is an imperative issue. Sunlight holds an enormous potential as an abundant, free, and sustainable source. Development of solar cells using inorganic and organic materials is proceeded from various perspectives by many researchers [1]. Solar cells exchange light to electric energy by absorbing sunlight. On the other hands, a light-driven actuator is an energy transducer that can convert light to mechanical quantities such as displacement, strain, and stress [2]. Recently, photoinduced macroscopic movements of photochromic polymers were demonstrated

J.-i. Mamiya (✉)

Chemical Resources Laboratory, Tokyo Institute of Technology, R1-12, 4259, Nagatsuta, Midori-ku, Yokohama 226-8503, Japan

e-mail: jmamiya@polymer.res.titech.ac.jp

[3]. Photomechanical effect can be defined as reversible change in shape by absorption of light, which results in a significant macroscopic deformation and mechanical actuation. If light can be used as an external stimulus, remote control and rapid performance of deformation can be brought about. Furthermore, by the use of light as a stimulus, no wires and connections are necessary for the performance, which enables easy fabrication and lightweight of devices. Light-driven polymer actuators, therefore, are promising in a wide range of micro- and macro-scaled devices. Polymer materials meet requirements as artificial muscles due to its advantageous properties: high processability, flexibility, easy fabrication characteristics, and low manufacturing costs. Many actuators have been developed using polymers as base materials: polymer gels [4–6], conducting polymers [7–9], carbon nanotubes [10–13] and dielectric elastomers [14] that show response to various external stimuli. Polymer actuators have now reached the early stages of commercialization, particularly for use in MEMS devices [15]. The liquid-crystalline polymers have been considered for bioinspired materials and artificial muscle applications. Liquid-crystalline elastomers (LCEs) are unique materials due to their combination of the anisotropic aspects of LC phases and the rubber elasticity of polymer networks. There have been a number of excellent books and review articles published on the chemistry, physics and theory of LCEs [16–23]. LCEs have been a hot topic recently because one can induce large deformations of LCE materials by changing the alignment of mesogens in LCEs by external stimuli such as electric fields, temperature and light (Fig. 17.1). The LCEs contract along the alignment direction of mesogens by heating to the LC-isotropic phase transition temperature and cooling below the phase transition temperature they show expansion [24, 25]. Recently, not only contraction but various types of movements of the polymer actuators were achieved by control of shape of the polymers [26], molecular alignment of the mesogens [27], and polarization of light [28]. These characteristics are extremely useful as basic materials for soft actuators. However, weak mechanical strength and low stress generated by photoirradiation of the polymer films remain main issues. Now new polymer actuators that have overcome these problems are created.

In this chapter, we introduce the photomechanical energy conversion of polymers, gels, and LC elastomers aiming at an application for light-driven polymer actuators. We focused on classification and application of the polymer actuators, in particular light-driven polymer actuators.

17.2 Light-Driven Polymer Actuators

17.2.1 Photochromism

Photochromism is defined as a reversible photoinduced transformation of a molecule between two isomers whose absorption spectra are distinguishably different

Fig. 17.1 Concept and illustration of anisotropic deformation of liquid-crystalline polymers by external stimuli

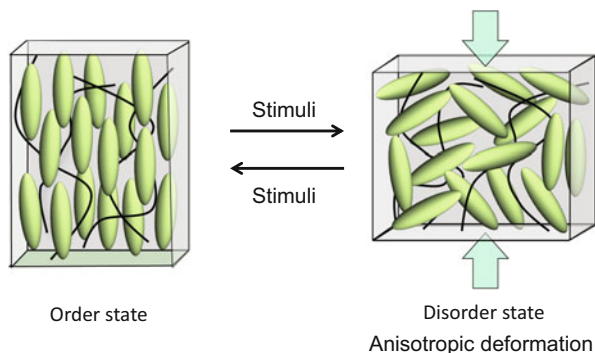


(Fig. 17.2a) [29]. Physical property of photochromic molecules can be controlled by photoinduced structural changes. An azobenzene, which is one of the common photochromic molecules, exhibits reversible *trans*–*cis* isomerization by light [30–32]. When amorphous azobenzene polymers were irradiated with a light interference pattern, mass transport took place, which leads to a sinusoidal surface pattern. The azobenzene-based polymer systems are excellent candidates for photomechanical actuation for many applications involving small size, localized actuation, remoteness of the power source. Deformation of polymer colloid particles containing azobenzenes by light was also reported by Wang et al. [33, 34]. The spherical polymer particles changed from a sphere into an ellipsoid upon exposure to interfering linearly polarized laser beams. The elongation of the particles was induced along the polarization direction of the laser beam due to gradient force of the laser irradiation.

Polymer gels have attracted much attention as artificial muscles because polymer gels contain fluid in their three-dimensional network structures, which provides softness, and exhibit a discontinuous change in volume between the swollen state and the collapsed state. This bistable characteristic of gels could be useful in the development of sensors and biomimetic materials. Prins et al. prepared a gel consisting of a low-molecular-weight chrysophenine dye and a water-swollen gel of poly(2-hydroxyethyl methacrylate) cross-linked with ethylene glycol dimethylacrylate [35]. The polymer gel was found to contract upon exposure to UV light. It is because the *trans*–*cis* isomerization causes a reduction in hydrophobicity of the dye, liberating the dyes from the polymer chain to the surrounding solution. The same manner of the photoinduced deformations was also observed in poly(methacrylic acid) gels on which chrysophenine was absorbed [36].

17.2.2 Photochemical Reaction

Shape memory polymers are materials which can be deformed and fixed in a temporary shape, from which they recover their original shape only exposed to

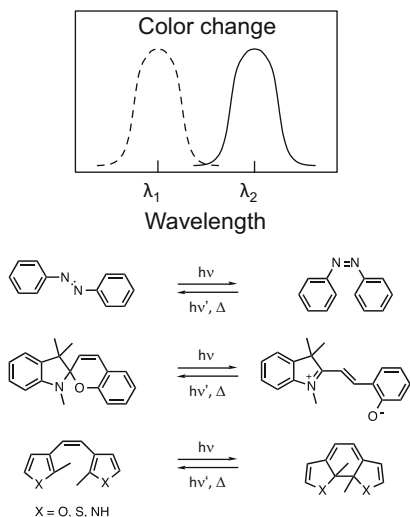
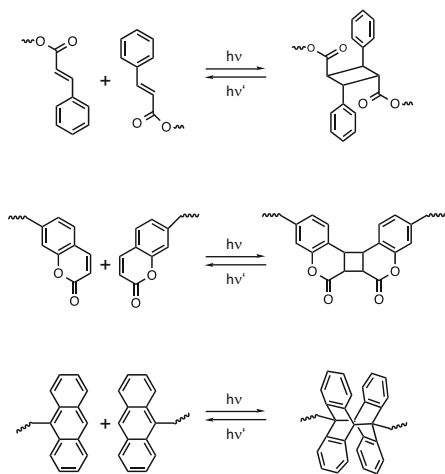
a Photochromism**b** Photochemical reactions

Fig. 17.2 (a) Change in absorption spectra and chemical structures of typical photochromic compounds and (b) reversible photodimerization and photocleavage under light irradiation at two different wavelengths

appropriate stimulus [37, 38]. The deformation is captured through a reversible morphology change induced by a suppression of molecular relaxation when the applied strain is released (through a glass transition or crystallization temperature). Photoinduced shape memory could be achieved via photochemistry. A number of studies have exploited the use of reversible photocrosslinking reactions based on the reversible photodimerization and photocleavage of such chromophores as cinnamoyl, coumarin, and anthracene (Fig. 17.2b). Lendlein et al. reported photoinduced shape memory polymers containing cinnamic acid groups. Exposure to UV light led to fixation of the elongated shape by a photoinduced [2+2] cycloaddition reaction after elongation of the polymer film by external force [37]. In photoresponsive polymers, the amorphous polymer network has coiled segments between two netpoints. When the polymer film is stretched, the coiled segments of the chains are elongated. Upon exposure to UV light, the elongated segments of the chains are partially fixed owing to formation of new photoresponsive crosslinks, resulting in an elongated new shape. The formed crosslinks can be reversibly cleaved by irradiation with UV light. As a result, the fixed elongated film can recover to the original permanent shape.

Zhao et al. have demonstrated that an amorphous polymer bearing coumarin groups can display large bending towards incident UV light [39]. Surface volume contraction generated by photocrosslinking of the polymer chains on one side of the films. Dimerization of two coumarin groups result in an increase in density only on the irradiated side of the films, leading to imbalanced surface stresses. Anthracene

is also a conventional photoreactive compound that undergoes [4+4] intermolecular dimerization upon irradiation with UV light. Polymer fibers with anthracene side groups were prepared, and their photomechanical properties were investigated [40]. Irradiation of the polymer fibers with UV light caused the fiber to bend toward the actinic light source. The bent fiber was undissolved in chloroform and maintained its shape for over 1 month. The photodimerization occurred more effectively with increasing temperature, suggesting that the enhancement of the mobility increased photoreactivity as well as macroscopic deformation.

17.2.3 Photothermal Effect

The photothermal effect means that light absorption of photoresponsive materials raises the internal temperature by non-radiative decay. Carbon nanotubes absorb a wide range of light from UV to near-infrared (NIR). The carbon nanotubes function as a nanoscale heat source to absorb the NIR light and then convert light energy to thermal energy. Polymer composites with both single and multi-walled carbon nanotubes have interesting insights into the possibility of designing nanomechanical systems [41–45]. The polymer composites with the carbon nanotubes produce a mechanical response to IR irradiation [41]. Large amplitude of photothermal actuation accomplished through heat transduction to polymer chains. Terentjev reported that change in temperature by IR heating reached $\Delta T \sim 15$ °C. This highlights an important question as to whether the response is due to photon absorption or heat transfer. It is difficult to distinguish these effects on IR actuation of the polymer composite. Photomechanical property of polyacrylamide-based fiber containing the graphite as a dye was investigated upon illumination with NIR [42]. The fiber bent and temperature increased about 10 °C during illumination. When the light source was turned off, the temperature returned to its initial value and the fiber recovered its initial shape. Energy conversion of NIR light into mechanical stress of the fiber with graphite was demonstrated by the photothermal effect. The photothermal effect has great potential as a driving force of polymer actuators.

17.3 Photomechanical Property of Cross-Linked Liquid-Crystalline Polymers

17.3.1 Fabrication of Cross-Linked LC Polymers

LCEs are usually lightly cross-linked networks. It has been known that the crosslinking density has a great influence on the macroscopic properties and the phase structures [46]. The mobility of chain segments is reduced with an increase of

crosslinking points and consequently the mobility of mesogens in the vicinity of a crosslink is suppressed. The concept of LCEs was first proposed by de Gennes [47] and the first example of the LCE was prepared by Finkelmann [48]. A variety of LCEs have been prepared with various structures of main chains in polymer networks and various kinds of mesogens. There are in general two ways of preparation of LCEs: two-step method [24, 49, 50] and one-step method [51]. In the former, well-defined weak networks are synthesized in the first step. These networks are deformed with a constant load to induce the network anisotropy. In the second reaction step, crosslinking reactions fix the network anisotropy. This two-step process benefits from the reproducibility of the induced network anisotropy before well-aligned elastomers are obtained. Uniformly aligned mesogenic monomers containing two reactive groups or prepolymers with reactive groups can be photochemically or thermally polymerized or cross-linked with the addition of non-mesogenic crosslinking agents, which gives rise to macroscopically aligned LCEs and anisotropic LC networks with different crosslinking densities with macroscopic orientation of the LC states fixed in the solid samples [52].

Broer et al. developed the one-step method to prepare highly oriented side-chain LC polymers [51]. This one-step process is in situ photopolymerization of macroscopically aligned LC monomers. When polymerization is carried out in ordered LC monomers, highly ordered polymers may be obtained.

17.3.2 Photoinduced Deformation of LC Polymers

If the LC polymers are cross-linked to fix LC phase structure, the LC polymers show macroscopic deformation by external stimuli due to strongly correlation between main chain and molecular alignment of the polymers. When exposure to the monodomain LC polymer film with UV light, the films bent toward an actinic light source along the rubbing direction, and the bent film reverted to the initial flat state after exposure to Vis light (Fig. 17.3). This bending and unbending behavior was reversible just by changing the wavelength of the incident light. The bending direction was also controlled by the alignment direction of mesogens [27, 28]. The cross-linked LC polymers deformed by disorder of molecular alignment with photoisomerization of the photochromic moiety and motion of the polymer chain. When the feed ratio of azobenzene moieties in the polymers decreases, the degree of the isomerization and penetration depth of incident light are enhanced, which leads to an effective photoinduced deformation. Mechanical stress induced by the deformation in the polymers was generated the times higher than that of natural muscles. This photoinduced bending could be induced repeatedly over 5,000 times [53].

Changes in birefringence and mechanical stress in the polymer films were investigated simultaneously to evaluate relationship between molecular alignment of the mesogens and contraction of the films upon photoinduced bending [54]. The intensity of a probe beam from He-Ne laser was monitored with a photodiode

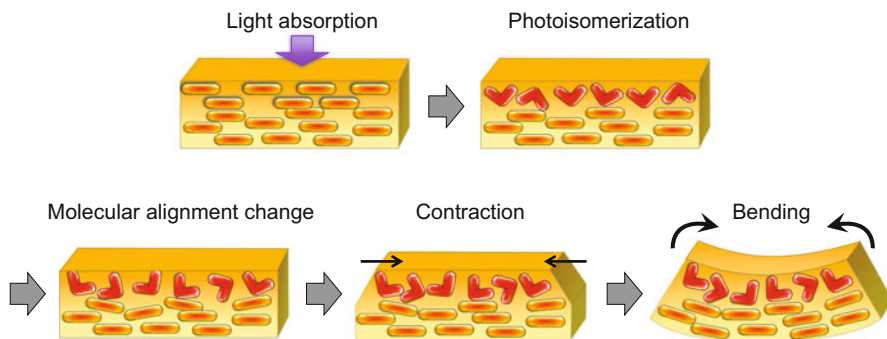


Fig. 17.3 Illustration of mechanism of photoinduced bending in the cross-linked liquid-crystalline polymers

through a polymer film between crossed polarizers (Fig. 17.4). The photoinduced stress was measured with thermomechanical analyzer by clamping the films at both ends along the alignment direction of the mesogens. The generated stress and the birefringence changes followed the same time dynamics. This means that the disorder of the molecular alignment induced by the *trans*–*cis* photoisomerization of the azobenzene moieties causes a mechanical stress in the cross-linked LC polymers. The photoinduced stress exhibited a clear dependence on the crosslinker concentration.

Recently, fast and large amplitude bending of an azobenzene polymer was induced, which leads to oscillations of the azobenzene cantilever. The oscillations of the polymers can be tuned on and off by switching polarization direction of a laser beam. The frequency of the photodriven oscillation is about 30 Hz [55]. The oscillation would be expected to cause photoinduced flying of the polymer films. In addition, large area molecular ordering of a polymer brush carrying azobenzene LCs could be fabricated by one-step hot-pressing with uniaxially stretched Teflon sheets, and the photomechanical response was achieved by the resultant wide-range bimorph configuration and photoisomerization of azobenzenes [56].

17.3.3 Light-Driven Polymer Actuators Based on Cross-Linked LC Polymers

There are many problems such as mechanical strength, shape and size of the polymers to apply the cross-linked LC polymers to the actuators. By preparing a laminated structure composed of a photoactive layer and a flexible polymer substrate, both photoresponsive and good mechanical properties can be provided simultaneously, leading to complicated movements of the films [57, 58]. A plastic belt was prepared by connecting both ends of the film laminated by thermal compression of the cross-linked LC polymer with azobenzene moiety and an

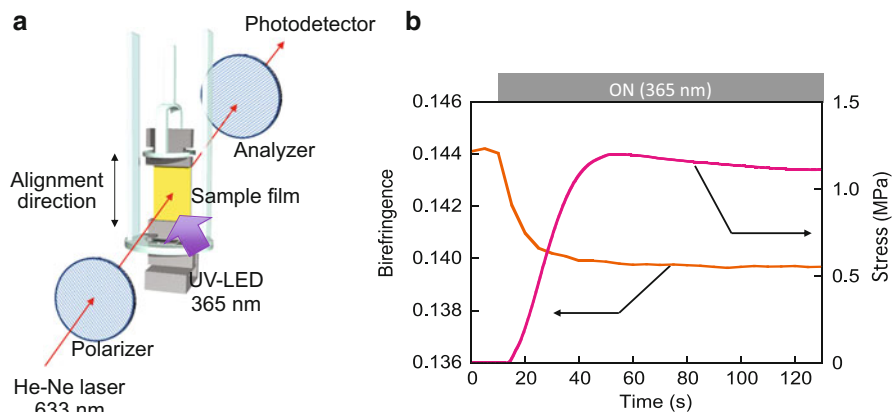


Fig. 17.4 Illustration of experimental setup for simultaneous evaluation of change in birefringence of the mesogens (a) and stress generated by photoinduced deformation of the polymers (b)

unstretched low-density polyethylene film (PE) with an adhesion layer. Simultaneous irradiation of the belt with UV and visible light induced a rotation of the belt to drive two pulleys in a one direction at room temperature (Fig. 17.5a). Contraction and expansion forces produced simultaneously at the different parts along the long axis of the belt give rise to the rotation of the pulleys and the belt with the same direction [57]. The rotation brings new parts of the belt to be exposed to UV and visible light, which enables the motor system to rotate continuously. By partially laminating with photoactive layer into a plastic substrate, the laminated films moved freely such as flexible robotic arm upon photoirradiation (Fig. 17.5b) [58]. Light-driven microrobots consisting of a photoactive polymer layer and PE film were fabricated. Photoinduced movements of the microrobots were achieved by the combination of the bilayer film with different initial shapes and molecular alignment and manipulated to pick, lift, move, and place a milligram-scale object by irradiating different parts of the microrobot [59].

All-polymer microdevices can be fabricated using lithographic techniques in combination with LC polymer actuators. LC monomers that are sensitive to two different wavelengths of light were deposited with ink-jet printer on a glass coated with polyvinyl alcohol (PVA). The reactive monomers can be cured after printing. The cilia released from the substrate by dissolving the PVA layer in water. The microactuators with different subunits can be selectively addressed by changing the wavelength of light. The artificial cilia have potential to create flow and mixing in wet environments such as lab-on-a-chip applications [60]. A two-dimensional microarray was fabricated from a cross-linked LC polymer by replica technique. After photoirradiation with UV light, the array showed a photoinduced deformation, leading to increase in the diameter of pillars. The microarray showed switchable behavior on reflection spectra by alternate irradiation of UV and Vis light due to the change in the order of the microarray. The reversible switching indicates that

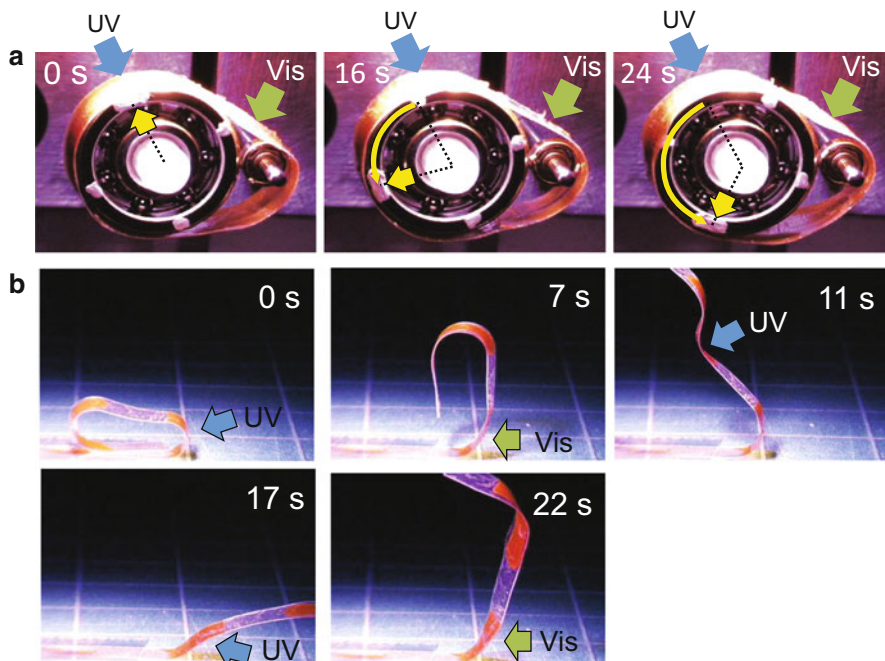


Fig. 17.5 Photographs of photoinduced rotation in a light-driven plastic motor (a) and photographs showing time profiles of flexible motion in a robotic arm (b) composed of cross-linked liquid-crystalline polymers and a polyethylene sheet

the cross-linked LC polymers with azobenzene moieties have potential applications in optical actuators [61].

Cross-linked LC polymer films were prepared by photopolymerization of aligned LC monomers in a glass cell. However, the glass cells must be carefully opened to afford freestanding LC films after polymerization. Crosslinking of polymers by means of electron beams (EB) has been widely used for industrial technology as an alternative to chemical methods for crosslinking in polymers. EB irradiation induced formation of intra- and inter-layer crosslinks in photoactive and substrate layers. Photomobile materials with adhesive-free bilayer structure were fabricated by EB irradiation directly [62]. After EB irradiation polymer films with bilayer structures became almost insoluble in chloroform, indicating the formation of crosslinks. The EB-cross-linked polymer films showed a reversible bending upon photoirradiation with no fatigue. A simple method for fabrication of photomobile polymer materials was proposed with large-area, smooth surface and controlled thickness of both photoactive and substrate layers.

In order to develop light-driven artificial muscles using the cross-linked LC polymers, polymer fibers containing azobenzene moieties were fabricated (Fig. 17.6). An LC copolymer was mixed with low-molecular-weight crosslinker containing two isocyanate moieties at the end of molecules, and the mixtures were

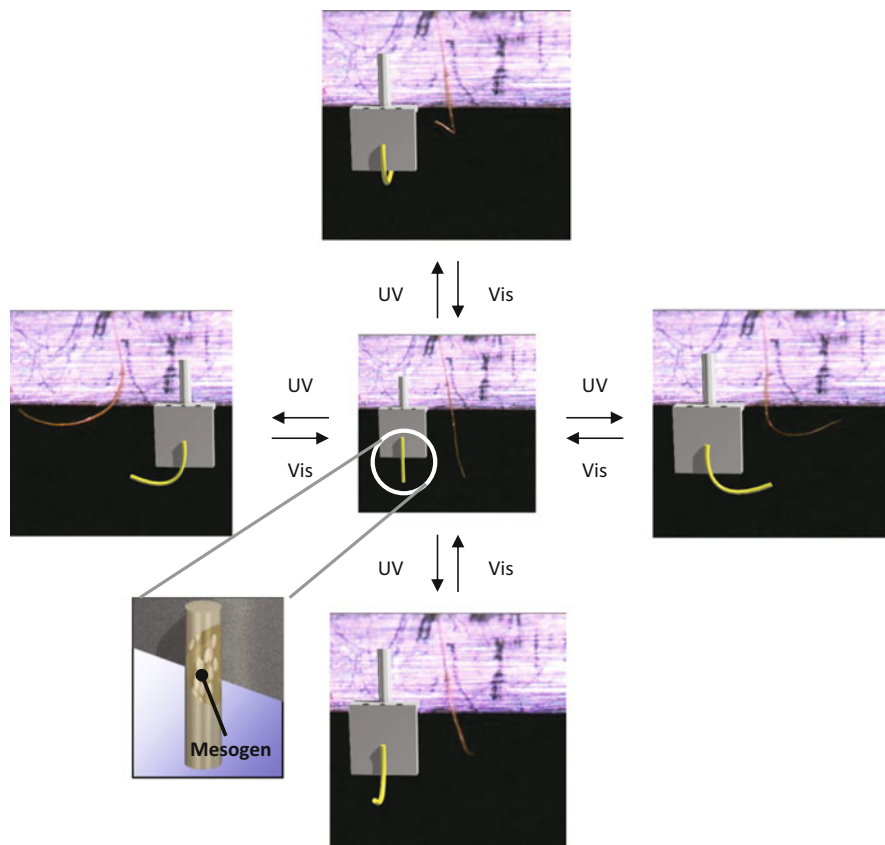


Fig. 17.6 Preparation of cross-linked liquid-crystalline polymer fibers and photographs of three-dimensional motions of light-driven artificial muscles

formed into fibers by pulling the mixtures with toothpick as quick as possible. The polymer fibers had uniaxial molecular alignment along the fiber axis. When the fibers were heated above the T_g of the polymers, the fibers contracted along the fiber axis. On the other hands, the fibers exhibited reversible bending above $90\text{ }^\circ\text{C}$ upon alternative irradiation with UV and visible light. Since the shape of the fibers was approximately cylindrical, the fiber could be irradiated with light under the same conditions from every side. The directional control in photomobility of the fibers may lead to potential applications in artificial muscles and polymer actuators [26].

17.4 Conclusion

Polymer actuators have a great potential for energy conversion systems due to excellent formability. In addition, light is an efficient power source for many applications, and can induced deformation of photoresponsive polymers remotely. In light-driven polymer actuators, structural change at a molecular level could be amplified to a macroscopic motion of the materials, leading to generation of mechanical stress through photomechanical energy conversion. Various materials and driving methods have been investigated for polymer actuators with mechanical properties. We described the photomechanical effects of the cross-linked liquid-crystalline polymers containing photoresponsive groups. Cross-linked liquid-crystalline polymers showing various movements by photoirradiation are promising materials for artificial muscles and soft actuators. Various macroscopic actuations have been achieved by skillful material design and fabrication of devices. However, many problems still remain unsolved, such as conversion efficiency and fatigue resistance. Various researchers will address the problems for these issues in the light-driven polymer actuators. New applications in medical and electrical fields will open up by continuous progress of the photomechanical energy conversion system.

References

1. Hagfeldt A, Boschloo G, Kloo L, Pettersson H (2010) Dye-sensitized solar cells. *Chem Rev* 110:6596–6663
2. Li M-H, Keller P, Li B, Wang X, Brunet M (2003) Light-driven side-on nematic elastomer actuators. *Adv Mater* 15:569–572
3. Ikeda T, Mamiya J, Yu Y (2007) Photomechanics of liquid-crystalline elastomers and other polymers. *Angew Chem Int Ed* 46:506–528
4. Osada Y, Okuzaki H, Hori H (1992) A polymer gel with electrically driven motility. *Nature* 355:242–244
5. Osada Y, Derossi DEE (2000) *Polymer sensors and actuators*. Springer, Berlin/Heidelberg
6. Osada Y, Khokhlov AR (2002) *Polymer gels and networks*. Marcel Dekker, New York
7. Baughman RH (1996) Conducting polymer artificial muscles. *Synth Met* 78:339–353
8. Lu W, Fadeev AG, Qi B, Smela E, Mattes BR, Ding J, Spinks GM, Mazurkiewicz J, Zhou D, Wallace GG, MacFarlane DR, Forsyth SA, Forsyth M (2002) Use of ionic liquids for π -conjugated polymer electrochemical devices. *Science* 297:983–987
9. Smela E (2003) Conjugated polymer actuators for biomedical applications. *Adv Mater* 15:481–494
10. Baughman RH, Cui C, Zakhidov AA, Iqbal Z, Barisci JN, Spinks GM, Wallace GG, Mazzoldi A, De Rossi D, Rinzler AG, Jaschinski O, Roth S, Kertesz M (1999) Carbon nanotube actuators. *Science* 284:1340–1344
11. Kim P, Lieber CM (1999) Nanotube nanotweezers. *Science* 286:2148–2150
12. Zhang Y, Iijima S (1999) Elastic response of carbon nanotube bundles to visible light. *Phys Rev Lett* 82:3472–3475
13. Spinks GM, Wallace GG, Fifield LS, Dalton LR, Mazzoldi A, De Rossi D, Khayrullin II, Baughman RH (2002) Pneumatic carbon nanotube actuators. *Adv Mater* 14:1728–1732

14. Pelrine R, Kornbluh R, Pei Q, Joseph J (2000) High-speed electrically actuated elastomers with strain greater than 100 %. *Science* 287:836–839
15. Liu C (2007) Recent developments in polymer MEMS. *Adv Mater* 19:3783–3790
16. Zentel R (1989) Liquid-crystalline elastomers. *Adv Mater* 10:321–329
17. Kelly SM (1995) Anisotropic networks. *J Mater Chem* 5:2047–2061
18. Warner M, Terentjev EM (1996) Nematic elastomers - a new state of matter? *Prog Polym Sci* 21:853–891
19. Cotton JP, Hardouin F (1997) Chain conformation of liquid crystalline polymers studied by small-angle neutron scattering. *Prog Polym Sci* 22:795–828
20. Terentjev EM (1999) Liquid-crystalline elastomers. *J Phys Condens Matter* 11:R239–R257
21. Xie P, Zhang R (2005) Liquid crystal elastomers, networks and gels: advanced smart materials. *J Mater Chem* 15:2529–2550
22. Finkelmann H (1998) Physical properties of liquid crystalline elastomers. Wiley-VCH, New York
23. Warner M, Terentjev EM (2003) Liquid crystal elastomers. Oxford University Press, UK
24. Küpfer J, Finkelmann H (1994) Liquid crystal elastomers: influence of the orientational distribution of the crosslinks on the phase behavior and reorientation processes. *Macromol Chem Phys* 195:1353–1367
25. Wernter H, Finkelmann H (2001) Liquid crystalline elastomers as artificial muscles. *e-Polymers* no. 013
26. Yoshino T, Kondo M, Mamiya J, Kinoshita M, Yu Y, Ikeda T (2010) Three-dimensional photomobility of crosslinked azobenzene liquid-crystalline polymer films. *Adv Mater* 22:1361–1363
27. Kondo M, Yu Y, Ikeda T (2006) How does the initial alignment of mesogens affect the photoinduced bending behavior of liquid-crystalline elastomers? *Angew Chem Int Ed* 45:1378–1382
28. Yu Y, Nakano M, Ikeda T (2003) Directed bending of a polymer film by light. *Nature* 425:145
29. Irie M (2000) Photochromism: memories and switches – introduction. *Chem Rev* 100:1683
30. Ikeda T (2003) Photomodulation of liquid crystal orientations for photonic applications. *J Mater Chem* 13:2037–2057
31. Natansohn A, Rochon P (2002) Photoinduced motions in azo-containing polymers. *Chem Rev* 102:4139–4175
32. Shibaev V, Bobrovsky A, Boiko N (2003) Photoactive liquid crystalline polymer systems with light-controllable structure and optical properties. *Prog Polym Sci* 28:729–836
33. Li Y, He Y, Tong X, Wang X (2005) Photoinduced deformation of amphiphilic azo polymer colloidal spheres. *J Am Chem Soc* 127:2402–2403
34. Li Y, He Y, Tong X, Wang X (2006) Stretching effect of linearly polarized Ar⁺ laser single-beam on azo polymer colloidal spheres. *Langmuir* 22:2288–2291
35. Van der Veen G, Prins W (1971) Photomechanical energy conversion in a polymer membrane. *Nat Phys Sci* 230:70–72
36. Van der Veen G, Prins W (1974) Photoregulation of polymer conformation by photoshromic moieties – I. Anionic ligand to an anionic polymer. *Photochem Photobiol* 19:191–196
37. Lendlein A, Kelch S (2002) Shape-memory polymers. *Angew Chem Int Ed* 41:2034–2057
38. Lendlein A, Jiang H, Jünger O, Langer R (2005) Light-induced shape-memory polymers. *Nature* 434:879–882
39. He J, Zhao Y, Zhao Y (2009) Photoinduced bending of a coumarin-containing supramolecular polymer. *Soft Mater* 5:308–310
40. Kondo M, Matsuda T, Fukae R, Kawatsuki N (2010) Photoinduced deformation of polymer fibers with anthracene side groups. *Chem Lett* 39:234–235
41. Ahir SV, Terentjev EM (2005) Photomechanical actuation in polymer-nanotube composites. *Nat Mater* 4:491–495

42. Nakata K, Sakai M, Ochiai T, Murakami T, Fujishima A (2012) Bending motion of a polyacrylamide/graphite fiber driven by a wide range of light from UV to NIR. *Mater Lett* 74:68–70
43. Torras N, Zinoviev KE, Marshall JE, Terentjev EM, Esteve J (2011) Bending kinetics of a photo-actuating nematic elastomer cantilever. *Appl Phys Lett* 99:254102
44. Wang W, Sun X, Wu W, Peng H, Yu Y (2012) Photoinduced deformation of cross-linked liquid-crystalline polymer film oriented by a highly aligned carbon nanotube sheet. *Angew Chem Int Ed* 51:4644–4647
45. Loomis J, Fan X, Khorsavi F, Xu P, Fletcher M, Cohn RW, Panchapakesan B (2013) Graphene/elastomer composite-based photo-thermal nanopositioners. *Sci Rep*. doi:10.1038/srep01900
46. Küpfer J, Nishikawa E, Finkelmann H (1994) Densely cross-linked liquid-crystal elastomers. *Polym Adv Technol* 5:110–115
47. de Gennes P-G (1975) *Physique moleculaire*. C R Acad Sci B 281:101–103
48. Finkelmann H, Kock H-J, Rehage G (1981) Investigation on liquid crystalline polysiloxanes 3 liquid crystalline elastomers – a new type of liquid crystalline material. *Makromol Chem Rapid Commun* 2:317–322
49. Zentel R, Reckert G (1986) Liquid crystalline elastomers based on liquid crystalline side group, main chain and combined polymers. *Makromol Chem* 187:1915–1926
50. Zentel R, Benalia M (1987) Stress-induced orientation in highly cross-linked liquid-crystalline side group polymers. *Makromol Chem* 188:665–674
51. Broer DJ, Finkelmann H, Kondo K (1988) In-situ photopolymerization of an oriented liquid-crystalline acrylate. *Makromol Chem* 189:185–194
52. Küpfer J, Finkelmann H (1991) Nematic liquid single crystal elastomers. *Makromol Chem Rapid Commun* 12:717–726
53. Kondo M, Miyasato R, Naka Y, Mamiya J, Kinoshita M, Yu Y, Barrett C, Ikeda T (2009) Photomechanical properties of azobenzene liquid-crystalline elastomers. *Liq Cryst* 36:1289–1293
54. Shimamura A, Priimagi A, Mamiya J, Ikeda T, Yu Y, Barrett CJ, Shishido A (2011) Simultaneous analysis of optical and mechanical properties of cross-linked azobenzene-containing liquid-crystalline polymer films. *ACS Appl Mater Interfaces* 3:4190–4196
55. White TJ, Tabiryan NV, Serak SV, Hrozhyk UA, Tondiglia VP, Koerner H, Vaia RA, Bunning TJ (2008) A high frequency photodriven polymer oscillator. *Soft Mater* 4:1796–1798
56. Hosono N, Kajitani T, Fukushima T, Ito K, Sasaki S, Takata M, Aida T (2010) Large-area three-dimensional molecular ordering of a polymer brush by one-step processing. *Science* 330:808–811
57. Yamada M, Kondo M, Mamiya J, Yu Y, Kinoshita M, Barrett CJ, Ikeda T (2008) Photomobile polymer materials: towards light-driven plastic motors. *Angew Chem Int Ed* 47:4986–4988
58. Yamada M, Kondo M, Miyasato R, Naka Y, Mamiya J, Kinoshita M, Shishido A, Yu Y, Barrett CJ, Ikeda T (2009) Photomobile polymer materials-various three-dimensional movements. *J Mater Chem* 19:60–62
59. Cheng F, Yin R, Zhang Y, Yen C, Yu Y (2010) Fully plastic microrobots which manipulate objects using only visible light. *Soft Mater* 6:3447–3449
60. van Oosten CL, Bastiaansen CWM, Broer DJ (2009) Printed artificial cilia from liquid-crystal network actuators modularly driven by light. *Nat Mater* 8:677–682
61. Yan Z, Ji X, Wu W, Wei J, Yu Y (2012) Light-switchable behavior of a microarray of azobenzene liquid crystal polymer induced by photodeformation. *Macromol Rapid Commun* 33:1362–1367
62. Naka Y, Mamiya J, Shishido A, Washio M, Ikeda T (2011) Direct fabrication of photomobile polymer materials with an adhesive-free bilayer structure by electron-beam irradiation. *J Mater Chem* 21:1681–1683

Chapter 18

Photoredox Reaction

Tetsu Tatsuma

Abstract A photoelectrochemical actuator based on poly(acrylic acid) gel loaded with TiO₂ nanoparticles and copper(II) ions swells in a water-ethanol mixed solution under ultraviolet (UV) light due to photocatalytic reduction of copper (II) to copper(0) nanoparticles and oxidation of ethanol. After removal of UV light, the hydrogel gradually shrinks again due to aerobic oxidation of copper nanoparticles to copper(II) ions. A photoelectrochemical actuator based on poly(acrylic acid) gel loaded with TiO₂ nanoparticles and silver(I) ions also swells in water under UV light due to photocatalytic reduction of silver(I) to silver(0) nanoparticles and oxidation of water. The hydrogel shrinks again under visible light due to re-oxidation of silver nanoparticles to silver(I) ions and reduction of oxygen molecules by the plasmon-induced charge separation. Partial swelling and shrinking of the hydrogel are also possible.

Keywords Electrochemical actuators • Localized surface plasmon resonance • Photoelectrochemical actuators • Plasmon-induced charge separation • TiO₂ photocatalysis

18.1 Introduction

Electrochemical actuators function based on redox reactions, which can be induced by relatively small changes in electrode potentials. The electrochemical actuators are therefore operated by a small voltage (e.g. about 1 V or smaller). Redox reactions can also be induced by light, by using semiconductors and or semiconductor coupled with metal nanoparticles. Since energy of generally available photons is around 1–3 eV, available photovoltage is lower than 3 V. Electrochemical actuators are therefore suitable for driving by the photons.

In this chapter, photoelectrochemical actuators in which interaction between polymer chains of a hydrogel is controlled by photoinduced reactions of a metal

T. Tatsuma (✉)

Institute of Industrial Science, University of Tokyo, Komaba, Meguro-ku,
Tokyo 153-8505, Japan

e-mail: tatsuma@iis.u-tokyo.ac.jp

ion/metal nanoparticle redox couple. This class of actuator exhibits extremely large volume changes, without wiring. Site-selective volume changes are also possible by focusing the light.

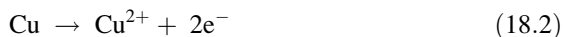
18.2 Electrochemical Swelling and Shrinking of the Gel

Swelling and shrinking of an ionic hydrogel can be controlled by redox reactions of ions entrapped in the gel. A typical example is a poly(acrylic acid) gel loaded with copper(II) ions [1]. A poly(acrylic acid) gel is swollen in pure water (Fig. 18.1, right). If it is loaded with copper(II) ions, it is shrunken if the concentration of copper(II) is higher than the threshold value, due to electrostatic interaction and coordination linkage between the carboxyl groups of the gel and copper(II) ions (Fig. 18.1, left).

If the hydrogel is immobilized on a flexible electrode surface, copper(II) ions can be reduced at the electrode surface to metallic copper(0), which is deposited on the electrode surface, by applying a potential more negative than the redox potential for the copper(II/0) couple (Eq. 18.1).



As a result, the hydrogel is swollen because the copper(II) concentration in the gel is lowered (Fig. 18.1, right). The hydrogel can be shrunken again by oxidizing the metallic copper(0) to copper(II) ions (Fig. 18.1, left) (Eq. 18.2).



The electrochemical control of the gel volume can also be explained in terms of electrochemical control of the copper(II) ion concentration in the gel. As shown in Fig. 18.2, the volume phase transition of the poly(acrylic acid) gel is induced at a certain concentration. The redox reaction changes the effective concentration of copper ion in the gel, resulting in the volume changes.

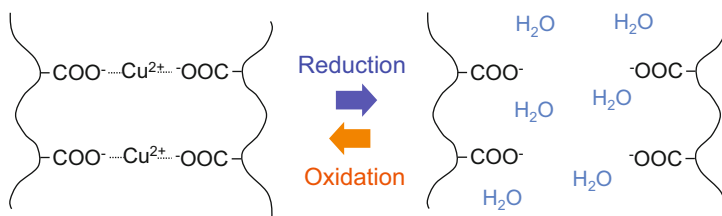
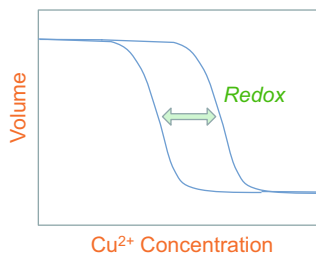


Fig. 18.1 Mechanisms of an electrochemical soft actuator based on poly(acrylic acid) gel and copper(II) ions. In the reduced state, copper(0) is deposited on the electrode

Fig. 18.2 Schematic graph for volume changes of the poly(acrylic acid) gel loaded with copper(II) ions



18.3 UV-Induced Swelling of the Gel and Shrinking in the Dark

Copper(II) ions can also be reduced photoelectrochemically by TiO₂ photocatalysis. TiO₂ is a colorless material, which absorbs no visible light. However, it absorbs ultraviolet (UV) light and electrons in its valence band are excited to its conduction band (Fig. 18.3) [2]. The excited electrons in the conduction band are consumed by ambient oxygen molecules or some metal ions. Oxygen molecules are reduced to hydrogen peroxide, superoxide anions, or water. Copper(II) ions are reduced to metallic copper(0) nanoparticles (Eq. 18.1). On the other hand, the positive holes in the valence band drive oxidation reactions of water or most organic compounds. Water molecules are oxidized to oxygen molecules and organic compounds are oxidized to, for instance, carbon dioxide molecules. Since TiO₂ drives those redox reactions under UV light, it is practically used as a photocatalyst.

In the present actuator, TiO₂ is used for reduction of copper(II) ions. However, electrons used for the reduction of copper(II) ions are supplied from electron donors such as water or organic compounds. In the present case, ethanol is used as the electron donor.

A poly(acrylic acid) gel containing TiO₂ nanoparticles is prepared, and is loaded with copper(II) ions [3]. The gel is shrunken by the loading (Figs. 18.4 and 18.5, left) as is the poly(acrylic acid) gel without TiO₂. If the shrunken gel is immersed in a mixture of water and ethanol and irradiated with UV light, TiO₂ absorbs light and drives redox reactions. The excited electrons in the conduction band are accepted by copper(II) ions, resulting in reduction to metallic copper(0) nanoparticles (Fig. 18.3). As a result, the shrunken gel is swollen because the copper (II) concentration is lowered in the gel and its color is changed from blue to dark brown (Figs. 18.4 and 18.5, right) due to plasmon resonance of the copper nanoparticles. The holes in the valence band are consumed chiefly by oxidation of ethanol (Fig. 18.3).

After the UV light is removed, the swollen gel is gradually shrunken again and the color of the gel reverts to blue (Figs. 18.4 and 18.5, left). These changes are explained in terms of re-oxidation of copper nanoparticles deposited on TiO₂ nanoparticles by dissolved oxygen in the solution (Eq. 18.3).

Fig. 18.3 Mechanisms of UV light-induced photocatalytic reactions at TiO_2

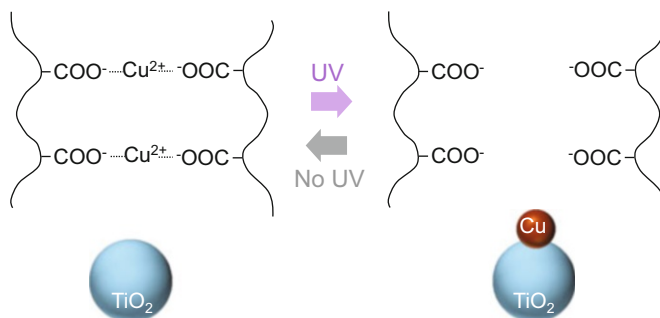
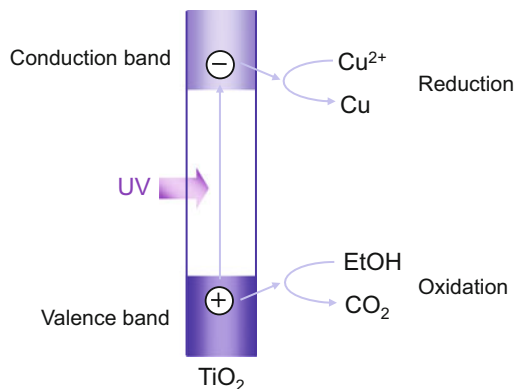


Fig. 18.4 Mechanisms of a photoelectrochemical soft actuator based on poly(acrylic acid) gel, TiO_2 nanoparticles, and copper(II) ions

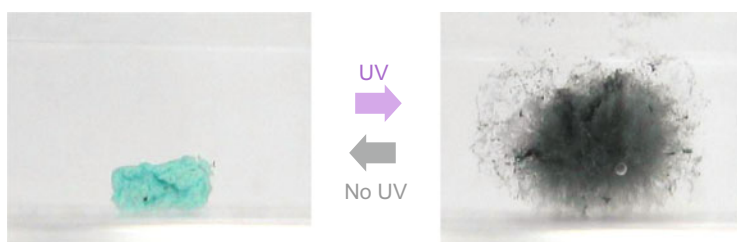
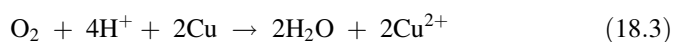


Fig. 18.5 Volume changes of the photoelectrochemical soft actuator based on poly(acrylic acid) gel, TiO_2 nanoparticles, and copper(II) ions



Actually, the gel is not shrunken in the absence of dissolved oxygen.

18.4 Partial Changes of the Gel Morphology

One of the most significant advantages of light-driven soft actuators is site-selective actuation. For instance, “ears” can be formed by using two UV spotlights and a “jelly bear” can be prepared (Fig. 18.6a). The ears disappear gradually after removal of the spotlights due to the aerobic re-oxidation of the copper nanoparticles [3].

In the case of a poly(acrylic acid) gel loaded partially with TiO_2 nanoparticles, irradiation of the whole gel with UV light results in partial swelling of the loaded part (Fig. 18.6b) [3].

18.5 Application of the Plasmonic Photoelectrochemistry to Actuators

In the case of the above-mentioned photoelectrochemical actuator based on the copper(II/0) redox reactions swells under UV light and shrinks after the UV light is shut off. To maintain the swollen state, the gel must be irradiated continuously. However, the continuous irradiation could be undesirable for certain uses. In

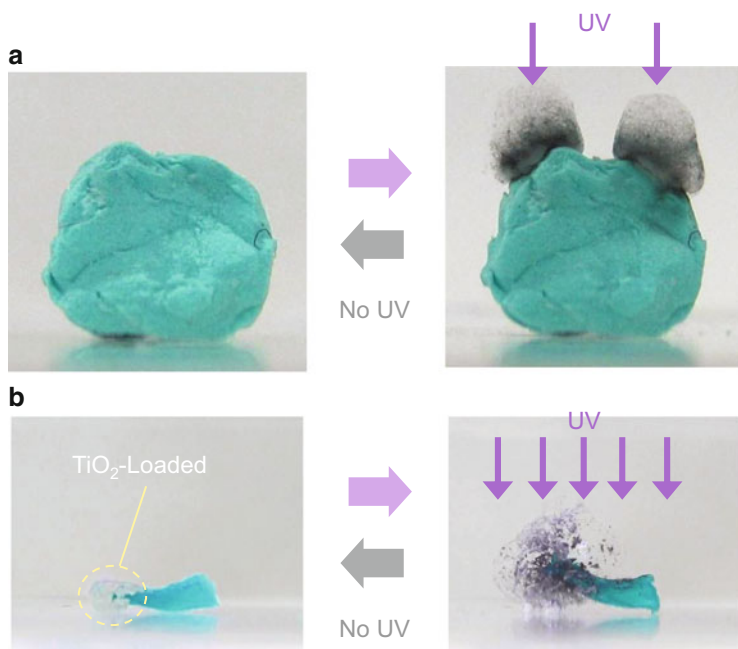


Fig. 18.6 Partial actuation of the photoelectrochemical soft actuator based on poly(acrylic acid) gel, TiO_2 nanoparticles, and copper(II) ions

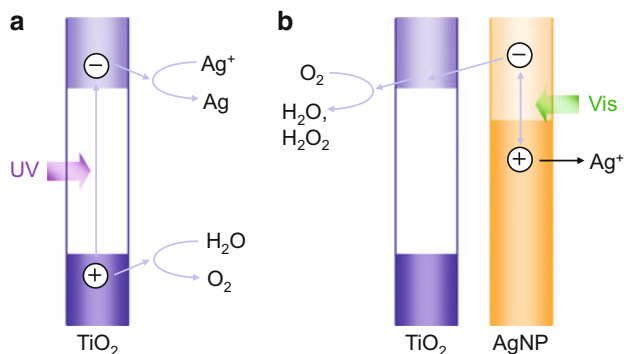
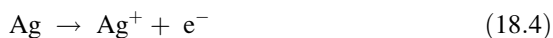


Fig. 18.7 Mechanisms of (a) UV light-induced photocatalytic reactions at TiO₂ and (b) plasmon-induced charge separation at the silver nanoparticle-TiO₂ interface

addition, excessive irradiation might damage polymer chains by photocatalytic reactions. Therefore, reversible reduction and oxidation reactions driven by light of different wavelengths are desired.

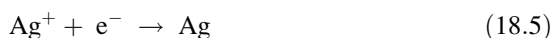
A poly(acrylic acid) gel is therefore coupled with a TiO₂-silver(I/0) system [4, 5]. The system is driven by plasmon-induced charge separation [5, 6]. It is known that gold, silver, and copper nanoparticles absorb visible light on the basis of localized surface plasmon resonance. Conduction electrons of the nanoparticles oscillate in resonance with oscillation of incident electromagnetic field. If the resonant plasmonic nanoparticles are in contact with a wide-bandgap semiconductor like TiO₂, electrons transfer from the resonant nanoparticles to the conduction band of the semiconductor (i.e. plasmon-induced charge separation) (Fig. 18.7b).

In the case of the gold nanoparticle, positive charges left on the nanoparticle as a result of the plasmon-induced charge separation are used for oxidation of electron donors such as alcohols [6]. On the other hand, in the case of copper nanoparticle, it is aerobically oxidized even in the dark, as described above [3], although the plasmon-induced charge separation could accelerate the oxidation [7]. In the case of silver, the charge separation results in oxidation and dissolution of silver nanoparticles (Eq. 18.4) (Fig. 18.7b) [8].



The electrons transferred to TiO₂ are consumed by reduction of oxygen molecules [8].

The dissolved silver(I) ions can be re-reduced to silver(0) nanoparticles by irradiating the TiO₂ with UV light (Eq. 18.5) (Fig. 18.7a).



The TiO₂-silver(I/0) system is therefore a pseudo-reversible redox system, oxidation of which is driven by visible light-induced plasmonic

photoelectrochemistry and reduction of which is driven by UV light-induced TiO_2 photocatalysis. The pseudo-reversible reaction is applied to, for instance, multicolor photochromism [4].

18.6 UV-Induced Swelling and Visible Light-Induced Shrinking of the Gel

Copper(II) ions of the above-mentioned light-driven hydrogel actuator are replaced with silver(I) ions (Fig. 18.8). The hydrogel with TiO_2 nanoparticles loaded with silver(I) ions [9] are initially shrunken (Figs. 18.8 and 18.9a left). The gel is immersed in water and irradiated with UV light. As a result, the hydrogel is swollen gradually (Figs. 18.8 and 18.9a right), as is the case for the hydrogel loaded with copper(II) ions. The hydrogel stop swelling upon the removal of UV light. The hydrogel does not shrink even when the gel is left in the dark for a while.

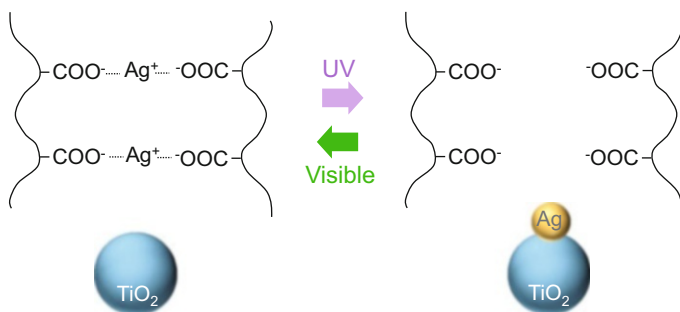


Fig. 18.8 Mechanisms of a photoelectrochemical soft actuator based on poly(acrylic acid) gel, TiO_2 nanoparticles, and silver(I) ions

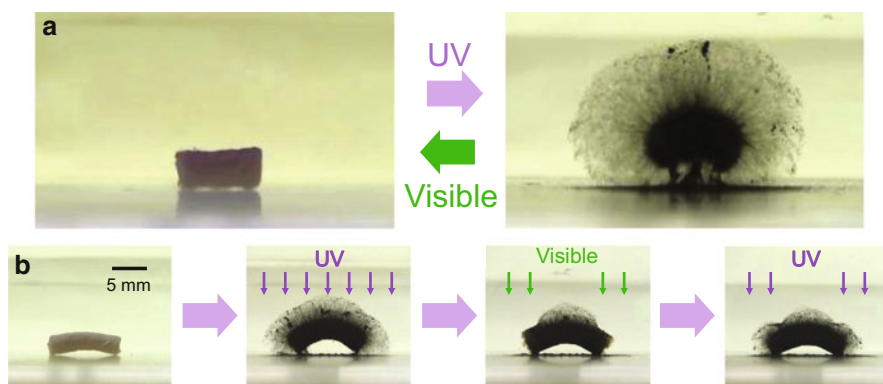


Fig. 18.9 (a) Volume changes and (b) partial actuation of the photoelectrochemical soft actuator based on poly(acrylic acid) gel, TiO_2 nanoparticles, and silver(I) ions

However, the hydrogel starts to shrink when it is irradiated with visible light, due to oxidative release of silver(I) ions from the silver nanoparticles as a result of the plasmon-induced charge separation (Figs. 18.8 and 18.9a left).

Partial swelling and shrinking of the hydrogel are also possible (Fig. 18.9b). When the upside of the gel is irradiated with UV light, the upside swells and the hydrogel bends. If the edges of the gel are irradiated with visible light, the edges shrink. The edges swell again by irradiating those with UV light. Thus, partial swelling and partial shrinking are both possible by UV and visible light, respectively.

18.7 Conclusions

The light-driven soft actuators can be developed by combining an ionic hydrogel with a photoinduced redox system. Those actuators could be applied to tactile graphic displays, rewritable stamps, active catheters, and microvalves for lab-on-a-chip and micro-TAS systems.

References

1. Takada K, Tanaka N, Tatsuma T (2005) A redox actuator based on reversible formation of bond between poly(acrylic acid) gel and Cu^{2+} ion. *J Electroanal Chem* 585:120–127. doi:[10.1016/j.jelechem.2005.07.024](https://doi.org/10.1016/j.jelechem.2005.07.024)
2. Fujishima A, Honda K (1972) Electrochemical photolysis of water at a semiconductor electrode. *Nature* 238:37–38. doi:[10.1038/238037a0](https://doi.org/10.1038/238037a0)
3. Takada K, Miyazaki T, Tanaka N, Tatsuma T (2006) Three-dimensional motion and transformation of a photoelectrochemical actuator. *Chem Commun* 2006:2024–2026. doi:[10.1039/b600442c](https://doi.org/10.1039/b600442c)
4. Ohko Y, Tatsuma T, Fujii T, Naoi K, Niwa C, Kubota Y, Fujishima A (2003) Multicolor photochromism of TiO_2 films loaded with Ag nanoparticles. *Nat Mater* 2:29–31. doi:[10.1038/nmat796](https://doi.org/10.1038/nmat796)
5. Tatsuma T (2013) Plasmonic photoelectrochemistry: functional materials based on photoinduced reversible redox reactions of metal nanoparticles. *Bull Chem Soc Jpn* 86:1–9. doi:[10.1246/bcsj.20120256](https://doi.org/10.1246/bcsj.20120256)
6. Tian Y, Tatsuma T (2005) Mechanisms and applications of plasmon-induced charge separation at TiO_2 films loaded with gold nanoparticles. *J Am Chem Soc* 127:7632–7637. doi:[10.1021/ja042192u](https://doi.org/10.1021/ja042192u)
7. Yamaguchi T, Kazuma E, Sakai N, Tatsuma T (2012) Photoelectrochemical responses from polymer-coated plasmonic copper nanoparticles on TiO_2 . *Chem Lett* 41:1340–1342. doi:[10.1246/cl.2012.1340](https://doi.org/10.1246/cl.2012.1340)
8. Kawahara K, Suzuki K, Ohko Y, Tatsuma T (2005) Electron transport in silver-semiconductor nanocomposite films exhibiting multicolor photochromism. *Phys Chem Chem Phys* 7:3851–3855. doi:[10.1039/b511489f](https://doi.org/10.1039/b511489f)
9. Tatsuma T, Takada T, Miyazaki T (2007) UV light-induced swelling and visible light-induced shrinking of a TiO_2 -containing redox gel. *Adv Mater* 19:1249–1251. doi:[10.1002/adma.200602386](https://doi.org/10.1002/adma.200602386)

Part V
Materials of Soft Actuators:
Magneto-Driven Soft Actuators

Chapter 19

Magnetic Fluid Composite Gels

Toshihiro Hirai

Abstract Polymer gels in which magnetic fluid is immobilized have been considered as a possible candidate of useful actuators or sensors. Particularly, remote actuation is possible without any harmful damage to the body in medical actuation. This means the system can also be applied for energy harvesting system, too. In this chapter the author summarize the some characteristics of magnetid fluid (or ferrofluid) which implies super paramagnetic property. Then the immobilization of these material in polymer gels, and the structural changes induced in the magnetic gels by applying magnetic field or gradient of magnetic field. Some applications of these gels are introduced in the last section.

Keywords Artificial muscle • Ferrofluid • Gel actuator • Hydrogel • Polyvinyl alcohol

19.1 Introduction

Material is magnetized by a magnetic field in general, and the magnitude and direction of the magnetization depend on the material. There are several types of magnetization [1]. Magnetism of ion is classified as ferromagnetic, diamagnetic, paramagnetic, and antimagnetic. Iron, a ferromagnetic material, is strongly magnetized in the direction of the magnetic field and is attracted strongly to the magnet, as is well known. Copper, a diamagnetic material, what is magnetized slightly in the direction opposite to the magnetic field, is repelled as a consequent. Some of the magnetic material, that is attracted to the magnet depending on the magnetic field, and weakly magnetized, and does not have any magnetization under the absence of magnetic field, is called paramagnetic. Antimagnetism is a magnetism induced by applying a magnetic field, is similar to paramagnetic, but the direction of the magnetization is opposite. Magnetic particles with diameter of nanometer size is monodomain particle and shows paramagnetic property. The particle coated with

T. Hirai (✉)

Fiber Innovation Incubator, Faculty of Textile Science and Technology,
Shinshu University, Nagano, Japan
e-mail: tohirai@shinshu-u.ac.jp

surfactant can be stabilized in solution, which is called magnetic fluid. The magnetic fluid shows characteristic functions [2]. These functions are attractive, and are very useful when we can apply them for the gels [3–5]. The polymer gel is defined as a material which has a shape and/or three dimensional network structure and not solubilize in solution with large amount solution that swell the network structure of polymer. In this chapter, the author will introduce the characteristics of the magnetic fluid, and some of the characteristic properties and functions of the gel. These information can be useful for the emerging research field of “magnetic fluid composite gel” [6–8].

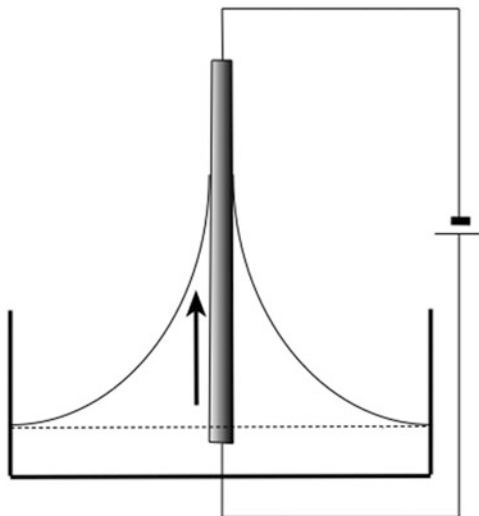
19.2 Magnetic Fluid

Now, nano-sized ferromagnetic particles can be stably suspended in a liquid, and the suspension is called magnetic fluid (or ferro-fluid). Nano particles with diameter of several nm implies super-paramagnetism. Super-paramagnetism is the magnetism that shows the characteristics of ferromagnetic under the presence of magnetic field, but paramagnetic under the absence of magnetic field. These properties can be observed in the dispersion of very small particles with single magnetic domain. Magnetic fluid is a fluidic material composed of colloidal dispersion of solid magnetic particles with the diameter of subdomain size suspended in a liquid medium with sufficient stability. We treated the concentration of the particle reaches ca. $10^{23}/\text{m}^3$. Magnetic fluid analogue was initially a dispersion of ferromagnetic particle with diameter of 0.5–40 μm suspended in a mineral oil. The dispersion aggregates under the magnetic field, and their application for the technical field was investigated. Magnetic fluid the author mentioned in this chapter is the dispersion of far smaller than the initial one with magnitude of thousandth, with particle diameter of 5–20 nm. The fluids of such fine particles can be not only stable from aggregation but also durable in storage. Moreover, they change physical properties reversibly by turning on-and-off the magnetic field, without having any residual magnetization, that is, they implies the characteristics of super paramagnetism.

19.2.1 *Various Hydrodynamic Characteristics and Behavior*

Various investigations on the interesting hydrodynamic behaviors of magnetic fluid were carried out. Some of them are introduced as follows.

Fig. 19.1 Conical meniscus formation. When electric current is applied to the rod wire, magnetic fluid climb up the wire



19.2.2 Deformation of Magnetic Fluid by Magnetic Field

19.2.2.1 Conical Meniscus

When an electrically conductive wire is dipped in the magnetic fluid and the current is turned on through the wire, the magnetic field climbs up the wire and forms a conical meniscus (Fig. 19.1) [9]. The mechanism was analyzed and quantitatively simulated [10, 11].

19.2.2.2 Swelling of the Interface by the Magnetic Field

When a magnetic field is applied to the interface of magnetic fluid, the surface of the magnetic fluid swells up with the magnitude of Δh (Fig. 19.2). The shape of the interface was analyzed and estimated.

19.2.2.3 Magnetic Levitation

Non-magnetic objects can be levitated in the magnetic fluid under the presence of a magnetic field (Fig. 19.3). And even in the absence of the magnetic field, permanent magnets can levitate by themselves [12]. Necessary conditions for magnetic levitation were discussed by Jones [13].

Fig. 19.2 Inflation of magnetic fluid in the magnetic field

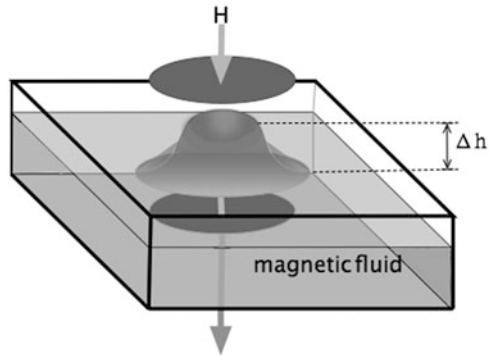
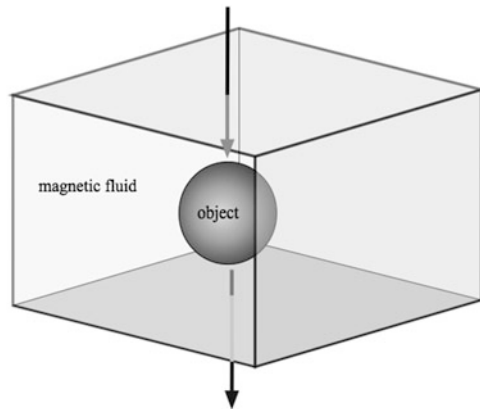


Fig. 19.3 Levitation of non-magnetic object in magnetid fluid



19.2.2.4 Application of Magnetic Fluid

These phenomena can be applied for the practical applications [2]. For instance [1], Seal Bearing: Sealing two compartments is the successful application of magnetic fluid. The mechanism is based on the levitation, and there is almost no wear compared with ball bearing [2]. Damper: Mechanical energy is dissipated as thermal energy using viscosity of the magnetic fluid [3], Transducer: Magnetic fluid can convert a property into another property, such as acoustic converter, pressure generator, position sensor, current detector, accelerometer, level meter, magneto sensor, and strain sensor etc. [4]. Actuators: Magnetic fluid can be used as actuators using fluid property and magneto-rheological phenomena. The device have advantage with actually no wearing as far as fluid characteristic holds.

19.3 Magnetic Fluid Composite Gels

From the viewpoint of gel materials, magnetic gels are considered to be attractive when we can utilize the functions of the magnetic fluid in gel as soft matter. We investigated the properties of these gels from the viewpoint of magneto-strictive actuator. Here the author will introduce some research on the magnetic fluid immobilized gels, and their characteristics. Recently the research field has been revived and getting back its popularity with the results as possible candidates for practical applications [14–17].

19.3.1 Magnetostriction of Magnetic Fluid Immobilized Gel

Various trials had been carried out in order to apply to the magnetic fluid for the gels. Zryinyi found phase transition phenomena in the magnetostrictive deformation process [4]. We show our cases on two types of the gels [3, 4, 18]. One is the gel in which the magnetic fluid immobilized as it is and the other gel is the magnetic particles immobilized under aggregated form. The gel network investigated is poly (vinyl alcohol) (PVA) with degree of polymerization of 1,700 and 7,600, and the solvents used for dispersion are water and dimethylsulfoxide (DMSO).

19.3.1.1 Immobilization Magnetic Fluid in the Gels

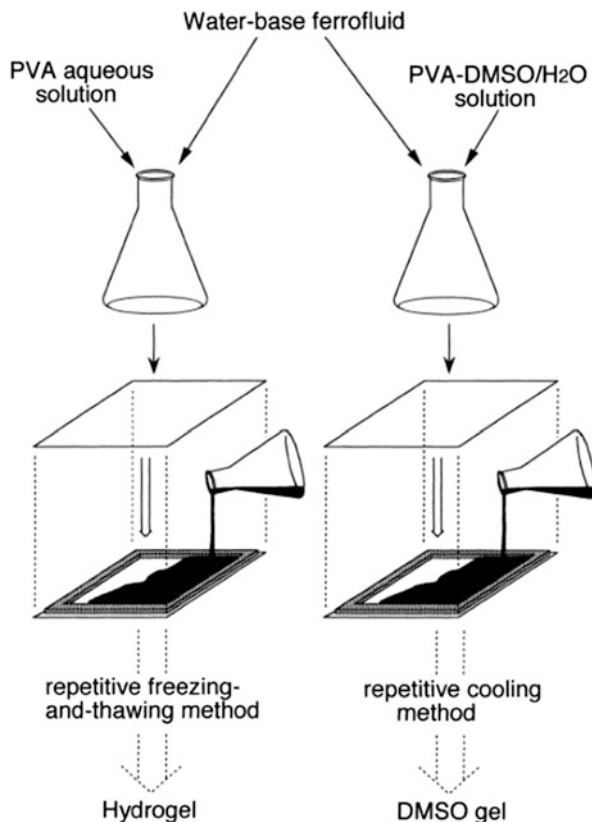
Magnetic fluid from magnetic particles coated or stabilized with oleic acid was dispersed in PVA aqueous solution, and the hydrogel was prepared by repeating freeze-and-thaw process (Fig. 19.4). When $DP = 1,700$ was employed, PVA concentration less than 8 % is not adequate since the gel is not bearable for use. However we employ PVA with higher molecularweight such as 7,600, polymer content can be depressed down to 4 %.

Magnetic fluid can also be immobilized in DMSO gel in aqueous DMSO by repetitive freeze-and-thaw method as the same manner as PVA hydrogel (Fig. 19.4). In both cases, no chemical cross-linking treatment is applied, and polymer gel network is formed only by physical cross-links. Elasticity of the gels can be controlled by varying polymer content and/or magnetic fluid content. Generally speaking, the increase of polymer concentration and degree of polymerization and the decrease of magnetic fluid content lead the stiffness of the gel higher.

19.3.1.2 Morphology of the Magnetic Fluid Gels

The gels, in which magnetic fluid was immobilized, showed almost the same in appearance as that of PVA hydrogels. By immobilizing the magnetic fluid, the surface of became slightly rough, but no big difference. The feature is almost the same in the case of magnetic fluid immobilized DMSO gel, too.

Fig. 19.4 Sample gel preparation methods

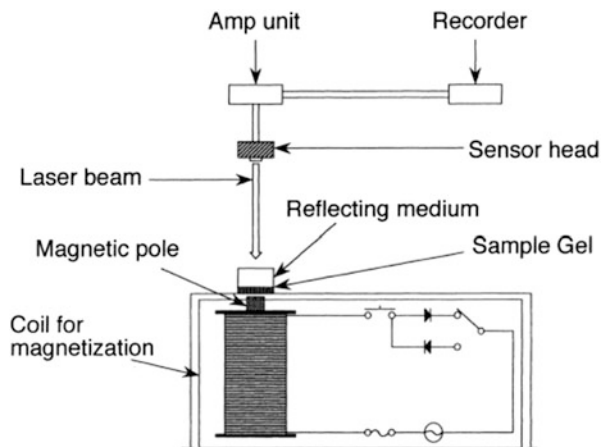


When these gels were immersed in acetone and changed into xerogels, the SEM image of them showed some difference. Xerogels from hydrogels are similar to each other irrespective of the presence of magnetic fluid, but those of from DMSO gels showed aggregate structure of magnetic particles. These difference reflect the difference in the gel structure though indirectly.

19.3.1.3 Magneto-Striction of Magnetic Fluid Immobilized Gel

Effect of magnetic fluid on the strain is measured as shown in Fig. 19.5. Magneto-striction are small in both gels, but the different characteristics are shown. Hydrogels expand in the direction of magnetic field, while DMSO gels shrink (Fig. 19.6). Both gels showed swift motility, that is, 90 % deformation was attained in 0.1 s. The deformation depends on the content of magnetic fluid, polymer content and elasticity of the gel. Such a big discrepancy between hydrogel and DMSO gel in the deformation direction is originated from the state of the magnetic fluid immobilized (Figs. 19.7, 19.8, and 19.9). Magnetorheological phenomena was detected in

Fig. 19.5 Measurement of strain induced by applying magnetic gradient



hydrogel although it is small (Fig. 19.10). From morphological observation, magnetic fluid forms aggregates in DMSO gel, while it is coated as homogeneous dispersion in the hydrogel. The difference suggests that the magnetic fluid keeps its original property as fluid. In the micrograph of xerogel of hydrogel, we could not see the aggregate suggesting the magnetic fluid is occluded in the PVA network homogeneously. In the DMSO gel, aggregates of magnetic fluid is clearly observed in SEM. For PVA hydrogel, little difference was observed in secondary electron image (SEI) and backscattered electron image (BEI), while SEI and BEI showed difference in DMSO gel, and suggested the magnetite localization or aggregation in the gel. From TEM observation, the magnetic particle in the magnetic fluid has the size of 5–20 nm. The magnetic fluid of the size distribution has super paramagnetic property, and been known to show the expansion in the direction of the magnetic field by orientation and chain alignment formation in the parallel direction of the magnetic field or the gradient of the field. The deformation of hydrogel observed in our case can be explained by the nature of the magnetic fluid with super paramagnetic property. While in the case of DMSO gel, the contractile deformation in the direction of the magnetic field can be explained according to the phenomena of the ferromagnetic aggregates.

19.3.2 Structural Change of Magnetic Fluid Gels Induced by Magnetic Field [19]

The magnetic gels deforms in different manner, depending on the mode of immobilization. We carried out direct observation of the structural deformation of the gels under the magnetic field by small angle X-ray scattering. The information is useful for designing the magnetic field sensitive gel materials. Sample gels were hydrogel and DMSO gel, the contents of magnetic fluid were 5 and 25 %. Higher

Fig. 19.6 Strain induced in hydrogel and DMSO gel by applying magnetic field gradient. (a) hydrogel (PVA:8 wt%) expand in the direction of magnetic field. (b) DMSO gel (PVA:8 wt%) and (c) DMSO gel (PVA:4 wt%) shrinks in the direction. At room temperature. Magnetic field: 1.26×10^4 A/m

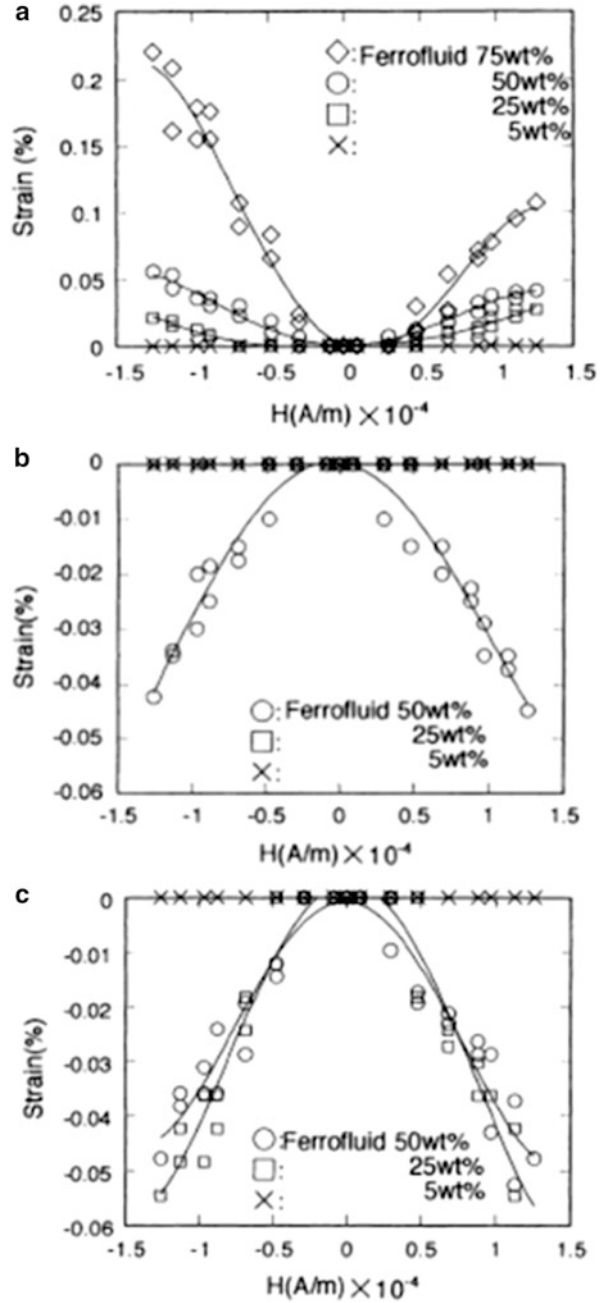


Fig. 19.7 Effect of elasticity on ferrofluid content. PVA content was fixed. DMSO gel is stiffer than hydrogel

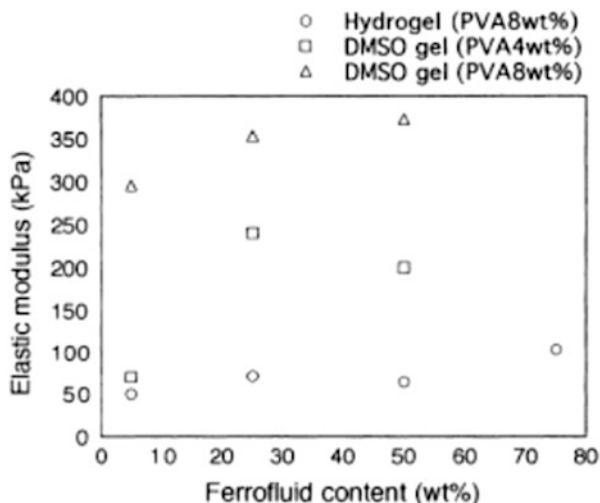
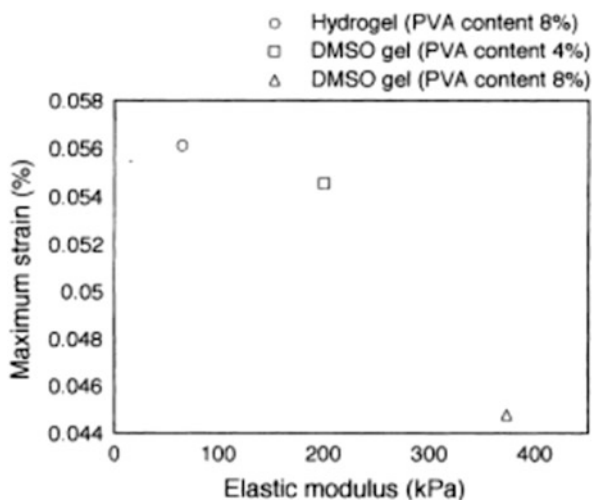
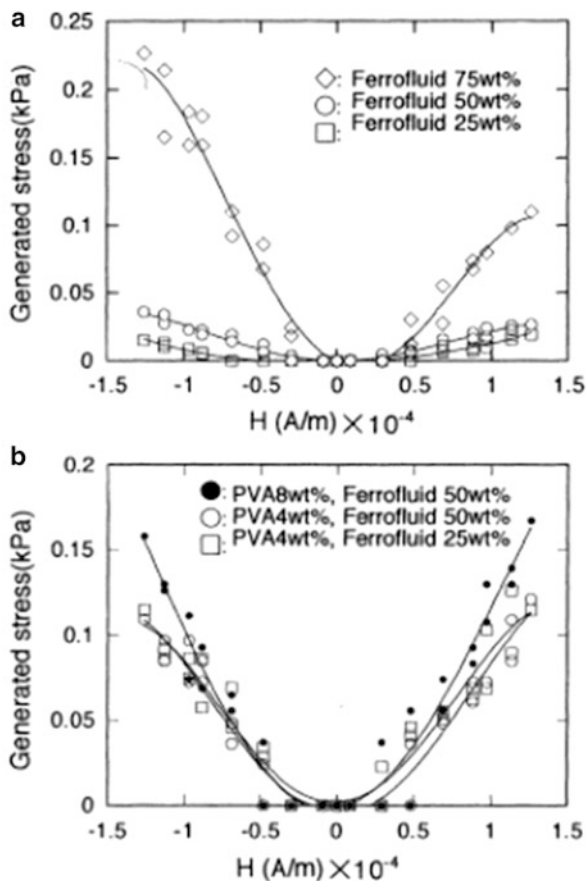


Fig. 19.8 Strain at break depends on modulus of the gel. Hydrogel showed the highest elongation among the three samples. Ferrofluid content = 50 wt%



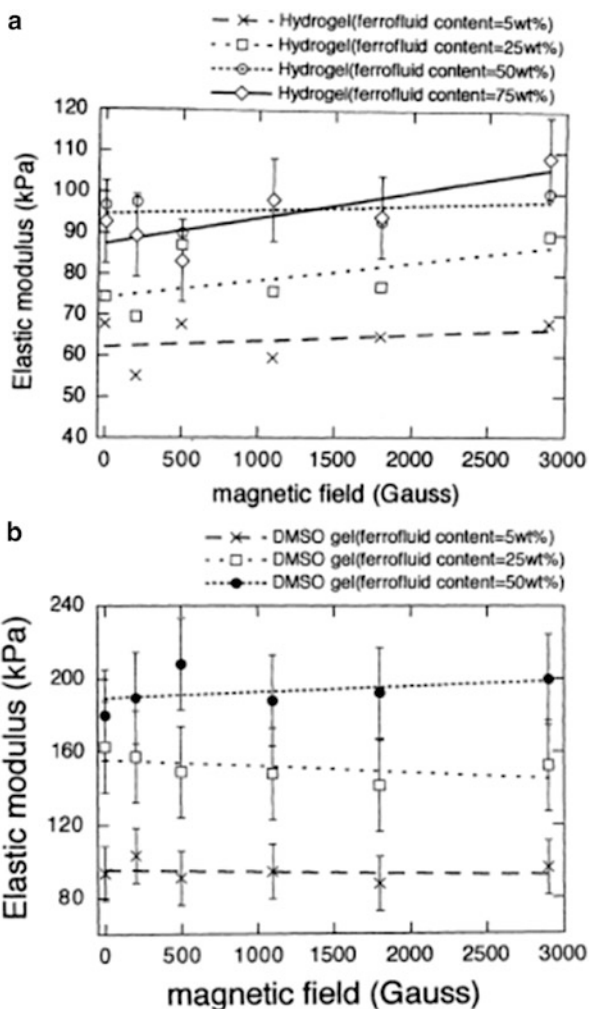
content of magnetic fluid is not adequate for the X-ray scattering observation because of strong X-ray absorption by the magnetic particles. The in situ observation became possible by using strong X-ray from synchrotron radiation. Scattering range in scattering vector q_s is $0.006 < q_s < 0.2$. The scattering showed a shoulder around $q_s = 0.075 \text{ \AA}^{-1}$, that is, ca. 80 \AA in actual size. This shoulder suggests that the relatively weak closest particle interaction exists. The shoulder peak is stronger in DMSO gel than that in hydrogel, suggesting that the dispersion is higher in hydrogel (Fig. 19.11). TEM image also showed particle size of ca. 80 \AA . DMSO gel did not show clear shoulder peak, suggesting aggregates formation or wide distribution of the particle size. The scattering profile is subjected for Fourier

Fig. 19.9 Stress induced by applying magnetic field gradient. (a) hydrogels, (b) DMSO gels



inversion, and the distribution function is obtained (Fig. 19.12). Parameters obtained were summarized in the Table 19.1. The results suggests the different effect of magnetic field between hydrogel and DMSO gel. Maximum vector length reaches 500–600 Å. The scattering bodies in both gels have similar dimension in size despite of the different reactions to the magnetic field. In the gel of 25 % magnetite content in which the magnetically induced deformation was observed, the size of the scattering body increased in hydrogel and decreased in DMSO gel. The tendencies can explain the magnetically induced motility of the gels. Value of maximum vector length D_{\max} and Porod slope (α_p) (Fig. 19.13) is summarized in the table. The value gives the information of the fractal structure of the scattering body. In the table, the gradient in the region of $0.022 < q_s < 0.045$. The value is $\alpha_p = -3.2$. The range of $-4 < \alpha_p < -3$ corresponds to the rough surface fractal structure with the dimension of 140–290 Å. The results show α_p value increases in the hydrogel and decrease in DMSO gel by applying magnetic field to the gel with magnetic fluid content of 25 %. Guinier analysis shows the value of the radius of gyration R_g increases in hydrogel and decreases in DMSO gel by magnetic field

Fig. 19.10 Effect of elastic modulus of the gels on magnetic field. (a) for hydrogel, and (b) for DMSO gel. Modulus of hydrogel slightly increased with magnetic field



application (Table 19.1). These changes in the structural parameters induced by magnetic field are in agreement with the magneto-mechanical behavior of the gels.

19.4 The Applications of Magnetic Fluid Composite Gels

19.4.1 Magnetite Immobilization in the Gel by Complexation Reaction

Magnetite particles with nano-size can be immobilized by the other method, too. Complexation reaction of PVA with iron (Fe(III) and Fe(II)) can be applied for this

Fig. 19.11 Small angle X-ray scattering of PVA gels containing ferrofluid under magnetic field

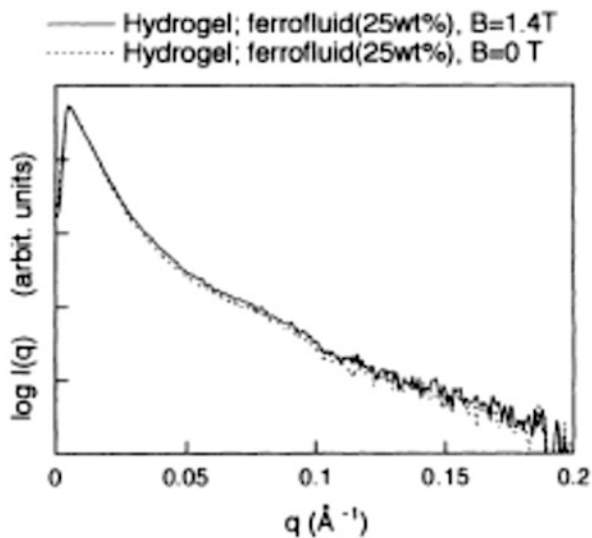
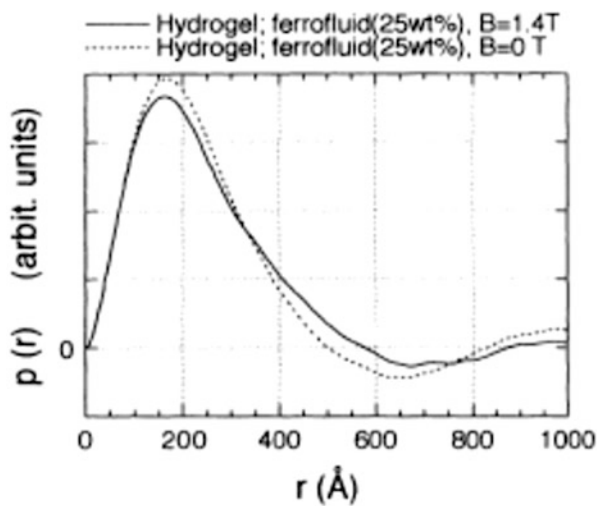


Fig. 19.12 Distance distribution function $p(r)$ of PVA gels containing magnetic fluid. By applying magnetic field, $p(r)$ increased slightly

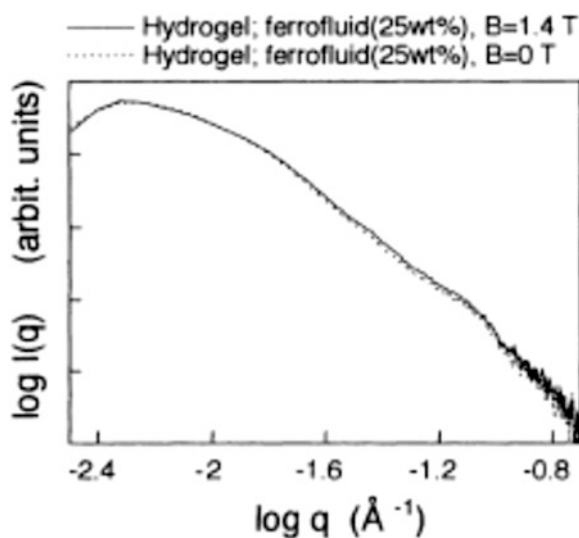


purpose. Complexation reaction can also function as crosslinking reacton. By titrating PVA-ion solution into an NaOH aqueous solution, the PVA-magnetite gel can easily be formed. The gel beads have the diameter of 2 mm, and showed ferro-magnetic property. After throughly rinsing the gel beads in water, we employed this magnetite gel as a carrier.

Table 19.1 Characteristic parameters of PVA hydrogels and DMSO gels

	Magnetic field (T)	R_g (Å)	D_{max} (Å)	Porod slope at $0.022-0.045 \text{ \AA}^{-1}$	Peak position of $p(r)$ (Å)
Hydrogel (magnetic fluid:5 wt%)	0	200	579	-3.003	213
	1.4	199	576	-2.978	214
Hydrogel (magnetic fluid:25 wt%)	0	162	503	-3.256	168
	1.4	175	580	-3.146	163
DMSO gel (magnetic fluid:5 wt%)	0	193	582	-3.181	191
	1.4	193	575	-3.154	188
DMSO gel (magnetic fluid:25 wt%)	0	197	598	-3.152	181
	1.4	184	558	-3.168	178

Fig. 19.13 Porod plot. Slope value suggests the scattering body has rough surface structure



19.4.2 Release Control by Magnetic Field

By immersing the magnetic gel particles in an aqueous solution of bovine serum albumin (BSA) as a depot for a while, the sample gel with BSA was prepared. The magnetic gel particles were subjected for release measurement. As has been suggested in previous section, magnetic gel can be actuated by applying magnetic field, when it is immobilized homogeneously. The mechanical deformation of the gel can induce fluctuation of diffusivity of the species in the gel, thus leads to the possibility of release control by magnetic field. Figure 19.14a illustrated the system, and the results are shown in Figs. 19.14b, c. The release of BSA was not detected in the gel beads from PVA with $DP = 7,600$, but detected in the PVA gels with

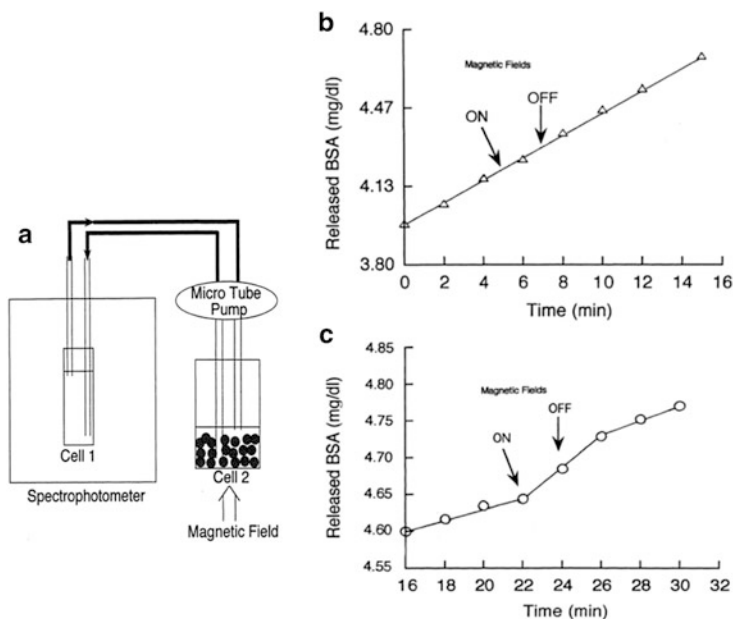


Fig. 19.14 Release control measurement by applying magnetic field. Spheric magnetic gel particles obtained by complexation method were investigated. (a) Experimental set up. Releases of BSA from the hydrogels (PVA:8 wt%, magnetic fluid:25 wt%) were shown. (b) hydrogel from DP = 7,600. (c) hydrogel from DP = 1,700. Magnetite content were the same. At room temperature. Release rate increased by applying magnetic field for the gel from DP = 1,700. Release rate of hydrogel gel from low molecularweight PVA was controllable by magnetic field

DP = 1,700 by applying magnetic field. The difference between the two can be explained from the gel network density, that is, the gels from DP = 1,700 have loose structure that allows the diffusion of BSA. Thus, by applying the magnetic field, enhancement of protein release was observed when the network structure is not tight.

19.4.3 Encapsulation of Magnetic Fluid for Display Device

For a magnetically active device, encapsulation of magnetic fluid has been carried out. By conventional encapsulation method, content of magnetic fluid in the capsule is usually not high enough for display device. A method proposed in the Fig. 19.15 was proposed, which can be a possible way of encapsulation with very high content magnetic fluid [20]. When the content of magnetic fluid is high enough and can be mixed with white powder such as TiO_2 , the particles can be applied for magnetically controlled display as illustrated [21].

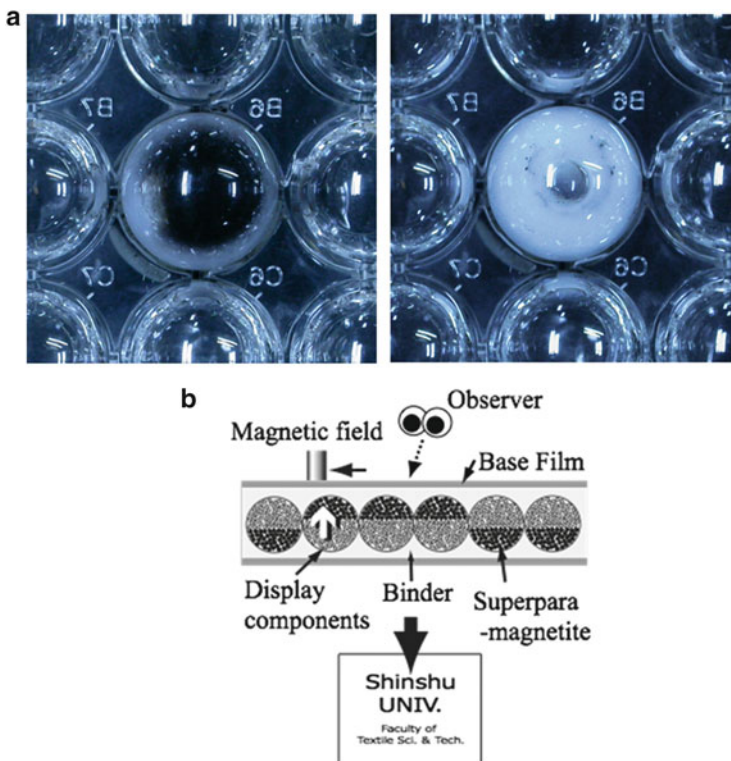


Fig. 19.15 Magnetically induced color change (*black* and *white*) for demonstration of display function (a). Microcapsule contains ferro fluid (*black*) and TiO_2 (*white*). *Left*: magnetic field was applied from the top. *Right*: magnetic field was applied from the other side. Thus, *black* and *white* color changed by magnetic field. Concept was illustrated in (b). Super paramagnetic property has advantage to realize clear and stable image. Otherwise interaction among the magnetic particles causes indistinct image

19.5 Conclusion

The research of magnetic fluid immobilization are rather limited particularly in the soft composites of polymer, for such as gels. But it has big possibility for not only actuator but also for various applications. Particularly, for the medical use, remote control of aggregate formation of the magnetic fluid immobilized gels by focusing magnetic field will be a good candidate. One of the other interesting applications is the magneto-rheological function such as elasticity control, that can be applied magnetically controlled dumper. Stability control against oxidation will be one of the remaining issues for the practical application, and that can be expected to be overcome with applying non-aqueous organo-gel systems.

References

1. Coey JMD (2009) Magnetism and magnetic materials. Cambridge University Press, New York
2. Rosensweig RE (1979) Fluid dynamics and science of magnetic liquid. Advances in electronics and electron physics, vol 48. Academic, New York
3. Hirai T, Takamizawa T, Hirai M et al (1995) Magnetically induced structure change of polymer gel. Res Prog Polym Phys Jpn 38:163–166
4. Zrinyi M, Barsi L, Buki A (1996) Deformation of ferrogels induced by nonuniform magnetic fields. J Chem Phys 104:8750–8756
5. Zrinyi M (2011) Patterns in soft magnetic matter, Euromech Colloquim, p 526, Dresden
6. Horkay F, Zrinyi M (1989) Mechanochemical energy conversions of neutral polymer gels. Makromol Chem Makromol Symp 30:133–143
7. Frank S, Lauterbur PC (1993) Voltage-sensitive magnetic gels as magnetic resonance monitoring agents. Nature 363:334–336
8. Zrinyi M, Barsi L, Biiiki A (1998) Ferrogel: a new magneto-controlled elastic medium. Polym Gel Netw 5:415–427
9. Neuringer JL, Rosensweig RE (1964) Ferrohydrodynamics. Phys Fluids 7:1927
10. Krueger DA, Jones TB (1974) Hydrostatic profile of ferrofluid around a vertical current-carrying wire. Phys Fluids 17:1831–1833
11. Rosensweig RE (1987) Magnetic fluids. Annu Rev Fluid Mech 19:437–453
12. Rosensweig RE (1966) Buoyancy and stable levitation of a magnetic body immersed in a magnetizable fluid. Nature 210:613–614
13. Jones TB (1979) A necessary condition for magnetic levitation. J Appl Phys 50:5057
14. Tasoglu S, Kavaz D et al (2012) Paramagnetic levitational assembly of hydrogels. Adv Mater 25(8):1137–1143
15. Terech P, Friol SE (2007) Rheometry of an androstanol steroid derivative paramagnetic organogel, methodology for a comparison with a fatty acid organogel. Tetrahedron 63:7366–7374
16. Xie Z-L, Jeličić A, Wang F-P et al (2010) Transparent, flexible, and paramagnetic ionogels based on PMMA and the iron-based ionic liquid 1-butyl-3-methylimidazolium tetrachloroferrate(III) [Bmim][FeCl₄]. J Mater Chem 20:9543–9549
17. Zrinyi M (2000) Intelligent polymer gels controlled by magnetic fields. Colloid Polym Sci 278:98–103
18. Takamizawa T (1995) Study on actuation of ferro fluid immobilized PVA hydrogel by applying magnetic field. Master Thesis of Shinshu University
19. Glatter O, Kratky O (1982) Small-angle X-ray scattering. Academic, New York
20. Takada T, Hirai T (2004) A novel preparation method for capsules containing a high proportion of magnetite using a magnetic field. Polym Bull 52:437–442
21. Takada T, Shoubara T et al (2003) Paper presented at the – the International Display Workshop (IDW '03), Fukuoka, Japan

Chapter 20

Magnetic Particle Composite Gels

Tetsu Mitsumata

Abstract Magnetic soft materials containing solid state magnetic particles demonstrate various motions and magnetorheological behavior in response to magnetic fields. When a rotational magnetic field is applied to magnetic gels containing with magnetized particles, the magnetic gels exhibit rotational motion. When a non-uniform magnetic field is applied to magnetic gels, the elongation of magnetic gels is observed. The rotational motion of magnetic gels can be applied to a fluid pump that delivers water in straight and spiral tubes. A bead of magnetic gels loaded with drugs undergoes accelerated drug release depending on the rotation rates. The elongational motion of magnetic gels can be applied to an elongation-contraction actuator or a microvalve. Under uniform magnetic fields, the magnetic gels show variable viscoelastic behavior depending on the field-strength, which is called the magnetorheological effect. The dynamic modulus of magnetic hydrogels increases by two orders of magnitude synchronized with magnetic fields. The magnetorheological effect of magnetic gels can be applied to haptic devices or intelligent dampers. Actuators and magnetorheological effects of magnetic soft materials consisting of solid state magnetic particles are described.

Keywords Composite gel • Elastomer • Magnetic gel • Magnetic particle • Stimuli-responsive gel

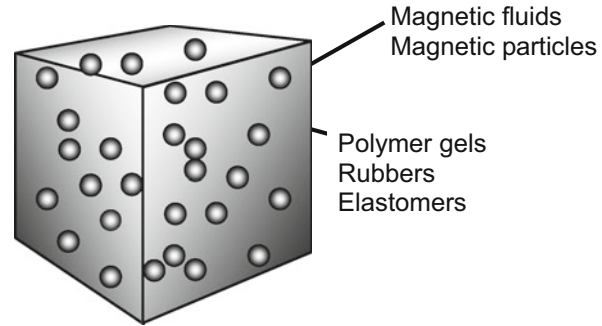
20.1 Introduction

Polymer gels or elastomers are three-dimensional networks of polymer chains swollen by a large amount of solvent. Due to this, these materials are rich in elasticity and are called the soft material. By dispersing magnetic particles or magnetic fluids into the soft materials (Fig. 20.1), an intelligent material that responds to magnetic fields can be obtained, which is called the magnetic soft material. Magnetic soft materials exhibit various magnetic response which is useful for actuators with innovative functionalities, for example, elongation-contraction

T. Mitsumata (✉)

Department of Materials Science and Technology, Faculty of Engineering, Niigata University,
8050 Ninocho, Ikarashi, Nishi-ku, Niigata 950-2181, Japan
e-mail: tetsu@eng.niigata-u.ac.jp

Fig. 20.1 Schematic illustration representing the constituent of magnetic soft materials



Magnetic soft materials

motion [1–3], rotational motion [4, 5], and variable elasticity [6–11]. These phenomena originate from the magnetic interaction between magnetic fields and the magnetization (magnetic moment) of magnetic particles. Since the magnetic soft materials are extremely soft compared to plastics or metals, the phenomena induced by magnetic fields are seen to be drastic. Magnetic soft materials provide many advantages on the use of actuators. The force generated by magnetic fields is strong because the magnetic field directly acts on the magnetic dipole of solid state magnetic particles. The speed of magnetic response is fast compared to the other actuators consisting of stimuli-responsive soft materials. Magnetic soft materials can be worked by a remote control, this avoids troubles of electric wiring between materials and electric magnets. The remote control by magnetic fields is quite simple however it is really useful on a practical use. Recently, unique example was reported that a magnetic foam can be driven by a permanent magnet and removes effectively oil contaminants spread on water surface [12]. Beside these, the motion or reaction of magnetic soft materials can be designed easily by the magnetism of magnetic particles. When the magnetic particles with large remanent magnetization are used, the actuator of magnetic soft materials can be driven by weak magnetic fields. The application of magnetic soft materials would be widely and rapidly spread in a recent decade using these advantages. In this review, the actuators and variable elasticity of magnetic soft materials are described.

20.2 Magnetically Driven Actuators Made of Soft Materials

20.2.1 Magnetic Gel Pumps

Figure 20.2 displays the photographs of gel-pump made of a gel-rotor, a pair of permanent magnet, and an electric motor [13]. The rotor is made from polyvinyl alcohol (PVA) hydrogels containing solid state magnetic particles. The magnetic particle is barium ferrite which is a hard ferrite with high remanent magnetization.

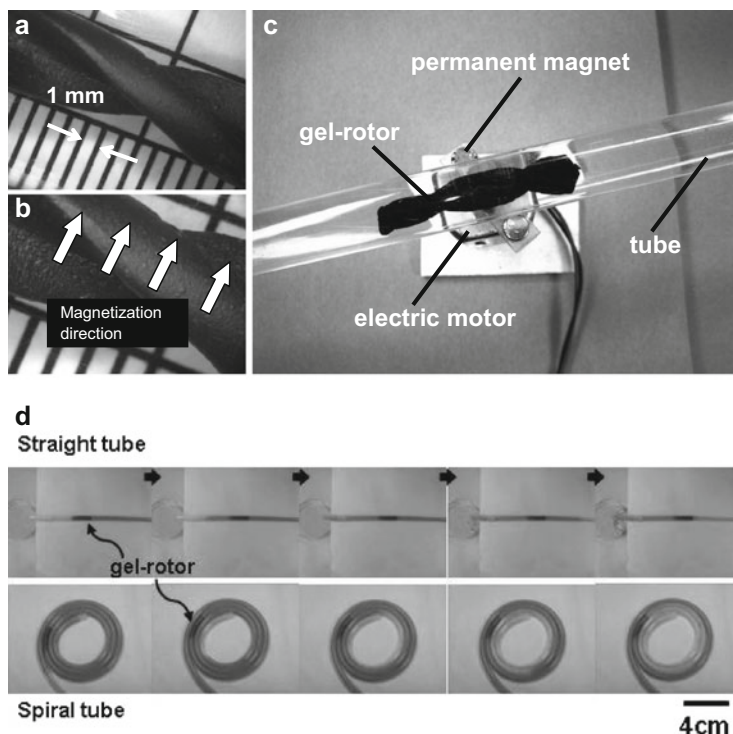


Fig. 20.2 (a, b) Rotor of magnetic hydrogels magnetized in the direction of arrows. (c) Photograph of gel-pump driven by rotational magnetic fields. (d) Photographs representing water flow by gel-pump in a straight (*tops*) and spiral tubes (*bottoms*)

The rotor as synthesized has no magnetization, therefore the rotor does not rotate when rotational magnetic fields are applied. After the synthesis, the rotor is put under a uniform magnetic field of 1 T for 1 min in order to give the rotor a remanent magnetization. The top photos of Fig. 20.2d show the gel-pump in a straight tube. The gel-rotor is in the center of the tube. The water flows to a laboratory dish at the end of the tube within 8 s. The bottom photos of Fig. 20.2d show the gel-pump in a spiral tube. The gel-pump delivers water even in spiral tubes because the elastic modulus of the gel-rotor is extremely low ($\sim 10^4$ Pa). The pump made of magnetic soft materials can be worked without direct contact between the gel-rotor and electromagnet. This would be useful for microfluidic applications such as μ -TAS.

20.2.2 Rotational Motion of Magnetic Gel Beads

A bead of hydrogel containing magnetized magnetic particles demonstrates rotational motion by applying rotational magnetic fields. When the bead is synthesized loaded with a drug, the drug release is accelerated by the rotation of magnetic fields.

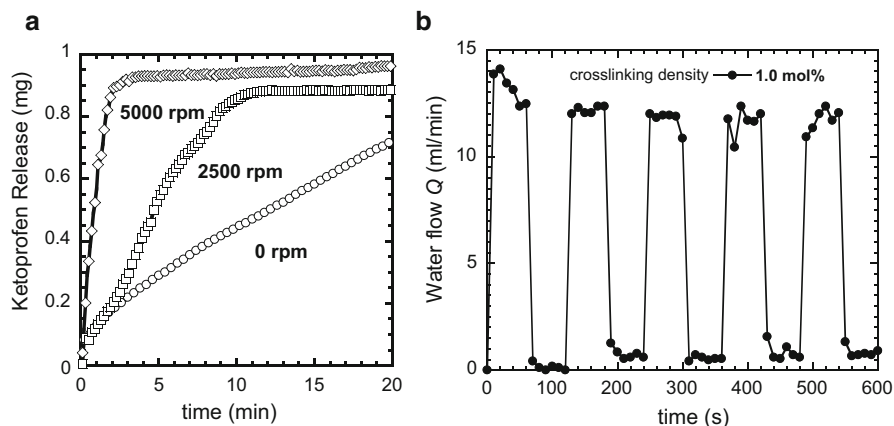


Fig. 20.3 (a) Time profiles of drug (ketoprofen) release for magnetic-gel beads at various rotation rates. (b) Pulsatile water flow by open-close switching of magnetic-gel valves ($P = 0.3$ MPa)

The amount of drug released from the bead at various rotation rates is presented in Fig. 20.3a [5]. The bead is a saccharide gel of sodium alginate containing magnetized particles of barium ferrite and drugs (ketoprofen). As seen in the figure, the amount of drug clearly increases with the rotation rates of magnetic fields. Without rotation, the drug release reaches a saturation value of 0.90 mg at 25 min, which corresponds to 92 % of the drug in feed. When the magnetic beads are rotated at 5,000 rpm, the time to achieve the saturation is approximately 3 min, which corresponds to 1/8 of the time without rotation.

20.2.3 Magnetic Gel Valves

Magnetic gels containing magnetic particles or magnetic fluids exhibit an elongational motion by a gradient magnetic field. The elongation is induced by the magnetic force acting between magnetization of magnetic particles and magnetic fields. The magnetic force is proportional to the multiple of magnetization M and the magnetic field gradient $\partial H/\partial x$. By using the elongational motion, a pulsatile water flow in a tube can be realized by using weak magnetic fields. The elongation is also observed for magnetic gels containing magnetic particles without having remanent magnetization such as soft ferrites. The flow rate of water in a microtube is shown in Fig. 20.3b when pulsatile magnetic fields with 80 mT are applied to the magnetic gel-valve every 60 s under a water pressure of 0.3 MPa [13]. The magnetic gel consists of iron oxide (Fe_3O_4), and the size of the gel is 3 mm in long and 1 mm in diameter, and the diameter of the microtube is 1 mm. The water flow is obstructed by the magnetic gel which was elongated into the microtube by the magnetic fields. The valve made of magnetic gels works under water pressures up to 1.6 MPa.

20.3 Magnetic Soft Materials with Variable Viscoelasticity

When a uniform magnetic field is applied to magnetic gels, the elastic modulus of the magnetic gels alter basically due to the magnetic interaction between magnetization of magnetic particles and magnetic fields. Figure 20.4a illustrates the storage modulus G' for carrageenan (CA) magnetic gels containing carbonyl iron (CI) particles when pulsatile magnetic fields were applied [14]. The gel demonstrates huge, exceeding two orders of magnitude, and reversible changes in storage modulus synchronized with the magnetic field. The absolute change in storage modulus due to the magnetic field $\Delta G'$ is 4.5 MPa, which corresponds to 500 times higher than the off-field modulus. Similar field response and huge increase in the modulus are also seen in the loss modulus G'' as shown in Fig. 20.4b.

Figure 20.5 depicts the volume fraction dependence of the storage modulus G' for CA/CI magnetic gels in the presence and absence of a magnetic field [15]. The solid line in the figure represents the storage modulus calculated by the Krieger–Dougherty equation [16] for a random dispersion of magnetic particles. At 0 mT, the storage modulus of the magnetic gel almost obeys the equation up to $\phi \sim 0.33$, indicating the magnetic particles are homogeneously dispersed in the matrix gel. This brings the magnetic gel a giant and reversible changes in the dynamic

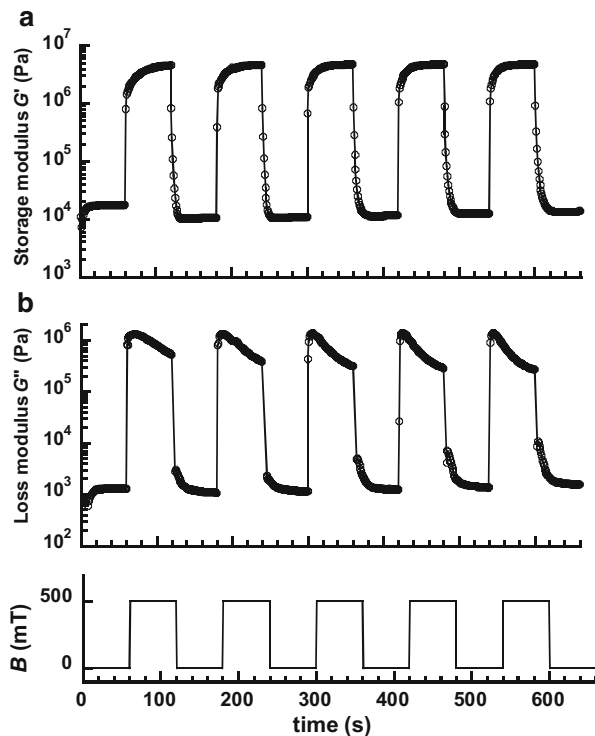
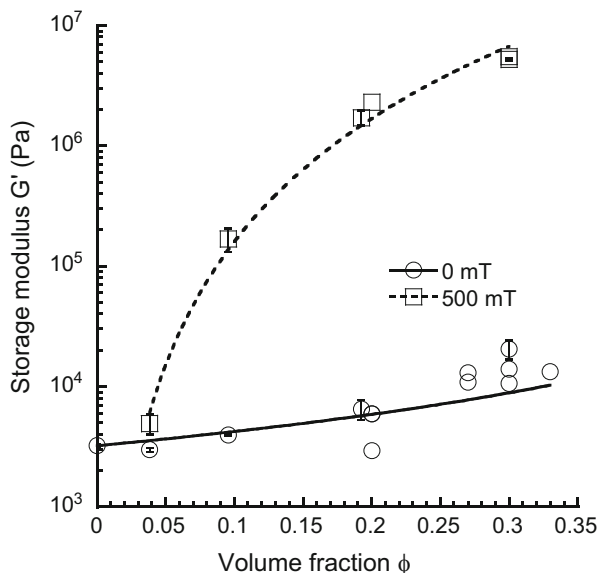


Fig. 20.4 (a) Storage modulus and (b) loss modulus for magnetic gels in response to pulsatile magnetic fields (carrageenan 0.7 wt%, $\gamma \sim 10^{-4}$, $\phi = 0.34$)

Fig. 20.5 Storage modulus for CA/CI magnetic gels at 0 and 500 mT as a function of the volume fraction of magnetic particles



modulus. At 500 mT, the storage moduli for the magnetic gels are higher than those at 0 mT. When the volume fraction is at $\phi < 0.04$, no significant increase in the storage modulus is observed upon an application of a magnetic field. The storage modulus at 500 mT can be well fitted by a power law (broken line), which is an indication of the percolation threshold at $\phi \sim 0.04$.

Figure 20.6 displays the scanning electron micrographs for CA/CI magnetic gels freeze-dried under a magnetic field with field-strengths of 0 and 320 mT [15]. No alignment is observed for the CI particles when the magnetic field is 0 mT. On the other hand, it can be seen at 320 mT that the CI particle aligns in the direction of magnetic fields, which is called a chain structure. This evidence clearly indicates that the magnetic particles are able to move within the matrix gel which was cross-linked by the physical bond. A similar phenomenon is observed for carrageenan/ γ - Fe_2O_3 hydrogels that the storage modulus is reduced remarkably by the particle movement [17]. This movement of magnetic particles must accompany the local deformation of gel network since the magnetic particles are immobilized by the network. The arrangement of magnetic particle changes from random to a chain structure without changing its shape macroscopically. Indeed, the carrageenan network is found to be stretched in the direction of the magnetic field, as indicated by white arrows in Fig. 20.6c. Conversely, this evidence tells us that there arises a strong interaction of adhesion between magnetic particles and the carrageenan gel.

The reversibility of storage modulus and absolute change in storage modulus are strongly affected by the viscoelastic properties of the matrix. Figure 20.7 displays the storage modulus as a function of matrix (CA) concentration when the volume

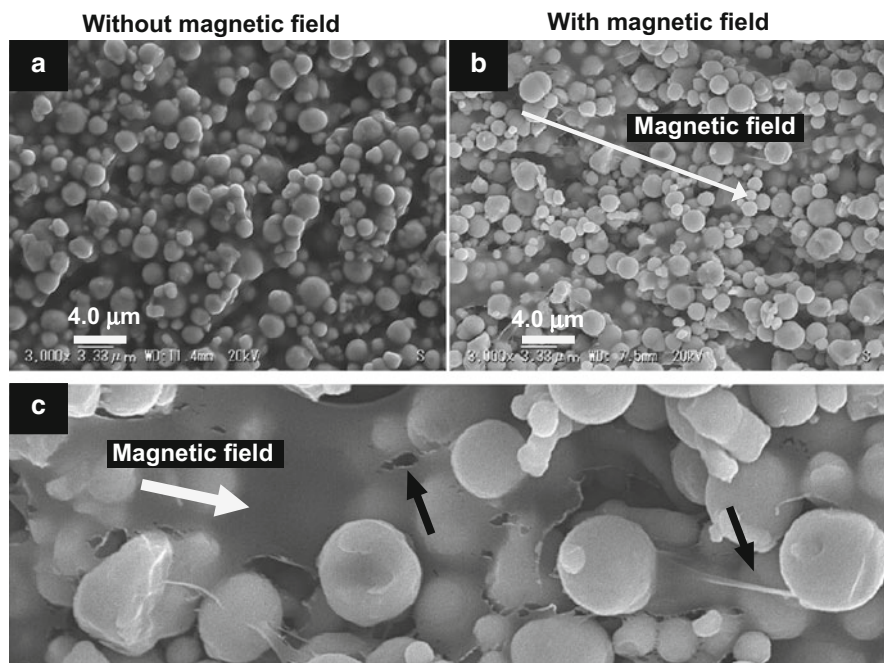
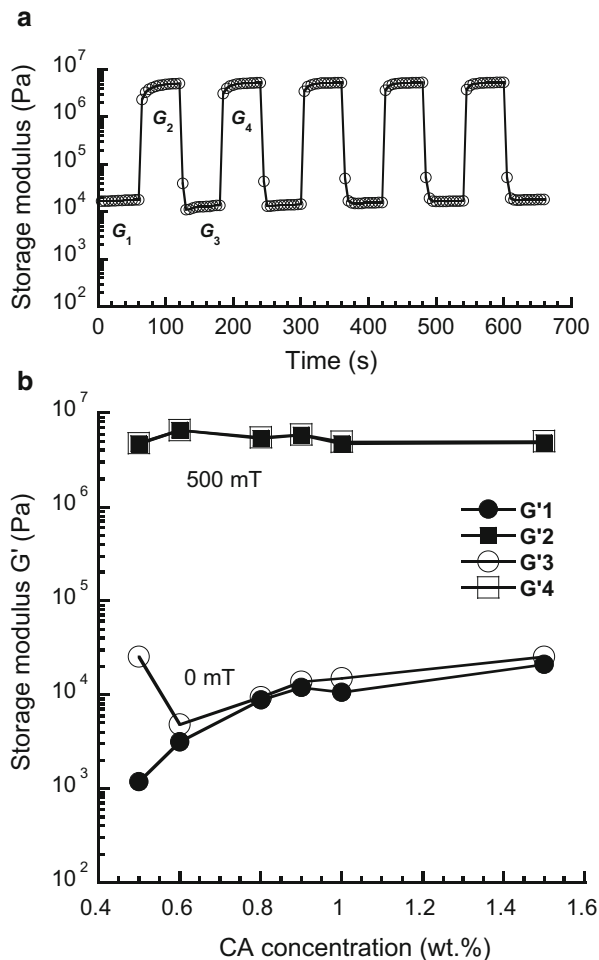


Fig. 20.6 Dispersibility of magnetic particles in carrageenan gels at (a) 0 mT and (b and c) 320 mT for CA/CI magnetic gels ($\phi = 0.27$). *White arrows* indicate the direction of magnetic fields. *Black arrows* indicate a ripped part and the stretched part by the chain formation

fraction of magnetic particles is constant at 0.30 [15]. In Fig. 20.7a, the storage moduli G'_1 and G'_2 show the modulus at the first application of a magnetic field of 500 mT; the storage moduli G'_3 and G'_4 represent the modulus at the second application of the magnetic field. At 0 mT, the G'_1 for magnetic gels above 0.6 wt% is almost the same as that of G'_3 , suggesting that the distribution of the magnetic particles is recovered to the original arrangement. When the CA concentration is 0.5 wt%, the storage modulus after applying the magnetic field G'_3 is 2.5×10^4 Pa, which is 20 times higher than that of G'_1 . This indicates that the matrix was destructed by the movement of magnetic particles, and the chain structure fails to remain after removing the magnetic field. The storage modulus at 500 mT (G'_2 , G'_4) is approximately of 5.4×10^6 Pa, independently of the CA concentration, suggesting a chain structure of magnetic particles with a perfect alignment. When the CA concentration is 3.0 wt%, the value of G'_1 significantly increases while the G'_2 decreased to a low value of 1.7×10^6 Pa because the movement of magnetic particles is obstructed due to high elasticity of the matrix.

So far, many attempts have been carried out to obtain magnetorheological soft materials that the elastic modulus changes by magnetic fields, however, the modulus change was not significant. The magnetic gel presented here, CA/CI magnetic

Fig. 20.7 (a) Definition of storage moduli G'_1 – G'_4 and (b) storage moduli G'_1 – G'_4 as a function of carrageenan concentration for CA/CI magnetic gels ($\gamma = 10^{-4}$, $\phi = 0.30$)



gel, exhibits giant changes in elasticity compared to the other magnetic soft materials. Why does the CA/CI magnetic gel undergo a wide range modulation of elastic modulus? Of course, significant changes in elasticity are observed when magnetic particles with high magnetization are employed. However, it is easily found that this magnetization effect is not dominant for the magnetorheological effect of CA/CI magnetic gels since the $\Delta G'$ is described by $\Delta G' = \mu_r \mu_0 (M\phi)^2$ [15], μ_r : relative magnetic permeability, μ_0 : magnetic permeability in vacuum, M : magnetization, ϕ : volume fraction of magnetic particles. Most important factor is the dispersibility of magnetic particles in CA gels, that is, random dispersion makes magnetic gels a wide range modulation of dynamic modulus. When magnetic particles are embedded in gels with high volume fractions, the storage modulus fails to be high with an order of 1 MPa because the magnetic particle forms a particle network consisting of magnetic particles. In addition, it has been cleared

that the particle network is destroyed by magnetic fields, resulting in a significant reduction of the on-field modulus [18, 19]. On the other hand, magnetic gels with a random dispersion of magnetic particles do not demonstrate both effects that are negative factors for magnetorheological effects. Another factor is adhesion property between magnetic particles and the matrix. The magnetorheology of carrageenan gels with iron oxide (CA/IO gels) is one order of magnitude lower than that of CA/CI gels [20], although there is no significant difference in both magnetism and particle dispersibility. For example, the saturation magnetization of CI particles (~ 214 emu/g) is only twice that of IO particles (~ 94 emu/g). The off-field modulus for the CA/IO gels is nearly equal to that for the CA/CI ($\sim 10^4$ Pa), which is an indication of random dispersion of magnetic particles as well as CA/CI gels. The IO particle might be strongly bound within the matrix and the particle cannot form chains effectively under magnetic fields. Besides those factors, it has been found that the size of magnetic particles, not only primary particles but also secondary particles, strongly affects the magnetoelastic behavior for magnetic soft materials [21, 22].

Thus, the viscoelastic properties of magnetic hydrogels can be tuned by magnetic fields, however, hydrogels are not suitable for industrial use due to water evaporation and low mechanical toughness. A magnetic elastomer synthesized using polyurethane also exhibits wide range modulation of elasticity in air. Figure 20.8 shows the absolute change in storage modulus $\Delta G'$ and relative changes in the storage modulus G'_{B500}/G'_{B0} for magnetic elastomers as a function of the volume fraction of magnetic particles [23]. The $\Delta G'$ for magnetic carrageenan gels demonstrating giant magnetorheology is also shown in the figures for comparison. The increment in the storage modulus increases with the volume fraction and saturated to approximately 4.8 MPa at $\phi > 0.30$. The relative change in the storage

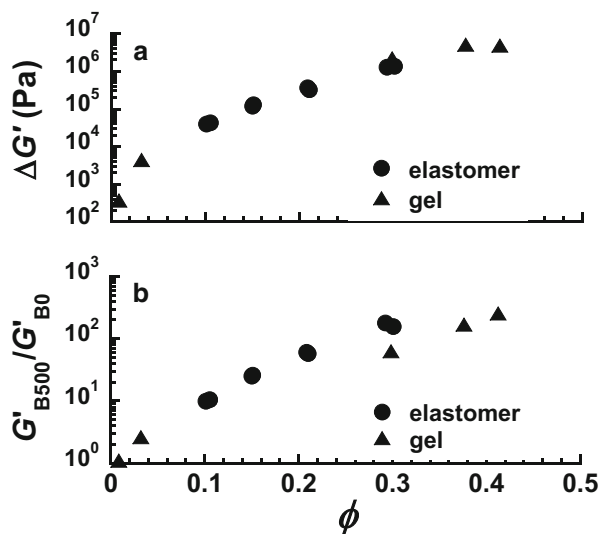


Fig. 20.8 (a) Absolute change in storage modulus and (b) relative change in storage modulus for magnetic polyurethane elastomers and magnetic carrageenan gels as a function of the volume fraction of magnetic particles ($\gamma = 10^{-4}$, 500 mT)

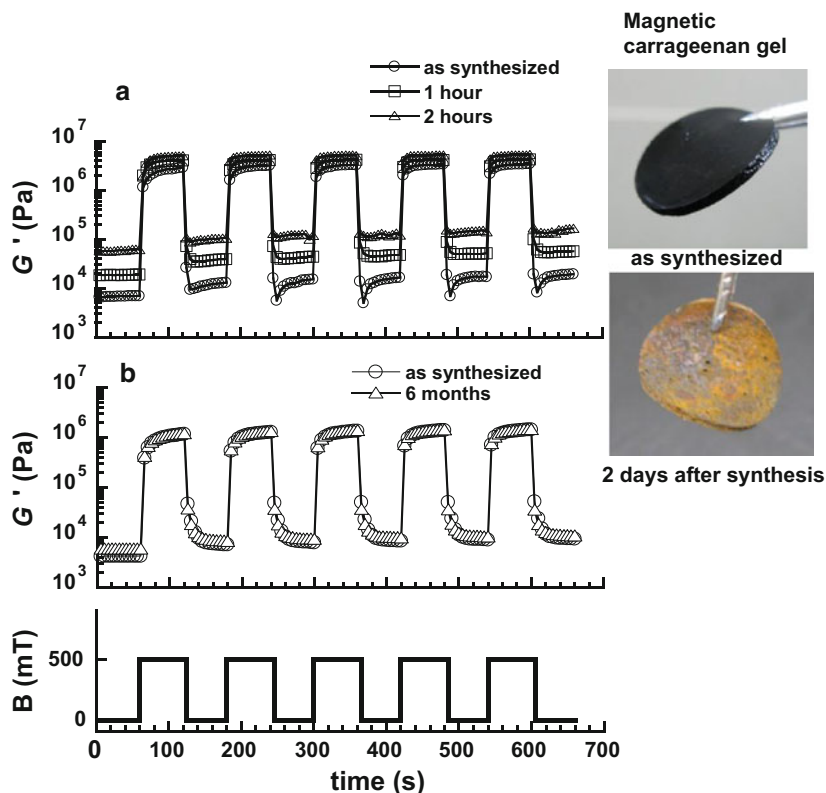


Fig. 20.9 Degradation of magnetorheological response for (a) magnetic carrageenan gel and (b) magnetic polyurethane elastomer. Pulsatile magnetic field with 500 mT was applied to the samples ($\phi = 0.29$, $\gamma = 10^{-4}$). *Photo*: magnetic gels as synthesized (*top*) and 2 days after synthesis (*bottom*)

modulus increases with the volume fraction, and the value is similar to that for magnetic carrageenan gel. This strongly suggests that the CI particles are able to align along the magnetic lines of force within the polyurethane elastomer, as well as magnetic carrageenan gels.

Figure 20.9a, b display the influence of degradation on the magnetorheological properties for magnetic carrageenan gels and elastomers, respectively [23, 24]. The storage modulus of magnetic gels stored in air increases significantly within 2 h because of water evaporation from the gel; as a result, the magnetorheological effect is diminished. After 3 h, the magnetic gel lose its softness (solidified), and the magnetorheological response is not observed. Contrary to this, the magnetic elastomer maintains its field-response even after half a year from synthesis. Not only water evaporation but also freezing of water limits the usage of magnetic gels. The magnetic gel is solidified at the freezing point of the swelling medium i.e. water, but the obtained magnetic elastomer keeps its softness below $0\text{ }^{\circ}\text{C}$ ($T_g \sim -40\text{ }^{\circ}\text{C}$). Other serious problems for the practical use of magnetic hydrogels are degradations of the

magnetic particle and the polymer matrix. The photos in Fig. 20.9 show the material degradation due to the rust of CI particles. The color of the magnetic gel is black when at synthesis and changes to dark yellow within a few days, caused by the oxidation of CI particles. This leads to a decrease in the magnetic permeability of the magnetic gel as a bulk state; as a result, the magnetorheological response is markedly weakened. In near future, it would be important to investigate that both the oxidative stability of the present elastomer and the stability of iron particles against humidity. Thus, a magnetic soft material with significant magnetorheology, high toughness, and durability was obtained. Recently, magnetic elastomers enabled high mechanical toughness and durability are applied to intelligent shoes and walking guidance systems with variable haptic sense of sole [25], which are greatly expected for walking rehabilitations and next-generation games with virtual reality.

Generally, a chain structure of magnetic soft materials consists of only magnetic particles, however, nonmagnetic particles are able to participate in forming the chain structure of magnetic particles. A few years before, Klingenberg et al. have carried out a systematic investigation and found that the yield stress of magnetorheological fluids is enhanced by the presence of nonmagnetizable particles [26]. Figure 20.10a demonstrates the relationship between the absolute changes in the storage modulus $\Delta G'$ and the mixing ratio r for bimodal magnetic hydrogels [27]. At $r < 0.34$, the $\Delta G'$ keeps a high value with 0.8 MPa, and it decreases with the

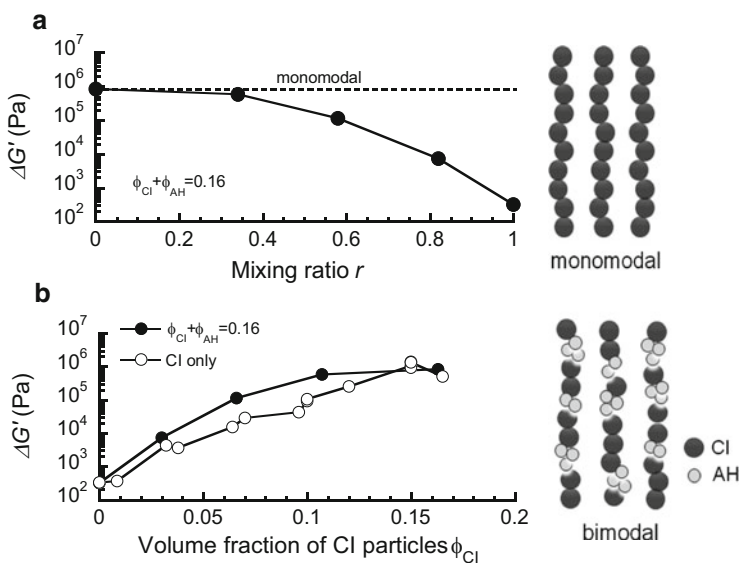


Fig. 20.10 Absolute change in storage modulus as a function of (a) mixing ratio and (b) volume fraction of CI particles for bimodal magnetic hydrogels consisting of magnetic and nonmagnetic particles. *Inset:* Schematic illustration representing the substitution of magnetic particles with nonmagnetic particles at $r = 0.34$

mixing ratio at $r > 0.34$. According to the magnetic measurement, the relative magnetic permeability at a certain mixing ratio can be expressed a linear combination of μ_{CI} (~ 5.48) and μ_{CA} (~ 1.0), i.e. $\mu_r = (1 - r)\mu_{\text{CI}} + r\mu_{\text{CA}}$. Not only the relative permeability but also the saturation magnetization can be written by a linear combination of each magnetization. This clearly suggests that the high values of $\Delta G'$ cannot be explained by the magnetic interaction acting between magnetic dipoles of the magnetic particles.

Figure 20.10b depicts the relationship between the absolute change in the storage modulus $\Delta G'$ and the volume fraction of CI particles ϕ_{CI} for bimodal magnetic hydrogels [27]. It is obvious that the $\Delta G'$ for bimodal magnetic gels are higher than those for monomodal one (CI only) at all volume fractions of CI particles. This is probably due to a reduction of percolation threshold of chain formation by embedding nonmagnetic particles. Bimodal magnetic gels give us an important insight that a weight of materials can be reduced by 21 % without sacrificing magnetoelastic properties. It was found by theoretically and experimentally [28, 29] that the resonance frequency of vibration can be shifted by changing the elastic modulus of materials. This material would be used for vibration controllable devices that the damping factor can be controlled by the intensity of magnetic fields.

20.4 Conclusion

The various motions and the variable elasticity of magnetic gels containing magnetic particles were described. The magnetic gel rotates by rotational magnetic fields and elongates by non-uniform magnetic fields. The rotational motion originates from the magnetic interaction between the remanent magnetization of magnetic particles and magnetic fields, and the motion can be used for fluid pumps and drug capsules. The elongational motion is caused by the magnetic interaction between magnetization and gradient magnetic fields, and the motion can be applied to expansion-contraction actuators and microvalves. Under uniform magnetic fields, the magnetic gel undergoes variable viscoelasticity depending on the field intensity. The storage modulus of magnetic gels can be altered by 500 times with respect to the off-field modulus. Similar to the storage modulus, the loss modulus of magnetic gels can be changed reversibly by magnetic fields. This variable viscoelasticity can be applied for haptic devices and intelligent dampers that control vibration effectively. Magnetic elastomers made from polyurethane are rich in mechanical properties and durability compared to magnetic hydrogels. Serious problem currently is a size effect on the application of magnetic soft materials. The magnetic field response decreases remarkably as increasing the thickness of magnetic soft materials. The improvements are needed so that magnetic particles effectively form a chain structure even under weak magnetic fields. Compact and power-saving electromagnets to generate strong and uniform magnetic fields are also expected as well as the development of materials.

Acknowledgment This research was partially supported by a Grant-in-Aid for Scientific Research of Priority Areas 438 from Next-Generation Actuators Leading Breakthroughs and a Grand-in-Aid for Scientific Research (B) (Proposal No. 23360051). The author is grateful for Dr. T. Okazaki of Bando Chemicals, Mr. T. Hojo and Mr. K. Yamamoto of Panasonic Electric Works for valuable discussion.

References

1. Zrinyi M, Szabo D, Filipcsei G, Feher J (2002) Electrical and magnetic field-sensitive smart polymer gels. In: Osada Y, Khokhlov AR (eds) *Polymer gels and networks*. Marcel Dekker, New York, pp 309–355
2. Zrinyi M (2000) Intelligent polymer gels controlled by magnetic fields. *Colloid Polym Sci* 278:98–103
3. Mitsumata T, Horikoshi Y, Negami K (2007) High-power actuators made of two-phase magnetic gels. *Jpn J Appl Phys* 43:7257–7261
4. Mitsumata T, Horikoshi Y, Takimoto J (2007) Flexible fluid pump using magnetic composite gels. *e-Polymers* 147:1
5. Mitsumata T, Kakiuchi Y, Takimoto J (2008) Fast drug release using rotational motion of magnetic gel beads. *Res Lett Phys Chem*. doi:[10.1155/2008/671642](https://doi.org/10.1155/2008/671642)
6. Shiga T, Okada A, Kurauchi T (1995) Magnetroviscoelastic behavior of composite gels. *J Appl Polym Sci* 58:787–792
7. Jolly MR, Carlson JD, Munoz BC (1996) A model of the behaviour of magnetorheological materials. *Smart Mater Struct* 5:607–614
8. Ginder JM, Clark SM, Schlotter WF, Nichols ME (2002) Magnetostrictive phenomena in magnetorheological elastomers. *Int J Modern Phys B* 16:2412–2418
9. Bossis G, Bellan C (2002) Field dependence of viscoelastic properties of MR elastomers. *Int J Modern Phys B* 16:2447–2453
10. Lokander M, Stenberg B (2003) Improving the magnetorheological effect in isotropic magnetorheological rubber materials. *Polym Test* 22:677–680
11. Mitsumata T, Ikeda K, Gong JP, Osada Y, Szabo D, Zrinyi M (1999) Magnetism and compressive modulus of magnetic fluid containing gels. *J Appl Phys* 85:8451–8455
12. Calcagnile P, Fragouli D, Bayer IS, Anyfantis GC, Martiradonna L, Cozzoli PD, Cingolani R, Athanassiou A (2012) Magnetically driven floating foams for the removal of oil contaminants from water. *Nano Lett* 6:5413–5419
13. Horikoshi Y, Mitsumata T, Takimoto J (2007) Developments for a fluid valve using magnetic gels. *Trans Mater Res Soc Jpn* 32:843–844
14. Mitsumata T, Abe N (2009) Magnetic-field sensitive gels with wide modulation of dynamic modulus. *Chem Lett* 38:922–923
15. Mitsumata T, Honda A, Kanazawa H, Kawai M (2012) Magnetically tunable elasticity for magnetic hydrogels consisting of carrageenan and carbonyl iron particles. *J Phys Chem B* 116:12341–12348
16. Krieger IM, Dougherty TJ (1959) A mechanism for non-Newtonian flow in suspensions of rigid spheres. *Trans Soc Rheol* 3:137–152
17. Mitsumata T, Kosugi Y, Ouchi S (2009) Effect of particles alignment on giant reduction in dynamic modulus of hydrogels containing needle-shaped magnetic particles. *Prog Colloid Polym Sci* 136:163–170
18. Mitsumata T, Sakai K, Takimoto J (2006) Giant reduction in dynamic modulus of κ -carrageenan magnetic gels. *J Phys Chem B* 110:20217–20223

19. Mitsumata T, Wakabayashi T, Okazaki T (2008) Particle dispersibility and giant reduction in dynamic modulus of magnetic gels containing barium ferrite and iron oxide particles. *J Phys Chem B* 112:14132–14139
20. Mitsumata T, Abe N (2011) Giant and reversible magnetorheology of carrageenan/iron oxide magnetic gels. *Smart Mater Struct.* doi:[10.1088/0964-1726/20/12/124003](https://doi.org/10.1088/0964-1726/20/12/124003)
21. Stepanov G, Borin D, Odenbach S (2009) Magnetorheological effect of magneto-active elastomers containing large particles. *J Phys Conf Ser* 149:012098
22. Chiba N, Yamamoto K, Hojo T, Kawai M, Mitsumata T (2013) Wide-range modulation of dynamic modulus and loss tangent for magnetic elastomers containing submillimeter magnetic particles. *Chem Lett* 42:253–254
23. Mitsumata T, Ohori S (2011) Magnetic polyurethan elastomers with wide range modulation of elasticity. *Polym Chem* 2:1063–1067
24. Mitsumata T, Ohori S, Honda A, Kawai M (2013) Magnetism and viscoelasticity of magnetic elastomers with wide range modulation of dynamic modulus. *Soft Mater* 9:904–912
25. Masuda Y, Kikuchi T, Kobayashi W, Amano K, Mitsumata T, Ohori S (2012) Design and evaluation of unit for haptic device on foot. Paper presented at the 2012 IEEE/SICE international symposium on system integration, Fukuoka, 16–18 December 2012
26. Ulicny JC, Snavelly KS, Golden MA, Klingenberg DJ (2010) Enhancing magnetorheology with nonmagnetizable particles. *Appl Phys Lett.* doi:[10.1063/1.3431608](https://doi.org/10.1063/1.3431608)
27. Ohori S, Fujisawa K, Kawai M, Mitsumata T (2013) Magnetoelastic behavior of bimodal magnetic hydrogels using nonmagnetic particles. *Chem Lett* 42:50–51
28. Walsh PL, Lamancusa JS (1992) A variable stiffness vibration absorber for minimization of transient vibrations. *J Sound Vib* 158:195–211
29. Negami K, Mitsumata T (2011) Magnetorheological behavior of magnetic carrageenan gels against shear and compression strains. *e-Polymers* 034:1

Part VI

Modeling

Chapter 21

Molecular Mechanism of Electrically Induced Volume Change of Porous Electrodes

Kenji Kiyohara, Takushi Sugino, and Kinji Asaka

Abstract Electroactive soft actuators that make use of the volume change of porous electrodes on applying voltage are recently drawing attention. We discuss the mechanism of the volume change of the porous electrodes on applying voltage by using the Monte Carlo simulation. We show that, when the pore size of the electrode is so small that it is comparable to the size of the electrolyte ions, slight change in the molecular structure or in the external field can drastically change the thermodynamic properties in porous electrodes. The pressure exerted inside the porous electrodes can be two or three orders of magnitude larger than the atmospheric pressure. Those behaviors are explained by the balance between the volume exclusion interaction and the electrostatic interaction.

Keywords Monte Carlo simulation • Polymer actuator • Porous electrode

21.1 Introduction

Electroactive soft actuators are recently drawing attention as new kinds of actuators [1]. They are flexible and light weight because they are usually made of polymers or carbon materials, in contrast to conventional hard actuators that are made of metals or ceramics. The typical driving voltage for most electroactive soft actuators is as low as 1 V. The performance of the soft actuators at the moment, however, needs improvement before they are used in our daily life. In order to design the materials and the structures for a soft actuator that show desirable performance, one would need to understand the mechanism at the molecular level. Clarifying the mechanisms of the actuations at the level of molecular interaction is one of the general issues of the electroactive soft actuators.

One of the promising electroactive soft actuators is a three layered polymer actuator, of which two of the layers act as the anode and the cathode and these are

K. Kiyohara (✉) • T. Sugino • K. Asaka

Health Research Institute, National Institute of Advanced Industrial Science and Technology (AIST), 1-8-31, Midorigaoka, Ikeda, Osaka 563-8577, Japan

e-mail: k.kiyohara@aist.go.jp

separated by an ion conductive polymer layer. On applying voltage, the electrode layers change their volume in an asymmetric fashion and, as a result, the actuator as a whole shows bending motion. In order to clarify the mechanism of this type of actuators, one would need to understand the thermodynamics in the electrode layers at the molecular level. The molecular simulation techniques such as the Monte Carlo simulation or the molecular dynamics simulation are useful tools for this purpose. The Monte Carlo simulation is particularly useful for studying electrodes because it can represent the situation most realistically: unlike the molecular dynamics simulation, the Monte Carlo simulation can deal with the change in the numbers of ions in the electrodes efficiently by choosing the appropriate thermodynamic ensemble [2]. Since all three layered polymer actuators are composed of electrodes with porous structures in one or another way, we discuss the mechanism of the volume change of porous electrodes on applying voltage is discussed based on the results of the Monte Carlo simulation. Some of the examples of the three layered actuators made of porous carbon electrodes are the carbon nanotube paper [3] and the Bucky gel actuator [4]. The mechanisms of those actuators are not necessarily the same just because they are composed of porous electrodes. By analyzing the mechanism of volume change in porous electrodes at the molecular level, it would be possible to clarify the similarities and the differences for the actuators with different porous electrodes at the same basic grounds of the molecular interactions.

21.2 Model

In the Monte Carlo simulation, any model for the molecular interaction can be used. The usual strategy is to start with the simplest possible molecular interaction, rather than realistic ones, in order to extract the basic physics of the system, and then to refine the model later as needed. If one uses an elaborated model from the start, such as the one that includes all the detailed molecular structure or the electronic states, the required computational time could be extremely long, even though more quantitative description of the soft actuator may be aimed. In our study, the porous electrodes were modeled by slit porous electrodes that are formed by two hard plates that are set parallel to each other (see Fig. 21.1). Those plates are uniformly chargeable. The electrolyte ions were modeled by hard spheres that have a positive or negative charge at the center, which are called the primitive model. Those electrode plates and the ions interact in a uniform medium of a fixed dielectric constant. Obviously, there are two kinds of interactions in this model; the volume exclusion interaction and the electrostatic interaction. The volume exclusion interaction acts only repulsively but the electrostatic one acts both repulsively and attractively, depending on the signs of the charge of the pair of interacting objects. Although the detailed molecular structure of electrodes and ions and more detailed interactions such as the van der Waals interaction or the effect of polarizability were

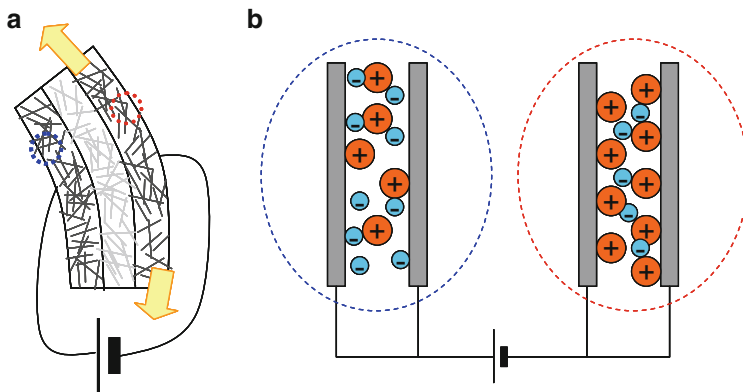


Fig. 21.1 (a) Schematic picture of the three layer actuator. *Yellow arrows* indicate that the cathode expands relative to the anode. (b) Schematic picture of the inside of the electrodes of the three layer actuator at the molecular scale. A small portion of the anode of the three layer actuator (the *blue circle* in (a)) and that of the cathode (the *red circle* in (a)) are magnified in the *blue* and the *red circle*, respectively

neglected in this model, it is a good place to start: the thermodynamic behaviors in porous electrodes are not well understood even for such a simple model of a porous electrode with electrolyte ions.

21.3 The Monte Carlo Simulation

Once the model of molecular interaction is chosen, thermodynamic properties of the system can be calculated by the Monte Carlo simulation. The Monte Carlo simulation is a computational method to calculate the thermodynamic properties at equilibrium according to the statistical mechanics for the given molecular models and external conditions: It makes a bridge between the microscopic properties (molecular interaction) and the macroscopic properties (thermodynamic properties). For the case of the porous electrodes, the energy is exchanged with the outside of the system in three forms; heat, insertion and removal of ions, and induction of surface charge. Therefore, the fundamental equation that defines the thermodynamics of the porous electrodes is

$$dE = TdS + \mu dN + \Phi dq \quad (21.1)$$

where E denotes the energy of the porous electrodes, T the temperature, S the entropy, μ the chemical potential of a minimum set of ions that make the whole charge neutral (a pair of a cation and an anion for the case of singly valenced ions), N the number of the ion sets, Φ the voltage and q the charge induced on the surface of the electrode. The thermodynamic ensemble represented by this equation is the

constant-voltage grand-canonical ensemble [2], where the thermodynamic fields are temperature, chemical potential of ions, and voltage.

We note here that specifying μ corresponds to specifying the concentration of ions in the bulk electrolyte, because chemical potential of ions is closely related to the concentration of the ions. At equilibrium, the value of μ of the ions in the bulk electrolyte and that in the porous electrodes should be the same, because ions can freely move between the bulk electrolyte and inside the porous electrodes. This also means that, once we specify μ , the thermodynamic potential of the ions are completely specified and it is not necessary to calculate the molecular interaction in the bulk electrolyte during the Monte Carlo simulation. In the ensemble that we used, the volume of the porous electrodes was fixed during the simulation. The pressure exerted inside the porous electrodes were calculated for different pore sizes separately. Whether the porous electrode tends to expand or contract for the given condition can be determined by plotting the pressure as a function of the pore size. It is possible to use an ensemble that allows the volume change of the porous electrodes by adding “ $-p dV$ ” on the right hand side of Eq. (21.1), where p is the pressure and V is the volume. However, using such an ensemble is not very meaningful unless the elastic strength of the porous electrodes is properly specified. Since the detailed information about the elastic strength for the real system is not available, we chose to use the ensemble for which dV is always zero.

The procedure of the Monte Carlo simulation is described as the following. For the model specified above, each configuration of the system is characterized by three kinds of properties; the number of ions, the position of those ions, and the surface charge density on each electrode plates. The values of those properties are randomly changed by the computer to generate configurations and each configuration is weighted by the Boltzmann factor of the corresponding ensemble in order to calculate the thermodynamic average of a physical property. Typically, tens of millions of configurations are generated by the computer for the system size that contains hundreds to a thousand pairs of ions. The Boltzmann factor that corresponds to the constant-voltage grand-canonical ensemble has the form $\exp[-(\mu N - E + \Phi q)/k_B T]$, where k_B is the Boltzmann constant.

21.4 Thermodynamic Behaviors of Ions in Porous Electrodes

21.4.1 Effects of Porosity

It would be worth while to speculate how the porosity of the electrode would affect the thermodynamics based on the molecular interactions of the model, before discussing the detail of the simulation results. If the electrode is plane and adjacent to a bulk electrolyte, when voltage is applied to the electrode, electrical double layers (EDLs) form on the electrode surface. The typical thickness of the EDLs

would be a few times the diameter of the electrolyte ions. The counterions accumulate near the electrode surface with a high concentration on applying voltage. Apart from the electrode surface by the thickness of the EDLs, the concentration of the ions are no different from the bulk before applying the voltage, because the electrostatic potential caused by the electrode surface is shielded by the EDLs. Consequently, for the case of planar electrodes, thermodynamic properties in the electrolyte do not significantly change on applying voltage: the pressure acting on the electrode is virtually the same as before applying the voltage.

On the other hand, if the electrode has a porous structure and the pore size is similar to or smaller than the thickness of the EDLs, the EDLs develop from the both sides of the pore and, for a sufficient applied voltage, they may overlap. In this case, the thermodynamic properties inside the pore are not the same as those before applying voltage nor those in the bulk. It might be tempting to think that, in such small porous electrodes, the pressure inside the pore would always increase when voltage is applied because the concentration of the counterions would become higher. However, such a theory misses the consideration of electrostatic interaction.

The simple model that we used has two kinds of interactions; the volume exclusion interaction and the electrostatic interaction. When concentration of ions in the pore increases, the pressure increases due to the volume exclusion interaction. The electrostatic interaction among the counterions tends to increase the pressure because they are similarly charged. On the other hand, the electrostatic interaction between the counterions and the electrode surface tends to decrease the pressure because they are oppositely charged. This speculation shows that, even if the model is simple, whether the pressure in the porous electrode increases or decreases on applying voltage is by no means obvious.

21.4.2 Some Simulation Results and Their Implications

In the following, we show the results of the Monte Carlo simulation and discuss the thermodynamics in porous electrodes [5]. For the electrolyte ions, we used the primitive model for which the ratio of the diameter of cations, d_+ , and that of anions, d_- , is $d_-/d_+ = 0.8$. For such an asymmetric electrolyte ions, the ionic structure and the thermodynamics in the cathode and those of the anode are different. For the case of the three layer actuators, the asymmetric generation of pressure and resulting volume change cause the bending motion. Here, the unit of length was chosen to be d_+ and the unit of energy $e^2/(4\pi\epsilon d_+)$, where e is the electron charge and ϵ is the dielectric constant of the medium. Using these units, the molecular interaction is completely defined once the distance between the ions and the electrodes is specified. The external fields, which are denoted by T , μ , and Φ in Eq. (21.1), are specified as the following. If d_+ is chosen to be 4.2 Å and ϵ to be 10, the thermal energy, T , of 300 K corresponds to 0.075 times the unit energy. Considering that the unit of voltage is made by dividing the unit of energy by the electron charge, 1 V corresponds to $\phi = 0.232$, where $\phi = \Phi/4\pi$. The chemical potential, μ , was chosen

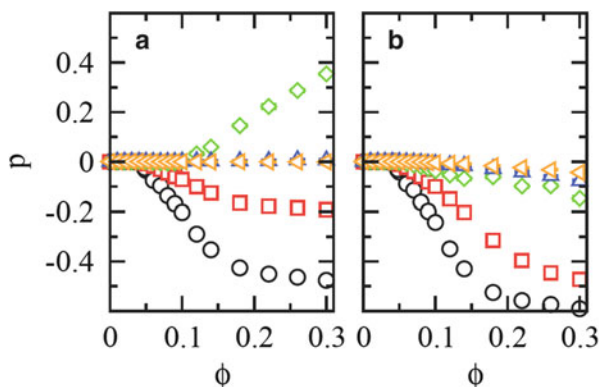


Fig. 21.2 Pressure as a function of voltage for electrolyte ions with cation diameter $d_+ = 1.0$ and anion diameter $d_- = 0.8$ in the anode (a) and that in the cathode (b). The results for pore sizes $W = 1.1, 1.5, 2.0, 4.0$ and 8.0 are denoted by *circles, squares, diamonds, up-triangles, and left-triangles*, respectively. The scale in the vertical axis is the same for (a) and (b). Reproduced with permission from Kiyohara and Asaka [5]. Copyright Taylor & Francis (2013)

in such a way that the concentration of ions in the bulk was chosen to be 0.5 mol/dm^3 by preliminary simulations. The porosity of the electrodes is defined by W , which is the pore size or the separation of the two electrode plates in the unit of d_+ . In this study, W was chosen to be the same for the anode and the cathode.

Figure 21.2 shows the pressure in the cathode and the anode at equilibrium as a function of voltage for five different pore sizes; $W = 1.1, 1.5, 2.0, 4.0$, and 8.0 . Pressure has the unit of energy divided by cubed length. For the unit specified above, the atmospheric pressure or 10^5 Pa corresponds to $p = 1.35 \times 10^{-4}$. The variation of the pressure shown in Fig. 21.2 is two to three orders of magnitude larger than the atmospheric pressure. Although we do not expect quantitative agreement with the real systems, it would not be surprising if a large magnitude of pressure is exerted inside the pore. It is also interesting to find that the voltage dependence of the pressure is significantly different for different pore sizes. For the same pore size, the voltage dependence of the pressure is different for the cathode and for the anode. For $W = 1.1$, the pressure decreases with voltage both in the anode and the cathode. The pressure also decreases for $W = 1.5$ and it does so more significantly in the cathode for the large voltages. For $W = 2.0$, the pressure in the anode shows near zero values for small voltages and it starts to increase near $\phi = 0.1$ and the pressure in the cathode decreases with voltage. For $W = 4.0$ and 8.0 , the change of pressure as a function of voltage is small. If the pressures of different pore sizes are compared for a fixed pressure, it becomes apparent that the pressure significantly changes for a small change of the pore size. For example, the pressure in the anode at $\phi = 0.3$ shows a large negative values for $W = 1.1$ and 1.5 but a large positive value for $W = 2.0$. It then shows near zero values for large pores of $W = 4.0$ and 8.0 .

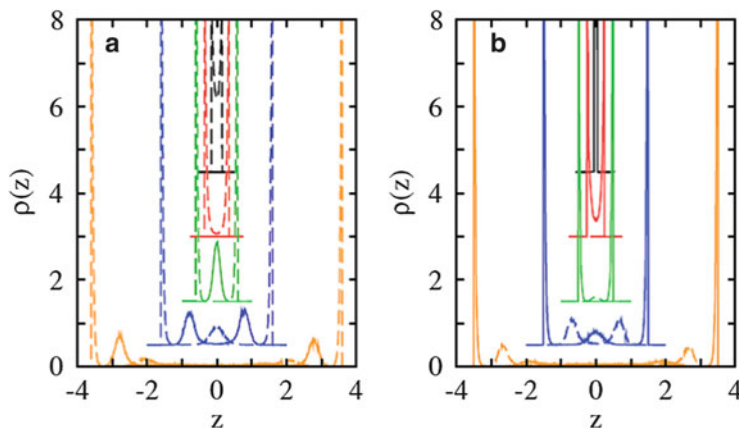


Fig. 21.3 Ion density profile in the anode (a) and the cathode (b) for electrolyte ions with cation diameter $d_+ = 1.0$ and anion diameter $d_- = 0.8$ at voltage $\phi = 0.30$. The results for $W = 1.1, 1.5, 2.0, 4.0$ and 8.0 are denoted by *black, red, green, blue* and *orange*, respectively. *Dashed lines* denote the anion density and *solid lines* the cation density. The results for pore sizes other than $W = 8.0$ are shifted in the vertical direction. The highest peaks are truncated. Reproduced with permission from Kiyohara and Asaka [5]. Copyright Taylor & Francis (2013)

As discussed in Sect. 21.4.1, it is reasonable that the pressure is similar for large pore sizes, because the EDLs in the same pore do not significantly overlap. For small pore sizes, the pressure significantly changes as a function of voltage and pore size. The pressure exerted due to the volume exclusion interaction is always positive by construction. The pressure exerted due to the electrostatic interaction can in principle be positive or negative. In the detailed analysis of the pressure, we found that the pressure due to the electrostatic interaction is negative for all the conditions that we used. The sign of the pressure is determined by the balance between the volume exclusion interaction, which exerts positive pressure, and the electrostatic interaction, which exerts negative pressure.

The reason for the non-monotonical change of pressure as a function of the pore size can be explained by the ionic structure inside the pore. Figure 21.3 shows the concentration profile of the ions for $W = 1.1, 1.5, 2.0, 4.0$, and 8.0 at $\phi = 0.3$. In the anode of pore size $W = 1.1$ (Fig. 21.3a), only the anions (dashed line) are distributed. The high concentration in the middle indicates that the EDLs on the both sides are so close that they overlap. When the pore size increases to $W = 1.5$, the structure is somewhat relaxed in packing, showing the region of small concentration in the middle of the pore. For $W = 2.0$, there appears a peak of coions (solid line) in the middle of the pore. The coions interact with neighboring counterions by both the volume exclusion (repulsive) and the electrostatic (attractive) interaction, in addition to the long range interaction with the electrode surfaces. For $W = 4.0$, the peak of the coions splits with decrease of the height, showing the relaxation in the packing, and there appears a small peak of counterions in the middle of the pore. For $W = 8.0$, there appears a large region of flat concentration in the middle of the

pore, showing the EDLs on the both sides are separately and almost completely formed. The ionic structure of this large pore size should be no different from that of a planar electrode adjacent to the bulk electrolytes.

It is notable that, in Fig. 21.3, a sharp peak of coions in the anode of $W = 2.0$ is present. The volume exclusion interaction between those coions and neighboring counterions is the main cause of the positive pressure that is shown in Fig. 21.2. The peaks of coions in the anode for $W = 4.0$ are as low as those of $W = 8.0$. This shows that $W = 4.0$ is large enough for the structure of coions to relax and for the EDLs to form separately. The ionic structure for $W = 1.1$, for which the concentration is high in the middle, also indicates significant packing and resulting large volume exclusion (repulsive) interaction between the counterions and the electrode surfaces. However, the electrostatic (attractive) interaction is also large in this case, because the counterions are close to the electrode surfaces on the both sides. The electrostatic interaction turned out to overcome the volume exclusion interaction in this case.

These examples show that the counterions form the first peak of concentration and coions form the second peak on the electrode surfaces. Such behaviors cannot be found in mean field theories such as the Guoy–Chapman theory, which neglects the size of the ions. Accumulation of coions near the electrode surface, which is an example of the correlation effect [6, 7], occurs only when the electrostatic interaction is strong. When the temperature or the dielectric constant of the medium is large enough, the electrostatic interactions is weak and the correlation effect is invisible. The non-monotonical behavior of the pressure as a function of the voltage and the pore size is a manifestation of the correlation effect and the confined environment. For a large enough value of the dielectric constant of the medium, the pore size dependence of the pressure has been found to be monotonical because the volume exclusion interaction dominates.

21.4.3 Comparison with Experimentally Proposed Theories

The mechanism of volume change in porous electrodes has been explained in several different ways. Oren et al. have studied the volume change of graphite in aqueous solution of electrolytes [8]. They found that the volume of the graphite electrodes expand for both positive and negative voltage. They also found that the expansion rate is closely related to the amount of charge that is induced on the electrode surface. So, they explained that the expansion of graphite is caused by the surface tension caused by the accumulation of counterions on the electrode surface. Intercalation of various atoms and molecules in carbon materials and associated volume change during the formation of the graphite intercalated compounds have been studied and the mechanism of the volume change has been explained both by the volume exclusion effect and the charge transfer [9]: the volume of carbon materials increases by the amount and the size of the intercalants and also carbon-carbon bond length changes due to the charge transfer associated with the intercalation.

The mechanisms of volume change of porous carbon materials on applying voltage can be categorized in three groups; (1) surface tension due to counterions on the electrode surface, (2) change of carbon-carbon bond length on charging, and (3) volume exclusion effect due to intercalation. Surface tension of counterions changes the pressure in the direction parallel to the electrode surface, but it can create pressure in the vertical direction as well if the surface is curved. Unfortunately, however, this mechanism does not seem to have been explored in detail. Change of carbon-carbon bond length has been studied both theoretically [10] and experimentally [11]. According to this mechanism, the carbon material expands when it is charged negatively and contracts when charged positively. This mechanism seems to be well accepted, but the experimental results of the actuator with carbon nanotube sheet cannot be explained solely by this mechanism when the applied voltage is large: when a large positive charge is induced on the carbon nanotube sheet, it expands. Baughman et al. have developed the polymer actuator of which the electrode is composed of carbon nanotube sheet and the mechanism of volume change of the electrodes was explained by both the volume exclusion effect and the charge transfer [3]. Fukushima et al. have developed the polymer actuator with the Bucky-gel and the mechanism of volume change of the electrodes was explained by the asymmetry of the volume exclusion effect between the anode and the cathode [4].

Volume exclusion effect due to intercalation of counterions primarily explains the expansion of the electrode. In some discussions, de-intercalation of coions, which should cause contraction, is similarly treated. Since the size of anions and that of cations are different, this asymmetry, which is present in both intercalation and de-intercalation, may explain the bending motion of the three layer actuators. However, some studies show that the relative volume change of the cathode and the anode significantly depends on the duration of applying voltage. This means that the mechanism of volume change depends not only on the molecular structure but also on the transient relaxation process. This fact complicates the analysis of the mechanism of volume change of porous electrodes.

Our study using the Monte Carlo simulation is most closely related to the theory of the volume exclusion effect due to intercalation, because we calculated the pressure that acts perpendicular to the electrode surface and we did not include the effect of change of bond length in the electrode. However, we also explicitly included the electrostatic interaction between the ions and the electrodes in the model. The simulation results show that, in porous electrodes with small pore sizes, slight change in the molecular structure or in the external field can drastically change the thermodynamic properties in porous electrodes. The reason for that is because the pressure exerted by the volume exclusion interaction and that of the electrostatic interaction are opposite in sign but similar in magnitude. We also note that there is an experimental study that discusses the effect of the electrostatic interaction on the volume change of graphite. In that study, it was found that, on applying voltage, the graphite expanded as it was intercalated with ions, but on further raising the voltage, the graphite contracted [12]. This is an experimental evidence that shows the importance of the electrostatic interaction in the volume change of the porous electrode.

21.5 Conclusions

The three layered actuators show bending motion on applying voltage due to the asymmetric volume change of the two electrode layers. In order to analyze its mechanism at the molecular level, we performed Monte Carlo simulations in the constant-voltage grand-canonical ensemble with simple models of ions and porous electrodes. In this method, the volume exclusion interaction and the electrostatic interaction between the electrolyte ions and the electrode surfaces are explicitly taken into consideration at the molecular level.

We found that, when the pore size of the electrode is so small that it is comparable to the size of the electrolyte ions, slight change in the molecular structure or in the external field can drastically change the thermodynamic properties in porous electrodes. The reason for that is because the pressure exerted by the volume exclusion interaction and that of the electrostatic interaction are opposite in sign but similar in magnitude. The pressure exerted inside the porous electrodes can be two or three orders of magnitude larger than the atmospheric pressure. These findings show that the balance between the volume exclusion interaction and the electrostatic interaction is the key concept in considering the thermodynamics in porous electrodes. This concept would be useful in designing actuators at the molecular level.

References

1. Bar-Cohen Y (ed) (2001) Electroactive polymer actuators as artificial muscles. SPIE, Washington
2. Kiyohara K, Asaka K (2007) Monte Carlo simulation of porous electrodes in the constant voltage ensemble. *J Chem Phys* 126:214704–214720
3. Baughman RH, Cui C, Zakhidov AA, Iqbal Z, Barisci JN, Spinks GM, Wallace GG, Mazzoldi A, De Rossi D, Rinzler AG, Jaschinski O, Roth S, Kertesz M (1999) Carbon nanotube actuators. *Science* 284:1340–1344
4. Fukushima T, Asaka K, Kosaka A, Aida T (2005) Fully plastic actuator through layer-by-layer casting with ionic-liquid-based Bucky gel. *Angew Chem Int Ed* 44:2410–2413
5. Kiyohara K, Asaka K (2013) Voltage induced pressure in porous electrodes. *Mol Phys* 111:297–308
6. Levin L (2002) Electrostatic correlations: from plasma to biology. *Rep Prog Phys* 65:1577–1632
7. Grosberg AY, Nguyen TT, Shklovskii BI (2002) The physics of charge inversion in chemical and biological systems. *Rev Mod Phys* 74:329–345
8. Oren Y, Glatz I, Livnat A, Kafri O, Soffer A (1985) The electrical double layer charge and associated dimensional charges of high surface area electrodes as detected by more deflectometry. *J Electroanal Chem* 187:59–71
9. Dresselhaus MS, Dresselhaus G (2002) Intercalation compounds of graphite. *Adv Phys* 51:1–186

10. Chan CT, Kamitakahara WA, Ho KM (1987) Charge-transfer effects in graphite intercalates: ab initio calculations and neutron-diffraction experiment. *Phys Rev Lett* 58:1528–1531
11. Flandrois S, Hauw C, Mathur RB (1989) Charge transfer in acceptor graphite intercalation compounds. *Synth Metal* 34:399–404
12. Shioyama H, Fujii R (1987) Electrochemical reactions of stage 1 sulfuric acid-graphite intercalation compound. *Carbon* 25:771–774

Chapter 22

Material Modeling

Yutaka Toi

Abstract Attention has been focused on ionic conducting polymer-metal composites (IPMCs) as intelligent materials for artificial muscles and robotics for recent years. The two-dimensional finite element formulation based on the Galerkin method is conducted for the basic field equations governing electrochemical response of IPMC beams with two pairs of electrodes upon applied electric field. The three-dimensional finite element analysis is conducted for the deformation of IPMC beams due to water redistribution in the beams associated with the electrochemical response. Some numerical studies are carried out in order to show the validity of the present formulation. A computational modeling is also established for the electrochemical-poroelastic behavior of conducting polymers such as polypyrrole. The three-dimensional continuum modeling given by Della Santa et al. for the passive, poroelastic behavior of conducting polymers is extended to the formulation for the active, electrochemical-poroelastic formulation according to Onsager-like laws, which is combined with the one-dimensional equation for ionic transportation. The validity of the finite element formulation for these governing equations has been demonstrated by numerical studies for the passive and active responses of polypyrrole membranes.

Keywords Actuator • Computational mechanics • Conducting polymer • Electrochemical-mechanical analysis • Finite element method

22.1 Ionic Conducting Polymer Actuators

Much attention has been focused on ionic conducting polymer-metal composites (IPMCs) as intelligent materials for artificial muscles, robotics, and MEMS in recent years [1]. The bending motion of an ionic conducting polymer gel film (ICPF), both sides of which are galvanized with platinum electrodes, was first found by Oguro et al. [2]. Since then, the electrochemical-mechanical behaviors

Y. Toi (✉)

Institute of Industrial Science, University of Tokyo, 4-6-1 Komaba, Meguro-ku,
Tokyo 153-8505, Japan
e-mail: toi@iis.u-tokyo.ac.jp

of IPMC materials consisting of polyelectrolyte membrane such as Nafion and Flemion have been theoretically and experimentally studied by many researchers.

The in-plane bending of the IPMC beam when a weak electric field is applied between its top and bottom faces is dominated by internal water redistribution. Internal water redistribution is associated with two phenomena, electroosmosis of hydrated ions to the cathode side and self-diffusion of water molecules to the anode side.

Kanno et al. [3] discussed the dynamics of ICPF actuators by black-box linear modeling. Shahinpoor et al. [4] presented a number of models for the micro-electromechanics of IPMCs as electrically controllable artificial muscles. Nemat-Nasser and Li [5] developed a micromechanical model that accounts for the coupled ion transport, electric field, and elastic deformation to predict the response of IPMCs. Tadokoro et al. [6] proposed a white-box actuator model on the basis of physicochemical hypotheses, in which the travel of sodium ions and water molecules in the actuator membrane is assumed to generate eigenstrains causing the deformation of IPMCs. Popovic and Taya [7] proposed a simulation model of Nafion-Pt (platinum) actuation behavior in dry conditions based on the effect of charge and water redistribution upon the applied electric field and self-diffusion of water molecules due to concentration gradients. Toi and Kang [8, 9] discretized the basic one-dimensional equations governing the electrochemical behavior of IPMC beams and plates by the Galerkin finite element method [10]. The three-dimensional finite element analysis based on the initial strain method for the deformation response of the IPMC beams and plate is conducted by using the evaluated eigenstrain due to water redistribution as an initial strain.

22.2 Computational Modeling of Electrochemical Response of Ionic Conducting Polymer Actuators

When an IPMC beam composed of a Nafion membrane and two pairs of platinum electrodes as shown in Fig. 22.1 is subjected to a step voltage as shown in Fig. 22.2; it exhibits the bending deformation response, which consists of the following two processes. The first process is the forward motion in which the beam bends toward the anode side on a short time scale. This bending deformation is due to the swelling of Nafion near the cathode side and the contraction near the anode side, which are caused by the sudden movement of hydrated cations to the cathode sides. The forward motion is followed by the second process, called the backward motion, in which slow recovery of the bending deformation takes place by the diffusion of free water molecules to the anode side. In this section, the finite element formulation based on the Galerkin method is applied to the electrochemical differential equations governing these two processes.

Fig. 22.1 Platinum-plated Nafion membrane

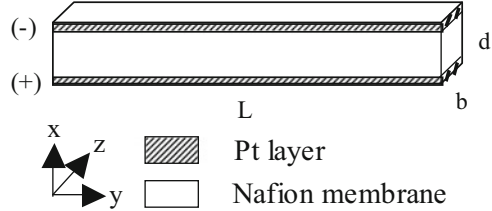
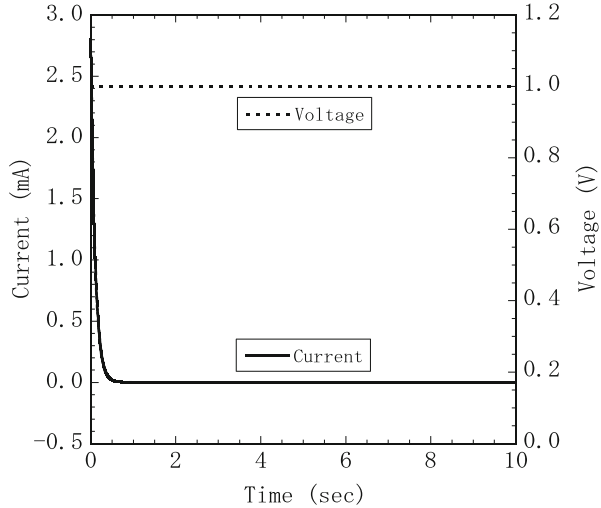


Fig. 22.2 Input step voltage and electric current waveform



22.2.1 Forward Motion

When a Nafion membrane is under an electric field caused by the step voltage on the platinum electrodes, hydrated sodium cations are subjected to electric forces toward the cathode side. The hydrated cations are also subjected to a viscous resistance force and a diffusion force in the anode direction. Based on the balance of these forces, the total charge $Q(x, t)$ is expressed as follows:

$$\eta_1 \frac{\partial Q(x, t)}{\partial t} = kT \frac{\partial^2 Q(x, t)}{\partial x^2} - \frac{\partial Q(x, t)}{\partial x} \left\{ \frac{e}{\epsilon_e \mathcal{S}_x} \left[\int_0^t i(\tau) d\tau + Q(x, t) - Q(x, 0) \right] \right\} \quad (22.1)$$

In Eq. (22.1), i is the electric current as shown in Fig. 22.2. The initial and boundary conditions are given as follows:

Table 22.1 Material parameters and calculation conditions for forward motion analysis

Coefficient of viscosity for hydrated Na ⁺	$\eta_1 = 1.18 \times 10^{-11} \text{ (N} \cdot \text{s/m}^2\text{)}$
Boltzmann constant	$k = 1.380 \times 10^{-23} \text{ (N} \cdot \text{m/K)}$
Absolute temperature	$T = 293 \text{ (K)}$
Elemental charge	$e = 1.6 \times 10^{-19} \text{ (C)}$
Dielectric constant of hydrated Nafion membrane	$\epsilon_e = 2.8 \times 10^{-3} \text{ (C}^2\text{/N} \cdot \text{m}^2\text{)}$
Cross-section area	$S_x = 34.2 \times 10^{-6} \text{ (m}^2\text{)}$
Avogadro's number	$N_a = 6.02 \times 10^{23} \text{ (/mol)}$

$$\{Q(x, 0)\} = N_a e S_x c_0 x, \quad \{Q(0, t)\} = 0, \quad \{Q(d, t)\} = N_a e S_x c_0 d \quad (22.2)$$

Table 22.1 shows the material constants and calculation conditions used for solving Eqs. (22.1) and (22.2) in which it is assumed that $c_0 = c(x, 0) = 1147 \text{ mol/m}^3$. The charge density $c(x, t)$ is calculated from the total charge using the following equation:

$$Q(x, t) = N_a e S_x \int_0^x c(\xi, t) d\xi \quad (22.3)$$

It should be noted that, when necessary, the density of water molecules $w(x, t)$ during the forward motion can be given by

$$w(x, t) = w_1 + w_2(x, 0) + nc(x, t) \quad (22.4)$$

The following equation for the total charge $\{Q_N(x, t)\}$ is obtained by the finite element formulation of Eq. (22.1) based on the Galerkin method:

$$\begin{bmatrix} A_{11}^{(e)} & A_{12}^{(e)} \\ A_{21}^{(e)} & A_{22}^{(e)} \end{bmatrix} \{Q_N(x, t + \Delta t)\} = \begin{bmatrix} B_{11}^{(e)} & B_{12}^{(e)} \\ B_{21}^{(e)} & B_{22}^{(e)} \end{bmatrix} \{Q_N(x, t)\} \quad (22.5)$$

The following equation for the charge density $\{c_N(x, t)\}$ is obtained by the Galerkin finite element formulation for Eq. (22.3):

$$\begin{bmatrix} C_{11}^{(e)} & C_{12}^{(e)} \\ C_{21}^{(e)} & C_{22}^{(e)} \end{bmatrix} \{c_N(x, t)\} = \begin{bmatrix} D_{11}^{(e)} & D_{12}^{(e)} \\ D_{21}^{(e)} & D_{22}^{(e)} \end{bmatrix} \{Q_N(x, t)\} \quad (22.6)$$

22.2.2 Backward Motion

The second process is the slow diffusion of water molecules in the anode direction. The density of water molecules $w(x, t)$ is calculated with the following equation:

Table 22.2 Material parameters and calculation conditions for backward motion analysis

Concentration of water bound to the fixed SO_3^- groups	$w_1 = 4381 \text{ (mol/m}^3\text{)}$
Concentration of free water molecules	$w_2 = 4381 \text{ (mol/m}^3\text{)}$
Time that the first stage ends and the second stage begins	$t_1 = 0.11 \text{ s}$
Hydration number of Na^+ ions in swollen Nafion	$n = 4.7$
Coefficient of viscosity for free water molecules	$\eta_2 = 11.6 \times 10^{-11} \text{ (N} \cdot \text{s/m}^2\text{)}$

$$\frac{\partial w(x, t)}{\partial t} = \frac{kT}{\eta_2} \frac{\partial^2 w(x, t)}{\partial x^2} \quad (22.7)$$

The initial and boundary conditions are given by Eq. (22.8).

$$w(x, 0) = w_1 + w_2(x, 0) + nc(x, t_1), \quad \frac{\partial w(0, t)}{\partial x} = 0, \quad \frac{\partial w(d, t)}{\partial x} = 0 \quad (22.8)$$

Table 22.2 shows the material parameters and calculation conditions for the backward motion.

The finite element formulation of Eq. (22.7) based on the Galerkin method leads to the following equation for the water molecule density $\{w_N(x, t)\}$:

$$\begin{bmatrix} A_{11}^{(e)} & A_{12}^{(e)} \\ A_{21}^{(e)} & A_{22}^{(e)} \end{bmatrix} \{w_N(x, t + \Delta t)\} = \begin{bmatrix} E_{11}^{(e)} & E_{12}^{(e)} \\ E_{21}^{(e)} & E_{22}^{(e)} \end{bmatrix} \{w_N(x, t)\} \quad (22.9)$$

22.3 Three-Dimensional Mechanical Response Analysis of Nafion Actuators

The three-dimensional finite element deformation analysis with an eight-noded hexahedron element can be conducted for the IPMC beam under given boundary conditions by using an estimated eigenstrain $\{\varepsilon_i(x, t)\}$ that is proportional to $w(x, t)$ as the initial strain in the IPMC beam. The incremental stiffness equation for the initial strain increment $\{\Delta\varepsilon_i\}$ is expressed as follows:

$$[k]\{\Delta u_N\} = \{\Delta f_i\} \quad (22.10)$$

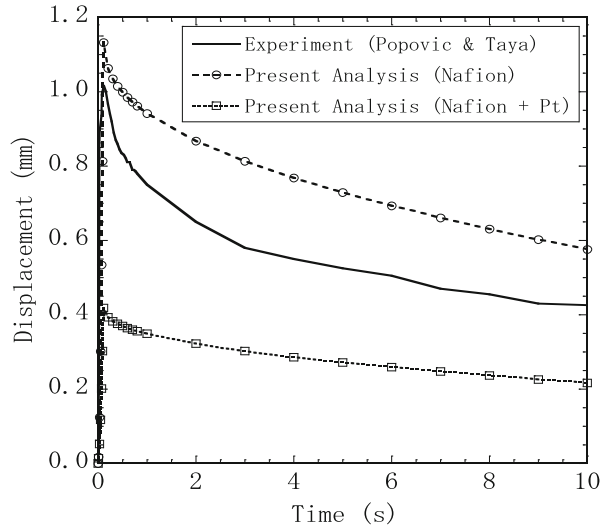
where

$$\{\Delta f_i\} = \int_{V_e} [B]^T \{\Delta\sigma_i\} dV, \quad \{\Delta\sigma_i\} = [D]\{\Delta\varepsilon_i\} \quad (22.11)$$

where the following symbols are used: $[k]$, the incremental element stiffness matrix; $\{\Delta u_N\}$, the incremental nodal displacement vector; $\{\Delta f_i\}$, the incremental apparent external force vector; $[B]$, the strain–nodal displacement matrix; and $[D]$, the elastic stress–strain matrix for the Nafion membrane or platinum electrodes.

Table 22.3 Mechanical properties of IPMC

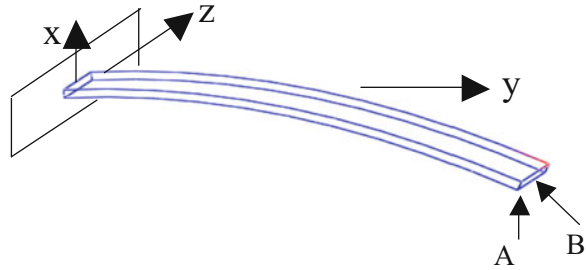
	Young's modulus (GPa)	Poisson's ratio
Nafion membrane	0.23	0.49
Platinum layer	146.8	0.39

Fig. 22.3 Time-history of displacement of the platinum-plated Nafion membrane

The IPMC beam model shown in Fig. 22.1 is analyzed under the electric voltage and current input shown in Fig. 22.2. The material constants and calculation conditions necessary for the electrochemical analysis are shown in Tables 22.1 and 22.2. The mechanical properties of the Nafion membrane and the platinum electrodes are given in Table 22.3. The dimensions of the model are as follows: length $L = 20$ mm, depth of the Nafion membrane $d = 200$ μm , breadth $b = 1.8$ mm, and thickness of the platinum electrode $t = 0.25$ μm .

In Fig. 22.3, the calculated time-histories of the tip displacement are compared with the experimental result obtained by Popovic and Taya [7]. The deformation process through the forward and the backward motion has successfully been simulated by the finite element analysis. Figure 22.3 contains two kinds of calculated results, one of which shows the mechanical response of a pure Nafion membrane and the other, the mechanical response of a Nafion membrane with platinum electrodes. The actual rigidity of the IPMC beam can be considered to be between the two calculated cases because some of the platinum particles are dispersed inside the Nafion membrane [11]. Therefore the correspondence between the calculated and experimental results shown in Fig. 22.3 can be considered to be reasonable. As the eigenstrain near the cathode side where the water molecules gather is larger than that on the anode side, the beam deflects to the anode side, as shown in Fig. 22.4, which is a reasonable result.

Fig. 22.4 Schematic depiction of the deformation of a platinum-plated Nafion membrane



The references include details of the present analysis [8, 9], two-dimensional equations for the electrochemical response [12], and an extension to an IPMC actuator analysis using other materials such as Flemion [13, 14].

22.4 Conducting Polymer Actuators

Actuators using conducting polymers such as polypyrrole have the following advantages: (1) generation of large forces (that are several tens of times as large as the forces of human muscles), (2) structural simplicity and light weightness, (3) noiselessness, and (4) operation by low voltage (1–2 V). The development, application, and production of such actuators are expected in the fields of robotics, biomedical engineering, and micro-electromechanical systems [15–19].

Deformation of the expansion and contraction of a conducting polymer membrane in an electrolyte bath occurs due to the inward and outward flow of electrolyte caused by the pressure difference between the inside and outside of the membrane. This is a passive, poroelastic behavior [15–17]. When turning on the electrical current between a conducting polymer membrane and the electrolyte, the deformation of the expansion and contraction of the conducting polymer membrane is accelerated by the insertion and de-insertion of ions, which is an active, electrochemical-poroelastic behavior [15–17]. The polypyrrole that is doped with relatively small anions such as ClO_4^- expands and contracts due to the insertion and de-insertion of the anions (oxidation and reduction), which is classified as anion-driven actuation [18, 19]. On the other hand, anions do not move in the polypyrrole doped with relatively large anions such as DBS (docecylbenzene sulfonate), which expands and contracts due to the insertion and de-insertion of cations (reduction and oxidation). This process is classified as cation-driven actuation [18, 19].

Della Santa et al. [15–17] derived the governing equations of continuum modeling based on poroelasticity theory for the response of conducting polymer actuators using polypyrrole. They compared one-dimensional theoretical solutions for the passive, poroelastic behavior with the experimental results, however, details of the formulation for the active, electrochemical-poroelastic behavior were not given.

Toi and Jung [20, 21] extended the three-dimensional continuum modeling given by Della Santa et al. [15–17] based on Biot’s poroelasticity theory [22] to the formulation for the active, electrochemical-poroelastic behavior according to Onsager’s law [23], which was combined with the one-dimensional ionic transportation equation given by Tadokoro et al. [6] to construct the system of governing equations. The governing equations were discretized by the finite element method. Numerical calculations were conducted for the passive, poroelastic behavior and the active, electrochemical-poroelastic behavior, the results of which were respectively compared with the theoretical solution [15] and the experimental results [16] to illustrate the validity of the present modeling.

22.5 Computational Modeling of Electrochemical-Poroelastic Response of Conducting Polymer Actuators

22.5.1 Stiffness Equation of Poroelastic Solid

According to Biot’s theory [22], the equilibrium equation of poroelastic solids containing fluid is given as follows:

$$\frac{\partial \sigma_{ij}^t}{\partial x_j} = 0 \quad (22.12)$$

where

$$\sigma_{ij}^t = \sigma_{ij}^s + \sigma_{ij}^f, \quad \sigma_{ij}^s = \frac{E}{1 + \nu} \epsilon_{ij}^s + \frac{\nu E}{(1 + \nu)(1 - 2\nu)} e^s \delta_{ij}, \quad \sigma_{ij}^f = -\beta P \delta_{ij} \quad (22.13)$$

in which the following notations are used: σ_{ij}^t , total stress; σ_{ij}^s , partial (average) stress of the solid phase; σ_{ij}^f , partial (average) stress of the liquid phase; x_j , Cartesian coordinates; E , Young’s modulus; ν , Poisson’s ratio; ϵ_{ij}^s , strain of the solid phase; e^s , volumetric strain of the solid phase; δ_{ij} , Kronecker’s delta; β , porosity; and P , pressure. It is noted that the coefficients E and ν in Eq. (22.13) have a substantial difference from those of a conventional elastic system: they are variable with the porosity β [15].

The displacement increment $\{\Delta u\}$ and the pressure increment ΔP in each element are assumed to have the following forms:

$$\{\Delta u\} = [N_u] \{\Delta u_N\}, \quad \Delta P = [N] \{\Delta P_N\} \quad (22.14)$$

where $[N_u]$ and $[N]$ are the shape function matrices of the eight-node hexahedron elements. $\{\Delta u_N\}$ and $\{\Delta P_N\}$ are the nodal displacement increment vector and the

nodal pressure increment vector, respectively. Using Eq. (22.13), the solid stress increment vector $\{\Delta\sigma^s\}$ and the fluid stress increment vector $\{\Delta\sigma^f\}$ are respectively expressed by the following equations:

$$\{\Delta\sigma^s\} = [D^s]\{\Delta\varepsilon\} = [D^s][B]\{\Delta u^N\}, \quad \{\Delta\sigma^f\} = -\beta[H]^T \Delta P \quad (22.15)$$

where $[B]$ is the strain-nodal displacement matrix for solids, $[D^s]$ is the stress-strain matrix for solids, and $[H]$ is the coefficient matrix determined by Eq. (22.13).

Substituting Eq. (22.15) into Eq. (22.12), the following three-dimensional element stiffness equation for poroelastic solids can be obtained:

$$[K]\{\Delta u_N\} = \beta[B^*]\{\Delta P_N\} \quad (22.16)$$

where

$$[K] = \int_{V_e} [B]^T [D^s] [B] dV, \quad [B^*] = \int_{V_e} [B]^T [H] [N] dV \quad (22.17)$$

22.5.2 Poisson's Equation for Pressure

According to Onsager's law [23], the relations among the ionic flux J , the mass flux V^f , the electric potential gradient $\nabla\varphi$, and the pressure gradient ∇P can be expressed as follows:

$$J = K_{11}\nabla\varphi + K_{12}\nabla P, \quad V^f = K_{21}\nabla\varphi + K_{22}\nabla P \quad (22.18)$$

Calculating the divergence of both sides of Eq. (22.18) and eliminating $\nabla^2\varphi$, the following equation is used:

$$\text{div}V^f = \frac{\partial e^f}{\partial t} \quad (22.19)$$

Then, using the relation concerning the passive, poroelastic behavior [15]:

$$\frac{\partial e^f}{\partial t} = -\frac{(1-\beta)}{f}\nabla^2 P \quad (22.20)$$

and Biot's equation of continuity (Biot 1954):

$$\frac{\partial e^s}{\partial t} = -\frac{\beta}{1-\beta}\frac{\partial e^f}{\partial t} \quad (22.21)$$

the following Poisson's equation for pressure in the case of electrochemical response can be derived:

$$\frac{\partial e^s}{\partial t} = C_1 \frac{-\beta}{(1-\beta)} \nabla J + C_2 \frac{\beta}{f} \nabla^2 P \quad (22.22)$$

where f is a coefficient representing permeability of fluid in porous solids, which is called the frictional coefficient between solid and fluid [15].

Implementing the finite element formulation of Eq. (22.22) based on the Galerkin method, the following equation for the volumetric strain rate of solids $\{\dot{e}_N^s\}$, the rate of change of the charge density $\{\dot{c}_N\}$, and the pressure $\{P_N\}$ can be obtained:

$$[S]\{\dot{e}_N^s\} = C_1 \frac{\beta}{(1-\beta)} [S]\{\dot{c}_N\} - C_2 \frac{\beta}{f} [A]\{P_N\} \quad (22.23)$$

22.5.3 Evolution Equation for Volumetric Strain Rate

Substituting Eq. (22.22) into the following form of the motion law for the passive, poroelastic behavior [15]:

$$\frac{(1-\nu)E}{(1+\nu)(1-2\nu)} \nabla^2 e^s = \beta \nabla^2 P \quad (22.24)$$

the following evolution equation of the volumetric strain for the electrochemical-poroelastic behavior can be derived:

$$L \nabla^2 e^s = \frac{1}{C_2} \frac{\partial e^s}{\partial t} + \frac{C_1}{C_2} \frac{\beta}{(1-\beta)} \nabla J \quad (22.25)$$

where

$$L = \frac{(1-\nu)E}{f(1+\nu)(1-2\nu)} \quad (22.26)$$

Implementing the finite element formulation of Eq. (22.25) based on the Galerkin method, the following equation for the volumetric strain rate of solids $\{\dot{e}_N^s\}$, the rate of change of the charge density $\{\dot{c}_N\}$, and the volumetric strain $\{e_N^s\}$ can be obtained:

$$[S]\{\dot{e}_N^s\} = C_1 \frac{\beta}{(1-\beta)} [S]\{\dot{c}_N\} - C_2 J [A]\{e_N^s\} \quad (22.27)$$

22.5.4 Ionic Transport Equation

The changes of the total charge and the charge density accompanied by the ionic movement in a solid or a liquid electrolyte are expressed by Eqs. (22.5) and (22.6), respectively.

22.5.5 Computational Procedure

The computational procedure for the active, electrochemical-poroelastic behavior using the finite element equations given in the preceding subsections is as follows. The electric charge density is obtained from the global system forms of Eqs. (22.5) and (22.6). The volumetric strain rate is obtained from the global system form of Eq. (22.27) by using the electric charge density rate and the volumetric strain. The pressure is calculated from the global system form of Eq. (22.23) by using the volumetric strain rate and the rate of change of the charge density. The displacement increment is calculated from the global system form of Eq. (22.16) by using the pressure increment. The stress increments in solid and fluid are calculated from Eq. (22.15) by using the displacement increment and the pressure increment. These procedures are repeated after each small time increment until the final time is reached.

22.6 Electrochemical-Poroelastic Response Analysis of Polypyrrole Actuators with Solid Electrolyte

The solid electrolyte actuator as shown in Fig. 22.5 is a PPy membrane pasted on a polymer gel electrolyte, such as PVDF, or the solid electrolyte, which can be operated in air. The contraction of the PPy volume takes place by the release of the PF_6^- ions near the cathode at a negative voltage. Conversely, the volume expansion of the PPy occurs by the inflow of the PF_6^- ions near the anode at a positive voltage.

The model dimensions and the physical constants used in the present analysis are shown in Fig. 22.6 and Table 22.4, respectively. Figure 22.7 shows the electric current history measured at the voltage of 1 V [24, 25], which is substituted into $i(\tau)$ in Eq. (22.1) to solve the ionic transport equation. The current values corresponding to the voltages 0.25, 0.5, and 0.75 V are assumed to be the values obtained by multiplying the current corresponding to 1 V by factors of 0.25, 0.5 and 0.75, respectively. The coefficients in Eq. (22.23) are assumed to be $C_1 = 0.5 \text{ m}^3/\text{mol}$ and $C_2 = 28/\text{m}^3$ to fit the model with the experimental results obtained at the voltage of 1 V. Figure 22.8 shows the bending deformation profiles at the voltages of 0.25, 0.5,

Fig. 22.5 Schematic diagram of a polypyrrole actuator with solid electrolyte

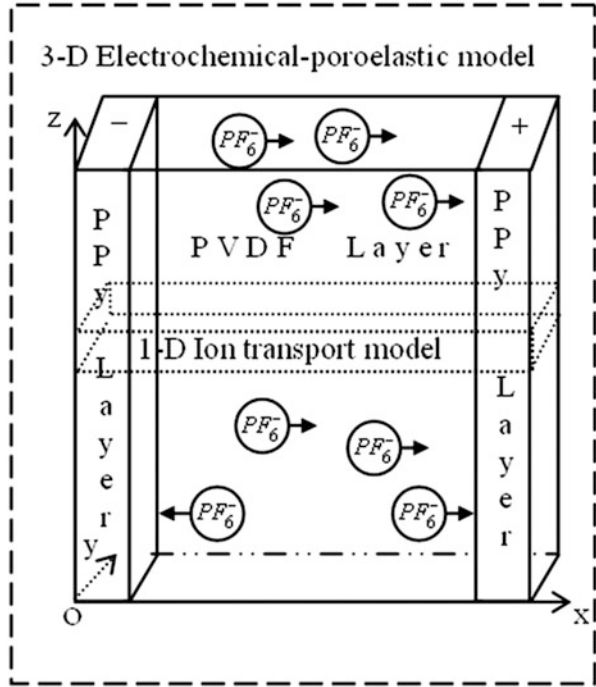


Fig. 22.6 Dimensions of a polypyrrole actuator with solid electrolyte

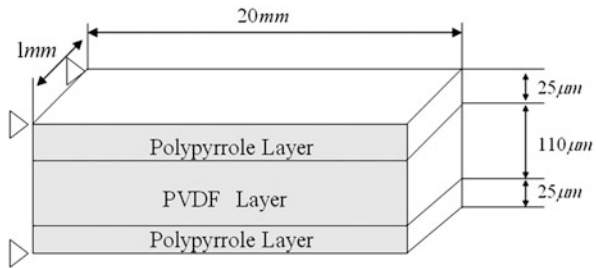


Table 22.4 Material parameters for poroelastic analysis

Friction coefficient	$f = 1.29 \times 10^{20} \text{ (Nsm}^{-4}\text{)}$
Porosity	$\beta = 0.108$
Elastic constants for PPy	$E_{PPy} = 80 \text{ MPa, } \nu_{PPy} = 0.42$
Elastic constants for PVDF	$E_{PVDF} = 440 \text{ MPa, } \nu_{PVDF} = 0.412$

0.75, and 1 V. The calculated results correspond well with the experimental results [24–26] by considering the large deformations.

Details of the present analysis [21, 22, 27] and the application to other conducting polymers such as polyaniline [28] are given in the references.

Fig. 22.7 Input electric current waveform

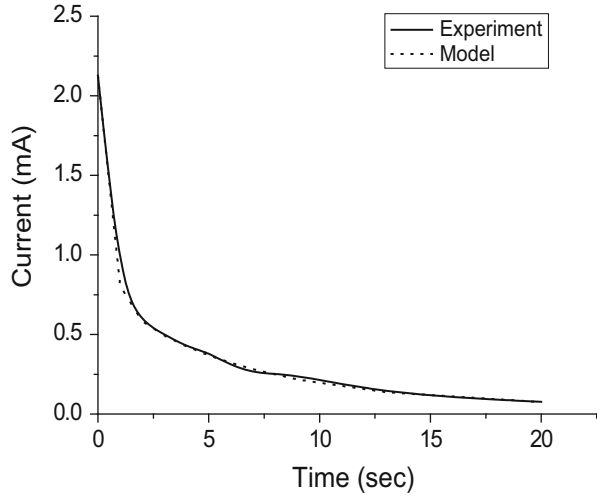
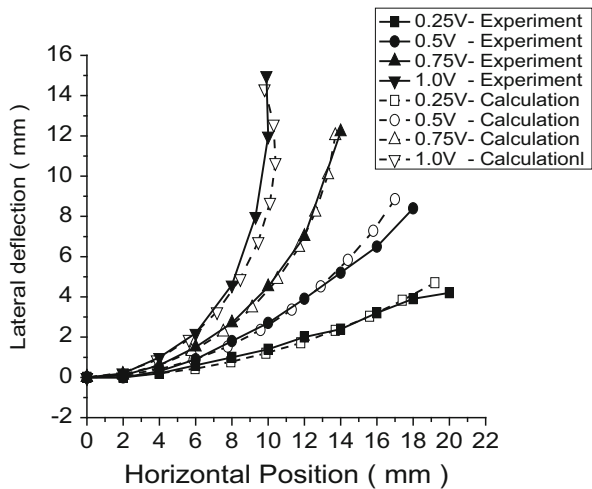


Fig. 22.8 Deformation of a polypyrrole actuator with solid electrolyte



References

1. Uchida M et al (2002) SPIE conference on electroactive polymer actuators and devices, vol 4695, pp 57–66
2. Oguro K et al (1992) Bending of an ion-conducting polymer film-electrode composite by an electric stimulus at low voltage. *J Micromach Soc* 5:27–30
3. Kanno T et al (1996) Modeling of ICPF (Ionic Conducting Polymer Gel Film) actuator (1st report, fundamental characteristics and black-box modeling). *Trans JSME Ser C* 62 (598):2299–2305

4. Shahinpoor M et al (1998) Ionic polymer-metal composites (IPMCs) as biomimetic sensors, actuators and artificial muscles – a review. *Mater Struct* 7:R15–R30
5. Nemat-Nasser S, Li JY (2000) Electromechanical response of ionic polymer-metal composites. *J Appl Phys* 87(7):3321–3331
6. Tadokoro S et al (2000) An actuator model of ICPF for robotic applications on the basis of physicochemical hypotheses. In: Proceedings of the 2000 I.E. International conference on robotics and automation, San Francisco, pp 1340–1346
7. Popovic S, Taya M (2001) 2001 Mechanics and materials summer conference, UCSD, San Diego
8. Toi Y, Kang SS (2004) Finite element modeling of electrochemical-mechanical behaviors of ionic conducting polymer-metal composites. *Trans JSME Ser A* 70(689):9–16
9. Toi Y, Kang SS (2005) Finite element analysis of two-dimensional electrochemical-mechanical response of ionic conducting polymer-metal composite beams. *Comput Struct* 83:2573–2583
10. Finlayson BA (1972) The method of weighted residuals and variational principles. Academic, New York
11. Nemat-Nasser S (2002) Micromechanics of actuation of ionic polymer–metal composites. *J Appl Phys* 92(5):2899–2915
12. Kang SS, Toi Y (2005) Finite element analysis of two-dimensional electrochemical-mechanical response of ionic conducting polymer actuators. *Trans JSME Ser A* 71(702):225–232
13. Kang SS, Toi Y (2006) Finite element analysis of electrochemical-mechanical response of Flemion-based ionic conducting polymer actuators. *Trans JSME Ser A* 72(716):397–404
14. Jung WS et al (2010) Computational modeling of electrochemical-mechanical behaviors of Flemion-based actuators considering the effects of electro-osmosis and electrolysis. *Comput Struct* 88(15/16):938–948
15. Della Santa A et al (1997) Passive mechanical properties of polypyrrole films: a continuum, poroelastic model. *Mater Sci Eng C* 5:101–109
16. Della Santa A et al (1997) Performance and work capacity of a polypyrrole conducting polymer linear actuator. *Synth Met* 90:93–100
17. Della Santa A et al (1997) Characterization and modelling of a conducting polymer muscle-like linear actuator. *Smart Mater Struct* 6:23–34
18. Cortes MT, Moreno JC (2003) Artificial muscles based on conducting polymers. *e-Polymers* 41:1–42
19. Hara S et al (2004) Artificial muscles based on polypyrrole actuators with large strain and stress induced electrically. *Polym J* 36(2):151–161
20. Toi Y, Jung WS (2006) Finite element modeling of electrochemical-poroelastic behaviors of conducting polymer films. *Trans JSME Ser A* 72(719):1065–1071
21. Toi Y, Jung WS (2007) Finite element modeling of electrochemical-poroelastic behaviors of conducting polymers. *Comput Struct* 85(19/20):1453–1460
22. Biot MA (1954) Theory of elasticity and consolidation for a porous anisotropic solid. *J Appl Phys* 26:182–185
23. Katchalsky A, Curran PF (1967) Non-equilibrium thermodynamics in biophysics. Harvard University Press, Cambridge
24. Alici G et al (2006) Bending modeling and its experimental verification for conducting polymer actuators dedicated to manipulation applications. *Sens Actuators A* 126:396–404
25. Metz P et al (2006) A finite element model for bending behaviour of conducting polymer electromechanical actuators. *Sens Actuators A* 130–131:1–11
26. Alici G, Huynh NN (2006) Towards improving positioning accuracy of conducting polymer actuators. In: International workshop on advanced motion control, pp 478–483
27. Toi Y, Jung WS (2008) Computational modeling of electrochemical-poroelastic bending behaviors of conducting polymer (PPy) membranes. *Trans JSME Ser A* 74(740):513–519
28. Jung WS, Toi Y (2010) Finite element analysis of electrochemical-poroelastic behaviors of polyaniline fibers. *Trans JSME Ser A* 76(770):1263–1269

Chapter 23

Distributed Parameter System Modeling

Kentaro Takagi, Gou Nishida, Bernhard Maschke, and Kinji Asaka

Abstract This chapter discusses a distributed parameter system modeling of ionic polymer-metal composite actuators based on modified Yamaue's electro-stress diffusion coupling model. The lowest order linear time invariant state equation with the spatial variable is derived to carry out the simulation. An introductory method for simulation based on the state space model is also shown. The results of the simulation demonstrate the effectiveness of the derived model by showing the differences of the responses for the different cation species.

Keywords Distributed port-Hamiltonian system • Ionic polymer-metal composite • Simulation • State space equation

23.1 Introduction

Modeling electro-active polymers (EAPs) [1] is a challenging research topic because of the complex multi-physics behavior of the electro-mechanical transduction of the polymer materials. The physics of EAPs may be usually represented by partial differential equations that include spatial and temporal variables. Such systems are

K. Takagi (✉)

Department of Mechanical Science and Engineering, Graduate School of Engineering,
Nagoya University, Furo-cho, Chikusa-ku, Nagoya 464-8603, Japan
e-mail: takagi@nuem.nagoya-u.ac.jp

G. Nishida

Department of Applied Analysis and Complex Dynamical Systems, Graduate School
of Informatics, Kyoto University, 36-1, Yoshidahonmachi, Sakyo-ku, Kyoto 606-8501, Japan
e-mail: g.nishida@acs.i.kyoto-u.ac.jp

B. Maschke

Laboratoire d'Automatique et de Génie des Procédés, Université Claude Bernard Lyon 1,
F-69622 Villeurbanne Cedex, Lyon, France
e-mail: maschke@lagep.univ-lyon1.fr

K. Asaka

Health Research Institute, National Institute of Advanced Industrial Science
and Technology (AIST), Midorigaoka, Ikeda, Osaka 563-8577, Japan
e-mail: asaka-kinji@aist.go.jp

sometimes referred as distributed parameter systems. Not only revealing the physics of the actuation principle, but also constructing an easy-to-use model is expected for the modeling study from the point of view of practical applications. Previous studies on modeling EAPs, especially focused on ionic polymer-metal composites (IPMCs) [2], have been reported from black-box or gray-box models [3–12] to white-box models [13–18]. The terms such as black-box, gray-box, and white-box modelings represent the methodology of the modeling [19]. Generally speaking, the black-box or the gray-box models are suitable for analysis or design of actuators because they are usually represented by state space equations or transfer functions, that are well studied in the field of control engineering. State space model is a canonical form of ordinary differential equations [19, 20]. The state space model is suitable for numerical computation, analysis and control system design. In contrast, the white-box models are usually represented by partial differential equations, that are not easy to treat directly via state space equations or transfer functions. Recent years, distributed port-Hamiltonian system modeling, a unified framework that can represent physical distributed parameter system from the point of view of analytical mechanics and control theory, has been proposed [21, 22]. Nishida et al. showed that the distributed port-Hamiltonian scheme could effectively model the physics of IPMC actuators [23].

This chapter introduces the lowest order state space equation based on the model proposed by [23–25]. Especially, we focus on showing how the distributed-parameter model can be approximated by a simple state space equation. Once the state space equation can be obtained, it can be easily used for simulations or control system design. For the numerical simulations, an introductory guide will be sketched for the readers who are not familiar with state space equations. In this chapter the physics of the actuator is firstly shown. The physical (white-box) model consists of electrical, electro-mechanical coupling and mechanical functions of IPMCs. The essential part of the actuator which transforms the electrical quantity to the mechanical quantity, i.e. electro-mechanical coupling system, is modeled using electro-stress diffusion coupling model proposed by Yamaue et al. [17]. According to the power balance of the system [23], Yamaue's model is slightly modified in the model derivation. The model can predict the relaxation behavior which is a characteristic phenomenon of ionic polymers. In the latter part of this chapter, the state space approximation is shown using the method of separation of variables. In order to obtain the simplest model, we approximate each sub-system by only the first eigen mode. A simulation result demonstrates the effectiveness of the proposed model and illustrates the variation of the relaxation behavior due to the ion species such as sodium or tetraethylammonium.

23.2 Physics of Ionic Polymer-Metal Composite

23.2.1 *Electrical Model*

The electrical model represents the response from the input voltage to the flowing current (or charge). For the simplicity let us assume the chemical reactions at the electrodes do not occur. The simplest equivalent circuit may consist of the

membrane resistance $R_m(\Omega\text{m}^2)$ and the series electric double layer capacitance $C_d(\text{F}/\text{m}^2)$. Let $v_a(\text{V})$ be the input voltage. $Q(\text{C}/\text{m}^2)$ represents the amount of the charge stored in the unit area of the surface. Using Kirchhoff's second law, the circuit equation is represented as:

$$R_m\dot{Q}(t) + \frac{1}{C_d}Q(t) = v_a(t). \quad (23.1)$$

Equation (23.1) is an admissible model as the first order approximation, however, it does not result a good approximation. For improving the modeling accuracy, some studies have been reported. As the black-box models, constant phase elements or irrational transfer functions have been studied [26, 27]. In the white box models, transport model is commonly used to model the ionic motion [11, 28]. In addition to the dynamics of the ion movement, the roughness of the electrode may contribute to the electrical response. The fractal structure of the electrode or the distribution of the electric double layers may be modeled as a distributed RC circuit [4, 27]. The modeling approaches focusing on the distributed RC circuit can be found in [23, 25, 29]. In this chapter, the detailed electrical models are omitted for the simplicity and Eq. (23.1) will be used in the simulation shown later.

23.2.2 *Electro-Mechanical Coupling Model: Electro-Stress Diffusion Coupling Model (Yamaue's Model)*

The electro-mechanical coupling model represents the system from the input current density $j_e(= \dot{Q})$ (A/m^2) to the actuation bending moment $M_a(\text{Nm})$ as the output. We extend the electro-stress diffusion coupling model [17] from the point of view of the power conservation and the distributed port-Hamiltonian systems theory. The obtained diffusion equation of the swelling ratio (or bulk strain) f_s in the thickness direction $z(\text{m})$ is given by [23]:

$$\frac{\partial f_s(x, z, t)}{\partial t} = D' \frac{\partial^2 f_s(x, z, t)}{\partial z^2} - z \frac{\partial^3 w(x, t)}{\partial x^2 \partial t}, \quad (23.2)$$

$$\left. \frac{\partial f_s(x, z, t)}{\partial z} \right|_{z=\pm h/2} = \frac{\lambda_c}{D' \sigma_e} j_e(t) - \frac{4G}{K + \frac{4}{3}G} \frac{\partial^2 w(x, t)}{\partial x^2}, \quad (23.3)$$

where D' (m^2/s) is the diffusion coefficient, $K = Y/3(1 - 2\nu)$ is the bulk modulus, $G = Y/2(1 + \nu)$ is the shear modulus, Y (Pa) is the Young's modulus, and ν is the Poisson's ratio. λ_c (m^2/Vs) is the coupling coefficient and σ_e ($1/\Omega\text{m}$) is the conductivity. $h(\text{m})$ is the thickness of the membrane. It should be noted that the additional term $-z\partial^3 w/\partial x^2 \partial t$ that does not appear in Yamaue's model is introduced in the right hand side part of Eq. (23.2) by considering the power balance. The detailed discussion is found in [23].

The actuation bending moment generated by the swelling can be calculated as:

$$M_a(x, t) = W(x) \int_{-h/2}^{h/2} \left(K - \frac{2}{3} G \right) f_s(x, z, t) b z dz, \quad (23.4)$$

where $b(m)$ is the width and $W(x)$ is a window function which specifies the effective length $L(m)$ of the generated moment as below.

$$W(x) = u_s(x) - u_s(x - L) \quad (23.5)$$

where u_s is a unit step function.

23.2.3 Mechanical Model

We derive the equation of motion of which inputs are the actuation bending moment $M_a(Nm)$ and the external force $F_e(N/m)$ and of which output is the deflection $w(m)$. Assuming the deflection w is sufficiently small to be approximated the curvature as $\theta \approx \partial w / \partial x$, we employ the Euler-Bernoulli beam model. The equation of motion in the z direction and the boundary conditions are given by:

$$\rho b h \frac{\partial^2 w(x, t)}{\partial t^2} + \frac{Y I_b}{1 + \nu} \frac{\partial^4 w(x, t)}{\partial x^4} = \frac{\partial^2 M_a(x, t)}{\partial x^2} + F_e(x, t), \quad (23.6)$$

$$w|_{x=0} = 0, \quad \left. \frac{\partial w}{\partial x} \right|_{x=0} = 0, \quad \left. \frac{\partial^2 w}{\partial x^2} \right|_{x=L} = 0, \quad \left. \frac{\partial^3 w}{\partial x^3} \right|_{x=L} = 0 \quad (23.7)$$

where $\rho(kg/m^3)$ denotes the mass density and $Y I_b(N m^2)$ is the bending stiffness.

23.3 The Simplest Approximation: Linear Time Invariant State Space Equation

23.3.1 General Description of State Space Model and Method of Numerical Simulation

In order to carry out a numerical simulation or/and designing a control system, one may wish to transform a partial differential equation into a set of ordinary differential equations (ODEs) with the method such as separation of variables. Once one obtains a set of ODEs, one can rewrite them into a set of first-order

simultaneous differential equations. When a model of a system is represented by a first-order simultaneous differential equation, the model is called as a state space model [19, 20]. If the system is linear time invariant, the state equation is given by:

$$\dot{x}(t) = Ax(t) + Bu(t), \quad (23.8)$$

$$y(r, t) = C(r)x(t) + D(r)u(t) \quad (23.9)$$

where $x \in \mathbb{R}^n$ is called the state (vector), $u \in \mathbb{R}^m$ is the input (vector), and $y \in \mathbb{R}^p$ is the output (vector). $A, B, C(r), D(r)$ are the corresponding constant matrices including the spatial variable r . In this chapter, the spatial variable r corresponds to the longitudinal position of the IPMC cantilever.

In general, initial value problem of state equations, i.e. a system of first-order simultaneous differential equations, can be solved numerically by softwares or by programming languages. MATLAB is a well known product for numerical computation. Octave[30] and Scilab [31] are famous free softwares similar to MATLAB. For Fortran or C users, libraries for numerical computation may be found at e.g. [32]. Algorithm for solving the state equation in the softwares is based on such as Runge-Kutta method or Adams's method [19].

23.3.2 *Approximation of Partial Differential Equations: Separation of Variables and Derivation of the State Space Model*

23.3.2.1 Electrical System

From Eq. (23.1), the state space representation of the electrical system Σ_e is obtained as

$$\Sigma_e : \begin{cases} \dot{x}_e(t) = A_e x_e(t) + B_e v_a(t) \\ j_e(t) = C_e x_e(t) + D_e v_a(t) \end{cases} \quad (23.10)$$

$$A_e = -\frac{1}{R_m C_d}, \quad B_e = \frac{1}{R_m}, \quad C_e = A_e, \quad D_e = B_e \quad (23.11)$$

where the state variable is defined as $x_e = Q$.

23.3.2.2 Electro-Mechanical Coupling System

Equations (23.2) to (23.5) can be solved by the method of separation of variables [23–25]. We assume the solution of the boundary-value problem described by Eqs. (23.2) and (23.3) in the form:

$$f_s(x, z, t) = \sum_{i=0}^{\infty} \varphi_i(z) \xi_i(x, t) + g_1(z) e_1(x, t) + g_2(z) e_2(x, t). \tag{23.12}$$

The function $g_1(z)$ and $g_2(z)$ are chosen to render the boundary conditions homogeneous as:

$$g_1(z) = -[-z - (h/2 - \varepsilon)] u_s[-z - (h/2 - \varepsilon)], \tag{23.13}$$

$$g_2(z) = [z - (h/2 - \varepsilon)] u_s[z - (h/2 - \varepsilon)]. \tag{23.14}$$

where ε is a small quantity. e_1, e_2 are the right hand side part of Eq. (23.3).

Solving the eigenvalue problem of Eqs. (23.2) and (23.3), we obtain the eigenvalues λ_{d_i} and eigenfunctions $\varphi_i(z)$.

$$\lambda_{d_i} = \frac{(2i + 1)\pi}{h} \quad (i = 0, 1, 2, \dots) \tag{23.15}$$

$$\varphi_i(z) = \sin(\lambda_{d_i} z) \quad (i = 0, 1, 2, \dots) \tag{23.16}$$

Note that the even modes of Eq. (23.15), which does not contribute to generate bending moment, are neglected. Using the standard method of the eigenfunction expansion, we obtain the infinite set of ordinary differential equations.

$$\dot{\xi}_i(r, t) + \lambda_{d_i}^2 D' \xi_i(r, t) = k_{J_i} j_e(t) - k_{R_i} \frac{\partial^2 w(r, t)}{\partial r^2} - k_{W_i} \frac{\partial^3 w(r, t)}{\partial r^2 \partial t} \tag{23.17}$$

where

$$k_{J_i} = (-1)^i \frac{4\lambda_c}{h\sigma_e}, \quad k_{R_i} = (-1)^i \frac{16D'G}{h(K + \frac{4}{3}G)}, \quad k_{W_i} = (-1)^i \frac{4h}{(2i + 1)^2 \pi^2} \tag{23.18}$$

Though Eq. (23.17) has the right hand side terms which are the function with respect to x , Eq. (23.17) can be treated as an ordinary differential equation utilizing the linear superposition of the solution. As we will discuss in the next section, the deflection $w(x, t)$ can be separated into the spatial function and the temporal function.

$$w(x, t) = \sum_{j=1}^{\infty} \phi_j(x) \eta_j(t). \tag{23.19}$$

Therefore the variables in the solution can be separated in the form:

$$\xi_i(x, t) = \xi_{ic}(t) + \sum_{j=1}^{\infty} \frac{\partial^2 \phi_j(x)}{\partial x^2} \xi_{ij}(t) \quad (i = 0, 1, 2, \dots), \tag{23.20}$$

because the basis of the input $\partial^2 w / \partial x^2$ are $\partial^2 \phi_j / \partial x^2$ ($j = 1, 2, 3, \dots$). According to the linearity of Eq. (23.17) and Eq. (23.20), we obtain that:

$$\dot{\xi}_{ic}(t) + \lambda_{d_i}^2 D' \xi_{ic}(t) = k_{J_e} j_e(t) \quad (i = 0, 1, 2, \dots) \quad (23.21)$$

$$\dot{\xi}_{ij}(t) + \lambda_{d_i}^2 D' \xi_{ij}(t) = -k_{R_i} \eta_j(t) - k_{W_i} \dot{\eta}_j(t) \quad (i = 0, 1, 2, \dots, \quad j = 1, 2, 3, \dots) \quad (23.22)$$

Substituting Eq. (23.12) into Eq. (23.4), we obtain:

$$M_a(x, t) = W(x) \sum_{i=0}^{\infty} C_{MF_i} \xi_i(x, t). \quad (23.23)$$

The integration in Eq. (23.23) is calculated as:

$$C_{MF_i} = K_{MF} \int_{-h/2}^{h/2} \varphi_i(z) z dz = \frac{2K_{MF} h^2 (-1)^i}{\pi^2 (2i+1)^2} \quad (23.24)$$

where $K_{MF} = b(K - 2G/3)$.

In summary, the electro-mechanical coupling system has the inputs j_e , $\partial^2 w / \partial x^2$, and the output $M_a(x, t)$. After the separation of the variables x and t , the inputs are represented by the mechanical state variables $\eta_j(t)$. The state space representation is as follows:

$$\Sigma_{em} : \begin{cases} \dot{x}_{em}(t) = A_{em} x_{em}(t) + B_{em1} j_e(t) + B_{em2} x_m(t) \\ M_a(x, t) = C_{em1}(x) x_{em}(t) \end{cases} \quad (23.25)$$

In this chapter, consider the simplest case in which only the first modes exist, i.e., ($i=0$) and ($j=1$).

$$x_{em} = \begin{bmatrix} \xi_{0c} \\ \xi_{01} \end{bmatrix} \quad (23.26)$$

$$A_{em} = \begin{bmatrix} \lambda_{d1} & 0 \\ 0 & \lambda_{d1} \end{bmatrix}, \quad B_{em1} = \begin{bmatrix} k_{J_0} \\ 0 \end{bmatrix}, \quad B_{em2} = \begin{bmatrix} 0 & 0 \\ -k_{R0} & -k_{W0} \end{bmatrix}, \quad (23.27)$$

$$C_{em1}(x) = W(x) \begin{bmatrix} C_{MF0}, & \frac{\partial^2 \phi_1(x)}{\partial x^2} C_{MF0} \end{bmatrix}.$$

23.3.2.3 Mechanical System

For the mechanical system, the eigenvalue problem consists of Eqs.(23.6) and (23.7). Assuming the solution of Eq. (23.6) as in Eq. (23.19), we apply separation of variables in order to isolate the spatial and temporal terms. The eigenfunction $\phi_j(x)$ is derived from Eqs. (23.6) and (23.7).

$$\phi_j(x) = (\cos \beta_j x - \cosh \beta_j x) - \frac{\cos \beta_j L + \cosh \beta_j L}{\sin \beta_j L + \sinh \beta_j L} (\sin \beta_j x - \sinh \beta_j x) \quad (23.28)$$

where β_j satisfies

$$\cos \beta_j L \cosh \beta_j L + 1 = 0. \quad (23.29)$$

The constants $\beta_j(j = 1, 2, \dots)$ can be searched by numerical computation. For the case of $j = 1$, $\beta_1 L = 1.875$. Substituting Eq. (23.19) into Eq. (23.6) and integrating with respect to x over the domain after multiplying the eigenfunction $\phi_j(x)$, we obtain the temporal differential equation:

$$\ddot{\eta}_j(t) + 2\zeta_j \omega_j \dot{\eta}_j(t) + \omega_j^2 \eta_j(t) = F_{aj}(t) + k_f f_d(t) \quad (23.30)$$

where

$$F_{aj}(t) = \frac{\int_0^L \phi_j(x) \frac{\partial^2 M_a(x,t)}{\partial x^2} dx}{\rho b h \int_0^L \phi_j^2(x) dx} = \sum_{i=1}^{\infty} C_{MFi} (l_{Jj} \xi_{ic}(t) + l_{Wj} \xi_{ij}(t)) \quad (23.31)$$

and

$$\omega_j^2 = \frac{\beta_j^4 Y I}{\rho b h (1 + \nu)}, \quad k_{fj} = \frac{\phi_j(x_f)}{\rho b h \int_0^L \phi_j^2(x) dx} \quad (23.32)$$

$$l_{Jj} = \frac{\int_0^L \frac{\partial^2 \phi_j(x)}{\partial x^2} dx}{\rho b h \int_0^L \phi_j^2(x) dx}, \quad l_{Wj} = \frac{\int_0^L \left(\frac{\partial^2 \phi_j(x)}{\partial x^2} \right)^2 dx}{\rho b h \int_0^L \phi_j^2(x) dx} \quad (23.33)$$

Here the external force $F_e(x, t)$ is assumed as a concentrated load at $x = x_f$ and described as $F_e(x, t) = f_d(t)\delta(x - x_f)$. Accounting for the damping, we added the damping term with the modal damping ratio ζ_j . The input to the mechanical system F_{aj} , which is the output of the electro-mechanical system, can be written using the state vector of the electro-mechanical coupling system.

$$F_a(t) = C_{em2}x_{em}(t) \quad (23.34)$$

$$C_{em2} = [I_{J1} \quad I_{W1}] \begin{bmatrix} C_{MF0} & 0 \\ 0 & C_{MF0} \end{bmatrix} \quad (23.35)$$

As the result, the state space representation for the mechanical system Σ_m , can be written as followings;

$$\Sigma_m : \begin{cases} \dot{x}_m(t) = A_m x_m(t) + B_{m1}f_d(t) + B_{m2}F_a(t) \\ w(x, t) = C_{m1}(x)x_m(t) \end{cases} \quad (23.36)$$

where

$$x_m = \begin{bmatrix} \eta_1 \\ \dot{\eta}_1 \end{bmatrix} \quad (23.37)$$

$$A_m = \begin{bmatrix} 0 & 1 \\ -\omega_1^2 & -2\zeta_1\omega_1 \end{bmatrix}, \quad B_{m1} = \begin{bmatrix} 0 \\ k_{f1} \end{bmatrix}, \quad B_{m2} = \begin{bmatrix} 0 \\ 1 \end{bmatrix}, \quad C_{m1}(x) = [\phi_1(x) \quad 0] \quad (23.38)$$

23.3.2.4 Interconnection of Sub-Systems

The overall system, which has two inputs (v_a and f_d) and two outputs (j_e and w), is derived from above three systems Eqs. (23.10), (23.25) and (23.36), as follows:

$$x(t) := \begin{bmatrix} x_e(t) \\ x_{em}(t) \\ x_m(t) \end{bmatrix}, \quad u(t) := \begin{bmatrix} v_a(t) \\ f_d(t) \end{bmatrix}, \quad y(x, t) := \begin{bmatrix} j_e(t) \\ w(x, t) \end{bmatrix} \quad (23.39)$$

$$\frac{dx(t)}{dt} = \begin{bmatrix} A_e & O_{1 \times 2} & O_{1 \times 2} \\ B_{em1}C_e & A_{em} & B_{em2} \\ O_{2 \times 1} & B_{m2}C_{em2} & A_m \end{bmatrix} x(t) + \begin{bmatrix} B_e & 0 \\ B_{em1}D_e & O_{2 \times 1} \\ O_{2 \times 1} & B_{m1} \end{bmatrix} u(t) \quad (23.40)$$

$$y(x, t) = \begin{bmatrix} C_e & O_{1 \times 2} & O_{1 \times 2} \\ 0 & O_{1 \times 2} & C_{m1}(x) \end{bmatrix} x(t) + \begin{bmatrix} D_e & 0 \\ 0 & 0 \end{bmatrix} u(t) \quad (23.41)$$

The interconnection of the subsystems is shown in Fig. 23.1.

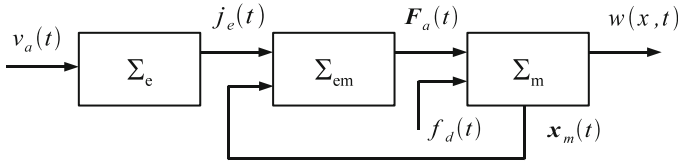


Fig. 23.1 Block diagram of the interconnected systems

Table 23.1 Model parameters

	Na ⁺ Case	TEA ⁺ Case
L (m)	43.5×10^{-3}	←
b (m)	5×10^{-3}	←
h (m)	200×10^{-6}	←
ρ (kg/m ³)	1.633×10^3	←
Y (MPa)	90	←
ν	0.3	←
ζ_1	0.033	←
R_m (Ωm^2)	9.821×10^{-4}	53.14×10^{-4}
C_d (F/m ²)	61.09	282.3
λ_e/σ_e (m ³ /A s)	2.895×10^{-10}	5.070×10^{-10}
D' (m ² /s)	32.62×10^{-11}	1.375×10^{-11}
Modification of B_{em1}	$0.8B_{em1}$	$0.2B_{em1}$

23.3.3 Simulation

In order to check the validity of the proposed model, this section shows a numerical simulation of actuating an IPMC cantilever. The voltage of 1(V) is periodically switched on and off with every 10(s) in the simulation. Table 23.1 shows the model parameters [24, 25] used in the simulation.

Figure 23.2 shows the time response of the tip deflection at $x = 0.035$. The solid and the dashed lines are in the cases of sodium (Na⁺) ion and tetraethylammonium (TEA) ion. When the counter ion is Na⁺, the response is oscillatory due to the sharp increase of the electro-active force development. The relaxation phenomenon is clearly shown in the both cases. Slow and less relaxation response of the TEA case is typically observed also in the experiment [24, 25]. Figure 23.3 shows the deflection shape $w(x, t)$ captured at $t = 5$ (s). Once the state $x(t)$ is computed from Eq. (23.40), the output $w(x, t)$ which is the function of the spatial variable x can be computed after the simulation.

Fig. 23.2 Simulation of the tip deflection $w(x = 0.035, t)$

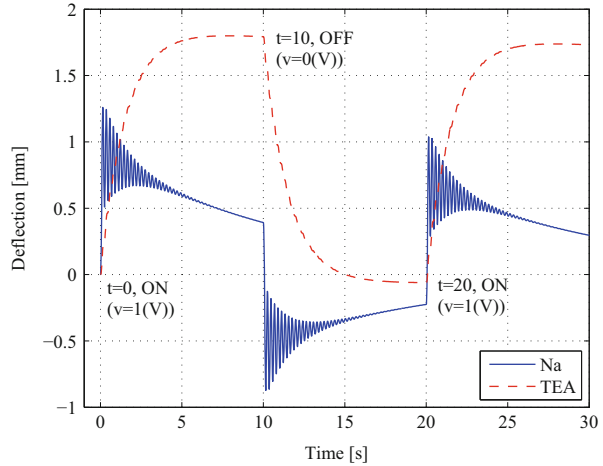
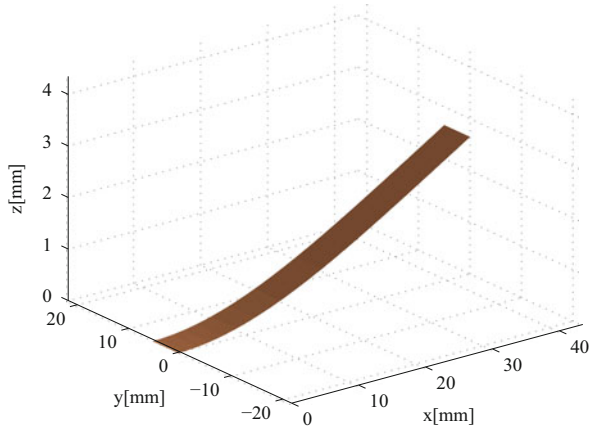


Fig. 23.3 Simulation of the deformation shape $w(x, t = 5)$ (TEA ion)



23.4 Conclusion

This chapter has discussed a distributed parameter system modeling of IPMC actuators and the introductory method for simulation based on the state space model. The state space representation of the electro-mechanical coupling system based on modified Yamaue’s electro-stress diffusion coupling model was shown. As the simplest case of the proposed model, the fifth-order linear time invariant state equation with the spatial variable was obtained. Note, if necessary, it is easy to derive an arbitrary higher order state equation instead of the fifth-order system. The results of the simulation demonstrated the effectiveness of the proposed model.

Being compared with the black-box modeling, the distributed parameter system modeling, so-called control-oriented physics-based modeling, has great advantages

of scalability and usefulness. The proposed model in this chapter has still some neglected physics such as the nonlinear impedance and the non-relaxation force in the electro-mechanical transduction, therefore further developments of the modeling from the view point of both physics and control theory are expected.

Acknowledgements The authors appreciate Mr. Takaaki Osada for his work on the simulation and the experiment during his master program.

References

1. Bar-Cohen Y (ed) (2004) Electroactive polymer (eap) actuators as artificial muscles: reality, potential, and challenges. 2nd edn. SPIE Press, Washington
2. Shahinpoor M, Kim KJ (2001) Ionic polymer-metal composites: I fundamentals. *Smart Mater Struct* 10:819–833
3. Mallavarapu K, Leo D (2001) Feedback control of the bending response of ionic polymer actuators. *J Intell Mater Syst Struct* 12:143–155
4. Bao X, Bar-Cohen Y, Lih SS (2002) Measurements and macro models of ionomeric polymer-metal composites. *Proc SPIE* 4695:220–227
5. Newbury KM, Leo DJ (2003) Linear electromechanical model of ionic polymer transducers-part I: model development. *J Intell Mater Syst Struct* 14:333–342
6. Yamakita M, Kamamichi N, Kaneda Y, Asaka K, Luo ZW (2004) Development of an artificial muscle linear actuator using ionic polymer-metal composites. *Adv Robot* 18(4):383–399
7. Chen Z, Tan X, Shahinpoor M (2005) Quasi-static positioning of ionic polymer-metal composite (IPMC) actuators. Proceedings of the 2005 IEEE/ASME international conference on advanced intelligent mechatronics, pp 60–65
8. Kothera C, Leo D (2005) Bandwidth characterization in the micropositioning of ionic polymer actuators. *J Intell Mater Syst Struct* 16(1):3–13
9. Kang S, Shin J et al. (2007) Robust control of ionic polymer-metal composites. *Smart Struct Mater* 16:2457–2463
10. Chen Z, Tan X (2008) A scalable dynamic model of ionic polymer metal composite actuators. *Proc SPIE* 6927:69270I
11. Chen Z, Tan X (2008) A control-oriented and physics-based model for ionic polymer-metal composite actuators. *IEEE/ASME Trans Mechatron* 13(5):519–529
12. Yamakita M et al. (2008) Integrated design of an ionic polymer-metal composite actuator/sensor. *Adv Robot* 22:913–928
13. Asaka K, Oguro K (2000) Bending of polyelectrolyte membrane platinum composites by electric stimuli part ii. response kinetics. *J Electroanal Chem* 480:186–198
14. de Gennes PG, Okumura K, Shahinpoor M, Kim KJ (2000) Mechanoelectric effects in ionic gels. *Europhys Lett* 50(4):513–518
15. Nemat-Nasser S, Li JY (2000) Electromechanical response of ionic polymer-metal composites. *J Appl Phys* 87(7):3321–3331
16. Tadokoro S, Yamagami S, Takamori T, Oguro K (2000) Modeling of nafion-Pt composite actuators (ICPF) by ionic motion. *Proc SPIE* 3987:262–272
17. Yamaue T, Mukai H, Asaka K, Doi M (2005) Electrostress diffusion coupling model for polyelectrolyte gels. *Macromolecules* 38:1349–1356
18. Wallmersperger T, Leo DJ, Kothera CS (2007) Transport modeling in ionomeric polymer transducers and its relationship to electromechanical coupling. *J Appl Phys* 101:024912
19. Ljung L, Glad T (1994) Modeling of dynamic systems. Prentice Hall, Englewood Cliffs
20. H. Khalil (2002) Nonlinear systems. 3rd Ed., Prentice Hall, Englewood Cliffs

21. van der Schaft A, Maschke B (2002) Hamiltonian formulation of distributed parameter systems with boundary energy flow. *J Geom Phys* 42:166–194
22. Macchelli A, Maschke B (2009) Infinite-dimensional port-hamiltonian systems. Modeling and control of complex physical systems—the port-hamiltonian approach. Springer, New York
23. Nishida G, Takagi K, Maschke B, Osada T (2011) Multi-scale distributed parameter system modeling of ionic polymer-metal composite soft actuator. *Contr Eng Pract* 19:321–334
24. Osada T, Takagi K, Hayakawa Y, Luo ZW, Asaka K (2008) State space modeling of ionic polymer-metal composite actuators based on electrostress diffusion coupling theory. *Proceedings of 2008 IEEE/RSJ international conference on intelligent robots and systems*, pp 119–124
25. Takagi K, Osada T, Asaka K, Hayakawa Y, Luo ZW (2009) Distributed parameter system modeling of IPMC actuators with the electro-stress diffusion coupling theory. *Proc SPIE* 7287:72871Q
26. Asaka K, Fujiwara N, Oguro K, Onishi K, Sewa S (2011) State of water and ionic conductivity of solid polymer electrolyte membranes in relation to polymer actuators. *J Electroanal Chem* 505:24–32
27. Takagi K, Nakabo Y, Luo ZW, Asaka K (2007) On a distributed parameter model for electrical impedance of ionic polymer. *Proc SPIE* 6524:652416
28. Farinholt KM, Leo DJ (2005) Electrical impedance modeling of ionic polymer transducers. *Proc SPIE* 5761:69–80
29. Takagi K, Jikuya I, Nishida G, Maschke B, Asaka K (2009) A study on the discretization of a distributed RC circuit model. *Proceedings ICCAS-SICE 2009*, pp 677–680
30. <http://www.gnu.org/software/octave/>
31. <http://www.scilab.org/>
32. <http://www.netlib.org/>

Chapter 24

Modeling and Feedback Control of Electro-Active Polymer Actuators

Norihiro Kamamichi, Kentaro Takagi, and Shigenori Sano

Abstract Electro-active polymers (EAPs) are functional polymeric materials which respond to electrical stimuli with shape change. Since EAPs can be activated by the electric field, driving equipments and implementation of control are easily achievable. However, a modeling and a feedback control are needed for practical applications such as a positioning control or a force control with high speed and high precision. In this chapter, we will show the basics of modeling and feedback control methods for ionic polymer-metal composites (IPMCs) from a viewpoint of control engineering. First, general modeling and actuation methods are briefly explained. Then, feedback control methods for output force or deformation are illustrated such as a PID controller, a feed-forward and feedback controller based on an identified model, a servo controller, and a robust PID controller considering uncertainty of the actuator.

Keywords Electro-active polymer • Feedback control • Ionic polymer-metal composite • Modeling

24.1 Introduction

Electro-active polymers (EAPs) [1, 2] are functional polymeric materials which respond to electrical stimuli with shape change. EAPs have potential capabilities as soft actuators, and are sometimes called artificial muscles due to their biotic smooth

N. Kamamichi (✉)

Department of Robotics and Mechatronics, Tokyo Denki University, 5 Senju-asahi-cho,
Adachi-ku, Tokyo 120-8551, Japan
e-mail: nkama@fr.dendai.ac.jp

K. Takagi

Department of Mechanical Science and Engineering, Nagoya University, Furo-cho, Chikusa-
ku, Nagoya 464-8603, Japan
e-mail: takagi@nuem.nagoya-u.ac.jp

S. Sano

Department of Mechanical Engineering, Toyohashi University of Technology, 1-1
Hibarigaoka Tenpaku-cho, Toyohashi, Aichi 441-8580, Japan
e-mail: sano@me.tut.ac.jp

motions. Since EAPs can be activated by the electric field, driving equipments and implementation of control are easily achievable.

There are many types of EAP materials, generally classified into three categories, as a dielectric type, a conductive polymer type and an ionic polymer type. Although dielectric type EAPs need to high-voltage for actuation, the conductive type and the ionic polymer type EAPs can be activated by low-voltage in several volts. We focus on the ionic polymer-metal composite (IPMC) [3], which is one of the ionic polymer type EAP. Ionic polymer actuators can be activated easily. If you just activate the actuator, only an electric battery and a switch are needed. If you do not require accuracy of movements, a model of the actuator may not be needed. Here, the term “model” is a mathematical expression of a target system, i.e. a mathematical equation or data to characterize dynamics of the actuator system. The dynamic characteristics of ionic polymer actuators vary depending on environmental conditions. Therefore, it is considered that a feedback control is needed for practical applications. In such case, an analysis and a design based on the model are effective. The control based on the model is needed to realize a positioning control or a force control with high speed and high precision.

In this chapter, we will show the basics of modeling and feedback control methods for ionic polymer actuators from a viewpoint of control engineering. Although various studies for control have been conducted in recent years, simple and fundamental control approaches are introduced in this chapter. First, general modeling and actuation methods are explained. Then, feedback control methods for output force or deformation are illustrated such as a PID controller, a feed-forward and feedback controller based on an identified model, a servo controller, and a robust PID controller considering uncertainty of the actuator.

24.2 Modeling and Actuation Methods for Electro-Active Polymer Actuators

24.2.1 Modeling Methods

To control actuators with satisfactory accuracy, modeling of actuators is important. The modeling means to construct numerical models which characterize behaviors of the actuator. In this chapter, numerical models indicate transfer functions or differential equations [4, 5]. In control engineering, there are two main types of modeling methods as a white-box modeling and a black-box modeling.

The white-box modeling is also called first principle modeling or physics modeling, and to derive detailed models based on the physical principles. Various researches of the white-box modeling for ionic type EAPs were conducted [6–12]. However, there are demerits that the white box model is commonly complex and it is hard to use directly for analysis and design of control systems.

On the other hand, the black-box modeling is to treat the system as a black-box without consideration of physical principles, and to derive models based on the input–output data obtained from experiments. Various researches of the black-box modeling for ionic type EAPs were also reported [13–19]. The black-box modeling is also called system identifications. It is useful as the control-oriented modeling method, and can be applied to any kinds of EAPs. However, system identifications need to be conducted for each actuator sample because of no consideration of the physical parameters.

There exists an intermediate method called gray-box modeling, which has advantages of white-box and black-box methods. The gray-box modeling is the method based on the partial phenomenological model considering the physical principles and estimations of unknown parameters from experimental data. This methods lead to simplification of mathematical explanations. There are many researches on the gray-box modeling for ionic polymer actuators [20–23].

24.2.2 Actuation Method

Ionic polymer actuators bend in response to electrical field. The deformation arises from the internal stress generated according to the movement of ions. Basically, it is possible to drive these actuators with a driving circuit similar to that for the electromagnetic motor. General driving methods such as voltage control, current control and PWM control are applicable.

Figure 24.1 shows an example of a control system. To drive the actuator, the input signal, generated in the computer, is applied to the actuator through the driving circuit such as a power amplifier. Furthermore, to construct a control system, suitable sensors are needed for measuring the state of the actuator. The information from the sensor is sent to the computer, and the input signal is calculated based on appropriate control algorithm.

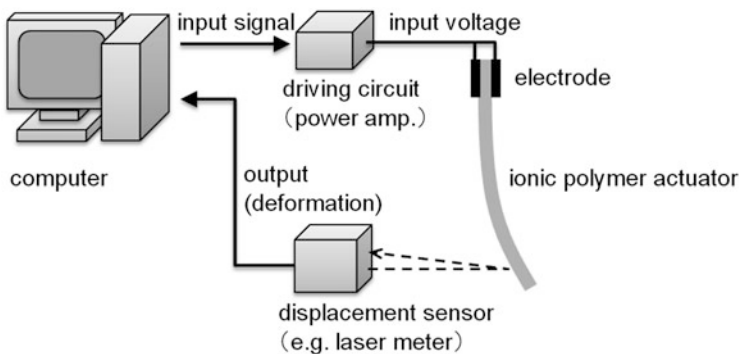


Fig. 24.1 Configuration example of control systems

24.2.3 Control Research for Ionic Polymer Actuators

There are various researches on controls of EAP actuators. In this section, we briefly introduce the control researches on IPMC actuators. As we shall demonstrate in the next section, fundamental control algorithms have been applied to regulate the deformation and/or the output force.

The simplest and powerful control method is a PID (proportional-integral-derivative) control [24, 25]. In fact, the PID control can be implemented easily and realized the sufficient performance with a certain range. On the assumption that dynamics of the IPMC is represented by linear time-invariant systems, typical control algorithms such as a state feedback control with a linear quadratic regulator (LQR) [14, 15], a lead-lag compensator [26], a feed-forward compensator [16, 27, 28] were applied. These model-based controls lead to improve the transient and stationary responses.

From another viewpoint, characteristics of IPMCs vary by environmental changes or iterative activation, the control performance may degrade or even the system may become unstable. Therefore, robust control approaches were applied [18, 29]. The robust controls aim to keep the stabilities and/or performances even with the existence of modeling errors, uncertainties, or parameter variations of the system. As defining the bounds of uncertainties, the robust controller guarantees the control performance as long as the modeling error is within the bounds. As another approach, adaptive controls were also applied to deal with the uncertainties and time-varying behaviors [30–32]. The basic idea of the adaptive control is on-line parameter estimations, and estimated parameters are used on the control system.

24.3 Deformation Control

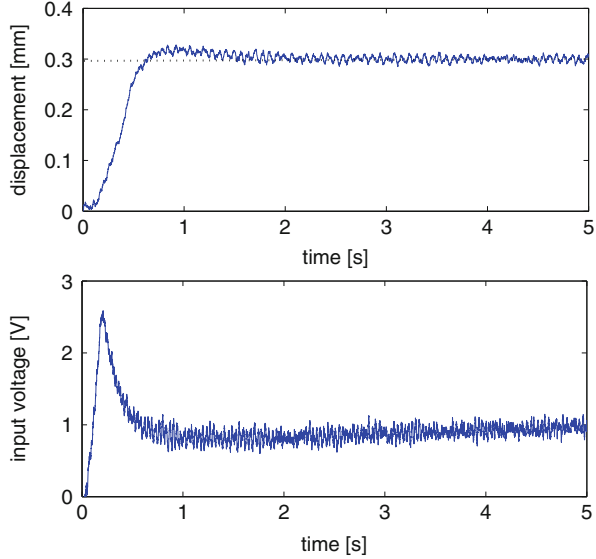
In this section, deformation control methods of IPMC actuators are explained. There are many algorithms for control, and fundamental control methods are explained [33].

24.3.1 PID Control

A PID control is one of the most simple and practical feedback control method, and widely applied in industry. The control input is calculated based on an error which is the difference between a measured output signal and a desired value. To vanish the error, the control input is determined by weighted sum of proportional, integral and derivative values of the error.

Defining the measured deformation as $y(t)$, the desired value as $y_r(t)$, the error is set as $e(t) = y_r(t) - y(t)$. The input signal of the PID controller is defined by

Fig. 24.2 Experimental result of PID control



$$u(t) = K_p e(t) + K_i \int_0^t e(\tau) d\tau + K_d \dot{e}(t) \quad (24.1)$$

where K_p, K_i, K_d are tuning parameters, which are the proportional gain, the integral gain, the derivative gain, respectively.

Figure 24.2 shows the experimental result. As shown in the Fig. 24.1, a strip of IPMC is fixed in a cantilever, and the displacement at a point near the tip is measured and controlled. In this experiment, the desired value was set as 0.3 mm, and PI control was applied. The displacement and the input voltage are shown in the Fig. 24.2. It is observed that smooth transient response and convergence to the desired value were realized. The response characteristics and stability can be adjusted by feedback gains.

24.3.2 2DOF Control Based on the Identified Model

Next, a tracking controller based on an identified model is explained, which is a 2-dof controller and has a feed-forward loop and a feedback loop. The identified model is used in feed-forward loop. Figure 24.3 shows the block diagram of the control system. $P(s)$ is the model of the actuator system. Feed-forward part of the controller consists of the inverse system of actuator's dynamics $P^{-1}(s)$ and a low-pass filter $L(s)$. $K(s)$ is a feedback part, and the feedback acts in the variation between the output and the reference signal which is a desired value filtered by the low-pass filter $L(s)$.

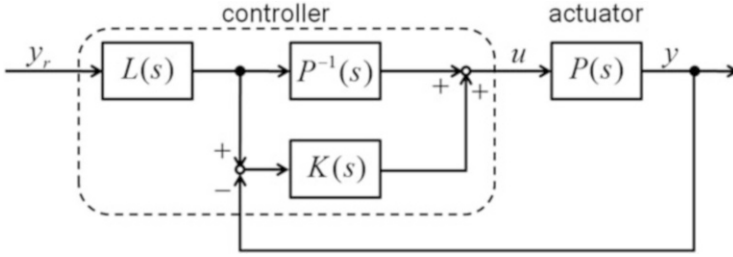
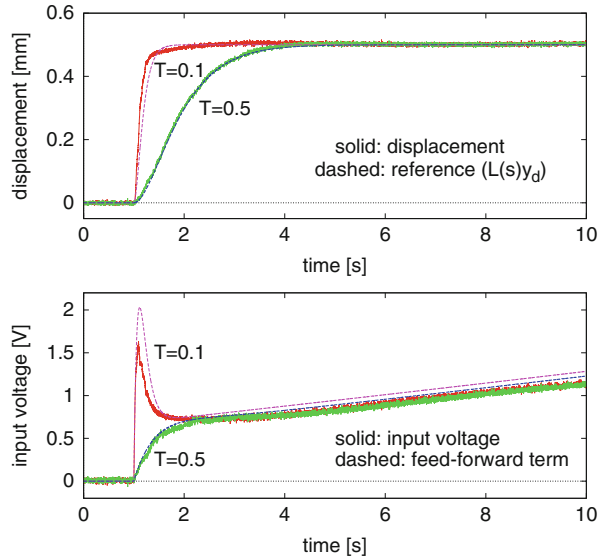


Fig. 24.3 Block diagram of the 2DOF control system

Fig. 24.4 Experimental result of 2DOF control



The feed-forward controller plays a role in shaping of desired response and improvement of controlled performance. The feedback controller plays a role in reducing of influence of disturbance or modeling errors.

Figure 24.4 shows the experimental result. The actuator model was identified from the experimental data of step response as the third-order transfer function:

$$P(s) = \frac{b_1s + b_0}{s^3 + a_2s^2 + a_1s + a_0}. \tag{24.2}$$

The low-pass filter in the controller is set as second-order system:

$$L(s) = \frac{1}{(Ts + 1)^2} \tag{24.3}$$

where T is a constant. In the feedback part, PI controller is applied, where feedback gain was set as $K_p = 5$ and $K_i = 3$.

From the results of Fig. 24.4, it is observed that each displacement fits with the reference signals and converges to the desired values. The input voltages consist chiefly of feed-forward inputs. Therefore, the identified model of the actuator is confirmed to be valid.

24.3.3 Servo Control

A servo control is applied for tracking to desired signals or stabilizing systems under the conditions of persisting disturbances. In this section, a controller design method based on state space models in modern control theory is explained.

The model of the actuator is assumed to be represented as a linear time-invariant system. Consider the system of the actuator defined by

$$\begin{aligned} \dot{x} &= Ax + Bu \\ y &= Cx \end{aligned} \quad (24.4)$$

where y is the output signal (displacement), u is the input signal (input voltage) and x is the state of the system. A , B , and C are constant matrixes, and the system is assumed to be controllable and observable. The system given by the transfer function can be represented in state space.

Let us consider the servo system problem for tracking to a constant reference signal. Defining a new input signal as $\dot{u} = v$, and an augmented system can be defined by

$$\begin{aligned} \begin{bmatrix} \dot{x} \\ \dot{u} \end{bmatrix} &= \begin{bmatrix} A & B \\ 0 & 0 \end{bmatrix} \begin{bmatrix} x \\ u \end{bmatrix} + \begin{bmatrix} 0 \\ 1 \end{bmatrix} v \\ y &= [C \quad 0] \begin{bmatrix} x \\ u \end{bmatrix}. \end{aligned} \quad (24.5)$$

The feedback controller to the augmented system (24.5) can be designed by appropriate feedback methods such as pole placement or optimal control methods. Defining the feedback gain matrix for the augmented system as F , then the matrix F is separated to the following:

$$[F_1 \quad F_2] = FZ^{-1}, \quad Z = \begin{bmatrix} A & B \\ C & 0 \end{bmatrix}. \quad (24.6)$$

Finally, the feedback controller to the system (24.4) is calculated by

$$u = -F_1x + F_2 \int_0^t e(\tau) d\tau \quad (24.7)$$

where the error between the reference signal and the output signal, $e(t) = y_r(t) - y(t)$

Fig. 24.5 Experimental result of servo control

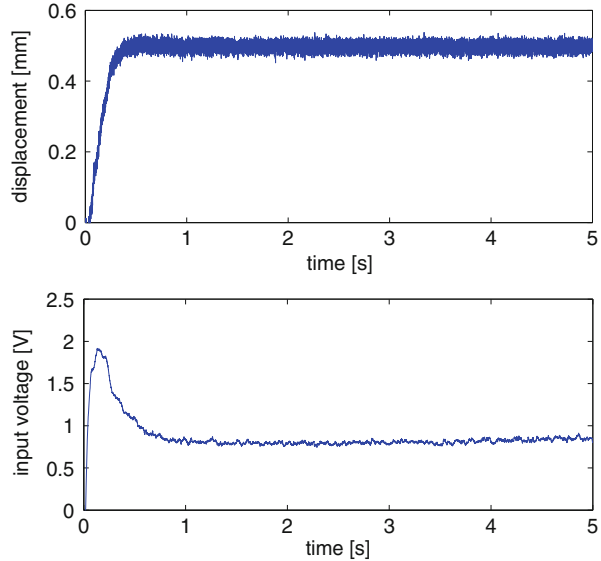


Figure 24.5 shows the experimental results of the servo control. In this experiment, the reference signal was set to the constant value as 0.5 mm. It is observed that the displacement converged to the reference signal, and tracking control was realized.

24.4 Force Control

IPMC actuators are kinds of bending type EAP actuators. A force control is considered to be useful from the viewpoint of utilizing the flexibility of IPMCs. However, characteristics of IPMCs vary by environment such as humidity or by iterative activation, the control performance may degrade or even the system may become unstable. Therefore, applications of robust control methods are awaited in order to cope with the uncertainty or the variation of the system. The term “robust” means the characteristics that control systems keep the stabilities and/or performances even with the existence of the uncertainties or the variations of the system. In this section, a simple transfer function model and a robust PID tuning method for force control are introduced [34].

24.4.1 Modeling Method for Force Control

For force control of IPMC actuators, a simple time-invariant model is derived with considering IPMC dynamics which consist of an electrical system and an electro-mechanical system.

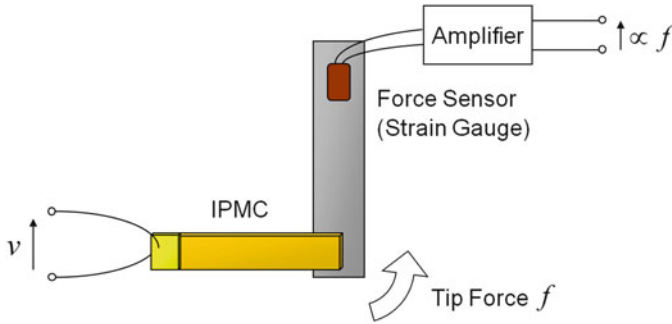


Fig. 24.6 Schematic view of the blocked force measurement

In this section, we consider a condition that a blocked force generated at the tip of a beam-shaped IPMC actuator is measured. Figure 24.6 shows a schematic view of the blocked force measurement using a strain gauge. In the figure, v [V] and f [N] are the applied voltage and the generated tip force of the IPMC, respectively. Being applied voltage, the IPMC bends to generate force on a force sensor. The force sensor is a thin steel cantilever bonded strain gauges. Because the tip force is proportional to the sufficiently small strain, the force can be estimated from the measured strain.

The dynamics from the applied voltage v to the measured force f are considered to be divided into subsystems of electrical part, electro-mechanical part and sensing part.

Electrical impedances of IPMCs are capacitive. The capacitive impedance corresponds to electric double layers between the polymers and the electrodes of IPMCs [21, 22]. A resistive element also appears in the impedance model due to the ion conductivity of the polymer. Using the electric double layer capacitance, C_d , and the membrane resistance, R_m , we model the electrical admittance as a first-order linear approximation. Let $G_e(s)$ be a transfer function from the voltage v to the current i :

$$G_e(s) = \frac{C_d s}{T_e s + 1} \quad (24.8)$$

where $T_e = R_m C_d$ is a time constant of the electrical (admittance) system.

Next, we model the electro-mechanical part, $G_{em}(s) = F(s)/I(s)$, which is the system from the input current to the output force. We consider two components in the model. The first term is proportional to the current i , and the second term is proportional to the charge. The current-proportional term is modeled as a first order transfer function. This term slowly converges to zero if the current is zero, therefore it can represent stress relaxation. The stress relaxation is a phenomenon that the bending stress gradually converges to zero even under constant voltage because of the diffusion of water (or solvent) in the polymer [6, 7]. The second charge-

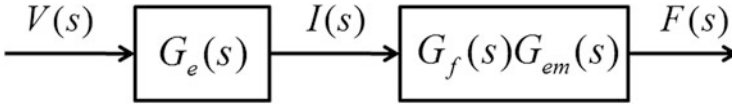


Fig. 24.7 Block diagram of the dynamics of IPMC

proportional term keeps steady stress [9] under constant voltage, and it is modeled as an integration of the current. Let $G_{em}(s)$ be a transfer function from i to f . Taking the components into $G_{em}(s)$, we have

$$G_{em}(s) = \frac{K_r}{T_{em}s + 1} + \frac{K_s}{s} \quad (24.9)$$

where T_{em} is a time constant of stress relaxation, and K_r, K_s are constants.

Because the force is measured by a strain-gauge based force sensor, the model of the sensor should be considered. Typical amplifiers for strain gauges have low pass filters; therefore the dynamics of the force sensor can be approximated by a first order system. Let $G_f(s)$ be a transfer function of the sensor:

$$G_f(s) = \frac{1}{T_f s + 1} \quad (24.10)$$

where T_f is a time constant of the sensor.

Figure 24.7 shows a block diagram of the proposed model. The first block, G_e , is the transfer function of the electrical model. The second block, $G_f G_{em}$, shows a transfer function of the electro-mechanical model and the sensor model. Let $G(s)$ be a transfer function from v to f . From Eqs. (24.8), (24.9) and (24.10), we obtain

$$G(s) = G_f(s)G_{em}(s)G_e(s) = \frac{(K_r + K_s T_{em})C_d s + K_s C_d}{(T_f s + 1)(T_{em} s + 1)(T_e s + 1)}. \quad (24.11)$$

The obtained transfer function $G(s)$ of Eq. (24.11) shows that the numerator is first order and the denominator is third order. In consideration of an application to feedback control, we treat the model as a black-box. Therefore, the coefficients of the transfer function $G(s)$ can be simplified as:

$$G(s) = \frac{s + b_0}{a_3 s^3 + a_2 s^2 + a_1 s + a_0}, \quad (24.12)$$

where the coefficients a_i ($i = 0, 1, 2, 3$) and b_0 can be obtained from Eq. (24.11) dividing both the numerator and the denominator by $(K_r + K_s T_{em})C_d$.

In Eqs. (24.11) and (24.12), assuming $K_r + K_s T_{em} > K_s$, we approximate as $b_0 \approx 0$. Thus the model for force control is given by

$$G(s) = \frac{s}{a_3s^3 + a_2s^2 + a_1s + a_0}. \quad (24.13)$$

Note that the model of Eq. (24.13) is effective in the case that the dynamics of stress relaxation is dominant.

24.4.2 Robust PID Force Control [34]

The parameters of the transfer function varies so much by environmental changes, therefore it is desirable to construct a robust control system even with the uncertainties of the model. We first show a representation of the parametric uncertainty and a closed loop transfer function with a PID controller. The coefficients of the transfer function in Eq. (24.12) are set as $\theta = [a_0 \ a_1 \ a_2 \ a_3]$. Assuming $a_3 > 0$, and the parameter θ is a member of a set of parameter Θ defined as

$$\Theta = \{\theta \mid \alpha_i \leq a_i \leq \beta_i \quad (i = 0, 1, 2, 3)\} \quad (24.14)$$

where α_i and β_i are the lower and upper bounds of a_i . The input signal of a PID controller is given by

$$v(t) = K_p e(t) + K_i \int_0^t e(\tau) d\tau + K_d \dot{e}(t) \quad (24.15)$$

where $e(t) = f_r(t) - f(t)$, and f_r is the reference of force. From Eqs. (24.13) and (24.15), the closed loop transfer function from the reference f_r to the actual force f is obtained as

$$\frac{F(s)}{F_r(s)} = \frac{K_d s^2 + K_p s + K_i}{a_3 s^3 + (a_2 + K_d) s^2 + (a_1 + K_p) s + (a_0 + K_i)}. \quad (24.16)$$

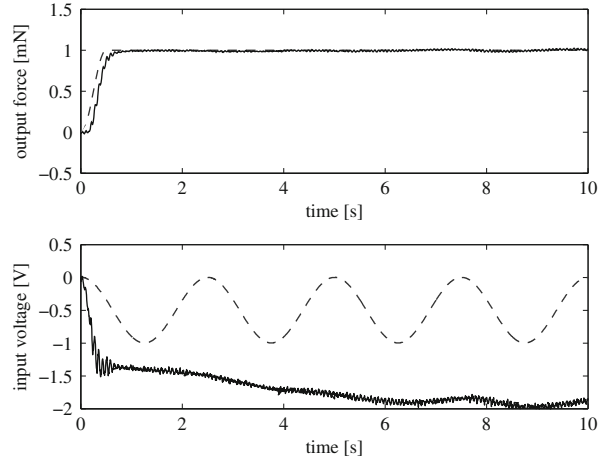
To a step reference input, the steady state error that equals $(K_i / (a_0 + K_i) - 1) F_r$ appears, however it is negligible because we can design $a_0 < < K_i$.

The closed loop transfer function of Eq. (24.16) has parametric uncertainties as in Eq. (24.15) and the characteristic equation of the closed loop system is a member of a set of polynomial, which is referred as an interval polynomial family. The characteristic equation of the closed loop system of Eq. (24.16) is given by

$$K(s, \theta) = a_3 s^3 + (a_2 + K_d) s^2 + (a_1 + K_p) s + (a_0 + K_i). \quad (24.17)$$

In this case, the interval polynomial, denoted by $K(s, \Theta)$, is defined as

Fig. 24.8 Experimental results of robust PID force control



$$\begin{aligned}
 K(s, \Theta) &= \{K(s, \theta) \mid \theta \in \Theta\} \\
 &= [\alpha_3 \quad \beta_3]s^3 + [\alpha_2 + K_d \quad \beta_2 + K_d]s^2 + [\alpha_1 + K_p \quad \beta_1 + K_p]s \\
 &\quad + [\alpha_0 + K_i \quad \beta_0 + K_i].
 \end{aligned} \tag{24.18}$$

The control objective is that the system is robust stable for the parametric uncertainties of Eq. (24.14). Therefore, the control system design problem is to find PID gains K_p , K_i , K_d such that the interval polynomial of Eq. (24.18) is robust stable polynomial family.

According to Kharitonov's theorem, for the third order system, any members of the interval polynomial of Eq. (24.17) are stable if and only if the following polynomial is stable [35].

$$K_2(s) = \beta_3 s^3 + (\alpha_2 + K_d)s^2 + (\alpha_1 + K_p)s + (\beta_0 + K_i) \tag{24.19}$$

As the result, if we design the PID gains K_p , K_i , K_d to make $K_2(s)$ stable, the closed loop system of Eq. (24.16) is stable for any parametric uncertainties of Eq. (24.14).

In a practical application, the controller design of the proposed method is conducted through the following steps:

1. Estimate the bound of the parameters, α_i and β_i ($i = 0, 1, 2, 3$) of Eqs. (24.13) and (24.14) by carrying out several identification experiments.
2. Determine the PID gain to make $K_2(s)$ of Eq. (24.19) stable by appropriate methods such as a pole placement.

Experimental result of the robust PID force control is shown in the Fig. 24.8. In this experiment, two IPMC samples were used for control and disturbance generation. Identification experiment was repeated five times to obtain the bound of

parameters. And then, the PID gains were chosen by the pole placement, and the control experiment was conducted.

Figure 24.8 shows the case with a disturbance. The upper graph of Fig. 24.8 plots the output force; the solid line is the controlled force f , and the dashed line is the desired force f_r . The controlled force f is well kept to the desired force during the experiment. The lower graph of Fig. 24.8 plots the input voltage; the solid line is the control voltage, and the dashed line is the disturbance input. It is observed that the desired force can be kept even if the disturbance acts. For details of verification experiments, please see the reference [34].

24.5 Conclusion

In this chapter, the basics of modeling and feedback control methods for ionic polymer actuators are explained. As the PID controller is a simple feedback method, widely used in practical applications, and it is also effective on the control of polymer actuators. The characteristics of ionic polymer actuators vary by environmental conditions, therefore robust controllers are useful. The modeling of the dynamics of the actuator is significantly important for analysis and control design.

The methods explained in this chapter are simple and fundamental approaches, however, various researches for controls of polymer actuators have been conducted to develop application systems of polymer actuators on practical levels. In order to apply the polymer actuator to practical robotic and mechatronics systems, there exist many problems such as limitation of output force or durability; however, mutual evolutions of improvements on the actuator technology and the design of the control system are important for further applications.

Acknowledgment The authors would like to express the deepest appreciation to Dr. Kinji Asaka and Professor Masaki Yamakita for their supports throughout the research.

References

1. Bar-Cohen Y (ed) (2004) Electroactive polymer (EAP) actuators as artificial muscles: reality, potential, and challenges, 2nd edn. SPIE Press, San Diego
2. Kim KJ, Tadokoro S (eds) (2007) Electroactive polymers for robotic applications: artificial muscles and sensors. Springer, London
3. Oguro K, Kawami Y, Takenaka H (1992) Bending of an ion-conducting polymer film-electrode composite by an electric stimulus at low voltage. *J Micromach Soc* 5:27–30 (in Japanese)
4. Ljung L, Glad T (1994) Modeling of dynamic systems. Prentice Hall, Englewood Cliffs
5. Goodwin GC, Payne RL (1997) Dynamic system identification: experiment design and data analysis. Academic, New York

6. Asaka K, Oguro K (2000) Bending of polyelectrolyte membrane platinum composites by electric stimuli part II. Response kinetics. *J Electroanal Chem* 480:186–198
7. Yamaue T, Mukai H et al (2005) Electrostress diffusion coupling model for polyelectrolyte gels. *Macromolecules* 38:1349–1356
8. de Gennes PG, Okumura K et al (2000) Mechanoelectric effects in ionic gels. *Europhys Lett* 50(4):513–518
9. Nemat-Nasser S, Li JY (2000) Electromechanical response of ionic polymer-metal composites. *J Appl Phys* 87(7):3321–3331
10. Tadokoro S, Yamagami S et al (2000) Modeling of Nafion-Pt composite actuators (ICPF) by ionic motion. In: *Proceedings of the SPIE*, vol 3987, pp 262–272
11. Toi Y, Kang SS (2005) Finite element analysis of two-dimensional electrochemical–mechanical response of ionic conducting polymer–metal composite beams. *Comput Struct* 83(31–32):2573–2583
12. Wallmersperger T, Leo DJ, Kothera CS (2007) Transport modeling in ionomeric polymer transducers and its relationship to electromechanical coupling. *J Appl Phys* 101:024912
13. Kanno R, Kurita A et al (1994) Characteristics and modeling of ICPF actuator. In: *Proceedings of the Japan–USA symposium on flexible automation*. Kobe, Japan, pp 691–698
14. Mallavarapu K, Leo D (2001) Feedback control of the bending response of ionic polymer actuators. *J Intell Mater Syst Struct* 12:143–155
15. Yamakita M, Kamamichi N et al (2004) Development of an artificial muscle linear actuator using ionic polymer-metal composites. *Adv Robot* 18(4):383–399
16. Chen Z, Tan X, Shahinpoor M (2005) Quasi-static positioning of ionic polymer-metal composite (IPMC) actuators. *Proceedings of the IEEE/ASME international conference on advanced intelligent mechatronics*. Monterey, USA, pp 60–65
17. Kothera C, Leo D (2005) Bandwidth characterization in the micropositioning of ionic polymer actuators. *J Intell Mater Syst Struct* 16(1):3–13
18. Kang S, Shin J et al (2007) Robust control of ionic polymer-metal composites. *Smart Mater Struct* 16:2457–2463
19. Yamakita M, Sera A et al (2008) Integrated design of an ionic polymer–metal composite actuator/sensor. *Adv Robot* 22:913–928
20. Kanno R, Tadokoro S et al (1996) Linear approximate dynamic model of ICPF (ionic conducting polymer gel film) actuator. *Proceedings of the international conference on robotics and automation*. Minneapolis, USA, pp 219–225
21. Bao X, Bar-Cohen Y, Lih S (2002) Measurements and macro models of ionomeric polymer-metal composites. In: *Proceedings of the SPIE*, vol 4695. San Diego, USA, pp 220–227
22. Newbury KM, Leo DJ (2003) Linear electromechanical model of ionic polymer transducers – part I: model development. *J Intell Mater Syst Struct* 14:333–342
23. Chen Z, Tan X (2008) A scalable dynamic model of ionic polymer metal composite actuators. In: *Proceedings of the SPIE*, vol 6927. San Diego, USA, p 69270I
24. Richardson R, Levesley M et al (2003) Control of ionic polymer metal composites. *IEEE/ASME Trans Mechatron* 8(2):245–253
25. Yun K, Kim WJ (2006) Microscale position control of an electroactive polymer using an anti-windup scheme. *Smart Mater Struct* 15(4):924–930
26. Bhat N, Kim WJ (2004) Precision force and position control of an ionic polymer metal composite. *IMEchE J Syst Control Eng* 218(6):421–432
27. Shan YF, Leang KK (2009) Frequency-weighted feedforward control for dynamic compensation in ionic polymer–metal composite actuators. *Smart Mater Struct* 18:125016
28. Fleming MJ, Kim KJ, Leang KK (2012) Mitigating IPMC back relaxation through feedforward and feedback control of patterned electrodes. *Smart Mater Struct* 21:085002
29. Lin HH, Fang BK et al (2009) Control of ionic polymer–metal composites for active catheter systems via linear parameter-varying approach. *J Intell Mater Syst Struct* 20(3):273–282
30. Brufau-Penella J, Tsiakmakis K et al (2008) Model reference adaptive control for an ionic polymer metal composite in underwater applications. *Smart Mater Struct* 17:045020

31. Lavu BC, Schoen MP, Mahajan A (2005) Adaptive intelligent control of ionic polymer–metal composites. *Smart Mater Struct* 14:466–474
32. Fang BK, Lin CK, Ju MS (2011) Adaptive control of ionic polymer–metal composite in air and under water using a modified direct self-tuning regulator embedded with integral action. *Smart Mater Struct* 20:105016
33. Ogata K (2009) *Modern control engineering*, 5th edn. Prentice Hall, New York
34. Sano S, Takagi K et al (2010) Robust PID force control of IPMC actuators. In: *Proceedings of the SPIE*, vol 7642. San Diego, USA, p 76421U
35. Barmish BR (1994) *New tools for robustness of linear systems*. Macmillan Publishing Company, New York

Chapter 25

Motion Design-A Gel Robot Approach

Mihoko Otake

Abstract The main focus of this chapter is to propose methods for motion design of deformable machines, using a particular electroactive polymer gel. They are deformable like mollusk that can locomote dynamically or manipulate things softly. Such a machine has been a dream in the past but is now experimentally possible. Mechanisms consisting of the gel, hereafter called ‘gel robots’, were designed, developed, and controlled experimentally. It includes: (1) a mathematical model of the gel to be applied for design and control of distributed mechanisms, (2) gel robots driving systems, (3) control of gel robots for dynamic deformations. This chapter overviews a gel robot approach based on agent model for motion design of deformable robots utilizing electroactive polymers with simulation and experimental results.

Keywords Agent model • Gel robot • Motion design • Simulation

25.1 Gel Robot Approach

The best way to discover concrete methods is to prototype machines from existing material. Real things tell us many things. Deformable robots were experimentally developed made entirely of electroactive polymer gel, hereafter called, “gel robots”. The purpose of gel robots is to discover fundamental principles for designing and controlling deformable machine made of actively deformable materials. From among variety of actively deformable materials, we selected electroactive polymer gel, Poly (2-acrylamido-2-methylpropane sulfonic acid) gel (PAMPS gel) [1, 2] which is capable of large deformations although the response speed is not so fast. The main advantage of this material is that transformation can be halted if required. Ideas are explored which solve motion design problems of

M. Otake (✉)

Department of Mechanical Engineering, Graduate School of Engineering,
Chiba University, 1-33 Yayoi-cho, Inage-ku, Chiba 263-8522, Japan
e-mail: otake@chiba-u.jp

robots with infinite degrees of freedom. This chapter introduces the essence of the study on electroactive polymer gel robots [3]¹.

25.2 Agent Model of Electroactive Polymers

In the field of artificial intelligence, agent is defined that anything that can be viewed as perceiving its environment through sensors and acting upon that environment through actuators [4]. The definition of agent applies to smart materials as well as robots[5]. Among various types of agents, we can model smart materials as model-based reflex agents, which maintain some sort of internal state that depends on the percept history and thereby reflects at least some of the unobserved aspects of the current state. Internal state functions are determined based on the electrochemomechanical property of each material. Fig. 25.1 a gives the structure of the reflex agent with internal state, showing how the current percept is combined with the old

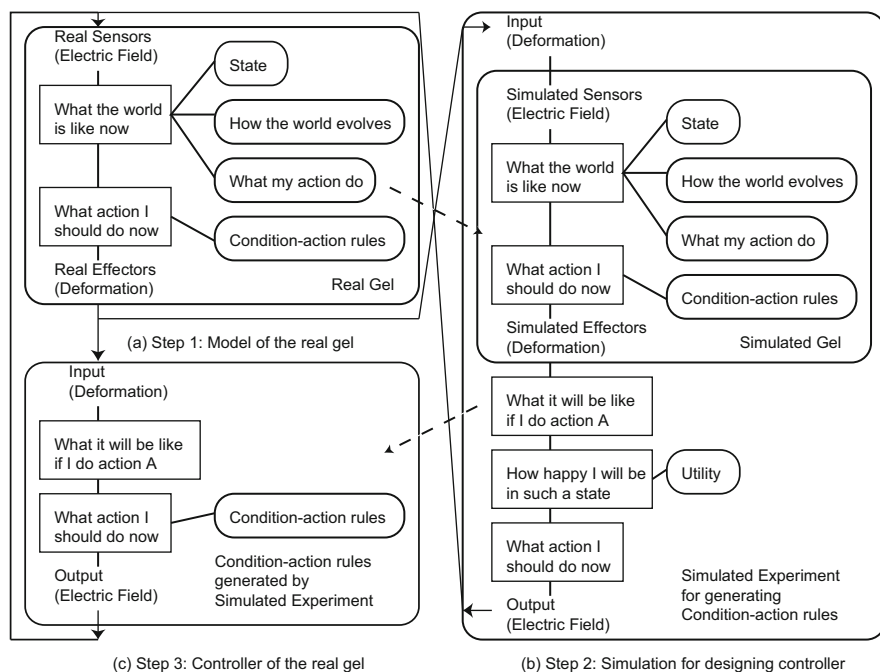


Fig. 25.1 Control system based on the agent model of electroactive polymers

¹ This chapter was adapted from in part, by permission, Mihoko Otake, *Electroactive Polymer Gel Robots - Modelling and Control of Artificial Muscles*, Springer-Verlag, 2009.

internal state to generate the updated description of the current state. Rectangles denote the current internal state of the agent's decision process and ovals to represent the background information used in the process.

25.3 Control System Design based on the Agent Model

Knowing about the current state of the environment is not always enough to decide what to do. The agent needs some sort of goal information that describes situations that are desirable. The agent program can combine this with information about the results of possible actions in order to choose actions that achieve the goal. However, goals alone are not really enough to generate high-quality behavior in most environments. Goals just provide a crude binary distinction between desirable and undesirable states, whereas a more general performance measure should allow a comparison of different world state according to exactly how desirable they would make the agent if they could be achieved. If one world state is preferred to another, then it has higher utility for the agent. A utility function maps a state onto a real number, which describes the associated degree of desirability.

Control system for electroactive polymers should contain modules which represent goal or utilities, since smart materials are modeled as simple reflex agents with internal state without goal or utility by its nature. Therefore, we model electroactive polymers, and include the model into control systems (Fig. 25.1b top half). Then, the utility function is added in order to determine the appropriate action or electrical stimuli to the material from the control system (Fig. 25.1b bottom half). Simulation would be conducted in various situations so that condition action rules are determined (Fig. 25.1c). The last module of (c), the controller with condition action rules is necessary for real-time operation.

25.4 Turning Over Motion Design

Here we describe the turning over motion design for the purpose of describing the implementation of control system design based on the agent model.

25.4.1 *Simulation of Deformation of the Electroactive Polymer Gel in Applied Electric Field*

The first step for motion design is simulation of deformation of the electroactive polymer gel in applied electric field, which is illustrated in Fig. 25.1b top half.

An ionic polymer gel in an electric field deforms through penetration of the surfactant solution [6]. This process is characterized by the following three steps.

1. Migration of surfactant molecules into the gel driven by the electric field
2. Adsorption of surfactant molecules to the polymers
3. Gel deformation caused by adsorption of surfactant molecules

We derive a constitutive equation of the second step to contain common variables to those of the first and third steps. This is to demonstrate consistent model from voltage input to gel deformation. Complex adsorption reaction [7] is approximated in a simple manner. The adsorption-induced deformation model gives a theoretical foundation.

25.4.1.1 Migration of Surfactant Molecules Driven by the Electric Field

The surfactant molecules move toward the cathode by electrophoresis when dc voltage is applied. Under static or quasi-static conditions, we assume current density i is proportional to electric field E ,

$$i = \varepsilon E, \quad E = -\nabla \Phi, \quad (25.1)$$

where electric conductivity ε and electric potential Φ appear.

25.4.1.2 Adsorption of Surfactant Molecules to the Polymers

Gong et al. theoretically analyzed the cross-linking effect on the polyelectrolyte–surfactant interaction [7]. They derived stability constant K on the basis of the free-energy minimum principle to predict concentration of bound surfactant molecules at equilibrium. Narita et al. analyzed kinetics of the cationic surfactant uptake into an anionic polymer network in order to discuss transient states [8]. Although the previous models well describe the binding of surfactant with the polymer network, they do not explain the issue of the electric field and deformation in the first and third steps. We propose and introduce the adsorption equation based on the Langmuir's theory for the second step. The model of simplicity explains the connection between the first and third steps. Adsorption state transition of the gel is approximated in the following local nonlinear differential equation [3]:

$$\frac{d\alpha}{dt} = v_a - v_d = -ai \cdot n - d\alpha. \quad (25.2)$$

where α is the adsorption rate defined as the molar ratio of bound surfactants to the local sulfonates group of the polymer chains inside the gel; i is the current density vector on the gel surface; n is the normal vector of the gel surface; a and d are

association and dissociation constants. The equation shows that the effect of an electric field to a gel is determined by the geometry of the equi-potential surface and the gel surface.

25.4.1.3 Gel Deformation Caused by Adsorption of Surfactant Molecules

Kitahara derived a formula for the plate deformation due to surface stress caused by atom adsorption on the surface [9]. We replace atoms with plates by surfactant molecules with gels respectively. On one side of the gel, adsorbed molecules give rise to surface stress. The formula for the bending in the case of uniform surface stress was provided by Stoney [10] as follows:

$$\frac{1}{R} = \frac{6(1-\nu)\sigma\Delta}{Eh^2}, \quad (25.3)$$

where R is the radius of curvature, ν is the Poisson's ratio, σ is the surface stress, Δ is the width of the adsorbate, E is the Young modules, and h is the width of the substrate. We approximate that the width of adsorbate and that of substrate are the same. Substituting $\nu = 0.5$ and $\Delta = h$ into equation (25.3), we have

$$\frac{1}{R} = \frac{3\sigma}{Eh}. \quad (25.4)$$

We approximate that surface stress is proportional to the adsorption rate, and obtain with constant b ,

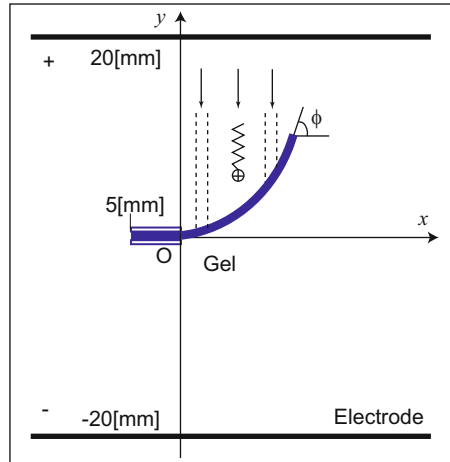
$$\sigma = b\alpha. \quad (25.5)$$

Equation (25.5) shows a linearized form of the stress as a nonlinear function of the adsorption rate in the neighborhood of $\alpha = 0$.

25.4.1.4 Summary

To summarize, in order to determine the deformation of the gel, we have to solve the set of equations (25.1), (25.2), (25.4) and (25.5). We obtain (1) current density from the voltage of electrodes, (2) the adsorption rate from the current density, (3) surface stress and strain from the adsorption rate, respectively. Figure 25.2 describes the deformation process of the beam of gel in uniform electric fields. Three arrows are current density vectors. Molecular density on the gel is large near the root and small near the tip of the gel.

Fig. 25.2 Deformation process of a surfactant driven ionic polymer gel illustrated with experimental setup



25.4.2 Definition of Utility Function for Achieving Turning Over Motion

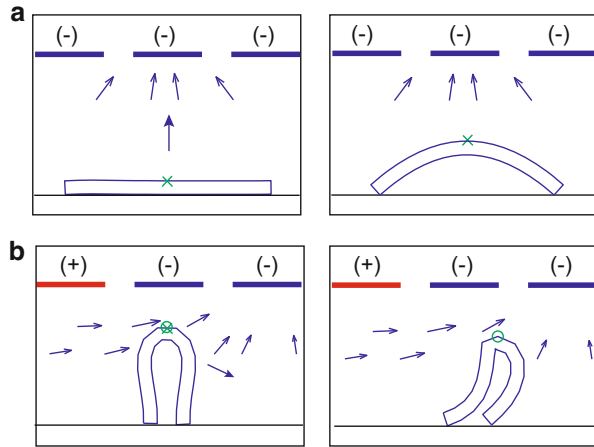
The second step for motion design is the definition of utility function for achieving objective motion, which is illustrated in Fig. 25.1b bottom half.

25.4.2.1 Abstraction of the Objective Motion

The key to achieve turning over motion is to coordinate each part of the body. If we get back to the objective of the motion, we do not have to control every part of the body in each step. The assumption is that only one or a few points are controlled by overall deformation of the other parts, which work cooperatively. We focus on the central position based on the preliminary experiment [11]. If one observes the trajectory of the center of the starfish-shaped gel robot while it turns over, it lifts up and moves above the tip. The orientation of the center rotates and reversed in final state. This observation leads us to regard turn over motion as a kind of locomotion along with rotation.

Our strategy to generate objective motion in a simple manner is to divide the motion into two processes, preparation process and transition process. At preparation process, we apply the electric field to move the center upward and to make the distance smaller between the center and the tip along the ground (Fig. 25.3a). At transition process, the electric field is switched so as to make the center rotates about the tip (Fig. 25.3b).

Fig. 25.3 Process of turn over motion



25.4.2.2 Spatially Varying Electric Field to Move the Center of the Gel

We previously found that spatially varying electric field generated by multiple electrodes arranged in a planar array can drive free-ended gels [11]. We describe the deformation in this configuration based on the model, because we use this configuration to drive gel robots. Initially, we placed a strip of gel material on the bottom of the water tank. Then, we suspended multiple electrodes in a planar configuration above the gel.

Figure 25.3a also shows assumed deformation of the gel below multiple electrodes and distribution of cationic surfactant molecules. If the electrode above the center of the gel is cathode, cationic surfactant molecules adsorb on the surface of the anionic gel facing the ground; which cause the center of the gel to move toward the cathode electrode. This is because the cathode electrode above the center of the gel attracts the surfactant molecules. We can see that the cathode electrode above the gel may move the center of the gel upward.

25.4.2.3 Selection of a Set of Operators

Turning over motion is divided into two processes, preparation process and transition process. Operators for each process were selected.

The effective operator to move the center of the gel upward was selected whose central region contains three cathode electrodes for preparation process (Fig. 25.3a), since the one whose central region is wider generates stronger electric field towards the electrodes. Then, the operator to move the center of the gel toward right was moved one step toward right direction (Fig. 25.3b), since the gel may bend toward right direction.

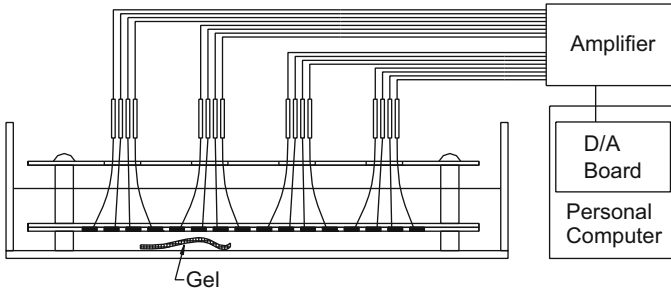
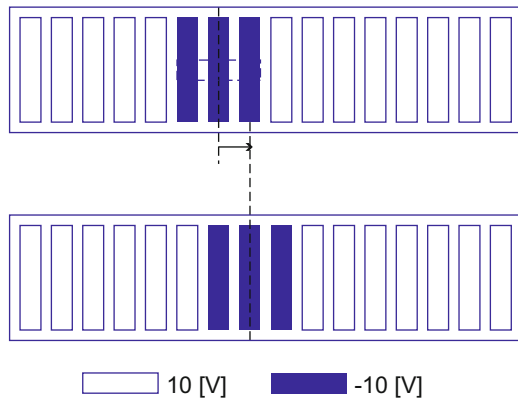


Fig. 25.4 16-channel array electrode system (side view)

Fig. 25.5 Applied voltage input sets



Multiple electrodes arranged in an array that looks like a ladder generate spatially varying electric fields. Figure 25.4 is a side view of the developed system. The size of each electrode is 4[mm] \times 20[mm], and the space between the electrodes is 2[mm]. The gel is located under the array of electrodes. Figure 25.5 illustrates a selected set of operators.

25.4.2.4 Phase Diagram for Switching of Operators

After a set of operators was selected, the timing for switching these operators was made clear. Condition was: the size of the gel, 16[mm] in length, 4[mm] in width and 1[mm] in thickness; polarity of central electrodes was cathodic; distance between the electrodes and the gel was 15[mm]; horizontal distance of the center of gels and electrodes was 0[mm].

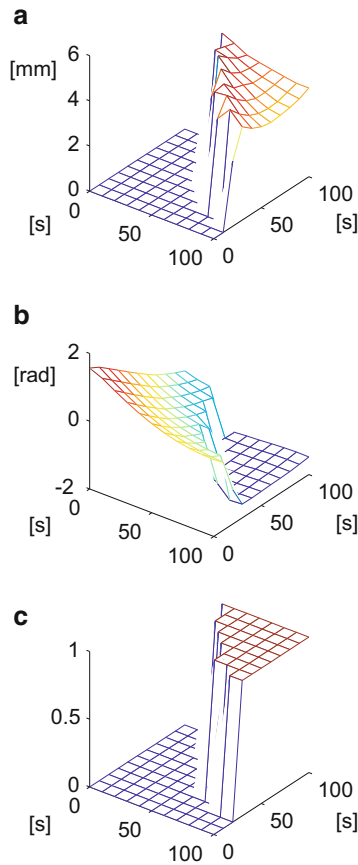


Fig. 25.6 Phase diagram of a beam-shaped gel: (a) height of the left edge of the gel, (b) angle of the normal vector on the right edge of the gel, (c) final state of the turnover (1: success, 0: failure). Applied electric field was generated by up operator which contains three cathodic electrodes. Applied period of each step was from 0 to 100 [s]. X-axis on the left is an applied period of the first operator. Y-axis on the right is an applied period of the second operator

Phase diagrams were drawn through simulation. The condition was that the timing for switching for 0 to 100 [s], and period to apply electric field after switching for 0 to 100[s]. The graph is shown in Fig. 25.6. The top graph illustrates the height of the left tip h ; the middle graph represents orientation of the tip θ . Turn over state was defined as follows: the state which meets both conditions that left tip is set free from the ground ($h > 0$), and right tip facing on the ground ($\theta < -\pi$), when it turns over toward right direction. Utility function is defined as $f(h, \theta) = -h(\theta + \pi)$. $f > 0$ when both variables meet the conditions. The bottom graph shows whether the turn over motion was

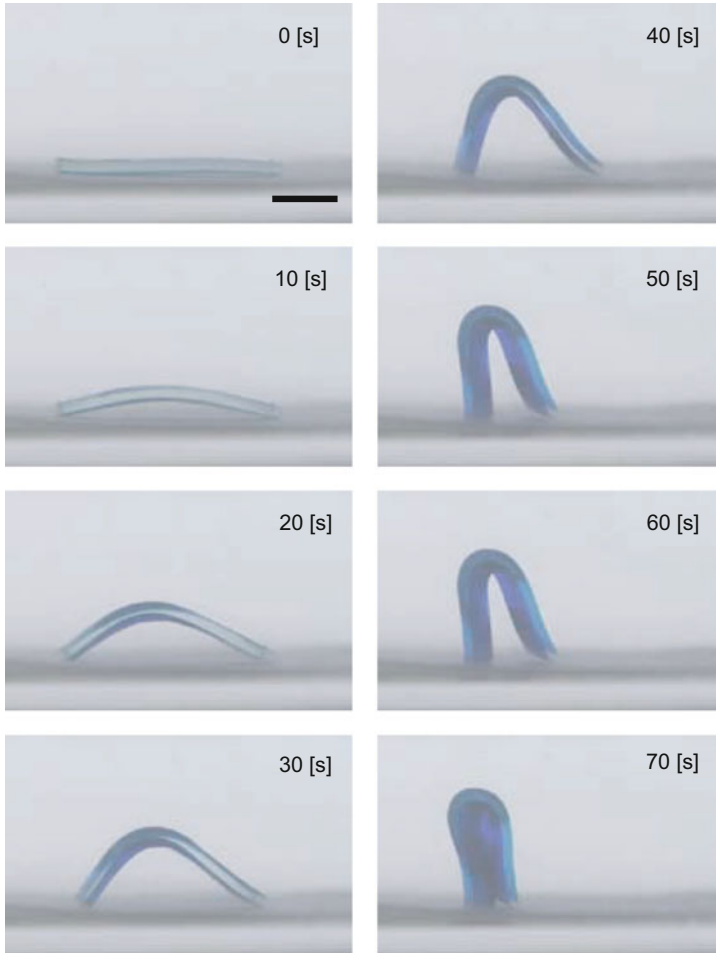


Fig. 25.7 Preparation process of turning over motion generation of beam-shaped gel: The time for switching was 70 [s]. The gel deformed into hairpin shape. The horizontal distance between the tip and center of the gel became smaller. The scale bar is 5 [mm]

successfully derived (plotted as 1 when $f > 0$) or not (plotted as 0 when $f \leq 0$) in simulation.

25.4.3 Application of Condition Action Rules

For the purpose of applying the simulation results to experiments, the calibration method was applied. The period to reach the switching point scatters because

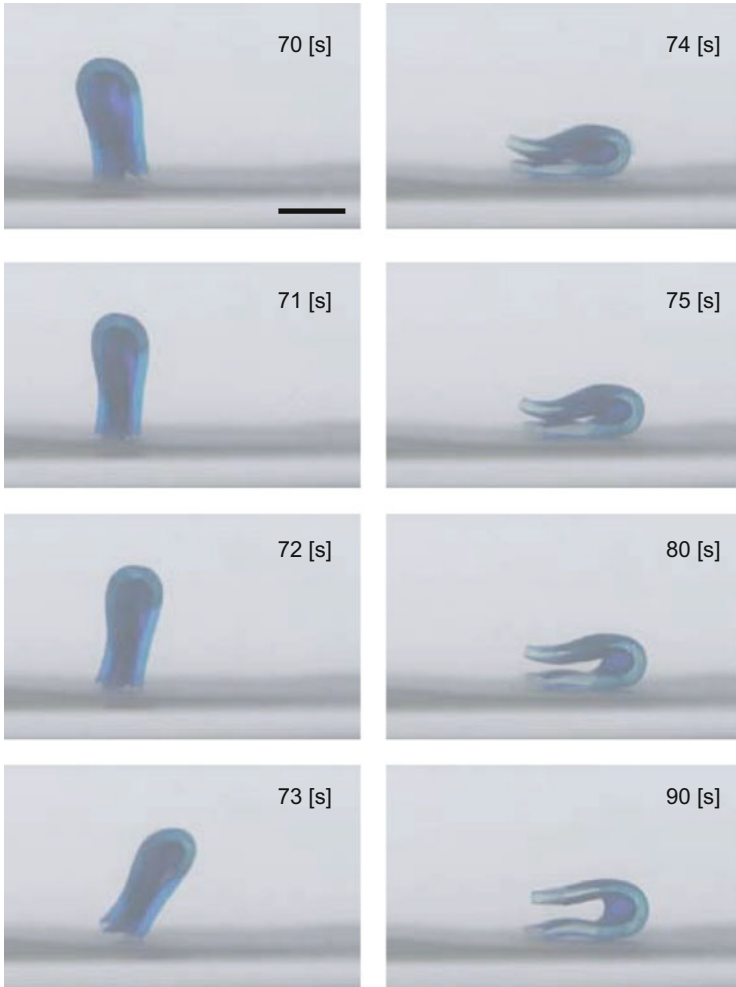


Fig. 25.8 Transition process of turning over motion generation of beam-shaped gel: The rotating motion occurred just after switching the operator in 70 [s]. It took 5 [s] to turn over. The scale bar is 5 [mm]

the parameters of the gel scatter. The model suggests that the deformation response of the same shape of gel is the same. The strategy is to switch the operator based on the position of the center of the gel or orientation of the tip of the gel, which are condition action rules illustrated in Fig. 25.1c. In this way, we can apply the simulation results to experimental results.

Turning over motion generation of free-ended gel was generated successfully based on the proposed method. Figure 25.7 shows preparation process of turn over motion. It took 70[s] to reach timing for switching. It took 5[s] after switching the operator for transition process (Fig. 25.8).

25.5 Discussion

The hairpin-shape of the gel was generated for the first time through the experiment. It should be emphasized that the originally known motion was only swinging motion of beam-shaped gel between pairs of electrodes. By applying this approach to three dimensional space, starfish-shaped gel robots turned over toward different directions. The curling around an object motion of a beam-shaped gel was also generated based on agent model [3]. Internal state of electroactive polymers keeps the history of electric input, which is the origin of potential smartness. With this in mind, we can bring out intelligence from smart materials and making use of this characteristics to operate infinite degrees of freedom. Movies on various motions of gels and gel robots are available on the gelrobot website [12].

Acknowledgements This work was supported by the Japan Society for the Promotion of Science Grant for Research on Gel Robots 13450100. The author express deep appreciation to Dr. Y. Kagami, Prof. H. Inoue, Prof. Y. Kakazu, and Prof. Y. Osada who give us suggestions of this research.

References

1. Osada Y, Okuzaki H, Hori H (1992) A polymer gel with electrically driven motility. *Nature* 355:242
2. Osada Y, Okuzaki H, Gong J, Nitta T (1994) Electro-Driven gel motility on the base of cooperative molecular assembly reaction. *Polymer Sci.* 36:340
3. Otake M (2009) *Electroactive polymer gel robots-modelling and control of artificial muscles.* Springer, Newyork
4. Russell S, Norvig P (1995) *Artificial intelligence: a modern approach.* Prentice-Hall, Inc., Upper Saddle River, NJ
5. Yeates C (1994) Are smart materials intelligent? *INSPEC Matters* 77:4
6. Okuzaki H, Osada Y (1994) Effects of hydrophobic interaction on the cooperative binding of a surfactant to a polymer network. *Macromolecules* 27:502
7. Gong JP, Osada Y (1995) Theoretical analysis of the cross-linking effect on the polyelectrolyte - surfactant interaction. *J Phys Chem* 99:10971
8. Narita T, Gong JP, Osada Y (1998) Kinetic study of surfactant binding into polymer gel - experimental and theoretical analyses. *J Phys Chem B* 102:4566
9. Kitahara K (1994) General formula for the deformation of a plate due to surface stress. *Japan J Appl Phys* 33:3673
10. Stoney GG (1909) The tension of metallic films deposited by electrolysis. *Proceed Roy Soc Lond A* 82, 172
11. Otake M, Kagami Y, Inaba M, Inoue H (2002) Motion design of a starfish-shaped gel robot made of electro-active polymer gel. *Robot. Autonom. Syst.* 40:185
12. Otake M, *Electroactive polymer gel robots-modelling and control of artificial muscles* (<http://www.gelrobot.net/>, 2011)

Chapter 26

Motion Control

Minoru Hashimoto

Abstract Poly vinyl chloride (PVC) gel actuators show great potential because of such positive characteristics as movement in the air, large deformation, and being lightweight. We propose a configuration of a contraction type actuator and investigate its various characteristics. The contraction strain is 10–15 %, the response frequency is 3–7 Hz and the applied voltage 200–600 V. The generating stress is proportional to the number of layers, and the stress is then about 10 kPa when the actuator height is 10 mm. To use this actuator as a control element, we develop a mathematical model. Based on these results, we develop a position feedback control technique for the actuator and investigate the validity of the control method. The control law included a feed forward term to compensate for the elastic characteristic of the PVC gel actuator. The control method had good performance.

Keywords Cole–Cole plot • Gel • Motion Control • Polymer actuator • Position control • PVC

26.1 Introduction

Polymeric materials have received special attention as materials for creating artificial muscles because they are flexible, lightweight, and can be easily molded. There have been many studies in this field, however most of the actuators using polymeric materials work only in water, and the linear deformation strain is very small.

We believe the characteristics of artificial muscles should approximate those of human muscles. Human muscles include the following characteristics, 30 % contraction strain, 0.3 MPa output stress and 10 Hz response rate [1]. For contraction strain, we can consider the following three materials as candidates for artificial muscles: dielectric elastomer [2], polypyrrole [3], and poly vinyl chloride (PVC) gel [4]. The PVC gel is the most promising material for an artificial muscle in terms of the applied dc field and response rate. A continuous supply of solvent is

M. Hashimoto (✉)

Department of Bioscience and Textile Technology, Interdisciplinary Graduate School of Science and Technology, Shinshu University, 3-15-1 Tokida, Ueda, Nagano 386-8567, Japan
e-mail: hashi@shinshu-u.ac.jp

necessary for typical gels, but PVC gel including the plasticizer does not need any solvent and is able to operate in air. Because the PVC gel deforms when subjected to an electric field, it is easy to create a fast response.

Hirai et al. studied the bending deformation of the PVC gel actuator [4, 5]. They established the principles and the characteristics of the bending deformation. However, it is necessary to cause deformation of expansion and contraction in an artificial muscle. In this chapter, we propose an electrode arrangement for the PVC gel actuator for an artificial muscle and investigate the characteristics of the proposed actuator experimentally to establish the validity of the PVC gel actuator as an artificial muscle. In addition, we build a linear mathematical model of the PVC gel actuator and design a control law for position control of the actuator.

An outline of this chapter follows. First, we introduce a configuration of the contraction type PVC gel actuator using mesh-type anodes. The characteristics of the actuator are then measured experimentally. Based on the experimental results of the characteristics, a linear mathematical model is built. A control law for position control based on the mathematical model is then designed. Finally, conclusions are drawn.

26.2 Contraction Type PVC Gel Actuator

26.2.1 Configuration of a Contraction Type Actuator

The PVC was plasticized with dibutyl adipate (DBA), a typical plasticizer. The PVC was dissolved with the DBA in tetrahydrofuran (THF) solvent. The weight ratios of PVC and DBA were adjusted to 1:4. The plasticized PVC is called PVC gel in this chapter.

Both sides of the PVC gel are sandwiched by electrodes. Electric charges (electrons) are injected from the cathode of the electrode into the gel, and the gel deforms along the anode. When the electric field is discharged, the PVC gel returns to its original shape. Before discharging the anode, the accumulation of electric charges promotes the electrostatic adhesiveness of the gel onto the anode, and creeping deformation appears on the anode surface [4]. The mechanism of creeping deformation is different from the deformation mechanisms of dielectric elastomer and conductive polymer [2, 6].

Based on this property of the PVC gel, we developed a configuration of the PVC actuator which facilitates the deformation of expansion and contraction [7, 8]. The PVC gel is sandwiched between a stainless mesh as an anode and stainless foil as a cathode. Figure 26.1 shows cross sections of the unit configuration when the dc field is applied and removed. A cathode is located on the right under the PVC gel, and an anode is above the gel. When the dc field was applied, the PVC gel creeps up the anode and moves into the mesh holes. When the dc field is removed, it returns to its former shape as a result of its elasticity. The displacement is increased by stacking

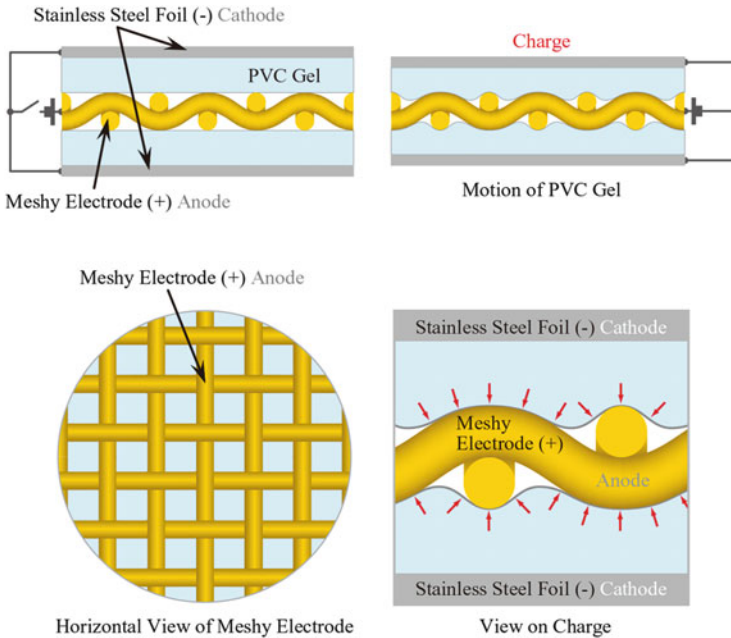


Fig. 26.1 Cross section of the deformation of the actuator

up the layers and it is operated as an expansion and contraction type actuator (Fig. 26.2).

We use mesh electrodes made from stainless steel. The mesh size is #100-#20 which stands for number of wires per inch. The diameter of the wires is 0.09–0.2 mm. Stainless foil whose thickness is 0.01 mm was used as the cathode. The thickness of PVC gel is from 0.25 to 0.7 mm. We confirmed that even if the anode is not a mesh electrode, a similar type of deformation occurs, providing the anode has an uneven shape and there is a flow path of air between the gel and the anode.

26.2.2 Characteristics of the PVC Gel Actuator

This contraction type of PVC gel actuator moves in the air, and the contraction strain is 10–15 %, the response frequency is 3–7 Hz and the applied voltage 200–600 V. The weight of the unit structure is about 1–2 g when the diameter is 20–30 mm. The electric current reaches up to 0.03 mA. Examples of the displacement and the recovery force are shown in Figs. 26.3 and 26.4. The actuator sample has the unit configuration shown in Fig. 26.1, and the applied voltage is 240 V. The generating stress is proportional to the number of layers, and the stress is then about 10 kPa when the actuator height is 10 mm. The modulus of the longitudinal elasticity of the layered type of PVC gel actuator increases in proportion to the

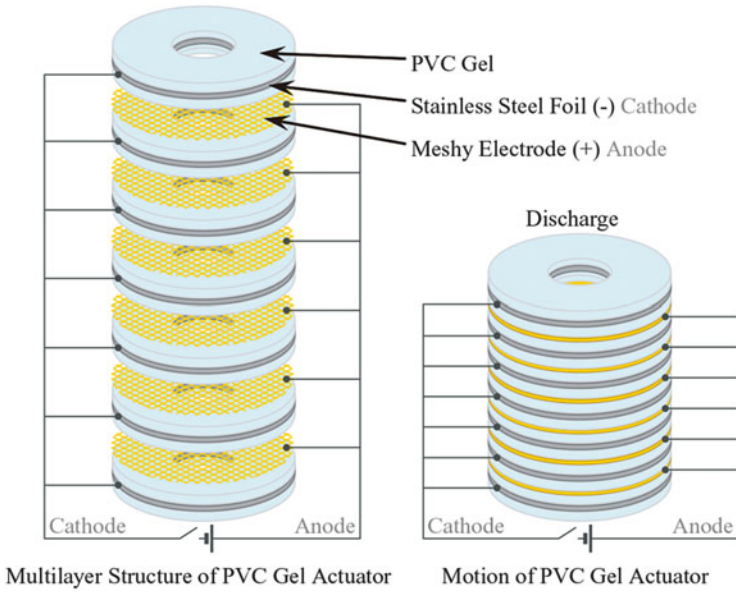


Fig. 26.2 Schematic drawing of the electrodes arrangement of the contraction type of PVC gel actuator

Fig. 26.3 Displacement of the actuator

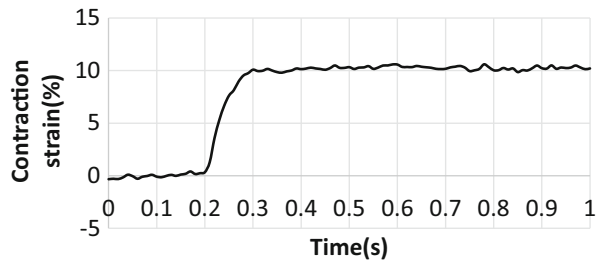
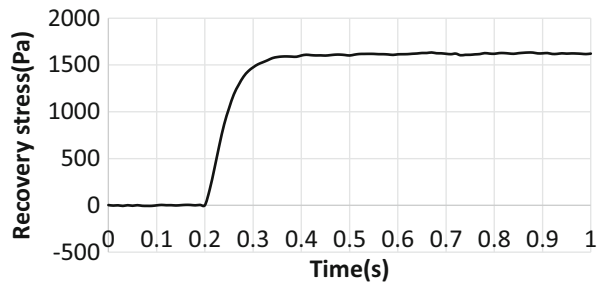


Fig. 26.4 Recovery stress of the actuator



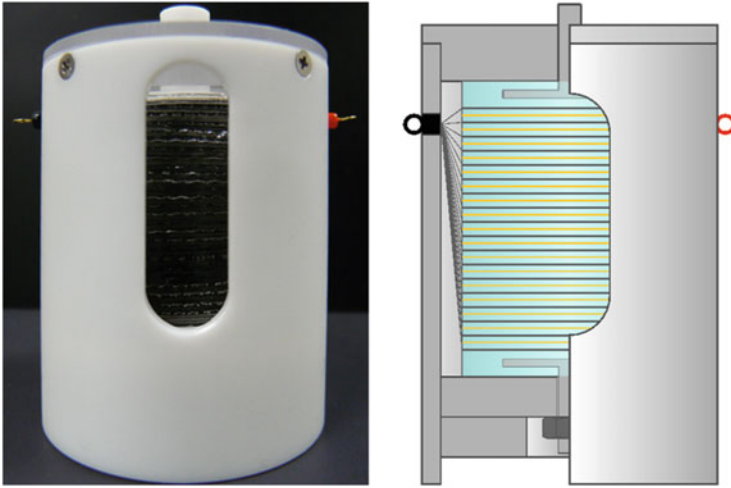


Fig. 26.5 Overview of the Multilayer-type PVC gel actuator

applied voltage as a human muscle. The stiffness when the larger voltage is applied is about ten times greater than that of the actuator without voltage. We deduced that this change of elasticity was caused by the increasing contact area between the mesh anodes and gels when the voltage was applied.

We believe the characteristics of the contraction type PVC actuators are unique. The proposed actuator will form the genesis of next-generation actuators, smart actuators and artificial muscles. The contraction type of PVC gel actuator can operate in air, and has the characteristics of flexibility, lightness and silence, so various applications are possible. Similar applications have been performed such as linear actuators, small size brakes [9] and an wearing assist garments with variable stiffness [10].

Figure 26.5 shows the overview of the contraction type PVC gel actuator as an example. The actuator has a diameter of 30 mm and is 38 mm high. The weight without the case is 41 g, and the number of stacking layers is 28. The contraction strain is 10 % and the output force is about 11 N when the applied voltage is 600 V. The electronic current is about 1 mA and its power consumption is 0.6 W.

There have been many studies in the field of artificial muscles. We list the general characteristics of the various artificial muscles compared with those of human muscles in Table 26.1. The PVC gel has good performances in contraction strain and response rate. The conductive polymer [6] has good properties for contraction strain and output force, but not for the response rate. The dielectric elastomer [2] has notable properties in response rate and output force, however it is necessary to apply a very high dc field to operate. Therefore, the proposed PVC gel is unique in its characteristics compared with the other artificial muscles. We believe that the unique characteristics of the proposed actuator may lead to it being used in many applications such as a micro pumps and micro valves.

Table 26.1 Characteristics of soft actuators comparing with human muscle

	Contraction	Force	Response	DC field
Conducting polymer	+	+	–	1 V/mm
Dielectric elastomer	–	+	++	100 V/ μ m
PVC gel	+	–	+	1 V/ μ m

26.3 Modeling and Motion Control

26.3.1 Modeling of the PVC Gel Actuator

We derive a mathematical model of the electrical and dynamic characteristics of a PVC gel actuator to enable us to apply it as a control element. The dynamic property of the PVC gel actuator is expressed by Σ . The input signal is the electric field E , and output signals are the stress F_{ext} and the displacement X .

This system can be divided into three components: the electrical component Σ_E , the electrical–mechanical energy conversion component Σ_{E-M} , and the mechanical component Σ_M as shown in Fig. 26.6. When the DC field E is applied, an electric current I is generated from Σ_E and the contraction stress F is generated by the input I . Finally the displacement x is created by Σ_M with the input F_{ext} . To determine the model for the complete characteristics of the PVC gel actuator, we derive a model for each component.

26.3.1.1 Modeling by the Electric Impedance Measurement

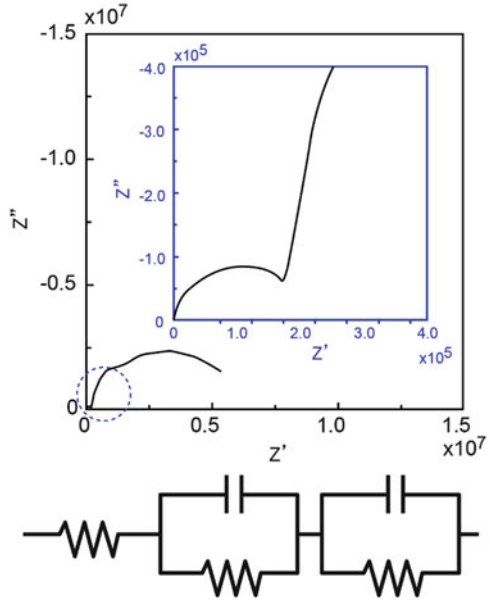
First, we estimated the electrical equivalent circuit for the component Σ_E using an electric impedance method. This impedance method characterizes the internal electrical state of the system using an AC voltage. DC and AC voltages were applied to the PVC gel actuator. The PVC gel actuator contracted when the DC voltage was applied. The AC voltage was used to measure the electrical impedance for various voltages. The frequency of the AC voltage was swept. The impedances for the various frequencies were plotted on a complex plane. The graph of the impedance plotted on the complex plane is called a Cole–Cole plot. We can estimate the equivalent circuit from the shape of the Cole–Cole plot. Thus, using this approach, the equivalent circuit model can be derived even if the object has complicated configurations.

We measured the impedance of the PVC gel actuator (DBA40, ten layers) applying a DC field of 200 V/mm. The AC voltage to measure the impedance was 3 V, the frequency was swept from 100 Hz to 1 kHz. Figure 26.7 shows the Cole–Cole plots for the PVC gel actuator. There were two arcs in the Cole–Cole plot. This means that the electrical equivalent circuit of a PVC gel actuator has two parallel circuits constructed with a resistance and a capacitor. However, in modeling the mechanical properties of the PVC gel actuator, the influence of the high

Fig. 26.6 Block diagram of PVC gel actuator using the three components



Fig. 26.7 Impedance spectrums



frequency region can be ignored because the response rate of the PVC gel actuator is under the 10 Hz. We then employed a single parallel circuit model. In addition, the distance between the origin of the complex plane and the impedance on the real axis corresponds to a series resistance. Combining these two models, we estimated an equivalent circuit as shown in Fig. 26.8.

Based on the equivalent circuit shown in Fig. 26.8, we estimate the transfer function Σ_E where the input is the electric field $E(s)$, the output is the electric current $I(s)$. The transfer function that we obtained is written as Eq. (26.1). R_1 is the resistance in a series and i is the current in the series circuit. In the parallel circuit, C is the capacitance of the capacitor, and R_2 is the resistance of the parallel resistor.

$$\frac{I(s)}{E(s)} = \frac{R_2Cs + 1}{R_1R_2Cs + R_1 + R_2} \tag{26.1}$$

The step response was simulated using the transfer function written by Eq. (26.1) (Fig. 26.9). Initially the capacitor stores the electric charge, and if the charge is then stored completely in the capacitor, the slope of the curve then becomes flat.

Fig. 26.8 Equivalent circuit of the PVC gel

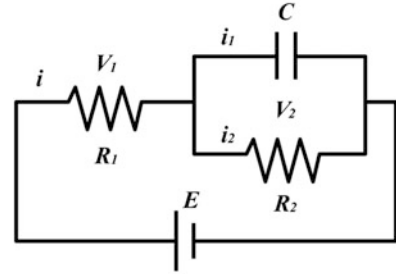
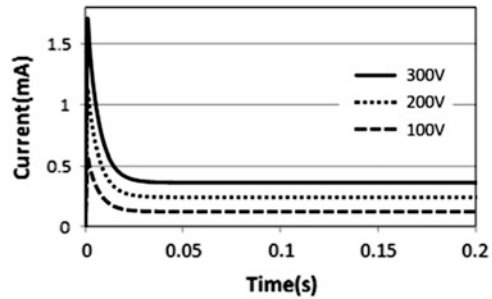


Fig. 26.9 Simulated results for the electric current i using Eq. (26.1)



26.3.2 Relationship Between the Current and Contraction Stress

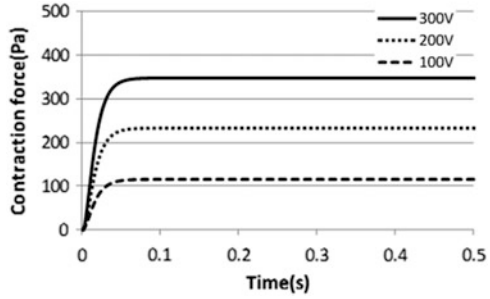
The relationship between the electric current and contraction stress was investigated to determine the transfer function of the electrical–mechanical energy conversion component Σ_{E-M} . The contraction stress and the electric current were measured when the various DC voltages were applied. The contraction stress was almost a linear function of the electric current. We assume that only the electric current i_2 shown in Fig. 26.8 contributes to the contraction stress. The electric current i_2 is the electric current running through the parallel resistor R_2 . The electric current i_2 is given by Eq. (26.2). The dynamic response of the contraction stress is expressed as a first order lag component. The relationship between contraction stress f and the electric current i_2 is given by Eq. (26.3).

$$I(s) = \frac{R_2Cs + 1}{R_1R_2Cs + R_1 + R_2}E(s) \tag{26.2}$$

$$F(s) = \frac{\alpha}{T_\alpha s + 1}I_2(s) \tag{26.3}$$

We performed a simulation of the step response of the contraction stress based on Eqs. (26.2) and (26.3). The simulated results for the contraction stress are shown in Fig. 26.10. The simulated results agree with the experimental results.

Fig. 26.10 Simulated results for the contraction stress f using Eqs. (26.2) and (26.3)



26.3.3 Relationship Between the Contraction Stress and Strain

In this subsection, we determine the relationship between the contraction stress and strain to establish a model for the mechanical component Σ_M . We measured the contraction displacement and contraction stress of the PVC gel actuator applying various DC fields. The contraction stress changed as a linear function of the contraction strain without any time delay [11]. Therefore, we can create a model of the transfer function as written by Eq. (26.4).

$$F(s) = \beta X(s) \tag{26.4}$$

26.3.3.1 Modeling the Whole System of the PVC Gel Actuator

To establish the model for the whole system of the PVC gel actuator, we combined the models for the three components.

The contraction stress f is determined by the contraction strain x of the PVC gel actuator and the external stress f_{ext} . The contraction stress is determined by the contraction strain and external stress as shown in Eq. (26.5). By substituting Eqs. (26.2), (26.3) and (26.4) into Eq. (26.5), we obtain Eq. (26.6), which is a model of the whole PVC gel actuator. If there is no external stress, the contraction strain $X(s)$ occurs as a result of the applied voltage $E(s)$. If the displacement of the PVC gel actuator is constrained from the environment, the output stress $F_{ext}(s)$ is generated according to Eq. (26.6).

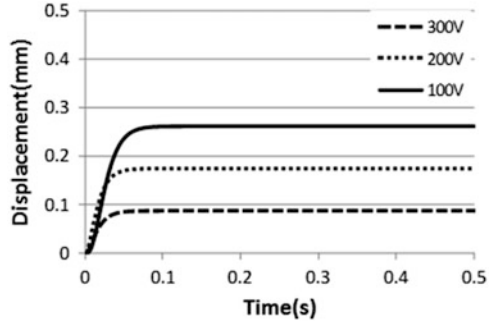
We simulated the contraction strain using Eq. (26.6) with the same conditions as those of the experiment. The simulated results are shown in Fig. 26.11. The simulated results agree with the experimental results.

$$F(s) = \beta X(s) + F_{ext}(s) \tag{26.5}$$

$$\frac{\alpha}{T_\alpha s + 1} \cdot \frac{1}{R_1 R_2 C s + R_1 + R_2} E(s) = \beta X(s) + F_{ext}(s) \tag{26.6}$$

A detailed description of the modeling of the PVC gel actuator can be found in reference [11].

Fig. 26.11 Simulated results for the contraction strain



26.3.4 Control of the PVC Gel Actuator

We design a control law for the PVC gel actuator using the mathematical model derived previously.

26.3.4.1 Control Law

Since PVC gel has an elastic characteristic, we introduce a feed forward term which is described by Eq. (26.7):

$$E_d = x_d / \gamma \quad (26.7)$$

where, x_d is the desired displacement, γ is the inclination of the approximate linear relationship. The whole control law is then written by Eq. (26.8):

$$E = k_p(x_d - x) + k_d(\dot{x}_d - \dot{x}) + E_d \quad (26.8)$$

where, E is the input voltage to the PVC gel and k_p , k_d are the proportional and derivative gains.

26.3.4.2 Determination of Gains

The values of the proportional and derivative gains are determined using the mathematical model for the PVC gel actuator, Eq. (26.6). Figure 26.12a, b show the simulated results for the feedback control using various values for the gains, k_p , k_d . Based on the results, we determined the values of gains as, $k_p = 300$, $k_d = 0.5$.

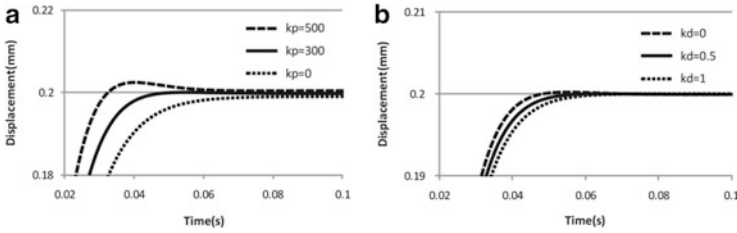
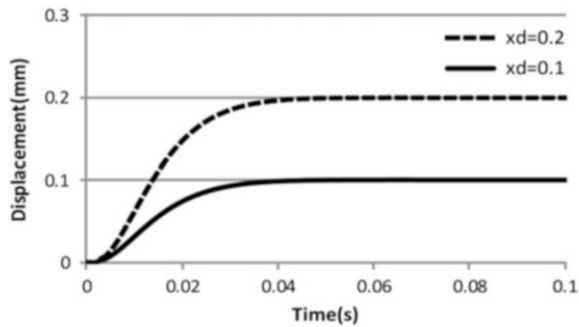


Fig. 26.12 Response with the various gains. (a) Proportional gains. (b) Derivative gains

Fig. 26.13 Simulated results for the feedback control



26.3.4.3 Feedback Control

We applied the control law described above to the PVC gel actuator. The simulations for the feedback control were performed (Fig. 26.13). The desired displacements were 0.1 and 0.2 mm. The results converged to the desired values.

We performed similar experiments to investigate the performance of the proposed control method. A laser displacement sensor was used to measure the displacement of the PVC gel actuator. DC voltages were applied to the PVC gel actuator by a linear amplifier according to a command signal, which was determined in a PC. The PC computed the command signal using Eq. (26.6) and outputted it to a digital-to-analog converter. The overview of the experimental setup is shown in Fig. 26.14. We used an eight-layered structure for the PVC gel actuator whose diameter was 50 mm and thickness of PVC gel was 1 mm.

The experimental results for the position feedback control are shown in Figs. 26.15 and 26.16. The desired trajectory was a sinusoidal curve whose frequency was 1 Hz and amplitude 0.4 mm. The experimental results for the closed and open loop control are shown in Fig. 26.15. The results for the closed loop control show that the control error was very small, while the open loop control error was very large. Figure 26.16 shows the gain diagrams for the closed and open loop control. Using the proposed control, the bandwidth of the frequency response increased. The bandwidth for the closed loop control was about 10 Hz, while that for the open loop was 3 Hz.

Fig. 26.14 Experimental setup for the feedback control

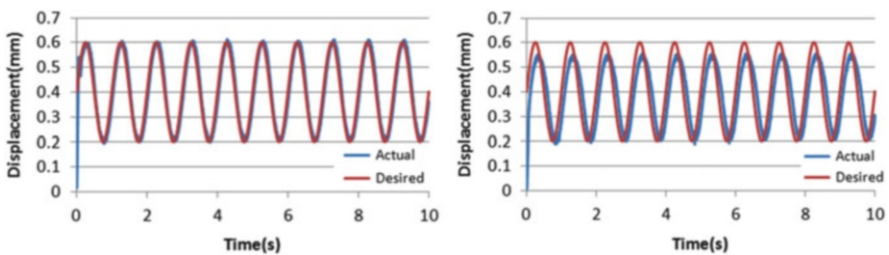
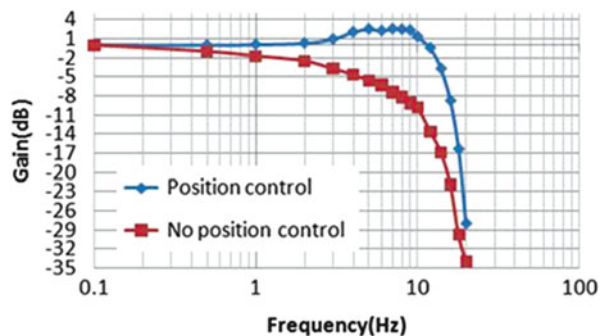


Fig. 26.15 Experimental results with and without feedback control. (a) Closed loop control. (b) Open loop control

Fig. 26.16 Gain diagram with and without the feedback control



26.4 Conclusions

We proposed a configuration for a contraction type of PVC gel actuator in which the PVC gel was sandwiched between an anode using a stainless mesh and a cathode using a stainless foil. The mesh type anode drew the PVC gel into the mesh hole

when the dc field was applied, and the actuator then contracted. We measured the characteristics of the actuator and showed that the PVC gel actuator displayed good performance such as a good response rate, large displacement, and being light in weight. The contraction strain was 14 %, the output stress was 4 kPa and the response rate was 7 Hz.

We investigated a model for a Contraction type PVC gel actuator. First, Cole–Cole plots were measured by an impedance meter to obtain the equivalent circuit of the electrical characteristics. Second, the relationship between the electric current and contraction stress was obtained experimentally to determine the conversion model from electrical energy into mechanical energy, and the mechanical deformation model of the PVC gel actuator was obtained. The mathematical model for the whole of the PVC gel actuator was derived by combining the models of the three components. Finally, we proposed a control method based on the proposed model. The control law included a feed forward term to compensate for the elastic characteristic of the PVC gel actuator. The control method had good performance. The response rate was increased by the feedback control, and the hysteresis of the PVC gel actuator was removed.

For future work, we will investigate a nonlinear model and the control method. The PVC gel actuator can be operated in air, and has the characteristics of flexibility and lightness, so various applications are possible.

Acknowledgments This research was supported by Nagano and the farmland region intellectual cluster creation business (Second period). Prof. Toshihiro Hirai of Shinshu University provided critical advice on this research. We are grateful to them for their support.

References

1. Kaneto K (2006) Macromolecule actuator. *Polymer* 55(12):956
2. Carpi F, Rossi DD, Kornbluh R, Pelrine R, Sommer-Larsen P (2008) Dielectric elastomers as electromechanical transducers. Elsevier, Amsterdam
3. Hara S, Zama T, Tkashima W, Kaneto K (2005) Free-standing gel-like polypyrrole actuators doped with bis (perfluoroalkylsulfonyl) imide exhibiting extremely large strain. *Smart Mater Struct* 14:1501–1510
4. Uddin Md Z, Watanabe M, Shirai H, Hirai T (2002) Creeping and novel huge bending of plasticized PVC. *J Robot Mechatr* 14(2):161–166
5. Watanabe M, Wakimoto N, Shirai N, Hirai T (2003) Bending electrostriction and space-charge distribution in polyurethane films. *J Appl Phys* 94(4):2494–2497
6. Sansinena J-M, Olazabal V (2004) In: Bar-Cohen Y (ed) Conductive polymers, electroactive polymer [EAP] actuators as artificial muscles. SPIE, Washington, pp 231–259
7. Ogawa N, Hashimoto M, Takasaki M, Hirai T (2009) Characteristics evaluation of PVC gel actuators. In: The 2009 IEEE/RSJ international conference on intelligent robots and systems (IROS2009) St. Louis, USA, pp 2898–2903
8. Yamano M, Ogawa N, Hashimoto M, Takasaki M, Hirai T (2009) A contraction type soft actuator using poly vinyl chloride gel. In: Proceedings of the IEEE international conference on robotics and biomimetics (ROBIO 2008), Bangkok, Thailand, pp 745–750

9. Shibagaki M, Matsuki T, Hashimoto M (2010) Application of a contraction type PVC gel actuator to brakes. In: Proceedings of the 2010 IEEE. international conference on mechatronics and automation, Xi'an, China, August 4–7, pp 39–44
10. Maeda Y, Li Yi, Yasuda K, Hashimoto M (2013) Development of a variable stiffness gel spats for walking assistance. In: The 2013 IEEE/RSJ international conference on intelligent robots and systems (IROS2013), November 3–8, Tokyo, Japan, 2013
11. Shibagaki M, Ogawa N, Hashimoto M (2010) Modeling of a contraction type PVC gel actuator. In: Proceedings of the 2010 IEEE. international conference on robotics and biometrics, December 14–16, Tianjin, China, pp 1434–1439

Part VII

Applications

Chapter 27

Application of Nano-Carbon Actuator to Braille Display

Isao Takahashi, Tomomasa Takatsuka, and Munemitsu Abe

Abstract Ionic electro-active polymer(EAP) actuators based on nano-carbon electrodes, which are comprised of materials such as carbon nano-tubes, ionic liquid and polymer are characterized by their thin, light and low-voltage properties. Alps had developed an ultra-thin and ultra-light Braille display for vision-impaired people utilizing this technology, in collaboration with AIST, Tokyo Univ., and Keio Univ. from fiscal 2009 to 2010, with the support of Ministry of Health, Labor and Welfare (MLHW), Japan.. In addition, for the purpose of improving the readability of display on the part of vision-impaired people who lost vision later in life, or those with finger paralysis, we developed a Braille display with a latching mechanism to move Braille dots.

Keywords Braille display • Carbon nano-tube • Electro-active polymer • Ionic liquid • Nano carbon • Polymer actuator

27.1 Introduction

Braille is a read and write mechanism for vision-impaired people by touching raised dots with fingers. Braille display allows Braille dots to be refreshed within limited number of cells to show various characters on the display. Vision-impaired people tend to have more difficulties in recent years with the prevailing introduction of liquid-crystal displays for touch panels. Hence, practical application of easy-to-equip, ultra-thin and ultra-light Braille display for regular uses in household electrical appliances has been much sought for. From fiscal 2009 to 2010, together with teams at AIST (National Institute of Advanced Industrial Science and Technology), Tokyo Univ. and Keio Univ., our development team had participated in a MLHW project to develop ultra-thin, ultra-light Braille display for vision-impaired people by using ionic EAP actuators with nano-carbon electrodes, which have thin, light and low-voltage properties. General summary of development is described in this chapter.

I. Takahashi (✉) • T. Takatsuka • M. Abe
Group 1, Material Engineering Department, Sendai R&D Center, Engineering Headquarters,
ALPS Electric Co., Ltd, Sendai, Miyagi 981-3280, Japan
e-mail: isao.takahashi@jp.alps.com

27.2 Ionic Electro-Active Polymer (EAP) Actuators Based on Nano-Carbon Electrodes

Ionic electro-active polymer (EAP) actuator with nano-carbon electrodes is an actuator developed by Fukushima and Asaka et al. [1], which bends when voltage is applied. As shown in Fig. 27.1 [2], this actuator has a configuration composed of an ionic-gel electrolyte layer sandwiched by nano-carbon dispersed ionic-liquid gel electrode layers. When small voltage is applied to the tips of electrode, volume of both electrode layers change as ions move from a negative to positive side, and cause the actuator to bend (Fig. 27.2) [2]. The mechanism of motion is the compound force of ionic intercalation, expansion and contraction of nano-carbon material and electrostatic force, etc. This actuator is expected to be one of the leading next-generation actuators, as it has properties such as thin, light and low-voltage and provide large displacement.

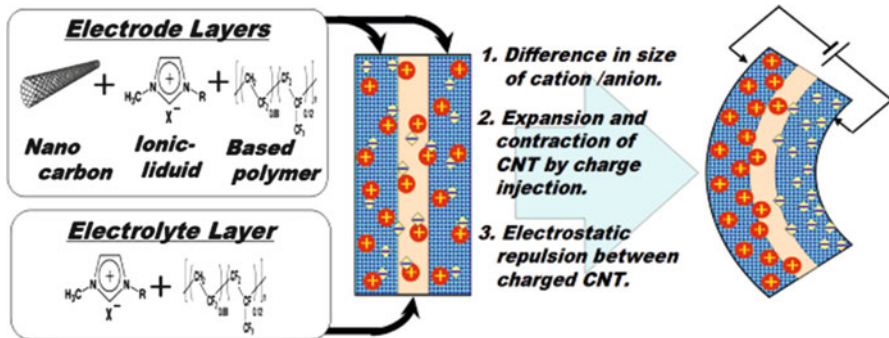


Fig. 27.1 Structure and motion mechanism of actuator

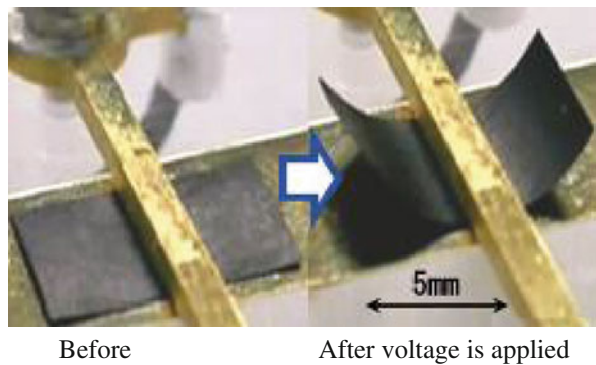


Fig. 27.2 Photograph of bending displacement

27.3 Goal of Braille Display Development

Our development concept is to develop a “thin and light Braille display which is usable by vision-impaired people” with the use of properties of nano-carbon EAP actuators. This concept was decided after discussing it with AIST, Tokyo Univ. and Keio Univ. teams.

27.3.1 *Specification of Braille Dots*

From the knowledge provided from Keio Univ. team, we selected the target specifications of Braille dots to be 0.3 mm or more height with 3 gf or more load with the shape of Braille dot illustrated in Fig. 27.3 [3].

27.3.2 *Specifications of Braille Size*

Initially, we considered our target to match Japanese or Perkins Braille specifications shown in Table 27.1 [3]. However, at an early stage of examination, we realized that it is significantly difficult to achieve those target Braille display specifications with the current actuator capacity. In consideration the Braille specifications in the world, we tried to identify the Braille size suitable to realize the target Braille dot height and load in a thin Braille display. As a result, we set an original Braille display size as our target.

27.4 Development of Direct Drive Type of Braille Display [4]

In order to develop a thinner Braille display, the structure is required to directly use bending displacement of actuator to move Braille dots. We came up with the new actuator wiring and layout and developed a 6 character display with an external driver and a 24 character display in a mobile phone mock-up.

27.4.1 *Layout and Shape of Actuators*

Figure 27.4 [4] shows the structure of the direct drive type of a Braille dot display. In this structure, actuators are placed on a flat base, but in consideration of a wide variety of actuator properties, all actuators may better be identical in shape for every dot. Thus, we need to figure out a right structure including a layout plan.

Fig. 27.3 Ideal shape of Braille dot (side view)

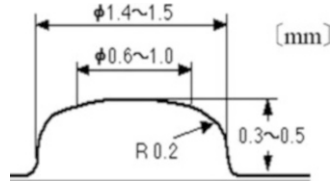


Table 27.1 Specifications of Braille size

	Braille size	Spec. type (mm)			
		Japan	Perkins	Giant	Original
	a: 1-4 Horizontal dot to dot	2.13	2.13	3.1	3.0
	b: 1-2 Vertical dot to dot	2.37	2.37	3.1	3.0
	c: 4-1 Cell to Cell	3.27	3.27	6.7	4.5
	d: 3-1 Line to line	9.17	9.17	6.2	—

After due consideration of the issues, we selected a structure where we cut the tips of actuators and place them in a slanting direction as shown in Fig. 27.5 [4]. By cutting the tips, we were able to gain 10 % more actuator width, which improved generated force by 10 %.

27.4.2 Support and Wiring of Actuators

In order to improve the assembly efficiency including the case for parts changes, wiring of flatly placed actuators is made to be a structure of paired FPC for both the upper and lower sides of actuator electrodes (Fig. 27.6 [4]).

Also, to support and fix actuators, we took a measure to sandwich wiring FPC with the upper and lower sides of Braille display. Those support points integrated

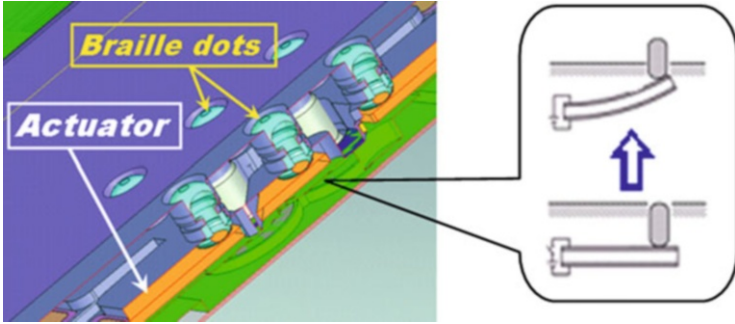


Fig. 27.4 Braille display structure and its motion

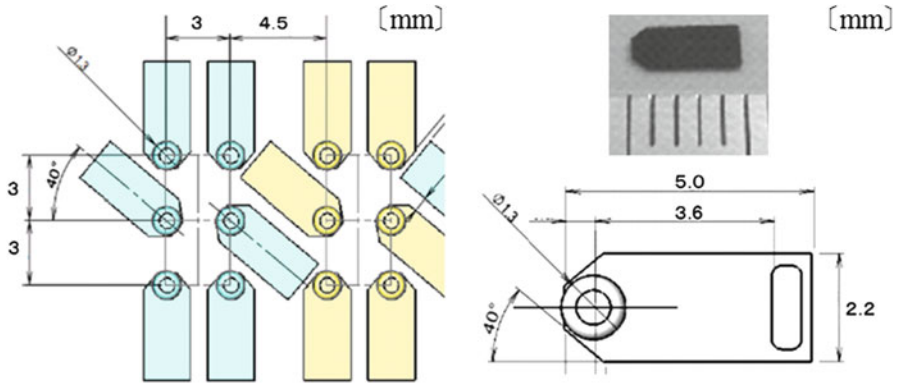


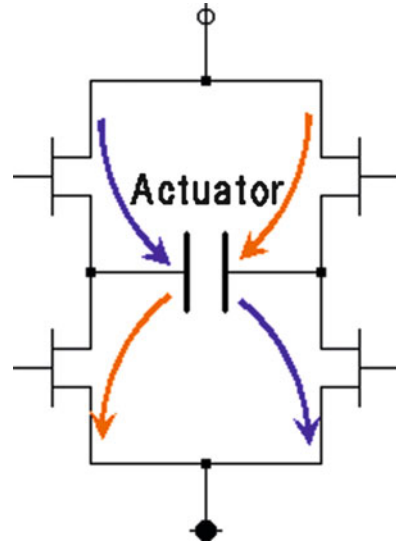
Fig. 27.5 Layout and shape of actuators



Fig. 27.6 FPC for wiring and wired actuators

into the main case with elasticity so that multiple actuators are supported with the same amount of pressure and achieve stable support and flow of electricity. FPC electrode terminals which feed electricity to actuators have a copper foil base covered with gold plating. On top of that, carbon polymer material is applied to improve the contact stability and anti-corrosiveness.

Fig. 27.7 H bridge circuit



27.4.3 Actuator Drive Circuit

Braille display functionally requires displacement (passage of electric current) to one direction only. Electric current to only one direction, however, causes distortion of materials or residual electric charge, which leads to the phenomenon such as changes to a default position when the power is off and longer time to return to the original position after displaced. An effective countermeasure to overcome these issues is to apply voltage to the opposite direction for a certain period of time when a dot is to be returned to the original position after raised or after back to the original position. Thus, we need to have both positive and negative power supply. As a result of examination, we introduced H bridge circuit, which easily enables a voltage to be applied in either direction (Fig. 27.7). This circuit type requires more distributing wires as it doesn't allow multiple actuators to share wires. Nevertheless, we selected H bridge as IC for motors with multiple circuits is readily available in the market and it is also easily adjustable (Fig. 27.8).

27.4.4 Braille Display Controller

We developed a Braille display controller which controls through an actuator drive by integrating the system in a notebook PC for the maintenance purpose. As shown in Fig. 27.9 [4], by keying in the text, the text is translated into Braille and appears on a Braille display. This controller has the following three modes: (1) direct key in mode which shows six characters in Braille (section a) in the operation display), (2) demo mode which sequentially shows Braille of 24 characters (6×4) repeatedly

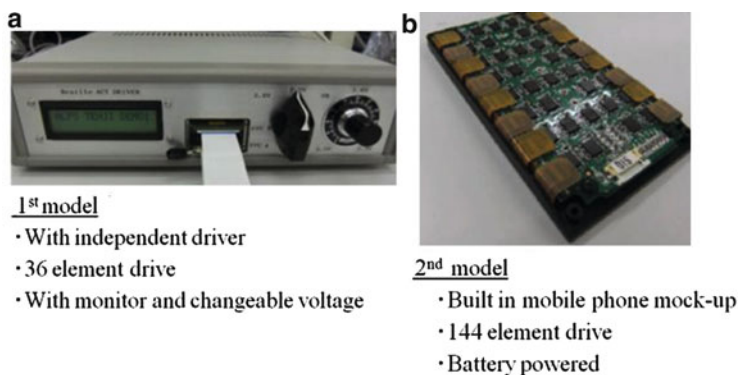


Fig. 27.8 Photograph of prototype driver [4]

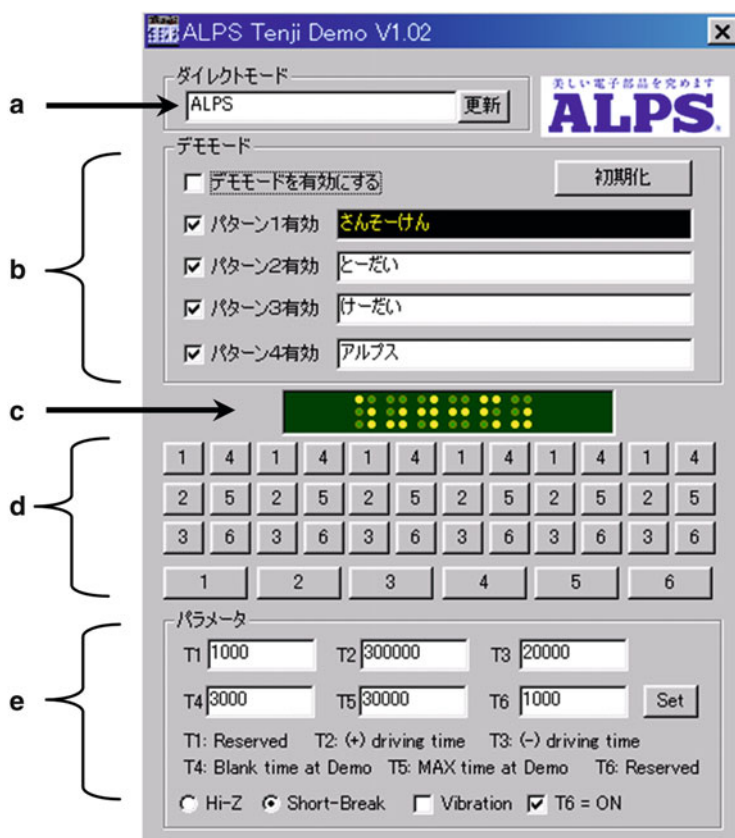
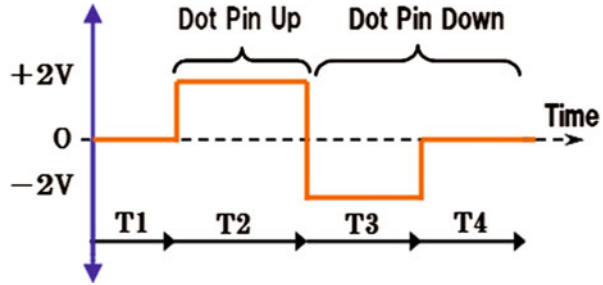


Fig. 27.9 Controller screeny

Fig. 27.10 Timing to introduce electric current to actuators



(section b) and (3) test mode which controls each Braille dots independently (section d). As for the control of electrified actuators, Fig. 27.10 [4] shows that timing to introduce electric current to actuators is to be set in the section e of the controller. This controller has been renewed its version several times as our display development progresses to have functions such as simultaneous display of 24 Braille characters and application of latching mechanism up to 12 characters.



27.4.5 *Direct Drive Type of Braille Display*

Table 27.2 [4] shows the developed prototype. We achieved our goal by creating a Braille display with six characters in a 3 mm-thick case. We consider this display can be less than 2 mm thickness when the case is simplified to integrate into equipment. Readability was found favorable from vision-impaired people who joined the evaluation test, but those who became vision-impaired later in life and not so familiar with reading in Braille found the readability deteriorated. Furthermore we found a new issue as we were requested to make the Braille size miniaturized to match the Perkins standard from the perspective of reading speed.

27.5 **Development of Braille Display with Latching Mechanism [5]**

The direct drive type of Braille display which moves Braille dots directly by nano-carbon EAP actuator showed enough readability to those who are born vision-impaired and used to reading Braille. However, for those who became vision-impaired later in life or people with paralyzed fingers as a result of suffering from diseases (such as diabetes) found this type less readable because of not enough Braille dot resiliencies. Then in order to make this display readable for more people, we improved the generated force of actuators itself in addition to adopting a latching mechanism to a Braille display.

Table 27.2 Prototype

Photograph of prototype	Specifications
	<ul style="list-style-type: none"> • Size: L30*W65*D3 mm • Dot to dot: 3.0 mm/Cell to cell: 4.5 mm • Dot height: 0.35–0.40 mm • Dot force: 4–5 gf
	<ul style="list-style-type: none"> • Size: L110*W55 *D24.5 mm (When folded) • Dot to dot: 3.0 mm/Cell to cell: 4.5 mm • Dot Height: 0.30–0.35 mm • Dot force: 3–4gf • Driver/controller built-in • Battery run

27.5.1 Policy of Developing Latching Mechanism

1. Latching move of a dot is handled by an actuator.
2. When a latch is in a static mode, actuator doesn't consume electricity.
3. The case thickness stays at around 5 mm even with the latching mechanism.
4. In addition to the original Braille size, this mechanism support the Perkins specifications as well.
5. A latch doesn't come off even when a Braille dot is pressed hard (100 gf or more)

27.5.2 Study and Decision on the Latching Mechanism

In line with the policies described above, we examined various types of latching mechanism and narrowed down the selection to the following four types shown in Table 27.3 [5]. Eventually, we selected Type C, which is light and also applicable to the Perkins specifications as shown in Table 27.4 [5] As shown in Fig. 27.11 [5], this Type C latching mechanism rotates a cam by using a horizontally placed actuator.

Figure 27.12 [5] shows inside of a Braille display with the type C latching mechanism. We structured the display to facilitate assembly and parts change by wiring and connecting actuators with FPC, which is the same method used for the direct drive type.

The size of actuator is L5.5*W1.6*D0.20 mm in Perkins specifications and L7.0*W2.0*D0.25 mm in the original specifications.

Table 27.3 Examination of latching mechanism options




	Type A	Type B	Type C	Type D
Means	Push-back 	Slide-Cam 	Rotary-Cam 	
Actuator placement	Horizontal	Side	Horizontal	Vertical
Direction of displacement	Two states U/D	Left/Right	Up/Down	Left/Right
Thickness of case	6–8 mm	4.5–5.5 mm	4.5–5.5 mm	11–13 mm

Table 27.4 Application to various Braille specifications

Braille spec.	A	B	C	D
Japan	×	×	×	△
Perkins	×	×	△	△
Original	○	○	○	○
Giant dots	○	○	○	○

Fig. 27.11 Latching mechanism with rotating cam

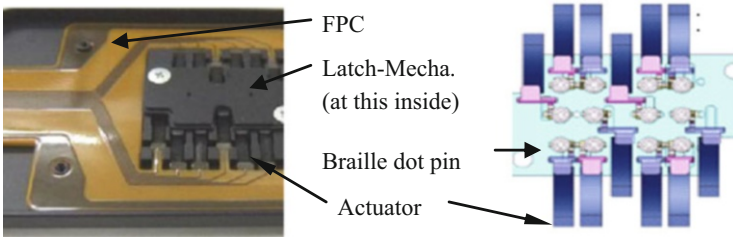
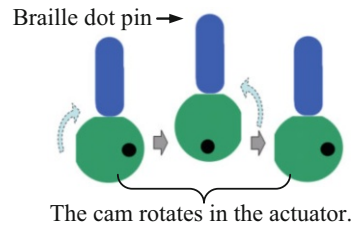






Fig. 27.12 Inside Braille display with latching mechanism

27.5.3 Braille Display with Latching Mechanism

The developed prototype is shown in Table 27.5 [5]. The case size is designed large enough to stabilize test uses by vision-impaired people. The structure can be reduced to 2/3 or less both horizontally and vertically. As we expected, the test

Table 27.5 Prototype

Appearance of prototype	Specifications
	<ul style="list-style-type: none"> • Size: L37*L67*D5 mm • Distance between dots: 3.0 mm/between cells: 4.5 mm • Dot height: 0.32 mm • Force generated: 100 gf and more (1 kgf and more in practice)
	<ul style="list-style-type: none"> • Size: L35*L62*D5 mm • Distance between dots: 2.3 mm/between cells: 4.2 mm • Dot height: 0.32 mm • Force generated: 100 gf and more (1 kgf and more in practice)
	<ul style="list-style-type: none"> • Size: L51*L150*D5 mm • Distance between dots: 3.0 mm/between cells: 4.5 mm • Dot height: 0.32 mm • Force generated: 100 gf and more (1 kgf and more in practice) • # of character: 12 (72 dots)
	<ul style="list-style-type: none"> Braille display driver/controller (without upper case) • Applicable to latch motion • Battery run/AC run

results showed better readability compared to the direct drive type. For Japanese texts, Perkins specifications showed a better readability result because it is closer to the Japanese specifications compared to our original one. We suppose Western texts that use a bigger Braille size may show different results.

27.6 Latest Status on Actuator Development [42]

Our actuator development team is working together with the counterpart team at AIST to realize practical applications of nano-carbon EAP actuator. Fiscal 2011 and onwards, improvements were seen in durability when continuously operated and in the displacement retention property when directly electrified in one direction. In fiscal 2013, they succeeded in achieving durability of more than 150,000 times with the displacement retention to last more than 3 h in a non-sealed environment by finding the best composition of high purity nano-carbon materials

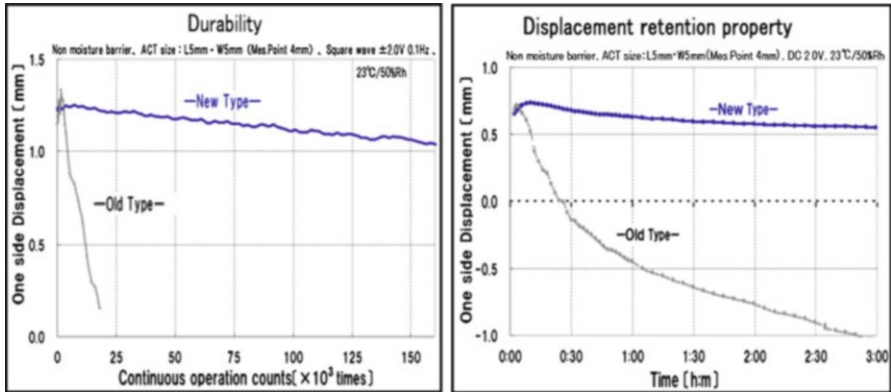


Fig. 27.13 Displacement retention property and durability of repeated operation (in not-sealed environment)

(Super-Growth CNT) [6] and electrode materials such as reformed carbon nanofibers and developing and improving their dispersion, stirring and film forming methods (Fig. 27.13 [2]). We conclude that these results accelerated the practical applications of Braille display using nano-carbon EAP actuators.

27.7 Ethical and Safety Issues in Test Environment

Development of Braille display requires prototype tests with the help of many vision-impaired people. In testing situation, a subject (vision-impaired person) must not feel uncomfortable or get injured as a result of the tests. Therefore, we must make sure to obtain informed consent beforehand, as well as to manage information properly. Furthermore, we must let “expert organizations” to review and check the ethical and safety conformance.

27.8 Conclusions

We have developed a 3 mm-thick direct drive Braille display and a 5 mm-thick Braille display with the latch mechanism which are readable to vision-impaired people by leveraging the features of nano-carbon EAP actuators.

This Braille display development project was successfully closed with the possibility of practical applications with some more issues to be solved. We believe the practical use of Braille display will come shortly with the actuator capacity improvement under further research and development. In the near future, we anticipate this type of Braille displays be integrated into various household electrical appliances and tablet PCs to solve daily inconveniences of vision-impaired

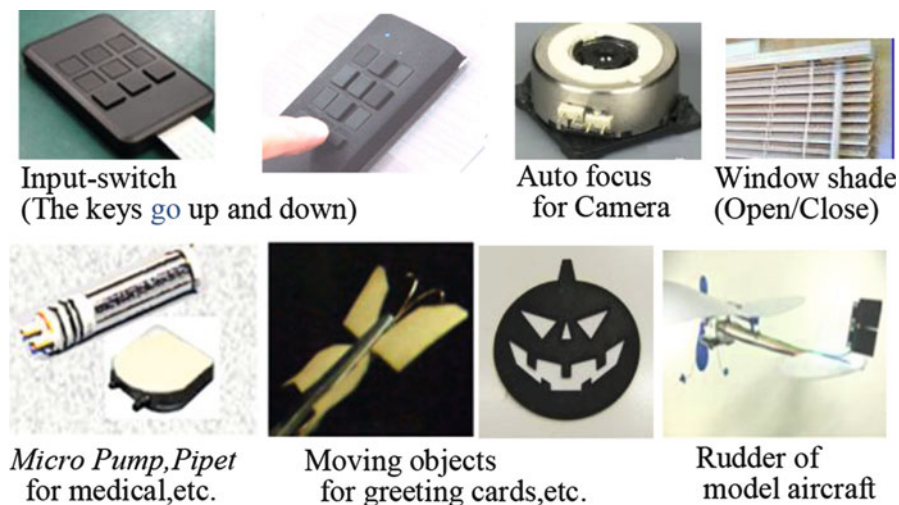


Fig. 27.14 Other examples of product application

people. legislative actions to enhance the absolute demand of Braille displays over the social infrastructures are sought for in order to help accelerate the materialization of the solution.

27.9 Other Examples of Actuator Application to Products

Lastly, we'd like to introduce some other examples of product applications of a nano-carbon EAP actuator. As actuator capacity and specifications required by various applications vary, we may raise the overall performance of actuators by promoting the development and verification of actuator capacity for various applications. Figure 27.14 [2] is the examples of product application other than a Braille display.

Acknowledgements The authors thank to Dr. Asaka K, Dr. Sugino T (Health Research Institute of AIST), Prof. Nakano Y, Assit.-Prof. Arai T (Keio Univ.), and Prof. Someya T, Dr. Sekitani T (Tokyo Univ.) for their collaborations in the Braille project (the grant from Ministry of Health, Labor and Welfare of Japan in 2009 FY and 2010 FY).

References

1. Fukushima T, Asaka K, Kosaka A, Aida T (2005) Layer-by-layer casting fabrication of soft actuator based on single-walled carbon nanotubes and ionic liquids. *Angew Chem Int Ed* 44:2410–2413

2. Takahashi I, Takatsuka T, Mitsumori K, Tokuchi N, Sugino T, Asaka K(2013) Research and development of nano-carbon based electroactive polymer actuators with high durability and response for practical applications. The 7th World Congress on Biomimetics, Artificial Muscles and Nano-Bio (BAMN 2013)
3. Mtohiro K, Tadayuki S, Hiroshi M, Yasushi N, Kouki C(1999) Development of Braille learning program for the adventitiously blind. Grants-in-aid for scientific research (Research Project Number: 07401007)
4. Abe M, Takahashi I, Asaka K, Sugino T, Someya T, Sekitani T, Nakano Y, Arai T(2009) Development of “Ultra-light and ultra-thin Braille device that can attach it also to mobile phone”. Final report in fiscal 2009 of MLHW project. http://www.mhlw.go.jp/bunya/shougaihoken/cyousajigyoyu/jiritsushien_project/seika/S04Report/Report_Mokuji04.htm
5. Abe M, Takahashi I, Tomomasa T, Asaka K, Sugino T, Someya T, Sekitani T, Fukuda K, Nakano T, Arai T, Oshima K (2010) Development of Ultra-thin Braille display for electronic Braille books (about B5 size). Final report in fiscal 2010 of MLHW project. http://www.mhlw.go.jp/bunya/shougaihoken/cyousajigyoyu/jiritsushienkiki/H22/S03/H22_seika-03.htm
6. Hata K, Futaba DN, Mizuno K, Namai T, Yumoto M, Iijima S (2004) Water-assisted highly efficient synthesis of impurity-free single-walled carbon nanotubes. *Science* 306:1362–1364

Chapter 28

Underwater Soft Robots

Kentaro Takagi, Zhi-Wei Luo, and Kinji Asaka

Abstract Two underwater soft robots using ionic polymer-metal composites (IPMCs), a ray-like robot and a quadruped robot, are introduced. For autonomous operation of the ray-like robot, miniaturized electrical devices are developed. A simple traveling wave input is employed to generate the motion of the fin. The propulsion speed of the robot is able to be controlled by the parameters of the traveling wave. In the experiment we observed that the amplitude of the fin increased toward the backward in spite of the uniform control input. This phenomenon may be the key to achieve the energy-efficient swimming of underwater robots by utilizing the elasticity of the actuator. The underwater quadruped robot is developed from a sheet of IPMC of which electrode is segmented into some parts to be controlled independently. We demonstrate the electro-discharge machining (EDM) method is useful to segment the electrode with the minimum damage to the polymer. In the experiment we found by accident that the deformation of the IPMC became gradually large by ion exchange with the copper electrode contact. Finally we show the gait of turtle is effective to control the developed quadruped robot.

Keywords Bio-mimetics • Ionic polymer-metal composite • Soft robotics • Underwater robot

K. Takagi (✉)

Department of Mechanical Science and Engineering, Graduate School of Engineering, Nagoya University, Furo-cho, Chikusa-ku, Nagoya 464-8603, Japan
e-mail: takagi@nuem.nagoya-u.ac.jp

Z.-W. Luo

Department of Computational Science, Graduate School of System Informatics, Kobe University, Nada-ku, Rokkodai-cho, Kobe 657-8501, Japan
e-mail: luo@gold.kobe-u.ac.jp

K. Asaka

Health Research Institute, National Institute of Advanced Industrial Science and Technology (AIST), Midorigaoka, Ikeda, Osaka 563-8577, Japan
e-mail: asaka-kinji@aist.go.jp

28.1 Introduction

Electro-active polymers (EAPs) are expected as soft actuators for robots that can mimic soft, smooth and various motions of living creatures. Ionic polymer-metal composite (IPMC), which is one of the EAPs, can be driven in water by applying low voltages around 2 or 3 volts [1, 2]. It is notable that IPMC is a very unique actuator because water is essential to work. An IPMC consists of an ion-exchange membrane of which surface is plated by thin rare metal layers. When voltage is applied across the electrodes, hydrated cations move toward the anode. The water movement causes the swelling of the ionic polymer at the anode side, therefore the bending moment is generated. Due to this working principle, IPMC actuators are suitable for underwater robots.

Bio-mimetic robotics or biologically inspired robotics are attractive research areas. A lot of studies of underwater robot have been reported. For example, Barrett et al. developed RoboTuna, that showed powerful and efficient propulsion [3]. Hirose et al. demonstrated the state of the art snake-like robot ACM-R5 [4, 5] at The 2005 World Exposition (EXPO 2005). They are both driven by geared motors, therefore their deformation shape are controlled to eliminate the force exerted by the environment. On the other hand, soft robots with muscle-like actuators can interact with environmental dynamics in contrast to the conventional robots with geared motors. In recent years, some underwater robots using soft actuators such as IPMCs have been reported. Nakabo et al. reported a snake-like robot using IPMC [6–8]. Yamakita et al. developed a three-link snake-like robot with IPMC joints [9]. Kim et al. developed TadRob, a small autonomous tadpole-like robot using IPMC [10]. Punning et al. developed a unique underwater robot like a ray fish [11]. Swimming style of rays or squids, called rajiform swimming (or rajiform locomotion) in which undulatory fin motions are used with pectoral fins [12, 13], has capability of various swimming such as forward, backward, rotational, upward and downward motions. As well as the swimming robots, some walking robots using IPMCs have been reported. For example, Yamakita et al. demonstrated a biped walking robot with linear muscle-like IPMCs [14]. Guo et al. developed an underwater multi-legged robot with a rigid plastic body and IPMC legs [15].

In this chapter, we introduce two underwater robots, an autonomous ray-like robot [16] and a quadruped robot with fully IPMC body [17]. In the first part of this chapter the autonomous ray-like swimming robot with two pectoral fins using IPMCs is shown. The advantage of the rajiform swimming is various motion, however, many control inputs are required for many IPMCs of the fins. In order to achieve the autonomous operation of the robot, we develop a small amplifier and employ a micro controller. The propulsion speed is measured under various control parameters to optimize them in the experiment. We observed a phenomenon that the deflection of the fin increased toward the backward although the amplitude of the input was spatially uniform. This phenomenon can also be observed in other robots [18, 19] whose bodies are elastic. Even in living creatures, undulatory motion with incremental wave can be observed [12, 13, 20]. Measuring the fin

amplitude, we confirm this phenomenon from the view point of interaction between elasticity of the actuator and fluid mechanics. In the latter part of this chapter, we show a small and light quadruped underwater walking robot fully made of IPMC. Utilizing the segmentation of the electrode, the IPMC robot achieves multi-degrees-of-freedom motion compared with the conventional IPMC walking robots. The segmented parts of the IPMC are driven via copper electrodes, by which unintended ion exchange occurs. The gait of the robot is designed to mimic a turtle of which gait is sufficiently slow. In the experiment, the gait of the robot is demonstrated and the walking speed is measured.

28.2 Autonomous Ray-Like Robot

28.2.1 Development of the Ray-Like Robot

28.2.1.1 Design of the Fin Using IPMC

IPMCs were fabricated from Nafion[®] N-117 membrane (DuPont) through five times gold plating process. The size of the each IPMC is 5 (mm) × 50 (mm). Thickness is about 200 (μm). The counter ion is exchanged to sodium ion aiming at the quick response of the actuators. Figure 28.1 shows the developed fin. It consists of eight IPMCs and a thin polyethylene film. Each IPMC is aligned at equal intervals and is clamped by the acrylic support with copper electrodes. The IPMCs are set into the slit of the film. The polyethylene film has sufficiently small thickness of about 12 (μm), therefore it does not inhibit the motion of the IPMCs. The entire size of the fin is about 75 (mm) × 45 (mm).

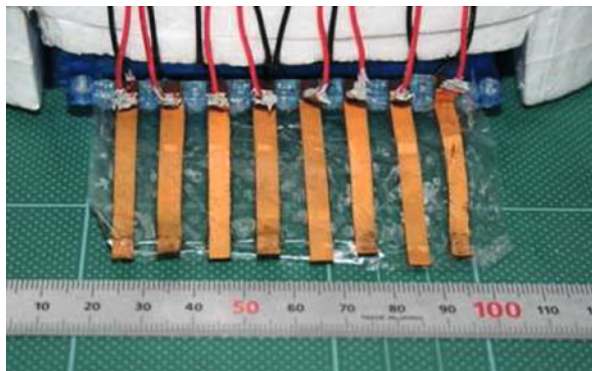


Fig. 28.1 Developed fin with eight IPMCs [16]

Fig. 28.2 Developed autonomous ray-like robot [16]



Table 28.1 Size of the ray-like robot

	Length (mm)	Width (mm)	Hight (mm)
Polystyrene float	180	100	55
Whole body of the robot	250	190	55

28.2.1.2 Electrical Devices for Autonomous Operation

Figure 28.2 shows the developed autonomous ray-like robot. The body is made of polystyrene foam that also acts as the float. The size of the robot is summarized in Table 28.1. A micro controller board named *C-CHIP* [16, 21], specially designed miniature linear amplifiers, a commercial DC/DC converter and a lithium-ion polymer battery are loaded onto the robot. The developed robot can swim without external control or power supply lines. The electrical devices and the body with the fins weigh about 200 (g) and 115 (g), respectively. The total weight of the robot is about 315 (g). The size of the robot is summarized in Table 28.1.

The sixteen IPMCs of the fins are independently driven by the miniature amplifier. The miniature amplifier has two channels on a printed-circuit board and has the output capability of ± 2.5 (V) and ± 500 (mA). The details of the developed electric devices are shown in [16].

28.2.2 Design of the Control Input

28.2.2.1 Traveling Wave of the Fin

The voltage applied to the IPMCs are designed as a prescribed waveform without feedback. In the previous studies on swimming robots [3, 6, 7], traveling wave input is commonly used. Note that there is a large difference between conventional swimming robots with geared motors and robots with soft actuators. The former ones usually control their deformation shapes, in contrast, the latter ones control

their actuation force. In other words, the robot with soft actuators has a flexible fin or/and body, therefore the deformation shape results from the interaction between the elasticity and the fluid mechanics. For example, the deformation of a snake-like robot using IPMC increases toward the tail while the applied voltages have uniformly same amplitudes [19]. This interesting phenomenon is observed in the experiment of the rajiform swimming robot, as will be shown in Sect. 28.2.3.2.

28.2.2.2 Design of the Voltage Input to the Actuators

Let M_{ai} be the generated bending moment of the i -th IPMC and v_i be the control voltage. The bending moment M_{ai} may be assumed to be proportional to the sinusoidal voltage at a frequency of around 1(Hz); $M_{ai}(t) \approx G_{M_{av_a}} \cdot v_i(t)$ where $G_{M_{av_a}}$ is a constant.

The designed voltage input is given as:

$$v_i(t) = v_0 \sin \left(2\pi f t - s_d \frac{2\pi n_w (i-1)}{N_a - 1} \right) \quad (i = 1, 2, \dots, N_a) \quad (28.1)$$

where v_0 , f , s_d , n_w and N_a denote the constant amplitude of the voltage, the frequency, the sign (± 1) of the direction, the body-length normalized wave number and the total number of the actuators, respectively. The body-length normalized wave number n_w is defined as: $n_w := L/\lambda$ where L is the length of the fin and λ is the wave length. n_w should hold

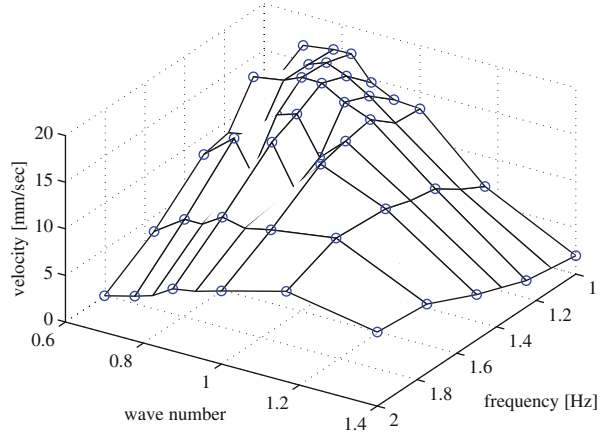
$$n_w < \frac{N_a - 1}{2} \quad (28.2)$$

in order to satisfy the sampling theorem because the actuators are aligned discretely. For the developed ray-like robot, n_w should hold $n_w < 3.5$.

28.2.3 Experiments

We carried out two experiments, the measurement of the swimming speed of the fin itself and the measurement of the deflection of each IPMC. The objective of the former experiment is to measure the swimming performance of the fin itself. The other reason is because the robot did not reach the steady speed due to the size of the robot compared with the size of the water tank. Just for reference, the average speed of the robot shown in Fig. 28.2 is about 8.0 ± 1.4 (mm/s) after swimming of 300(mm) with the initial speed of 0 (mm/s). The objective of the latter experiment is to observe the phenomenon that the amplitude of the fin increases from the head toward the tail.

Fig. 28.3 Propulsion velocity with respect to the control parameters [16]



28.2.3.1 Measurement of the Propulsion Speed

To measure the propulsion speed of the fin, we have developed a video capture system. A marker was attached to the fin to be detected by the developed real-time image processing system. The fin hanged by a light rod with a counter weight was put into a water tank. The control voltage to each IPMC of the fin was given by Eq. (28.1) with various values of $1.0(\text{Hz}) \leq f \leq 2.0(\text{Hz})$ and $0.70 \leq n_w \leq 1.40$. v_0 was set as 2.0 (V). The details of the experimental setup is shown in [16]. The tangential velocity of the trajectory data was estimated using numerical differentiation with twice moving average filtering whose window size was 20 points. The time averaged absolute value of the stationary state was used for the evaluation.

Figure 28.3 shows the result of the average propulsion velocity V with respect to several values of f and n_w . The optimal value of f and n_w , in the sense of maximizing the propulsion velocity, exists around $f = 1.25$ (Hz) and $n_w = 0.824$. The maximum value is 18.1 (mm/s). The wave velocity (phase velocity) V_p can be calculated as: $V_p = f\lambda = fL/n_w$. This ratio is associated with swimming efficiency [13]. The maximum value of the velocity ratio V/V_p equals 0.188 when $f = 1.0$ (Hz) and $n_w = 0.824$. From Fig. 28.3, we can also see that the propulsion velocity varies much with respect to the frequency and the wave number. From this fact, the propulsion performance may easily degrade by unexpected environmental changes or/and modeling errors. Adaptive feedback or learning control will be useful to search the parameters of the control input.

28.2.3.2 Measurement of the Amplitude of the Traveling Wave

To observe the increase of the amplitude of the wave generated on the fin, we measured the deflection of the fin using a laser displacement sensor. In the experiment, the support of the fin was fixed. The amplitude is calculated from the

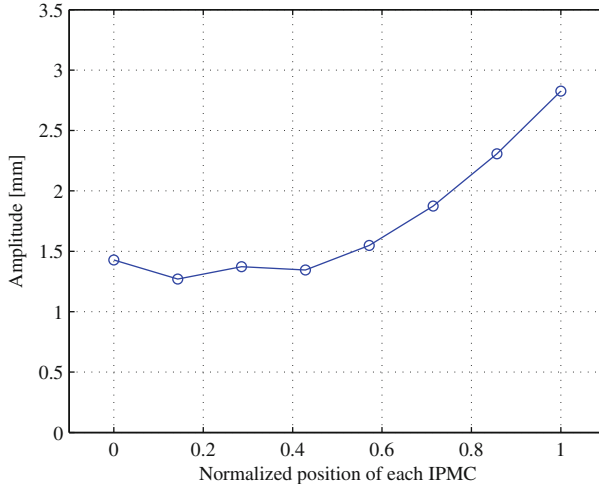


Fig. 28.4 Amplitude of the fin [16]

time history of the measured sinusoidal deflection. The details of the experimental setup is shown in [16].

Figure 28.4 shows the amplitude of the fin in the case of $f=1.0$ (Hz) and $n_w=0.85$. Clearly the amplitude of the fin increases toward the right hand side which is the direction of the wave propagation. The amplitudes of the head and the tail differs about twice. This phenomenon was also observed in the other values of the control parameters.

28.2.3.3 Discussions

We employed the traveling wave input with the constant amplitude v_0 , however we should keep in mind that the generated deflection shape of the fin is not necessarily same as the input shape. A schematic illustration is shown in Fig. 28.5. The amplitude of the output shape increases toward the tail (right), while the amplitude of the input wave is uniformly constant (left). This interesting phenomenon is also observed in a snake-like robot [19] or in an elastic fin with a motor [18]. Elasticity of the body plays an important role in the phenomenon because a simple beam model of the snake-like robot can simulate the incremental amplitude [19]. Furthermore, many natural animals such as slender fishes employ this incremental amplitude swimming form [12, 13]. Lighthill pointed out such swimming form is energy-efficient [20]. Cheng et al. showed that living fishes utilize the passive elasticity of the bodies [22]. Underwater robots with soft actuators like IPMCs have potentials to realize natural and highly efficient swimming as living fishes, that utilize the interaction between their elastic bodies and fluid mechanics.

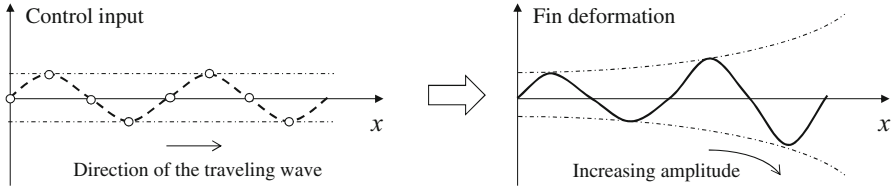


Fig. 28.5 Schematic view of the increase of deflection amplitude

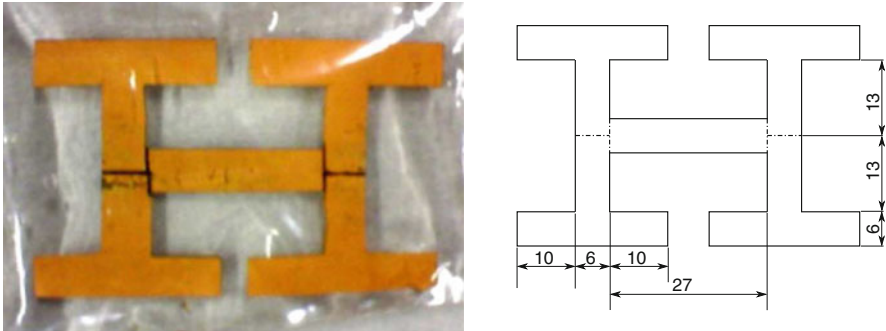


Fig. 28.6 Segmented IPMC (left) and its size (right, the unit is represented by (mm)) [17]

28.3 Quadruped Robot with Fully Polymer Body

28.3.1 Development of the Quadruped Robot

An IPMC sheet was fabricated from Nafion[®] N-117 membrane through gold plating process. The IPMC sheet was cut into the H shape as shown in Fig. 28.6 with a cutter knife. In order to be applied four independent control inputs, the surface electrodes should be segmented into five parts as shown in Fig. 28.6. In the figure the dashed lines indicate the removed electrode for the isolation. We employed the electro-discharge machining (EDM) [23], that can remove the surface metal with the minimum damage on the polymer. The segmented five portions of the IPMC can be used as the independent legs.

Using the skeletal wire shown in Fig. 28.7, we bent the H shaped IPMC sheet to stand by the four legs. By changing the angle of the skeletal wire, the ground angle of the legs can be adjusted. The front legs are set to be inclined and the hind legs are set to be almost vertical. The skeletal wire is made from a paper clip covered with plastic and is attached copper-tape contacts soldered to the power lines. The copper electrode that may cause ion exchange leads to an unexpected but useful effect to increase the deformation of the actuator. This effect of the copper-ion exchange will be mentioned again in the section of the experiment.

The assembled robot is shown in Fig. 28.8. Overall length of the robot is about 25 (mm). The four T-shaped legs can move independently. The bending motion of

Fig. 28.7 Skeletal wire and the copper electrode contacts [17]



Fig. 28.8 Developed quadruped robot with fully polymer body [17]

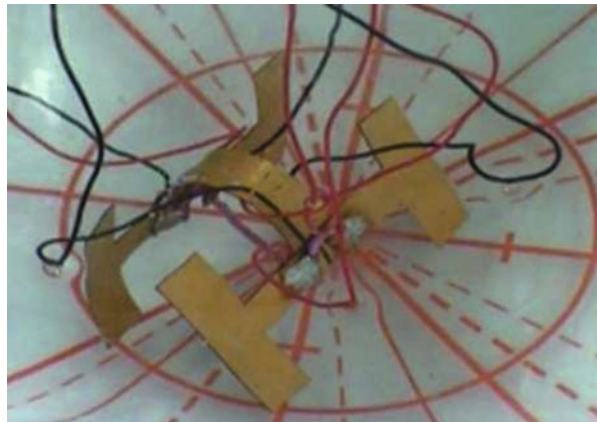
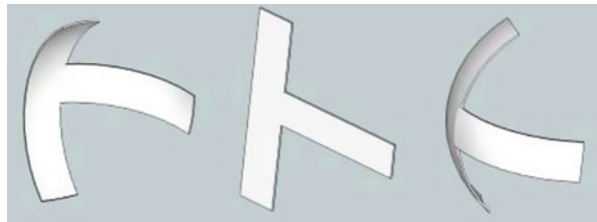


Fig. 28.9 Motion of the leg part [17]



a leg part is shown in Fig. 28.9. The T-shaped leg moves as if it has two joints since it consists of the horizontal and vertical parts. The horizontal part of the leg contributes to move the leg back and forth, and the vertical part make the leg up and down. Because of the T-shape, the leg can perform both motions of swing and kicking without complex mechanism. Being applied positive voltage, the hind legs move forward, and the front legs lift from the ground and move forward. Conversely, being applied negative voltage, the legs move backward and kick the ground.

28.3.2 Design of the Control Input

28.3.2.1 Design of the Walking Pattern, Gait

In order to walk, the robot requires an appropriate walking pattern, namely, gait. However, most of gaits, e.g. the gait of lizard [24], does not work for the developed robot. The lizard gait and many other gaits are dynamic walk, that is, they have such a period that two or less legs are on the ground. The developed quadruped robot can maintain the stance only if three or more legs are on the ground. This is because the robot has soft legs and does not have any balancing mechanism. Therefore the gait that always keeps three or four legs on the ground can only work for the developed robot. Such a gait is, for example, the turtle gait shown in Fig. 28.10. The gait of turtle is a kind of static walk. In the turtle gait, the legs move in order of the position of left front (LF), right hind (RH), right front (RF) and left hind (LH), with same phase differences in a cycle. If three legs except the swing leg are in contact with the ground and the center of gravity is always located within the triangle formed by the three legs, the quadruped robot maintains the equilibrium. It is known that the turtle gait enables slow animals to achieve the quadrupedal locomotion [24, 25].

Let the normalized position of a leg be \bar{x} . Considering the turtle gait, the desired position of a leg \bar{x}_d is designed as shown in Fig. 28.11. \bar{x}_d is positive or negative

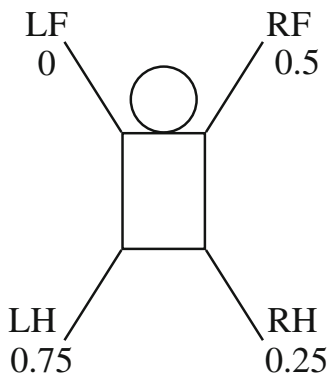


Fig. 28.10 Leg phase of a turtle [17]

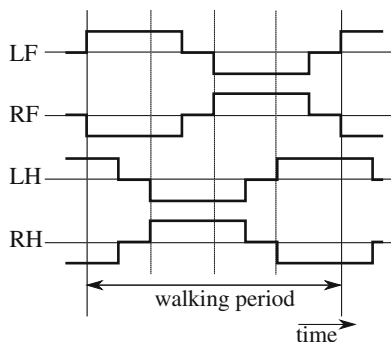


Fig. 28.11 Input waveform \bar{x}_d that mimics the gait of a turtle [17]

during $3/8$ of a period. \bar{x}_d is kept zero, during $1/8$ of a period, between the positive and the negative. The leg bends forward when \bar{x}_d is positive. The leg extends to kick the ground when \bar{x}_d is negative. Although the waveforms of \bar{x}_d have same shapes in all four legs, their phases have differences of 0.25 each other as shown in Fig. 28.10.

28.3.2.2 Feedforward Controller for Smoothing the Voltage Input

The legs are controlled without any sensors, by feedforward control. Because of the capacitive impedance of IPMC, large current flows when step voltage is applied to the IPMC. In order to prevent the impulsive current, a feedforward controller is useful to reduce the impulse. The response model of the tip displacement of the leg x from the input voltage v_a is modeled by a transfer function,

$$G_{xv_a}(s) = \frac{b}{s^2 + a_1s + a_0}. \quad (28.3)$$

With the model of Eq. (28.3), the feedforward controller is designed as:

$$K_{ff}(s) = \frac{\omega_{m1}\omega_{m2}\omega_{m3}}{(s + \omega_{m1})(s + \omega_{m2})(s + \omega_{m3})} \cdot G_{xv_a}^{-1}(s). \quad (28.4)$$

The parameters ω_{m1} , ω_{m2} and ω_{m3} were determined after considering the response in the simulation. The desired position of the tip of the leg is normalized to be 1 when the maximum admissible voltage is applied. Let the limit of the applied voltage be V_0 . The actuation voltage v_a is given by:

$$V_a(s) = K_{ff}(s) \cdot \frac{bV_0}{a_0} \cdot X_d(s). \quad (28.5)$$

28.3.3 Experiment

28.3.3.1 Method

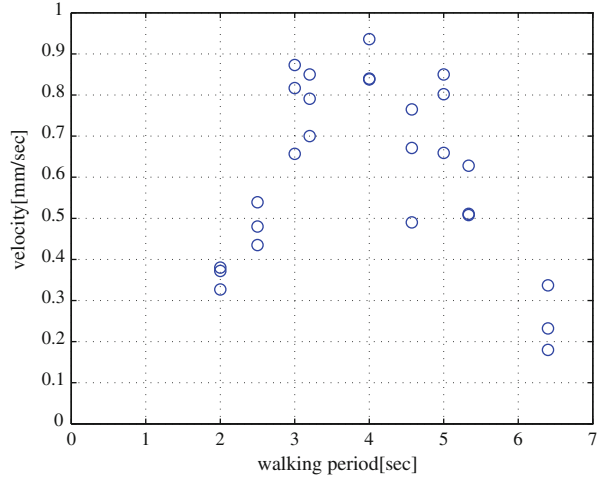
At the preliminary stage of the experiment, the counter ion was exchanged as sodium ion. Though the bending response was quick but was small at first, the deflection gradually increased large and the response becomes slow, even with the same level of the input voltage. This might be caused by the ion-exchange through the copper metal contact attached to the IPMC. We repeated the experiment until the actuator reached to exhibit same response. The effect of ion-exchange by copper metal is also found in some references [26–28].

The coefficients of the transfer function in Eq. (28.3) is estimated from the response of the swept sine test. Table 28.2 shows the estimated coefficients a_0 , a_1 and b . The feedforward controller is designed with the parameters ω_1 , ω_2 and ω_3 as shown in Table 28.2. The parameters of the controller is chosen to avoid the

Table 28.2 Parameters of the model and the feedforward controller [17]

a_0	a_1	b	ω_{m1}	ω_{m2}	ω_{m3}	V_0
61.03×10^{16}	1.868×10^{16}	1.9646×10^{16}	19	24	24	2.3

Fig. 28.12 Average walking speed versus walking period [17]



impulsive current from the observation in the simulation. The amplitude of the voltage V_0 is set as 2.3 (V).

The walking speed of the robot varies by the period of gait, or the period of \bar{x}_d shown in Fig. 28.11. The smallest value of the walking period is bounded by the actuator dynamics and the feedforward controller. The walking period becomes shorter, the displacements of the legs become smaller. Otherwise for the long walking period the displacements of the legs become large, however, the walking speed becomes slow. For much longer walking period, greater than 10 (s), the back-relaxation of the IPMC actuator appears and the displacements of the legs return to zero. Therefore there exists the optimal walking period to achieve the fastest locomotion. In order to estimate the average walking speeds for the various walking periods, we measure the elapsed time while the robot moves 30 (mm) long.

In the experiment, the robot is placed at the bottom of a water tank filled with deionized water of 40 (mm) depth. The control law shown in Eqs. (28.4), (28.5) and Fig. 28.11 is implemented to a digital signal processor. The control signals are amplified by an amplifier circuit using power operational amplifiers.

28.3.3.2 Results and Discussions

Figure 28.12 shows a graph of the average walking speed versus the walking period. There exists an apparent peak of the walking speed when the walking period is about 4 (s). The maximum velocity is 0.936 (mm/s) when the walking period is $T = 4$ (s).

The stride denoted by S of the quadruped robot is determined by multiplying the walking speed V and the walking period T , as $S = VT$. The peak of the stride S is located at $T = 5$ (s), that is different from Fig. 28.12 [17]. When the walking period is less than 4(s), the time when the voltage is kept applying is too short to move the legs sufficiently. Therefore, the walking speed decreases according to the short walking period in such case. When the walking period is from 4 to 5 (s), the stride is almost constant. If the strides are same, the robot walks faster by shorter walking period. When the walking period is greater than 5 (s), the stride becomes shorter because of the back-relaxation of the IPMC.

28.4 Conclusion

Two underwater soft robots using IPMCs, the ray-like robot and the quadruped robot, have been introduced. For autonomous operation of the ray-like robot, the miniaturized electrical devices were developed. A simple traveling wave input was employed to generate the moment on the fin. The propulsion speed of the robot was able to be controlled by the parameters f and n_w . It should be noted that the deformation of the fin increased toward the backward in spite of the uniform control input. This incremental wave phenomenon may be the key to achieve the energy-efficient locomotion of underwater swimming robots by utilizing the elasticity of the actuator. It may also be the key for understanding the energy-efficient swimming of living fishes. For more detailed discussion of the swimming dynamics of the robot, analysis using fluid mechanics is expected as the future work.

The quadruped robot was developed from a sheet of IPMC of which electrode was segmented into five parts to be controlled independently. The EDM method was useful to segment the electrode with the minimum damage to the polymer. Ion exchange by copper electrode was observed during the experiment. This unexpected phenomenon is useful to obtain large deformation of IPMC actuators. We have also demonstrated that the gait of turtle was effective for the developed quadruped robot.

The robot with fully IPMC body is resilient to interact with the environment and is even capable of working in deep sea [29]. Because of the unique characteristics of wet, soft, lightweight and robust actuators, IPMCs are expected as next-generation actuators for underwater robots.

Acknowledgements Mr. Masanori Yamamura developed the ray-like robot and carried out the experiment. Mr. Naoki Tomita developed the quadruped robot and carried out the experiment. Dr. Shinya Hirano and Dr. Masaki Onishi helped us to design the experimental setup. Prof. Jonathan Rossiter advised us about the EDM. The authors would like to appreciate Dr. Yoshihiro Nakabo for the valuable discussions and his generous help. Prof. Yoshikazu Hayakawa gave us some useful comments. The authors would also like to appreciate Dr. Toshiharu Mukai, Prof. Masaki Yamakita and Dr. Norihiro Kamamichi for their courtesy.

References

1. Bar-Cohen Y (ed) (2004) *Electroactive polymer (EAP) actuators as artificial muscles: reality, potential, and challenges*, 2nd edn., SPIE Press, Washington
2. Shahinpoor M, Kim KJ (2001) Ionic polymer-metal composites: I fundamentals. *Smart Mater. Struct.* 10:819–833
3. Barrett D, Grosenbaugh M, Triantafyllou M (1996) The optimal control of a flexible hull robotic undersea vehicle propelled by an oscillating foil. *Proceedings IEEE AUV symposium*, pp 1–9
4. Takayama T, Hirose S (2002) Amphibious 3D active cord mechanism “HELIX” with helical swimming motion. *Proceeding of 2002 IEEE/RSJ international conference on intelligent robots and systems (IROS2002)*, 775–780
5. Yamada H, Chigisaki S, Mori M, Takita K, Ogami K, Hirose S (2005) Development of amphibious snake-like robot ACM-R5. *Proceedings 36th international symposium on robotics, TH3C4*
6. Nakabo Y, Mukai T, Ogawa K, Ohnishi N, Asaka K (2004) biomimetic soft robot using artificial muscle. *Tutorial wtp3 electro-active polymer for use in robotics in ieee/rsj international conference intelligent robots and systems (iros2004)*
7. Ogawa K, Nakabo Y, Mukai T, Asaka K, Onishi N (2005) Snake-Like swimming artificial muscle. *Video proceedings IEEE international conference robotics and automation 2005 (ICRA2005)*
8. Nakabo Y, Mukai T, Asaka K (2010) Biomimetic soft robots using IPMC. In: Kim KJ, Tadokoro S (eds.) *Electroactive polymers for robotics applications*, 165–198, Springer, London
9. Yamakita M, Kamamichi N, Kozuki T, Asaka K, Luo ZW (2005) A Snake-Like Swimming Robot Using IPMC Actuator and Verification of Doping Effect, *Proceeding of 2005 IEEE/RSJ Int. Conf. on Intelligent Robots and Systems (IROS2005)*, pp 3333–3338
10. Jung J, Kim B, Tak Y, Park J (2003) Undulatory tadpole robot (TadRob) using ionic polymer metal composite (IPMC) actuator. *Proceeding of 2003 IEEE/RSJ international conference on intelligent robots and systems (IROS2003)*, pp 2133–2138
11. Punning A, Anton M, Kruusmaa M, Aabloo A (2004) A biologically inspired ray-like underwater robot with electroactive polymer pectoral fins. *Proceeding of the international IEEE conference mechatronics and robotics vol 2*, pp 241–245
12. Azuma A (1992) *The biokinetics of flying and swimming*. Springer, Tokyo
13. Sfakiotakis M, Lane DM, Davies JBC (1999) Review of fish swimming modes for aquatic locomotion. *IEEE J Oceanic Eng* 24(2):237–252
14. Yamakita M, Kamamichi N, Kaneda Y, Asaka K, Luo ZW (2004) Development of an artificial muscle linear actuator using ionic polymer-metal composites. *Adv Robot* 14(4):383–399
15. Guo S, Shi L, Asaka K, Li L (2009) Experiments and Characteristics Analysis of a Bio-inspired Underwater Microrobot. *Proceeding of international conference on mechatronics and automation (ICMA2009)*, pp 3330–3335
16. Takagi K, Yamamura M, Luo ZW, Onishi M, Hirano S, Asaka K, Hayakawa Y (2006) Development of a Rajiform swimming robot using ionic polymer artificial muscles. *Proceedings 2006 IEEE/RSJ international conference on intelligent robots and systems (IROS2006)*, pp 1861–1866
17. Tomita N, Takagi K, Asaka K (2011) Development of a quadruped soft robot with fully IPMC body. *2011 Proceedings of SICE annual conference (SICE2011)*, pp 1687–1690
18. Watanabe M, Muramatsu K, Kobayashi N (2002) Propulsion performance of an aquatic mobile robot using traveling-wave motion of a flexible fin (relationship between propulsion efficiency and flow pattern) (in Japanese). *Trans Japan Soc Mechanical Eng* 68(665):188–195
19. Takagi K, Nakabo Y, Luo ZW, Mukai T, Yamamura M, Hayakawa Y (2006) An analysis of increase of bending response in IPMC dynamics given uniform input. *Proc SPIE* 6168:616814
20. Lighthill MJ (1960) Note on the swimming of slender fish. *J Fluid Mech* 9: 305–317

21. Luo ZW, Odashima T, Takagi K, Yamamura M, Hayakawa Y, Hirano S, Kato A (2005) On recent developments and autonomous decentralized control of mobile robot. Proceedings of the IEEE ROBIO 2005 workshop presentations, pp 19–22
22. Cheng JY, Pedley TJ, Altringham JD (1998) A continuous dynamic beam model for swimming fish. *Philosophical transactions of the royal society of london, series b-biological sciences* vol. 353(1371), pp 981–997
23. Rossiter J, Mukai T (2011) Electrostatic and thermal segmentation of multi-segment IPMC sensor-actuators. *Proc SPIE* 7976:79761C
24. Alexander RM (1992) *Exploring biomechanics: animals in motion*. W. H. Freeman Publishers
25. Stewart I, Golubitsky M (1992) *Fearful symmetry: is god a geometer?*. Blackwell Publishing, Boston
26. Uchida M, Taya M (2001) Solid polymer electrolyte actuator using electrode reaction. *Polymer* 42:9281–9285
27. Johanson U, Maeorg U, Sammelseg V, Brandell D, Punning A, Kruusmaa M, Aabloo A (2008) Electrode reactions in Cu-Pt coated ionic polymer actuators. *Sensors and Actuators B* 131:340–346
28. Takagi K, Tomita N, Asaka K (2014) A simple method for obtaining large deformation of IPMC actuators utilizing copper tape. *Adv Robot* doi:10.1080/01691864.2013.876939
29. Nakabo Y, Takagi K, Mukai T, Yoshida H, Asaka K (2005) Bending response of an artificial muscle in high-pressure water environments. *Proc SPIE* 5759:388–395

Chapter 29

IPMC Actuator-Based Multifunctional Underwater Microrobots

Shuxiang Guo and Liwei Shi

Abstract A variety of microrobots have commonly been used in the fields of biomedical engineering and underwater operations during the last few years. Due to their compact structure, low driving power, and simple control systems, microrobots can complete a variety of underwater monitoring operations, even in restricted underwater environments. Generally speaking, compact structure, multi-functionality, flexibility and precise positioning are considered incompatible characteristics for underwater microrobots. Nevertheless, we have designed several novel types of bio-inspired locomotion, using ionic polymer metal composite (IPMC) and shape memory alloy (SMA) actuators. We reviewed a number of previously developed underwater microrobot prototypes that were constructed to demonstrate the feasibility of these types of biomimetic locomotion. Based on these prototypes, we summarized the implemented techniques and available results for efficient and precise underwater locomotion. In order to combine compact structure, multi-functionality, flexibility and precise positioning, we constructed a prototype of a new lobster-like microrobot and carried out a series of experiments to evaluate its walking, rotating, floating and grasping motions. Diving/surfacing experiments were performed by electrolyzing the water around the surfaces of the actuators. Three proximity sensors were installed on the microrobot to detect an object or avoid an obstacle while walking.

Keywords Bio-inspired locomotion • Bio-inspired underwater microrobot • Bio-medical robot • Biometrics • IPMC (Ionic Polymer Metal Composite) actuator

S. Guo (✉)

Faculty of Engineering, Kagawa University, 2217-20 Hayashi-cho, Takamatsu, Kagawa, Japan

School of Life Science, Beijing Institute of Technology,
Beijing 100081, China

e-mail: guo@eng.kagawa-u.ac.jp

L. Shi

School of Life Science, Beijing Institute of Technology,
Beijing 100081, China

e-mail: shiliwei@bit.edu.cn

29.1 Introduction

Robots have been used to carry out a wide range of underwater jobs that humans deem dangerous, dull and/or dirty, mostly because of their aptitude for multi-functionality and high accuracy. This trend has continued into underwater monitoring operations, including pollution detection, video mapping, exploration of unstructured underwater environments and other tasks [1, 2]. Various configurations, shapes and sizes of underwater robots are required for different applications or tasks. For underwater environmental detection or observation, a compact structure with multi-functionality and flexibility enables a robot to work in limited spaces. When a large range of motions and large load capacity are required, a traditional motor-actuated electromagnetic structure is essential. When large interior space and flexible multidirectional rotation in a restricted space are required, a spherical robot body is recommended. When high-speed cruising is required, a streamlined robot body may be the best choice [3].

If a robot is to be used in a complicated underwater environment, such as a narrow pipeline or a region filled with reefs, it should be endowed with the combined attributes of endurance, stable high speed, large load capability, flexibility, compact structure and multi-functionality. Many types of underwater robots have been developed in recent years. While the use of some of these robots involves changing the angles of rudders or adjusting the differential propulsive forces of thrusters, a number of vectored propeller-actuated underwater robots have also been introduced [4]. A multi-channel Hall-effect thruster has also been reported, involving vector composition of underwater robots [5]. Moreover, we have developed a spherical underwater robot equipped with three vectored water-jet-based thrusters [3]. However, most of these robots are steered by traditional electromagnetic thrusters, which are difficult to miniaturize.

Accordingly, motors are rarely found in microrobot applications [6, 7] and special actuator materials are used instead. A variety of smart materials, such as ionic polymer metal composite (IPMC), piezoelectric elements, pneumatic actuators and shape memory alloy, have been investigated for use as artificial muscles in new types of microrobots [8–14]. In this research, IPMC is used as actuator material to develop a microrobot with a compact structure, multi-functionality and flexibility. The actuation characteristics of IPMC, which include suitable response time, high bending deformation and long life, show significant potential for the propulsion of underwater microrobots [15–20].

For real-world applications, an underwater robot should possess the attributes of endurance, stable high speed, large load capacity, flexibility, compact structure and multi-functionality. To implement these characteristics, we propose a mother–son robot system, which includes several microrobots as sons and a newly designed amphibious spherical robot as the mother. This is an original concept and is inspired by the design of aircraft carrier systems. In this system, the mother robot is actuated by four water-jet propellers and eight servomotors, capable of providing a stable high speed and carrying the microrobots to a desired target location where tasks are

to be performed. When the mother robot reaches the desired location, or encounters a narrow channel that is difficult to navigate, it assumes a stable position and acts as a base station for the microrobots. Then, the microrobots exit the mother robot, proceed to the target position and carry out their tasks.

Compared with a single large robot, when the final tasks are carried out by microrobots, it is easier to adapt to narrow environments and implement relatively high positioning precision. In addition, compared with individual microrobots, the mother–son system offers the following advantages.

1. The range of motions of the overall system is expanded, owing to the relatively high speed and endurance of the mother robot.
2. The microrobots can obtain a relatively stable, high power supply via cables.
3. Since the microrobots are all controlled by the mother robot, communications between microrobots can be implemented by the mother when cooperation is needed.
4. Since the power supply and control units are installed in the mother robot, the microrobots can be designed with a more compact structure, suitable for restricted spaces such as narrow pipelines or channels.

We introduced a newly designed spherical amphibious mother robot in [21] and [22]. A spherical body has both a compact structure and maximum interior space, compared to a streamlined body. It can rotate and change direction more easily than a streamlined design, which is very important for microrobots in restricted spaces. To expand the range of motion of the overall system, we designed the mother robot for amphibious use. In this chapter, we will mainly focus on the microrobots.

Nature provides the best models for robots. Living creatures furnish an abundance of structures for biomimetic robot design. Aside from fish-like and manta-ray-like swimming locomotion, we have developed several microrobots that employ biomimetic locomotion to implement walking, floating and swimming motions [1, 2, 23–26]. However, each of these units implements only some of these motions and none of them are able to carry out simple tasks such as grasping and carrying objects to a desired position, detecting an object, or avoiding an obstacle. In order to create a compact structure with efficient and precise locomotion, and multi-functionality, we have developed a new microrobot with nine IPMC actuators, used as legs or fingers. This unit employs seven of its actuators to walk, rotate and float. The other two actuators are utilized to implement grasping. Moreover, the microrobot can detect the direction and distance of an object, and avoid an obstacle while walking, using three infrared proximity sensors. In this chapter, the ‘multifunctional locomotion’ means that the microrobot can perform walking, rotating, grasping and surfacing/diving motions. However, the term ‘multi-functionality’ means not only implementing these motions, but also carrying out simple tasks such as grasping and carrying objects to a desired position, detecting an object, or avoiding an obstacle.

The remainder of this chapter is divided into four parts. First, we describe the characteristics of IPMC actuators, review the feasibility results for several previously developed microrobots and summarize the implemented techniques of

underwater locomotion, as a guide to the next stage of microrobot design. Second, based on these techniques of biomimetic locomotion, we introduce a new type of microrobot with a compact structure and multi-functional locomotion, analyse its walking mechanism, and calculate its theoretical walking speed. Third, we discuss the development of a prototype of this underwater microrobot, together with a series of experiments to evaluate its walking and rotating speeds on a flat underwater surface. We also describe object detection and obstacle avoidance while walking, which is accomplished via three proximity sensors installed in the front of the microrobot. Finally, we present our conclusions.

29.2 Biomimetic Locomotion

29.2.1 IPMC Actuators

Ionic polymer metal composite (IPMC) is an innovative material made of an ionic polymer membrane, chemically plated with gold electrodes on both sides. Its actuation characteristics show significant potential for the propulsion of underwater microrobots. It is lightweight and has a suitable response time, high bending deformation and long life. IPMC is widely used in soft robotic actuators such as artificial muscles, as well as on dynamic sensors [15–20]. The ionic polymer metal composite adopted for this research consists of Au deposited on Nafion™ film with a thickness of 0.22 mm.

An IPMC actuator can be regarded as equivalent to a cantilever beam. Figure 29.1 shows the mechanical configuration and relevant geometrical parameters, which are as follows: L_c denotes the length of the clamped part of the IPMC, L_f is the total free length of the IPMC and w and h denote the width and the height of the IPMC cross-section. The pinned end is used to apply electrical voltages across the thickness.

According to mechanical analysis, bending deformation of an IPMC actuator results from the redistribution of internal water molecules. Under the influence of an applied stimulus, the water molecules in the actuator are re-distributed in the following two stages [27].

1. When an electrical stimulus is applied across the thickness of the IPMC, each hydrated sodium ion moves to the cathode side, accompanied by four hydrated

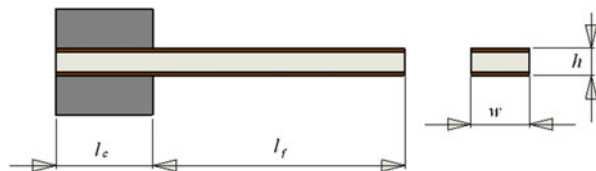


Fig. 29.1 Mechanical configuration of the actuator and relevant parameters

water molecules. Bending deformation is then generated by the expansion of Nafion117 near the cathode side and contraction near the anode side.

2. After a short time, the self-diffusion of water molecules causes free water molecules to gradually flow to the anode side, reducing the concentration of water molecules at the cathode and demonstrating the deformation recovery potential of the IPMC actuator.

We measured the free-end deflection of an IPMC actuator in a water tank for different applied square-wave signals. The sample IPMC actuator was 20 mm long, 4 mm wide and 0.22 mm thick. It was driven by a personal computer (PC) equipped with a digital-to-analogue converter card, and the deflection of the IPMC was measured via a laser displacement sensor. The laser sensor was used to translate the displacement to a voltage and then the voltages were recorded and translated to the PC by an analogue-to-digital converter card. We used the square-wave signals to drive the IPMC actuator.

We also measured the bending force generated at the free end of the equivalent cantilever beam by applying different signals. In this experiment, the sample IPMC actuator was 24 mm long, 19 mm wide and 0.22 mm thick. The actuator was driven by a PC equipped with a digital-to-analogue converter card, and the bending force of the IPMC was measured by an electronic balance. To reduce the torque on the electronic balance, we used a needle to transfer the press force from the IPMC actuator. The initial distance between the IPMC and the needle tip is set as 3 mm. The experimental results indicate that the tip-bending force increases as the driving voltage increases.

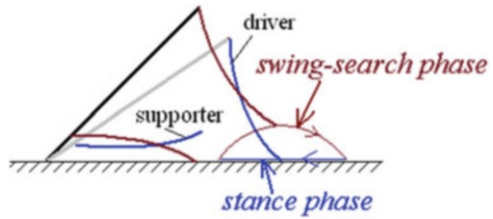
29.2.2 Bio-Inspired Locomotion

IPMC actuators can be used as oscillating or undulating fins for swimming microrobots when a fast response is required [15–17, 28, 29]. However, this type of swimming motion cannot ensure precise positioning of the robot. Fish-like robots cannot implement a backward swimming motion, which is essential in a restricted space. Furthermore, fish-like propulsion mechanisms simply mimic the undulating and oscillatory body/fin motions of a fish. Some simple underwater tasks are not easily carried out without hands or fingers. Therefore, in addition to swimming, other types of biomimetic locomotion are required for microrobots with compact structure, multi-functions and flexibility.

29.2.2.1 Stick Insect-Inspired Walking Locomotion

Nature provides perfect models for robots. Biomimetic robots borrow their senses and structure from animals, such as insects, fish and birds. In the case of the stick insect, each leg is composed of the coxa, femur, tibiae and tarsus. The tarsus

Fig. 29.2 Two-phase driving locomotion with IPMC actuators [24]



is also called the foot and does not contribute to its movements. The coxa offers the foot one degree of freedom (DOF) in the direction of movement. The femur and the tibiae offer the foot two DOF to enable it to find a reliable foothold during the swing–search phase to touch the ground and support the body during the stance phase.

A stick insect-inspired biomimetic locomotion prototype using two IPMC actuators was introduced in [1]. As Fig. 29.2 shows, the actuator in the vertical direction is called the driver, while the actuator in the horizontal direction is called the supporter. The free end of the driver is the foot. The driver and supporter are controlled by two channels of square waves, each with the same frequency. The phase of the supporter lags 90° behind that of the driver [1, 2, 24].

29.2.2.2 Jellyfish-Like Floating Locomotion

Jellyfish movement is dependent on floatation, ocean currents and winds, and is accomplished via a form of jet propulsion. Specifically, jellyfishes move by squeezing their bodies so that jets of water are ejected from underneath, propelling them forward.

A jellyfish-inspired biomimetic locomotion prototype with SMA actuators was introduced in [30]. The jellyfish-inspired body uses SMA actuators to imitate the circular muscles of a real jellyfish. The body shrinks when voltage is applied and water is squeezed out of it. This changes the buoyancy and produces an upward force. The body floats upward when the force reaches a certain value. The upward force can be changed by controlling the frequency of the actuator shrinkage and the voltage between its two ends. This means that the microrobot can be induced to float upward, remain neutrally buoyant, or sink as required.

29.2.2.3 Butterfly-Inspired Swimming Locomotion

Butterfly movement is accomplished by the counter force of air. Specifically, they flap their wings to push the air at different frequencies and speeds. In a single flapping period, there are two motions, folding and unfolding. Movement results from the fact that the folding motion pushes the air between their wings at a higher speed than the unfolding motion.

A butterfly-inspired biomimetic locomotion prototype with SMA actuator was also introduced to implement fast swimming. We use two pectoral fins to imitate the flapping motions of a butterfly. The fins are installed perpendicular to the horizontal plane, and the initial angle between them is set at $\pi/3$. They squeeze the water between them to create a counter force in the horizontal direction. In this way, the microrobot can be induced to implement a swimming motion. The horizontal propulsion can be changed by controlling the frequency of the actuator shrinkage and the driving voltage. The two pectoral fins are driven by separate SMA actuators, and thus the robot can swim or make turns via the cooperation of the fins [26].

29.2.2.4 Inchworm-Inspired Crawling Locomotion

Inchworms have smooth, hairless bodies, usually about 25 mm long. Also known as measuring worms, spanworms, or loopers, they lack appendages in their midsections, causing them to have a characteristic looping gait. They have three pairs of true legs at the front end, like other caterpillars, but only two or three pairs of prolegs at the rear end. An inchworm moves by drawing its hind end forward while holding on with its front legs, and then advancing its front section while holding on with its prolegs (<http://www.infoplease.com/ce6/sci/A0825073.html>, [25, 31]).

An inchworm-inspired biomimetic locomotion prototype with two IPMC actuators was introduced to implement fast creeping. The design was based on a one DOF leg. The structure of the one DOF walking mechanism is described in [31]. This mechanism can only implement crawling motion.

29.3 Developed Microrobots

Swimming motion is a universal motion in water for the underwater species. Up to now, majority of research work has been focused on fish-like propulsion mechanisms, fin materials, remote operation, multi-agent cooperation and mechanical structures. We have developed a robotic fish by using one IPMC actuator, which was reported by CCTV 10 in China. Figure 29.3 shows this fish-like microrobot, which can live with real fish in the same water tank.

However, the swimming motion cannot ensure the position precision for the robot. The fish-like robots cannot implement backward swimming motion, which is essential in limited space. Also, the fish-like propulsion mechanisms just mimic the undulating and oscillatory body/fin motions. It is hard to implement some simple underwater tasks without hands or fingers. So, besides the swimming, we proposed some other biomimetic locomotion.

Based on stick insect-inspired walking locomotion, a prototype of an eight-legged microrobot was developed, as shown in Fig. 29.4a [2]. It was 33 mm long, 56 mm wide and 9 mm high. Four legs were used as drivers and the other four actuators were used as supporters. It was capable of walking, rotating and diving/

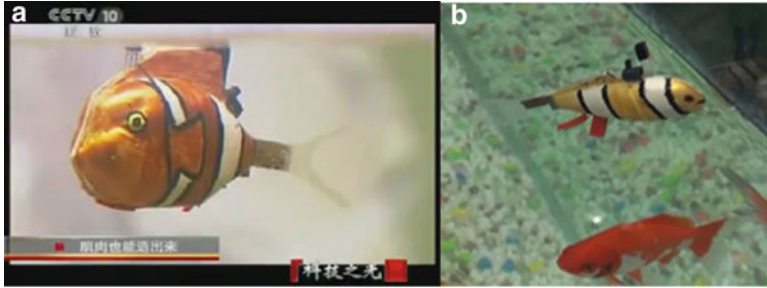


Fig. 29.3 Fish-inspired microrobot. (a) Fish-like microrobot, (b) Living with the real fish



Fig. 29.4 Prototype microrobots. (a) Stick insect-inspired [2], (b) Jellyfish-inspired [1], (c) Inchworm-inspired [25, 31]

surfacing. However, the floating efficiency of this microrobot was not high. To improve the floating motion, a prototype of a jellyfish-type microrobot was constructed, based on jellyfish-inspired locomotion, as shown in Fig. 29.4b [1]. It was 68 mm high, with a weight of 4.81 g in air. This biomimetic microrobot consisted of a two-ring body and four legs. The body was designed to imitate a jellyfish's diving/surfacing motions. Additionally, four IPMC actuators were fixed on the body to implement walking motion in two directions. Although the floating motion was improved, the prototype was unable to rotate, and the walking motion was unsatisfactory because the centre of gravity was located in one of the two halves of the body, causing an imbalance in the overall body and a large amount of slippage.

For the purpose of creating a microrobot with a compact structure and multi-functions, an inchworm-inspired microrobot with ten IPMC actuators was developed, as shown in Fig. 29.4c. It was 33 mm long, 14 mm wide and 14 mm high. Four outside actuators were used as legs to implement walking, rotating and floating motions. The other six actuators were used as fingers to grasp small objects [25, 31]. Figure 29.5 shows the hybrid motion of the inchworm-inspired microrobot. Compared with the jellyfish-like robot, this design offered the advantages of stability, compact structure, less water resistance and grasping motion implementation. However, because the rotating radii were not the same for the outside four legs, a large amount of slippage occurred while rotating and the rotating efficiency was not high. Only the outside four legs were used to electrolyze

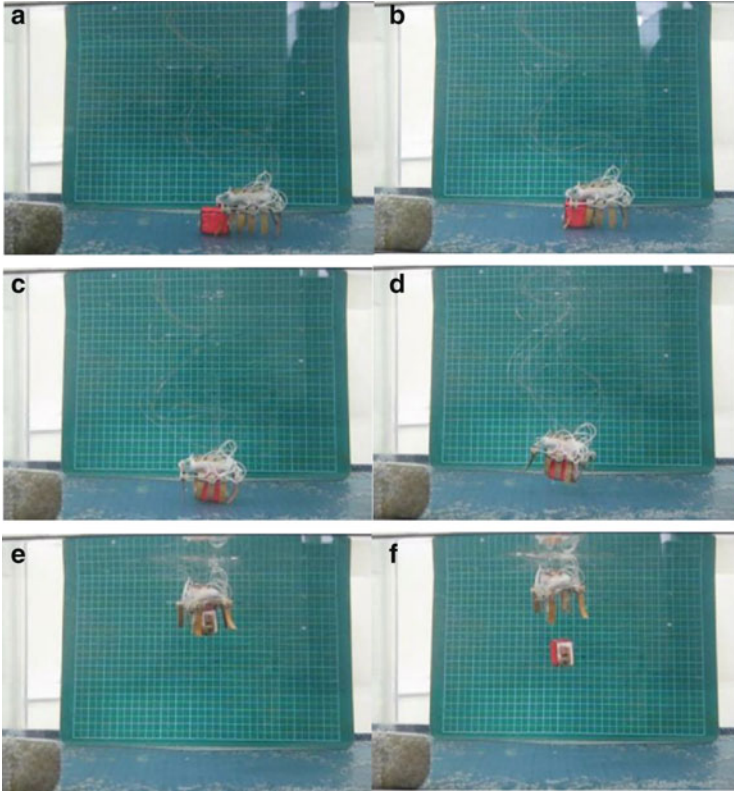


Fig. 29.5 Hybrid motion of the inchworm-inspired microrobot. (a) Initial position, (b) Walking motion, (c) Grasping motion, (d) Floating motion, (e) Reaching the surface, (f) Opening motion

the water around the IPMC surface, generating air bubbles, which became attached to the surfaces of the legs, increasing the buoyancy and implementing the floating motion. Due to the limitations of the structure, the inside six legs were used solely as fingers to grasp an object and could not contribute any buoyancy to the floating motion, so that the floating speed was slow. To overcome these difficulties, a new lobster-like microrobot is introduced in the following sections.

29.4 Proposed Multifunctional Lobster-Like Microrobot

29.4.1 Actual Lobsters

The lobster anatomy includes the cephalothorax, which fuses the head and the thorax, and the abdomen. Lobsters have five pairs of legs, of which the front three pairs have claws and the rear two pairs are used exclusively for walking. They live

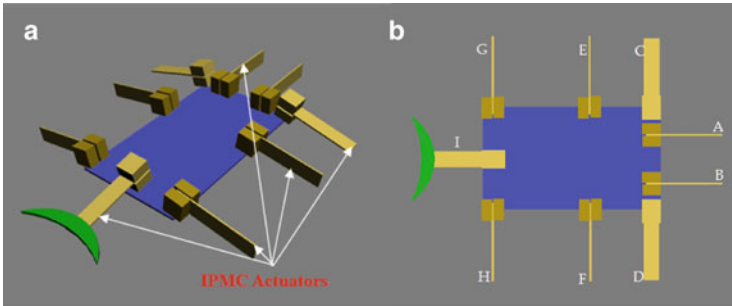


Fig. 29.6 Proposed structure of the lobster-like microrobot. (a) Side View, (b) Top View

in murky environments at the bottom of the ocean and their heads are equipped with a pair of antennae, which are used as sensors. The abdomen includes small swimmerets, and its tail is composed of uropods and the telson. While walking, the tail also provides some support to the abdomen. In general, lobsters are 25–50 cm long and move by walking slowly across the sea floor. However, when they flee, they swim swiftly backwards by curling and uncurling their abdomens (<http://en.wikipedia.org/wiki/Lobster>, http://en.wikipedia.org/wiki/File:Metanephrops_japonicus_edit.jpg).

29.4.2 Proposed Lobster-Like Microrobot

To inherit the multi-functions of the inchworm-inspired microrobot and overcome its disadvantages, a new lobster-like microrobot is proposed. The structure of the new microrobot is shown in Fig. 29.6. The microrobot uses nine IPMC actuators as legs or fingers, labelled A to I. Actuators A and B are used as fingers; actuators C, D, E, F, G and H are used as legs; and actuator I is used as a tail. The nine actuators are all 14 mm long, 3 mm wide and 0.22 mm thick. The total size of the microrobot is 65 mm long (including the two fingers and the tail), 50 mm wide and 9 mm high.

29.4.3 Crawling and Rotating Mechanism

The lobster-like microrobot employs a two-phase crawling motion, consisting of a stance phase and a swing–search phase, as with the stick insect. This stick insect-inspired crawling locomotion was proposed and utilized by Guo et al. in [24]. The details are reiterated here for the sake of clarity. While crawling, legs C and D, and the tail are supporters, while legs E, F, G and H are the drivers. The four drivers and three supporters are driven by square waves with the same frequency, and the phase

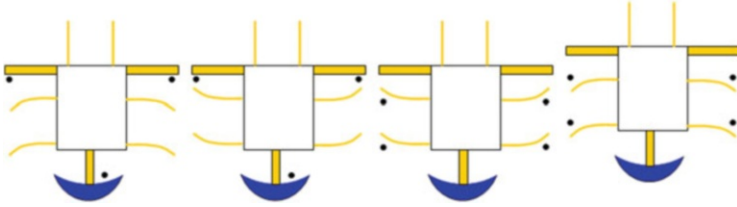


Fig. 29.7 Crawling mechanism. The *filled circle* indicate which legs contact the ground

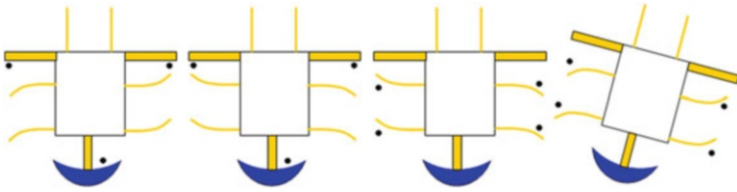


Fig. 29.8 Rotating mechanism. The *filled circle* indicate which legs contact the ground

of the three supporters lags 90° behind that of the four drivers. Each step cycle of the walking motion can then be separated into four periods, as shown in Fig. 29.7.

1. The three supporters lift the body up and the drivers are off the ground.
2. While the body is lifted by the three supporters, the four drivers bend forward.
3. The three supporters bend far enough upward so that they are off the ground and the four drivers contact the ground.
4. The four drivers bend backward to push the body forward [1].

By changing the bending directions of the drivers on opposite sides of the body, the proposed microrobot can crawl forward or backward and rotate clockwise or counter clockwise, in a manner similar to the slow crawling motion of an actual lobster on the sea floor. Figure 29.8 shows one step cycle of the rotational motion, which is also divided into four periods.

29.4.4 Floating Mechanism

The water around the surface of the IPMC actuators can be electrolyzed when the frequency of the driving voltage is below 0.3 Hz. The proposed microrobot electrolyzes the water around the IPMC surfaces of all six legs. Air bubbles are generated and become attached to the leg surfaces to increase the buoyancy and implement the floating motion. The tail fin is also used to provide buoyancy and to adjust the balance of the overall body while floating. The quantity of air bubbles

generated is determined by the frequency and driving voltage. The buoyancy of the microrobot can be controlled by the resulting change in volume to make the microrobot float upward, remain neutrally buoyant, or sink [1].

29.4.5 Grasping Mechanism

We use two IPMC actuators to imitate the front pair of claws of an actual lobster, as shown in Fig. 29.6. The distance between the pair of claws is 10 mm and they are attached to the front of the microrobot. The generated bending force of the IPMC actuator is determined by the driving voltage and the tip displacement. For a given driving voltage, when the deflection increases, the bending force decreases. Hence, the grasping capability is determined by the size of the object and the coefficient of friction when the stimulus is fixed.

29.4.6 Control System

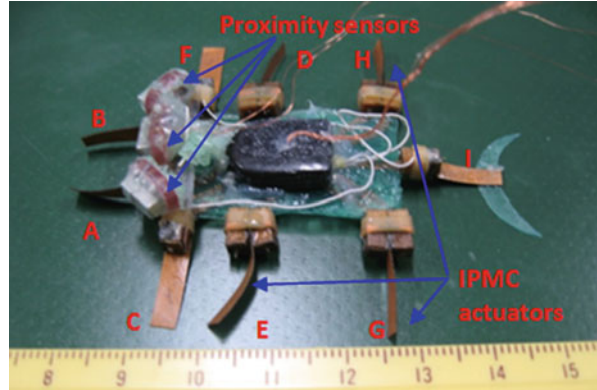
We use an AVR atmega164 as the control centre of the microrobot, and MOSFET FDS4935A and NDS9936 power sources to drive the IPMC actuator. Legs C–D, E–G and F–H are controlled separately by three square-wave signals, and tail I is controlled by another square-wave signal. The claws are stimulated by the same step signal. We use three proximity sensors to judge the direction and distance of an obstacle, and alter its motion accordingly [32].

29.5 Prototype Microrobot and Experiments

29.5.1 Prototype of the Lobster-Like Microrobot

In order to create a compact structure with efficient, precise locomotion and multi-functionality, we developed a new microrobot with nine IPMC actuators, used as legs or fingers. This unit employs seven of its actuators to walk, rotate and float. The other two actuators are utilized to implement grasping. The prototype is shown in Fig. 29.9. C, D and I are used as supporters to lift the robot, while E, F, G and H are drivers that bend forward or backward to implement walking and rotation. A and B can be used as two fingers to grasp an object. When floating, I is also used as the tail fin to adjust the balance of the body. The proximity sensor used in the present research is 8 mm long and 5 mm wide, with a weight of 0.5 g. The distance measurement range for one sensor is from 0 to 60 mm, and the output voltage ranges from 150 mV to the power voltage [32].

Fig. 29.9 Prototype lobster-like microrobot



29.5.2 Walking Experiments

Lobsters live at the bottom of the ocean, where the seawater is static. They move mostly by walking slowly across the sea floor. Accordingly, to evaluate the walking motion of the new lobster-like microrobot, we carried out experiments on a flat underwater surface and recorded the time required to crawl a distance of 50 mm with various applied signal voltages and frequencies. Legs C, D, E, F, G and H, and the tail I were used to implement the walking motion. C, D and I were used as supporters, and were driven by a square-wave voltage. The four drivers E–G and F–H received the same stimulus. The tests were repeated 10 times for each set of control signals, in order to determine the average speed in the same experimental environment. The experimental results are shown in Fig. 29.10a. We can see that: (1) the walking speeds increased when the input voltage increased; (2) with a voltage of 6 V, a maximum walking speed of 6.75 mm s^{-1} was attained at 2.5 Hz; and (3) with a voltage of 4 V, a maximum speed of 3.2 mm s^{-1} was attained at 4 Hz. A second peak point occurred at 5 Hz with a voltage of 6 V. When the frequency was higher than 10 Hz, the walking speed approached 0. The maximum operating frequency of the IPMC actuator is about 25 Hz as a simple cantilever in our experiments.

29.5.3 Rotating Experiments

The rotational motion of the microrobot was also examined on a flat underwater surface. We recorded the time required to rotate through an angle of 90° under the influence of various applied signal voltages and frequencies. These tests were also repeated ten times for each set of control signals, in order to calculate the average speed. The experimental results are shown in Fig. 29.10b. We can see that: (1) the rotating speeds increased when the voltage increased; (2) with a voltage of 6 V, a

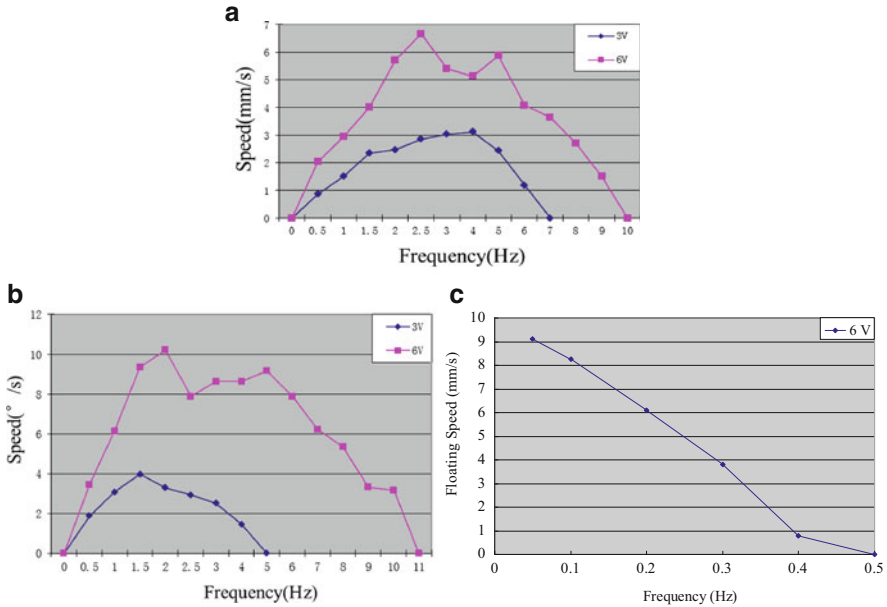


Fig. 29.10 Experimental results. (a) Walking speeds, (b) Rotating speeds, (c) Floating speeds

maximum speed of $10.3^\circ \text{ s}^{-1}$ was attained at 2 Hz; and (3) with a voltage of 3 V, a maximum speed of 4° s^{-1} was attained at 1.5 Hz. There was also a second peak point at 5 Hz for the rotational speed with a voltage of 6 V. When the frequency was higher than 11 Hz, the rotational speed approached 0. The displacement of the IPMC actuator would be smaller in a real-world application, due to the body loading, leg slippage and short response time at high frequencies.

29.5.4 Floating Experiments

While floating, legs C, D, E, F, G and H are used to electrolyze the water around their surfaces. To avoid permanent deformation of the IPMC actuator, a direct current (DC) stimulus was not utilized. The frequency of the applied voltage ranged from 0.05 to 0.5 Hz with a voltage of 6 V. The experimental environment was the same as that used with the inchworm-inspired robot. The experimental floating speed results are shown in Fig. 29.10c. The floating speed decreased when the frequency increased. The maximum floating speed was 9.1 mm s^{-1} at 0.05 Hz. Compared with the inchworm-inspired unit, the floating speed of the lobster-like microrobot was greatly improved. When the frequency was higher than 0.4 Hz, the microrobot was no longer able to float upward.

29.5.5 Walking, Rotating and Hand Manipulation Experiments

In these tests, first the microrobot walked toward the target object and the pair of claws at the front of the microrobot bent toward each other to grasp the object. Then the microrobot rotated clockwise and walked forward to the desired position while grasping the object. Finally, the microrobot opened its two fingers and walked backward, as shown in Fig. 29.11.

29.5.6 Obstacle-Avoidance Experiments

Lobsters live in murky environments and their heads are equipped with a pair of antennae, which are used as sensors. To imitate an actual lobster and walk through a relatively complex environment, the microrobot uses three short-range proximity sensors to detect the direction and distance of an object. The direction and distance of an obstacle can be determined from the output of the three sensors. The microrobot can then alter its motion, either by walking backward, or by rotating clockwise or counter clockwise.

An obstacle-avoidance experiment was also carried out with the inchworm-inspired microrobot [31, 32]. Due to the low rotating efficiency of this unit and the high installation position of the sensors on top of the body, it was difficult to detect an obstacle with a low profile, and a long time was required to avoid a very wide obstacle.

We carried out the obstacle-avoidance experiments for the lobster-inspired microrobot on a flat underwater surface. In these tests, first the microrobot walked toward the obstacle, using legs C to H at a frequency of 1 Hz and an input voltage of 6 V. When the distance between the microrobot and the obstacle decreased to about 20 mm, the three proximity sensors detected the obstacle. The microrobot then stopped and rotated clockwise, continuing until the right, middle and left sensors were successively unable to detect the obstacle. Once this was accomplished, the robot stopped rotating and walked forward.

The lobster-like microrobot implemented underwater walking, rotating, grasping and surfacing/diving motions. As the actual lobster usually crawls at the bottom of the ocean, it isn't good at swimming, which is just the auxiliary motion while fleeing. So, the developed lobster-inspired microrobot also had a low swimming efficiency by curling/uncurling its tail part and swinging its four swimmeret-like drivers to swim.

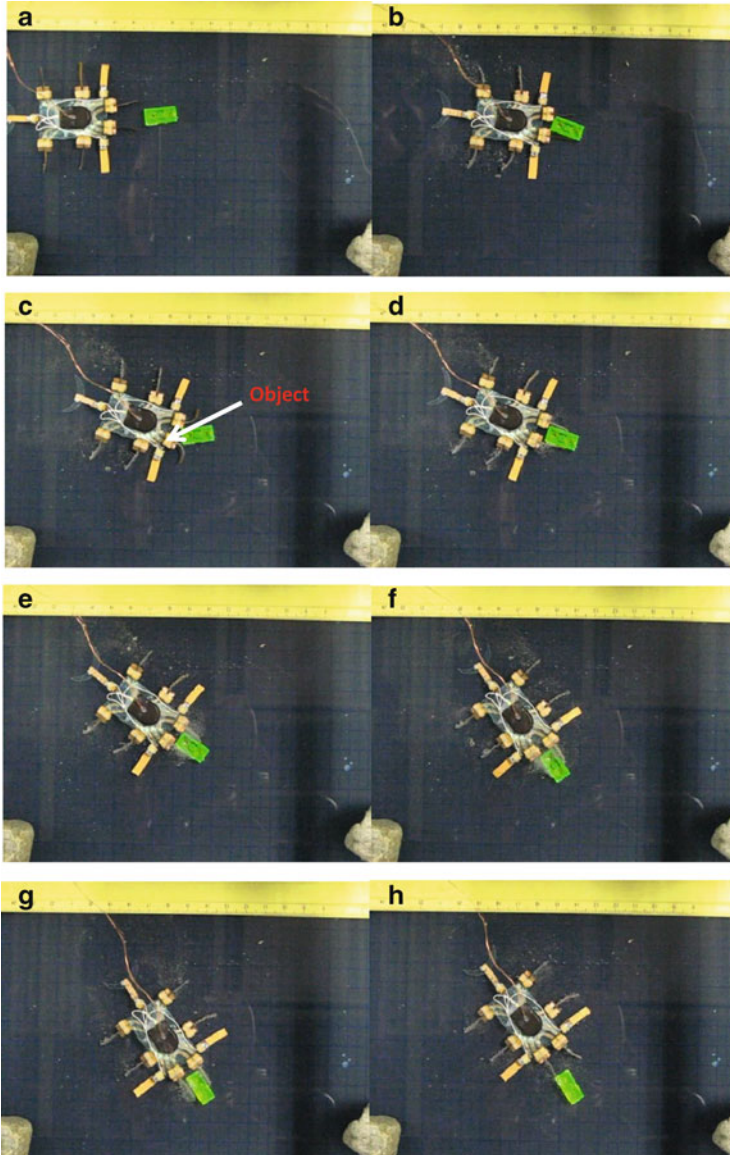


Fig. 29.11 Walking, rotating, and hand manipulation experiment. (a) Initial state, (b) Walking motion, (c) Opening two fingers, (d) Grasping motion, (e) Rotational motion, (f) Walking forward, (g) Opening two fingers, (h) Walking backward

29.6 Discussion

In Table 29.1, we summarize the underwater motions that have been developed for microrobot designs. Three methods of underwater walking have been implemented: inchworm-inspired, stick insect-inspired and lobster-inspired. All of these methods are driven by IPMC actuators and two IPMC actuators are used for one DOF legs. The position precision and flexibility are satisfactory, and the microrobot walking speeds are adjustable.

Floating can be achieved through the electrolysis characteristics of IPMC, or through jellyfish-inspired or fish bladder-inspired designs. The floating speeds of these three methods are adjustable. However, the position precision and flexibility are not satisfactory, except the flexibility of the jellyfish-inspired design.

Table 29.1 Types of underwater biomimetic locomotion

Underwater motions	Implemented methods	Actuators	Number of actuators	Position precision	Flexibility	Speeds
Walking motion	Inchworm-inspired [32]	IPMC	2	0.3 mm	Adjustable	Adjustable
	Stick insect-inspired [2]	IPMC	2	0.4 mm	Adjustable	Adjustable
	Lobster-inspired	IPMC	2	0.4 mm	Adjustable	Adjustable
Floating motion	Electrolysis characteristics of IPMC [32]	IPMC	4	No	No	Adjustable
	Jellyfish-inspired [1, 33–35]	SMA or IPMC	SMA (1) or IPMC (6)	No	Adjustable	Adjustable
	Fish bladder-inspired [29]	SMA	1	No	No	Adjustable
Swimming motion	Fish-inspired [29]	SMA or IPMC	SMA (2) or IPMC (1)	No	Adjustable	Adjustable
	Snake-like [15]	IPMC	≥ 2	No	No	Adjustable
	Butterfly-inspired [26]	SMA	2	No	Adjustable	Fast
	Manta ray-inspired [36]	IPMC	8	No	Adjustable	Adjustable
Grasping motion	Human finger-inspired [37]	IPMC	3	0.3 mm	Adjustable	Adjustable
		SMA		No		
	Lobster-inspired	IPMC	2	0.2 mm	Flexible	Adjustable
	Inchworm-inspired [32]	IPMC	6	0.3 mm	Adjustable	Adjustable

Similar to the body and/or caudal fin (BCF), and median and/or paired fin (MPF) type motion in fish classification, robots can be classified into a body and/or caudal actuator (BCA), and median and/or paired actuator (MPA), respectively [38]. Swimming is achieved through fish-inspired, snake-inspired, butterfly-inspired or manta ray-inspired designs (the first of which has received most attention). Fish-inspired and snake-inspired designs are actuated by a body and/or caudal actuator (BCA). Butterfly-inspired and manta ray-inspired designs are actuated by a median and/or paired actuator (MPA). The butterfly-inspired design achieves the fastest swimming speed. The flexibility and swimming speeds of four methods are satisfactory, except the snake-like design. For the mechanism limitation of oscillatory and the undulatory motions, none of these four methods can achieve a satisfactory position precision.

Human finger-inspired, inchworm-inspired and lobster-inspired finger locomotions have been proposed for grasping, and can be used to grasp and carry some underwater objects. These results can guide us in the design of microrobots with different dimensional and functional requirements [39–45].

29.7 Conclusion

In this chapter, stick insect-inspired two-phase walking locomotion, jellyfish-inspired floating/diving locomotion and inchworm-inspired crawling and grasping locomotion were discussed. The feasibility results for three previously developed prototype microrobots were then reviewed. The floating efficiency of a stick insect-inspired robot was not high. A jellyfish-like robot could not rotate and its walking motion was unsatisfactory, although its floating motion was improved. For an inchworm-inspired robot, there were large differences in the rotational radii of the outside four legs, leading to a large amount of slippage while rotating and low rotating efficiency. In addition, the inside six legs were used solely as fingers to grasp an object and could not contribute any buoyancy to the floating motion, so that the floating speed was slow.

To inherit the multi-functions of the inchworm-inspired microrobot and overcome its disadvantages, we introduced a new lobster-like microrobot, intended for underwater exploration in a restricted space. It uses nine IPMC actuators as legs or claws. Seven actuators are used as legs to implement walking, rotating and floating. The other two actuators are used as claws to grasp small objects. To imitate the antennae of actual lobsters, three infrared proximity sensors are installed on the head of the microrobot to detect an obstacle. We constructed a prototype of this microrobot, carried out experiments and measured the walking and rotating speeds on a flat underwater surface. Compared with the inchworm-like robot, its rotating motion was greatly improved. Diving/surfacing experiments were also conducted by electrolyzing the water around the actuator surfaces. From the results of these experiments, we demonstrated that the floating efficiency was higher than that of the inchworm-like robot. By inheriting the grasping motion of the inchworm-like

design, the lobster-inspired microrobot was also able to grasp small objects while walking or floating. Obstacle-avoidance experiments were also conducted, using three proximity sensors to detect the direction and distance of an obstacle. Thanks to the low installation position of the sensors and the high rotating efficiency, the lobster-inspired microrobot was able to detect an obstacle with a low profile and avoid the obstacle to realize closed-loop control.

We have included a summary of the implemented methods of underwater biomimetic locomotion. This can guide us in the design of microrobots with various purposes. Since these methods are driven by low voltages, they are safe and economical, and are suitable for actual applications, such as toys or devices used in an aquarium.

As the next step in our research, we will introduce a mother–son robot system to solve microrobot design problems requiring as low speeds and short operating times in restricted operating areas.

Acknowledgments This research is supported by Kagawa University Characteristic Prior Research Fund 2012.

References

1. Shi L, Guo S, Asaka K (2011) Development of a new jellyfish-type underwater microrobot. *Int J Robot Autom* 26(2):229–241
2. Guo S, Shi L, Asaka K, Li L (2009) Experiments and characteristics analysis of a bio-inspired underwater microrobot. In: Proceedings of the 2009 I.E. international conference on mechatronics and automation, Changchun, China, 9–12 August 2009
3. Lin X, Guo S (2012) Development of a spherical underwater robot equipped with multiple vectored water-jet-based thrusters. *J Intell Robot Syst* 67(3–4):307–321
4. Cavallo E, Micheline R, Filaretov V (2004) Conceptual design of an AUV equipped with a three degrees of freedom vectored thrusters. *J Intell Robot Syst* 39(4):365–391
5. Duchemin O, Lorand A, Notarianni M, Valentian D, Chesta E (2007) Multi-channel hall-effect thrusters: mission applications and architecture trade-offs. In: Proceedings of the 30th international electric propulsion conference, Florence, Italy, 17–20 September 2007
6. Behkam B, Sitti M (2006) Design methodology for biomimetic propulsion of miniature swimming robots. *J Dyn Syst Meas Control* 128(1):36–43
7. Zhang W, Guo S, Asaka K (2006) A new type of hybrid fish-like microrobot. *Int J Automat Comp* 3(4):358–365
8. Heo S, Wiguna T, Park H, Goo N (2007) Effect of an artificial caudal fin on the performance of a biomimetic fish robot propelled by piezoelectric actuators. *J Bionic Eng* 4(3):151–158
9. Villanueva A, Joshi K, Blottman J, Priya S (2010) A bio-inspired shape memory alloy composite (BISMAC) actuator. *Smart Mater Struct* 19(025013):1–17
10. Wang Z, Hang G, Li J, Wang Y, Xiao K (2008) A micro-robot fish with embedded SMA wire actuated flexible biomimetic fin. *J Sens Actuators A Phys* 144(2):354–360
11. Lee S, Kim K, Park I (2007) Modeling and experiment of a muscle-like linear actuator using an ionic polymer–metal composite and its actuation characteristics. *J Smart Mater Struct* 16(3):583–588

12. Liu S, Lin M, Zhang Q (2008) Extensional ionic polymer conductor composite actuators with ionic liquids. In: *Electroactive polymer actuators and devices (EAPAD)*, vol 6927, p 69270H
13. Nakadoi H, Sera A, Yamakita M, Asaka K, Luo Z, Ito K (2007) Integrated actuator-sensor system on patterned IPMC film: consideration of electronic interference. In: *Proceedings of the 2007 4th IEEE international conference on mechatronics*, 8–10 May 2006
14. McGovern ST, Spinks GM, Xi B, Alici G, Truong V, Wallace GG (2008) Fast bender actuators for fish-like aquatic robots. In: *Electroactive polymer actuators and devices (EAPAD)*, vol 6927, p 69271L
15. Kamamichi N, Yamakita M, Asaka K, Luo Z (2006) A snake-like swimming robot using IPMC actuator/sensor. In: *Proceedings of the 2006 I.E. international conference on robotics and automation*, Orlando, Florida, USA, 15–19 May 2006
16. Kim B, Kim D, Jung J, Park J (2005) A biomimetic undulatory tadpole robot using ionic polymer–metal composite actuators. *J Smart Mater Struct* 14:1579–1585
17. Ye X, Su Y, Guo S, Wang L (2008) Design and realization of a remote control centimeter-scale robotic fish. In: *Proceedings of the 2008 IEEE/ASME international conference on advanced intelligent mechatronics*, Xi'an, China, 2–5 July 2008
18. Yim W, Lee J, Kim KJ (2007) An artificial muscle actuator for biomimetic underwater propulsors. *J Bioinspir Biomim* 2(2):S31–S41
19. Ye X, Hu Y, Guo S, Su Y (2008) Driving mechanism of a new jellyfish-like microrobot. In: *Proceedings of 2008 I.E. international conference on mechatronics and automation*, Takamatsu, Japan, 5–8 August 2008
20. Kamamichi N, Kaneda Y, Yamakita M, Asaka K, Luo ZW (2003) Biped walking of passive dynamic walker with IPMC linear actuator. In: *Proceedings of SICE annual conference in Fukui*, Fukui University, Japan, 4–6 August 2003
21. Guo S, Mao S, Shi L, Li M (2012) Development of an amphibious mother spherical robot used as the carrier for underwater microrobots. In: *Proceedings of the 2012 ICME international conference on complex medical engineering*, Kobe, Japan, 1–4 July 2012
22. Guo S, Mao S, Shi L, Li M (2012) Design and kinematic analysis of an amphibious spherical robot. In: *Proceedings of 2012 I.E. international conference on mechatronics and automation*, Chengdu, China, 5–8 August 2012
23. Guo S, Okuda Y, Zhang W, Ye X, Asaka K (2006) The development of a hybrid underwater micro biped robot. *J Appl Bionics Biomech* 3(3):143–150
24. Zhang W, Guo S, Asaka K (2006) Development of an underwater biomimetic microrobot with both compact structure and flexible locomotion. *J Microsyst Technol* 13(8):883–890
25. Shi L, Guo S, Asaka K (2010) A novel multifunctional underwater microrobot. In: *Proceedings of the 2010 I.E. international conference on robotics and biomimetics*, Tianjin, China, 14–18 December 2010
26. Shi L, Guo S, Asaka K (2012) A novel jellyfish- and butterfly-inspired underwater microrobot with pectoral fins. *Int J Robot Autom* 27(3):276–286
27. Gong Y, Fan J, Tang C, Tsui C (2011) Numerical simulation of dynamic electro-mechanical response of ionic polymer-metal composites. *J Bionic Eng* 8:263–272
28. Gao B, Guo S (2010) Development of an infrared ray controlled fish-like underwater microrobot. In: *Proceedings of the 2010 I.E. international conference on automation and logistics*, Hong Kong & Macau, China, 16–20 August 2010
29. Gao B, Guo S, Ye X (2011) Motion-control analysis of ICPF-actuated underwater biomimetic microrobots. *Int J Mechatr Automat* 1(2):79–89
30. Shi L, Guo S, Asaka K (2011) A novel butterfly-inspired underwater microrobot with pectoral fins. In: *Proceedings of the 2011 I.E. international conference on mechatronics and automation*, Beijing, China, 7–10 August 2011
31. Shi L, Guo S, Asaka K (2011) A bio-inspired underwater microrobot with compact structure and multifunctional locomotion. In: *Proceedings of 2011 IEEE/ASME international conference on advanced intelligent mechatronics (AIM 2011)*, Budapest, Hungary, 3–7 July 2011

32. Guo S, Shi L, Xiao N, Asaka K (2012) A biomimetic underwater microrobot with multifunctional locomotion. *Robot Autonom Syst* 60(12):1472–1473
33. Yeom S, Oh I (2009) A biomimetic jellyfish robot based on ionic polymer metal composite actuators. *J Smart Mater Struct* 18(085002):1–16
34. Villanueva A, Priya S, Anna C, Smith C (2010) Robojelly bell kinematics and resistance feedback control. In: *Proceedings of the 2010 I.E. international conference on robotics and biomimetics*, Tianjin, China, 14–18 December 2010
35. Villanueva A, Smith C, Priya S (2011) A biomimetic robotic jellyfish (Robojelly) actuated by shape memory alloy composite actuators. *Bioinspir Biomim* 6(3):1–16
36. Chen Z, Um TI, Bart-Smith H (2011) A novel fabrication of ionic polymer-metal composite membrane actuator capable of 3-dimensional kinematic motions. *Sens Actuators A Phys* 168(1):131–139
37. Jain RK, Patkar US, Majumdar S (2009) Micro gripper for micromanipulation using IPMCs (ionic polymer metal composites). *J Sci Ind Res* 68(1):23–28
38. Chu W, Lee K, Song S, Han M, Lee J, Kim H, Kim M, Park Y, Cho K, Ahn S (2012) Review of biomimetic underwater robots using smart actuators. *Int J Precis Eng Manuf* 13(7):1281–1292
39. Shi L, Guo S, Mao S, Li M, Asaka K (2013) Development of a lobster-inspired underwater microrobot. *Int J Adv Robot Syst* 10:1–15. doi:[10.5772/54868](https://doi.org/10.5772/54868)
40. Shi L, Guo S, Li M, Mao S, Xiao N, Gao B, Song Z, Asaka K (2012) A novel soft biomimetic microrobot with two motion attitudes. *Sensors* 12(12):16732–16758
41. Guo S, Li M, Shi L, Mao S (2012) A smart actuator-based underwater microrobot with two motion attitudes. In: *Proceedings of 2012 I.E. international conference on mechatronics and automation*, Chengdu, China, 5–8 August 2012
42. Shi L, Guo S, Asaka K (2012) Modeling and experiments of IPMC actuators for the position precision of underwater legged microrobots. In: *Proceedings of the 2012 I.E. international conference on automation and logistics*, Zhengzhou, China, 15–17 August 2012
43. Park I, Kim S, Kim D, Kin K (2007) The mechanical properties of ionic polymer-metal composites. In: *Journal of electroactive polymer actuators and devices (EAPAD)*, vol 6524, p 65241R
44. Pan Q, Guo S, Okada T (2011) A novel hybrid wireless microrobot. *Int J Mechatr Automat* 1(1):60–69
45. Ha NS, Goo NS (2010) Propulsion modeling and analysis of a biomimetic swimmer. *J Bionic Eng* 7(3):259–266

Chapter 30

Medical Applications

Tadashi Ihara

Abstract Current applications of soft actuators in medical fields are discussed. Included here are polymer, elastomer, and gel actuators along with biocompatibility issues. The applications expands to a wide range of medical devices: artificial muscles, muscle alternatives, prosthetic devices, catheters, stents and surgical instruments. With the nature of medical applications, shown here are not only from articles but from many patent documents.

Keywords Actuator • Biocompatibility • Elastomer • Gel • Medical device • Polymer

30.1 Medical Applications of Soft Actuators

Current medical devices utilize a variety of actuators including electric, pneumatic, hydraulic, or mechanical actuators. For example, many blood pumps and surgical assist robots use electric motors, precision injection pumps use mechanical actuators, patient lifts use pneumatic or hydraulic actuators, to name a few.

They are applied not only externally but also internally implanted such as seen in left ventricular assist device (LVAD) used for heart failure patients. However, those conventional actuators are usually bulky, heavy, and require external energy supply.

Recent advances in soft actuator technology are paving way to overcome the limitations of those conventional actuators. In actual biological muscles, either skeletal, smooth or cardiac muscles, actuation is quite different from conventional mechanical actuators. While conventional actuators create either rotational, linear or combined motions, biological muscles contract and expand generating bending, stretch and rotational motions [1–4].

Soft actuators currently under study provide non-conventional actuation devices that are small in size, light weighted, least energy consuming which enable noiseless motion of contraction, bending, or linear motions. Soft actuators would provide innovative medical applications such as artificial muscles, implantable pumps, new

T. Ihara (✉)

Department of Clinical Engineering, Suzuka University of Medical Science, Suzuka, Japan
e-mail: ihara@suzuka-u.ac.jp

catheter devices and drug delivery systems. Those new devices designed for medical applications may in turn provide novel industrial applications.

A number of materials has been investigated for use as medical devices including dielectric gels, ion polymer gels, dielectric elastomers, liquid crystal elastomers, conductive polymers and carbon nanotubes. This article reviews current studies of medical applications of soft actuators by materials. Also, a brief review on biocompatibility of soft actuator materials is provided.

30.2 Polymer Film/Resin Actuators

Polymer actuators have many advantages in medical use; thin, light weight, quick in response, operates on very small voltage, and flexible in shaping. Numerous medical applications with polymer actuators have been proposed and some are in practical use.

One of the earliest medical application of polymer actuators is a catheter driving ion polymer metal compound (IPMC). National Institute of Advanced Industrial and Science and Technology (AIST) has developed a catheter bending mechanism by attaching a pair of IPMC membrane onto a catheter enabling 4 directional bending motion by applying voltage on the membranes [5]. Conventionally, catheters are directed by a twisting motion at the hand of a doctor to place it at a precise location guiding it to the correct branching blood vessels under fluoroscopy. By using IPMC actuator, quick and precise operations can be achieved by bending them to a desired direction (Fig. 30.1).

Boston Scientific Limited had developed a localized drug delivery system using drug-loaded nanocapsules [6]. An electroactive-polymer-actuated (EAP-actuated) stent, which shrinks with applied potential and expands to contact a body lumen upon releasing the potential (Fig. 30.2). With this apparatus, precision drug delivery such as anti-inflammatory agents, anti-thrombotic agents, anti-neoplastic agents, or anesthetic agents can be achieved at desired target sites for sustained length of time.

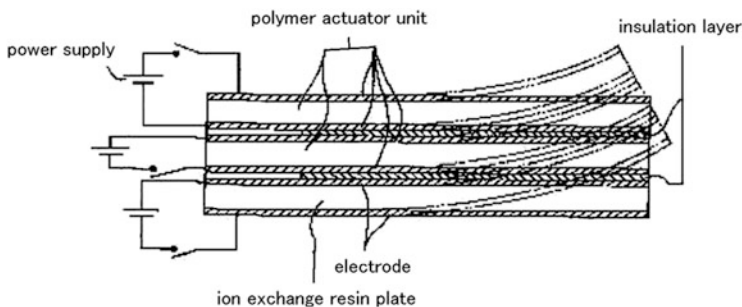


Fig. 30.1 A catheter device that changes the bending direction arbitrarily by IPMC

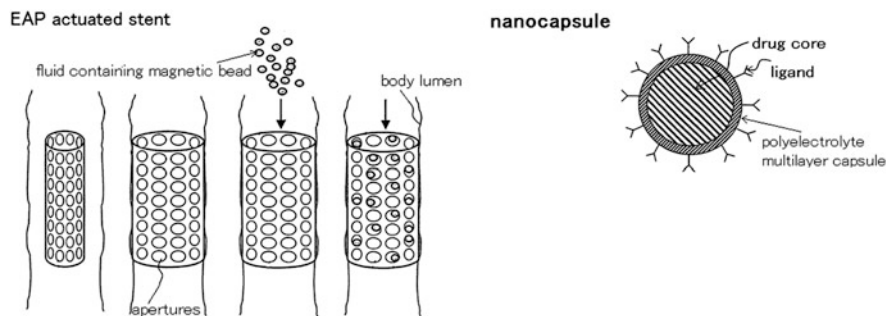


Fig. 30.2 Electroactive polymer actuated drug eluting stent: schematic illustration of expansion of the stent and the release of drug containing nanocapsule (*left*) and the structure of the nanocapsule (*right*)

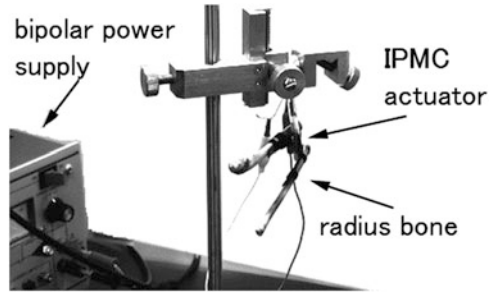
Eidenschink et al. has developed a mechanism to expand a balloon used for percutaneous transluminal coronary angioplasty (PTCA) using conductive polymer [7]. The balloon reopens the occluded coronary artery by inflating it with 5–6 atmospheric pressure. By using conductive polymer, the new PTCA device enables: (1) compact folding of the balloon at the time of retrieval of the balloon by twisting the catheter, (2) precise shape formation of the balloon by controlling the expansion and contraction of the balloon by the conductive polymers equipped along the axial direction of the balloon, (3) step by step expansion of the balloon adjusting to the morphology of coronary artery driven by the conductive polymers, (4) expansion and folding of a stent used with PTCA balloon driven by the conductive polymers.

Another catheter related application include the control of a balloon for atherectomy [8]. Atherectomy is applied when the clot of the coronary artery could not be removed by the balloon catheter, e.g., PTCA. It scrapes the clot by a multiple tiny blades arranged outside the balloon. Conductive polymers provide precise control of the blade movement.

Conductive polymers are also applied for aortic aneurism coil placed to prevent rupture of thoracic or abdominal aortic aneurism. Boston Scientific SciMed Inc. has developed a method to utilize conductive polymer as an actuator that expand and contract the filter element which retrieves the dislodged blood clot. Also it is used as a lock and release switch of a fixation connector at the anastomosis site of blood vessels [9] as well as an expansion-contraction mechanism of a sleeve which protects a catheter [10]. Related application is a non-radiopaque expandable marker by a conductive polymer used to identify the position of stents or grafts within the patient body [11].

Another important medical application of polymer actuators is the control of medical pumps such as the micro-pumps for drug delivery system, drainage pumps, blood pressure control pumps. Soltanpour et al. has devised a way to control the chamber volume of a micro-pump using IPMC, particularly for the use of implantable intraocular pressure control [12]. Searete developed an implantable, remote control osmotic pressure pump [13].

Fig. 30.3 An artificial joint actuated by ion polymer metal compound



Developing artificial muscle by polymer actuators has been a challenge due mainly to its relatively small generating force. Despite its inherent difficulty, its numerous advantages as an artificial muscle actuator including its quick response, flexibility in shaping, low driving voltage, and biocompatibility may be an important factor in implementing them in clinical use.

Ihara et al. succeeded in driving a small radius bone by an IPMC membrane: the developed force was enhanced by adjusting the thickness of the IPMC [14–16] (Fig. 30.3).

Shahinpoor et al. has developed a mechanism in which an IPMC membrane is controlled by biological signal such as nerve action potentials [17]. Scorvo et al. has developed a mechanism that controls the bending and stretching motion of a plaster cast by conductive polymers [18]. Furthermore, a cardiac muscle assist device with conductive polymer was developed by Mower et al. [19]. This is called an active cardiac envelope that assists a failing heart by wrapping it and help contracting it. It has a self battery charging function by the motion of the heart as well as sensing function of cardiac muscle contraction using the sensing function of conductive polymers.

Pavad Medical, Inc. developed a unique medical application of conductive polymer. They developed a tethered airway implants using conductive polymers by which sleep apnea patients can keep the airway open by releasing the occluding tongue [20, 21]. Hegde et al. announced an application of conductive polymer for actuation of sphincter anus that enables release of anus at defecation as well as holding anus at rest [22].

Shahinpoor et al has developed a polyacryl nitrile (PAN) artificial muscle to treat ptosis patients by inserting the PAN membrane under the palpebral conjunctiva. Using acid solution drip the PAN membrane contracts and raises the eyelid [23] (Fig. 30.4).

Ethicon Endo-Surgery has utilized conductive polymers for the driving mechanism of hydraulic actuator of a scalpel that operates by holding tissues and blood vessels [24] (Fig. 30.5).

Boston Scientific Scimed, Inc. had developed electroactive polymer based artificial sphincters and artificial muscle patches [25]. The artificial urethral sphincter treats patients with incontinence that arises from malfunction of the patient's urethral sphincter or anal canal. The artificial sphincter comprises a cuff that comprises one or more electroactive polymer actuators and placed around a body lumen, and a control unit that expand or contract the cuff (Fig. 30.6).

Fig. 30.4 Ptosis correction artificial muscle by polyacryl nitrile (PAN) membrane

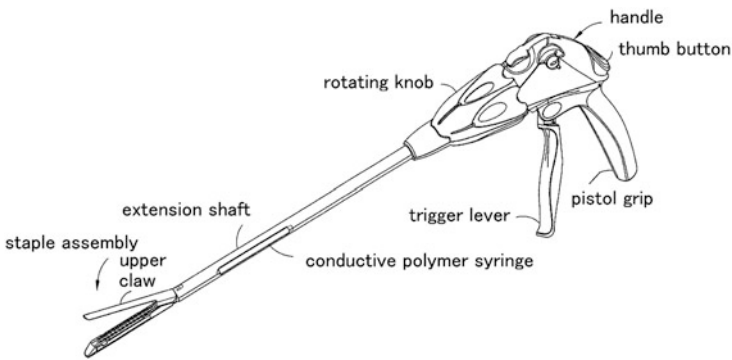
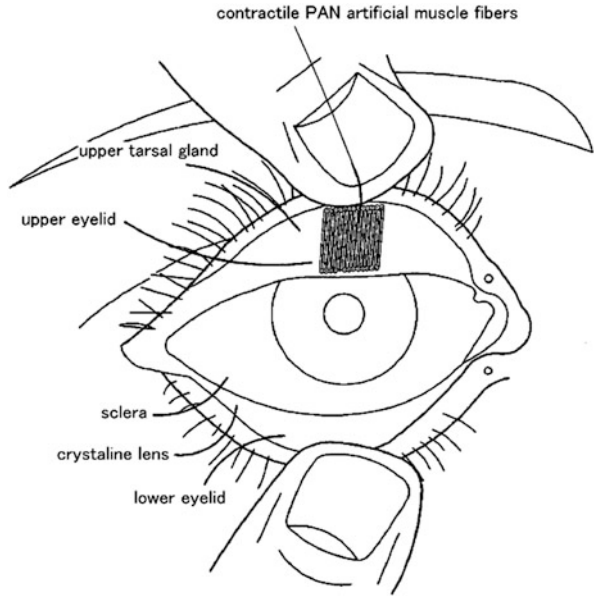


Fig. 30.5 Stapling scalpel using conductive polymer syringe

Fig. 30.6 Electroactive polymer based artificial sphincters

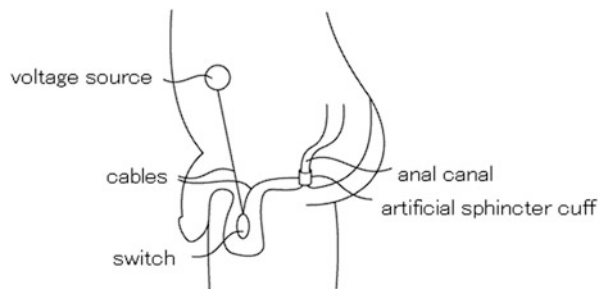


Fig. 30.7 Electroactive polymer based patches for cardiac assist device

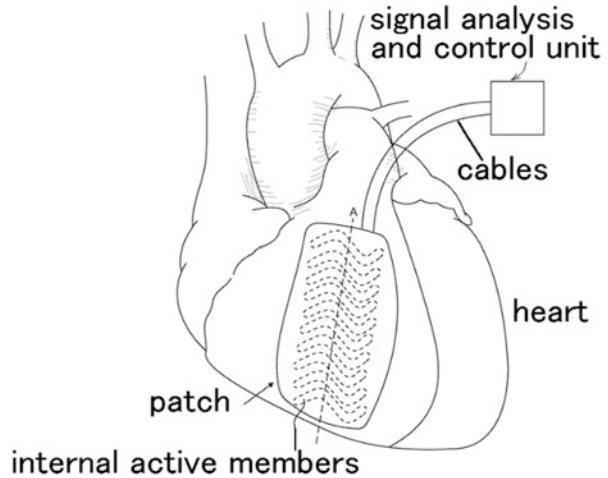
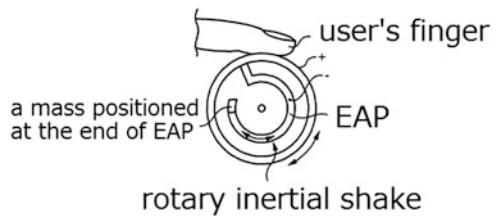


Fig. 30.8 A haptic device with a wheel rotated by EAP



In other embodiments, the electroactive polymer (EAP) units are used to assist heart failure patients. EAP units are arranged on a patch and each internal active members of EAP is controlled by a signal analysis and control unit (Fig. 30.7).

An indirect medical assist device using conductive polymers has also been investigated. Shcena et al. developed a haptic stylus for automatic braillewriter. In one embodiment, a wheel with EAP and an inertial mass is rotationally moved by the electroactive polymer actuator [26]. Also, in other embodiment, polymer material enables a constantly renewable media for Braille (Fig. 30.8) [27].

30.3 Elastomer Actuators

Elastomer is a popular material in medicine; bandages, liners used in limb prosthetics, and artificial blood vessels are some of the typical applications. The elastic material features expandable sheet or tube that fits to the organ's shape and self-fixation mechanism. The application of medical elastomer material would be extended when they are actuated and controlled with external signals. Potentially, elastomer has very high force generating capacity and would be very suitable when

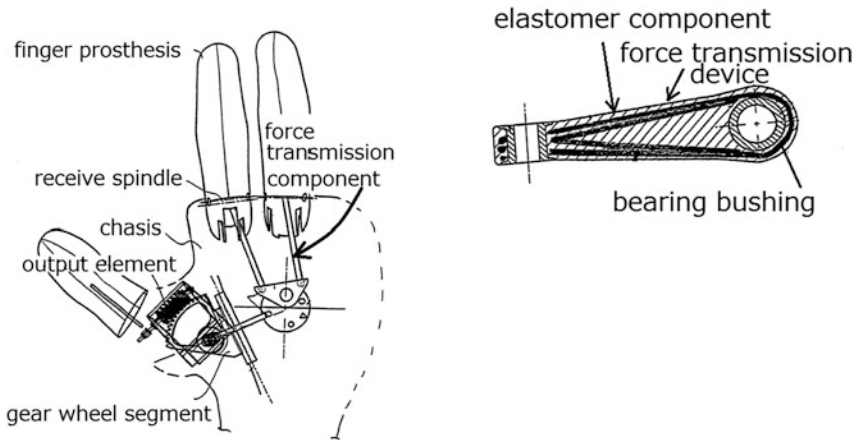


Fig. 30.9 Schematic illustration of the finger prosthesis unit with the force transmission component (*left*) and the structure of the force transmission device with elastomer component (*right*)

used as artificial muscle [28]. However, to generate large force, elastomer requires high voltage or high energy and has not been preferred as an implantable device.

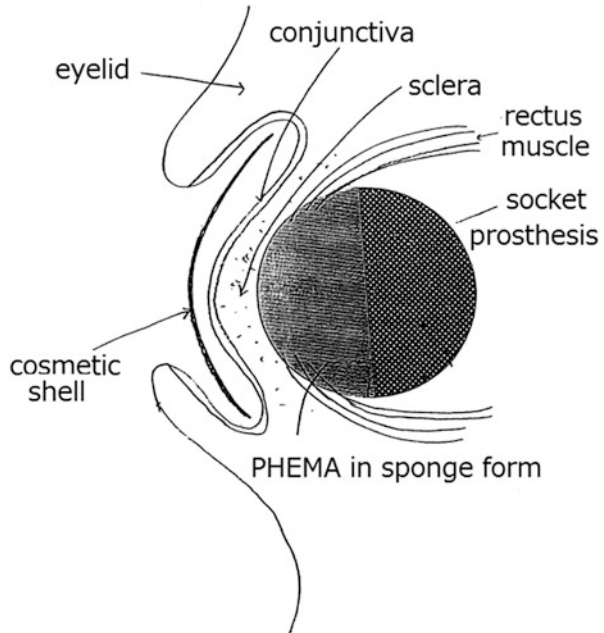
Puchhammer has invented a hand/finger prosthesis device using elastomer component [29]. The elastomer component in the force transmission device provides actuation of finger prosthesis unit around the swiveling axis (Fig. 30.9).

30.4 Gel Actuators

Gels are also widely used material for medical use including ointment, skin lotion, ultrasound conductive gel, cooling gel, gel pads and others. As an actuator, gel actuators demonstrate relatively large generated force and has been studied as a promising artificial muscle material. On the other hand, its relative slowness in response compared to biological muscle had been the obstacle to the practical implementations. Gels respond to electric field, temperature, pH, or chemical solvent and can swell or shrink as much as 1,000 times [30, 31]. Also these displacement changes are reversible. Recent gel actuators demonstrate much faster response and are rigorously studied as practical artificial muscle material.

Lions Eye Institute invented an ocular socket prosthesis using hydrophilic polymer [32]. It is designed to place a prosthetic eyeball when a patient had to remove his/her eye because of severe trauma, infection, tumor, or untreatable glaucoma. The prosthetic eye globe is then pushed into the ocular socket, and the muscles are attached to the prosthesis device, and covering tissues are sutured over the outside. Once the tissues have healed, an external cosmetic shell can be worn over this surface under the eyelids, and give reasonable natural appearance and “eye” movement (Fig. 30.10).

Fig. 30.10 Ocular socket prosthesis device



Chiarelli et al. has developed an artificial urethral sphincter driven by antagonistic polyvinyl-alcohol contractile elements powered by changes in acetone concentration [33]. Also, Beebe et al. has announced a micro-pump using hydrogel [34]. A drug delivery system using hydrogel is also devised [35].

30.5 Biocompatibility

In applying soft actuators for medical use, it is imperative to verify their biocompatibilities. Thorough examination of biocompatibility in each actuators are just in its early phase. Wang et al. evaluated biocompatibility of polypyrrole (PPy) in vitro and in vivo and found that PPy extraction solution showed no evidence of acute and subacute toxicity, pyretogen, hemolysis, allergen, and mutagenesis; only light inflammation was found during 6 months of the postoperation, when the PPy-silicone tube bridged across the gap of the transected sciatic nerve [36]. Miriani et al. examined cell toxicity of conductive polymers for use as a coating material of electrodes. They found no cell toxicity of poly 3,4 ethylenedioxythiophene (PEDOT) in either cases of using polystyrene sulfonate (PSS) or phosphate buffered saline (PBS) as doping ion [37].

Morishima et al. has developed a contraction enhancement device for cardiac muscle cell culture using ion polymer metal compound (IPMC) and found no cytotoxicity of IPMC [38].

Ferraz N. et. al. investigated cytotoxicity of polymer polypyrrole (PPy) that may be used in electrochemically controlled hemodialysis. The biocompatibility evaluation was conducted on indirect toxicity assays with fibroblasts and monocyte cell lines and an acute toxicity test in mice. They found no cytotoxic response in vitro or in vivo. However, it was shown that aging of the composite had a negative effect on biocompatibility, regardless of the storage condition.

Moura RM and de Queiroz AA studied biocompatibility of polyaniline nanotubes (PANINTs) that may be used for cardiac tissue engineering applications [39]. PANINTs are combined with the highly hydrophilic polyglycerol dendrimers (PGLDs) to improve its electroactive functionalities. The PGLD-coated PANINTs showed no cytotoxic effects to Chinese hamster ovary cells.

30.6 Conclusion

Medical actuators by soft materials including gels, elastomers, and polymers have a number of advantages over conventional metal or plastic actuators either externally applied or implanted in patient's body.

In most medical applications, the goal of soft actuators is to provide artificial muscle or in other words, alternative devices to biological muscles. However, practical implementation of soft actuators are investigated in diverse area of medical field such as pump actuation module, pump valve control, micromanipulator for gene therapy, catheter motion assist device.

To answer the questions on whether the given soft actuators meet required response, force, durability, electrical safety and biocompatibility, still more rigorous investigations are needed. Despite the difficulties in implementation and required studies in biocompatibilities some soft actuator devices are already in clinically application and still more will come.

References

1. Carpi F, Smela E (2009) Biomedical applications of electroactive polymer actuators. Wiley, Chichester
2. Kim KJ, Tadokoro S (2007) Electroactive polymers for robotics applications: artificial muscles and sensors. Springer, London
3. Shahinpoor M, Kim KJ (2007) Artificial muscles: applications of advanced polymeric nanocomposites. CRC, Boca Raton
4. Higuchi T, Suzumori K, Tadokoro S (2010) Next-generation actuators leading breakthroughs. Springer, London

5. Agency of Industrial Science and Technology, Ministry Of International Trade and Industry (1999) Polymeric actuators and process for producing the same. EP 0943402 A2, 1999
6. Boston Scientific Limited (2013) Localized drug delivery using drug-loaded nanocapsules and implantable device coated with the same. EP20040706932, 2013
7. Eidenschink T, Wise D, Sutermeister D, Prairie E, Alkhatib Y, Gregorich D, Jennings A, Heidner M, Godin D, Gunderson RC, Blix J, Jagger KA, Volk AK (2008) Medical balloon incorporating electroactive polymer and methods of making and using the same. US Patent Application 20080086081A1, Apr 10, 2008
8. Weber J, Eidenschink T, Elizondo D, Simer L (2005) Electrically actuated medical devices. US Patent Application 0165439 A1, Jul 28, 2005
9. Boston Scientific SciMed Inc. (2008) Electroactive polymer actuated medical devices. US Patent 6,969,395 B2. Mar 4, 2008
10. Boston Scientific SciMed, Inc. (2007) Protection by electroactive polymer sleeve. US Patent Application 0032851 A1, Feb 8, 2007
11. Eidenschink T, Jagger KA, Sutermeister D, Volk AK, Wise D, Heidner M, Boston Scientific SciMed, Inc. (2008) Electroactive polymer radiopaque marker. US Patent Application 0021313 A1, Jan 24, 2008
12. Soltanpour D, Shahinpoor M (2003) Implantable micro-pump assembly. US Patent 6,589,198 B1, Jul 8, 2003
13. Searete LLC (2007) Osmotic pump with remotely controlled osmotic flow rate. US Patent Application 0135797 A1, Jun 14, 2007
14. Ihara T, Nakamura T, Horiuchi T, Mukai T, Asaka K (2009) Simulated muscle type actuator using IPMC (2009). In: The 10th SICE system integration division annual conference, Tokyo, Dec. 24, 2009, pp 598–599
15. Nakamura T, Ihara T, Horiuchi T, Mukai T, Asaka K (2009) Measurement and modeling of electro-chemical properties of ion polymer metal composite by complex impedance analysis. SICE J Contr Meas Syst Integ 2(6):373–378
16. Ihara T, Nakamura T, Ikada Y, Asaka K, Oguro K, Fujiwara N (2004) Application of a solid polymer electrolyte membrane-gold to an active graft. In: Proceedings of the 2nd international conference on artificial muscle, Ikeda, 2004
17. Shahinpoor M (2005) Bio-potential activation of artificial muscles. US Patent Application 0085925 A1, Apr 21, 2005
18. Scorvo SK (2005) Adjustable orthotic brace. US Patent 6,969,365 B2, Nov 29, 2005
19. Mower MM, Roberts JL, Light ED (2006) Cardiac contractile augmentation device and method therefor. US Patent Application 0217774 A1, Sept 28, 2006
20. Pavad Medical, Inc. (2007) Tethered airway implants and methods of using the same. US Patent Application 0246052 A1, Oct 25, 2007
21. Pavad Medical, Inc. (2008) Self charging airway implants and methods of making and using the same. US Patent Application 0046022 A1, Feb 21, 2008
22. Hegde AV, Choi GY, Buch WS (2006) Artificial sphincter. US Patent Application 0047180 A1, Mar 2, 2006
23. Shahinpoor M, Soltanpour D (2009) Surgical correction of ptosis by polymeric artificial muscles. US Patent 7,625,404B2, Dec 1, 2009
24. Ethicon Endo-Surgery, Inc. (2006) Surgical instrument having fluid actuated opposing jaws. US Patent Application 0289600 A1, Dec 28, 2006
25. Boston Scientific SciMed, Inc. (2012) Electroactive polymer based artificial sphincters and artificial muscle patches. EP1503703A2, 2012
26. Schena BM (2008) Haptic devices using electroactive polymers. US Patent 7339572 B2, 2008
27. Schena BM, Immersion Corporation (2010) Haptic stylus utilizing an electroactive polymer. US Patent 7,679,611 B2, Mar 16, 2010
28. Anderson IA, Gisby TA, McKay TG, O'Brien BM, Calius EP (2012) Multi-functional dielectric elastomer artificial muscles for soft and smart machines. J Appl Phys 112:041101
29. Puchhammer G (2009) Hand prosthesis, EP20060828626, 2009

30. Tanaka T, Nishio I, Sun ST, Ueno-Nishio S (1982) Collapse of gels under an electric field. *Science* 218:467
31. Ogawa N, Hashimoto M, Takasaki M, Hirai T (2009) Characteristics evaluation of PVC gel actuators. In: IEEE/RSJ international conference on intelligent robots and systems, Oct 2009
32. Lions Eye Inst. Australia Inc. (1998) Ocular Socket Prosthesis. Patent WO1998008549 A1, Mar 5, 1998
33. Chiarelli P, De Rossi D, Umezawa K (1989) Progress in the design of an artificial urethral sphincter. In: Proceedings of the 3rd Vienna international workshop on functional electrostimulation, Vienna, Sept 1989
34. Beebe DJ, Moore JS, Bauer JM, Yu Q, Liu RH, Devadoss C, Jo BH (2000) Functional hydrogel structures for autonomous flow control inside microfluidic channels. *Nature* 404:588–590
35. Peppas NA, Bures P, Leobandung W, Ichikawa H (2000) Hydrogels in pharmaceutical formulations. *Eur J Pharm Biopharm* 50:27–46
36. Wang X, Gu X, Yuan C, Chen S, Zhang P, Zhang T, Yao J, Chen F, Chen G (2004) Evaluation of biocompatibility of polypyrrole in vitro and in vivo. *J Biomed Mater Res A* 68:411–422
37. Miriani RM, Abidian MR, Kipke DR (2008) Cytotoxic analysis of the conducting polymer PEDOT using myocytes. *Proc IEEE Eng Med Biol Soc* 1841–1844:2008
38. Ferraz N, Strømme M, Fellström B, Pradhan S, Nyholm L, Mhryanyan A (2012) In vitro and in vivo toxicity of rinsed and aged nanocellulose-polypyrrole composites. *J Biomed Mater Res A* 100(8):2128–2138
39. Moura RM, de Queiroz AA (2011) Dendronized polyaniline nanotubes for cardiac tissue engineering. *Artif Organ* 35(5):471–477

Chapter 31

Micro Pump Driven by a Pair of Conducting Polymer Soft Actuators

Masaki Fuchiwaki

Abstract Micro pumps are regarded as key components of many MEMS devices. They are widely used in the fluid operations systems of fields ranging from chemistry and biotechnology to mechanical engineering. The micro pumps developed to present generally incorporate piezoelectric-element, thermopneumatic, electrostatic, electromagnetic, electroosmotic, electromagnetic-fluid, and various other drives, but along with their reduced size they have increased in component number and structural complexity. The conducting polymer soft actuator based on polypyrrole opens widely and closes completely as a result of electrochemical oxidation and reduction, respectively. The opening and closing movement of the soft actuator, inside which the cation-driven layer is arranged, becomes large because the anion-driven layer that is arranged outside is the predominant driver. We developed a micro pump that is driven by a pair of conducting polymer soft actuator based on polypyrrole and clarified the fundamental characteristics and transport mechanism of the micro pump. The proposed micro pump can transport fluids unidirectionally without backflow by means of a pair of conducting polymer soft actuators that open and close. Furthermore, a wider range of flow rates and a greater maximum delivery head was obtained with the proposed micro pump. The energy consumption rate of the proposed micro pump is dramatically lower than the energy consumption rates of conventional micro pumps because the conducting polymer soft actuator can be driven with a low voltage.

Keywords Conducting polymer • Micro pump • Polypyrrole • Soft actuator

31.1 Introduction

Micro pumps are regarded as key components of many MEMS devices. They are used in μ -TAS (micro total analysis systems) and other chemical analysis systems and as insulin injectors and other medical devices. They are also widely used in the fluid operations systems of fields ranging from chemistry and biotechnology to

M. Fuchiwaki (✉)
Kyushu Institute of Technology, Fukuoka, Japan
e-mail: futiwaki@mse.kyutech.ac.jp

mechanical engineering. This has brought a rising demand for a greater range of flow rates, higher precision in flow resolution, continuous constant-flow transport, and other advances in micro pump performance [1, 2].

The micro pumps developed to present generally incorporate piezoelectric-element, thermopneumatic, electrostatic, electromagnetic, electroosmotic, electromagnetic-fluid, and various other drives [3, 4], but along with their reduced size they have increased in component number and structural complexity. Piezoelectric elements have also led to problems in increased electric power consumption. This has led to a need for micro pumps that are simpler in structure and higher in energy efficiency, and for actuators that can drive them with higher efficiency and precision by a simple mechanism.

In the present study, we propose and investigate the development of a micro pump driven by conducting polymer soft actuators. Conducting polymers are known for their capability to shift between resistive and metallic conductivity together with swelling and contraction (electrochemomechanical deformation) under electrochemical redox reactions [5, 6]. These properties have led to strong interest in their development for use as soft actuators and artificial muscle [7–19]. Conducting polymer soft actuators are thin films and are therefore small and lightweight. They are also characterized by high responsiveness and durability, flexibility, plasticity, and capability for operation with low driving voltages.

Soft actuator films composed of polypyrrole (PPy) conducting polymers in particular are a focus of interest as a new functional material [20–25] because of their high mechanical strength and their drive capability in solutions in a broad range of pH levels as well as in air and water [26]. Conducting polymer soft actuators in various configurations envisioned for practical application have recently been developed, and studies have been reported on their application to micro pumps. Ramirez et al. [27] have developed a flexural soft actuator and constructed a micro pump using them in pairs. Wu et al. [28] have developed a tubular soft actuator and applied it to micro pump development. Fuchiwaki et al. [29] have developed a flat soft actuator that undergoes local deformation and reported the oscillation volume of a micro pump driven by this actuator.

In the present study, the objective is to investigate the development of an open/close PPy soft actuator, by constructing a micro pump driven by a pair of these actuators and elucidating its basic properties in terms of the relation between flow characteristics and developed pressure head and the rate of energy consumption.

31.2 Experimental

31.2.1 Preparation for Conducting Polymer Soft Actuator

A conducting polymer soft actuator was created by electrochemical polymerization, as shown in Fig. 31.1. Pyrrole was used as a monomer, and dodecylbenzenesulfonic acid (DBS) and tetra-*n*-butylammonium bis (trifluoromethanesulfonyl) imide

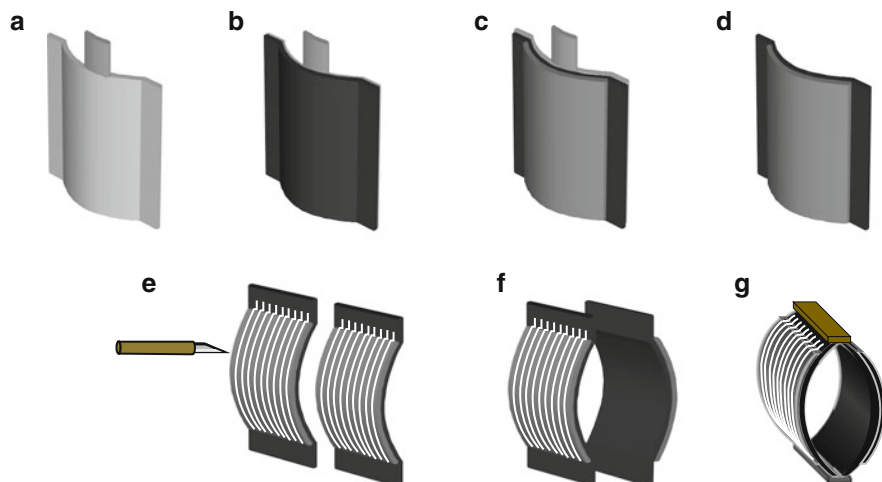


Fig. 31.1 Preparation of the conducting polymer soft actuator that opens and closes as a driving source for the micro pump

(TFSI) were used as the supporting electrolytes. Titanium plate (Ti), platinum plate, and silver wires were used for the work electrode, the counter electrode, and the reference electrode, respectively.

We first performed electrodeposition on a $20 \times 20 \text{ mm}^2$ Ti plate by aqueous electrolyte solution containing 0.15 M of pyrrole monomer and 0.25 M of DBS. The deposition was conducted in galvanostatic mode with a current density of 1.0 mA cm^{-2} for 2,000 seconds at room temperature. PPy.DBS film with a thickness of approximately $30 \mu\text{m}$ was deposited on the Ti plate (Fig. 31.1a, b), the cation-driven layer film. Both sides of the PPy.DBS film were then covered with tape insulated by fluorine resin, and an aqueous electrolyte solution containing 0.15 M of pyrrole monomer and 0.25 M of TFSI was used for electrodeposition on a $10 \times 15 \text{ mm}^2$ piece of PPy.DBS film. PPy.TFSI film with a thickness of approximately $30 \mu\text{m}$ was deposited on the PPy.DBS film, the anion driven layer film (Fig. 31.1c). PPy.TFSI/PPy.DBS film having a bimorph structure was deposited on the center part on the Ti plate to a thickness of approximately $60 \mu\text{m}$. The deposited PPy.TFSI/PPy.DBS film was then removed from the Ti plate to obtain the conducting polymer soft actuator film (Fig. 31.1d). Finally, slits were made in the soft actuator film at intervals of 1.0 mm (Fig. 31.1e). We prepared two PPy.TFSI/PPy.DBS films with slits and installed these films face to face (Fig. 31.1f). The upper and lower parts of these films were fixed by platinum sheets. This procedure produces a single soft actuator that opens and closes (Fig. 31.1g).

31.3 Results and Discussions

31.3.1 Opening and Closing Movement of the Soft Actuator

The deformations of the proposed conducting polymer soft actuator are shown in Fig. 31.2. In the present study, the platinum plate and silver wire were used as counter and reference electrodes, respectively. The soft actuator was driven in a mixture solution of water and a LiTFSI solution of 0.5 mol L^{-1} and a sine wave having a frequency of 0.005 Hz was given to the applied voltages of from -1.2 to 1.0 V .

The conducting polymer soft actuator opens and closes by electrochemical oxidation and reduction, respectively. The actuator completely closes in reduction and opens widely in oxidation. In reduction, Li^+ (as cations) are doped, causing the cation-driven layer to expand, and TFSI $^-$ (as anions) are de-doped, causing the anion-driven layer to contract. As a result, the soft actuator closes. In oxidation, Li^+ are de-doped in the cation-driven layer, causing the cation-driven layer to contract, and TFSI $^-$ are doped in the anion-driven layer, causing the anion-driven layer to expand. As a result, the soft actuator opens. Opening and closing the soft actuator in which the anion-driven layer and cation-driven layer were placed adversely was difficult. The expansion ratio of the PPy.TFSI film used as the anion-driven layer was greater than that of the PPy.DBS film used as the cation-driven layer [30–33]. Furthermore, since the conducting polymer soft actuator produces a greater force in contraction than in expansion, opening and closing of the soft actuator having the inner cation-driven layer becomes large because the outer anion-driven layer becomes the predominant driver.

31.3.2 Micro Pump Driven by Two Conducting Polymer Soft Actuators

A micro pump with a pair of the conducting polymer soft actuator that opens and closes to provide the driving source is shown in Fig. 31.3. The pump is a capsule-type pump with a length of 60.0 mm and a diameter of 21.0 mm. Two conducting polymer soft actuators are situated inside the pump as a driving source.

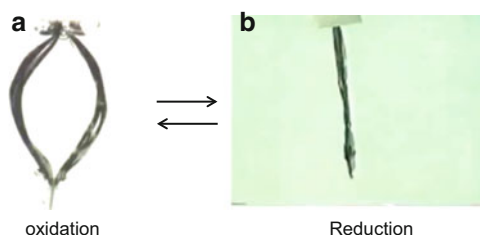


Fig. 31.2 Deformations of the proposed conducting polymer soft actuator

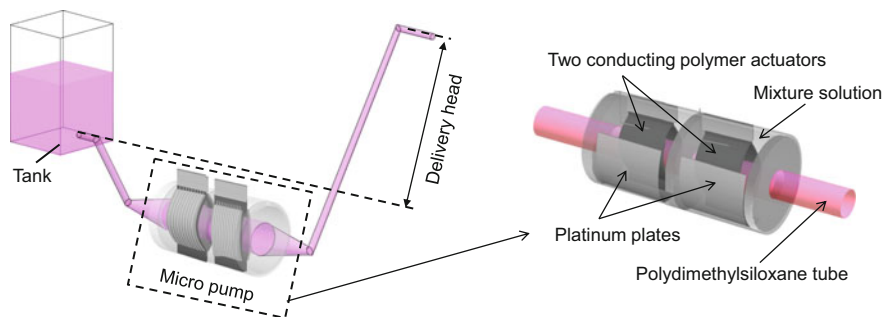


Fig. 31.3 Micro pump with conducting polymer soft actuators

A polydimethylsiloxane tube with an outside diameter of 5.0 mm and a thickness of 20 μm is incorporated. A platinum plate as a counter electrode and a silver wire as a reference electrode are arranged outside the soft actuator. The tube was filled with the red-colored water to be transported, and the capsule was filled with the mixture solution of water and 0.5 mol L^{-1} LiTFSI solution. The pump is not equipped with a valve. The micro pump, with its drive consisting of two tube open/close actuators in a flexible (polydimethylsiloxane) tube, is shown schematically in Fig. 31.3. Red-colored water is pumped from the head tank by the actuator action to obtain a unidirectional flow to the tube outlet, which is used to determine the pressure head developed by the pumping action. The applied voltages for actuators Inlet and Outlet ranged from -1.2 to $+1.0$ V and from -0.6 to $+0.5$ V, respectively, and the frequency was 0.005 Hz. Moreover, a phase difference of 180° was given to actuators Inlet and Outlet.

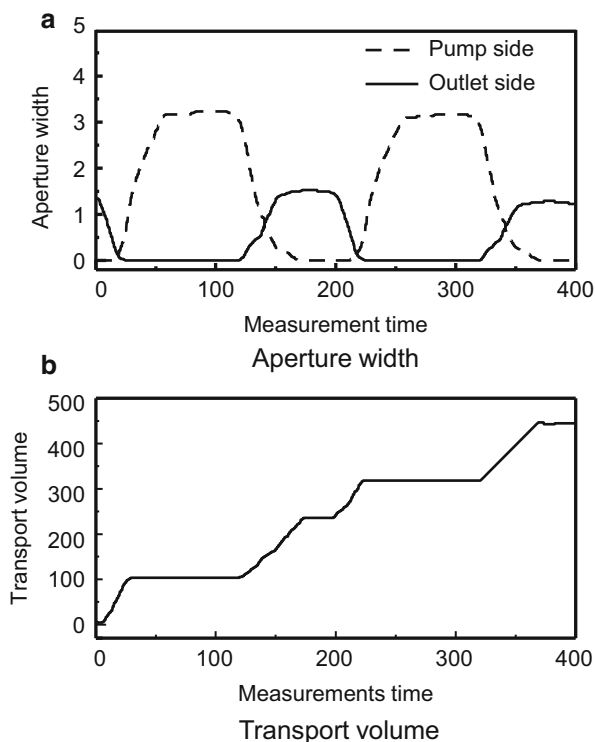
31.3.3 Unidirectional Fluid Transport of the Micro Pump

Figure 31.4a, b show the relation between the actuator aperture widths (defined as the greatest distance between the two PPy film components of each actuator at a given time) (Fig. 31.4a) and the micro pump transport volume (Fig. 31.4b). The horizontal and vertical axes in Fig. 31.4a indicate the measurement time and the actuator aperture widths at that time, respectively, with the upstream aperture width (on the pump side) shown by the broken line and the downstream aperture width (on the outlet side) by the solid line. The horizontal and vertical axes in Fig. 31.4b indicate the measurement time and the cumulative transport volume at that time, respectively.

As shown by Fig. 31.4a, the maximum aperture widths attained by the upstream and downstream actuators were $d_1 = 3.2$ mm and $d_2 = 1.4$ mm, respectively, and the ratio between the two, d_1/d_2 , was thus approximately 2.9.

The results, as shown in Fig. 31.4b indicate that the micropump induces unidirectional fluid transport free from backflow. Comparison of this graph with the

Fig. 31.4 (a) Variation with time of the actuator aperture widths. (b) Variation with time of the transport volume of the micro pump driven by the conducting polymer soft actuator



aperture widths in Fig. 31.4a shows the relation between the transport volume and the aperture widths during a complete pump cycle. In the time from $t = 0$ to 20 s, the transport volume is approximately 100 μL . During this period, the upstream actuator is fully closed and the downstream actuator effectively propels the fluid farther downstream, toward the outlet. During the period from $t = 20$ to 100 s, the upstream actuator opens and thus draws fluid into the tube from the tank, but the downstream actuator remains closed and thereby effectively prevents any change in cumulative transport volume. From $t = 110$ to 170 s, the upstream actuator is closing while the downstream actuator is opening, and the fluid is again transported downstream by the micropump. The fluid transport during this period up to full closure of the upstream actuator is approximately 150 μL . With the upstream actuator then closed, the cumulative volume flow remains constant with no reverse flow until the downstream actuator again begins to close and thus completes the pump cycle. In one complete cycle of the soft actuator pair opening and closing, i.e., a pump cycle, approximately 250 μL of the fluid is transported. With repetition of this cycle, the unidirectional fluid transport proceeds without backflow.

It was also found possible to obtain unidirectional transport of the fluid with a phase difference of 210° between the two actuators, but the flow rate was lower. With other inter-actuator phase differences, backflow arose and unidirectional transport could not be obtained. The ratio d_1/d_2 between the upstream and

downstream actuator aperture widths also strongly affected the fluid transport. The maximum transport volume occurred with a d_1/d_2 ratio of approximately 2.9, and unidirectional transport could not be obtained with d_1/d_2 ratios of 1.0 or lower.

31.3.4 Transport Mechanism of the Micro Pump

The transport mechanism was investigated by Computational Fluid Dynamics (CFD) analysis, as it was not possible to visualize the flow field in the micropump tube. The mechanism was elucidated using ANSYS CFX 11.0 to simulate the flow field generated in the tube by the actuator pair. The equations governing the fluid movement are the continuous (1) and Navier–Stokes equations (2). Discretization was performed by finite volume. The computation mesh number was approximately 250,000, with a structured mesh used for mesh generation. The assumed boundary conditions were no-slip boundaries at the walls and free boundaries open to the atmosphere at the open tube ends. The frequency of actuator open/close movement was taken as 0.005 Hz, with an inter-actuator phase difference of 180° . The computational period and time interval were three pump cycles (one cycle per 200 s) and 1.0 s, respectively. A laminar-flow model was used in view of the relatively low Reynolds number.

$$\frac{\partial \rho}{\partial t} + \nabla \cdot (\rho U) = 0 \quad (31.1)$$

$$\frac{\partial \rho U}{\partial t} + \nabla \cdot (\rho U \otimes U) = \nabla \cdot (-P\delta + \mu(\nabla U + (\nabla U)^T)) \quad (31.2)$$

Figure 31.5 shows the time series of the flow field generated during a single pump cycle, in terms of velocity vectors on the x – z cross-section passing through the centerline of the micro pump tube with the transport direction to the right, as obtained in the simulation.

Figure 31.5a–d show the flow field as the downstream actuator closes with the upstream actuator remaining closed throughout. As shown, velocity vectors are substantially absent in the tube on the upstream side of the pump but quite large on the downstream side. This clearly indicates that the downstream actuator is propelling the fluid as it closes while the upstream actuator blocks related backflow. Figure 31.5e–g show the flow field as the upstream actuator opens while the downstream actuator is fully closed. Large velocity vectors now appear in the region leading into the upstream actuator but no velocity vectors are visible in or beyond the downstream actuator. This indicates that the upstream actuator is drawing fluid from the holding tank while the downstream actuator blocks any backflow from its own region. Figure 31.5i–l show the next stages of the flow field, in which the upstream actuator closes as the downstream actuator opens. In the initial stage of these actuator movements, velocity vectors exit the tube region in the

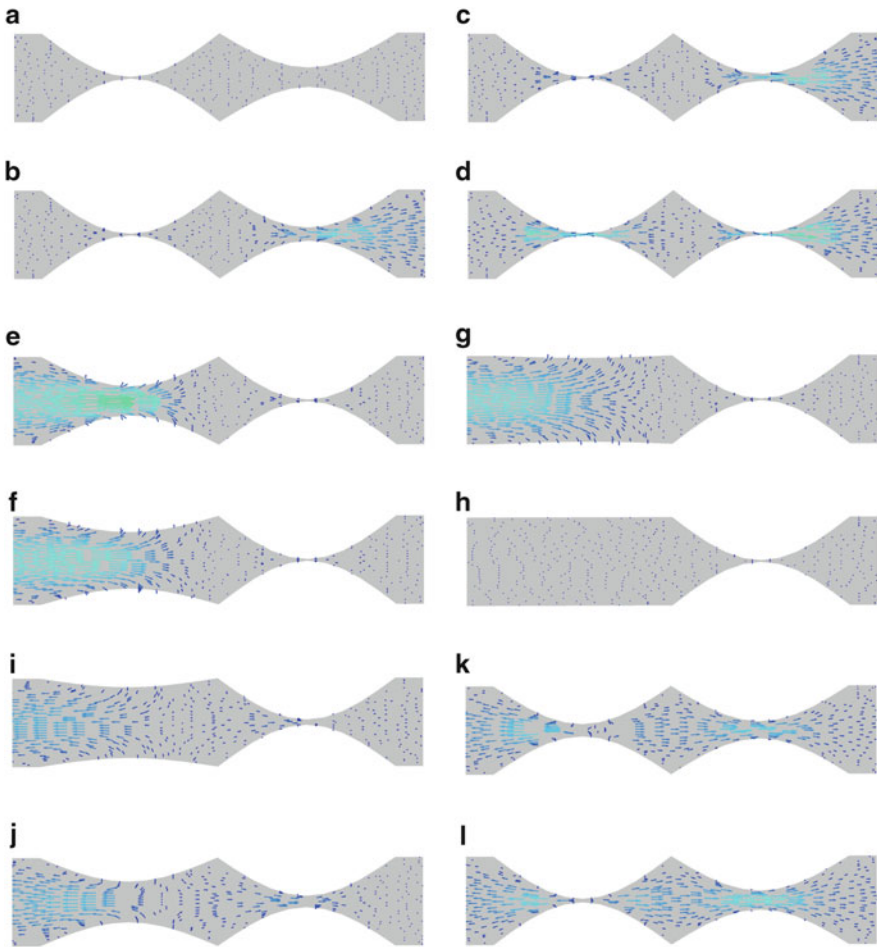
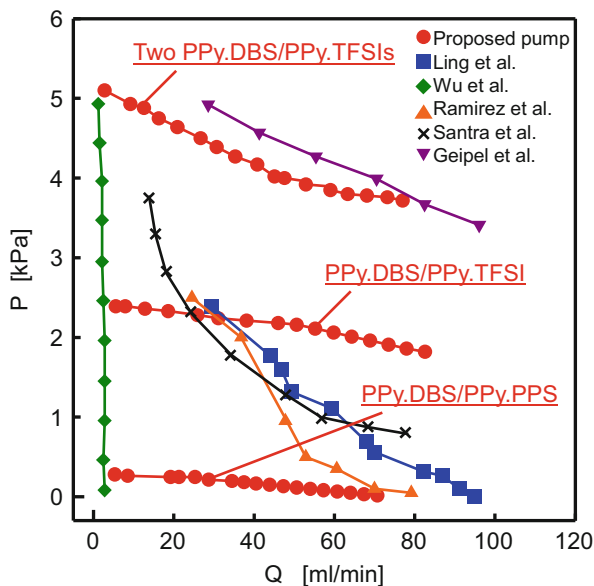


Fig. 31.5 (a)–(d) Flow field as the downstream actuator closes with the upstream actuator remaining closed throughout. (e)–(h) Flow field as the upstream actuator opens while the downstream actuator is fully closed. (i)–(l) Next stages of the flow field, in which the upstream actuator closes as the downstream actuator opens

upstream actuator on both sides just as other velocity vectors enter the tube region in the downstream actuator from both sides. This indicates that the upstream actuator is propelling the fluid in both directions just as the downstream actuator is drawing fluid toward itself from both directions. The overall flow, however, is governed by the action of the upstream actuator movement because, as shown in Fig. 31.5a and also evident from these figures, its deformation volume is substantially larger than that of the downstream actuator. The fluid flow is thus in the desired direction of transport. The end result is unidirectional transport under pump-cycle repetition.

Fig. 31.6 Relationship between pressure of the delivery head and flow rate for the micro pump driven by the conducting polymer soft actuator



31.3.5 Pressure and Flow Rate Characteristics of the Micro Pump

The relationship between pressure of the delivery head and the flow rate for a micro pump driven by a pair of the conducting polymer soft actuator is shown in Fig. 31.6. PPy.DBS/PPy.PPS indicates the result obtained using *p*-phenolsulfonic acid (PPS) in NaCl solution, rather than TBATFSI, as the supporting electrolyte, and two PPy.DBS/PPy.TFSIs indicates the case in which two PPy.DBS/PPy.TFSI films are laminated.

In all cases, the pressures of the delivery head decreased with the increase in flow rate in the range of approximately 2.0–83.0 $\mu\text{L min}^{-1}$. However, when TBATFSI was used as the supporting electrolyte, the pressures ranged from 1.8 to 2.4 kPa, which is approximately five times greater than that in the case of PPS. When TBATFSI is used as the supporting electrolyte, the ion radius of TFSI⁻ is larger than that of Cl⁻ [30–33]. Therefore, significant deformations of the conducting polymer actuator occurred and the occurrence power of the conducting polymer actuator is great. Furthermore, the pressures became approximately ten times greater than in the case of PPS, when two PPy.DBS/PPy.TFSI actuators were used as a driving source. In the case of two PPy.DBS/PPy.TFSI actuators, since two PPy.DBS/PPy.TFSI films were laminated, the occurrence power of the conducting polymer actuator increases.

31.3.6 Energy Consumption Rate of the Micro Pump

Energy consumption rate was calculated in order to evaluate the fundamental characteristics of the micro pump. The energy consumption rate indicates the energy consumed while the micro pump transports fluids at a unit flow rate. Therefore, the performance of the pump increases as the energy consumption rate decreases. The energy consumption rate E_c $\text{J } \mu\text{L}^{-1}$ was calculated by the following Eqs. (31.3) and (31.4).

$$E = \frac{\int VI dt}{t} \quad [\text{J s}^{-1}] \quad (31.3)$$

$$E_c = E/Q \quad [\text{J } \mu\text{L}^{-1}] \quad (31.4)$$

where E , I , V , t , E_c and Q represent the energy consumed per unit time J s^{-1} , current A, voltage V, time s, energy consumption rate $\text{J } \mu\text{L}^{-1}$, and flow rate $\mu\text{L s}^{-1}$, respectively. The energy consumption rate of the proposed micro pump and those of the conventional micro pumps [27, 34–36] at approximately $28 \mu\text{L min}^{-1}$ are listed in Table 31.1.

The energy consumption rate of the proposed micro pump is dramatically lower than the energy consumption rates of the conventional micro pumps. These results indicate that the energy consumption rate of the proposed micro pump driven by the conducting polymer soft actuator is much lower than the energy consumption rates of the conventional micro pumps and that the efficiency of the proposed micro pump is higher than the efficiencies of the conventional micro pumps. In particular, the energy consumption rate of the proposed micro pump is much lower than those of the micro pumps with piezo actuators [36] and permanent magnet actuators [35] as driving sources. As shown in Table 31.1, the operating voltage of the conducting polymer soft actuator is much lower than the operating voltages of piezo actuators and permanent magnet actuators. Therefore, the power consumption of the conducting polymer soft actuator is lower, which may lead to the realization of a high-efficiency micro pump.

Table 31.1 Energy consumption rate of the proposed micro pump compared with data for selected conventional micropumps at approximately $28 \mu\text{L min}^{-1}$

	Our pump (28.7 [mL/min])	Ling et al. [35] (29.4 [mL/min])	Ramirez et al. [27] (24.5 [mL/min])	Santra et al. [34] (24.4 [mL/min])	Geipel et al. [36] (28.6 [mL/min])
Energy consumption rate [mJ/mL]	68	1,396	181	4,666	154

31.4 Conclusion

We developed a micro pump that is driven by a pair of conducting polymer soft actuator based on polypyrrole and clarified the fundamental characteristics and transport mechanism of the micro pump. The proposed micro pump can transport fluids unidirectionally without backflow by means of a pair of conducting polymer soft actuators that open and close. Furthermore, a wider range of flow rates and a greater maximum delivery head was obtained with the proposed micro pump. The energy consumption rate of the proposed micro pump is dramatically lower than the energy consumption rates of conventional micro pumps because the conducting polymer soft actuator can be driven with a low voltage.

References

1. Teymoori MM, Ebrahim AS (2005) Design and simulation of a novel electrostatic peristaltic micromachined pump for drug delivery applications. *Sens Actuators A* 117:222–229
2. Jeong OC, Konishi S (2007) Fabrication and drive test of pneumatic PDMS micro pump. *Sens Actuators A* 135:849–856
3. Nguyen N, Huang X, Chuan TK (2002) MEMS-micropumps: a review. *ASME J Fluids Eng* 124:385–392
4. Lee CJ, Tu KZ, Lei U, Hsu CJ, Sheen HJ (2005) A valveless micropump with asymmetric Obstacles. In: Proceedings of the 16th international symposium on transport phenomena, Prague, 2005
5. Chiang CK, Druy MA, Gau SC, Heeger AJ, Louis EJ, MacDiarmid AG, Park YW, Shirakawa H (1978) Synthesis of highly conducting films of derivatives of polyacetylene. *J Am Chem Soc* 100:1013–1021
6. Nigrey PJ, MacDiarmid AG, Heeger AJ (1979) Electrochemistry of polyacetylene, $(\text{CH})_x$: electrochemical doping of $(\text{CH})_x$ films to the metallic state. *J Am Chem Soc Chem Commun* 594–595
7. Otero TF, Broschart M (2006) Polypyrrole artificial muscles: a new rhombic element. Construction and electrochemomechanical characterization. *J Appl Electrochem* 36:205–214
8. Otero TF, Martínez JG (2012) Artificial muscles: a tool to quantify exchanged solvent during biomimetic reactions. *Chem Mater* 24:4093–4099
9. Otero TF, Martínez JG, Zaifoglu B (2013) Using reactive artificial muscles to determine water exchange during reactions. *Smart Mater Struct* 22:104019
10. Otero TF, Alfaro M, Martinez V, Perez MA, Martinez JG (2013) Biomimetic structural electrochemistry from conducting polymers: processes, charges, and energies. Coulovol-tammetric results from films on metals revisited. *Adv Funct Mater* 23:3929–3940
11. Baughman RH (1991) Conducting polymers in redox devices and intelligent materials systems. *Makromol Chem Macromol Symp* 51:193–215
12. Otero TF, Rodriguez J, Angulo E, Santamaria C (1993) Artificial muscles from bilayer structures. *Synth Met* 57:3713–3723
13. Kaneto K, Kaneko M, Min Y, MacDiarmid AG (1995) “Artificial muscle”: electromechanical actuators using polyaniline films. *Synth Met* 71:2211–2212
14. Baughman RH (1996) Conducting polymer artificial muscles. *Synth Met* 78:339–353
15. Otero TF, Sansihena JM (1997) Bilayer dimensions and movement in artificial muscles. *Bioelectrochem Bioenerg* 42:117–122

16. Lewis TW, Moulton SE, Spinks GM, Wallace GG (1997) Optimisation of a polypyrrole based actuator. *Synth Met* 85:1419–1420
17. Careema MA, Vidanapathirana KP, Skaarup S, West K (2004) Dependence of force produced by polypyrrole-based artificial muscles on ionic species involved. *Solid State Ion* 175:725–728
18. Smela E, Lu W, Mattes BR (2005) Polyaniline actuators: Part I. PANI(AMPS) in HCl. *Synth Met* 151:25–42
19. Spinks GM, Truong VT (2005) Work-per-cycle analysis for electromechanical actuators. *Sensor Actuators A* 119:455–461
20. Madden JD, Cush RA, Kanigan TS, Brenan CJ, Hunter IW (1999) Encapsulated polypyrrole actuators. *Synth Met* 105:61–64
21. Hutchison S, Lewis TW, Moulton SE, Spinks GM, Wallace GG (2000) Development of polypyrrole-based electromechanical actuators. *Synth Met* 113:121–127
22. Fuchiwaki M, Takashima W, Kaneto K (2001) Comparative study of electrochemomechanical deformations of poly(3-alkylthiophene)s, polyanilines and polypyrrole films. *Jpn J Appl Phys* 40:7110–7116
23. Bay L, West K, Skaarup S (2002) Pentanol as co-surfactant in polypyrrole actuators. *Polymer* 43:3527–3532
24. Otero TF (2013) Reactions drive conformations. Biomimetic properties and devices, theoretical description. *J Mater Chem B* 1:3754–3767
25. Otero TF, Martinez JG (2013) Structural and biomimetic chemical kinetics: kinetic magnitudes include structural information. *Adv Funct Mater* 23:404–416
26. Kaneto K, Sonoda Y, Takashima W (2000) Direct measurement and mechanism of electrochemomechanical expansion and contraction in polypyrrole films. *Jpn J Appl Phys* 39:5918–5926
27. Ramirez GS, Diamond D (2006) Biomimetic, low power pumps based on soft actuators. *Sens Actuators A* 135:229–235
28. Wu Y, Zhou D, Spinks GM, Innis PC, Megill WM, Wallace GG (2005) TITAN: a conducting polymer based microfluidic pump. *Smart Mater Struct* 14:1511–1516
29. Fuchiwaki M, Tanaka K, Kaneto K (2009) Planate conducting polymer actuator based on polypyrrole and its application. *Sens Actuators A* 150:272–276
30. Hara S, Zama T, Ametani A, Takashima W, Kaneto K (2004) TFSI-doped polypyrrole actuator with 26 % strain. *J Mater Chem* 14:1516–1517
31. Hara S, Zama T, Takashima W, Kaneto K (2004) Artificial muscles based on polypyrrole actuators with large strain and stress induced electrically. *Polym J* 36:151–161
32. Hara S, Zama T, Takashima W, Kaneto K (2004) Gel-like polypyrrole based artificial muscles with extremely large strain. *Polym J* 36:933–936
33. Hara S, Zama T, Ametani A, Takashima W, Kaneto K (2004) Enhancement in electrochemical strain of a polypyrrole–metal composite film actuator. *J Mater Chem* 14:2724–2725
34. Santra S, Holloway P, Batich CD (2002) Fabrication and testing of a magnetically actuated micropump. *Sens Actuators B* 87:358–364
35. Ling SJ, Yuan JL, Sung JL, Yi CH, Wu SY, Mi CT, Ching CH (2007) A stand-alone peristaltic micropump based on piezoelectric actuation. *Biomed Microdevices* 9:185–194
36. Geipel A, Goldschmidtboing F, Doll A, Jantschke P, Esser N, Massing U, Woias P (2008) An implantable active Microport based on a self-priming high-performance two-stage micropump. *Sens Actuators A* 145:414–422

Chapter 32

Elastomer Transducers

Mikio Waki and Seiki Chiba

Abstract Dielectric elastomers, transducers that couple the deformation of a rubbery polymer film to an applied electric field, show particular promise with features such as simple fabrication in a variety of size scales, high strain and energy density, high efficiency and fast speed of response, and inherent flexibility, environmental tolerance, and ruggedness. A variety of actuator configurations has been demonstrated at various size scales including rolled “artificial muscle” actuators, framed and bending beam actuators for efficient opto-mechanical switches, and diaphragm and thickness mode actuators for pumps and valves. The performance benefits of dielectric elastomers can allow for new generations of devices in microrobotics, communications, and biotechnology.

Dielectric elastomer has also been shown to operate in reverse as a generator. It has several characteristics make it potentially well suited for power takeoff systems using wave, water current, wind, human motion, etc.

Keywords Actuators • Artificial Muscles • Dielectric elastomers • Direct drive • EAP • Electroactive polymers • Generators • Renewable energy • Sensors

32.1 Introduction

Population growth and the quest for better living standards are expected to cause a surge in demand for energy in the twenty-first century. This increase in demand, combined with global warming and other environmental impacts suggests the need for new approaches to meeting our energy needs. Among the diverse measures proposed to meet our energy needs, we may take two possible approaches, i.e., (1) the use of high efficient actuators, and (2) the use of renewable energy. Dielectric elastomer (DE) transducers might be able to solve the both issues, as follows;

M. Waki
Wits Inc, 880-3 Oshiage, Sakura-City, Tochigi, Japan
e-mail: waki@wits-web.com

S. Chiba (✉)
Chiba Science Institute, 3-8-18 Yagumo, Meguro-ku, Tokyo, Japan
e-mail: schiba947@gmail.com

1. Using a DE transducer makes it possible to achieve a highly efficient transduction from electric energy into mechanical energy (the theoretical transduction efficiency is 80–90 %), which translates into a considerable energy saving compared with other actuator technologies such as electric motors with gearboxes [1].
2. Recently, the use of DE actuator in the reverse mode, in which deformation of the elastomer by external mechanical work is used to generate electrical energy, has been gaining more attention. DE has shown considerable promise for harvesting energy from environmental sources such as ocean waves, wind, water currents, human motion, etc. [2].

We will discuss possible applications of DE actuators, DE sensors, and DE generators in this chapter.

32.2 Background on DE Transducers

DE transducers are a new transducer technology that has been began an investigation by SRI International (R. Perline, S. Chiba et al.) in 1991 [3].

DE transducers that couple the deformation of a rubbery polymer film to an applied electric field, show particular promise with features such as simple fabrication in a variety of size scales (from micro to several meter scale), high strain (up 380 %) and energy density of 1 W/g (for comparison, electric motor with gearbox is 0.05 W/g), high efficiency (80–90 %) and fast speed of response (over 50 kHz), and inherent flexibility, environmental tolerance, and ruggedness [1] (see the detail of the principal in Chap. 13: Dielectric Elastmers).

As shown in Fig. 32.1 [1], DE technology occupies a unique performance space for actuation, giving much higher actuation pressure/densities than electrostatic and electromagnetic actuation, and much higher strains than piezoelectric and magnetostrictive actuation. It also is interesting to note that DE stress–strain performance is comparable to that of nature muscle. Hence the name “artificial muscle” is an appropriate description for DE technology.

DE transducers have moved from the research and development stage to the commercial domain with research and development on practical applications, and furthermore to the mass production stage.

32.3 DE Actuators and DE Sensors

As elastomers are light and deform like rubbers, they can show flexible movements like bionic actions. They can express “flexible and natural feeling” which systems with motors cannot imitate.

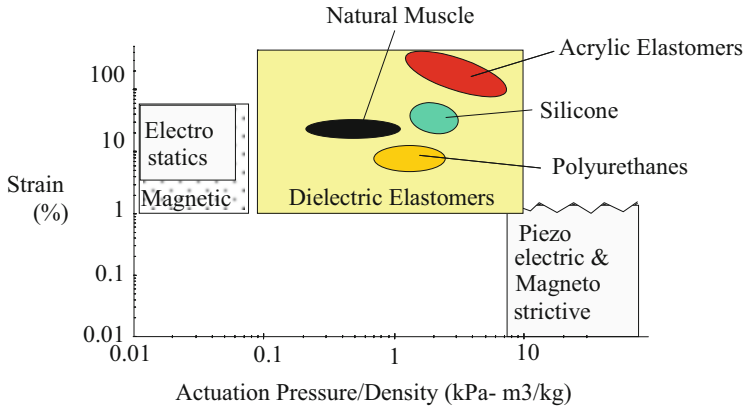


Fig. 32.1 Performance comparison of existing fast actuator technology, natural muscle, and DE

In addition to above, DE actuators do not use any gears and cams, thus enabling high efficiency and safe and smooth driving even if the speed or direction of movement are suddenly changed.

32.3.1 *Application of Robots (Include Care and Rehabilitation Purpose) and Sensors*

A wide array of proof-of-principle devices (see Fig. 32.2) for use in leg robots, swimming robots, snake like robots, compact inspection robots, gecko like robots for climbing up perpendicular walls or across ceilings, and flying robots, as well as in achieving compatibility with living organisms are currently developed [1].

The leg robot is particularly unique [4]. It has role actuators having 3-DOF, as shown in Fig. 32.3 [5], so it enables sideways stepping like a crab without turning around, when it collides with wall.

In near future, the DE technology will be applied to robots for medical treatments, rescue, care, personal use and industrial purpose in the near future.

We have already noted that DE actuators are also intrinsically position or strain sensors in Chap. 13, Dielectric Elastomers, since there is a direct proportionality between the change in the capacitance and elongation of DE actuators. As sensors, DEs can be used in all of the same configurations as actuators, as well as generators. In near future, therefore, smart shape robots or care equipments shown in SF movies may be appeared.

The ribbon form actuators having a sensor function can be used to measure force, or pressure as well as motion at the same time. This actuator can assist human motion. At the same time, it can work as motion feedback sensor. We hope that it may be useful for smart rehabilitation equipments for hands, legs, and fingers. Such equipments may be used to evaluate a recovery situation exactly. Figure 32.4 shows sensor grove for rehabilitation purpose [6].

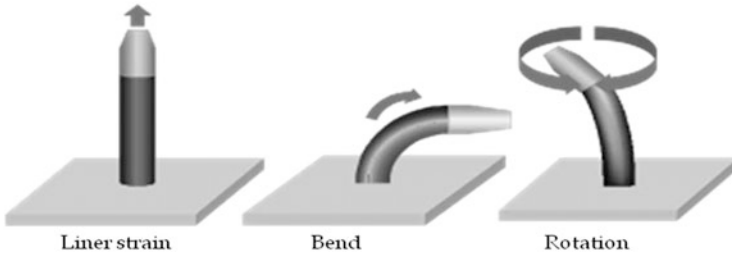


Fig. 32.2 A wide array of proof-of-principle devices

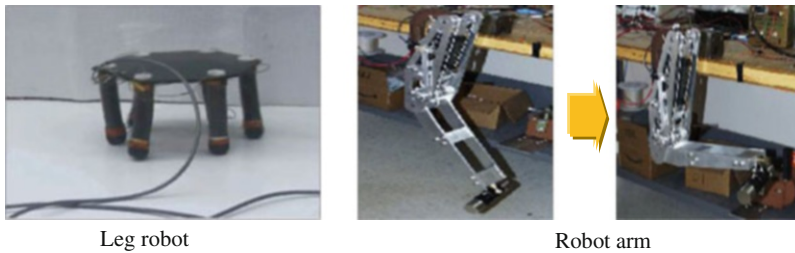


Fig. 32.3 Role actuator having 3-DOF

32.3.2 Application to Audio Equipment

DE has a very wide frequency range, from DC to 50 kHz, far beyond the audible range. Applications using the wide frequency of the DE include musical instruments, acoustic equipment, and vibration devices. The operation principle of the DE as a loudspeaker is very simple. The sound signal is superimposed on a DC bias voltage and the resulting voltage signal is applied across the electrodes of the DE. As the displacement of the DE can follow the temporal variation of the signals, sounds can be reproduced. There are several possible methods for the sound reproduction. Indeed, loudspeakers based on DE have already been demonstrated [7]. Here we describe a method using dipole speakers. This method has a very simple structure and effective performance.

Figure 32.5 shows a dipole speaker that has two opposed diaphragms located symmetrically about a central plane. The diaphragms can be operated in push-pull mode. Figure 32.6 shows how the voltage signal (comprised of the audible signal superimposed on the DC bias) can be used to drive the DE to produce sound.

A prototype of the dipole speaker made by Wits Inc. (Tochigi, Japan) uses DE cartridges (diaphragm with frame shown in Fig. 32.5). The outer diameter of the diaphragm is 100 mm and the inner diameter is 50 mm. The bias voltage and the maximum of the input signals are set to be 2 kV and $1 \text{ kV}_{\text{p-p}}$, respectively.

Fig. 32.4 DE sensor grove

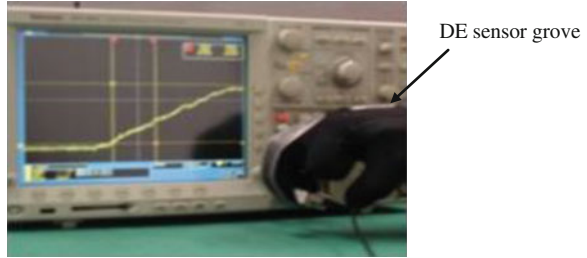


Fig. 32.5 Dipole speaker

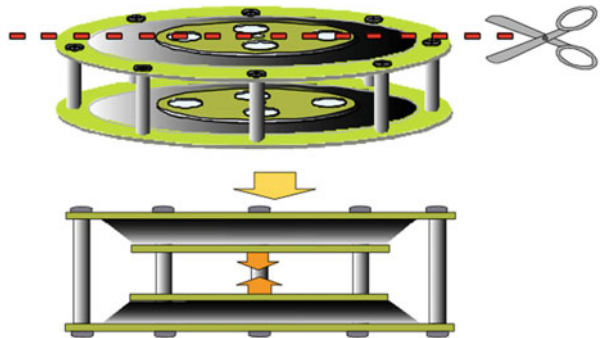
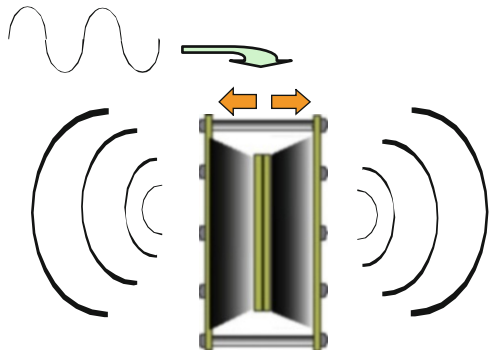


Fig. 32.6 Operations image of dipole speaker



The performance of this DE speaker was evaluated in the anechoic chamber of the Science and Technical Research Laboratories of Japan Broadcasting Corporation [8]. The loudspeaker was found to have moderately satisfactory frequency response from 0.5 kHz to more than 10 kHz (about 15 dB variation in SPL measured at 50 cm). The directionality of the speaker shows a significant difference between back-and-forth and right-and-left, confirming its expected desirable performance as a dipole speaker.

The harmonic distortion components are very small over the wide frequency range. This is another desirable feature of a DE dipole speaker. We believe that the performance of DE dipole speakers can be further improved by refining the design.

Fig. 32.7 DE Cartridge (left); DE stereo speaker system (right)



We are currently evaluating the performance of the speaker mounted in enclosures, and plan to evaluate next-generation speaker designs including spherical ones.

The DE cartridge used in the loudspeakers is thin and lightweight. When two pieces of the cartridge are used, the driving force that can be generated is up to 4 N. Thus, applications such as in sound insulation and vibration proofing, which use these cartridges as vibrators, also have been investigated [7]. Such application devices enable sound insulation and vibration proofing in the following manner. Actual vibrations and noise are detected by microphones or vibration pickups and converted into electric signals. Then, signals for canceling the electric signals are created and applied to the DE vibrators. The DE vibrators can act on the outer walls of buildings, the frames of equipment, and car bodies to counteract their vibrations or noise. In simple experiments with cars, it has been confirmed that sonic pressures larger than 50 dB can be reduced in a low frequency region (100–300 Hz) by setting up a DE vibrator in the roof of the car.

Since DE is a rubber like film, it is lightweight and its shape can be easily changed. Thus, a DE loudspeaker could be made to conform to almost any shape or surface contour. DE loudspeakers might be incorporated in housing, cars, industrial machines, and electric home appliances. Figure 32.7 shows how a DE dipole speaker might be used as a home stereo system [7].

Recently, we have developed DE transparent Dipole-speakers, as shown in Fig. 32.8 [9].

32.3.3 Other Applications

Many other applications have been identified, and, in some cases, investigated including

- variable texture surfaces for fluid flow control, displays, and other novel applications such as smart skin [10–12].
- micro-nano devices such as inkjets, microfluidics, valves, pumps, switches, sensors, motor and micro generators [10–13].
- Micro-nano robots [12, 13].

We also note our recent progress that a DE actuator having only 0.1 g of DE lifted the weight of 1.0 kg using carbon system electrodes [14] (see Fig. 32.9).

Fig. 32.8 DE transparent dipole speaker using transparent electrodes

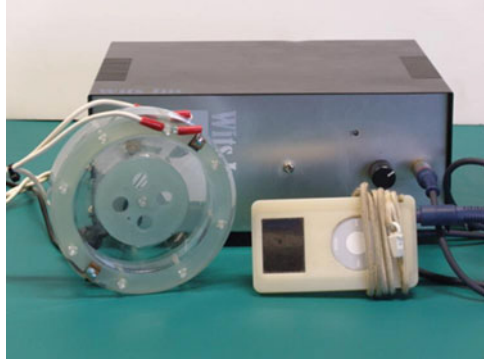
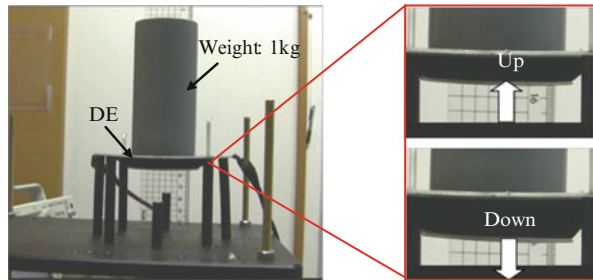


Fig. 32.9 DE lifted the weight of 1.0 kg using carbon system electrodes



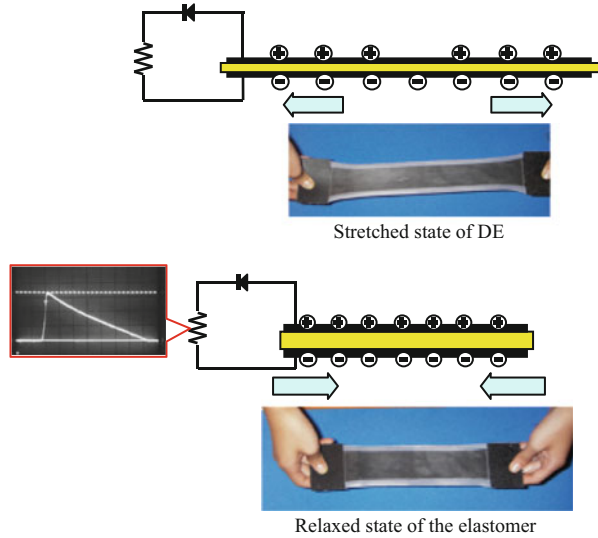
32.4 Application of DE Generation Devices

Another working mode of the DE artificial muscle is the power generation mode [2]. This is operatively the opposite of the actuator function. Application of mechanical energy to DE to stretch it causes compression in thickness and expansion of the surface area. At this moment, electrostatic energy is produced and stored on the polymer as electric charge. When the mechanical energy decreases, the recovery force of the dielectric elastomer acts to restore the original thickness and to decrease the in-plane area. At this time, the electric charge is pushed out to the electrode direction. This change in electric charge increases the voltage difference, resulting in an increase of electrostatic energy (see the detail in Chap. 13: Dielectric Elastomers)

Figure 32.10 shows the operating principal of DE power generation [5].

DE can be used for traditional generator applications as a direct replacement for electromagnetic generators. One can, for example, connect a DE generator to an internal combustion engine to make a fuel-powered generator. For these traditional generator applications, DE may offer lower cost, lighter weight, smaller size, or other advantages. However, it must be acknowledged that for these traditional high frequency applications, DE is a new technology competing against a mature technology that is well suited for the task. Hence, while DE may eventually become

Fig. 32.10 Operating principle of DE power generation



competitive in traditional high-speed generator applications, other uses for both point and distributed generators may better exploit the advantages of DE in the nearer term (see the detail in Chap. 13: Dielectric Elastomers).

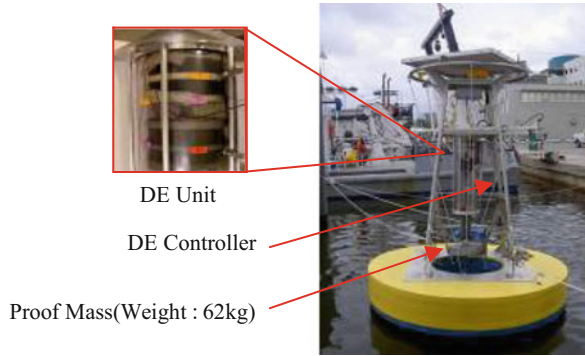
For point generator applications, DE is much more competitive if the mechanical input is intrinsically low frequency or variable speed. For these applications, conventional generators must use transmissions with their added cost, complexity, and size, thus making DE more competitive in the low frequency domain. Linear, as opposed to rotary motion, also favors DE.

Since this power generation phenomenon is not dependent on the speed of transformation, its power generation device can generate electric energy by utilizing natural energies such as up-and-down motions of waves, slowly flowing river water, human and animal movements, and vibration energies produced from vehicles and buildings [2, 7, 15].

32.4.1 DE Wave Generation

In spring 2006, the first prototype for a wave power generator using DE was developed and tested in a tank having dimensions of 1.5 m width, 1.2 m depth and 20 m length. Two DE sheets of 58×20 cm (total weight 40 g) were set at the center of the tank. A wave of 12 cm in height occurring every 3 s generated 1.8 W (one wave's energy is 5.4 J) of electricity. The conversion efficiency (the ratio of generated energy to applied force) is approximately 46 % [16].

Fig. 32.11 DE Generator system on the buoy used in December 2007



In August 2007 in Tampa Bay, Florida, USA, we carried out the world's first marine experiment into power generation by natural sea waves using a power generator having 150 g of DE [2]. The maximum measured electrical output capacity, verified in laboratory tests, was 12 J per stroke for the generator. However, wave activity was minimal during the test period. Wave heights were on the order of few centimeters, which made it very difficult to carry out tests for wave-powered generators. On occasion the weather generated waves 10 cm high. Even with the wave height of 10 cm, we were able to generate a peak power of 3.6 J at a bias voltage of 2,000 V (see Fig. 32.11).

The generator uses a proof-mass to provide the mechanical forces that stretch and contract the DE, as shown in Fig. 32.11 [2, 5].

Based on data from laboratory testing, we estimated that the energy conversion efficiency of DE generator is 70–75 % (not including hydrodynamic losses).

We should note that these measurements were made with a small bias voltage of 2,000 V applied to the DEs. By simply raising the applied voltage to the 6,000 V, we can estimate that a peak power of 11 W and an average power of 2.2 W could have been generated under these same small wave conditions [17].

In December 2008, oceanic tests were also carried out in California, USA, and it was confirmed that generated electric power was constantly stored in a battery.

An estimate based on data from our sea trial demonstration experiments has shown that even in seas where the wave height is only 1 m throughout the year (e.g., the sea close to Japan), if there are spaces of approximately 400 m in length and 60 m in width, the establishment of a sea-based facility generating 8.5 MW of power is possible [18]. Figure 32.12 shows the conceptual rendering of the DE wave power generator system [19].

The power generation efficiency estimated on the basis of the data obtained from our experiments is approximately 19 US cents/kWh [17]. In the near future, we expect that the electric power generation per unit mass or volume of DE material can double, and that the expected power generation cost per kilowatt-hour is 5–7.5 US cents [17]. This value is comparable to that for fossil fuel thermal power plants. Of course, the wave power systems have the additional benefit of not releasing any pollution or greenhouse gasses.

Fig. 32.12 Conceptual rendering of DE wave power generator system

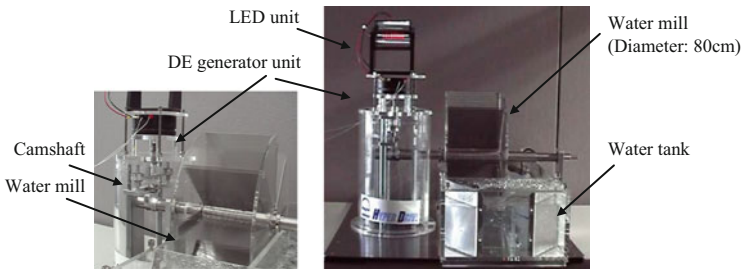
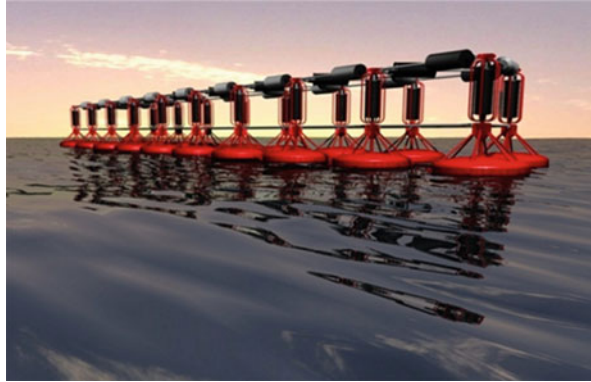


Fig. 32.13 Water mill generator using DE

32.4.2 DE Water Mill Generators

Large-scale hydroelectric power generation is a clean and renewable energy resource, but it has a great environmental impact as a result of the dam, reservoir, and modification of the riverbed. Also, there are few new suitable locations for hydroelectric power. In contrast to “big hydro,” with so-called micro hydro, generators are placed into flowing rivers or streams without the need for large dams (or in many cases, any dam at all) or modification to the riverbed.

A DE generator can be well suited for micro hydro [7]. As with wave power, the fact that DE can operate efficiently over a range of frequencies suggests that a DE generator can operate efficiently in the widely varying flow rates of many undammed streams and rivers. Since the DE material has a high energy density, DE generators do not require high-speed rotation from a converter. A simple structure that induces stretching and contracting of the DE is enough to generate electricity.

Figure 32.13 shows a water mill device that is 80 cm in diameter. This proof-of-principle device was tested in Wits corp. A small water pump (1.12 L/s flow rate) was fixed to a test tank to move water that spun the waterwheel.

Fig. 32.14 Small power generation device

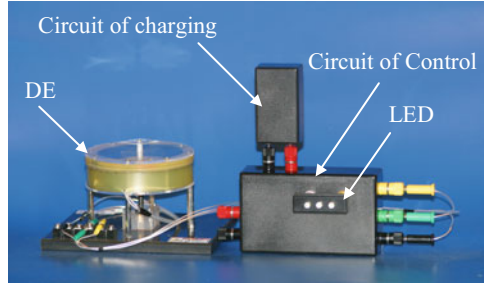
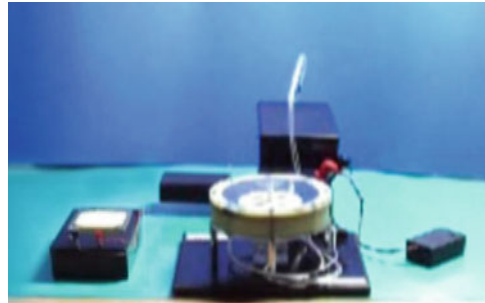


Fig. 32.15 Small-scale power-generation device and LED controlled by wireless signals



The waterwheel was attached to a crankshaft with a push rod that was then attached to a diaphragm-type of DE device. The up and down motion of the push rod stretched and contracted the DE in the diaphragm. In this simple test, each turn of the wheel produced 5 J of electricity.

32.4.3 *Portable DE Generators*

A small electric power generator developed by Wits Corp. uses the DE Cartridge (see Fig. 32.7) [7]. By pushing the central part of DE by 4–5 mm once a second, a power of approximately 0.12 W can be generated (see Fig. 32.14). The energy generated by this device can light several LEDs, and it is also possible to control ON/OFF operations of a remote device by coupling to a wireless system. In this case, the DE supplies electricity to the devices only when it receives mechanical energy. Thus it can be used as a switching system and this simple structure can be easily incorporated into a wireless network (see Fig. 32.15) [5].

32.4.4 *Wearable Generators*

In a power generation experiment, a thin artificial muscle film (25 cm long \times 5 cm wide, weight about 0.5 g) attached a human arm was able to generate 80 mJ of

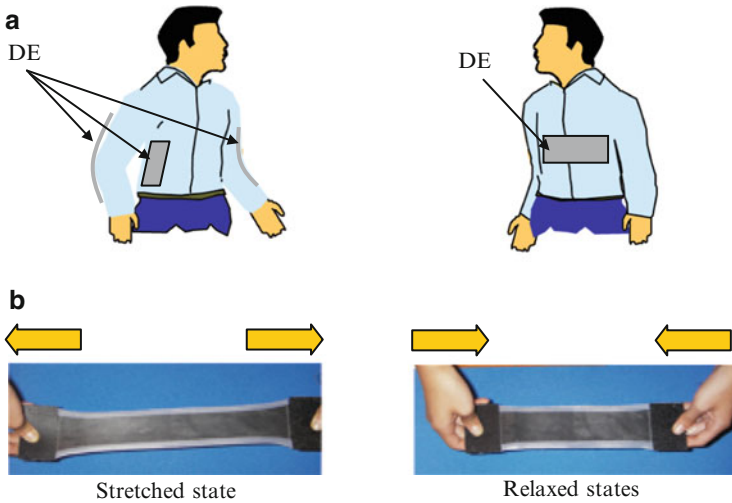


Fig. 32.16 Harvesting energy system from human body. (a) Conceptual rendering of DEs put up to side and chest of arm and body. (b) Stretched state of DE (*left*) and Relaxed state of the elastomer (*right*)

electrical energy with one arm movement (see Fig. 32.16b) [5]. It is also possible to make them generate electricity putting up dielectric elastomers besides the arm to the side and the chest of the body (see Fig. 32.16a) [5].

Furthermore, in an experiment using different power generation equipment, artificial muscle film attached to the bottom of a shoe was verified to generate electricity when the artificial muscle was distorted while walking. When an adult male took one step per second, one shoe was able to produce about 1 W of electrical power [20].

This confirmed that by utilizing human movement, enough electrical power could be obtained to recharge batteries for mobile telephones and similar devices [15]. In addition, electrical energy from the movements of animals could be used to construct livestock management systems. Other applications of animal-generated energy being investigated include scientific surveys of ecosystems of migratory birds and fish, among others.

32.4.5 Production of Hydrogen

We also carried out experiments on hydrogen production. In the experiments, the generated energy was first stored in a small battery (12 V/600 mAh) [17]. This battery was connected to a hydrogen generation system via a DC–DC converter. The hydrogen generation equipment used in the experiments was a simple

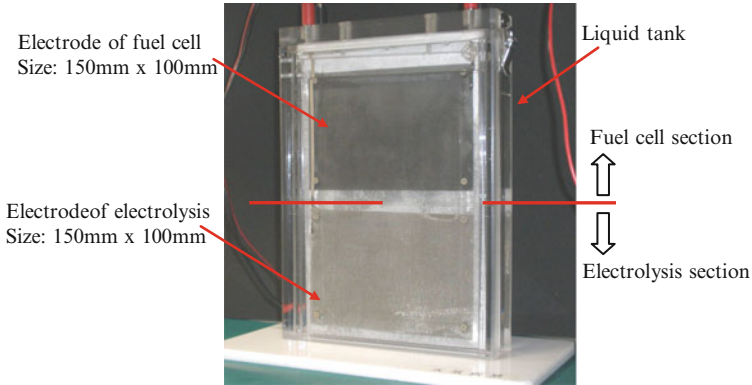


Fig. 32.17 Hydrogen generation equipment by electrolysis

electrolytic cell that used nickel electrodes of a mesh of 0.1 mm (150×100 mm) (Fig. 32.17). A 3 % aqueous solution of sodium hydroxide was used as a raw material. Applied voltages were reduced to 3 V by a DC–DC converter.

32.5 Future of DE

Helping to address critical issues such as global warming through the enabling of effective harvesting of highly distributed natural power sources is clearly a great potential benefit of DE. We are expecting the DE generators may become one of the promising technologies not only produce the power, but also to produce hydrogen in ocean and deserts in future.

Next-generation DE actuators might enable the vibration reduction and control of entire large structures. Other future applications might include new vehicles driven by innovative methods, and construction machines or robots with more complex, yet dexterous motions.

References

1. Chiba S, Stanford S, Pelrine R, Kornbluh R, Prahlah H (2006) Electroactive polymer artificial muscle. *JRSJ* 24(4):38–42
2. Chiba S, Waki M, Kornbluh R, Pelrine R (2008) Innovative power generators for energy harvesting using electroactive polymer artificial muscles. In: Bar-Cohen Y (ed) *Electroactive polymer actuators and devices (EAPAD)*, Proceedings of the SPIE, vol 6927, 692715, pp 1–9
3. Pelrine R, Chiba S (1992) Review of artificial muscle approaches. In: Proceedings of the third international symposium on micromachine and human science, Nagoya, Japan
4. Pei Q, Rosenthal M, Pelrine R, Stanford R, Kornbluh R (2003) Multifunctional electroelastomer roll actuators and their application for biomimetic walking robots. In: Bar-Cohen Y

- (ed) Proceedings of the SPIE, smart structures and materials, electroactive polymer actuators and devices (EAPAD), San Diego, CA, March 2003
5. Chiba S, Waki M (2011) Extending application of dielectric elastomer artificial muscles to wireless communication systems. Recent advances in wireless communications and networks, Chapter 20, pp 435–454 (InTech)
 6. Chiba S, Waki M, Wada T (2012) Evolving dielectric elastomer artificial muscles. *Petrotech*, vol 35, No 7
 7. Chiba S et al (2007) Extending applications of dielectric elastomer artificial muscle. In: Proceedings of the SPIE, San Diego, 18–22 March, 2007
 8. Sugimoto T, Ono K, Ando A, Chiba S, Waki M (2010) Sound generator structure for low-elastic electroactive polymer. *Acoust Soc Jpn Acoust Sci Tech* 31(6):411–413
 9. Chiba S, Waki M, Asaka K, Suwa Y, Wada T, Hirakawa Y (2012) Challenges for Loud speakers using dielectric elastomers. (Invited), Abstract of IUMRS-ICEM 2012 C5—K125-002), C-5: electroactive polymer actuators, sensors and energy harvesters, 25–27 Sept 2012, Yokokama, Japan
 10. Kornbluh R, Bashkin J, Pelrine R, Prahlad H, Chiba S (2004) Medical applications of new electroactive polymer artificial muscles. *Seikei Kakou* 16(10):631–637
 11. Pelrine R, Kornbluh R, Prahlad H, Heydt R, Bashkin J, Chiba S (2006) Micro and nano fluidic devices using electroactive polymer artificial muscle. In: Proceedings of the 10th international conference on miniaturized system for chemistry and life science, 5–9 Nov 2006, Tokyo, Japan, pp 278–280
 12. Kornbluh R, Pelrine R, Chiba S (2004) Silicon to silicon: stretching the capabilities of micromachines with electroactive polymers. *IEEJ Trans SM* 124(8):266–271
 13. Kornbluh R, Pelrine R, Chiba S (2004) Artificial muscle for small robots and other micromechanical devices. *IEE Trans Jpn* 122-E(2):97–102
 14. Chiba S, Waki M (2011) Current status and future prospects of dielectric elastomer transducers. (Invited), Advanced Technology forum (Front line of Actuator Technology), Japan Society of Mechanical Engineers 2011, Tokyo, Japan
 15. Chiba S, Waki M (2011) Power generation by micro/small vibration using dielectric elastomer. *Funct Mater* 31(4):56–63
 16. Chiba S, Pelrine R, Kornbluh R, Prahlad H, Stanford S, Eckerle J (2007) New opportunities in electric power generation using electroactive polymers (EPAM). *J Jpn Insti Energ* 86(9):743–737
 17. Chiba S, Kornbluh R, Pelrine R, Waki M (2008) Low-cost hydrogen production from electroactive polymer artificial muscle wave power generators. In: Proceedings of the world hydrogen energy conference 2008, Brisbane Australia, 16–20 June 2008
 18. Chiba S, Waki M, Masuda K, Ikoma T, Osawa H (2011) Innovative wave power generation using dielectric elastomer artificial muscles. In: Proceedings of the WHTC 2011, Glasgow UK
 19. Chiba S, Waki M, Kornbluh R, Pelrine R (2009) Innovative wave power generation system using EPAM. In: Proceedings of the Oceans' 09, Bremen, Germany, 11–15 May 2009
 20. Harsha P, Kornbluh R, Pelrine R, Stanford S, Eckerle J, Oh S (2005) Polymer power: dielectric elastomers and their applications in distributed actuation and power generation. In: Proceedings of the ISSS 2005, international conference on smart materials structures and systems, Bangalore, India

Part VIII
Next-Generation Bio-Actuators

Chapter 33

Tissue Engineering Approach to Making Soft Actuators

Toshia Fujisato, Shunya Takagi, Tomohiro Nakamura, and Hiroshi Tsutsui

Abstract Recent innovation in the tissue engineering makes it real to construct the biological organ and tissue in vitro using proteins and living cells. This technology is not only for the regeneration of patients' organ and tissue but also for the actuation of any artificial machine. The living muscles driven by the activation of actin-myosin molecular motors transform biochemical energy of ATP into mechanical energy. They have excellent characteristics of lightweight, high flexibility, and remarkable efficiency for energy conversion compared to the mechanical actuators that require electricity as a power source. Therefore, a muscle cell-based bio-hybrid actuator termed bio-actuator has the potential of being flexible and highly efficient on a micro to macro scale. The aim of this chapter is to describe the bio-actuator made of cultured skeletal muscle cells in vitro based on our investigation. There are still several issues to be solved for getting large and powerful bio-actuator which works long term with proven reliability, however it must be done in the near future by intensive studies of vigorous tissue-engineers.

Keywords Bio-actuator • C2C12 • Collagen gel • Myoblast • Tissue-engineered muscle

33.1 Tissue Engineering

The human body is a nature-made wonderful machine achieved by the evolution over hundred millions of year. Proteins, lipids, polysaccharides, and some inorganic materials such as hydroxyapatite are its compositions except water that is holding about 60 % of total body weight. In terms of cell type, the body contains about 200 of different types of cells and their total number is about 60 trillion. All are differentiated from only one fertilized egg. The extracellular part, the space between cells in our tissue, is filled with extracellular matrix consisting of structural proteins of collagen and elastin, cell adhesion molecules, proteoglycan, and hyaluronic acid. When the organ or tissue is malfunctioned or to be removed by a

T. Fujisato (✉) • S. Takagi • T. Nakamura • H. Tsutsui
Biomedical Engineering, Osaka Institute of Technology, 5-16-1 Ohmiya,
Asahi, Osaka 535-8585, Japan
e-mail: toshiya.fujisato@oit.ac.jp

traumatic injury or cancer ablation, an artificial organ or tissue would be used for their substitution as well as organ or tissue transplantation. The current artificial organ and tissue are mainly made of plastics and/or metals and their composition is totally different from our body, despite some artificial bone are made of ceramics that are relatively similar to hydroxyapatite of our body. Their structure is also much different even if the outward appearance looks like the human organ or tissue. As a result, even after several years of their implantation, they may be remained as a foreign body without assimilation to the host tissue and sometimes cause infectious disease because of its poor vascularization responsible for our immune system.

The tissue engineering is an emerging approach to replace the human body by an artificial tissue made of the material close to it and to be replaced by it. It is recognized that the cell source, scaffold as an extracellular matrix, and cell growth factors are the key elements for the tissue engineering [1]. The human body except heart, brain, and spinal cord is always scrapped and built by the appropriate cells and then our body of today is not the same as that of yesterday. For example, the skin cells turn over in about 3 weeks and even the bone does in about a half of year. The engineered tissue may be assimilated and replaced by the host through this cellular turnover activity. However, myocardial cells organizing the heart and central nervous system cells organizing brain and spinal cord will work through the whole of our life with very limited turnover, so that it would be easily understood how difficult the cure of myocardial and cerebral infarction in which these cells died is.

Muscles are responsible for the most of our body motion and classified into three major types of cardiac, skeletal, and smooth muscles. The muscles are one of the linear actuators driven by the activation of actin-myosin molecular motors and transform biochemical energy of ATP, adenosine triphosphate, into mechanical energy. Therefore, they have excellent characteristics of lightweight, high flexibility, and remarkable efficiency for energy conversion compared to the artificial mechanical actuators that require electricity as a power source. A muscle cell-based bio-hybrid actuator, termed bio-actuator, has the potential of being flexible and highly efficient on a micro to macro scale. Some of the bio-actuators have already been reported [2, 3], however they have not been widely studied because of the difficulty to handle and maintain proteins and living cells in long term under the sterilized and wet conditions where a lot of mechanical and/or electrical equipment are not suitable to use.

On the other hand, muscle tissue itself had been extensively investigated to be used as an *in vivo* actuator for the treatment of myocardial infarction. In this procedure called dynamic cardiomyoplasty, skeletal muscles were taken from the patient's back or abdomen and wrapped around his or her heart and synchronized by electric stimulation from a device similar to a pacemaker [4]. At present, instead of using the muscle tissue directly, the method has been modified to utilize cells in the skeletal muscle tissue and some of them have already been clinically applied. In this procedure, skeletal myoblasts are collected from the patient's muscle tissue and the cell suspension is injected into the infarcted area or the cultured cell sheets are attached onto it [5]. By the technical advances in tissue engineering and regenerative

medicine to build a mammalian tissue *in vitro* especially with bioreactor for culturing cells for long time, it may be ready to realize the bio-actuator.

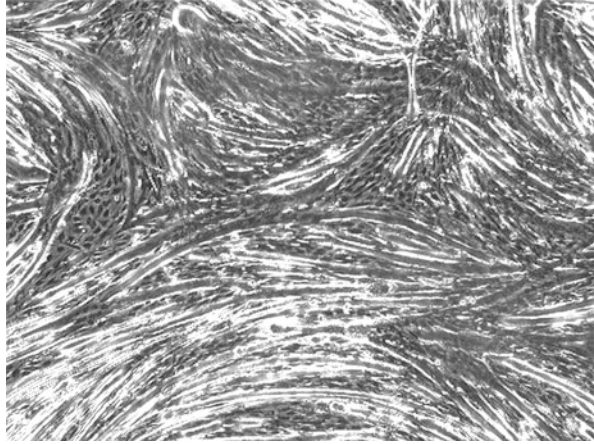
In this chapter, the bio-actuator made of cultured skeletal muscle cells *in vitro* is mainly described, neither made of muscle tissue directly nor proteins such as myosin and actin responsible for muscle contraction.

33.2 Actuator Made of Muscle Cells

Smooth and cardiac muscles are made up of smooth muscle cells and cardiomyocytes, respectively. The smooth muscle is found in internal organs and tissues like blood vessels, lymphatic vessels, the urinary bladder, uterus, and gastrointestinal tract. Smooth muscle cells are able to be easily obtained from animal tissues and also to be proliferated *in vitro*. It is very important in the tissue engineering field to reconstruct the smooth muscle tissue like esophagus and sphincter, however the smooth muscle cells may not be suitable for a bio-actuator since the contraction speed is much slower than that of the cardiac and skeletal muscles in spite of its expansion-contraction ratio is higher. There have already been several articles reported for the cardiomyocyte-based bio-actuators [6, 7]. But the cardiomyocytes are highly differentiated and have very low ability for proliferation as described above especially in adult, so that it is necessary to sacrifice fetal or neonatal animals for isolating them whenever they are needed. No progenitor cell has been established as well as its proliferation at present, although the differentiation to cardiomyocytes from the induced pluripotent stem cells, iPS cells, is vigorously investigated. In addition, controllability of cardiomyocytes has to be obtained since they have the involuntary movement. Skeletal muscle is made up of myocytes, also known as skeletal muscle cells or skeletal muscle fibers. Myocytes have also very low ability for proliferation as well as cardiomyocytes, however they are formed by the fusion of developmental myoblasts, also known as myosatellite cells, in a process of myogenesis. Moreover, since the myosatellite cells can easily be collected from skeletal muscle fibers and proliferated *in vitro*, they may be the best candidate for a cell source of bio-actuator.

The contraction of skeletal muscle in our body is controlled by the nervous system. Skeletal muscle cells are depolarized by acetylcholine that is the neurotransmitter released by motor neurons at the neuromuscular junction. By this depolarization, the ionic calcium is released from the sarcoplasmic reticulum in muscle cells and combined to the regulatory protein troponin. This interaction followed by its conformational change makes the movement of tropomyosin and exposing of the myosin-binding sites on actin. Then these bindings of actin and myosin molecules make contraction of the skeletal muscle. Whereas the cultured skeletal muscle does not have nerve system, the muscle cell membrane may be depolarized by the applied electrical signal in culture medium, and then the ionic calcium may be released from the sarcoplasmic reticulum and make the cells contract. As described above, myoblasts may differentiate into myotubes by the

Fig. 33.1 Cultured mouse myoblasts cell line C2C12



fusion of each cell and subsequently differentiate into muscle fibers by incubation in the appropriate culture medium [8]. However, when the myoblasts are cultured on an ordinary cell culture dish, they would randomly orient after their differentiation (Fig. 33.1). It may be very important to align the cells in one direction and bundle them in three dimensions in order to produce an effective cell-based bio-actuator.

There have been several reports published about the tissue-engineered skeletal muscles with or without scaffolds. The pioneer study had been reported in 2000 by Dennis and Kosnik. They made cultured three-dimensional skeletal muscle, called myooid, by spontaneous tissue formation in long-term cell culture and its contraction tetanus force was about 440 μN [9]. Huang et al. have improved the method and the contraction force had reached about 805 μN [10]. Yan et al. have obtained cultured skeletal muscle having a contraction force of about 500 μN by lamination of myoblasts cultured on aligned collagen [11]. Collagen is the main component of the extracellular matrix accounting for about 30 % of the protein content of the human body. Its affinity for cells is so high that it is used for a substrate of the cell culture by coating onto the tissue culture dishes, and also often used as a substrate for three-dimensional cell culture in a gel form.

33.3 Our Tissue-Engineered Bio-Actuator

We have constructed a three-dimensionally cultured skeletal muscle with collagen gel as cell substrate and also extracellular matrix. Generally, the cell-embedded collagen gel shrinks gradually and isotropically with the incubation time and the muscle cells may orient randomly as well as in the two-dimensional cell culture on culture dish. However, the cell-collagen conjugate may shrink heterotropically when it is fixed at some points onto the substrate because the gel around fixed

points is not able to move but at others is free [12]. In our tissue-engineered muscle, the viscous cell suspension of collagen was applied onto the substrate in rectangular shape and the both longitudinal ends were held on the substrate to allow the gel to shrink heterotropically. We have introduced two artificial tendons at the both ends in order to fix and handle the gel firmly. The artificial tendons were made up of acellular porcine blood vessel consisting of collagen fiber having high affinity to the collagen gel containing cells. Thanks to the pinhole of artificial tendons, the cultured muscle could be easily set to the stimulation and measurement apparatuses through the pinholes for the quantitative evaluation of contraction and relaxation kinetics and also to the driving points of actuator. The C2C12 cell line that is immortalized mouse skeletal myoblasts [13] has been chosen for without sacrificing any animal in our cultured muscle.

A purchased porcine aorta was digested in an enzymatic solution of elastase to remove elastic fibers and cells inside. The acellular aorta was cut into circular forms having diameter and thickness of 3 and 1.5 mm, respectively and pinholes of 1 mm diameter were punched out at their center to get an artificial tendon. The culture substrate was made of polycarbonate plate on which a thin silicone sheet was attached and two stainless steel pins were provided at distance of 13 mm on the substrate. Type-I collagen gel (Cellmatrix[®], Nitta Gelatin Inc., Osaka, Japan) was used as a scaffold of C2C12 cells and the cells were embedded in a cold gel solution at density of 1.0×10^7 cells/mL. After insertion of two artificial tendons into pins on the substrate, the cell suspension of 100 μ L was applied between two tendons by a micropipette (Fig. 33.2). After gelation of the cell suspension at 37 °C, the construct was put into the growth medium (GM) consisted of high-glucose Dulbecco's modified Eagle's medium (DMEM) solution supplemented with 10 % fetal bovine serum and 1 % antibiotics and cultured to allow the trypsinized cells to repair and proliferate. After 2 days in culture, the GM was shifted to the differentiation medium (DM) consisting of high-glucose DMEM solution supplemented with 7 % horse serum to allow C2C12 myoblasts to differentiate to myofibers. The culture was performed at 37 °C in 5 % CO₂ atmosphere and the medium was replaced every two days. The cell-collagen gel composite started to shrink

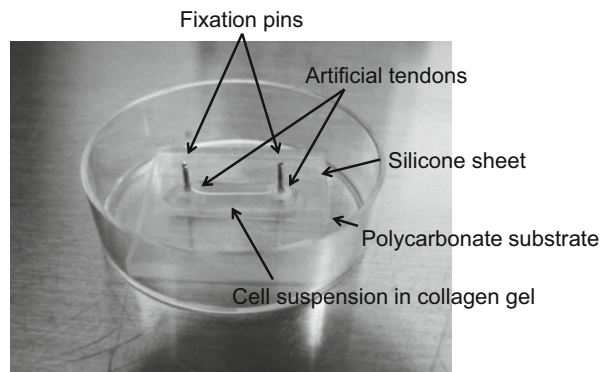
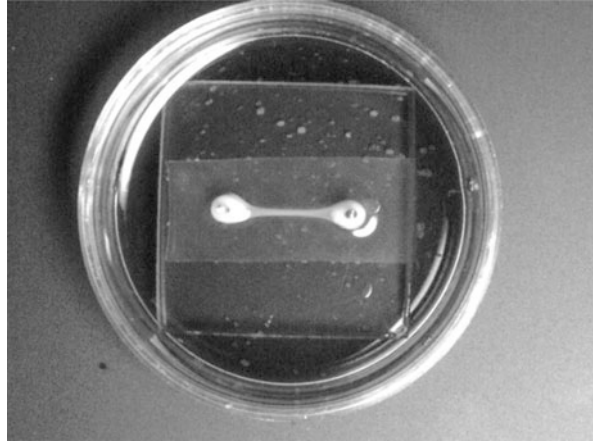


Fig. 33.2 Construction of tissue-engineered skeletal muscle

Fig. 33.3 Tissue-engineered skeletal muscle in 35 mm culture dish



gradually and since it was fixed with a pin at both ends, it shrunk anisotropically without changing longitudinal length. Furthermore, since the silicone sheet was just laid on the substrate, the gel came detached gradually from the substrate, resulting cultured skeletal muscle was a small dumbbell-like shape having approximately 15 mm in length and 0.5 mm in diameter at the 14 days after gelation (Fig. 33.3) [14].

33.4 Contractile Force Measurement of Bio-Actuator and Its Drive of Micro-Object

It is not easy to measure the contractile force of tissue-engineered muscle *in vitro* because of the necessity for its connection to the measurement device in the wet condition. Some researchers utilize the image processing system to avoid this issue [12], however this must not be avoided for its application to the bio-actuator. We have connected our bio-actuator through the artificial tendons to a force measurement device equipped with a load cell and electrical signal generator (Fig. 33.4). Contraction and relaxation movements of tissue-engineered skeletal muscle would be observed when a monopolar electrical stimulation pulses through the culture medium was applied.

It was found that the isometric force of the engineered muscle had increased when the applied voltage, pulse width, and frequency of the pulse signal increased. There might be several stages of differentiation in the myotubes formed by the fusion of C2C12 myoblasts and the threshold of myotubes in response to electrical stimulation would depend on the stage. So that the more the applied voltage and pulse width increased, the more the number of myotubes participated in the contraction might increase and as a result, the contractile force might increase.

Fig. 33.4 Force measurement device for tissue-engineered skeletal muscle

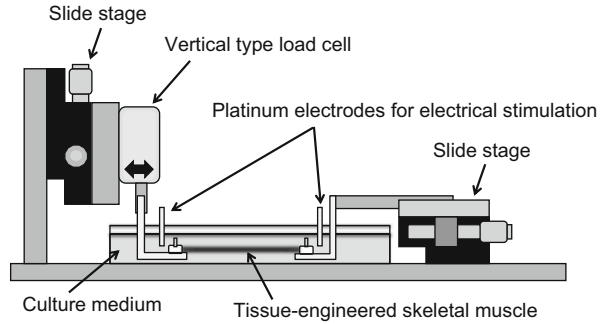
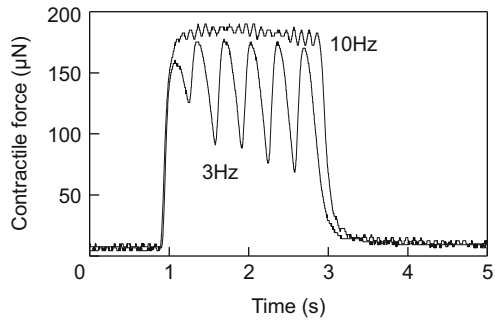


Fig. 33.5 Contractile force of tissue-engineered skeletal muscle



When the tissue-engineered muscle was stimulated by the electric signal of applied voltage of 50 V and a pulse width of 2 ms, if the signal frequency was 10 Hz or less, it showed the synchronized contraction force with the signal pulse. However, if the frequency was more than 10 Hz, the muscle showed almost the constant contraction force (Fig. 33.5). In the living skeletal muscle tissue, the signal frequency from the motor neurons is about 50 Hz and the muscle shows the tetanic contraction by the signal. Our tissue-engineered muscle might also show the tetanic contraction when the frequency of applied electric signal was more than 10 Hz. Whereas the maximum contractile force of our engineered muscle was lower than that of previously described groups, it might be equivalent if the condition such as the number of cells and culture period was similar to them.

Our bio-actuator had been preliminarily applied for driving a micro-object prepared by the micro stereolithography apparatus. Two base objects of a rectangular-shaped anchor of which the length, width, and height was 2.8, 2.1, and 1.2 mm, respectively and a rotatable lever of 14.8, 2.1, and 1.2 mm, respectively were located at distance of 13 mm as same as the length of bio-actuator on the substrate plate. The artificial tendons of bio-actuator were tied firmly to the base objects by the top objects of 2.8, 2.1, and 1.3 mm (Fig. 33.6a). When the lever-like preliminary actuator device was immersed in the culture medium and the electrical pulse stimulation to cause tetanus contraction was added to the medium, the bio-actuator had contracted about 15 % and be able to drive the lever object for

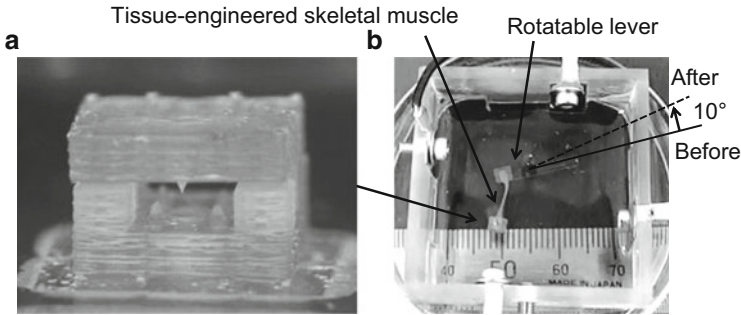


Fig. 33.6 (a) Anchor parts and (b) whole structure of bio-actuator before electrical stimulation

the rotation about 10° (Fig. 33.6b). However, the lever object had not been returned to the original position even after the removal of electric pulse signal. The most muscle tissues work in pairs located in opposite sides of a joint or bone, called agonist and an antagonist. When they work, the agonist generates the specific movement and the antagonist acts in opposition and then returns the movement to its initial position. This is because the muscle tissue can make a pulling force only and cannot push itself back into the original position. Therefore, in order to perform the bio-actuator device effectively, it is necessary to have two tissue-engineered muscles that work in turn different from the mechanical actuator which is movable to both directions. The electrical stimulation is applied through the culture medium in our current system, so that even if two bio-actuators were prepared, the device may not be driven properly. Not through the medium but direct stimulation to each bio-actuator may be necessary.

33.5 Further Study of Bio-Actuator

One of the goals of this study is to develop the tissue-engineered skeletal muscle consisted of fully matured myofibers. From the histological observations of cross-sectional view of our tissue-engineered skeletal muscle at 3 weeks after the incubation, it was found that the polynuclear myotubes differentiated from C2C12 myoblasts were oriented parallel to the longitudinal direction (Fig. 33.7a). In addition, from the microstructural observations by transmission electron microscopy, it was also confirmed to have sarcomeres that are the contractile units of skeletal muscle tissue composed of fibrous proteins that slide each other during its contraction and relaxation (Fig. 33.7b). The maturation of the cultured cells was also confirmed by a Real-time PCR, a device for detecting specific gene expression, of MyoD, Myogenin, and Myf6 that are myogenic regulatory factors in the process of myogenesis and then differentiation markers for skeletal muscle cells from myoblasts. Their expressions were clearly detected 2 weeks after the tissue culture (Fig. 33.8) and these results indicate that C2C12 myoblasts has started to

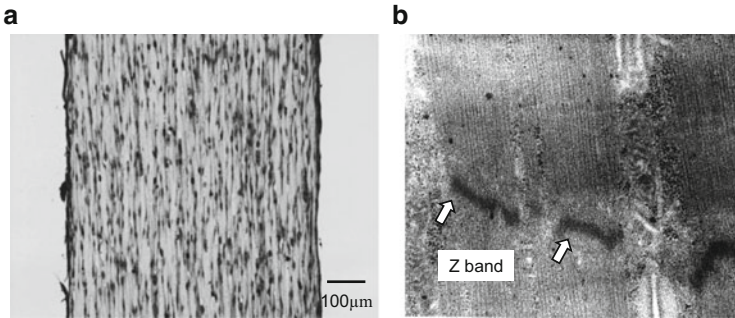
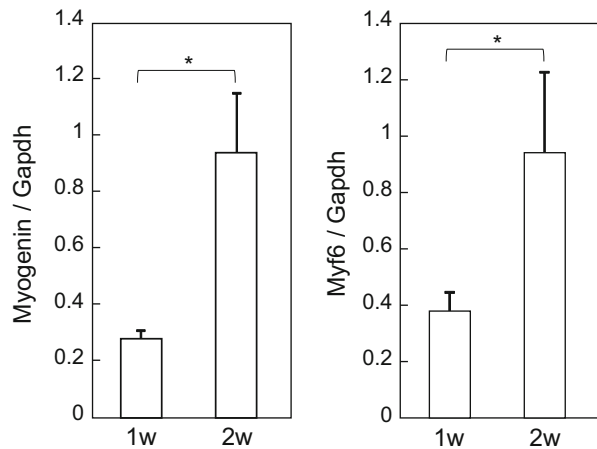


Fig. 33.7 (a) Micro and (b) ultrastructure of tissue-engineered skeletal muscle

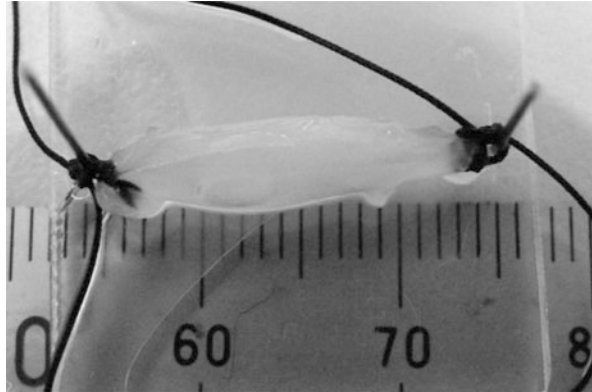
Fig. 33.8 Gene expression in tissue-engineered skeletal muscle



differentiate just after medium transfer from GM to DM and the mature myocytes have emerged at least 3 weeks after the cell culture.

One of the biggest problems to be solved in the tissue engineering research is that it is still not possible to construct a capillary network inside the artificial tissue. Capillary network runs throughout every part in the human body and supplies nutrients and oxygen through the blood components for the individual cells to survive. Diameter of our tissue-engineered muscle was about 0.5 mm and since they had no capillary network inside and nutrients and oxygen were just supplied from the surrounding media, this size might be the largest. If the initial volume of the collagen gel and the number of cells inside had been increased in order to have thicker tissue, the resulting artificial tissue would not become thick because of the necrosis inside. We are now challenging to develop a novel collagen sponge scaffold having capillary-like structure inside with medium-circulating bioreactor (Fig. 33.9). Currently, the maximum contractile force of our tissue-engineered

Fig. 33.9 Tissue-engineered skeletal muscle with collagen sponge scaffold



skeletal muscle is about 0.2 N/cm^2 and is less than 5 % of the biological muscle of the same size from 15 to 40 N/cm^2 . Several works have already been reported about enhancement of cultured muscle cells, we also introducing electric and mechanical stimulations as a training of the engineered muscle in order to enhance differentiation and maturation and as a result, contractile force.

As a conclusion, it was successfully prepared of the bio-actuator made of tissue-engineered skeletal muscle especially connecting through the artificial tendons at its both ends. It was made of three-dimensionally aligned myotubes and myofibers and was possible to drive micro-object. However, it needs further improvements in order to be utilized as practical bio-actuator as described already. In the usual cell culture, the culture medium has to be replaced every two days and there is a potential for contamination at that time. It may also important issue to establish an automatic long term cell culture system to avoid any contamination for the applicable bio-actuator.

Acknowledgments This work was partly supported by JSPS KAKENHI Grant Number 24500521.

References

1. Ikada Y (2006) Challenges in tissue engineering. *J R Soc Interface* 3(10):589–601
2. Kakugo A, Shikinaka K, Gong JP (2008) Integration of motor proteins - towards an ATP fueled soft actuator. *Int J Mol Sci* 9(9):1685–1703
3. Akiyama Y, Iwabuchi K, Furukawa Y, Morishima K (2009) Long-term and room temperature operable bioactuator powered by insect dorsal vessel tissue. *Lab Chip* 7(9):140–144
4. Chiu RC, Kochamba G, Walsh G, Dewar M, Desrosiers C, Dionisopoulos T, Brady P, Ianuzzo CD (1989) Biochemical and functional correlates of myocardium-like transformed skeletal muscle as a power source for cardiac assist devices. *J Card Surg* 4(2):171–179
5. Miyagawa S, Saito A, Sakaguchi T, Yoshikawa Y, Yamauchi T, Imanishi Y, Kawaguchi N, Teramoto N, Matsuura N, Iida H, Shimizu T, Okano T, Sawa Y (2010) Impaired myocardium

- regeneration with skeletal cell sheets—a preclinical trial for tissue-engineered regeneration therapy. *Transplantation* 90(4):364–372
6. Horiguchi H, Imagawa K, Hoshino T, Akiyama Y, Morishima K (2009) Fabrication and evaluation of reconstructed cardiac tissue and its application to bio-actuated microdevices. *IEEE Trans Nanobiosci* 8(4):349–355
 7. Tanaka Y, Sato K, Shimizu T, Yamato M, Okano T, Kitamori T (2007) A micro-spherical heart pump powered by cultured cardiomyocytes. *Lab Chip* 7(2):207–212
 8. Kubo Y (1991) Comparison of initial stages of muscle differentiation in rat and mouse myoblastic and mouse mesodermal stem cell lines. *J Physiol* 442:743–759
 9. Dennis RG, Kosnik PE 2nd (2000) Excitability and isometric contractile properties of mammalian skeletal muscle constructs engineered in vitro. *In Vitro Cell Dev Biol Anim* 36(5):327–335
 10. Huang YC, Dennis RG, Larkin L, Baar K (2005) Rapid formation of functional muscle in vitro using fibrin gels. *J Appl Physiol* (1985) 98(2):706–713
 11. Yan W, George S, Fotadar U, Tyhovych N, Kamer A, Yost MJ, Price RL, Haggart CR, Holmes JW, Terracio L (2007) Tissue engineering of skeletal muscle. *Tissue Eng* 13(11):2781–2790
 12. Vandenburg H (2010) High-content drug screening with engineered musculoskeletal tissues. *Tissue Eng Part B Rev* 16(1):55–64
 13. Yaffe D, Saxel O (1977) Serial passaging and differentiation of myogenic cells isolated from dystrophic mouse muscle. *Nature* 270(5639):725–727
 14. Yamasaki K, Hayashi H, Nishiyama K, Kobayashi H, Uto S, Kondo H, Hashimoto S, Fujisato T (2009) Control of myotube contraction using electrical pulse stimulation for bio-actuator. *J Artif Organs* 12(2):131–137

Chapter 34

ATP-Driven Bio-machine

Daisuke Inoue, Arif Md. Rashedul Kabir, Kazuki Sada, Jian Ping Gong,
and Akira Kakugo

Abstract *Biomolecular motor systems* microtubule/kinesin, actin/myosin are constituent components of biological power unit, which can perform mechanical work by converting chemical energy obtained from hydrolysis of adenosine triphosphate (ATP). The biomolecular motors are organized into highly complex and ordered structures as observed in muscle, stress fiber, contractile ring which exhibit various functions. Performance of these natural machines are much attractive compared to man-made machine. Therefore, to utilize the advantage of these natural machines biological motors have been proposed as the building blocks of *ATP-driven bio-machine*. In this chapter, different methodologies for designing biomolecular motor based bio-machines through non-equilibrium self-organization process are described.

Keyword Active self-organization • Biomolecular motor • Kinesin • Microtubule • Non-equilibrium system

34.1 Biomolecular Motors

Biomolecular motor systems (actin/myosin, microtubule/kinesin and dynein) are constituent components of eukaryotic cytoskeleton that play important roles in cell motility [1], cytokinesis [2], cellular transport [3] and so on. The most outstanding

D. Inoue
Graduate School of Chemical Sciences and Engineering, Hokkaido University,
Sapporo 060-0810, Japan

A.M.R. Kabir
Faculty of Science, Hokkaido University, Sapporo 060-0810, Japan

K. Sada • A. Kakugo (✉)
Graduate School of Chemical Sciences and Engineering, Hokkaido University,
Sapporo 060-0810, Japan

Faculty of Science, Hokkaido University, Sapporo 060-0810, Japan
e-mail: kakugo@sci.hokudai.ac.jp

J.P. Gong
Faculty of Advanced Life Science, Hokkaido University, Sapporo 060-0810, Japan

property of biomolecular motor systems is their ability to convert chemical energy of ATP into mechanical work with high efficiency. Biomolecular motors can provide high specific power [4] which is almost 100 times larger than that of widely used electric motors; hence, these natural machines have been considered promising candidates for constructing ATP-driven bio-machine. Nowadays, biomolecular motors are being used in developing new devices for serving the following purposes: nanoscale molecular transportation [5, 6], surface imaging [7], force measurement [8], and lab-on-a-chip sensor design [9]. Biomolecular motors can amplify their performance through active self-organization process as observed in muscles, stress fibers and mitotic spindle [10]. Self-organization of biomolecular motors into multi-molecular assemblies expands the utility of biomolecular motors as larger actuators compared to a nano device constructed from a single biomolecular motors. Various methods of self-organization have been developed in order to assemble biomolecular motors into highly organized structures which might offer integrated functions as observed in natural systems.

34.1.1 Active Self-Organization of Biomolecular Motors

Active components in living system including biomolecular motors form multi-molecular assemblies through active self-organization (AcSO) process. The AcSO proceeds in the presence of continuous supply of energy inside the system. After assembly formation, the assembled structures maintain their stability in a non-equilibrium steady state. AcSO process has several advantages with respect to adaptability with the change of environment [11], self-healing [12–16], and self-replication, etc. AcSO also offers a promising method for the self-assembly of biomolecular motor systems as discussed in the subsequent sections where microtubules/kinesin system has been treated as a model system.

Microtubules are cytoskeletal filaments polymerized from tubulin dimer (α and β tubulin), whereas kinesin super family constitutes a structurally diverse group of microtubule-based motor proteins that use the energy of ATP hydrolysis for moving along microtubules [17]. In vitro studies demonstrated that microtubules can exhibit translational motion on a kinesin coated surface [18], which is called in vitro motility assay of microtubules (Fig. 34.1). To integrate the microtubule/kinesin systems into a more ordered structure, an active self-organization method was developed based on the in vitro motility assay by employing streptavidin (St)-biotin(Bt) interaction [19, 20] (Fig. 34.2a). This method allowed to obtain a wide variety of assembled structures, e.g. bundles, networks, and ring-shaped microtubule assemblies that differ in size or shape depending on the experimental condition such as microtubule density and St-Bt modification ratio, etc. (Fig. 34.2b) [21, 22]. Bundles, networks, and ring-shaped microtubule assemblies offer diverse functions, quite different from that of a single microtubule filament, as reflected

Fig. 34.1 Schematic representation of in vitro motility assay of microtubules driven on a kinesin coated surface

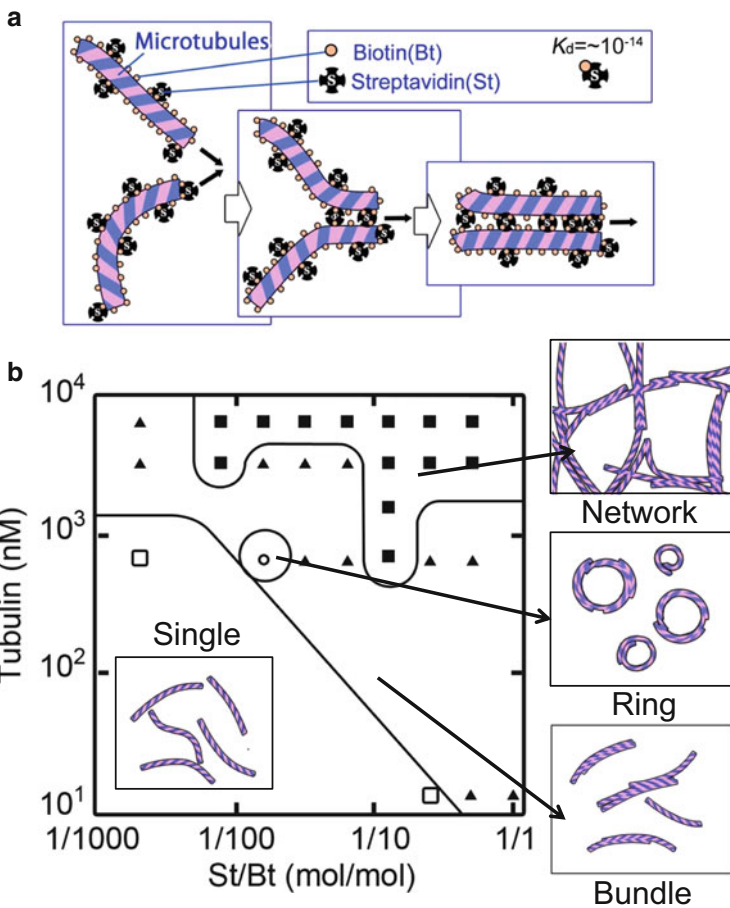
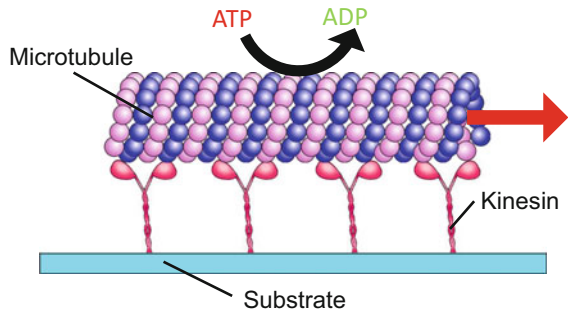


Fig. 34.2 Active self-organization (AcSO) of microtubules. Schematic representation of active self-organization of microtubules by employing streptavidin (St)/biotin (Bt) interaction (a). Phase diagram for the morphology of microtubule assemblies (b)

through translational, amoeboid and rotational motion, respectively (Fig. 34.2b). The average velocity of bundled microtubule assemblies ($0.19 \pm 0.05 \mu\text{m s}^{-1}$) was almost similar to that of single filaments ($0.17 \pm 0.05 \mu\text{m s}^{-1}$) [20]. This result indicates that during AcSO single microtubules are assembled into ordered structure based on their polarity and hence these assembled structures are capable of showing integrated and diverse functions [20, 23].

The rotational motion obtained from the ring-shaped structure could be of great importance in future nano-technological applications because only the ring-shaped microtubule structure continuously provides mechanical work without changing the position of the mass centre [21–28]. In subsequent paragraph we introduce the characteristic features of ring-shaped microtubule assemblies.

34.1.2 Controlling the Direction of Rotational Motion of the Ring-Shaped Microtubule Assemblies

The AcSO of microtubules successfully produced ring-shaped microtubule assemblies with a wide range of size distribution (Fig. 34.3a) [28]. An inherent characteristic of ring-shaped microtubule assemblies is that they can generate rotational motion both in the counter clockwise (CCW) and clockwise (CW) direction. However the ratio of ring-shaped microtubule assemblies rotating in CCW and CW direction was approximately CCW: CW = 3:1 and under optimized conditions the ratio was as high as CCW: CW = 9:1 [28]. In vivo, a microtubule is usually composed of 13 protofilaments (PFs) in which α - and β -tubulin heterodimers (tubulins) are arranged head-to-tail in a polar fashion. These PFs are aligned parallel to the longitudinal axis of the microtubule [29–31]. When microtubules are reconstructed from tubulin in the presence of guanosine triphosphate (GTP) in vitro, they consist of various numbers of PFs [30, 31]. With the number of PFs differing from 13, the microtubules are known to have a left- or right-handed supertwist in the PF arrangement [32–34]. The ring-shaped microtubule assemblies obtained by AcSO showed preferential rotation in the clockwise or counterclockwise direction depending on the handedness of the PFs within the microtubule lattice.

Cytoskeletal proteins are known to govern handedness related asymmetry observed in nature [35–37]. Inhibition of the functions of these proteins reverses or even breaks the asymmetry. There were efforts to tune the handedness of ring-shaped microtubule assemblies. PFs number in a microtubule lattice, which determines the handedness of microtubules and also ring-shaped microtubules, was controllable by changing experimental conditions [38]. It was revealed that preferential rotation of the ring-shaped microtubules assembly obtained through AcSO process is significantly affected by the incubation time for microtubules preparation. The ratio of ring-shaped microtubule assemblies rotating into CCW

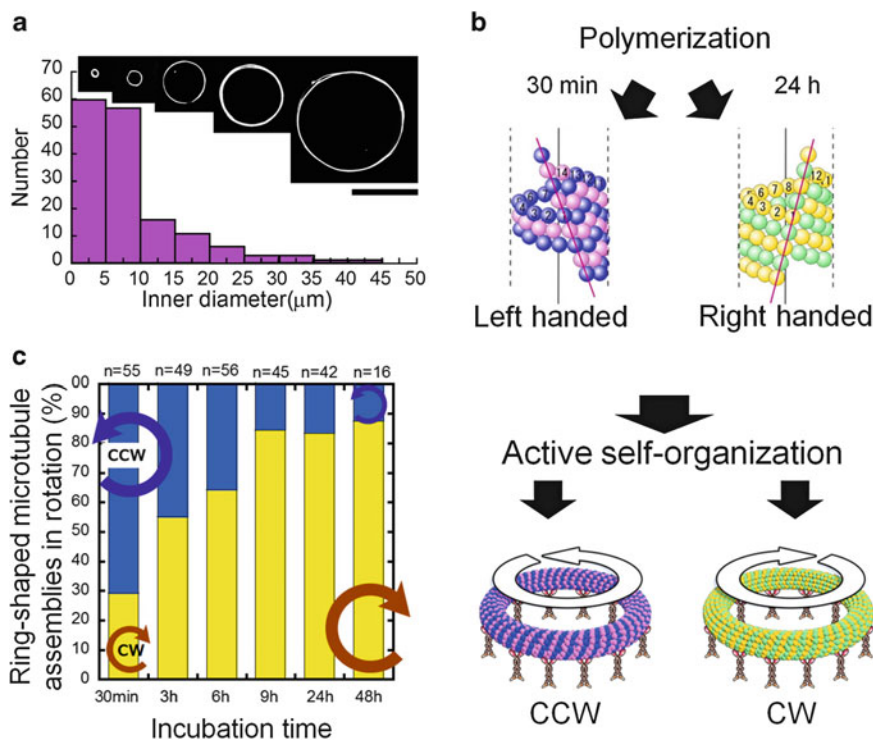


Fig. 34.3 Ring-shaped microtubule assemblies obtained from AcSO of microtubules. Images of the ring-shaped microtubule assemblies with various sizes and their size distribution (**a**). Schematic representation of the investigation on the effect of incubation time for microtubules preparation on the preferential rotation of the ring-shaped microtubule assemblies Scale bar: 25 μm (**b**). Effect of incubation time of microtubules preparation on the preferential rotation of the ring-shaped microtubule assemblies formed by AcSO. The ring-shaped microtubule assemblies rotating in counter-clockwise (CCW) and clockwise (CW) directions are shown as percentage of total number of rings (**c**)

or CW direction was $\text{CCW}:\text{CW} = 7:3$ when the incubation time for microtubule polymerization was 30 min. On the other hand, by changing the incubation time for microtubule polymerization to 24 h, the ratio was dramatically changed to $\text{CCW}:\text{CW} = 1:9$ (Fig. 34.3b, c). It was observed that change in the incubation time also brought change in the size of ring-shaped microtubule assemblies, which is associated with the rearrangement of the PFs in microtubules lattice. These findings would not only reveal the obscure mechanism that governs the formation of such ring-shaped organized structures and their preferential rotation but also provide an insight in understanding the handedness observed in highly ordered and complex assemblies of natural systems. Thus, controlled handedness of ring-shaped microtubule assemblies will widen the opportunity for developing future bio-machine.

34.2 Prolonged In Vitro Lifetime of Biomolecular Motor in a Reactive Oxygen Species Free Inert Atmosphere

Performances of biomolecular motors are quite sensitive to their environment and different types of factors such as biochemical factors (enzyme), physical factors (temperature and pressure) or chemical factors (pH, oxidation and reduction) are known to affect the lifetime of biomolecular motors. Nowadays it is possible to keep the harmful effects of most of the factors minimum. Fluorescence microscopy has been widely used for investigating various aspects of biomolecular motor system. However generation of reactive oxygen species (ROS) under fluorescence microscopy has been a great concern for the lifetime of biomolecular motors. ROS can cause serious damage to biomolecular motors and terminate their activity [39–42]. A combination of glucose, glucose oxidase, and catalase has been commonly used so far as scavenger to minimize the oxidative stress on biomolecular motors [43]. This scavenger system, however, can work only for a limited period of time (approximately a few hours). To minimize the effect of ROS on biomolecular motors inert chamber system (ICS) was developed that allowed the investigation keeping the specimen in an inert nitrogen gas atmosphere free of ROS [44]. Using ICS, the active lifetime of the microtubule/kinesin system was prolonged for a longer time by protecting it from oxidative damage (Fig. 34.4c). The lifetime of microtubule assemblies was also prolonged successfully in the inert atmosphere [45]. Prolonged in vitro lifetime of biomolecular motors will foster their future industrial applications at a great extent. Moreover prolonged lifetime of biomolecular motors opened the door to perform further investigation on the AcSO of microtubules specially where the time length of AcSO plays a crucial role.

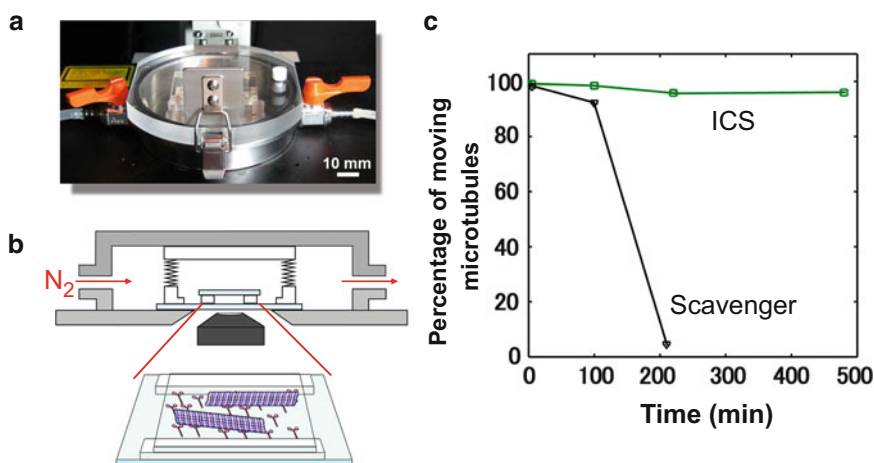


Fig. 34.4 Inert chamber system (ICS) used to prolong the active life time of biomolecular motor system. Image of ICS (a). Schematic diagram of ICS and a flow cell used for motility assay of microtubules (b). Effects of different experimental conditions on the moving ability of microtubules. Motility assays were performed using only scavengers and using ICS (c)

34.2.1 Growth of Ring-Shaped Microtubule Assemblies Through Stepwise Active Self-Organization in an Inert Atmosphere

Thickness of the ring-shaped microtubule assemblies is significantly important in consideration of force integration by biomolecular motors and their sustainable practical use. One way to increase dimensionality, e.g., thickness of ring-shaped microtubule assemblies is to let the AcSO process proceed for a longer period of time by continuously supplying microtubule filaments in a stepwise manner [46]. Stepwise method, that was proved successful in the self-organization of organic, inorganic and biological systems [47–49], allows the ring-shaped microtubule assemblies grow further. Stepwise AcSO can be performed by using the ICS where new microtubule filaments, streptavidin (St) and ATP were added before in a stepwise manner it reached a thermodynamically stable steady state (Fig. 34.5a). This process was performed nine times in a consecutive manner, and as the result thickness of ring-shaped microtubule assemblies was found to increase without affecting the distribution of their inner radii (Fig. 34.5b, c). After the fifth AcSO, thickness of ring-shaped microtubule assemblies was found to decrease and this has been accounted for by the loss of viability of microtubule assemblies after

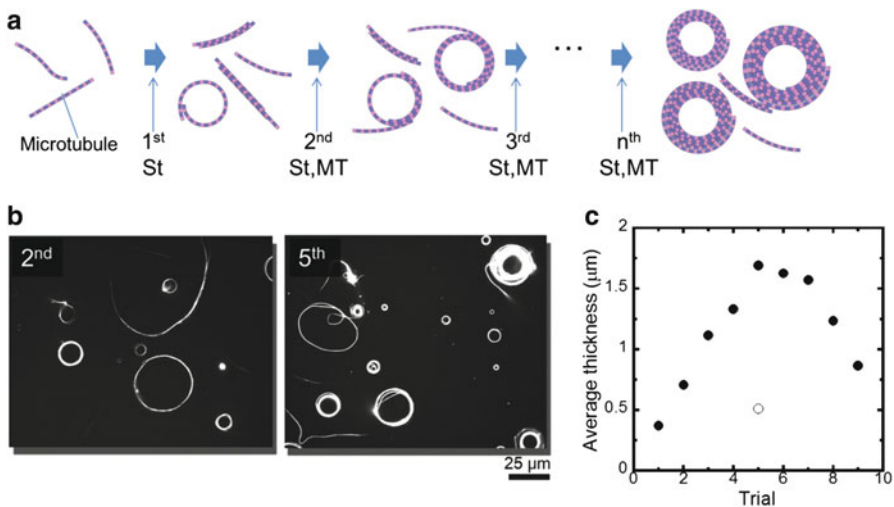


Fig. 34.5 Stepwise active self-organization of microtubules can produce thicker ring-shaped microtubule assemblies. Schematic representation of the stepwise AcSO of microtubules (a). Representative fluorescence images showing the change in the number and thickness of ring-shaped microtubule assemblies obtained after the second and fifth stepwise AcSOs (b). Average thickness of ring-shaped microtubule assemblies obtained after the first to ninth stepwise AcSOs (closed circle) and non-stepwise AcSO (open circle) (c). Standard deviations of the first to ninth stepwise AcSOs and the non-stepwise AcSO are 0.15, 0.39, 0.93, 0.89, 1.12, 1.18, 1.14, 1.01, 0.48 and 0.26, respectively

fifth AcSO. The loss of viability of the ring-shaped microtubule assemblies might have arisen from the high probability of collision of the ring-shaped microtubule assemblies with microtubule bundles, which might have resulted in the association of microtubules of opposite polarity. Thus stepwise AcSO of microtubules successfully produced thicker ring-shaped microtubule assemblies, which could not be observed in a non-stepwise AcSO.

34.3 Spatiotemporal Control of Active Self-Organization of Biomolecular Motors

With a view to have a spatiotemporal control on the self-organization process of biomolecular motors, effects of various external factors on the AcSO have been investigated. Self-organization of biomolecular motors was successfully controlled by utilizing various external factors that include temperature gradient or air-buffer interface, as discussed in the following sections.

34.3.1 Formation of Well-Oriented Microtubules with Preferential Polarity Under a Temperature Gradient

Generally, tubulin polymerization is carried out in the presence of chemical energy of GTP hydrolysis at a homogeneous thermal environment (constant temperature) *in vitro*. Polymerization of tubulin under asymmetric conditions, achieved by applying a temperature gradient with spatial restriction, produced well-oriented microtubule assemblies having preferential polarity (Fig. 34.6) [50]. The formation of a microtubule array with preferential polarity was based on the premise that the propagation of heat for the nucleation process towards the cold end was slower than the polymerization rate of microtubules. When the former value exceeded the latter, nucleation was faster than microtubule growth, thereby leading to a random polarity. Initially when heat propagation was much faster than the microtubule polymerization rate, the nucleation kinetics was the rate determining factor for the growth process. Under a temperature gradient, microtubules started to elongate from thermally induced nuclei and aligned themselves parallel to the long axis of space available. In the later stages, when heat propagation was slower than the microtubule polymerization rate, no nuclei were formed at the growth front and microtubule growth depended exclusively on the polymerization. At that time, a tubulin concentration gradient was developed at the growth front. Since microtubules grow at a faster rate at the plus end than at the minus end, the plus end grew preferentially, and the growth of the minus end was suppressed in the absence of excess free tubulin. Consequently, microtubules were formed with their plus ends oriented

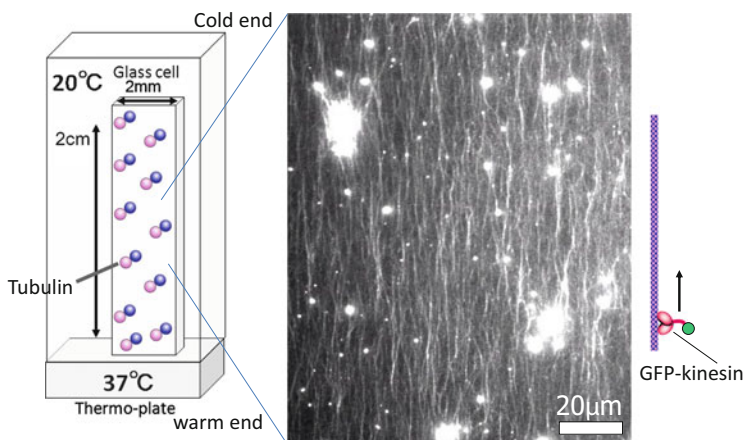


Fig. 34.6 Formation of well-oriented microtubules through polymerization under a temperature gradient. Schematic illustration of the experimental setup used for preparing well-oriented microtubules under asymmetric polymerization conditions (a temperature gradient) in a confined space (*left*). Fluorescence microscopy image of GFP-kinesins on oriented microtubules (*right*)

towards the cold end. The preferential polarity of the microtubules assembly was elucidated by the unidirectional motion of green fluorescent protein fused kinesin (GFP-kinesin) their a unidirectional motion along the oriented microtubule tracks under fluorescent microscope. Most (90 %) of the GFP-kinesins moved along the microtubules toward the cold end (Fig. 34.6 (left)). Thus, application of temperature gradient in microtubule polymerization can control not only the orientation of microtubules but also their polarity.

34.3.2 *Formation of Ring-Shaped Assembly of Microtubules with a Narrow Size Distribution at an Air-Buffer Interface*

As already discussed, ring-shaped microtubules assemblies are obtained through the AcSO process by employing St/Bt interaction. However, the size of the ring-shaped microtubule assemblies obtained was widely distributed and the yield of ring formation was also quite low, which appeared as a significant drawback for the development of future artificial biomachine. Instead of using St/Bt interaction, AcSO of microtubules at an air–buffer interface resulted in ring-shaped microtubule assemblies with a narrow size distribution and high yield (Fig. 34.7a, b) [51]. Using an “air–buffer interface control system” combined with the “inert chamber system (ICS)” the reversible conformational transition between ring- and bundle-shaped microtubules at the air–buffer interface was successfully observed.

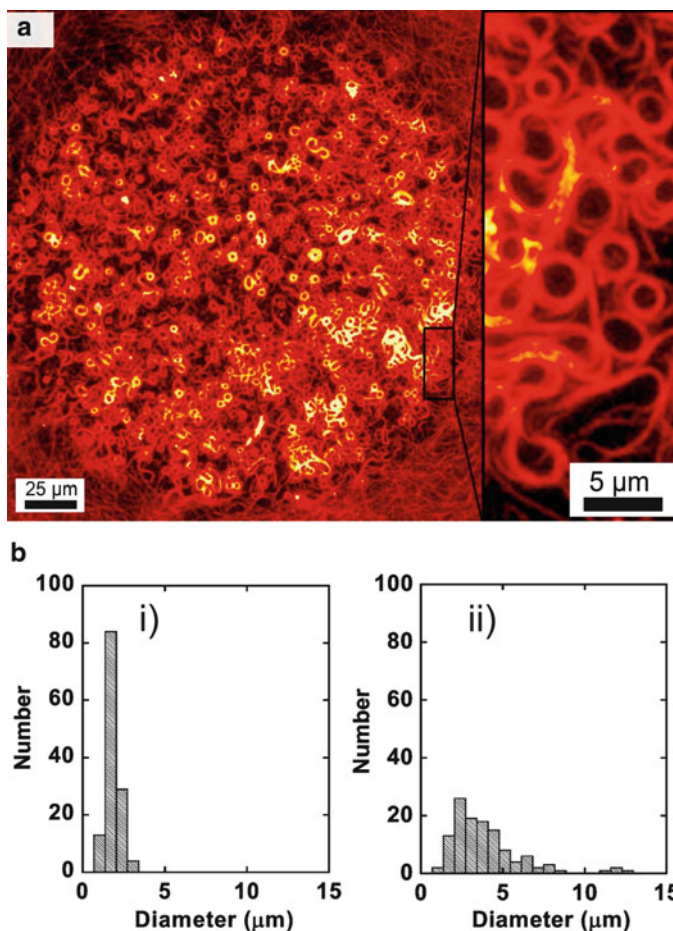


Fig. 34.7 Formation of ring-shaped microtubule assemblies at an air-buffer interface. (a) Fluorescence microscopy image of the ring-shaped microtubule assemblies formed at the air-buffer interface through AcSO. Distribution of diameter of ring-shaped microtubule assemblies formed through AcSO (b): (i) at the air-buffer interface, and (ii) in aqueous medium using the St-Bt interaction

Formation mechanism of the ring-shaped microtubules from the elongated filaments at the air-buffer interface is accounted for by the free energy arguments. Here the air-buffer interface and buffer are treated as poor and good solvent for microtubules respectively. In free-energy arguments, the free energy for microtubule ring formation is treated as the sum of surface energy of elongated and ring-shaped microtubules, volume energy of a ring, conformation energy, rigidity of the ring, coulomb energy between charges on the coil and translational energy of counterions distributed around the coil part. The free energy of the formation of the ring-shaped microtubule assemblies was defined as-

$$\Delta G \approx -\alpha\rho + \frac{\beta}{\rho^{2/3}} + \kappa L\rho^{2/3} + \frac{3}{2}k_B T(\rho^{-2/3} + \rho^{2/3}) + \frac{e^2}{\epsilon l_s \rho^{2/3}} + \frac{k_B T}{3\rho^{2/3}} \ln \rho \quad (34.1)$$

where α : effective binding energy, β : effective surface energy, ρ : density of the polymer chain, κ : rigidity of the polymer chain, L : contour length, ϵ : dielectric constant, l_s : bjerrum length (the charges of the coil part are neutralized by mono-valent counterions, while the counterions are condensed onto microtubule in poor solvent)

The first and second terms in Eq. (34.1) are the bulk and the surface energy of the ring respectively. The third term is rigidity energy of the ring, fourth is conformation energy, fifth is coulomb energy between charges on the coil and sixth is translational energy of counterions. When the air-buffer interface (permittivity ~ 0) contact with microtubules, the ΔG increases due to the increase in fourth terms of Eq. (34.1), and microtubules tend to decrease their surface energy by forming ring-shape structure.

The ring-shaped microtubule assemblies with a narrow size distribution obtained at the air-buffer interface holds prospect for serving as a promising candidate as building blocks a for ATP driven bio-machine.

34.4 Conclusion

Active self-organization has been a promising technique to integrate biomolecular motor system into ordered structure which can offer assembled structures with functions of a wide range as observed in natural systems. All these efforts are expected to collectively foster the development of biomolecular motor based ATP-driven bio-machine and at the same time will help understand the development process of hierarchical structures and origin of various emergent functions observed in nature.

References

1. Cooper JA (1991) The role of actin polymerization in cell motility. *Annu Rev Physiol* 53:585–605
2. Umeda M, Emoto K (1999) Membrane phospholipid dynamics during cytokinesis: regulation of actin filament assembly by redistribution of membrane surface phospholipid. *Chem Phys Lipids* 101:81–91
3. Bachand M, Trent AM, Bunker BC, Bachand GD (2005) Physical factors affecting kinesin-based transport of synthetic nanoparticle cargo. *J Nanosci Nanotechnol* 5:718–722
4. Mahadevan L, Matsudaira P (2000) Motility powered by supramolecular springs and ratchets. *Science* 288:95–100
5. Turner DC, Chang C, Fang K, Brandow SL, Murphy DB (1995) Selective adhesion of functional microtubules to patterned silane surfaces. *Biophys J* 69:2782–2789

6. Ramachandran S, Ernst KH, Bachand GD, Vogel V, Hess H (2006) Selective loading of kinesin-powered molecular shuttles with protein cargo and its application to biosensing. *Small* 2:330–334
7. Hess H, Clemmens J, Howard J, Vogel V (2002) Surface imaging by self-propelled nanoscale probes. *Nano Lett* 2:113–116
8. Hess H, Howard J, Vogel VA (2002) A Piconewton force meter assembled from microtubules and kinesins. *Nano Lett* 2:1113–1115
9. Martin GL, Heuvel VD, Dekker C (2007) Motor proteins at work for nanotechnology. *Science* 317:333–336
10. Alberts B, Johnson A, Lewis J, Raff M, Roberts K, Walter P (2008) *Molecular biology of the cell*, 5th edn. Garland Press, New York
11. Lasker GW (1969) Human biological adaptability. *Science* 166:1480–1486
12. Martin P (1997) Wound healing—aiming for perfect skin regeneration. *Science* 276:75–81
13. Gutsmann T, Hassenkam T, Cutroni JA, Hansma PK (2005) Sacrificial bonds in polymer brushes from rat tail tendon functioning as nanoscale velcro. *Biophys J* 89:536–542
14. Boncheva M, Whitesides GM (2003) Self-healing systems having a design stimulated by the vertebrate spine. *Angew Chem Int Ed* 42:2644–2647
15. Chen X, Dam MA, Ono K, Mal A, Shen H, Nutt SR, Sheran K, Wudl F (2002) A thermally re-mendable cross-linked polymeric material. *Science* 295:1698–1702
16. White SR, Sottos NR, Geubelle PH, Moore JS, Kessler MR, Sriram SR, Brown EN, Viswanathan S (2001) Autonomic healing of polymer composites. *Nature* 409:794–797
17. Vale RD, Fletterick RJ (1997) The design plan of kinesin motors. *Annu Rev Cell Dev Biol* 13:745–777
18. Howard J, Hudspeth AJ, Vale RD (1989) Movement of microtubules by single kinesin molecules. *Nature* 342:154–158
19. Hess H, Clemmens J, Brunner C, Doot R, Luna S, Ernst KH, Vogel V (2005) Molecular self-assembly of “Nanowires” and “Nanospoools” using active transport. *Nano Lett* 5:629–633
20. Kawamura R, Kakugo A, Osada Y, Gong JP (2010) Selective formation of a linear-shaped bundle of microtubules. *Langmuir* 26:533–537
21. Kawamura R, Kakugo A, Osada Y, Gong JP (2010) Microtubule bundle formation driven by ATP: the effect of concentrations of kinesin, streptavidin and microtubules. *Nanotechnology* 21:145603
22. Tamura Y, Kawamura R, Shikinaka K, Kakugo A, Osada Y, Gong JP, Mayama H (2011) Dynamic self-organization and polymorphism of microtubule assembly through active interactions with kinesin. *Soft Matter* 7:5654–5659
23. Hess H (2006) Self-assembly driven by molecular motors. *Soft Matter* 2:669–677
24. Liu H, Spoerke ED, Bachand M, Koch SJ, Bunker BC, Bachand GD (2008) Biomolecular motor-powered self-assembly of dissipative nanocomposite rings. *Adv Mater* 20:4476–4481
25. Luria I, Crenshaw J, Downs M, Agarwal A, Seshadri SB, Gonzales J, Idan O, Kamcev J, Katira P, Pandey S, Nitta T, Phillpota SR, Hess H (2011) Microtubule nanospool formation by active self-assembly is not initiated by thermal activation. *Soft Matter* 7:3108–3115
26. Idan O, Lam A, Kamcev J, Gonzales J, Agarwal A, Hess H (2012) Nanoscale transport enables active self-assembly of millimeter-scale wires. *Nano Lett* 12:240–245
27. Liu H, Bachand GD (2012) Effects of confinement on molecular motor-driven self-assembly of ring structures. *Cell Mol Bioeng* 6:98–108
28. Kawamura R, Kakugo A, Shikinaka K, Osada Y, Gong JP (2008) Ring-shaped assembly of microtubules shows preferential counterclockwise motion. *Biomacromolecules* 9:2277–2282
29. Amos LA, Klug A (1974) Arrangement of subunits in flagellar microtubules. *J Cell Sci* 14:523–549
30. Amal I, Wade RH (1995) How does taxol stabilize microtubules? *Curr Biol* 5:900–908
31. Ray S, Meyhöfer E, Milligan RA, Howard J (1993) Kinesin follows the microtubule’s protofilament axis. *J Cell Biol* 121:1083–1093

32. Chrétien D, Wade RH (1991) New data on the microtubule surface lattice. *Biol Cell* 71:161–174
33. Chretien D, Kenney JM, Fuller SD, Wade RH (1996) Determination of microtubule polarity by cryo-electron microscopy. *Structure* 4:1031–1040
34. Chretien D, Fuller SD (2000) Microtubules switch occasionally into unfavorable configurations during elongation. *J Mol Biol* 298:663–676
35. Vogan KJ, Tabin C (1999) A new spin on handed asymmetry. *Nature* 397:295–298
36. Shibazaki Y, Shimizu M, Kuroda R (2004) Body handedness is directed by genetically determined cytoskeletal dynamics in the early embryo. *Curr Biol* 14:1462–1467
37. Thitamadee S, Tuchiara K, Hashimoto T (2002) Microtubule basis for left-handed helical growth in *Arabidopsis*. *Nature* 417:193–196
38. Kakugo A, Kabir AMR, Hosoda N, Shikinaka K, Gong JP (2011) Controlled clockwise–counterclockwise motion of the ring-shaped microtubules assembly. *Biomacromolecules* 12:3394–3399
39. Dixit R, Cyr R (2003) Cell damage and reactive oxygen species production induced by fluorescence microscopy: Effect on mitosis and guidelines for non-invasive fluorescence microscopy. *Plant J* 36:280–290
40. Sporn LA, Foster TH (1992) Photofrin and light induces microtubule depolymerization in cultured human endothelial cells. *Cancer Res* 52:3443–3448
41. Juarranz A, Villanueva A, Diaz V, Cañete MJ (1995) Photodynamic effects of the cationic porphyrin, mesotetra(4 N-methylpyridyl)porphine, on microtubules of HeLa cells. *J Photochem Photobiol B* 27:47–53
42. Stockert JC, Juarranz A, Villanueva A, Cañete M (1996) Photodynamic damage to HeLa cell microtubules induced by thiazine dyes. *Cancer Chemother Pharmacol* 39:167–169
43. Kishino A, Yanagida T (1988) Force measurements by micromanipulation of a single actin filament by glass needles. *Nature* 334:74–76
44. Kabir AMR, Inoue D, Kakugo A, Kamei A, Gong JP (2011) Prolongation of the active lifetime of a biomolecular motor for in vitro motility assay by using an inert atmosphere. *Langmuir* 27:13659–13668
45. Kabir AMR, Inoue D, Kakugo A, Sada K, Gong JP (2012) Active self-organization of microtubules in an inert chamber system. *Polym J* 44:607–611
46. Inoue D, Kabir AMR, Mayama H, Gong JP, Sada K, Kakugo A (2013) Growth of ring-shaped microtubule assemblies through stepwise active self-organisation. *Soft Matter* 9:7061–7068
47. Ueda T, Gao QZ, Yamaichi E, Yamagishi C, Akiyama M (1994) Growth of GaAs microcrystal by Ga droplet formation and successive As supply with low-pressure metalorganic chemical vapor deposition. *J Cryst Growth* 145:707–713
48. Lvov Y, Decher G, Sukhorukov G (1993) Assembly of thin films by means of successive deposition of alternate layers of DNA and poly(allylamine). *Macromolecules* 26:5396–5399
49. Knoll W (1996) Self-assembled microstructures at interfaces. *Curr Opin Colloid Interface Sci* 1:137–143
50. Kakugo A, Tamura Y, Shikinaka K, Yoshida M, Kawamura R, Furukawa H, Osada Y, Gong JP (2009) Formation of well-oriented microtubules with preferential polarity in a confined space under a temperature gradient. *J Am Chem Soc* 131:18089–18095
51. Kabir AMR, Wada S, Inoue D, Tamura Y, Kajihara T, Mayama H, Sada K, Kakugo A, Gong JP (2012) Formation of ring-shaped assembly of microtubules with a narrow size distribution at an air-buffer interface. *Soft Matter* 8:10863–10867

Chapter 35

Employing Cytoskeletal Treadmilling in Bio-Actuator

Ken-Ichi Sano, Ryuzo Kawamura, and Yoshihito Osada

Abstract In this chapter, we describe treadmilling bio-actuators. The principle of treadmilling actuator is, filamentous protein complex formation by actin or tubulin accompanying a sequence of nucleotide triphosphate hydrolysis is to alter the critical concentration of polymerization at the two ends of the filament. Recently, we have succeeded in the creation of hydrogels which autonomously oscillate owing to the treadmilling of actin or tubulin. These hydrogels have great potential as bio-actuators because they are easy to make on a centimeter scale.

Keywords Actin • Bio-actuator • Cytoskeleton • Hydrogel • Microtubules • Treadmilling

35.1 Introduction

To understand and to create efficient bio-actuator systems, it is critical to understand the mechanisms that generate movement within a system. To learn these mechanisms and the functional relationship of each component it is useful to isolate each element and evaluate it [1]. Biologically, this is done in vitro by studying various proteins individually and applying those functions to tissues. A group of proteins called motor proteins, generate biological movement in the living

K.-I. Sano (✉)

Molecular and System Life Science Unit, RIKEN Advanced Science Institute, Saitama, Japan

Department of Innovative Systems Engineering, Nippon Institute of Technology, Saitama, Japan

e-mail: kisano@nit.ac.jp

R. Kawamura

Molecular and System Life Science Unit, RIKEN Advanced Science Institute, Saitama, Japan

Department of Chemistry, Saitama University, Saitama, Japan

e-mail: ryuzo@mail.saitama-u.ac.jp

Y. Osada

Molecular and System Life Science Unit, RIKEN Advanced Science Institute, Saitama, Japan

e-mail: osadayoshi@riken.jp

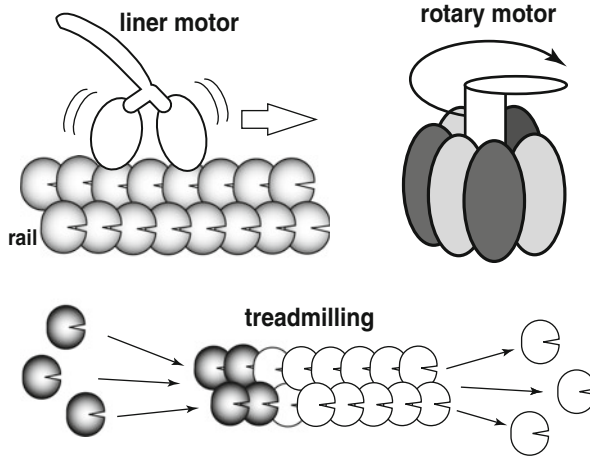


Fig. 35.1 Schematic illustrations of classified motor proteins, linear motors, rotary motors, and treadmilling. Linear motor protein slides on the rail proteins such as filamentous actin and microtubules using the energy of ATP hydrolysis. Rotary motor protein usually rotates the stalk shaft using ions (including proton) flow from outer to inner cell and the energy of ATP hydrolysis. In treadmilling, filamentous protein complex formation accompanying a sequence of nucleotide triphosphate hydrolysis is to alter the critical concentration of polymerization at the two ends of the filament

organism [2]. Therefore, the assessment and reconstruction of motor proteins *in vitro*, has received increasing attention in the field of bio-actuator research [3–5].

Generally, motor proteins are classified into one of three groups (Fig. 35.1) [1, 2]. (1) The linear motor proteins, such as myosin, kinesin, and dynein. These progress linearly along filamentous actin or microtubules using energy from ATP (adenosine triphosphate) hydrolysis. (2) There are rotary motor proteins, such as $F_1(F_0)$ -ATPase or the bacterial flagella motor. These create rotational movement through the hydrolysis of ATP and an ion gradient. (3) Finally, there are treadmilling proteins. These proteins work through the polymerization and depolymerization of filamentous actin or microtubules. To create a bio-actuator using motor proteins they must act cooperatively to generate force, similar to the muscular system in animals [6]. Although the flagella motor itself can propel bacteria [7], and linear motor proteins have been tested *in vitro* [8], the output of these proteins in trials was very low, and the movement is on a microscopic scale [9–12]. Recently, we have succeeded in the creation of hydrogels which oscillate owing to the treadmilling of actin or tubulin. These hydrogels have great potential as bio-actuators because they are easy to make on a centimeter scale. In this chapter, we describe treadmilling bio-actuators, including our recent progress with the treadmilling oscillator.

35.2 What Is Treadmilling?

A treadmill is an athletic machine for walking or running in one place. In biology, a treadmill is the continuous polymerization and depolymerization of an actin or tubulin filament such that a given subunit traverses from the point of addition (polymerization) along the filament and is eventually removed by depolymerization [2].

Here, we would like to explain actin treadmilling as an example. Actin is the most abundant protein in eukaryotes and is responsible for maintaining the integrity and motility of eukaryotic cells [13–15]. Actin can exist in a globular monomeric state called G-actin when stored in low ionic conditions *in vitro*. When salt is added to this solution, polymerization of G-actin will occur and a double-helical, stable, filamentous structure (called F-actin) is formed [16]. Actin is an ATP hydrolysis protein, and hydrolysis of ATP is accelerated by the polymerization of actin. After the polymerization, even if elongation reaches a stationary state (not equilibrium), there still exists a certain concentration of G-actin depending on the ionic strength of the solution and actin concentration [17]. That is, actin is polymerizing and depolymerizing, moving from monomeric G-actin to filamentous F-actin regularly. Furthermore, since there is polarity to the structure of the F-actin, polymerization takes place preferentially at one end of the filament and depolymerization occurs preferentially at the other. Consequently, the length of an F-actin will not change when in a stationary state, but the actin monomers move (Fig. 35.2). This phenomenon is called “treadmilling” which is associated with the idea of the athletic treadmill.

Locomotion by actin treadmilling is not limited in an *in vitro* reconstruction system, but is seen occurring in cellular motility events [15, 18]. When an animal cell moves on a solid surface or alters its morphology, the shape of the cell membrane dynamically changes, extending pseudopodia. The rearrangement of the F-actin underlying the cell membrane determines the shape and movement of the cell. For example, filaments that are in spiky bundles generate filopodia; and flat protrusive F-actin fans create lamellipodia [2]. These changes in F-actin network structure are induced through F-actin treadmilling and filament remodeling inside the cells. Studies of these phenomena are well documented and have revealed that these events are driven by the actin treadmilling. Of course, it is known that many actin associated proteins are required as well. Especially, actin depolymerization proteins such as ADF/cofilin which promote severing of F-actin and accelerate G-actin dissociation, promoting treadmilling.

It is also important to consider the output power and speed capabilities of a treadmilling bio-actuator [19]. Most bio-actuator research has used linear motor proteins, such as myosin which constitutes muscles, or kinesin and dynein which move along microtubules. The linear motor proteins move at a speed of about 4 and 1 $\mu\text{m/s}$ for conventional myosin (myosin from skeletal muscle) and conventional kinesin (kinesin from brain), respectively. The output power of a single myosin motor reaches 10 pN and kinesin reaches 6 pN (Table 35.1). A single F-actin

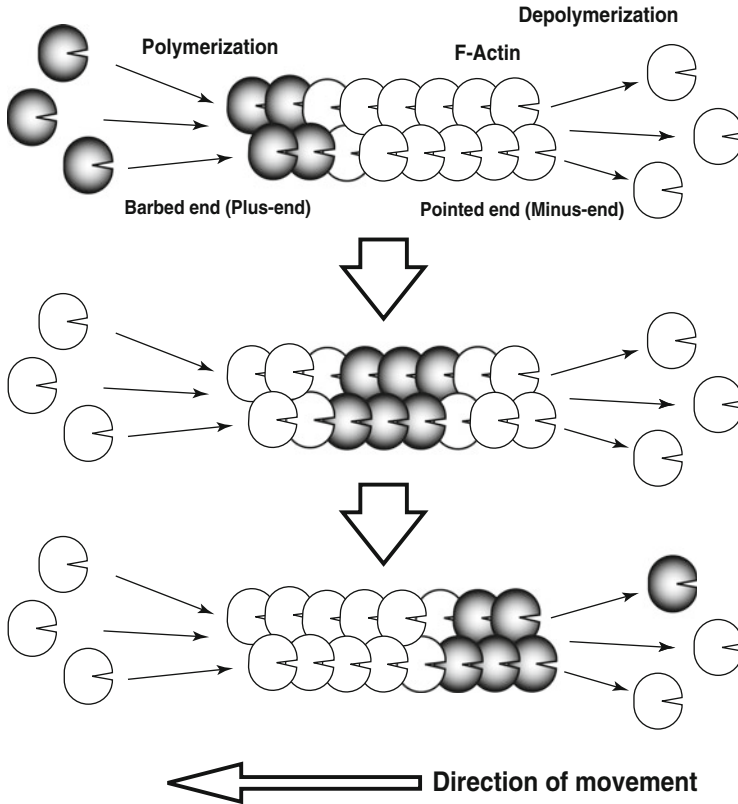


Fig. 35.2 Schematic illustrations of actin treadmilling. The two ends of actin filament have different rate constant for polymerization and depolymerization. The fast-growing end is called barbed end or plus end, whereas the slow-growing end is called pointed end or minus end

Table 35.1 Comparison of performance between bio-actuators. Literature by Mahadevan and Matsudaira 2000 was modified

	Velocity ($\mu\text{m/s}$)	Output (pN)	Power density (J/sg)
MyosinII-Actin linear motor	1–10 (usually)	10	20
	50 (max)		
Kinesin-microtubules linear motor	1	6	7
Actin-treadmilling	1	10	100
Microtubules-treadmilling	0.02	4	50
Car engine			0.3

filament undergoing treadmilling has an output speed of $1 \mu\text{m/s}$ and a power output of 10 pN , these output characteristics are almost equivalent to the linear motor proteins. Note that the power density of actin treadmilling, however, greatly

exceeds that of the linear motor proteins. Thus, it appears that an actin treadmilling system has sufficient power and speed to be applicable as a bio-actuator.

Treadmilling is seen not only in actin filaments but also in microtubules. Hotani and co-workers have succeeded in the direct observation of the polymerization and depolymerization of a single microtubules under an optical microscope [20]. However, simple chemical equilibrium models do not explain the elongation and shortening of microtubules. This is called “dynamic instability” and illustrates the “softness” or “plasticity” of biological systems. The dynamic instability seen in microtubules is an interesting biological finding, and is an interesting consideration when designing hypothetical materials for bio-actuator systems. Although the output features of microtubule treadmilling are not very different from actin, the output speed is quite slow at a $0.02 \mu\text{m/s}$ in vitro. Even at the maximum speeds found in vivo microtubules are still slow at $0.2 \mu\text{m/s}$ which is almost $1/5$ that of actin.

35.3 Studies of Treadmilling Systems

Cell biology aims to elucidate the regulatory mechanism of actin treadmilling. As a result of several genetic analyses and molecular imaging studies, it has become clear that many actin associated proteins and small G-proteins are required for treadmilling [15]. Therefore, reconstruction of a treadmilling bio-actuator requires establishing a model system consisting of the key ingredients required for the movement. Hotani and co-workers built an excellent model system that used liposomes as a cell model [21]. They successfully engineered liposomes with various components inside (i.e., varied concentrations of actin, or ATP) and then analyzed the actin dynamics and the resulting liposome shape based on the precise conditions within the liposomes (Fig. 35.3). For example, when a certain actin bundling protein was added, the network structure of F-actin was changed and consequently the morphology of liposome also changed. Some systems biology studies have also been applied to actin treadmilling in recent years, because it is so difficult to control each of these elements in vitro.

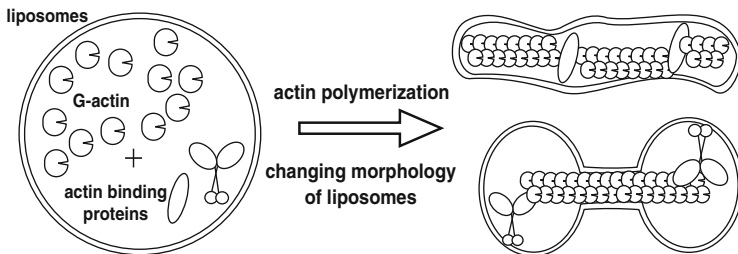


Fig. 35.3 Changing morphology of liposomes through actin polymerization and organization of actin filaments

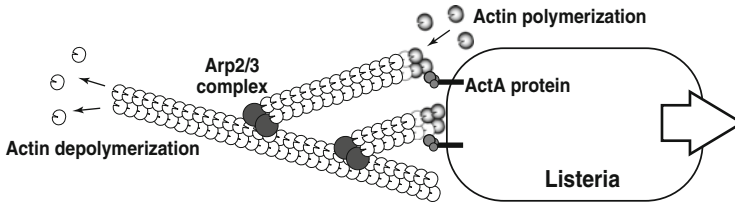


Fig. 35.4 Actin polymerization produces force for *Listeria* movement. *Listeria* uses the actin treadmilling machinery to move around inside the host cell. A transmembrane protein ActA is induced directed actin polymerization allowing to swim around bacteria in the host cell

Accordingly, research using whole cell lysates that contain all the components required for treadmilling are commonly used [22]. *Listeria* is a human pathogen that uses the host's actin treadmilling network to navigate around the inside of the cell. *Listeria* has an ActA protein on its cell surface which acts to nucleate actin filaments, then sequential treadmilling “pushes” *Listeria* around inside of the cell (Fig. 35.4) [23], even exploiting the host cell to help it reach a neighbor cell to infect it. This *Listeria*-based actin treadmilling movement can be reproduced as an artificial system. When polystyrene beads are coated in the ActA protein and added to *Xenopus laevis* extract supplemented with ATP, the polystyrene beads start to “swim”.

35.4 Supra-Macromolecular Hierarchical Cytoskeletal Protein Hydrogels

Recently, we succeeded in synthesizing chemically cross-linked hydrogels comprised of actin or tubulin [24, 25]. These hydrogels have complex multi-order structure different from conventional synthetic polymer hydrogels. Conventional hydrogels could be said to have only three orders of structure, that is the monomer units (zero order), the polymerized molecules (first order), films and sheets (second order), and finally a swollen hydrogel (third order). However, our actin hydrogel, for example, has more structural dimensions. G-actin has amino acid units (zero order), these form the polypeptide chain (first order), next the peptide forms α -helical and β -sheets (second order), and then the final structure of the protein would be the third order. Thus, G-actin itself has three levels of structure, making F-actin a fourth order, the PEG cross-linking then could be considered a fifth order in the structure (Fig. 35.5). We therefore named these hydrogels “supra-macromolecular hierarchical hydrogels” and we assess any emergent functions owing to this structural hierarchy.

Supra-macromolecular hierarchical protein hydrogels show high mechanical strength. The storage modulus of the supra-macromolecular hierarchical hydrogels is two–three orders of magnitude larger than that of conventional synthetic polymer

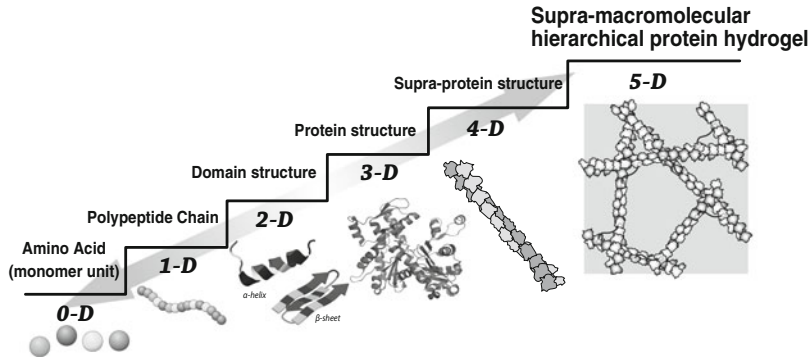


Fig. 35.5 Concept of Supra-macromolecular hierarchical protein hydrogel

hydrogels with flexible chain networks (e.g., polyacrylamide gel) [24, 25]. This is likely associated with the rigid filamentous nature of the initial chain assembled from G-actin. The gels can also undergo sol–gel transition by changing ionic strength and temperature inducing polymerization and depolymerization of actin and tubulin within the gel. Notably the supra-macromolecular hierarchical protein hydrogels displayed cooperative depolymerization against strain, and showed immediate recovery of the storage modulus when the strain was removed [25]. That is, they exhibit a self-repairing capability depending on the structural dimensions.

Furthermore, the storage modulus of supra-macromolecular hierarchical hydrogel autonomously oscillated for more than 10 h (Sano et al., unpublished results). Since such oscillations were not observed without chemical crosslinking, these appear to be essential for this oscillatory property. Treadmilling is also required to create these mechanical oscillations in the supra-macromolecular hierarchical hydrogel. When we added a drug to suppress treadmilling, the oscillations of the storage modulus stabilized. These results indicate that the oscillatory properties of the supra-macromolecular hierarchical protein hydrogels were based on both the treadmilling and gelation by chemical crosslinking of the filamentous structures. Importantly, the supra-macromolecular hierarchical protein hydrogels may yield a functional oscillatory treadmill bio-actuator.

The size of the treadmilling actuators described above, (liposomes, polystyrene beads, and *Listeria*) were up to 100 μm , however, the supra-macromolecular hierarchical protein hydrogels are built on a centimeter scale. This means that, with respect to size, the supra-macromolecular hierarchical protein hydrogels might accomplish actuation that is practical. Unfortunately, we have not succeeded in harvesting the output work from the oscillation of the supra-macromolecular hierarchical protein hydrogels at present. This is attributed to our lack of knowledge of the molecular mechanisms regulating the oscillatory phenomena of the supra-macromolecular hierarchical protein hydrogels.

Recently, we combined these supra-macromolecular hierarchical protein hydrogels with linear motor proteins [26]. We explored the specific motility of

the supra-macromolecular hierarchical microtubules hydrogel when combined with kinesin. As a result, we found that the cross-linked microtubules hydrogel showed enhanced velocity and power, with a prolonged persistent motion when compared with microtubules only mixtures. Importantly, no specific polarization or organizational control is required to generate the motion.

35.5 Conclusions

Here, we briefly described the possibility of harnessing the treadmilling actions of cytoskeletal proteins in the development of bio-actuator. The goals of this research are for the supra-macromolecular hierarchical protein hydrogels to contribute not only to the understanding of bio-actuators, but also to facilitate motility research.

Acknowledgments Actin and microtubules hydrogel studies were supported in part by TOYOTA motor corporation and KAKENHI from Japan Society for Promotion Science to K.-I. S. (20681013, 23570181).

References

1. Bray D (2001) Cell movements: from molecules to motility, 2nd edn. Garland Science, New York
2. Alberts B, Johnson A, Lewis J et al (2002) Molecular biology of the cell, 4th edn. Garland Science, New York
3. Howard J, Hudspeth AJ, Vale RD (1989) Movement of microtubules by single kinesin molecules. *Nature* 342:154–158
4. Vale RD, Reese TS, Sheetz MP (1985) Identification of a novel force-generating protein, kinesin, involved in. *Cell* 42:39–50
5. Sheetz MP, Spudich JA (1983) Movement of myosin-coated fluorescent beads on actin cables in vitro. *Nature* 303:31–35
6. Bagshaw CR (1993) Muscle contraction, 2nd edn. Springer, Heidelberg
7. Berg HC (2003) The rotary motor of bacterial flagella. *Annu Rev Biochem* 72:19–54
8. Valle RB (ed) (1991) Molecular motors and the cytoskeleton. In: *methods enzymol*, vol 196. Academic, San Diego
9. Diehl MR, Zhang K, Lee HJ, Tirrell DA (2006) Engineering cooperativity in biomotor-protein assemblies. *Science* 311:1468–1471
10. Hess H, Clemmens J, Brunner C et al (2005) Molecular self-assembly of “nanowires” and “nanospools” using active transport. *Nano Lett* 5:629–633
11. Kakugo A, Shikinaka K, Matsumoto K et al (2003) Growth of large polymer-actin complexes. *Bioconjug Chem* 14:1185–1190
12. Kawamura R, Kakugo A, Shikinaka K et al (2008) Ring-shaped assembly of microtubules shows preferential counterclockwise motion. *Biomacromolecules* 9:2277–2282
13. Sheterline P, Clayton J, Sparrow JC (1998) Actin, 4th edn. Oxford University Press, New York
14. Pollard TD (2007) Regulation of actin filament assembly by Arp2/3 complex and formins. *Annu Rev Biophys Biomol Struct* 36:451–477

15. Pollard TD, Borisy GG (2003) Cellular motility driven by assembly and disassembly of actin filaments. *Cell* 112:453–465
16. Frederiksen DW, Cunnungham LW (eds) (1982) Structural and contractile proteins Part B, the contractile apparatus and the cytoskeleton. In: *methods enzymol*, vol 85. Academic, San Diego
17. Pollard TD (1986) Rate constants for the reactions of ATP- and ADP-actin with the ends of actin filaments. *J Cell Biol* 103:2747–2754
18. Pollard TD, Cooper JA (2009) Actin, a central player in cell shape and movement. *Science* 326:1208–1212
19. Mahadevan L, Matsudaira P (2000) Motility powered by supramolecular springs and ratchets. *Science* 288:95–100
20. Horio T, Hotani H (1986) Visualization of the dynamic instability of individual microtubules by dark-field microscopy. *Nature* 321:605–607
21. Tanaka-Takiguchi Y, Kakei T, Tanimura A et al (2004) The elongation and contraction of actin bundles are induced by double-headed myosins in a motor concentration-dependent manner. *J Mol Biol* 341:467–476
22. Pantaloni D, Le Clainche C, Carlier MF (2001) Mechanism of actin-based motility. *Science* 292:1502–1506
23. Tilney LG, Portnoy DA (1989) Actin filaments and the growth, movement, and spread of the intracellular. *J Cell Biol* 109:1597–1608
24. Sano K, Kawamura R, Tominaga T et al (2011) Self-repairing filamentous actin hydrogel with hierarchical structure. *Biomacromolecules* 12:4173–4177
25. Sano K, Kawamura R, Tominaga T et al (2011) Thermoresponsive microtubule hydrogel with high hierarchical structure. *Biomacromolecules* 12:1409–1413
26. Kawamura R, Sano K, Ijro K, Osada Y (2014) Chemically cross-linked microtubule assembly shows enhanced dynamic motions on kinesins. *RSC Adv* DOI: 10.1039/C4RA04491F

Index

A

Acetylene black (AB), 137
AC impedance, 153
Acrylic rubber, 10, 192
ActA, 478
Actin, 12, 474, 475, 477, 478
Actin/myosin, 459
Activated carbon, 137
Activated carbon nanofiber (ACNF), 127
Active, electrochemical-poroelastic behavior, 293
Active self-organization (AcSO), 460
Actuation pressure, 180
Actuator, 29, 135, 248, 409
 application, 369
 drive circuit, 362
Additives, 128–131
Adenosine triphosphate (ATP), 12
Adsorption (or ion exchange), 334, 335
 process, 78
 rate, 334
Aerogel, 11
AFM phase image, 145
Agent, 332
Agent model, 332–333
Air-buffer interface, 467
Amoeba-like creep, 163
Anion drive, 92
Anion-driven actuation, 293
Anionic gel, 337
Anisotropic, 100
Anisotropic LC networks, 228
Antenna, 21
Application, 131
Aqueous electrolytes, 96

Arcomeres, 454
Artificial arm, 193
Artificial cilia, 59
Artificial muscles, 191, 231, 344, 412
Artificial pupil, 7
Asymmetric charge distribution, 165
Atomic force microscope (AFM), 41
ATP-driven bio-machine, 459
Automobiles, 23
Autonomous intestine-like motion, 66–67
Azobenzene, 7

B

Backward motion, 288
Barium ferrite, 8
Beam-shaped, 342
Belousov-Zhabotinsky (BZ) reaction, 4, 52
Bending motion, 123
Bimorph, 8, 91, 229
Bio-actuator, 12, 473–475, 477
Biocompatibilities, 416
Bioinspired, 1
Biomaterial, 2
Biomedical devices, 21–22
Biomimetic, 1, 5
Biomimetic robot, 389
Biomolecular motor, 459
Biotin, 460
Biot's theory, 294
Bis-peroxides, 30
Black-box modeling, 317
Block copolymer, 137
Blocking force, 94
Block-like, 42

- Body-length normalized wave number, 375
 Boltzmann factor, 278
 Braille cell, 117
 Braille display, 357
 Braille size, 359
 Breakdown strength, 181
 Brunauer-Emmett-Teller (BET), 107
 Bucky gel, 5, 84, 122
 Bucky gel actuators, 122, 276
 Bucky paper, 121
 Butterfly-inspired biomimetic locomotion, 393
 BZ reaction, 4
- C**
- Capillary network, 455
 Carbide-derived carbon (CDC), 128
 Carbon black (CB), 129
 Carbon microcoil (CMC), 29
 Carbon nanotubes (CNT), 2, 121
 Cardiomyocytes, 12
 Cardiomyoplasty, 448
 κ -Carrageenan, 8
 Carrageenan (CA), 265
 Catheter, 5, 410
 Cation drive, 92
 Cation-driven actuation, 293
 Cationic and anionic volumes, 141
 Cationic surfactant molecules, 337
 C2C12, 451
 Cellular PP, 206
 Chain structure, 266
 Charge transfer, 154–155, 282
 Chemical plating method, 78
 Chemical wave, 53
 Chemomechanical system, 4
 Chiral polymer, 202
 Chromophore, 7
Cis-trans isomerization, 7
 Coil-globule transition, 42
 Coions, 281
 Cole-Cole plot, 154, 348
 Collagen, 3
 Colloidal particle, 106
 Complexation, 255
 Compliant electrode, 10, 177
 Composite gel, 246
 Composite materials, 30
 Compression modulus, 154
 Condition action rules, 341
 Conducting polymer actuator, 19
 Conducting polymers, 89, 293
 Conductive polymers (CP), 2, 8, 121
- Conical meniscus, 247
 π -Conjugated polymer, 8
 Constant-voltage grand-canonical ensemble, 278
 Constitutive equation, 334
 Consumer electronics, 19–21
 Contractile force, 452
 Contractile strain, 115
 Contractile stress, 113
 Contraction force, 94
 Contraction type PVC gel actuator, 347
 Controller, 362–364
 Control system, 333
 Conversion efficiencies, 95
 Cooperative, 163
 Copolymer, 163
 Copolymerization, 40
 Coulomb force, 192
 Counterions, 281
 Crawling, 166
 Creep(ing), 99, 117
 Creeping deformation, 344
 Current density, 334, 335
 Cyclic voltammograms (CV), 157
 Cytoskeleton, 459
 Cytotoxicity, 417
- D**
- Damper, 248
 Damping factor, 272
 DE cartridges, 436
 Dedoping, 106
 Deformable machine, 331
 Deformation, 142, 335
 Deformation of the gel, 335
 Deformation ratio of DE, 183
 DE Generator system on the buoy, 441
 Degree of crosslinking, 3
D-E hysteresis loop, 200
 Desorption, 105
 DE stress-strain performance, 434
 DE transparent Dipole-speakers, 438
 DE vibrators, 438
 Diaphragm pump, 9
 Dibutyl adipate (DBA), 344
 Dielectric breakdown strength, 192
 Dielectric constant, 10, 192
 Dielectric elastomer actuators, 19, 191
 Dielectric elastomers (DEs), 10, 118, 178, 343
 Dielectric gels, 7
 Dielectric solvent, 165–166
 Diffusion coefficient, 40

Dimensional change, 41
Dimethyl sulfoxide (DMSO), 166
Dipole speakers, 436
Direct drive, 364
Dispersibility, 30
Dispersing/flocculating oscillation, 69
Displacement, 141
Distributed generator applications, 185
Dopant, 8
Doping, 106
Double-layer charging kinetic model, 124
Drug delivery systems, 39, 410
Drug release, 263
Durability, 147
Dynamic light scattering, 49
Dynamic sensors, 390

E

Effect of solvation, 96
Eigenfunction expansion, 306
Eigenvalue problem, 306
Elastic electrode layers, 192
Elasticity, 94
Elastic modulus, 145
Elastomers, 2, 10, 153, 414
Electret, 206
Electrical conductivity, 153, 334
Electrical double layers (EDLs), 278
Electric double layer, 303
Electric double-layer capacitor (EDLC), 137
Electric field, 334
Electric impedance measurement, 348–350
Electric potential, 334
Electric power density, 112
Electroactive polymer (EAP), 135, 152, 410
Electroactive polymer (EAP) actuators, 17
Electroactive polymer gel, 331
Electroactive polymer gel robots, 332
Electroactive soft actuators, 275
Electrochemical actuator, 237
Electrochemical (EC)-creeping, 99
Electrochemical doping, 8
Electrochemical kinetic model, 124
Electrochemical oxidation, 92
Electrochemical reaction, 5, 159
Electrochemical window, 98
Electrochemomechanical deformation (ECMD), 92
Electrodeposition, 96
Electro-discharge machining (EDM), 378
Electrohydrodynamic instability, 165
Electromagnetic waves, 29

Electro-mechanical, 163
Electro-mechanical coupling system, 305–307
 π -Electron, 91
Electronic EAPs, 17
Electro-optical, 163
Electroosmosis, 288
Electro-osmotic water flow, 80
Electrophoresis, 334
Electrophoretic polarization, 5
Electrophoretic transport, 5
Electro-rheological, 166
Electrospinning, 40
Electrostatic effect, 123
Electrostatic force, 43
Electro-stress diffusion coupling model, 80, 303
Emeraldine salt, 8
Encapsulation, 258–259
Energy conversion, 165, 223
Energy conversion efficiency, 441
Energy density, 179
Energy efficiency, 115
Energy harvesting, 23–24, 173
Engine, 1
Entanglement, 45
Equivalent cantilever beam, 391
Equivalent circuit, 154
Equivalent circuit model, 124
Ethical and safety issues, 368
1-Ethyl-3-methylimidazolium bis (trifluoromethylsulfonyl)imide, 152
1-Ethyl-3-methylimidazolium bis (trifluoromethylsulfonyl)imide ([EMI][TFSI]), 152
1-Ethyl-3-methylimidazolium tetrafluoroborate (EMIBF₄), 122
Euler-Bernoulli beam model, 304
Extracellular matrix, 447

F

Faradaic mechanism, 128
Faradic current, 156
Fast speed of response, 178
Feedback control, 315
Ferroelectret, 207
Ferroelectric, 10
Ferroelectricity, 198
Ferroelectric liquid crystal, 10
Ferromagnetic, 8
Ferromagnetic particle, 246
Field-activated polymers, 177
Finite element formulation, 288

Finite element method, 294
 Fish-like microrobot, 393
 Flemion, 288
 Flexible electrode, 156
 Flory-Huggins theory, 3
 Force control, 322
 Forward motion, 288
 Free-ended, 337
 Free volume, 7
 Frequency, 159
 Frequency dependence, 124

G

Gait of turtle, 380
 Galerkin method, 288
 Gel, 2, 415
 Gel deformation, 334
 Gel-fish, 5
 Gel-looper, 5
 Gel machine, 12
 Gel-pump, 262
 Gel robots, 337
 Gel-valve, 264
 Generative force, 146
 Grafting, 29
 Guide wire, 5

H

Hairpin-shape, 342
 Haptics, 20
 Haptic sense, 271
 Harvesting energy, 434
 Heat conduction, 49
 Heat of water condensation, 109
 Helical structure, 98
 Hierarchical structure, 106
 High energy efficiency, 193
 Highly efficient transduction, 434
 High strain rate, 178
 Hook law, 8
 Human arm, 443
 Human-machine interface (HMI), 197
 Hydrodynamic characteristics, 246–247
 Hydrogel, 5, 164, 237
 Hydrogen, 188
 Hydrogen bonding, 4
 Hydrogen generation system, 444
 Hydrolysis, 12
 Hydrophilic, 35
 Hydrophobic, 35
 Hydrophobic interaction, 46
 Hysteresis loss, 192

I

Image device and image apparatus, 19
 Immobilization magnetic fluid, 249
 Impact sensor, 172
 Inchworm-inspired microrobot, 394
 Inchworm-inspired crawling and grasping locomotion, 404
 Inchworm-inspired microrobot, 396
 Independent of wave period, 186
 Inert chamber system (ICS), 464
 Information apparatuses, 23
 Intercalation, 282
In vitro motility assay, 460
 Ion drag, 165
 Ion-exchange by copper metal, 381
 Ion gels, 136
 Ionic conducting polymer-metal composites, 287
 Ionic conductive polymer gel films (ICPF), 77
 Ionic conductive polymers, 75–84
 Ionic conductivity, 144, 156
 Ionic crosslink, 92, 100
 Ionic EAP (i-EAP), 17, 121
 Ionic EAP actuator, 121
 Ionic hydrogel, 238
 Ionic liquids (ILs), 5, 80–81, 98, 136, 153
 Ionic polymer actuator, 136
 Ionic polymer conductor network composite (IPCNC), 84
 Ionic polymer gel, 334
 Ionic polymer-metal composite (IPMC), 5, 75, 121, 372, 410
 Ionic polymer metal composite actuator, 19
 Ionic transport mechanism, 140
 Ionization, 3
 Isotheric heat of sorption, 109
 Isothermal sorption curve, 108

J

Jellyfish-inspired biomimetic locomotion, 392
 Jellyfish-inspired floating/diving locomotion, 404
 Joule heating, 10, 93, 106

K

Kerr effect, 171
 Ketjen black (KB), 137
 Kharitonov's theorem, 326
 Kinesin, 474, 475, 480

L

Laminated films, 230
Langmuir's theory, 334
Latching mechanism, 364–367
Leg slippage, 400
Lens, 168
Leucocyanide, 7
Leuco-emeraldine salt, 8
Leverage actuator, 105
Light-driven actuator, 223
Light-volume transduction, 212
Linear actuators, 115, 347
Liquid-crystalline elastomers (LCEs), 10, 224
Listeria, 478, 479
Lobster-like microrobot, 395, 397, 404
Loss modulus, 265
Lower critical solution temperature (LCST), 4, 29, 39

M

Macro azo-initiator, 30
Macro-fiber composite, 207
Macroscopic deformation, 228
Magnetic elastomer, 269
Magnetic field, 8
Magnetic fluid, 246, 261
Magnetic fluid composite gels, 249–255
Magnetic fluid gels, 251–255
Magnetic hydrogels, 269
Magnetic levitation, 247–248
Magnetic particles, 261
Magnetic soft material, 261
Magnetization, 245
Magnetorheological effect, 268
Magneto-rheological function, 259
Magnetorheology, 269
Magnetostriction, 249–251
Maxwell stress, 10
MCM-41 (mesoporous silica), 129
Measurement circuit of generated energy, 185
Mechanical strength, 144
Mechanism for deformation, 141
Mechanisms, 275
Mechanochemical engine, 3
Mechanochemical turbine, 3
Mechano-electric functions, 163
Medical devices, 409
Memory effects, 100
Mesh electrodes, 345
Metallic counter cations, 80
Metal nanoparticles, 237
Micelle-like, 42

Microactuators, 12
Microchannel, 218
Micro-electro-mechanical system (MEMS), 9
Microfluidic system, 217
Micro-nano devices, 438
Micropatterned irradiation, 216
Micro pump, 421
Microrelief formation, 216
Micro-soft gripper, 168
Microtubule/kinesin, 459
Microtubules, 474, 475, 480
Miniaturized IPMCs, 82–83
Model, 316
Modeling, 315
Molecular alignment, 228
Molecular assembly reaction, 5
Molecular weight, 42
Monodomain particle, 245
Monte Carlo simulation, 123, 276
Morphology, 40, 43, 249–250
Mother robot, 389
Motion, 336
Motion design, 331, 333–341
Motor, 1, 11
Motor proteins, 475, 479
Multi-functionality, 398
Muscles, 409, 448
8.5MW of power, 441
Myogenesis, 454
Myogenic regulatory factor, 454
Myooid, 450
Myosatellite, 449
Myosin, 12, 474, 475

N

Nafion, 5, 137, 288
Nano-Carbon Actuator, 357–369
Nanofibers, 40
National Institute of Advanced Industrial Science and Technology (AIST), 357
New generations of devices, 433
Next-generation DE actuators, 445
NMR, 141
Noble-metal electrodes, 75
Non-Faradaic mechanism, 128
Nylons, 170

O

Obstacle-avoidance experiments, 401
Onsager's law, 295

- Operating principal of DE power generation, 183, 439
- Operators, 337
- Ordinary differential equations (ODEs), 304
- Oscillation, 165
- Osmotic pressure, 3
- P**
- Paper actuator, 160
- Paramagnetic property, 245
- Passive, poroelastic behavior, 293
- Patents, 17
- Percutaneous transluminal coronary angioplasty (PTCA), 411
- Perfluorocarboxylic acid, 7
- Perfluorosulfonic acid, 77
- Peristaltic motion, 55
- Permanent deformation, 400
- Phase diagram, 338–340
- Phase separation, 168
- Phase transition, 5, 40, 117, 164
- Phase transition temperature, 4
- pH Change, 3
- Photocatalysis, 239
- Photochromism, 224
- Photocrosslinking, 226
- Photoelectrochemical actuator, 237
- Photoinduced proton dissociation, 213
- Photo-ionization, 7
- Photoisomerization, 211
- Photomechanical effect, 224
- Photon mode, 219
- Photo-polymerization, 32
- Photoresponsive actuators, 212
- Photoresponsive cell culture surfaces, 220
- Photoresponsive dehydration, 212
- Photoresponsive hydrogels, 212
- Photoresponsive hydrogel sheet, 218
- Photoresponsive microvalve, 218
- Photo-responsive shrinking, 211
- Photoresponsive swelling, 212
- Photothermal effect, 227
- Hydrophilicity/hydrophobicity, 7
- Physical cross-link, 45
- Physical crosslinking, 138
- PID control, 318
- Piezoelectric actuators, 118
- Piezoelectric polymers, 197
- Piezoelectric tensors, 199
- Plasmon-induced charge separation, 242
- Plasmon resonance, 242
- Plasticizer, 163
- PLLA fibers, 205
- Pockels effect, 171
- Point generator applications, 185
- Point group theory, 199
- Poisson's ratio, 11, 335
- Polarity, 7
- Polarization, 156
- Polaron or bipolaron, 91
- Poling process, 200
- Poly(3,4-ethylenedioxythiophene) (PEDOT), 91, 98, 152
- Poly(acrylamide) (PAAm), 3
- Poly(acrylic acid) (PAA), 3
- Poly(ethylene glycol) (PEG), 4
- Poly(ethylene terephthalate) (PET), 170
- Poly(methacrylic acid) (PMMA), 4
- Poly(methyl methacrylate) (PMMA), 138
- Poly(methyl methacrylate (MMA)-*b*-*n*-butylacrylate (nBA)-*b*-MMA), 167
- Poly(*N*-isopropylacrylamide), 53
- Poly(*N*-isopropylacrylamide) (PNIPAM), 4, 39
- Poly(vinyl methyl ether) (PVME), 4
- Poly(vinylidene fluoride-*co*-hexafluoropropylene) (P(VDF-*co*-HFP)), 137
- Poly(vinylidene fluoride-trifluoroethylene), 10
- Polyaniline (PANI), 8, 91, 105, 129, 298
- Polycarbonate, 193
- Polydispersity index, 41
- Polyether-segmented polyurethaneurea (PEUU), 140
- Poly (2-acrylamido-2-methylpropane sulfonic acid) gel (PAMPS gel), 331
- Polyimide, 144
- Poly-ion complex, 106
- Poly-L-lactic acid (PLLA), 198, 202
- Polymer, 410
 - actuator, 135
 - electrolyte, 136
 - fabrication methods, 181
 - gels, 18, 225, 246
 - motor, 9
- PolyMuscle, 117
- Poly(3,4-ethylenedioxythiophene)/poly(4-styrenesulfonate) (PEDOT/PSS), 9, 106
- Poly(vinylalcohol)-poly(acrylic acid)-poly(allylamine) (PVA-PAA-PAIAm), 3
- Polypyrrole (PPy), 8, 91, 105, 129, 293, 343
- Polystyrene, 138
- Polythiophene (PT), 8, 91, 105

- Polyurethane (PU), 10, 153, 269
 Polyvinyl alcohol (PVA), 3, 164, 262
 Poly vinyl chloride (PVC), 7, 164, 343
 Polyvinylidene fluoride (PVDF), 198, 200
 Polyvinylidene fluoride-co-hexafluoropropylene (PVDF-HFP), 122
 Porous electrodes, 276
 Porous polypropylene (cellular PP), 198
 Positioning, 99
 Power density, 3
 Power generation efficiency, 441
 Power generation mode, 439
 Power generation phenomenon, 440
 Precise locomotion, 398
 Preparation process, 336, 337
 Pressure-and position-sensors, 182
 Pressure gradient, 80
 Prestrain, 10
 Primitive model, 279
 Printed actuator, 160
 Printing method, 146
 Proof-of-principle devices, 435
 Properties and performance, 181
 Proportional-integral-derivative control (PID), 318
 Prosthesis, 415
 Protic ionic liquid (PIL), 72
 Protofilaments, 462
 Ptosis, 412
 Pulsed-field gradient spin-echo (PGSE), 140–141
 Pumps, 1, 411
 PVA-DMSO gel, 166
 PVA-NMP gel, 171
 PVA-PAA, 4
 PVC gel actuator, 344
- Q**
- Quadruped robot, 378–383
- R**
- Radiation force, 7
 Radius of curvature, 335
 Rajiform swimming, 372
 Rate-determining step, 9
 γ -Ray, 4
 Ray-like robot, 373–378
 Reactive oxygen species (ROS), 464
 Redox, 157
 Reduction (or primary plating) process, 78
 Refreshable Braille display, 131
 Relative water vapor pressure, 108
 Relaxation, 159
 Relaxation phenomenon, 310
 Release control, 257–258
 Remote control, 259
 Reproducibility, 117
 Resonance frequency, 272
 Resorption, 111
 Response speed, 147
 Ring opening and closing, 7
 Robot-hand, 5
 Robotics, 22–23
 Robust, 322
 Robust control, 325
 Rod-like hydrogel, 214
 Role actuators having 3-DOF, 435
 Roll-type structure, 193
 Rotation, 11
 Rotational motion, 462–463
 Ruthenium tris(2,20-bipyridine), 53
- S**
- Scalpel, 412
 Seal bearing, 248
 Selective gold plating, 82
 Selective plasma treatment, 82
 Self-assembly, 12, 138
 Self-deformation, 89
 Self-diffusion, 288
 Self-driven gel conveyer, 64
 Self-oscillating fluids, 68–72
 Self-oscillating gels, 51–72
 Self-oscillating micelle, 71
 Self-oscillating microgels, 58
 Self-oscillating polymer brushes, 67–68
 Self-propelled motion, 63
 Self-walking gel, 60–63
 Sensor, 23–24
 Sensor grove, 435
 Servo control, 321
 Shape memory, 100
 Shape memory alloy (SMA), 117
 Shape memory polymers, 225
 Short-range proximity sensors, 401
 Silicone, 10
 Silicone rubber, 192
 Simulation, 333, 340
 Single-walled carbon nanotubes (CNTs), 5, 11
 Sizes from micrometers to several meters, 182
 Skeletal muscle, 3, 89, 113

Skin layer, 46
 Slide ring materials (SRM), 191
 Small-angle neutron scattering, 49
 Small-scale power-generation device, 443
 Small size brakes, 347
 Smart materials, 332
 Smooth muscle, 449
 Soft actuators, 1, 17, 177
 Soft segment, 164
 Solvent flow, 163
 Sorption degree, 108
 Sorption isotherm, 107
 Specifications of Braille dots, 359
 Specific surface area, 107
 Spherical robot, 388
 Sphincter, 412
 Spirobenzopyrane, 7
 Spiropyran, 212
 State equation, 305
 State space model, 305
 Stearyl acrylate (SA), 40
 Stereolithography, 453
 Stick insect-inspired two-phase walking locomotion, 404
 Stirling engine, 187
 Storage modulus, 8, 265
 Strain difference, 123
 Streptavidin, 460
 Stress relaxation, 324
 Sulfonated polyimide, 144
 Super artificial muscle, 187
 Supercritical CO₂, 204
 Super-growth, 127
 Super-growth CNT, 368
 Super-paramagnetism, 246
 Supra-macromolecular, 478–480
 Surface stress, 335
 Surface stress and strain, 335
 Surface tension, 43
 Surfactant, 334
 Surfactant molecules, 334
 Swelling of the interface, 247
 Swelling ratio, 30

T

Tacking, 170
 Tactile display, 9
 Tendons, 451
 Terpyridine (tpy), 70
 Tetrahydrofuran (THF), 344
 The correlation effect, 282
 The electrical double layer, 123

The electrostatic interaction, 279
 The Guoy-Chapman theory, 282
 Thermal expansion, 112
 Thermal-mode, 212
 Thermodynamics, 276
 Thermo-sensitive polymer gels, 29
 The structure of the direct drive type, 359
 The volume exclusion interaction, 279
 Three-layered, 122
 Time constant (CR), 126
 Tissue engineering, 448
 Touch sensor, 165
 Tracking controller, 319
 Training, 100
 Training effect, 94
 Transducer, 89, 248
 Transference numbers, 141
 Transition process, 336, 337
 Transmittance, 42
 Traveling wave, 374–377
 Treadmilling, 474–479
 Tri-block copolymer, 167, 204
 Triboelectric series, 173
 Tubulin, 460
 Turning over, 336
 Typical scope trace, 185

U

Ultra-light and thin Braille display, 131
 Underwater monitoring operations, 388
 Unimorph, 8
 Utility function, 333

V

Vapor grown carbon fiber (VGCF), 127, 137
 Variable texture surfaces, 438
 Variable viscoelasticity, 265–272
 Vibration damping, 21
 Vibration device, 195
 Viscosity oscillation, 68–70
 Voltage of electrodes, 335
 Volume exclusion effect, 123

W

Warburg impedance, 155
 Water mill device, 442
 Water vapor, 93, 96, 109
 Water vapor sorption, 106
 Wearing assist garments with variable stiffness, 347

Welfare device, 193
Wet-process, 160
White-box modeling, 316
Wireless network, 443
Work capacity, 115

Y
Yamaue's model, 303–304
Yarns, 11
Young's modulus, 10, 94,
114, 335